Numerical MHD Simulations of Astrophysical Jets

Thomas Jannaud

THÈSE

Pour obtenir le grade de

DOCTEUR DE L'UNIVERSITÉ GRENOBLE ALPES

École doctorale : PHYS - Physique
Spécialité : Astrophysique et Milieux Dilués
Unité de recherche : Institut de Planetologie et d'Astrophysique de Grenoble

Simulations Numériques MHD de Jets Astrophysiques

Numerical MHD Simulations of Astrophysical Jets

Présentée par :

Thomas JANNAUD

Direction de thèse :

Jonathan FERREIRA — Directeur de thèse
Professeur des Universités, Université Grenoble Alpes

Rapporteurs :

FABIEN CASSE
PROFESSEUR DES UNIVERSITES, UNIVERSITE PARIS CITE
CHRISTIAN FENDT
SCIENTIST, MAX PLANCK INSTITUTE

Thèse soutenue publiquement le **11 octobre 2023**, devant le jury composé de :

FABIEN CASSE PROFESSEUR DES UNIVERSITES, UNIVERSITE PARIS CITE	Rapporteur
JERÔME BOUVIER DIRECTEUR DE RECHERCHE, CNRS DELEGATION ALPES	Examinateur
JULIEN MALZAC CHARGE DE RECHERCHE HDR, CNRS DELEGATION OCCITANIE OUEST	Examinateur
MANEL PERUCHO MAITRE DE CONFERENCES HDR, UNIVERSITAT DE VALENCIA	Examinateur
AURORE BACMANN ASTRONOME, UNIVERSITE GRENOBLE ALPES	Présidente
CHRISTIAN FENDT SCIENTIST, MAX PLANCK INSTITUTE	Rapporteur

Invités :

CLAUDIO ZANNI
INGENIEUR DOCTEUR, INSTITUTO NAZIONALE DI ASTROFISICA

Bill Watterson

Abstract

Astrophysical jets are certainly one of the most fascinating phenomena in the universe. These are flows of matter observed around very different objects, such as active galactic nuclei (AGNs), the compact objects in X-ray binary systems, or even protostars. Despite their extremely different scales, these jets have in common that they are linked to the presence of an accretion disc rotating around the central object (black hole or star), and that they can be collimated at great distances, with the matter remaining confined around the rotation axis of the disc.

The only model capable of reproducing all these flows is based on the presence of a large-scale magnetic field in the disc (Blandford and Payne, 1982). The plasma is first ejected from the accretion disc and then confined around its axis by the Laplace magnetic force. The theoretical framework for this seminal work is MagnetoHydroDynamics (MHD), which describes plasma as a fluid in motion. It gave rise to a number of semi-analytical studies, followed by numerical simulations of jets from accretion disks, in two or three dimensions, in the classical or relativistic regime... However, the collimation of large-scale jets remains largely unexplored. How can jets be collimated in asymptotic regions, when the current flowing through them is disconnected from the disc ? These regions could be separated from the accelerating circuit by a discontinuity that occurs after the plasma has been confined towards the axis: the recollimation shock. Predicted by semi-analytical solutions and probably observed in AGN and protostar jets, these shocks have not yet been reproduced by MHD numerical simulations.

During my thesis, I carried out 2D numerical simulations of jets using the MHD code PLUTO (Mignone et al., 2007). These simulations, in non-relativistic ideal MHD, extend to unprecedented scales in space and time. In the first part of the thesis, I use the self-similar Jet-Emitting Disk (JED) model of Ferreira, 1997 as a boundary condition. The simulations I obtain are the first to contain stationary recollimation shocks. These behave qualitatively as expected by the semi-analytical solutions, but they also show that the flow emitted by the central object (black hole or star) has a significant influence on the collimation of the jet emitted by the disc.

In the second part of the thesis, the ejection is truncated: the JED is now limited to the innermost regions of the disc, with the outer regions no longer launching a jet. This more realistic setup produces jets that also contain recollimation shocks, showing that these shocks are not due to a bias of self-similarity. In the third part of the thesis, I present a special case of truncated simulation: the jet is no longer stationary but is buffeted at regular time intervals. This creates perturbations that propagate along the up from the asymptotic regions down to the vicinity of the disc. Such perturbations may be at the origin of certain quasi-periodic oscillations (QPO) observed in X-ray binaries.

Résumé

Les jets astrophysiques sont certainement l'un des phénomènes de l'univers les plus fascinants. Il s'agit d'écoulements de matière observés autour d'objets très différents, comme les noyaux actifs de galaxie (AGN), les objets compacts d'un système binaire X ou même les proto-étoiles. Malgré des échelles extrêmement différentes, ces jets ont en commun d'être liés à la présence d'un disque d'accrétion en rotation autour de l'objet central (trou noir ou étoile), ainsi que de pouvoir être collimatés à grande distance, la matière restant confinée autour de l'axe de rotation du disque.

Le seul modèle capable de reproduire tous ces écoulements repose sur la présence dans le disque d'un champ magnétique à grande échelle (Blandford and Payne, 1982). Le plasma y est d'abord éjecté du disque d'accrétion puis confiné autour de son axe par la force magnétique de Laplace. Ce travail fondateur a comme cadre théorique la MagnétoHydroDynamique (MHD), description du plasma comme un fluide en mouvement. Il a suscité nombre de travaux semi-analytiques, puis de simulations numériques de jets issus de disques d'accrétion, en deux ou trois dimensions, en régime classique ou relativiste... Cependant, la collimation des jets à grande échelle reste encore largement inexplorée. Comment les jets peuvent-ils être collimatés dans les régions asymptotiques, alors que le courant qui les parcourt est déconnecté du disque ? Ces régions pourraient être séparées du circuit accélérateur par une discontinuité ayant lieu après que le plasma ait été confiné vers l'axe : le choc de recollimation. Prédits par les solutions semi-analytiques et probablement observés dans les jets d'AGN et de proto-étoiles, ces chocs n'ont pour l'instant pas été reproduits par des simulations numériques MHD.

Au cours de ma thèse, j'ai réalisé des simulations numériques 2D de jets en utilisant le code MHD PLUTO (Mignone et al., 2007). Ces simulations, en MHD idéale et non-relativiste, s'étendent à des échelles de temps et d'espace sans précédent. Dans la première partie de la thèse, j'utilise le modèle autosimilaire Jet-Emitting Disk (JED) de Ferreira, 1997 comme condition limite. Les simulations que j'obtiens sont les premières à contenir des chocs de recollimation stationnaires. Celles-ci se comportent qualitativement comme attendu par les solutions semi-analytiques, mais elles montrent également que l'écoulement émis par l'objet central (trou noir ou étoile) a une influence primordiale sur la collimation du jet émis par le disque.

Dans la deuxième partie de la thèse, l'éjection est tronquée : le JED est maintenant limité aux régions les plus internes du disque, les régions externes ne lançant plus de jet. Ce dispositif plus réaliste produit des jets contenant également des chocs de recollimation, montrant que ces chocs ne sont pas dus à un biais de l'autosimilarité. Dans la troisième partie de la thèse je présente un cas particulier de simulation tronquée. Dans celui-ci, le jet n'est plus stationnaire mais est ballotté à intervalles de temps réguliers. Cela créée des perturbations remontant le jet des régions asymptotiques jusqu'au voisinage du disque. De telles perturbations être à l'origine de certaines oscillations quasi-périodiques (QPO) observées dans les binaires X.

Remerciements

Avant de parler de physique, j'aimerais dire merci à quelques-unes des personnes qui m'ont aidé et supporté pendant ces trois ans de thèse. A écouter les doctorants se plaindre, on pourrait s'imaginer qu'une thèse est un sacerdoce. Une montagne dont le pic reste toujours aussi éloigné, même après une longue marche. Mon expérience a été bien différente, et ces trois années passées à Grenoble (et un peu à Turin) ont été sans aucun doute les plus heureuses de ma vie. Cette liste ne sera bien sûr pas exhaustive, et je n'oublie ce que je dois à ceux qui ne sont pas cités ici.

J'aimerais commencer par vous remercier, Jonathan et Claudio, pour la confiance que vous m'avez tout de suite accordée, et pour tout ce que vous m'avez appris au cours de ces trois années. Jonathan, pour ton énergie permanente, ton empathie sans pareille et ta patience à toute épreuve. Claudio, pour ton pragmatisme toujours bienvenu, tes compliments et encouragements et ta rigueur scientifique. Vos enseignements et vos caractères se complètent parfaitement. J'ai grandement apprécié nos discussions souvent longues mais toujours constructives. Je n'oserais pas encore me prétendre chercheur, mais grâce à vous ces trois ans ont été une excellente formation scientifique. Merci également pour votre sensibilité, votre bienveillance et votre ouverture d'esprit. A vos côtés, j'ai pu grandir en tant que scientifique et en tant qu'homme, et je vous en suis infiniment reconnaissant.

Merci aux membres du jury et notamment aux rapporteurs d'avoir pris le temps de lire et d'évaluer cette thèse un peu longue. J'ai beaucoup apprécié nos échanges lors de la séance de questions. Merci aussi à ceux qui se sont gentiment proposés pour relire ce manuscrit.

L'accueil que j'ai reçu dans l'équipe SHERPAS au premier confinement m'a tout de suite fait comprendre que j'étais au bon endroit. Merci notamment à Jonatan et Samuel pour votre aide bienvenue. Je ne connais pas de groupe où il y ait une meilleure atmosphère de travail, dans la bonne humeur et la confiance mutuelle. J'ai particulièrement apprécié l'attention mise sur la participation des doctorants aux réunions d'équipe et aux sherpiades qui m'ont permis de beaucoup apprendre, même sur des sujets éloignés de ma thèse. Merci aux petits nups, Adrien, Valentina, Joanna, Étienne, Marc pour tes jeux de mots douteux, Jonah pour ta gentillesse et ton enthousiasme ; et aux gros nups Clément, Gaylor pour leur recommandations cinémas et librairies python ; John, Nico et Greg pour vos conseils scientifiques, votre énergie et votre bienveillance.

Merci aux administratifs et techniciens du laboratoire dont le travail dans des conditions difficiles n'est pas toujours apprécié à sa juste valeur.

Merci aux jeunes chercheurs qui sont devenus pour moi des amis et des exemples à suivre, qui m'ont impressionné par leur gentillesse sans limite, leur énergie, leur rigueur et leur curiosité, en science ou ailleurs. Merci à Julien pour les sorties montagnes et les cours d'ornithologie. Merci à Ileyk pour tes conseils pour naviguer dans le monde parfois labyrinthique de la recherche.

J'ai eu la chance de trouver à l'IPAG une communauté de gens soucieux des autres, pleine d'écoute et d'entraide. Merci aux doctorants et postdocs qui m'ont accompagné au cours de ces trois années. La team bassin, Dorian Tituan, Pierre, Vittoria, Salma ; la team RU, Léopold, Lucie, Filip, Maxime, Benjamin ; la team manif (déso Simon pour le chemin alternatif au lac Achard) ; la team foot, Nathan, Valentin, Nico, Antoine, Rajeev ; et la team escalade. Merci à Maxime et Enzo pour les plans grimpe parfois douteux mais toujours marrants, à Thibault et Maxime pour votre générosité, à Nico et Lionel pour l'AstroCoffee et les PizzaPlanet, à Adrien pour les cookies, et à tous ceux que j'oublie. Julien et Célia, je suis ravi d'avoir croisé votre route. Votre attachement à faire le bien autour de vous, votre modestie, votre naturel et votre capacité à rire de tout m'ont fait beaucoup de bien. Merci.

Je voudrais aussi dire quelques mots à mes amis pour les bons moments passés pendant ces trois ans : Milla, Alicia, Sami, Guillaume, Henri, Maïmouma, Hanae, Bayane, Mathilde... Merci à Alice et Thomas pour les séances de surf, à Sylvain pour m'avoir hébergé et supporté le temps que je trouve un appart. Merci à Lucile pour tes talents de coiffeuse, à Pauline pour les bons moments passés en festival et à ski. Merci aux potes de prépa, dire que ça fait maintenant dix ans... Pierre pour ta bonne humeur et nos discussions interminables, je n'aurais pas pu rêver d'un meilleur parrain ; Alex et Étienne pour les parties d'Age Of Empires, les randonnées, les plans skis improvisés et les nuits de Walpurgis ; Sélim pour ton humour et ta gentillesse. Baptiste, merci pour toutes ces randos et ces soirées pas toujours bien préparées mais toujours pleines de bonnes surprises. Jarla, avec toi dans ma vie, je suis certain de jamais m'ennuyer. Stan, merci pour les souvenirs inoubliables aux quatre coins du monde, hâte que tu reviennes de ce côté de l'Atlantique. Suzie, t'es toujours aussi cool, je suis trop content que tu sois dans ma vie. Encore tant d'aventures ces trois dernières années, je n'arriverai pas dire en quelques mots tout ce que tu as fait pour moi. Merci pour tout.

J'aimerais continuer encore longtemps, pour remercier les professeurs qui m'ont encouragé à continuer dans la science puis en thèse, les amis rencontrés sur un quai de gare, dans une salle d'escalade ou au hasard d'une conférence. Mais j'ai promis de ne pas être exhaustif, et j'ai peur de pas tenir parole.

Merci à ma famille. A mes grands-parents, dont l'amour et la gentillesse donnent le baume au cœur. Je vous promets de progresser en peinture. A mon frère Alexandre, qui m'a beaucoup appris. Quand je regarde le chemin parcouru ces dernières années, je suis fier de voir à quel point on a grandi et on avance ensemble. A mes parents, pour m'avoir fait connaître et aimer la science et pour m'avoir fait confiance et m'avoir toujours soutenu. Je vous aime, et je ne vous remercierai jamais assez.

"Oh, I get by with a little help from my friends
Mm, I get high with a little help from my friends
Mm, gonna try with a little help from my friends"

The Beatles

Contents

Abstract iii

Résumé v

Remerciements vii

1 Introduction 1
- 1.1 Observations of astrophysical jets . . . 5
  - 1.1.1 Different objects and lifetimes . . . 5
  - 1.1.2 Accretion-ejection correlation . . . 9
- 1.2 Large-scale collimation properties . . . 12
  - 1.2.1 Fanaroff-Riley dichotomy . . . 12
  - 1.2.2 Jet morphology . . . 13
- 1.3 State of the art and pending questions . . . 15
  - 1.3.1 Funneling and outer pressure . . . 15
  - 1.3.2 The need for self-induced magnetic collimation . . . 16
  - 1.3.3 Launching a jet from an accretion disk . . . 17
  - 1.3.4 Performing large-scale numerical simulations . . . 20
  - 1.3.5 The self-similar approach and recollimation . . . 22
  - 1.3.6 Aims and contents . . . 25

2 Theoretical framework 27
- 2.1 Ideal MHD approximations . . . 31
  - 2.1.1 Astrophysical jets: plasmas ? . . . 31
  - 2.1.2 Fully ionized plasma . . . 33
  - 2.1.3 Kinetic approach . . . 33
  - 2.1.4 Non-relativistic electromagnetism . . . 34
  - 2.1.5 Ohm's law and resistivity . . . 34
  - 2.1.6 Euler equations . . . 35
  - 2.1.7 Energy equation . . . 36
- 2.2 Ideal MHD equations . . . 38
- 2.3 MHD waves . . . 39
- 2.4 Magnetic flux . . . 41
- 2.5 Axisymmetry and stationarity . . . 41
- 2.6 Invariants and dynamics of steady flows . . . 42
  - 2.6.1 MHD invariants . . . 42
  - 2.6.2 Critical points in ideal MHD . . . 44
  - 2.6.3 Asymptotic speeds . . . 45
  - 2.6.4 The self-similar approximation . . . 46
  - 2.6.5 Parameter space . . . 46
  - 2.6.6 Electric circuits and collimation . . . 48
  - 2.6.7 Jet transverse equilibrium . . . 50
- 2.7 Discontinuities . . . 50

2.8 Summary . . . 53

3 Numerical framework **55**
3.1 The PLUTO code . . . 59
3.1.1 Finite volume methods . . . 60
3.1.2 Constrained transport . . . 60
3.1.3 Riemann solvers . . . 62
3.1.4 Godunov scheme . . . 63
3.1.5 CFL condition and acceleration scheme . . . 64
3.1.6 Accounting . . . 66
3.2 Numerical setups . . . 67
3.2.1 Simulation domain and grid . . . 67
3.2.2 Initial conditions . . . 69
3.2.3 Boundary conditions . . . 69
3.2.4 Normalization . . . 73

4 Self-similar simulations: The Blandford & Payne case **75**
4.1 A standing collimated jet . . . 80
4.1.1 Description of the simulation . . . 80
4.1.2 Quasi steady state . . . 82
4.1.3 Radial layering . . . 84
4.2 Steady recollimation shocks . . . 86
4.2.1 Rankine-Hugoniot conditions . . . 86
4.2.2 Two kinds of stationary shocks . . . 89
4.2.3 Shock spacing . . . 90
4.3 Electric circuits . . . 91
4.4 Time evolution . . . 92
4.5 Large scale collimation . . . 95
4.6 Summary . . . 98

5 Self-similar simulations: Parameter dependence and discussions **99**
5.1 Parameter dependence . . . 103
5.1.1 Mass loading parameter κ . . . 103
5.1.2 Magnetic field distribution α . . . 109
5.1.3 Influence of the central object . . . 114
5.2 Discussions . . . 117
5.2.1 Setup limitations . . . 117
5.2.2 Comparison with other numerical works . . . 118
5.3 Summary . . . 122

6 Steady simulations of jets emitted from a truncated JED **123**
6.1 Introduction . . . 127
6.1.1 Reproducing the observations . . . 127
6.1.2 Disconnecting accelerating and asymptotic circuits . . . 128
6.2 Numerical setup . . . 129
6.2.1 A setup resembling the quasi self-similar one . . . 129
6.2.2 Different boundary conditions on the disk . . . 130
6.3 The reference simulation . . . 133
6.3.1 A two/three-component outflow . . . 133
6.3.2 Outflow properties . . . 137
6.3.3 Radial balance . . . 139

6.4 Parameter dependence . . . 141
6.4.1 Rotation on the axis . . . 142
6.4.2 External magnetic field . . . 145
6.4.3 Radial distribution of the vertical magnetic field . . . 148
6.5 Comparison with other numerical works . . . 151
6.6 Summary . . . 154

7 Time-dependent simulations of jets emitted from a truncated JED 157
7.1 Quasi-periodic oscillations in X-ray binaries . . . 161
7.1.1 Ubiquitous in the observations . . . 161
7.1.2 Secular oscillations on the disk time scales . . . 164
7.2 Oscillating simulations . . . 167
7.2.1 Ejection properties . . . 167
7.2.2 Periodic oscillations . . . 169
7.2.3 Origin of the oscillations . . . 172
7.2.4 Vertical propagation . . . 177
7.2.5 Radial propagation . . . 182
7.3 Summary . . . 184

8 Conclusions and perspectives 185
8.1 Summary of the main results . . . 189
8.2 Perspectives . . . 189
8.2.1 3D simulations: collimation stability . . . 189
8.2.2 Towards a realistic ejection from the central object . . . 190
8.2.3 Time-dependent features in jets . . . 191

A 2.5D MHD instabilities 195

B Limiting the disk toroidal magnetic field 199

C 3D jet simulations 201

D Article published in A&A 211

Bibliography 239

Physical units and constants

This thesis is written in Gaussian-CGS units.
Below is a list of the various constants used in the text.

Speed of light in vacuum	$c = 2.9979 \times 10^{10}\,\mathrm{cm \cdot s^{-1}}$
Electron mass	$m_e = 9.1094 \times 10^{-28}\,\mathrm{g}$
Proton mass	$m_p = 1.6726 \times 10^{-24}\,\mathrm{g}$
Solar mass	$M_\odot = 1.9885 \times 10^{33}\,\mathrm{g}$
Astronomical unit	$au = 1.4959 \times 10^{13}\,\mathrm{cm}$
Parsec	$pc = 3.0857 \times 10^{18}\,\mathrm{cm}$
Electron charge	$e = 4.8032 \times 10^{-10}\,\mathrm{g^{1/2} \cdot cm^{3/2} \cdot s^{-1}}$
Boltzmann constant	$k_B = 1.3807 \times 10^{-16}\,\mathrm{cm^2 \cdot g \cdot s^{-2} \cdot K^{-1}}$
Planck constant	$h_p = 6.6261 \times 10^{-27}\,\mathrm{cm^2 \cdot g \cdot s^{-1}}$
Gravitational constant	$G = 6.6726 \times 10^{-8}\,\mathrm{cm^3 \cdot g^{-1} \cdot s^{-2}}$

Chapter 1

Introduction

Contents

1.1 Observations of astrophysical jets 5
1.1.1 Different objects and lifetimes 5
Active Galactic Nuclei 6
Young Stellar Objects 6
X-ray binaries 8
1.1.2 Accretion-ejection correlation 9
1.2 Large-scale collimation properties 12
1.2.1 Fanaroff-Riley dichotomy 12
1.2.2 Jet morphology 13
Protostellar jets 13
AGN jets 14
1.3 State of the art and pending questions 15
1.3.1 Funneling and outer pressure 15
1.3.2 The need for self-induced magnetic collimation 16
1.3.3 Launching a jet from an accretion disk 17
A bead on a wire 17
The importance of the toroidal magnetic field and accretion 18
1.3.4 Performing large-scale numerical simulations 20
Acceleration and propagation zones 20
Global bottom-up simulations 21
1.3.5 The self-similar approach and recollimation 22
Recollimation at large scales 22
The impending recollimation shock 24
1.3.6 Aims and contents 25

"Il faut toujours s'envoyer des fleurs. On est sûr que ça vient de quelqu'un qu'on aime bien."

"You should always send yourself flowers. You can be sure it's from someone you like."

Danièle Perret-Gentil

Il existe un très grand nombre de jets astrophysiques. Le premier a été observé en 1918 autour de noyau du galaxie actif (AGN) M87. Les observations de cet AGN, et du jet qui en émerge ont été extrêmement nombreuses. En son centre se situe un trou noir, M87, dont la masse est plusieurs trillions de fois celle du Soleil. Il fut le premier à être observé, par la collaboration Event Horizon Telescope (EHT) en 2019. Depuis 1918, beaucoup d'autres jets d'AGN ont été imagés. Nombre d'entre eux sont très collimatés (rectilignes et fins) et s'étendent très loin du trou noir à leur source, à plus d'un million de parsecs. Lorsque l'imagerie est impossible, la présence d'un jet est trahie par une forte émission radio.*

Ces jets sont relativistes, tout comme ceux observés autour de binaires X. Une binaire X est très différente d'un AGN. Il s'agit d'une étoile semblable au Soleil autour de laquelle orbite un objet compact (trou noir ou étoile à neutrons). De part leur taille et luminosité beaucoup plus faible, ces objets ne peuvent être observés que dans notre galaxie. Pour certains d'entre eux, on peut voir l'objet compact émettre un jet, détectable grâce aux radio-télescopes. Dans cette thèse, on ne s'intéressera qu'aux binaires X dont l'objet central est un trou noir. Alors que les AGN et leurs jets sont persistants, les jets de binaires X n'apparaissent que lors de violentes éruptions.

Enfin, dans notre galaxie des jets sont également observés autour d'étoiles en formation, dans les premiers millions d'années de leur existence (classe 0, I et II). Ces jets stellaires sont mis en évidence par leur interaction avec le milieu interstellaire, où ils forment des nébulosités dites Herbig-Haro. Celles-ci sont observables dans les raies optiques et infrarouges. Nombre de ces jets apparaissent également très collimatés jusqu'à plusieurs dizaines d'unités astronomiques de l'étoile.

Ainsi, les jets sont observés autour d'objets extrêmement différents, les trous noirs et les étoiles. Une de leurs rares caractéristiques en commun et la présence d'un disque d'accrétion, composé de plasma gravitationellement attiré par et tournant autour de l'étoile ou le trou noir. Cela a incité à développer des modèles de jet où celui-ci provient non pas de l'objet central (étoile ou trou noir) mais du disque d'accrétion. De tels modèles sont également corroborés par les corrélations d'accrétion-éjection: plus l'accrétion dans le disque est puissante, plus l'éjection dans le jet l'est aussi.

Dans ces modèles, l'accrétion et l'éjection sont interdépendantes, et nécessitent la présence d'un champ magnétique à grande échelle dans le disque. La rotation de celui-ci entraîne les lignes de champ magnétique, créant un fort gradient de pression magnétique toroidale donnant naissance au jet. Le champ magnétique toroidal ainsi créé, couplé au courant électrique poloidal, peut au lancement collimater les lignes de champ magnétique, et donc le jet.

Cependant, cela ne permet d'expliquer la collimation du jet que dans sa partie la plus proche du disque, lorsqu'il existe un fort courant électrique poloidal créé par le disque, au voisinage de celui-ci. Or les jets restent collimatés à des distances plusieurs centaines de fois plus grandes que le disque. Aussi loin de la source, le courant ne peut plus être causalement relié à la source. Quel mécanisme pourrait alors entraîner la collimation ?

Les premiers modèles supposaient une collimation induite par le milieu extérieur, par le biais d'une pression thermique ou d'une pression magnétique. Cependant, de récentes observations ont montré que les densité et champ magnétique du milieu interstellaire sont bien trop faibles pour produire la collimation observée dans certains jets stellaires. Cependant, un champ magnétique transporté depuis le disque le long des lignes de champ peut produire le confinement nécessaire.

Dans cette thèse, je m'intéresse à la collimation asymptotique des jets, qui produit la forme asymptotique de ces derniers: parabolique si la collimation est présente, cylindrique si elle est absente. Cette région asymptotique est causalement déconnectée du disque d'accrétion, le plasma ayant dépassé toutes les vitesses critiques. Mais alors, comment est fixé le courant dans cette zone, et comment peut avoir lieu cette déconnexion causale ?

Une possibilité pour créer cette déconnexion est la présence d'un choc de recollimation, apparaissant lorsque les lignes de champ magnétique convergent vers l'axe du jet. De tels chocs stationnaires sont observés dans des jets d'AGN tels que M87. Ils ont été prédits mais n'ont pas pu être reproduits par les études analytiques autosimilaires. L'étape suivante naturelle est de produire des simulations numériques de jets, afin de voir si et dans quels conditions les chocs de recollimation stationnaire peuvent être reproduits. Le cadre théorique adapté est la MagnétoHydroDynamique (MHD), description du plasma comme un fluide magnétisé en mouvement. Dans mes simulations, le disque et l'objet central (étoile ou trou noir) est une condition limite. Ces simulations s'étendent à des échelles en espace et en temps sans précédent.

Dans cette thèse, je présenterai plusieurs simulations numériques conçues pour combler le fossé entre les conditions de lancement du jet et ses propriétés de collimation aux échelles observables. L'objectif est d'évaluer si les résultats génériques obtenus dans le cadre auto-similaire sont toujours valables dans les simulations 2D dépendantes du temps. En particulier, je chercherai à savoir si l'existence d'un choc de recollimation est inévitable pour les conditions attendues dans les disques d'accrétion képlériens, comme l'a proposé Ferreira, 1997.

En conséquence de cette approche, je me concentrerai principalement sur les jets en régime stationnaire, afin de confronter mes simulations à la théorie des jets MHD. Il est clair que la plupart des jets astrophysiques, sinon tous, présentent des caractéristiques dépendant du temps. Cependant, le but de ce travail n'est pas de reproduire un jet spécifique, mais plutôt d'étudier les comportements génériques des jets MHD émis par les disques d'accrétion képlériens.

Le manuscrit est organisé comme suit :

- *Le chapitre 2 définit le cadre théorique de la thèse: la MHD idéale non relativiste. Je justifie les approximations utilisées et souligne leurs limites. Ensuite, je montre quelques propriétés pertinentes de la théorie des jets MHD idéaux.*

- *Le chapitre 3 définit le cadre numérique de la thèse. Je présente les différentes caractéristiques du code MHD PLUTO (Mignone et al., 2007) que j'ai utilisé tout au long de la thèse. Ensuite, je décris la configuration numérique conçue pour les simulations, avec le Jet-Emitting Disk (JED) comme condition limite.*

- *Les chapitres 4 et 5 présentent des simulations de jet dans lesquelles le JED s'étend sur toute la frontière inférieure. Je montre que des chocs de recollimation sont effectivement obtenus, en accord avec la théorie analytique. Je présente ensuite une étude paramétrique, montrant une correspondance entre mes simulations et les solutions auto-similaires, mais soulignant également le rôle crucial de la colonne axiale dans la collimation globale du jet. Enfin, je compare mes résultats à ceux de la littérature.*

- *Le chapitre 6 présente des simulations de jets où le JED est maintenant limité aux régions les plus internes du disque. Je montre que cette configuration plus réaliste produit des jets avec des chocs de recollimation aux propriétés similaires. J'effectue également une étude paramétrique, mettant en évidence l'influence de la rotation de l'objet central et de la pression ambiante sur les propriétés de collimation des jets.*

- *Le chapitre 7 décrit des simulations numériques obtenues par sérendipité, montrant des oscillations créées dans le jet asymptotique qui se propagent jusqu'au disque. De telles perturbations arrivant sur le disque pourraient fournir une explication aux QPOs observés dans les binaires à rayons X, comme l'a proposé Ferreira et al., 2022.*

1.1 Observations of astrophysical jets

1.1.1 Different objects and lifetimes

Observing the active galaxy Messier 87 (M87), astronomer Herbert Curtis noted:

"A curious straight ray lies in a gap in the nebulosity in p.a. 20°, apparently connected with the nucleus by a thin line of matter. The ray is brightest at its inner end, which is 11" from the nucleus." Curtis, 1918.

This was the very first observation of an astrophysical jet. The Active Galactic Nucleus (AGN) he refers to is a very luminous region at the galaxy center. It has long been thought to be powered by matter accreting onto a supermassive black hole (Lynden-Bell, 1969).

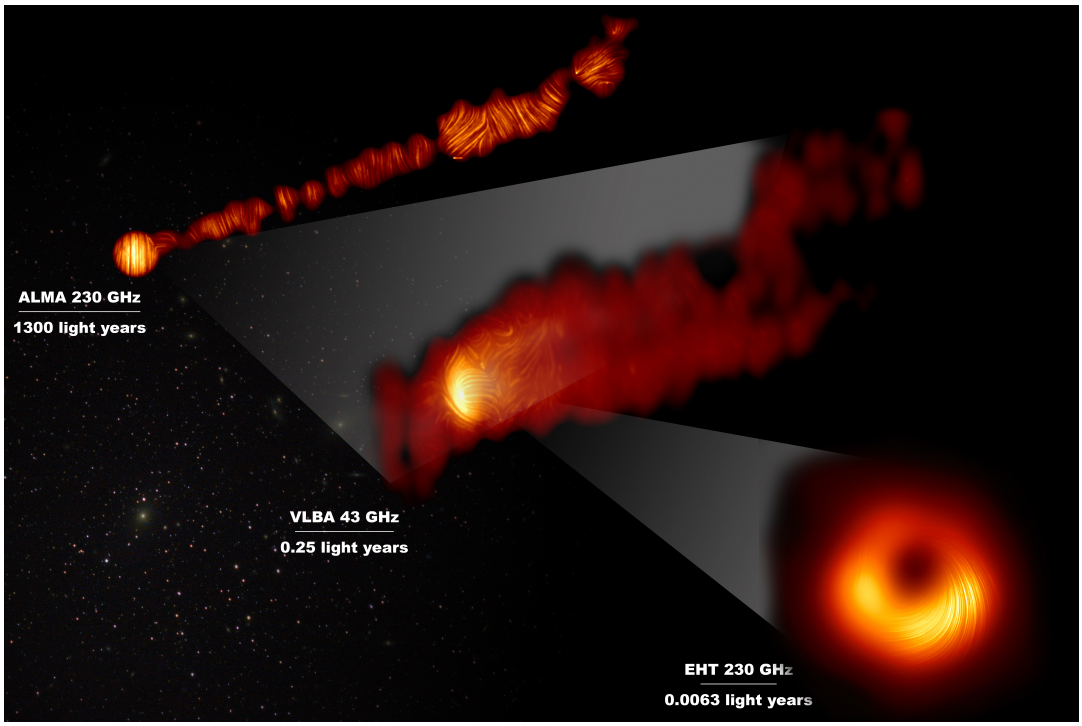

FIGURE 1.1: Composite image of the M87 central region from three radio telescopes (EHT et al., 2021a,b). The lines indicate polarization.

In the following century, the M87 jet has been closely observed, most notably thanks to the Hubble Space Telescope (HST) (see e.g. Biretta, Sparks, and Macchetto, 1999). But in recent years, the development of radio interferometry has allowed fast improvements. The Atacama Large Millimeter Array (ALMA) provided detailed imaging of the jet, and the Event Horizon Telescope Collaboration (EHT) allowed imaging of M87*, the supermassive black hole powering the AGN. Both images are shown on Figure 1.1.

Looking at these images, two remarks come to mind:

- The jet is very collimated, i.e. straight and thin, as noted by Curtis.
- It extends extremely far away, more than a million times the black hole size.

Perhaps even more striking, astrophysical jets are not only detected around AGNs. They are observed around most if not all types of accreting objects. In addition to AGNs (Blandford, Meier, and Readhead, 2019; Boccardi et al., 2017), jets are emitted from Young Stellar Objects (YSOs; Bally, Reipurth, and Davis, 2007; Frank et

al., 2014; Ray et al., 2007; Ray and Ferreira, 2021), close interacting binary systems (Fender and Gallo, 2014; Tudor et al., 2017), or even post-AGB stars (Asymptotic Giant Branch; Bollen, Van Winckel, and Kamath, 2017).

In this thesis, I will only consider the galactic jets emitted from protostars and binary systems, and the extragalactic jets emitted from AGNs, as they share a striking number of characteristics. In this section I will draw a short summary of their properties. For a more exhaustive overview, the curious reader is referred to the reviews listed in the paragraph above.

Active Galactic Nuclei

AGN jets are a relatively rare phenomenon. Active galaxies represent only 10% of all galaxies. They are characterised by a broad Spectral Energy Distribution (SED) from radio to γ-rays, and by a strong variability. And, only 10% of all active galaxies are considered radio-loud. Those are defined by huge radio emission, sometimes eight orders of magnitude stronger than that of regular galaxies, betraying the presence of a jet.

After the archetypal M87, jets were observed around many other AGNs. For instance, the left panel of Figure 1.2 represents the jet emitted from the nucleus of the active galaxy Hercules A. The radio flux associated with the jet is in blue. AGN jets are extremely large, reaching sizes up to 10^6 pc. Consequently, their growth should last tens to hundreds millions of years, and cannot be directly observed. The black hole at the core of the AGN being supermassive (i.e. between 10^6 and 10^{10} solar masses), those jets reach relativistic speeds.

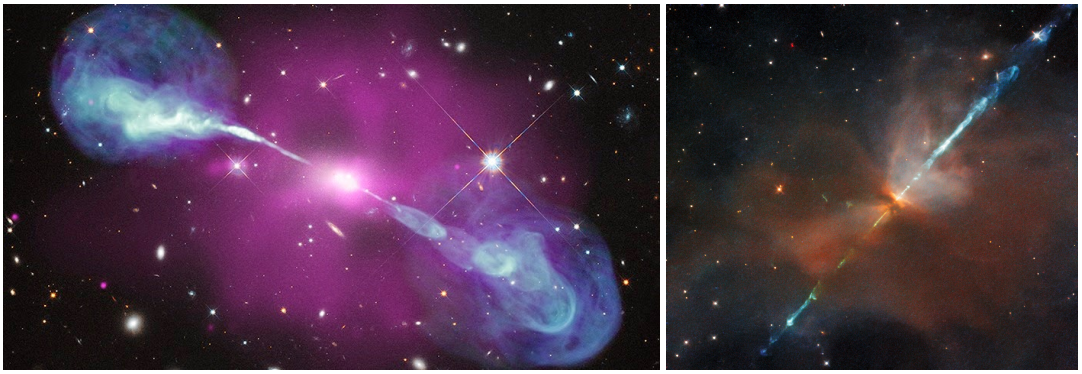

FIGURE 1.2: Astrophysical jet images. Left: Composite image of the radio galaxy Hercules A. In blue, radio emission (NSF/NRAO/VLA); in pink, X-ray emission (NASA/CXC/SAO); in white, orange, and blue, optical emission. Credit: Bia Boccardi. Right: Optical and infrared image of HH111 (WFC HST). Credit: Brunella Nisini.

Young Stellar Objects

On the other hand, jets emitted from forming stars are much smaller, most of them extending over less than one parsec. Thus, even though they are observed in our galaxy, they were first seen much later. While Herbig, 1950, 1951 and Haro, 1952, 1953 indirectly observed small emission nebulosities, the first direct observation was made by Snell, Loren, and Plambeck, 1980. Named Herbig-Haro (HH) objects, those nebulosities are formed by the interaction between a jet ejected from a newborn star with the interstellar medium. There are now more than a thousand detected Herbig-Haro objects, often observed in the optical by HST and in the infrared by the Spitzer

Space Telescope (SST). One of them, HH111, is represented in the right panel of Figure 1.2. We see that, like the AGN jets, YSO jets can also be very collimated and very large, extending up to thousands of stellar radii.

Other than their size, the main difference between AGN and YSO jets is their velocities. Protostars having masses roughly equal to the solar mass $M_\odot$, their jet speeds range from 100 to 600 km.s^{-1}. YSO jets are seen at the first three stages of star formation, as illustrated in Figure 1.3, and seen with different tracers at different stages.

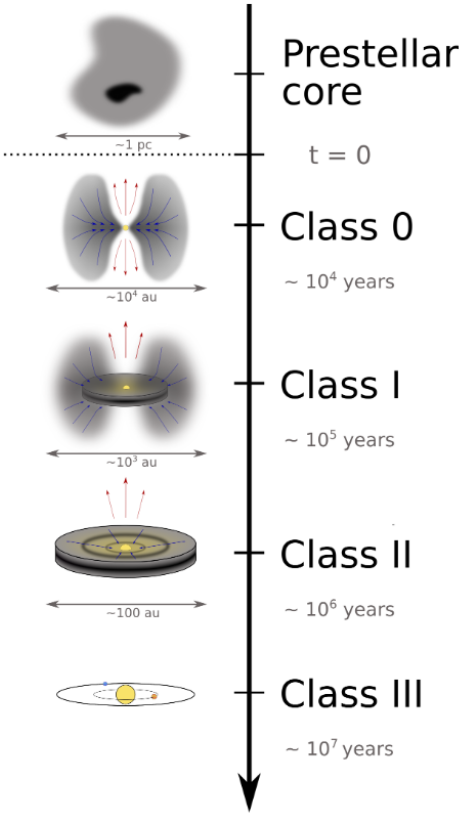

FIGURE 1.3: Early evolution of a solar type star until Class III. Jets are observed around Class 0, I and II stars. Adapted from Aloïs de Valon's PhD thesis.

- In Class 0, where the star mass is much smaller than that of the surrounding enveloppe. Molecular jets (SiO, CO, H_2) are visible in radio (mm-waves) and infrared.
- In Class I, where a sufficient amount of the enveloppe has collapsed onto the central star for it to be visible in the infrared. Atomic and molecular jets are seen in infrared (H_2, FeII) and optical ($H\alpha$, OI, NII, SII).
- In Class II, where the enveloppe has vanished, and the central star has become a classical T Tauri star. Jets can then be observed in optical very close to the central star.

The scales and durations of each class are represented in Figure 1.3. Of the objects presented in this section, HH212 is Class 0, DG Tau B and HH111 are Class I and HH30 is Class II.

X-ray binaries

X-ray binaries are binary systems composed by a donor star and a compact object (neutron star or black hole). The compact object accretes matter from the donor star, and releases the gravitational energy in the form of a strong X-ray emission. The X-ray band is usually decomposed in soft X-rays of lower energy (0.1 to 10 keV) and hard X-rays of higher energy (10 to 100 keV). Some X-ray binaries, called micro-quasars, also emit in radio. As in AGNs, this radio emission is often resolved as a pair of jets (see e.g. Espinasse et al., 2020; Mirabel and Rodríguez, 1994). Figure 1.4 is a sketch of such a radio-emitting X-ray binary. In such a system, the donor is a normal main sequence star and the mass of the compact object is only of a few solar masses.

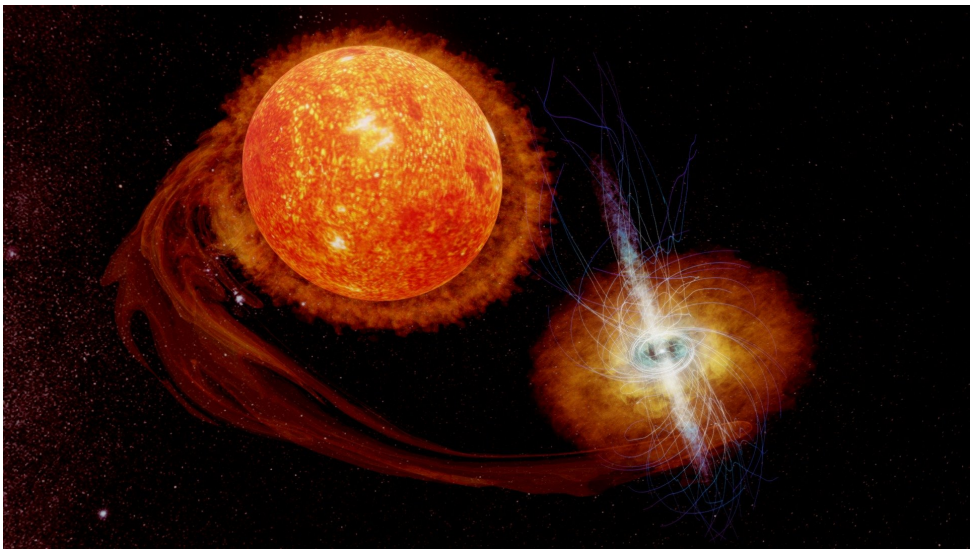

FIGURE 1.4: Sketch of a radio-loud Low-Mass X-ray Binary (LMXB), constitued by a compact object (black hole or neutron star) and a less massive donor star. The compact object accretes from the star via its Roche lobe, and ejects a powerful jet, perpendicular to its accretion disk. Credit: Salvatore Orlando.

Both black hole and neutron star binaries can produce powerful jets. But while most neutron star systems are persistent sources, black hole systems are generally transient (Done, Gierliński, and Kubota, 2007). In quiescence majority of the time, they occasionaly experience bright outbursts. These outbursts last weeks to months, and are spaced by months to decades. Over the course of the course of the outburst, the binary can emit mostly soft X-ray photons (soft state) or hard X-ray photons (hard state). Typical spectra are presented on Figure 1.5, for both soft (red) and hard (blue) states. The outbursts are most commonly followed in the Hardness Intensity Diagram (HID), an example of which is shown on Figure 1.6.

Hardness Intensity Diagrams are the equivalent for black hole outbursts of the Hertzprung-Russell (HR) diagram, that tracks the evolution of stars. In a HID is represented the total X-ray luminosity over the hardness ratio, at various times in the outburst. The hardness ratio is the number of hard X-ray photons of high energy over the total number of X-ray photons. It can thus be understood as a proxy for the energy or "color" of the binary. When this ratio is close to unity, the binary is in a hard state. When it is close to zero, it is in a soft state.

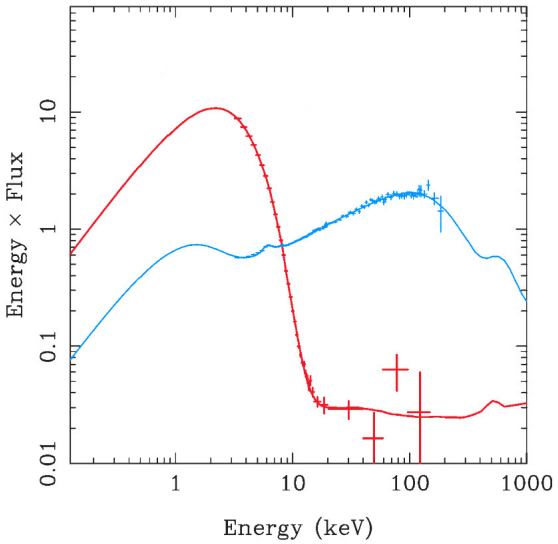

FIGURE 1.5: Spectra in the soft state (red) and hard state (blue) for the 2005 outburst of GRO J1655-40. Figure from Grégoire Marcel's PhD thesis, adapted from Zhang, 2013.

Black hole X-ray binary outbursts typically follow the q-shaped path in the HID shown in Figure 1.6. The evolution is counterclockwise, and starts in the low-luminosity hard state (A). The luminosity then increases while the spectrum is still dominated by the hard photons. In this hard state, steady radio jets can be observed. Then, the luminosity starts to decrease (B) and the system quickly moves from hard to soft state. During this transition the steady radio jets vanish, and we only observe transient flares that can be followed by Very Long Baseline Interferometry (VLBI, see e.g. Carotenuto et al., 2021). At some point (D) the luminosity decreases while the system remains in the soft state. Then occurs a transition from the soft to the hard state (E→F) leading to the reappearance of steady radio jets. Finally, the system goes back to quiescence while remaining in the hard state (F→A). Naturally, these are general behaviors, and some sources such as the very luminous Cygnus X-1 show more peculiar behavior. The curious reader is referred to Dunn et al., 2010 for more exhaustive spectral studies of black hole X-ray binaries.

1.1.2 Accretion-ejection correlation

X-ray binaries, AGNs and protostars all emit jets, collimated outflows that extend to very large scales compared to that of the central object. All those jets are almost-unidirectional and supersonic. The central objects they emerge from are quite different from one another, in terms of sizes, temperatures and velocities. AGNs and X-ray binaries are subject to relativistic effects, YSOs are not. One thing they do have in common however, is the presence of an accretion disk. It is composed of matter rotating around and falling into the central object (black hole or star) due to its gravitational attraction. Furthermore, for all these objects the power accreted in the disk is correlated to the power ejected in the jet.

These accretion-ejection correlations are illustrated in Figure 1.7, for X-ray binaries (top), AGNs (middle) and YSOs (bottom). In the case of a jet emitted from a compact object (black hole or neutron star), the accretion power is inferred from X-ray luminosity, in pink on Figure 1.2. Naturally, assumptions have to be made in order to convert a luminosity L into an accretion power $\dot{M}_{acc}c^2$, with $\dot{M}_{acc}$ the mass

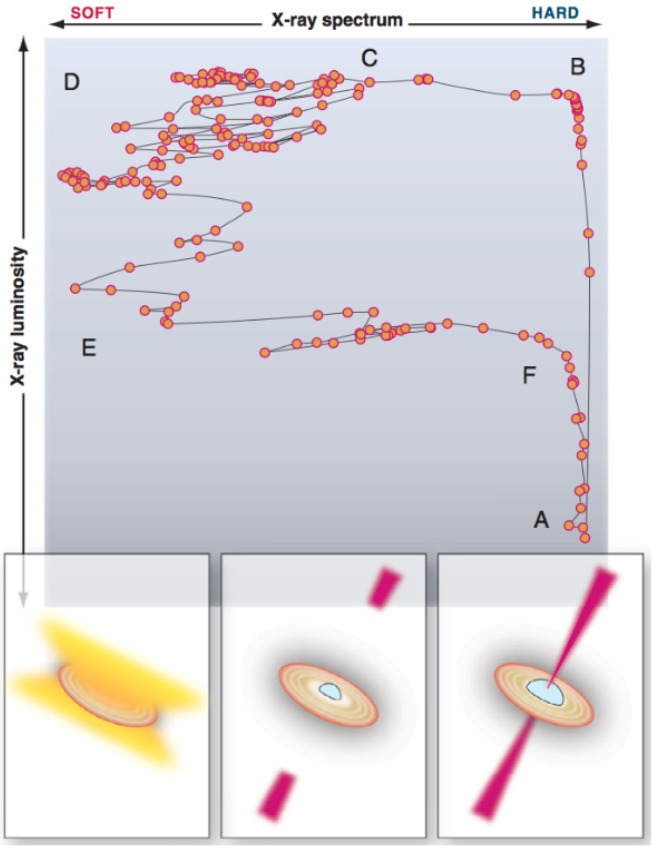

FIGURE 1.6: Hardness Intensity Diagram for an outburst of the Black Hole X-ray binary GRS 1915+105 (Fender and Belloni, 2012). Variation of the total X-ray luminosity with the hardness ratio (Hard X-ray flux over total X-ray flux). Each point corresponds to a single observation, and the evolution is counter-clockwise (A→B→...→F→A). In the bottom are the expected geometries: a strong jet is launched only in the hard state.

accretion rate in the disk. For instance, Ghisellini et al., 2014 assume a disk radiation efficiency $L/(\dot{M}_{acc}c^2)$ of 30%. The result is a strong correlation between the accretion and ejection powers. This correlation holds true whatever the mass of the compact central object, which can span over several decades ($M_{BH} = 10^6$ to $10^{10}\mathrm{M}_\odot$ for AGNs). On the top plot, we also see that neutron star and black hole X-ray binaries follow different correlations. A neutron star jet has a power smaller than a black hole jet with similar associated accretion power.

As shown in the bottom panel, the accretion-ejection correlation is also seen among YSOs. The jet mass loss rate $\dot{M}_{jet}$ and the disk mass accretion rate $\dot{M}_{acc}$ are proportional over a wide range of star masses and evolutionary stages.

Naturally, this does not mean that all the matter ejected in the jet must come from the disk. First, because correlation does not imply causation. But also because models of jets emitted from the central object can also explain this correlation, whether this object is a black hole (Blandford and Znajek, 1977) or a star (Matt and Pudritz, 2005). However, the universality of jet observations around objects subject to very different physics paired with the accretion-ejection correlation is a compelling argument in favor of models explaining jets with some of the matter accreted in the disk being released in the jet. In the following, I will mostly deal with jets emitted from an accretion disk.

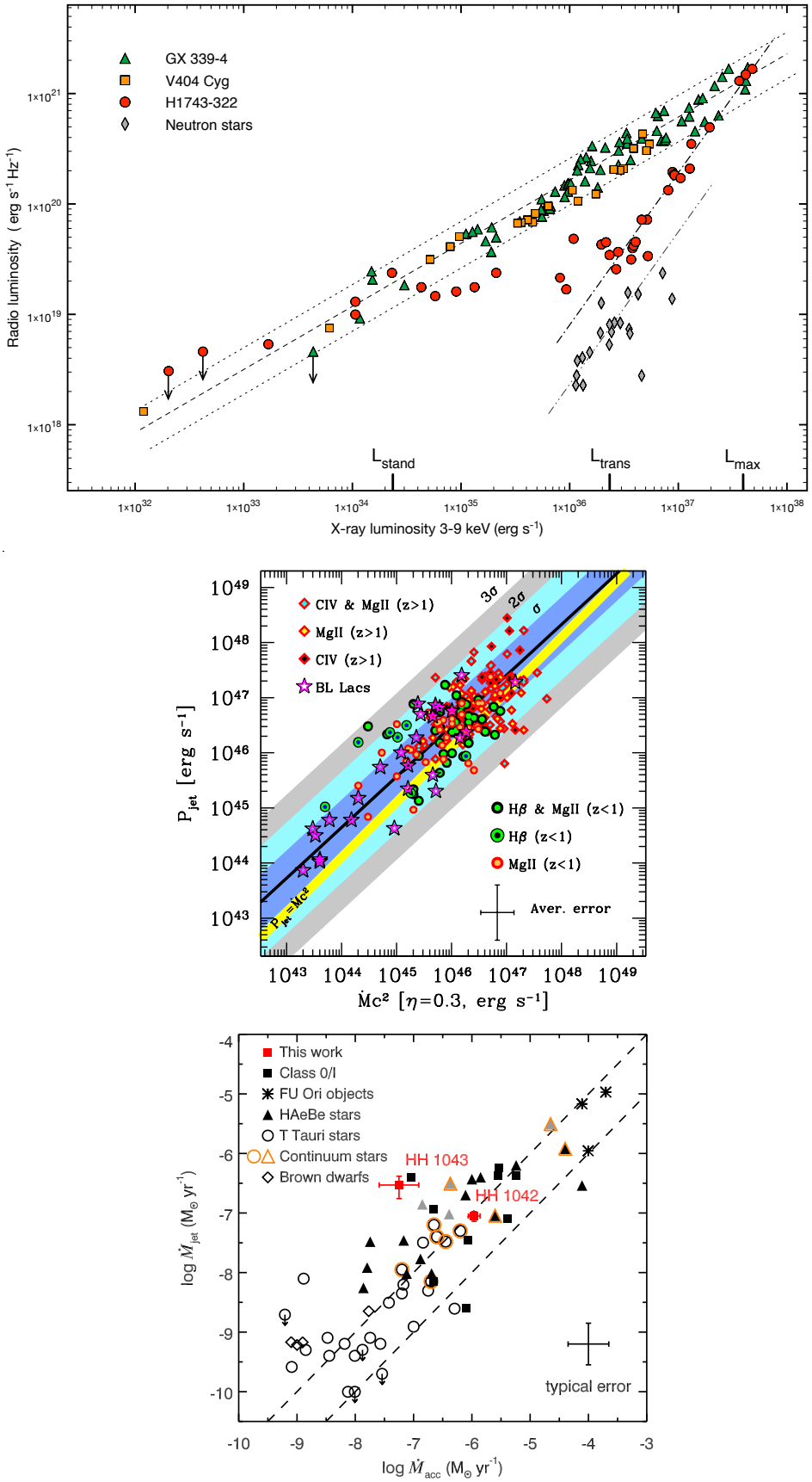

FIGURE 1.7: Accretion-ejection correlations. Top: Radio luminosity versus X-ray luminosity for several galactic black hole candidates and neutron stars (Coriat et al., 2011). Middle: Jet power versus accretion power for 217 AGNs (blazars) (Ghisellini et al., 2014). Bottom: Observed jet mass loss rate versus mass accretion rate for protostars of all classes (Ellerbroek et al., 2013).

1.2 Large-scale collimation properties

Let us now look at what will be the main topic of this thesis: the collimation of jets at their largest, asymptotic scales. Do they appear cylindrical, parabolic or conical ? What are the differences in collimation between jet types, and among each type ?

1.2.1 Fanaroff-Riley dichotomy

The large-scale collimation of AGN jets has been closely studied. The reference work of Fanaroff and Riley, 1974 classified them in two types based on their radio luminosity. They are defined as:

- The edge-darkened jets where the region of maximal luminosity is located closer to the AGN than to the edge of the jet. Those are FRI jets.
- The edge-brightened jets where the region of maximal luminosity is located closer to the edge of the jet than to the AGN. Those are FRII jets.

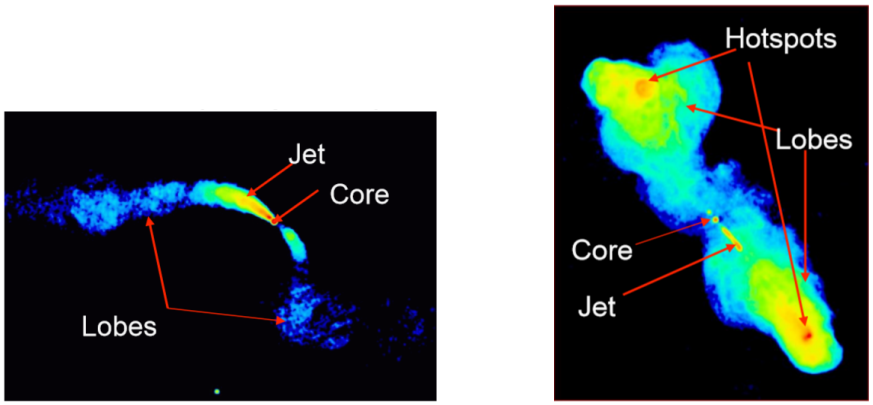

(A) FRI jet. (B) FRII jet.

FIGURE 1.8: AGN jet images of the two Fanaroff-Riley classes.

This classification is now known as the Fanaroff-Riley (FR) dichotomy. Detailed observations with radio interferometry have recently revisited this classification, showing the presence of another type, called FR0 (Garofalo and Singh, 2019), and that the division between FRI and FRII is not as rigid as previously thought (Mingo et al., 2019). For the sake of concision, I will only deal with the FRI and FRII classes.

Those two jet types are represented on Figure 1.8. The FRII jets appear more collimated, and are generally brighter and more extended than the FRI jets. The M87 jet (Figure 1.1) and Hercules A jet (Figure 1.2) are FRII. As their velocities are close to the speed of light, they can appear one-sided due to relativistic beaming. For instance, the counter jet of M87 pointed away from the Earth is very dim.

The differences between the shape of the emission maps for those two jet classes are generally associated with the discrepancy in jet power, the FRII jets being more luminous (Ledlow and Owen, 1996; Owen and Ledlow, 1994). The dichotomy would thus be caused by the accretion process (Ghisellini and Celotti, 2001), as the mass of the central black hole controls the optical emission of the galaxy (McLure and Dunlop, 2001). General Relativistic MagnetohydroDynamic (GRMHD; Bromberg and Tchekhovskoy, 2016; Tchekhovskoy and Bromberg, 2016) numerical simulations suggest the ambient medium also plays a role in setting this dichotomy.

1.2.2 Jet morphology

Protostellar jets

On the other hand, jets emitted from protostars do not show such a dichotomy. T Tauri jets (from Class II sources) are ejected with a large opening angle of 10 to 30 degrees, and become rapidly collimated. At 50 to 100 au from the star, the opening angle is only of a few degrees (Ray et al., 2007). Class I jets show similar opening angles in both ionized and molecular components (Davis et al., 2011). Studies of the HH212 jet point towards Class 0 jets being slightly more collimated than T Tauri jets.

Figure 1.9 shows this jet for different tracers and at different scales. HH212 appears cylindrical even at large scales, up to 10^5 au. At larger distances from the source appear large bow shocks. They are seen in most Herbig-Haro jets (see Reipurth and Bally, 2001 and references therein) and are signs of a conflicting interaction with the ambient medium. Figure 1.10 compares the radius of the HH212 jet with that of the jets from the T Tauri stars DG Tauri and RW Aur. The jet is indeed slightly more collimated, but the morphology is very similar to the jets of other classes.

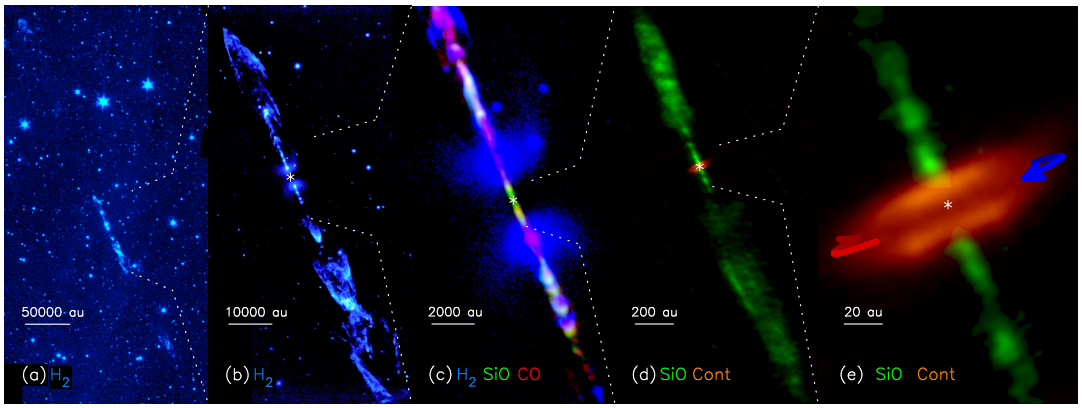

FIGURE 1.9: Different scales of the HH212 protostellar jet (Lee, 2020). (a): Reipurth et al., 2019, (b) and (c): Lee et al., 2015; McCaughrean et al., 2002, (d) and (e): Lee et al., 2017. The observed molecules and their associated colors are at the bottom.

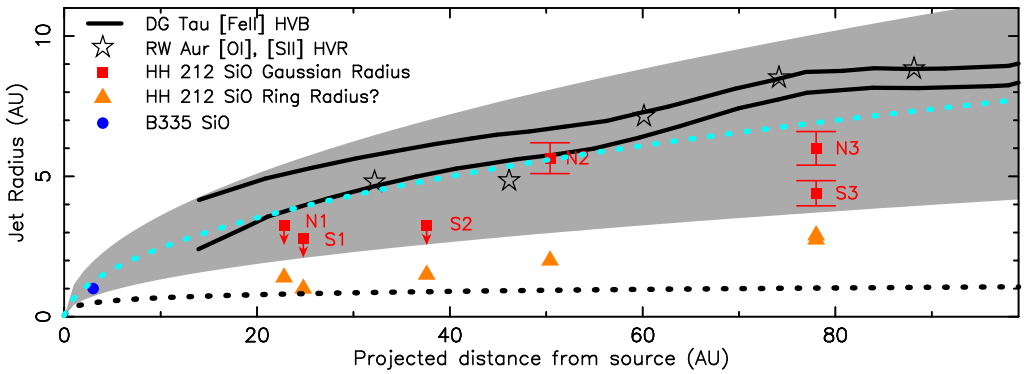

FIGURE 1.10: Distribution of various protostellar jet radii as a function of the distance from the star (Lee, 2020).

AGN jets

Extragalactic jets of both Fanaroff-Riley classes are also very collimated. Jets width and length are usually measured in units of gravitational radii $r_g \equiv GM/c^2$ or Schwarzchild radii $r_S \equiv 2GM/c^2$ where M is the mass of the supermassive black hole at the core of the AGN, G is the gravitational constant and c is the speed of light in vacuum. Such units act as a normalization of the distances by the black hole mass.

The left panel of Figure 1.11 shows the evolution of the M87 jet radius with the distance to the central black hole. The unit is the Schwarzchild radius and the evolution described below is generic to both Fanaroff-Riley classes. The jets are launched very close to the black hole, below $10^2 r_s$. They are then accelerated and collimated at scales of 10^3 to $10^5 r_s$. At the end of this process, the flow loses its collimation, and its energy is dissipated in radiation. This lasts until the formation of the lobes, beyond $10^9 r_s$. These lobes are visible on Figure 1.8, and sometimes accompanied by compact hotspots. Beyond those lobes, the jets vanish.

This dichotomy between an acceleration/collimation zone and a propagating zone is clear in the left panel Figure 1.11. We see a change in jet slope around $z_{coll} = 2.5 \times 10^5 r_s$:

- Upstream ($z < z_{coll}$), the jet is parabolic: $z \propto r^{1.73 \pm 0.05}$.
- Downstream ($z > z_{coll}$), the jet is conical: $z \propto r^{0.96 \pm 0.1}$.

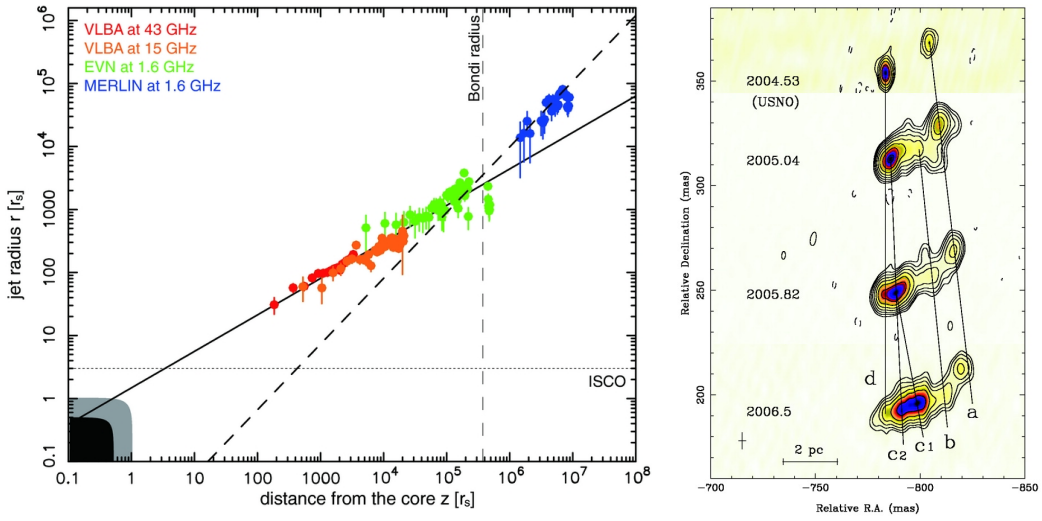

FIGURE 1.11: Left: Distribution of the M87 jet radius as a function of the deprojected distance from the core in units of Schwarzchild radius $r_s = 2GM_{BH}/c^2 = 120$ au (Asada and Nakamura, 2012). Right: VLBA imaging of the HST-1 knot at different times (Cheung, Harris, and Stawarz, 2007). The knot is located around $z = 5 \times 10^5 r_s$.

The transition between the two regions occurs at a strong shock, particularly prominent in the optical and thus named HST-1. As it happens at this transition, it was labeled **recollimation shock**. It also ejects superluminal features in radio, of which four observations are represented in the right panel of Figure 1.11. The vertical spacing is proportional to the time between the observations, and the vertical lines represent the apparent motions of the subfeatures HST-1a, HST-1b, HST-1c and HST-1d. These features are barely moving, and HST-1 is considered quasi-stationary.

1.3 State of the art and pending questions

While the observations unveiled how collimated the jets were, various scenarii and models were proposed to explain this large-scale confinement.

1.3.1 Funneling and outer pressure

Blandford and Rees, 1974 were the first to propose a model for extragalactic jets, that was adapted to YSO jets by Konigl, 1982. This "twin-exhaust" model is represented in Figure 1.12. A central hotspot (A, the black hole or star) ejects subsonic plasma in an isotropic manner. This plasma is later confined by a denser cloud (G), rotating around the central object: It is collimated along a channel of diminishing cross-section. This cross-section reaches a minimum at $z = R^*$ (N) where the flow becomes super-sonic.

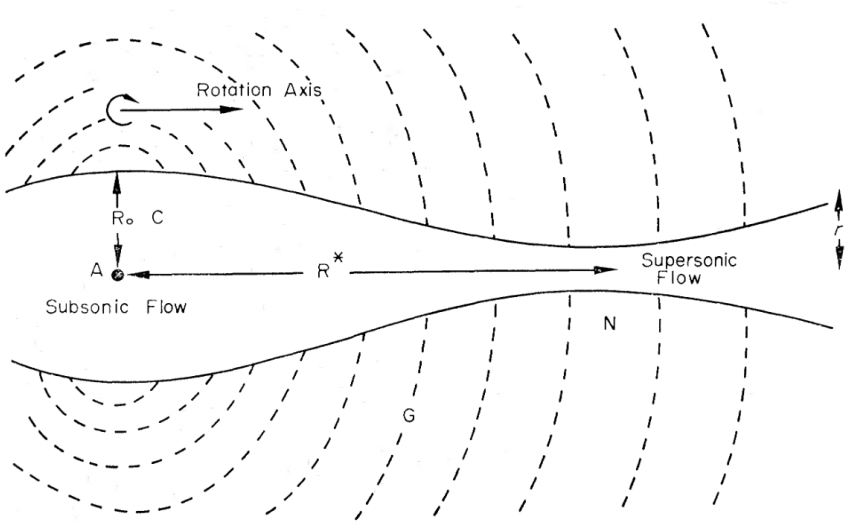

FIGURE 1.12: Scheme of the "twin-exhaust" model (Blandford and Rees, 1974). A hot plasma is emitted from a central region (A) in a central cavity (C). It is then collimated by an outer cloud in rotation around the central object (G), whose isobars are represented in dashed lines. The plasma is funneled into the nozzle (N), where it becomes supersonic. After that, the flow remains confined.

This model is very reminiscent of the de Laval nozzle, used for instance in rocket engines. In the same way that de Laval nozzle must have a very precise shape, the "twin-exhaust" model requires a specific vertical pressure profile. Slighltly different pressure profiles would result in strong Kelvin-Helmholtz shear instabilities, destroying the jet.

As a consequence, the following models assumed a supersonic ejection, which was later confirmed by radio interferometry. Barral and Canto, 1981 showed that the external pressure could reconfine an YSO jet. As the jet initially widens, its pressure drops and the constant external pressure eventually dominates. After an altitude z_{coll}, this leads to a refocusing of the jet towards its axis. They show that the external pressure P_{coll} required is

$$P_{coll} \simeq 5 \times 10^{-5} \left(\frac{\dot{M}_{jet}}{10^{-8} \mathrm{M}_\odot.\mathrm{yr}^{-1}} \right) \left(\frac{v_{jet}}{300 \mathrm{km.s}^{-1}} \right) \left(\frac{z_{coll}}{50 \mathrm{au}} \right)^{-2} \mathrm{Ba} \qquad (1.1)$$

where the barye Ba $= \mathrm{g.cm^{-1}.s^{-2}}$ is the CGS unit of pressure. As Cabrit, 2007, I consider a classical T Tauri star jet of mass loss rate $\dot{M}_{jet} = 10^{-8}\mathrm{M_\odot.yr^{-1}}$ and velocity $v_{jet} = 300\mathrm{km.s^{-1}}$, and assume a cloud temperature of $T = 10\mathrm{K}$. For the reconfinement to occur at $z_{coll} < 50\mathrm{au}$, the cloud density should be $n_{coll} > 2.4 \times 10^9 \mathrm{cm^{-3}}$, six hundred times higher than what is observed (see e.g. Hartigan, Edwards, and Ghandour, 1995). Thus while such a process may be invoked for younger Class 0 or Class I jets, it cannot be the universal mechanism for YSO jet collimation, as it does not hold for Class II jets.

1.3.2 The need for self-induced magnetic collimation

If thermal pressure of the ambient medium cannot explain the collimation, maybe magnetic pressure could. Replacing the thermal pressure P_{coll} by the magnetic pressure $B_{coll}^2/2$, one obtains

$$B_{coll} \simeq 10 \left(\frac{\dot{M}_{jet}}{10^{-8}\mathrm{M_\odot.yr^{-1}}}\right)^{1/2} \left(\frac{v_{jet}}{300\mathrm{km.s^{-1}}}\right)^{1/2} \left(\frac{z_{coll}}{50\mathrm{au}}\right)^{-1} \mathrm{mG} \tag{1.2}$$

This value is two to three orders of magnitude higher than the organized magnetic fields measured in dense prestellar cores (see e.g. Lee, Hull, and Offner, 2017). An isotropic turbulent magnetic pressure is also ruled out, as it would require a jet extremely magnetized at those large scales, with a magnetic pressure six hundred times higher than the thermal pressure (i.e. a magnetization $B^2/(4\pi P) \sim 600$).

However, such magnetic field values could be explained by a third mechanism, MagnetoHydroDynamics (MHD) self-collimation. In such a model, the collimating magnetic field is transported by the jet itself, carrying it from its launching point, at the vicinity of the central object (star or black hole), onto the collimation and propagation zones. As we will see in section 2.4, in steady-state ideal MHD the magnetic flux is conserved along the magnetic field lines (flux-freezing condition). To produce the magnetic field B_{coll} of equation 1.2 at the recollimation point, constant vertical magnetic field launched by the jet between $r_i = 0.1\mathrm{au}$ and $r_J = 1\mathrm{au}$ would be

$$B_l \simeq \left(\frac{r_{coll}}{r_J}\right)^2 B_{coll} = 10 \left(\frac{5\mathrm{au}}{1\mathrm{au}}\right)^2 \mathrm{mG} = 250\mathrm{mG} \tag{1.3}$$

The launch of MHD extended disk jets relies on strong magnetic fields brought by the accretion of matter in the vicinity of the central object. For the classical T Tauri star considered above, this vertical magnetic field would be close to equipartition (Ferreira and Pelletier, 1995)

$$B_{eq} \simeq 200 \left(\frac{M}{\mathrm{M_\odot}}\right)^{1/4} \left(\frac{\dot{M}_{acc}}{10^{-7}\mathrm{M_\odot.yr^{-1}}}\right)^{1/2} \left(\frac{r_J}{1\mathrm{au}}\right)^{-\frac{5}{4}+\frac{\xi}{2}} \mathrm{mG} \tag{1.4}$$

We see that the two magnetic fields B_{eq} and B_l are of the same order of magnitude. Here the crucial parameter is the ejection index ξ, radial exponent of the mass accretion rate in the disk $\dot{M}_{acc}(r) \equiv -4\pi \int_0^{h(r)} \rho u_r dz \propto r^\xi$, where $h(r)$ is the disk height at the radius r. This ejection index, as well as the jet extent ($r \in [r_i; r_J]$) determines the fraction of accreted mass that gets transferred into the jet

$$\frac{\dot{M}_{jet}}{\dot{M}_{acc}} \simeq \frac{\xi}{2} ln \left(\frac{r_J}{r_i}\right) \tag{1.5}$$

where the factor two comes from the fact that while there is only one disk, there are two jets, often called jet and counter-jet.

To compute B_{eq} (equation 1.4) I used a disk ejection index $\xi = 0.1$ and the same jet launching radii as above ($r \in [r_i = 0.1\text{au}; r_J = 1\text{au}]$). This gives a jet mass loss rate ten times smaller than the disk accretion rate, hence the choice $\dot{M}_{acc} = 10^{-7}\text{M}_\odot.\text{yr}^{-1}$.

1.3.3 Launching a jet from an accretion disk

This model of an extended disk/jet is called the Jet-Emitting Disk (JED). It allows the launching of powerful jets from highly magnetized accretion disks. It is a generalization by Ferreira, 1997 of the seminal work of Blandford and Payne, 1982, connecting the jet to a turbulent accretion disk and highlighting the importance of the ejection index ξ. Open magnetic field lines thread a thin keplerian disk. Along those lines, the plasma is lifted from the disk and transferred into the jet, extracting energy and angular momentum. Blandford & Payne initially built this model to explain the self-collimation of AGN jets by a magnetic field, but it also applies to jets of YSOs, XrBs, CVs...

These models use the framework of MagnetoHydroDynamics (MHD), describing the plasma as a fluid in motion. Because of the large degree of freedom of the problem, they make the hypothesis of radial self-similarity: values follow power laws with the distance to the central object (black hole or star). This approach will be detailed in Chapter 2, detailing its approximations, as well as the conclusions on jet behavior that can be retrieved from them. Here, I will only highlight a few points on jet launching that are useful to understand the aim of this thesis.

A bead on a wire

The mechanism these models rely on is often called magneto-centrifugal. The centrifugal force is exploited to eject matter from the rotating disk. I consider a poloidal plane perpendicular to the disk as in Figure 1.13. The central object is the origin O and the disk midplane is $z = 0$. Let us consider a magnetic field line anchored in the disk at r_0. Because of the flux freezing condition of steady-state ideal MHD, the velocity field lines are parallel to the magnetic field lines. The plasma has to follow the magnetic field lines, like a bead on a wire (Chan and Henriksen, 1980).

Let us immerse ourselves completely in this bead/wire analogy. The bead is only subject to the gravitational attraction of the central object and to the centrifugal force due to the rotation of the disk. Its potential energy is

$$\Phi(r,z) = -\frac{GM}{r_0}\left[\frac{1}{2}\left(\frac{r}{r_0}\right)^2 + \frac{r_0}{\sqrt{r^2+z^2}}\right] \tag{1.6}$$

where G is the gravitational constant and M the mass of the central object. The wire is considered in co-rotation with the disk at its anchoring point.

If the bead is at position ($r = r_0 + s\sin\theta; z = s\cos\theta$) where s is a small curvilinear abscissa on the wire and θ its colatitude, the angle between the wire and the normal to the disk $\vec{u_z}$, the bead potential becomes

$$\Phi(s) = -\frac{GM}{r_0}\left[\frac{1}{2}\left(\frac{r_0 + s\sin\theta}{r_0}\right)^2 + \frac{r_0}{\sqrt{r_0^2 + 2r_0 s\sin\theta + s^2}}\right] \tag{1.7}$$

To know which angles provide a stable equilibrium, I compute the second derivative of the energy potential

$$\left(\frac{d^2\Phi}{ds^2}\right)(s) = -\frac{GM}{r_0}\left[\frac{\sin^2\theta}{r_0^2} + \frac{r_0(3r_0^2\sin^2\theta - r_0^2 + 4r_0 s\sin\theta + 2s^2)}{(r_0^2 + 2r_0 s\sin\theta + s^2)^{5/2}}\right] \tag{1.8}$$

$$\left(\frac{d^2\Phi}{ds^2}\right)(s=0) = -\frac{GM}{r_0^3}\left[4\sin^2\theta - 1\right] \tag{1.9}$$

Therefore, if $\theta > \pi/6$ the equilibrium is stable and the bead stays on the disk. If $\theta < \pi/6$ the equilibrium is unstable and the bead is flung on the wire. This means that if the magnetic field line makes an angle with the disk greater than 60° and is directed outwards, a jet could be launched to infinity.

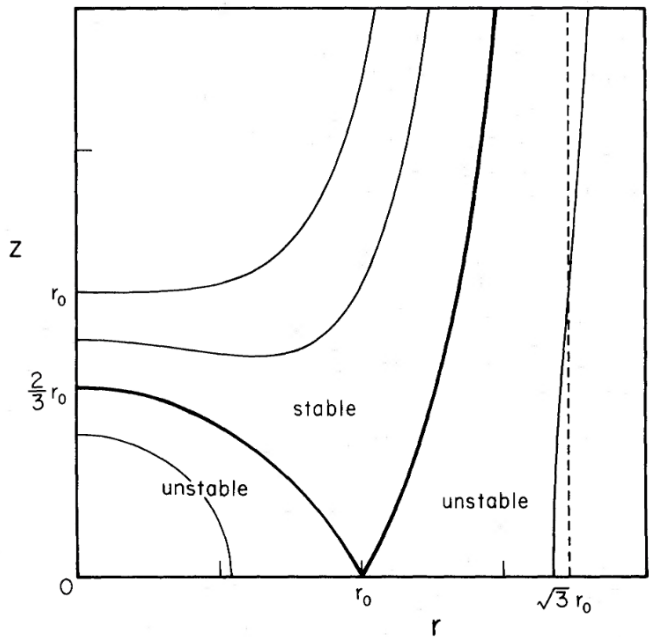

FIGURE 1.13: Isopotential surfaces for beads on a wire anchored at r_0 on a disk ($z = 0$) in Keplerian rotation around the origin O (Blandford and Payne, 1982). If the wire makes an angle greater than 60° with the disk, the equilibrium is stable and the bead stays close to the disk. If the angle is smaller than 60° and the wire is directed outwards, the bead can leave the disk and propagate to infinity.

The importance of the toroidal magnetic field and accretion

This simple analogy shows the possible poloidal magnetic field configurations able to launch a jet. But it hides the crucial role played by the toroidal magnetic field (i.e. in the direction perpendicular to the plane of Figure 1.13). This role is illustrated by the schemes of Figure 1.14. This is a very simplified picture, and the curious reader is referred to Ferreira and Pelletier, 1995 for a more exhaustive description.

The initial configuration is situation A. The magnetic field is initially purely poloidal and vertical, emerging from the disk (in grey). The magnetic field lines are rooted in the disk, and thus affected by the disk dynamics: the accretion along $-\vec{u_r}$ (due to the torque or infall) and the rotation along $+\vec{u_\varphi}$.

Thus, in the following configuration B, the anchoring points of the field lines have shifted inwards thanks to accretion. The rotation has twisted the field lines, and a toroidal component of the magnetic field has appeared, directed along $-\vec{u_\varphi}$. This toroidal component is naturally decreasing with altitude, as we move away from the disk, and the toroidal magnetic pressure $-\vec{\nabla} B_\varphi$ can drive the plasma upwards. Additionally, the poloidal magnetic field lines now tilted outwards can launch the plasma via the magnetocentrifugal ejection described above in the bead/wire analogy. This was already seen in early ideal MHD simulations (see e.g. Uchida and Shibata, 1985).

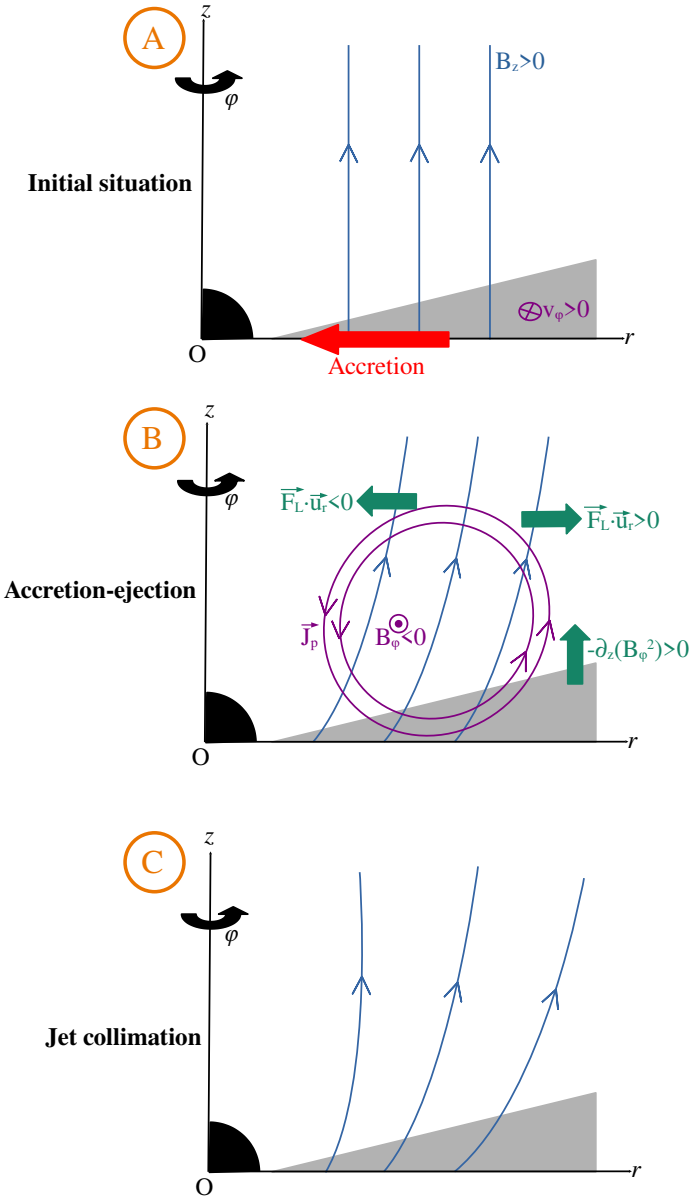

FIGURE 1.14: Scheme explaining the ejection mechanism and the subsequent collimation in a Magnetized Accretion-Ejection Structure (MAES). In blue are the poloidal magnetic field lines, initially vertical. In grey is the accretion disk, in Keplerian rotation around the axis Oz. The rotation velocity v_φ is in purple, as well as the subsequent toroidal magnetic field B_φ and poloidal current loops $\vec{j_p}$. In green are the Laplace force $\vec{F_L} = \vec{j} \times \vec{B}$ and magnetic pressure gradient $-\vec{\nabla} B_\varphi^2$.

The appearance of a toroidal magnetic field can then help launch the plasma. But it is also the driving force in jet collimation. The rotation induces an electric field $\vec{E}_{ind} = \vec{v}_\varphi \times \vec{B}_z$, directed towards $+\vec{u}_r$ in the disk. The associated current density $\vec{j}_p$ is represented in purple on situation B. Because of the current closure condition $\vec{\nabla} \cdot \vec{j} = 0$, counterclockwise current loops are created. The associated Laplace force $\vec{j}_p \times \vec{B}_\varphi$ is directed inwards (along $-\vec{u}_r$) on the innermost magnetic field lines, creating the initial jet collimation. The final situation is configuration C, where the innermost magnetic field lines are now collimated.

Additionally, the ejection powers the accretion, because of Lenz's law. In the disk, the Laplace force $\vec{j}_r \times \vec{B}_z$ is directed along $-\vec{u}_\varphi$. The conservation of angular momentum in the jet also brakes down the disk, reinforcing the accretion. In this disk+jet system, the accretion and ejection are intertwined: the jets drive the disk accretion, and the accretion feeds matter to the jets. It has been coined Magnetized Accretion-Ejection Structure (MAES, Ferreira and Pelletier, 1993a,b; Ferreira and Pelletier, 1995). Such an interdependence between accretion and ejection is naturally backed by the accretion-ejection correlations of section 1.1.2.

1.3.4 Performing large-scale numerical simulations

Acceleration and propagation zones

At this point, the reader might wonder why I am describing the ejection process, while my subject of interest is the large-scale jet collimation, far away from the central object or the disk. We have seen that the jet is collimated quickly after leaving the disk, beyond a few astronomical units for YSO jets, or a few Schwarzchild radii for AGN jets. The jet can be roughly summed up into a juxtaposition of two regions, corresponcould correspondding to the parabolic and conical shapes of M87 described in section 1.2.2. Figure 1.15 schemes a possible evolution of the vertical speed along the jet, assuming it has reached a steady state. The separation between the two zones happens at the altitude z_{coll}.

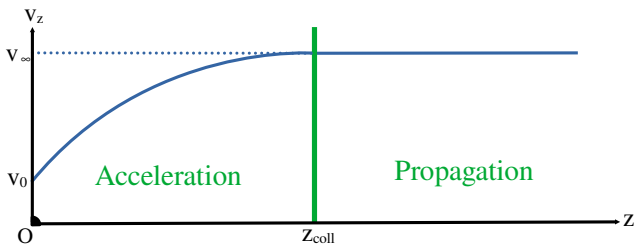

FIGURE 1.15: Simplified evolution of the vertical speed along a jet reaching an asymptotic state. The jet is ejected from the disk at speed v_0. It accelerates until a certain altitude z_{coll}, after which the speeds becomes constant at v_∞.

The two zones are:

- An "acceleration" zone, where the flow is accelerated and collimated. It is in this zone that the field lines go from their open configuration at launch (see the bead/wire analogy above) to their confined configuration ($|B_r/B_z| \ll 1$). It is also there that the flow crosses all critical surfaces (slow-magnetosonic, Alfvén and fast-magnetosonic, see section 2.6.2). This is crucial, as it allows a causal disconnection between the disk and the asymptotic jet, in the following zone.

- A "propagation" zone, where the poloidal magnetic field lines should be almost vertical. In Figure 1.15 I assume that the jet has reached a stationary state, and the vertical speed is constant in this propagation zone. The field lines have then reached their asymptotic state.

The self-similar models described above are stationary, and after their development, numerical simulations were required. These would reveal whether those steady states could be reached when starting out of an equilibrium, and highlight their possible instabilities.

There have been many numerical simulations studying jet collimation in the second "propagation" zone, starting relatively far away for the disk. Those were performed using either classical (see e.g. Matsakos et al., 2008, 2009; Stute et al., 2008; Stute et al., 2014; Teşileanu et al., 2014) or relativistic (see e.g. Komissarov and Falle, 1998; Perucho and Martí, 2007; Perucho et al., 2010; Porth and Komissarov, 2015) MHD. In those cases, the jet is already collimated at launch. The magnetic field lines are quasi-vertical, and the flow has already reached poloidal velocities above most critical speeds, if not all. Their intent was to study the stability of an already collimated jet, for instance to the various MHD instabilities, as well as the appearance of substructure such as shocks.

The aim of this thesis differs; it is focussed on the crucial importance of the launching conditions in setting the observable collimation properties of the jet. Simulations of a whole MAES have been performed (see e.g. Casse and Keppens, 2002, 2004; Murphy, Ferreira, and Zanni, 2010; Murphy, Zanni, and Ferreira, 2009; Sheikhnezami et al., 2012; Stepanovs and Fendt, 2016) where a simulated viscous or/and resistive accretion disk launches the jet/wind. But computing both the accretion and the ejection induces huge numerical constraints, and such simulations have not reached the jet asymptotic scales yet. The simulations presented in this thesis will extend from the disk upper boundary until the observable scales. Those scales would be equivalent to a few hundreds of astronomical units in the case of YSO jets, or a few thousands of Schwarzchild radii in the case of AGN jets.

Global bottom-up simulations

Lots of these "global" simulations have also been performed. As mine, they use the accretion disk as a boundary condition. Again, they were done using either classical (see e.g. Anderson et al., 2005, 2006; Fendt, 2006; Krasnopolsky, Li, and Blandford, 1999; Krasnopolsky, Li, and Blandford, 2003; Ouyed, Clarke, and Pudritz, 2003; Ouyed and Pudritz, 1997a,b, 1999; Pudritz, Rogers, and Ouyed, 2006; Ramsey and Clarke, 2011, 2019; Staff et al., 2015; Staff et al., 2010; Ustyugova et al., 1995, 1999) or relativistic (see e.g. Barniol Duran, Tchekhovskoy, and Giannios, 2017; Bromberg and Tchekhovskoy, 2016; Chatterjee et al., 2019; Porth and Fendt, 2010; Tchekhovskoy and Bromberg, 2016) MHD. Performing those types of simulations presents several difficulties.

First, they have a huge degree of freedom, as many distributions must be specified at the lower boundary condition. In the case of a 2.5D or 3D simulation, up to eight boundary conditions must be specified, one for each MHD variable (ρ, P, $\vec{B}$ and $\vec{v}$). Then, for each critical point that the flow is expected to cross, one of these conditions is relaxed. In our case, and that of most simulations in the paragraph above, this still leaves five or six distributions to fix. Such a large degree of freedom makes it hard to draw generic conclusions on jet collimation from specific simulations.

Second, performing such simulations is numerically challenging, because of the large discrepancy in scales. It requires a good resolution in the zone driving the

ejection, just above the inner disk regions (the "acceleration" zone of Figure 1.15). But it also needs to be on a grid large enough to capture the asymptotic jet regions, that will explain its observable shape (the "propagation" zone of Figure 1.15). In addition, launching jets from a Keplerian disk creates a discrepancy in timescales. The time increment must be small enough compared to the orbital period at the inner disk, but the simulation must run for a time long enough compared to the period at the outer disk. For this reason, the "global" simulations listed above either were performed on grids too small to see the jet asymptotics, or ran for a time too small to see a global steady state of the jet. This is due to either technical limitations (especially for the earlier works), or simply because this was not the intent of the authors. In my case, performing simulations at the required scales in space and time proved rather challenging, even with the usual methods of High Performance Computing (HPC). It required the development of a few numerical techniques, described in Chapter 3 and Appendix C.

1.3.5 The self-similar approach and recollimation

Recollimation at large scales

The self-similar solutions are a good starting point to study large-scale jet collimation, as, contrary to the numerical simulations, they are not subject to the technical limitations mentioned above. Since the seminal model of Blandford and Payne, 1982, it is known that a large-scale magnetic field threading a Keplerian accretion disk can accelerate the disk material into the jet up to super-fast magnetosonic speeds, thus crossing all MHD critical surfaces. This self-similar model was later generalized by modifying the magnetic field distribution (Contopoulos and Lovelace, 1994; Ostriker, 1997), or by adding thermal effects (Ceccobello et al., 2018; Vlahakis et al., 2000), and was transposed to relativistic MHD (Li, Chiueh, and Begelman, 1992; Polko, Meier, and Markoff, 2010, 2014; Vlahakis and Königl, 2003). Smoothly connecting self-similar jet models to a quasi-Keplerian accretion disk, Ferreira, 1997 showed that the super-fast magnetosonic jets systematically go through a recollimation towards their axis. As in Polko, Meier, and Markoff, 2010, this recollimation is due to the internal hoop stress caused by the self-induced Laplace force (see Figure 1.13). This is a generic result, later verified for warm outflows (Casse and Ferreira, 2000a) and weak magnetic fields (Jacquemin-Ide, Ferreira, and Lesur, 2019).

Some solutions are presented in Figure 1.16, each showing poloidal magnetic field lines. On the top panel are the highly magnetized solutions of Ferreira, 1997, with a magnetization (magnetic to thermal pressure ratio) $B^2/(4\pi P) \lesssim 1$ and various ejection indexes $\xi \in [0.005; 0.05]$. On the bottom panel is the lowly magnetized solution of Jacquemin-Ide, Ferreira, and Lesur, 2019, with $B^2/(4\pi P) = 5.7 \times 10^{-3}$ and $\xi = 0.1$.

After being launched outwards (see the bead/wire analogy in section 1.3.3), all field lines are eventually recollimated towards the axis. This recollimation is more pronounced for small values of the ejection index ($\xi \leq 0.012$) or of the magnetization ($B^2/(4\pi P) \sim 10^{-3}$, see also the other solutions of Jacquemin-Ide, Ferreira, and Lesur, 2019). In those solutions, the magnetic field lines eventually become almost horizontal ($|B_r/B_z| \gg 1$, with $B_r < 0$). But in those cases, recollimation happens very far away from the disk. The distances in both panels of Figure 1.16 are in units of r_0, radius of the field line at its anchoring point in the disk. This radius would correspond to the innermost point in the disk, which would be around 0.1 au for a YSO jet and at the Innermost Stable Circular Orbit (ISCO) for a black hole jet. The

location of the ISCO depends on the black hole spin, and is on the same scale as the Schwarzchild radius (see e.g. Bardeen, Press, and Teukolsky, 1972). Therefore, in those self-similar solutions, strong recollimation is only observed beyond 10^2 astronomical units for YSO jets, or beyond 10^3 Schwarzchild radii for AGN jets. Note however that the model is newtonian so this last number must be taken with caution.

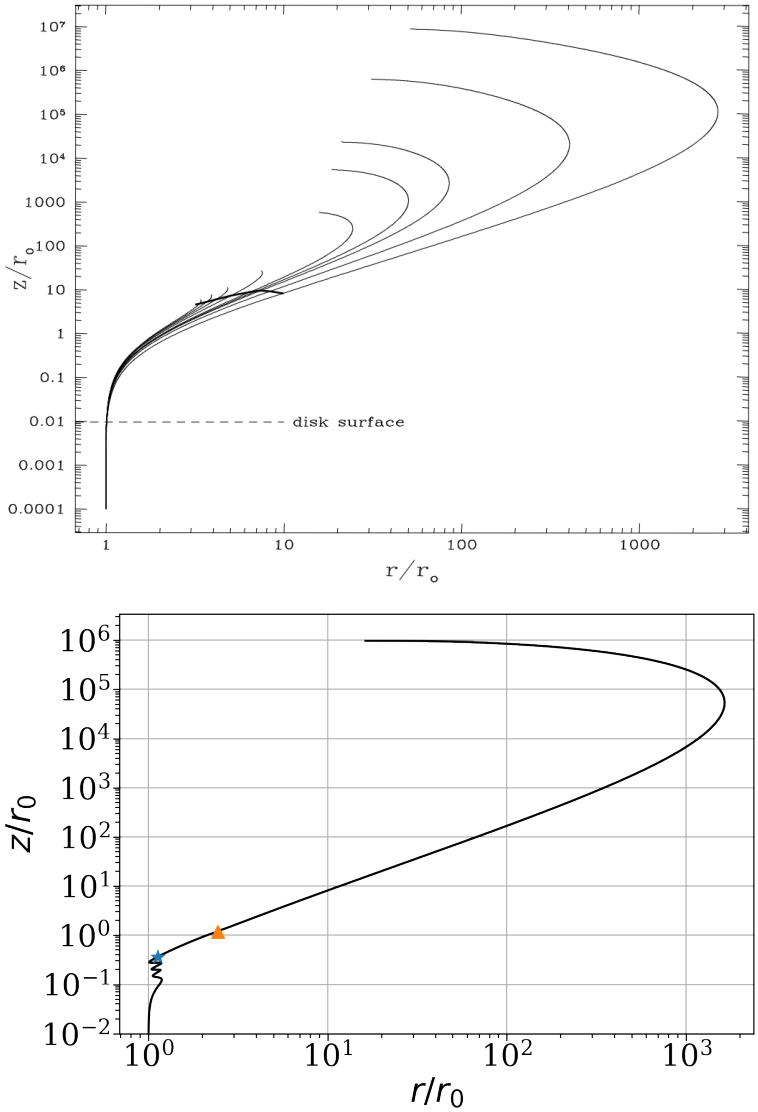

FIGURE 1.16: Top: Magnetic field lines for solutions of ejection indexes $\xi \in [0.05, 0.04, 0.03, 0.02, 0.012, 0.01, 0.009, 0.007, 0.005]$ (Ferreira, 1997). The smaller ξ, the higher cylindrical radii r are attained and the further away the recollimation. Bottom: Magnetic field line for the solution of low magnetization ($B^2/(4\pi P) = 5.7 \times 10^{-3}$) and ejection index $\xi = 0.1$ of Jacquemin-Ide, Ferreira, and Lesur, 2019). The slow-magnetosonic point is marked by a star and the Alfvén point is marked by a triangle. All solutions are super-SM in the conventional sense ($v_p > V_{FM_p}$).

The impending recollimation shock

Moreover, this recollimation happens on the same scale as the transition between the acceleration zone and the propagation, illustrated in Figure 1.15. The self-similar solutions cannot go further, as they would cross the fast-magnetosonic critical point, singularity in the MHD equations. Yet, the observations of the archetypal source M87 (Figure 1.11) show the presence of a quasi-stationary recollimation shock at the transition between the parabolic and conical phases of the jet. I argue this recollimation shock could be caused by the crossing of the fast-magnetosonic critical point in a self-collimated jet. Such standing recollimation shocks were already present in numerical simulations in which an already collimated jet is launched relatively far away from the disk (see e.g. Matsakos et al., 2008, 2009; Stute et al., 2008). However, they have yet to be seen in "global" jet simulations, in which a sub-Alfvénic flow is launched consistently with jet-launching models, such as the Jet-Emitting Disk (JED). As explained in the precedent section, this is most likely because those simulations were run in a domain too small compared to the recollimation scales (beyond 10^2 au for YSO jets or 10^3 r_s for AGN jets), or integrated on a time too small to reach a fully steady jet.

It is important to note that in such an approach, the dominant mechanism in the collimation is the internal hoop stress, caused by the toroidal magnetic field of the jet. It is at odds with the pressure mismatch at the interface between the jet and the ambient medium proposed as an explanation for the knots observed in AGN jets (Komissarov and Falle, 1998; Perucho and Martí, 2007; Perucho, 2020). Both can expected in MHD flows.

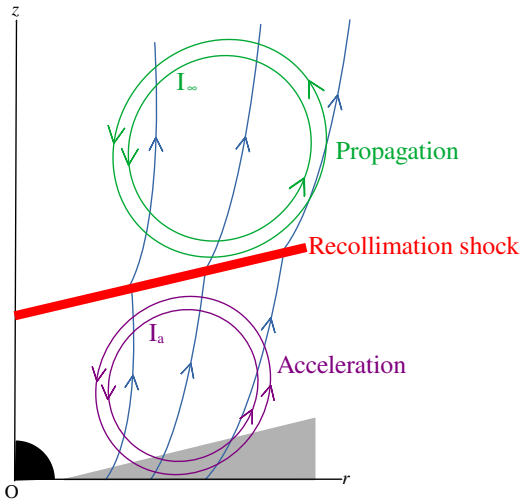

FIGURE 1.17: Configuration of the electric circuits in the presence of a recollimation shock (in red). The accelerating circuit (in purple) of maximal current I_a is upstream of the shock. The asymptotic circuit (in green) of maximal current I_∞ is downstream of the shock. The inner poloidal magnetic field lines (in blue) are collimated by the accelerating circuit in the acceleration zone. They are then refracted by the shock, and finally collimated by the asymptotic circuit.

One possible configuration of such a self-collimated jet is schemed on Figure 1.17. This is a zoomed-out view of configuration C of Figure 1.14. Beyond the recollimation shock (in red) and downstream of the accelerating electric circuit (in purple) appears a second asymptotic circuit (in green). The shock acts as a separatrix between

the acceleration zone near the disk, and the propagation zone at the largest, asymptotic scales. It is a discontinuity in all variables, in particular the magnetic field. The discontinuity in poloidal magnetic field induces a refraction of the poloidal magnetic field lines (in blue). The discontinuity in toroidal magnetic field induces a clear separation between the accelerating circuit, anchored in the disk, and the asymptotic circuit, at the observable scales.

In this situation, while the current I_a in the accelerating circuit is set by the launching conditions, it is not clear what fixes the current I_∞ in the asymptotic circuit. Yet, it this asymptotic current that dictates the jet shape. Heyvaerts and Norman, 1989 showed that all stationary axisymmetric magnetized jets will eventually collimate to a parabola, cone or cylinder, depending whether the asymptotic current I_∞ vanishes or not. This generic result has later been extended, taking into account current closure (Heyvaerts and Norman, 2003), as well as the geometry of the solution (collimating or decollimating, see Okamoto, 2003; Okamoto, 2001). It is tempting to use this feature to provide a simple explanation for the conical shape of the M87 jet beyond the recollimation shock (Figure 1.11): a vanishing asymptotic current $I_\infty = 0$ would lead to a ballistic propagation from the recollimation shock at $z \sim 10^5 r_s$, until the formation of the lobes at jet termination ($z \sim 10^9 r_s$). Naturally, Figure 1.17 shows a very simple picture, where there is a complete disconnection between the accelerating and asymptotic circuit. There could be a connection between the two circuits by current closing down on the jet axis, or via an external sub fast-magnetosonic outflow. Whether this scheme is realistic or not will be shown by the numerical simulations.

1.3.6 Aims and contents

This thesis aims at studying the large scale collimation of jets, that dictates their observable shape. The connection between the asymptotic current and the source remains a long standing pending issue. It is naturally studied with time-dependent MHD simulations, but previous works did not achieve a global steady state at these large scales, most likely because those simulations did not reach the required scales in space and time.

In this thesis, I will present several numerical simulations designed to bridge the gap between the jet launching conditions and its collimation properties at observable scales. The aim is to assess whether the generic results obtained within the self-similar framework still hold in full 2D time-dependent simulations. In particular, I will address whether the existence of recollimation shock is unavoidable for the conditions expected in Keplerian accretion disks, as proposed by Ferreira, 1997.

As a consequence of this approach, I will focus mostly on steady-state jets, in order to confront my simulations to MHD jet theory. It is clear that most if not all astrophysical jets exhibit time-dependent features. However, the aim of this work is not to reproduce a specific jet, but rather to investigate the generic behaviors of MHD jets emitted from Keplerian accretion disks.

The manuscript is organized as follows:

- Chapter 2 sets the theoretical framework of the thesis: non-relativistic ideal MHD. I justify the approximations used and highlight their limitations. Then, I show a few relevant properties of ideal MHD jet theory.

- Chapter 3 sets the numerical framework of the thesis. I present various features of the MHD code PLUTO (Mignone et al., 2007) I used throughout the thesis.

Then, I describe the numerical setup designed for the simulations, with the Jet-Emitting Disk (JED) as a boundary condition.

- Chapters 4 and 5 present jet simulations in which the JED extends on the whole lower boundary. I show that recollimation shocks are indeed obtained, in agreement with analytical theory. Then I present a parametric study, showing a correspondance between my simulations and the self-similar solutions, but also highlight the crucial role of the axial spine in global jet collimation. I also compare my results to the literature.

- Chapter 6 presents jet simulations where the JED is now limited to the innermost disk regions. I show that this more realistic configuration produces jets featuring recollimation shocks of similar properties. I also run a parametric study, highlighting the influence of the central object rotation and the ambient pressure on the jet collimation properties.

- Chapter 7 describes numerical simulations obtained serendipitously, showing oscillations created in the asymptotic jet that propagate down to the disk. Such perturbations arriving on the disk could provide an explanation to the QPOs observed in X-ray binaries, as proposed by Ferreira et al., 2022.

Chapter 2

Theoretical framework

Contents

2.1 Ideal MHD approximations . . . 31
2.1.1 Astrophysical jets: plasmas ? . . . 31
Electroneutrality . . . 31
Collisionality and ionization . . . 32
2.1.2 Fully ionized plasma . . . 33
2.1.3 Kinetic approach . . . 33
2.1.4 Non-relativistic electromagnetism . . . 34
2.1.5 Ohm's law and resistivity . . . 34
2.1.6 Euler equations . . . 35
2.1.7 Energy equation . . . 36
2.2 Ideal MHD equations . . . 38
2.3 MHD waves . . . 39
2.4 Magnetic flux . . . 41
2.5 Axisymmetry and stationarity . . . 41
2.6 Invariants and dynamics of steady flows . . . 42
2.6.1 MHD invariants . . . 42
2.6.2 Critical points in ideal MHD . . . 44
2.6.3 Asymptotic speeds . . . 45
2.6.4 The self-similar approximation . . . 46
2.6.5 Parameter space . . . 46
2.6.6 Electric circuits and collimation . . . 48
2.6.7 Jet transverse equilibrium . . . 50
2.7 Discontinuities . . . 50
2.8 Summary . . . 53

"Et saint Patrick d'ajouter froidement :
— You are Peter, and on that stone…
Saint Pierre ne le laisse pas achever."

"And Saint Patrick adds coldly:
— You are Peter, and on that stone…
Saint Peter does not let him finish."

Alphonse Allais

Dans ce chapitre, je dérive les équations de la MHD idéale non-relativiste, cadre usuel pour l'étude des jets astrophysiques. Je mets l'accent sur les différentes approximations utilisées et leur validité. Puis, je montre certaines propriétés pertinentes des jets obtenues dans ce cadre. Enfin, je donne les caractéristiques attendues des chocs de recollimation dans une approche entièrement autosimilaire.

Comme la taille caractéristique du jet est bien supérieure à la longueur de Debye, mais que les particules sont nombreuses dans une sphère de Debye, le plasma peut être considéré comme électriquement neutre. Comme le libre parcours moyen des particules est petit devant la taille caractéristique du jet, le plasma peut également être considéré comme collisionnel. Cependant, cela suppose de considérer le plasma comme complètement ionisé, ce qui est une hypothèse forte pour tous types de jets (AGN, étoiles jeunes, binaires X etc.). Dans ce cas, il n'y a pas de particules neutres. Cela permet alors d'utiliser l'approche monofluide, et de définir une unique densité et vitesse pour les ions et les électrons, et donc pour tout le plasma. Enfin, comme la taille caractéristique du jet est grande devant le rayon cyclotron, l'échelle macroscopique à laquelle le jet est observé est bien plus grande que l'échelle microscopique de rotation des particules autour du champ magnétique. Le jet est donc bien décrit par les équations de la dynamique des fluides.

Dans ce manuscrit, je négligerai les effets de la relativité et resterai dans le domaine de la physique newtonienne. Cette approximation est valable pour les jets protostellaires, mais ne fonctionne pas pour les jets d'AGN qui présentent de grands facteurs de Lorentz. La plupart des comparaisons directes avec les observations seront faites en utilisant des jets protostellaires. Les équations de la MHD dans le cadre de la relativité générale (GRMHD) sont différentes des équations newtoniennes. Dans l'équation du mouvement, par exemple, il y a un terme supplémentaire dû au champ électrique; et l'inertie, alors $(v/c)m$, est plus grande. Cela devrait compenser, au moins partiellement, le confinement causé par le champ magnétique toroïdal, en particulier pour des facteurs de Lorentz élevés. Ainsi, les structures (telles que les chocs de recollimation) observées dans mes simulations non relativistes devraient apparaître à des altitudes plus élevées dans des simulations GRMHD semblables. Cependant, il n'est pas évident que ces structures apparaissent, et si elles apparaissent, on ne sait de combien elles seraient déplacées vers le haut. Par conséquent, les comparaisons entre les résultats présentés dans cette thèse et les jets d'AGN ne peuvent être que qualitatives.

L'effet Hall et la pression des électrons peuvent être négligés dans tous types de jets. On néglige également la résistivité, ce qui est une hypothèse relativement forte au lancement, mais bien valide loin du disque, lorsque le jet se recollimate. Une telle approximation est appelée MHD idéale, et est le cadre usuel d'étude des jets astrophysiques. La viscosité du plasma est négligeable, et l'équation du mouvement est l'équation d'Euler. Et, dans le jet la densité est suffisamment faible pour négliger l'auto-gravité. On considère donc que seul l'objet central (trou noir ou étoile) produit un champ gravitationnel. Enfin, je suppose une équation d'état polytropique, le calcul des termes de chauffage et de refroidissement étant particulièrement complexe.

Dans un jet magnétisé supposé en MHD idéale, trois types d'ondes peuvent transporter de l'information. La plus lente, l'onde magnétosonique lente (SM) est semblable à une onde sonore dans le cas d'un plasma très magnétisé. L'onde d'Alfvén, de vitesse intermédiaire, est une onde de cisaillement. La plus rapide est l'onde magnétosonique rapide (FM), qui devient une onde d'Alfvén comprimant le plasma lorsque celui-ci est suffisament froid. C'est le passage du plasma à des vitesses supérieures à celles des ondes rapides qui déclenchent les chocs de recollimation auxquels on s'intéresse ici. L'écoulement devient stationnaire si et seulement si sa vitesse est supérieure aux vitesses de phase de toutes ces ondes. Un écoulement stable doit donc traverser trois points critiques. La présence d'un point critique produit une contrainte supplémentaire, introduisant ainsi une relation supplémentaire entre les paramètres du problème. En pratique, chaque ligne de champ magnétique ancrée dans le disque traversera les trois points critiques susmentionnés ou moins, en fonction des conditions d'éjection et des vitesses atteintes sur la ligne de champ. Chaque franchissement d'un point critique nécessite de laisser un paramètre libre à l'éjection, afin d'éviter de surcontraindre le problème.

Dans tout ce qui suit, les jets seront supposés axisymétriques. En MHD idéale, le jet peut être vu comme une succession de surfaces magnétiques imbriquées les unes dans les autres, à la manière de poupées russes. Une surface magnétique est l'ensemble des lignes de champ magnétique ancrées dans le disque à la même distance de l'objet central. La quantité définissant une surface magnétique est le flux magnétique. Celui-ci est conservé sur l'entièreté de la surface, de son lancement au niveau du disque, jusqu'à l'infini, dans la région asymptotique. De plus, la topologie des surfaces magnétiques est conservée au cours du temps. Celles-ci ne peuvent ni se rompre ni se reconnecter. Ainsi, les cinq invariants MHD, dépendant uniquement du flux, sont conservés au cours du temps et le long d'une surface magnétique. Ils peuvent être imposés à la source (disque ou objet central) comme une condition limite, en prenant en compte les problèmes de causalité expliqués dans le paragraphe précédent.

De nombreuses études analytiques ont permis de relier les propriétés du jet à celles du disque. Celles ayant eu le plus de succès sont dites radialement autosimilaires. Dans cette approche, on recherche des solutions stationnaires à l'écoulement 2D par séparation des variables, et on suppose que chaque quantité varie avec la distance à l'objet central par une loi de puissance. Pour cette approche, le travail de référence est le papier de Blandford and Payne, 1982. Il définit les paramètres clés du problème: le chargement en masse κ, le bras de levier magnétique λ et le paramètre α, exposant de la distance à la source pour le flux magnétique. De nombreux travaux autosimilaires ont suivi. En particulier, cette thèse s'appuie sur la généralisation de Ferreira, 1997, appelée Jet-Emitting Disk. Cependant, ces solutions ne peuvent pas traverser toutes les surfaces critiques, et ne reproduisent pas le jet asymptotique. L'état super-fast magnétosonique du jet devrait fortement dépendre de la distribution du courant au lancement, qui, par le paramètre α, définit où le courant se referme, et donc comment le jet est confiné.

Ce chapitre se conclut sur la dérivation des conditions de Rankine-Hugoniot pour des chocs de recollimation stationnaires et adiabatiques, après le passage du point magnétosonique rapide. Je décris les types de chocs possibles, ainsi que les relations entre les quantités pré et post-choc. On s'attend à des chocs relativement faibles, où le jet est légèrement compressé et réfracté au passage de la discontinuité. Ces considérations sont utiles pour comprendre les simulations qui seront décrites dans la suite du manuscrit.

In this chapter, I derive the equations of magnetohydrodynamics, highlighting why the approximations made are justified in our astrophysical objects, namely AGN and YSO jets. Then, I emphasize some properties of stationary flows relevant for this manuscript. This is obviously not intended to be a course on magnetohydrodynamics. For this purpose, I recommend the read of Goedbloed, Keppens, and Poedts, 2010; Goedbloed and Poedts, 2004 on which this chapter is based.

2.1 Ideal MHD approximations

2.1.1 Astrophysical jets: plasmas ?

In space, matter is not limited to the three most common states on Earth: solid, liquid and gas. Ignoring dark matter, around 90% of the matter in the universe is plasma, "a quasi-neutral gas of charged and neutral particles which exhibits collective behavior" (Chen, 1974). Although not freely existing under "normal" conditions, plasma can be generated on Earth, by lightning or flames for instance. Here, the charged particles are negatively charged electrons and positively charged ions. In all the following, quantities with a subscript i will refer to the ions, quantities with a subscript e will refer to the electrons and quantities with a subscript n will refer to the neutrals.

Electroneutrality

To study the electroneutrality of jets, I must introduce the Debye length:

$$\lambda_D = \sqrt{\frac{k_B T_e}{4\pi e^2 n_e}} \tag{2.1}$$

It is the typical size of a region over which charge imbalance due to thermal fluctuations may occur. For quasi-electroneutrality to hold, two conditions are required.

First, the plasma length scale should be much larger than the Debye length:

$$R_{jet} \gg \lambda_D \tag{2.2}$$

where R_{jet} is a typical radius of the jet.

In the case of AGN jets, I take $R_{jet} = 10^{18}\text{cm}(= 10^5 r_g)$, radius of the M87 jet at the HST-1 knot (see the left panel of Figure 1.11), and in the case of YSO jets, I take $R_{jet} = 10^{15}\text{cm}(= 10^2\text{au})$ as the asymptotic radius of a HH jet (see Louvet et al., 2018 or Figure 1.9). The values used for all calculations are listed in Table 2.1.

I then need an estimate of the jet temperature at the collimation point. In the case of YSO jets I use $T = 10^4$K (Bally, Reipurth, and Davis, 2007). In the case of AGN jets, estimating the temperature is quite harder as radio observations only give information on brightness temperatures of superthermal particles, around 10^{10}K (see e.g. Piner and Edwards, 2014, Homan et al., 2021). On the other hand, temperature of the interstellar medium surrounding the jet is estimated around $10^7\text{K}(= 1\text{keV})$ (Allen et al., 2006). Such values are usually assumed for thermal studies of AGN jets (see for instance Biretta, Stern, and Harris, 1991 or Asada and Nakamura, 2012). For lack of a better estimate, I will take this value as a proxy for the plasma temperature in the jet.

Second, there should be enough particles in a sphere of radius λ_D for statistical considerations to be valid:

$$n \gg \lambda_D^{-3} \tag{2.3}$$

For the sake of concision, all adimensioned parameters are written in Table 2.2. One can see that conditions 2.2 and 2.3 are verified for both AGN and YSO jets.

Collisionality and ionization

For particle motion to be long-range and collective rather than short-range and individual, either one pressure component (ion, electron or neutral pressure) dominates the others, or the plasma is thermalized: $T_i = T_e = T_n = T$. In that case, there needs to be a unique distribution function describing all the particles. This means that the plasma is collisional, which occurs when:

$$R_{jet} \gg \lambda_{coll} \tag{2.4}$$

where λ_{coll} is the collisional mean free path of the electrons.

In the case of a fully ionized plasma, I consider the collisions between electrons and ions, and the collisional mean free path is (Spitzer, 1962)

$$\lambda_{coll} = \lambda_{ei} \simeq 10^5 \frac{T_e^2}{n_e \ln \Lambda} \text{cm} \tag{2.5}$$

where $T_e = T$ is the temperature of the electrons, $n_e = n_i$ is the density of the electrons and $\ln \Lambda$ is the Coulomb logarithm. In all the following $\ln \Lambda = 10$.

In the case of a poorly ionized plasma the collisions between the electrons and the neutrals should also be considered, and the collisional mean free path becomes

$$\lambda_{coll} = \lambda_{en} \simeq 10^{15} n_n^{-1} \text{cm} \tag{2.6}$$

where n_n is the density of the neutrals.

For YSO jets, observations give a typical value of density $n = 10^3 \text{cm}^{-3}$, good estimate of n_e in a fully ionized jet and n_n in a poorly ionized jet.

For AGN jets, densities are harder to derive, but back-of-the-enveloppe calculations can give an estimate. For a jet of power L_j, density n, axial velocity v_j and outward velocity v_h, we have $L_j \sim \pi R_{jet}^2 n m_p v_j c^2$. By modeling the Spectral Energy Distribution (SED), the M87 jet power is estimated at $L_j \sim 10^{44} \text{erg.s}^{-1}$ (Owen, Eilek, and Kassim, 2000; Prieto et al., 2016). Taking $V_{jet} = c$ I obtain $n \sim 1 \text{cm}^{-3}$.

What are the values of λ_{coll}/R_{jet} ? In YSO jets, both fully ionized and poorly ionized plasmas can be considered collisional. On the other hand, fully ionized AGN jets are at the limit of validity of collisional plasma ($\lambda_{ei} \sim R_{jet}$). Assuming thermal equilibium, the ionization fraction can be computed via the Saha equation:

$$\frac{n_i}{n_n} = \left(\frac{2\pi m_e k_B}{h_p^2} \right)^{3/2} \frac{T^{3/2}}{n_i} e^{-U_i/(k_B T)} \tag{2.7}$$

where U_i is the ionization energy. For AGN jets, this gives $n_i \gg n_n$ and the plasma is fully ionized. AGN jets can thus be considered collisonial but would most likely end up non-fully collisional after a certain altitude.

In conclusion, both AGN and YSO jets can be considered collisional. As they are also electroneutral, they can be considered plasmas, according to definition of Chen above.

2.1.2 Fully ionized plasma

In all the following, I assume that the plasma is fully ionized. This means the plasma is only composed of ions and electrons, there are no neutrals. We have seen that this is a reasonable assumption for AGN jets. For YSO jets, the values in Table 2.1 give a fully ionized via the Saha equation 2.7. However, this equation is highly dependent on temperature, and colder jets are known to only be partially ionized. Hence, this assumption is rather strong.

Within the fully ionized and electroneutral assumptions, one can define a single plasma density $n_e = n_i = n$. As $m_i \gg m_e$ the density and velocity of the plasma become:

$$\rho = (m_i + m_e)n \simeq m_i n \tag{2.8}$$

$$\vec{v} = \frac{m_i \vec{v_i} + m_e \vec{v_e}}{m_i + m_e} \simeq \vec{v_i} \tag{2.9}$$

This approach is called "mono-fluid", the electrons and ions being treated as one single fluid. Because of their low mass, the electron motion is negligible and electrons only contribute to the current:

$$\vec{j} = en(\vec{v_i} - \vec{v_e}) \tag{2.10}$$

2.1.3 Kinetic approach

Describing the plasma as a single fluid, it should be considered on a macroscopic scale, i.e. on large length and time scales compared to fundamental phenomena happening to particles on small microscopic scales. One of such phenomena is the movement of a charged particle subjected to magnetic field, called cyclotron motion.

For a particle of charge q and mass m subjected to a magnetic field of intensity B and speed perpendicular to the magnetic field $v_\perp$, this motion is a gyration of radius $mv_\perp/(|q|B)$ and frequency $|q|B/m$. For an ion of charge e, those values are:

$$R_L = \frac{m_p v_\perp}{eB} \text{ and } \Omega_L = \frac{eB}{m_p} \tag{2.11}$$

Taking the thermal speed of the protons $c_{th} = \sqrt{k_B T/m_p}$ as an estimate for $v_\perp$, I can compare R_L to a typical length-scale of the jet, R_{jet}, and $1/\Omega_L$ to a typical time-scale of the jet, $t_{jet} = R_{jet}/V_{jet}$. Around YSOs, (Carrasco-González et al., 2010), $B = 10^{-4}$G is a good estimate of the magnetic field in the jet. For AGN jets (Araudo et al., 2018; Werner et al., 2012), it is in the 10^{-4} G range. For instance on the HST-1 knot of the M87 jet where the magnetic field should peak, X-ray variability measurments (Harris and Krawczynski, 2006; Perlman et al., 2003) give a field strength of $0.5 - 20$mG. This is consistent with the recent Event Horizon Telescope (EHT) of the central black hole M87* (EHT et al., 2021a). A magnetic field strength of $B \sim 1 - 30$G at launch and a poloidal magnetic field decreasing in $B_p \propto r^{-2}$ with the jet radius gives slightly lower magnetic fields at HST-1, in the 10^{-4}G range. As written in Table 2.2, the macroscopic scales at which we observe the jets are indeed much larger than the microscopic scales of particles cyclotron motion. They can thus be described by the equations of fluid dynamics.

2.1.4 Non-relativistic electromagnetism

In this manuscript, I will neglect the effects of relativity and stay in the realm of classical physics. As shown in Table 2.2, this approximation holds well for protostellar jets, but does not work for AGN jets exhibiting large Lorentz factors. Some qualitative consequences of our simulations can still be applicable to relativistic jets, for instance in the context of the two-flow model (Henri and Pelletier, 1991) where the inner spine emitted from the central object is highly relativistic (Lorenz factors around ten), and the outer jet launched by the accretion disk is sub-relativistic. Still, most of the direct comparison to observations will be made using protostellar jets.

The following four Maxwell equations are the foundation of classical electromagnetism (Heaviside, 1892; Maxwell, 1873). They link the electric field $\vec{E}$ and the magnetic field $\vec{B}$ with the charge density τ and the electric current density $\vec{j}$.

$$\vec{\nabla} \cdot \vec{E} = 4\pi\tau \qquad \textit{Gauss's law} \tag{2.12}$$

$$\vec{\nabla} \cdot \vec{B} = 0 \qquad \textit{Gauss's law for magnetism} \tag{2.13}$$

$$\vec{\nabla} \times \vec{E} = -\frac{1}{c}\frac{\partial \vec{B}}{\partial t} \qquad \textit{Faraday's law of induction} \tag{2.14}$$

$$\vec{\nabla} \times \vec{B} = \frac{1}{c}\left(4\pi\vec{j} + \frac{\partial \vec{E}}{\partial t}\right) \qquad \textit{Ampère's circuital law} \tag{2.15}$$

From Maxwell-Ampère we see that the electric current is due to both auto-induction and a variable electric field, called displacement current. Maxwell-Faraday then yields an estimate of this displacement current

$$\frac{E}{c^2 t_{jet}} \sim \frac{V_{jet} B}{c^2 t_{jet}} \sim \left(\frac{V_{jet}}{c}\right)^2 \frac{B}{R_{jet}} \text{ and } \frac{\left|\frac{1}{c}\frac{\partial \vec{E}}{\partial t}\right|}{\left|\vec{\nabla} \times \vec{B}\right|} \sim \left(\frac{V_{jet}}{c}\right)^2 \ll 1 \tag{2.16}$$

where $t_{jet} = R_{jet}/V_{jet}$ is a typical time-scale. In non-relativistic-jets with $V_{jet} \ll c$ the displacement current is negligible compared to the auto-induction and Ampère's law becomes

$$\vec{\nabla} \times \vec{B} = \frac{4\pi}{c}\vec{j} \tag{2.17}$$

This gives the current closure condition $\vec{\nabla} \cdot \vec{j} = 0$, meaning that all electric circuits are closed.

2.1.5 Ohm's law and resistivity

With this simplified version of Ampère's circuital law, we now miss an equation describing the time evolution of the electric field. Such an equation is obtained using the momentum conservation of the electrons. In a fully ionized plasma, neglecting the acceleration of the electrons and gravity because of their low mass yields

$$\vec{0} = -\vec{\nabla} P_e - n_e e(\vec{E} + \frac{1}{c}\vec{v}_e \times \vec{B}) + \frac{m_e n_e}{\tau_{ei}}(\vec{v}_i - \vec{v}_e) \tag{2.18}$$

where the last term is due to collisions with ions, τ_{ei} being the time-scale of such collisions. Using the definitions of current $\vec{j}$ and mean plasma speed $\vec{v}$ in the section 2.1.2 above, I get the generalized Ohm's law

$$\vec{E} + \frac{1}{c}\vec{v} \times \vec{B} = \eta_m \vec{j} + \frac{1}{en_e}(\vec{j} \times \vec{B} - \vec{\nabla} P_e) \tag{2.19}$$

where $\eta_m = m_e/(n_e e^2 \tau_{ei})$ is the plasma resistivity.

The Hall effect $\frac{1}{en_e}\vec{j} \times \vec{B}$ is negligible with respect to the left handside of the equation when

$$\Omega_L t_{jet} \gg \left(\frac{V_A}{V_{jet}}\right)^2 \tag{2.20}$$

The electron pressure is negligible with respect to the left handside of the equation when

$$\Omega_L t_{jet} \gg \left(\frac{c_{th}}{V_{jet}}\right)^2 \tag{2.21}$$

As these two conditions are satisfied in both AGN and YSO jets (see Table 2.2), these two terms can be dropped and we thus obtain a simpified version of Ohm's law

$$\vec{E} + \frac{1}{c}\vec{v} \times \vec{B} = \eta_m \vec{j} \tag{2.22}$$

Combining it with the Maxwell equations I get the induction equation

$$\frac{\partial \vec{B}}{\partial t} = (\eta_m \vec{\nabla} \times (\vec{\nabla} \times \vec{B}) - \vec{\nabla} \times (\vec{v} \times \vec{B})) \tag{2.23}$$

The plasma resistivity η_m can be expressed as in Spitzer, 1962

$$\eta_m = \frac{4\sqrt{2\pi}}{3} \frac{Ze^2 \sqrt{m_e} \ln \Lambda}{(k_B T_e)^{3/2}} \tag{2.24}$$

where Z is the ionization parameter and $ln\Lambda \sim 10$ is the Coulomb logarithm. The plasma is assumed to be fully ionized and $Z = 1$. I can now define the magnetic Reynolds number, quantifying the relative strengths of magnetic field advection and diffusion:

$$R_m = \frac{V_{jet} R_{jet}}{\eta_m} \tag{2.25}$$

The magnetic Reynolds number reported in Table 2.2 is very small in both AGN and YSO jets. The resistive term can thus be dropped and the induction equation becomes

$$\frac{\partial \vec{B}}{\partial t} = -\vec{\nabla} \times (\vec{v} \times \vec{B}) \tag{2.26}$$

describing the so-called ideal MHD regime.

2.1.6 Euler equations

As it exhibits collective behavior, the collisional plasma can be described as a fluid, and thus follows the equations of fluid dynamics, namely the continuity equation

$$\frac{\partial \rho}{\partial t} + \vec{\nabla} \cdot (\rho \vec{v}) = 0 \tag{2.27}$$

and the equation of motion

$$\rho\frac{\partial\vec{v}}{\partial t}+\rho(\vec{v}\cdot\vec{\nabla})\vec{v}=\frac{1}{c}\vec{j}\times\vec{B}-\vec{\nabla}P-\rho\vec{\nabla}\Phi_G \tag{2.28}$$

with only three volumic forces, the pressure gradient $-\vec{\nabla}P$, the gravitational potential gradient $-\rho\vec{\nabla}\Phi_G$ and the Laplace force $(1/c)\vec{j}\times\vec{B}$.

This expression for the equation of motion implies a non-viscous plasma. To verify this assumption, I compute the Reynolds number, ratio of inertial to viscous forces:

$$Re=\frac{V_{jet}R_{jet}}{\nu} \tag{2.29}$$

where ν is the kinematic viscosity. As in Frisch, 1995, I take $\nu\sim\lambda_{coll}c_{th}$, where λ_{coll} is the collisional mean free path between electrons and ions λ_{ei}, and $c_{th}=\sqrt{k_BT/m_p}$ is the thermal speed of the protons. The very large Reynolds numbers (see Table 2.2) justify the non-viscous assumption for both YSO and AGN jets. Using Ampère's law, the equation of motion becomes

$$\rho\frac{\partial\vec{v}}{\partial t}+\rho(\vec{v}\cdot\vec{\nabla})\vec{v}=\frac{1}{4\pi}(\vec{\nabla}\times\vec{B})\times\vec{B}-\vec{\nabla}P-\rho\vec{\nabla}\Phi_G \tag{2.30}$$

Gravity can be due to two terms: the attraction of the central object (black hole or star), or attraction of the plasma on itself, called self-gravity.

I seek for an estimate of the self-gravity potential compared to that of the central object (black hole or star). In the following, M is the mass of the central object (EHT et al., 2019 for AGNs) and Z_{jet} is the typical vertical length-scale of the jet (Asada and Nakamura (2012) for AGNs and Louvet et al., 2018 for YSOs). The gravitational potential at the center of a sphere of radius Z_{jet} and uniform mass density nm_p is $\Phi_S=-2\pi Gnm_pZ_{jet}^2$. The gravitational potential induced by the central object of mass M is $\Phi_*=-GM/Z_{jet}$. I thus computed the value of $nm_p/(M/Z_{jet}^3)$. Self-gravity being negligible for both types of jets, the gravitational potential is thus simply

$$\Phi_G=-\frac{GM}{R} \tag{2.31}$$

where G is the gravitational constant and R the distance to the source

This is natural, as self-gravity is already negligible in the disk, and the jet density is very small compared to that of the disk.

2.1.7 Energy equation

The exact energy equation is

$$\rho T(\frac{\partial S}{\partial t}+\vec{\nabla}\cdot(S\vec{v}))=\Gamma-\Lambda \tag{2.32}$$

where S is the specific entropy, and the entropy source $\Gamma-\Lambda$ describes the local effect of all possible heating Γ and cooling Λ terms.

The possible sources of heating are:

- Γ_{eff}, effective resistive and viscous heating
- Γ_{turb}, turbulent energy deposition

- Γ_{ext}, all external heating terms, such as protostellar UV/X-rays or cosmic rays

The possible sources of cooling are:

- Λ_{rad}, the radiative losses
- Λ_{turb}, the turbulent transport

As usually done in works on jets, I assume a polytropic equation of state

$$P = S\rho^{\Gamma} \tag{2.33}$$

where Γ is the polytropic index, varying between $\Gamma = 1$ in the isothermal case and $\Gamma = 5/3$ in the adiabatic case. This strong assumption makes the resolution of the energy equation much simpler, as there is then no need to compute Γ and Λ. The energy equation becomes

$$\frac{\partial S}{\partial t} + \vec{\nabla} \cdot (S\vec{v}) = 0 \tag{2.34}$$

Object	T(K)	n(cm^{-3})	B(G)	M(g)	R_{jet}(cm)	Z_{jet}(cm)	V_{jet}(cm.s^{-1})
AGNs	10^7	10^0	10^{-3}	10^{47}	10^{18}	10^{20}	10^{10}
YSOs	10^4	10^3	10^{-4}	10^{33}	10^{16}	10^{17}	10^7

TABLE 2.1: Typical physical conditions in AGN and YSO jets.

Object	V_{jet}/c	λ_D/R_{jet}	λ_D^{-3}/n_e	$1/(t_{jet}\omega_{ce})$	r_L/R_{jet}	$1/\mathscr{R}_m$	$(V_A/V_{jet})^2$
AGNs	1	10^{-14}	10^{-14}	10^{-9}	10^{-22}	10^{-47}	10^{-5}
YSOs	10^{-3}	10^{-13}	10^{-12}	10^{-20}	10^{-21}	10^{-40}	10^{-3}

Object	$(c_s/V_{jet})^2$	λ_{ei}/R_{jet}	λ_{en}/R_{jet}	$1/Re$	$m_p n_{jet}/(M/Z_{jet}^3)$
AGNs	10^{-7}	10^0	10^{-3}	10^{-3}	10^{-11}
YSOs	10^{-3}	10^{-4}	10^{-4}	10^{-5}	10^{-3}

TABLE 2.2: Adimensioned numbers in AGN and YSO jets.

2.2 Ideal MHD equations

We now have the full set of ideal MHD equations:

$$\frac{\partial \rho}{\partial t} + \vec{\nabla} \cdot (\rho \vec{v}) = 0 \qquad \textit{Continuity} \tag{2.35}$$

$$\rho \frac{\partial \vec{v}}{\partial t} + \rho(\vec{v} \cdot \vec{\nabla})\vec{v} = \frac{1}{4\pi}(\vec{\nabla} \times \vec{B}) \times \vec{B} - \vec{\nabla} P - \rho \vec{\nabla} \Phi_G \qquad \text{where } \Phi_G = -\frac{GM}{R} \qquad \textit{Motion} \tag{2.36}$$

$$\frac{\partial \rho S}{\partial t} + \vec{\nabla} \cdot (S \vec{v}) = 0 \qquad \text{where } S = \frac{P}{\rho^\Gamma} \qquad \textit{Energy} \tag{2.37}$$

$$\frac{\partial \vec{B}}{\partial t} = -\vec{\nabla} \times (\vec{v} \times \vec{B}) \qquad \text{where } \vec{\nabla} \cdot \vec{B} = 0 \qquad \textit{Induction} \tag{2.38}$$

Again, those equations were obtained in the non-relativistic case. There are several consequential differences to the relativistic case. In the equation of motion for instance there is an additional term due to the electric field and the inertia, then $(v/c)m$, is greater. This expected to compensate, at least partially, the confinement caused by the toroidal magnetic field (Figure 1.14), especially for high Lorentz factors. Thus, structures (such as recollimation shocks) seen in my non-relativistic simulations would be expected to appear at higher altitudes in similar GRMHD simulations. However it is not clear that those structures would appear at all, and if they do, by how much they would be displaced upwards. Consequently, comparisons between the results shown in this thesis and AGN jets can only be qualitative.

These ideal MHD equations can then easily be transformed in their conservation form

$$\frac{\partial \rho}{\partial t} + \vec{\nabla} \cdot (\rho \vec{v}) = 0 \qquad \textit{Continuity} \tag{2.39}$$

$$\frac{\partial \rho \vec{v}}{\partial t} + \vec{\nabla} \cdot \left[\rho \vec{v} \otimes \vec{v} + \left(P + \frac{B^2}{8\pi} \right) \bar{\bar{I}} - \frac{1}{4\pi} \vec{B} \otimes \vec{B} \right] = -\rho \vec{\nabla} \Phi_G \quad \text{where } \Phi_G = -\frac{GM}{R} \qquad \textit{Motion} \tag{2.40}$$

$$\frac{\partial S}{\partial t} + \vec{\nabla} \cdot (S \vec{v}) = 0 \qquad \text{where } S = \frac{P}{\rho^\Gamma} \qquad \textit{Energy} \tag{2.41}$$

$$\frac{\partial \vec{B}}{\partial t} + \vec{\nabla} \cdot (\vec{v} \otimes \vec{B} - \vec{B} \otimes \vec{v}) = \vec{0} \qquad \text{where } \vec{\nabla} \cdot \vec{B} = 0 \qquad \textit{Induction} \tag{2.42}$$

2.3 MHD waves

In a magnetized jet, several waves can transport information. To find out their properties, I will perform a linear analysis of the ideal MHD equations. For the sake of simplicity, gravity will be neglected in this section. The form of the equations better suited for this analysis is the following:

$$\frac{\partial \rho}{\partial t} + \vec{\nabla} \cdot (\rho \vec{v}) = 0 \qquad \textit{Continuity} \tag{2.43}$$

$$\rho \frac{\partial \vec{v}}{\partial t} + \rho(\vec{v} \cdot \vec{\nabla})\vec{v} = \frac{1}{4\pi}(\vec{\nabla} \times \vec{B}) \times \vec{B} - \vec{\nabla} P \qquad \textit{Motion} \tag{2.44}$$

$$\frac{\partial S}{\partial t} + \vec{\nabla} \cdot (S\vec{v}) = 0 \quad \text{where } S = \frac{P}{\rho^{\Gamma}} \qquad \textit{Energy} \tag{2.45}$$

$$\frac{\partial \vec{B}}{\partial t} = -\vec{\nabla} \times (\vec{v} \times \vec{B}) \quad \text{where } \vec{\nabla} \cdot \vec{B} = 0 \qquad \textit{Induction} \tag{2.46}$$

I consider an homogenous and static plasma with linear perturbations: $\vec{B} = \vec{B_0} + \vec{B_1}$, $\vec{v} = \vec{v_1}$, $P = P_0 + P_1$ and $\rho = \rho_0 + \rho_1$, where $|\vec{B_0}| \gg |\vec{B_1}|$, $P_0 \gg P_1$ and $\rho_0 \gg \rho_1$. The other quantities with subscript 0 are assumed constant while the perturbed quantities with subscript 1 vary in $e^{i(\vec{k}\cdot\vec{r}-\omega t)}$, with $\vec{k}$ and ω being respectively the wave vector and the wave frequency.

The ideal MHD equations then lead to:

$$\omega \rho_1 - \rho_0(\vec{k} \cdot \vec{u_1}) = 0 \tag{2.47}$$

$$\omega \rho_0 \vec{u_1} - P_1 \vec{k} + \frac{1}{4\pi}(\vec{k} \times \vec{B_1}) \times \vec{B_0} = \vec{0} \tag{2.48}$$

$$\omega \vec{B_1} - \vec{k} \times (\vec{u_1} \times \vec{B_0}) = \vec{0} \tag{2.49}$$

$$\frac{P_1}{P_0} - \Gamma \frac{\rho_1}{\rho_0} = 0 \tag{2.50}$$

Assuming $\omega \neq 0$, this yields

$$\rho_1 = \rho_0 \frac{\vec{k} \cdot \vec{v_1}}{\omega} \tag{2.51}$$

$$P_1 = P_0 \Gamma \frac{\vec{k} \cdot \vec{v_1}}{\omega} \tag{2.52}$$

$$\vec{B_1} = \frac{(\vec{k} \cdot \vec{v_1})\vec{B_0} - (\vec{k} \cdot \vec{B_0})\vec{v_1}}{\omega} \tag{2.53}$$

$$\tag{2.54}$$

Injecting those expressions into the linearized equation of motion, I obtain

$$\left[\omega^2 - \frac{(\vec{k} \cdot \vec{B_0})^2}{4\pi\rho_0}\right] \vec{v_1} = \left[\left(\frac{\Gamma P_0}{\rho_0} + \frac{B_0^2}{4\pi\rho_0}\right)\vec{k} - \frac{\vec{k} \cdot \vec{B_0}}{4\pi\rho_0}\vec{B_0}\right](\vec{k} \cdot \vec{v_1}) - \frac{(\vec{k} \cdot \vec{B_0})(\vec{v_1} \cdot \vec{B_0})}{4\pi\rho_0}\vec{k} \tag{2.55}$$

We place ourselves in cartesian coordinates (x, y, z) where z is the direction of $\vec{B_0}$ and the wave vector $\vec{k}$ lies in the $x - z$ plane. I define θ as the angle between $\vec{B_0}$ and $\vec{k}$. The problem is then reduced to the eigenvalue equation:

$$\begin{pmatrix} \omega^2 - k^2 V_A^2 - k^2 V_S^2 \sin^2\theta & 0 & -k^2 V_S^2 \sin\theta\cos\theta \\ 0 & \omega^2 - k^2 V_A^2 \cos^2\theta & 0 \\ -k^2 V_S^2 \sin\theta\cos\theta & 0 & \omega^2 - k^2 V_S^2 \cos^2\theta \end{pmatrix} \begin{pmatrix} v_1^x \\ v_1^y \\ v_1^z \end{pmatrix} = \begin{pmatrix} 0 \\ 0 \\ 0 \end{pmatrix} \tag{2.56}$$

where

$$V_A = \sqrt{\frac{B_0^2}{4\pi\rho_0}} \tag{2.57}$$

is the Alfvén speed and

$$V_S = \sqrt{\frac{\Gamma P_0}{\rho_0}} \tag{2.58}$$

is the sound speed.

Non-trivial solutions of the eigenvalue equation are obtained when the matrix determinant is zero. This yields the dispersion equation

$$(\omega^2 - k^2 V_A^2 \cos^2\theta)(\omega^4 - \omega^2 k^2 (V_A^2 + V_S^2) + k^4 V_A^2 V_S^2 \cos^2\theta) = 0 \tag{2.59}$$

This dispersion equation has three independent roots, corresponding to the three waves able to propagate through an ideal MHD plasma.

The first root is

$$\omega = k V_A \cos\theta \tag{2.60}$$

Its eigenvector being in the y direction, it is characterized by $\vec{v} \cdot \vec{B_0} = 0$ and $\vec{v} \cdot \vec{k} = 0$. From the equations above, we see that it does not perturb the density nor the pressure. This transverse wave, also orthogonal to the magnetic field, is called shear Alfvén wave.

The other two roots are

$$\omega = k V_\pm \tag{2.61}$$

where

$$V_\pm = \sqrt{\frac{1}{2}\left(V_A^2 + V_S^2 \pm \sqrt{\left(V_A^2 + V_S^2\right)^2 - 4 V_A^2 V_S^2 \cos^2\theta}\right)} \tag{2.62}$$

The first wave, associated with the root $\omega = k V_+$, is called fast-magnetosonic wave, with a phase speed $V_+ \equiv V_{FM}$. The second wave, associated with the root $\omega = k V_-$, is called slow-magnetosonic wave with a phase speed $V_- \equiv V_{SM}$. Their eigenvectors being in the $x - z$ plane, no straightforward characteristic can be derived from these general expressions. However, in a few extreme cases relevant for our jets, some properties can be derived.

For a cold plasma, in which V_S tends to zero, the slow wave disappears while the fast wave becomes an Alfvén compression wave of phase speed $V_{FM} = V_A$.

For highly magnetized plasma ($V_A \gg V_S$), the phase speed of the slow wave becomes $V_{SM} = V_S \cos\theta$ and the slow wave becomes a sound wave propagating along the magnetic field lines.

2.4 Magnetic flux

Through a contour $\mathcal{C}$ comoving with the plasma, the magnetic flux Ψ is defined by

$$\Psi \equiv \int_{\mathcal{S}} \vec{B} \cdot d\vec{\mathcal{S}} \tag{2.63}$$

where $\mathcal{S}$ is a surface spanning $\mathcal{C}$. The change of Ψ with time is due to two terms

$$\frac{d\Psi}{dt} = \int_{\mathcal{S}} \frac{\partial \vec{B}}{\partial t} \cdot d\vec{\mathcal{S}} + \int_{\mathcal{C}} \vec{B} \cdot (\vec{v} \times d\vec{\ell}) = \int_{\mathcal{S}} \frac{\partial \vec{B}}{\partial t} \cdot d\vec{\mathcal{S}} + \int_{\mathcal{C}} (\vec{B} \times \vec{v}) \cdot d\vec{\ell} \tag{2.64}$$

the first term results from the variation of the surface $\vec{\mathcal{S}}$ and the second from the motion of the contour $\mathcal{C}$. Using Maxwell-Faraday for the first term and Stokes theorem for the second term yield

$$\frac{d\Psi}{dt} = -\int_{\mathcal{S}} (\vec{\nabla} \times \vec{E}) \cdot d\vec{\mathcal{S}} + \int_{\mathcal{S}} \left(\vec{\nabla} \times (\vec{B} \times \vec{v})\right) \cdot d\vec{\mathcal{S}} = -\int_{\mathcal{S}} \left(\vec{\nabla} \times (\vec{E} + \vec{v} \times \vec{B})\right) \cdot d\vec{\mathcal{S}} \tag{2.65}$$

Using Ohm's law $\vec{E} + \vec{v} \times \vec{B} = \vec{0}$ yields

$$\frac{d\Psi}{dt} = 0 \tag{2.66}$$

This is known as the flux freezing condition: for any arbitrary contour, the magnetic flux Ψ is constant in time. This implies that magnetic field lines, defined as lines of constant magnetic flux, are moving with the plasma with the plasma: they are frozen into the plasma. Their topology is conserved with time: in ideal MHD, magnetic field lines can never break or reconnect. Similarly, magnetic flux tubes, also called magnetic surfaces, are embedded into the plasma. We can thus see jets as a multitude of magnetic surfaces anchored in the disk, nested within each other like Russian dolls, as illustrated in Figure 2.1.

2.5 Axisymmetry and stationarity

In all the following, I use the cylindrical coordinates (r, φ, z) and spherical coordinates (R, θ, φ), with the disk midplane is at $z = 0$ or $\theta = \pi/2$ and the jet axis at $r = 0$ or $\theta = 0$. In both geometries, the toroidal direction is along $\vec{u_\varphi}$ and the poloidal planes are orthogonal to that direction.

I further assume axisymmetry along the jet axis, and thus invariance along $\vec{u_\varphi}$. All developments will be made in the poloidal plane $\varphi = 0$. In addition, quantities with a subscript p are computed in the poloidal plane.

The magnetic flux is then equal to $\Psi = 2\pi r A_\varphi$ were A_φ is the φ-component of the magnetic vector potential $\vec{A}$ defined by $\vec{B} = \vec{\nabla} \times \vec{A}$. I assume that the outflow is stationary, and the magnetic flux Ψ is constant along any magnetic field line or magnetic surface.

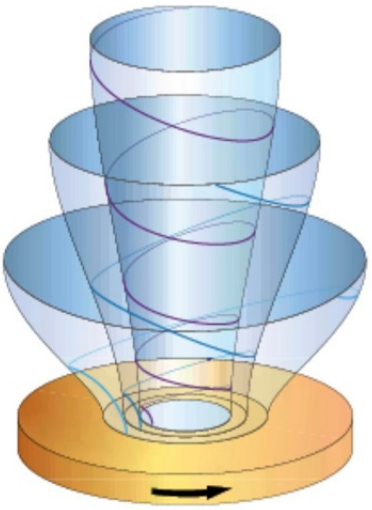

FIGURE 2.1: Axisymmetric jet composed of multiple magnetic surfaces (in blue) anchored in rotating disk (in orange)

2.6 Invariants and dynamics of steady flows

On top of the magnetic flux Ψ, a steady-state magnetic surface is characterized by five other quantities, called MHD invariants:

- The mass flux to magnetic flux ratio $\eta(\Psi) = 4\pi\rho v_p / B_p$.
- The rotation rate of the magnetic surface $\Omega_*(\Psi) = v_\varphi / r - \eta B_\varphi / (4\pi\rho r)$.
- the total specific angular momentum carried away by that surface $L(\Psi) = v_\varphi r - r B_\varphi / \eta$.
- The Bernoulli invariant $E(\Psi) = \frac{v^2}{2} + H + \Phi_G - \Omega_* r B_\varphi / \eta$.
- The specific entropy $S(\Psi) = P/\rho^\Gamma$.

Those invariants, constant on a magnetic field along the whole, can be imposed at their source as a boundary condition. This source where the invariants are set can be either the disk in the case of a disk jet, or central object in the case of a stellar or black hole jet. Changes from model to model or simulation to simulation will be the values and profiles of those invariants, along the central object or the disk. But first, let us derive the five MHD invariants.

2.6.1 MHD invariants

According to Ohm's law, $\vec{E} + \vec{v} \times \vec{B} = \vec{0}$, thus $E_\varphi = -\vec{v_p} \times \vec{B_p}$. With $\vec{A}$ and V being respectively the vector potential and the electric potential, we derive $\vec{E} = -\vec{\nabla} V - \frac{\partial \vec{A}}{\partial t}$ and thus $E_\varphi = -\frac{1}{r}\frac{\partial V}{\partial \varphi} - \frac{\partial A_\varphi}{\partial t}$. Axisymmetry and time-invariance lead to $E_\varphi = 0$. Thus $\vec{v_p}$ and $\vec{B_p}$ are colinear and

$$\vec{v_p} = l\vec{B_p} \tag{2.67}$$

Mass conservation then gives

$$\vec{\nabla} \cdot (\rho \vec{v_p}) = \vec{\nabla} \cdot (l\rho \vec{B_p}) = \vec{B_p} \cdot \vec{\nabla}(l\rho) + l\rho \vec{\nabla} \cdot \vec{B_p} = \vec{B_p} \cdot \vec{\nabla}(l\rho) = 0 \tag{2.68}$$

Thanks to the divergence condition on the magnetic field, $\eta \equiv 4\pi l\rho$ is invariant along a magnetic surface so that

$$\vec{v_p} = \frac{\eta}{4\pi\rho}\vec{B_p} \tag{2.69}$$

The mass flux at an altitude z between r and $r + dr$ is

$$d\dot{M}_{jet} = 2\pi r\rho v_z dr = \frac{\eta}{2} r B_z dr = \frac{\eta}{2}\frac{\partial\Psi}{\partial r}dr \tag{2.70}$$

η can thus be interpreted as the mass flux to magnetic flux ratio:

$$\eta = 2\frac{d\dot{M}_{jet}}{d\Psi} \tag{2.71}$$

Projected along the toroidal direction, the induction equation gives in cylindrical coordinates

$$\frac{\partial}{\partial z}\left(v_\varphi B_z - v_z B_\varphi\right) - \frac{\partial}{\partial r}\left(v_r B_\varphi - v_\varphi B_r\right) = \vec{\nabla}\cdot\frac{1}{r}\left(v_\varphi\vec{B_p} - B_\varphi\vec{v_p}\right) = 0 \tag{2.72}$$

Using the η invariant, I get

$$\vec{B_p}\cdot\vec{\nabla}\left(\frac{\eta B_\varphi}{4\pi\rho r} - \frac{v_\varphi}{r}\right) = 0 \tag{2.73}$$

I can define the invariant

$$\Omega_* \equiv \frac{v_\varphi}{r} - \frac{\eta B_\varphi}{4\pi\rho r} \tag{2.74}$$

Ω_* is a measure of the angular velocity of the magnetic field lines.

Projected along the toroidal direction, the equation of motion gives in cylindrical coordinates

$$\begin{aligned}\rho\vec{v}\cdot\vec{\nabla}u_\varphi &= \frac{1}{4\pi}\left(B_z\frac{\partial B_\varphi}{\partial z} + \frac{B_r}{r}\frac{\partial r B_\varphi}{\partial r}\right)\\ \frac{\rho}{r}\vec{v_p}\cdot\vec{\nabla}(ru_\varphi) &= \frac{1}{4\pi r}\vec{B_p}\cdot\vec{\nabla}(rB_\varphi)\end{aligned} \tag{2.75}$$

I derive

$$\vec{\nabla}\cdot\left(\rho r v_\varphi\vec{v_p} - \frac{rB_\varphi}{4\pi}\vec{B_p}\right) = \vec{0} \tag{2.76}$$

Using the η invariant, this gives

$$\vec{B_p}\cdot\vec{\nabla}\left(rv_\varphi - \frac{rB_\varphi}{\eta}\right) \tag{2.77}$$

I can then define the invariant

$$L \equiv rv_\varphi - \frac{rB_\varphi}{\eta} \tag{2.78}$$

It is the specific angular momentum, that consists in two parts: the classical kinetic part, and the magnetic part from the toroidal magnetic field.

To derive the energy invariant, I project the equation of motion along the poloidal velocity $\vec{v_p}$

$$\vec{v_p} \cdot \left((\vec{v} \cdot \vec{\nabla})\vec{v} + \frac{1}{\rho}\vec{\nabla}P + \vec{\nabla}\Phi_G \right) = \frac{1}{4\pi\rho}\vec{v_p} \cdot (\vec{\nabla} \times \vec{B}) \times \vec{B} \tag{2.79}$$

Using $(\vec{v} \cdot \vec{\nabla})\vec{v} = (\vec{\nabla} \times \vec{v}) \times \vec{v} + \frac{1}{2}\vec{\nabla}v^2$ I get

$$\vec{v_p} \cdot \vec{\nabla}(H + \Phi_G + \frac{v^2}{2}) = \frac{1}{4\pi\rho}\vec{v_p} \cdot (\vec{\nabla} \times \vec{B}) \times \vec{B} \tag{2.80}$$

where $H = \int \frac{1}{\rho}\vec{\nabla}P \cdot \vec{ds}$ is the enthalpy integrated over a field line, as there is no heating nor cooling term. I get

$$\frac{1}{4\pi\rho}\vec{v_p} \cdot (\vec{\nabla} \times \vec{B}) \times \vec{B} = \frac{\Omega_*}{4\pi\rho} \cdot \vec{\nabla}(rB_\varphi) = \frac{1}{4\pi\rho}\vec{B_p} \cdot \vec{\nabla}(\Omega_* r B_\varphi) = \vec{v_p} \cdot \vec{\nabla}\left(\frac{\Omega_* r B_\varphi}{\eta}\right) \tag{2.81}$$

Thus

$$\vec{v_p} \cdot \vec{\nabla}\left(\frac{v^2}{2} + H + \Phi_G - \frac{\Omega_* r B_\varphi}{\eta}\right) = 0 \tag{2.82}$$

The Bernoulli invariant is then defined as

$$E \equiv \frac{v^2}{2} + H + \Phi_G - \frac{\Omega_* r B_\varphi}{\eta} \tag{2.83}$$

It is the specific energy carried along a magnetic field line.

Finally, the energy equation directly implies that the specific entropy S is an invariant.

2.6.2 Critical points in ideal MHD

In section 2.3 we have seen the three types of waves can propagate in an ideal MHD flow: the slow-magnetosonic wave of speed V_{SM}, the Alfvén wave of speed V_{A_p} and the fast-magnetosonic wave of speed V_{FM}, with $V_{SM} < V_{A_p} < V_{FM}$. The flow becomes stationary if and only if its velocity is greater than the phase speeds of all these waves. A steady flow thus has to cross three critical surfaces, defined for each wave as the surface of mach number equal to one. The radii at which these crossings occur are noted respectively r_{SM}, r_A and r_{FM}. They are illustrated in Figure 2.2.

The critical Alfvén speed relevant for the flow is the poloidal alfvén speed:

$$V_{A_p} = \sqrt{\frac{B_p^2}{4\pi\rho}} \tag{2.84}$$

And the slow-magnetosonic and fast-magnetosonic speeds are respectively:

$$V_{SM} = \sqrt{\frac{1}{2}\left(V_A^2 + V_S^2 - \sqrt{\left(V_A^2 + V_S^2\right)^2 - 4V_{A_p}^2 V_S^2}\right)} \tag{2.85}$$

$$V_{FM} = \sqrt{\frac{1}{2}\left(V_A^2 + V_S^2 + \sqrt{\left(V_A^2 + V_S^2\right)^2 - 4V_{A_p}^2 V_S^2}\right)} \tag{2.86}$$

with $V_A = \sqrt{\frac{B^2}{4\pi\rho}}$ being the total Alfvén speed of the flow, poloidal and toroidal.

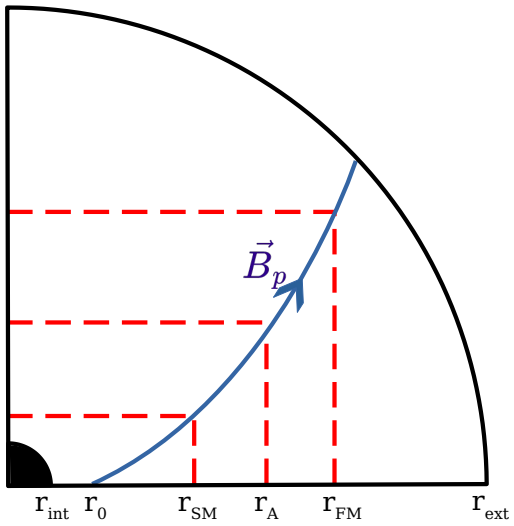

FIGURE 2.2: The Jet-Emitting Disk extends from an inner radius r_{int} to an outer radius r_{ext}. The magnetic field line, launched from the radius r_0, crosses at maximum three critical surfaces: super-slow at $r = r_{SM}$, Alfvén at $r = r_A$ and super-fast at $r = r_{FM}$.

The presence of a critical point produces an additional constraint, thus introducing an additional relation between the problem parameters. In practice, each magnetic field line anchored in the disk will cross the three aforementioned critical points or less, depending on the ejection conditions and on the speeds reached on the field line. Each crossing of a critical point requires to let a parameter free at the ejection, to avoid over-constraining the problem. Which parameters are free and fixed in our setup will be detailed in the following chapter.

Each of these three critical points is associated with a physical characteristic of the problem:

- The slow-magnetosonic constraint sets the mass flux emitted from the disk: a high jet mass flux lowers this point and brings it closer to the disk, while a low ejected mass brings it higher in the flow.
- The Alfvén constraint sets the angular momentum of the flow. The value of the MHD invariant being $L = \Omega_* r_A^2$, where Ω_* is a MHD invariant and r_A the jet radius where $v_p = V_{A_p}$, setting the value of V_{A_p} sets the value of L.
- The fast-magnetosonic constraint finally sets the total energy E of the flow (see e.g. Camenzind, 1986).

2.6.3 Asymptotic speeds

These critical surfaces are crossed in the first acceleration/collimation phase of the flow (see section 1.3.4). The jet has already become super-FM at the largest observable scales, where it is most collimated. There, it its maximal asymptotic speed v_∞ (see Figure 1.15).

How does this asymptotic speed depend on the ejection parameters ? Let us introduce the parameter g, defined by Pelletier and Pudritz, 1992 as $\Omega = \Omega_*(1 - g)$

and thus measuring the difference between the plasma rotation and the rotation of the magnetic field lines. It can be expressed as

$$g = \frac{m^2}{m^2 - 1}\left(1 - \frac{r_A^2}{r^2}\right) \tag{2.87}$$

This parameter is close to zero on the disk. At high altitudes, it rises to unity for highly super-Alfvénic ($m^2 \gg 1$) and highly collimated ($r \gg r_A$) jets. On a specific field line, the Bernoulli invariant becomes equal to the kinetic energy $E \simeq v_\infty^2/2$ and the poloidal asymptotic speed becomes

$$v_\infty \simeq \sqrt{2E} \tag{2.88}$$

This is a very generic result that dates back to Weber and Davis, 1967. It does not require any specific profile at launch. It simply says that in steady-state ideal MHD, the asymptotic speed of a highly super-Alfvénic and collimated jet is dictated by the Bernoulli invariant. As this Bernoulli invariant can be fixed at launch (on the disk or on the central object), the ejection conditions set the asymptotic jet speed.

2.6.4 The self-similar approximation

Unfortunately, not all results can be this generic, even though we have made quite a few approximations to obtain the ideal MHD equations. These equations remain heavy to solve with ordinary methods. The common method used to find solutions to axisymmetric ideal MHD flows is the separation of variables, searching for solutions of the form:

$$X = X_0 R^{\zeta_X} f_X(\theta) \tag{2.89}$$

One key assumption here is a power-law dependency with the spherical radius R, giving the property of scale invariance to the solution. Such an approach is known as the radially **self-similar ansatz**. Its justification relies on the expression of the gravitational potential. Since gravity is the main energy reservoir in accretion-ejection, it is indeed natural to expect the other quantities to follow a similar scaling.

I define the parameter $\alpha \equiv \zeta_\Psi$ as the radial exponent of the magnetic flux: $\Psi \propto R^\alpha$. The seminal paper of Blandford and Payne, 1982 corresponds to the case $\alpha = 3/4$. In our approach, all other radial exponents are expressed using this α parameter, as shown in Table 2.3.

Parameter X	Ψ	ρ	P	u_R	u_θ	u_φ	B_R	B_θ	B_φ
Exponent ζ_X	α	$2\alpha - 3$	$2\alpha - 4$	$-1/2$	$-1/2$	$-1/2$	$\alpha - 2$	$\alpha - 2$	$\alpha - 2$

TABLE 2.3: Values of the radial exponents ζ_X in $X \propto R^{\zeta_X}$ for the radially self-similar ansatz.

2.6.5 Parameter space

The importance of the ejection parameter ξ was already mentioned in the introduction. It is defined as the radial exponent of the mass flux $\dot{M}_{acc}(r) \equiv -4\pi \int_0^{h(r)} \rho u_r dz \propto r^\xi$, where $h(r)$ is the disk height at the radius r (Ferreira and Pelletier, 1995). This ejection index is linked to the α parameter through:

$$\alpha = \frac{3}{4} + \frac{\xi}{2} \tag{2.90}$$

This relation induces a few constraints on the values the self-similar parameter α can take. As material is only outflowing from the disk and not inflowing, $\xi > 0$. Moreover, there are no stationary super-SM self-similar solutions for $\xi \geq 1$. This gives the constraint $0 < \xi < 1$, thus $3/4 < \alpha < 5/4$.

In the continuation of Blandford and Payne, 1982, let us introduce a few relevant jet parameters, where the subscript 0 means that the quantity value is taken at its anchoring point in the disk, and the subscript A means that the quantity value is taken on the Alfvén surface.

$$\lambda \equiv \frac{\Omega_* r_A^2}{\Omega_0 r_0^2} \simeq \frac{r_A^2}{r_0^2} \simeq 1 - \frac{B_{\varphi_0}}{\eta \Omega_0 r_0} \tag{2.91}$$

This λ parameter is the magnetic arm lever, braking down the disk. It is the normalized specific angular momentum (i.e. the MHD invariant L). It also yields another expression of the asymptotic speed (equation 2.88) of highly super-Alfvénic and collimated jets

$$v_\infty = \sqrt{2\lambda - 3} V_{K_d} \tag{2.92}$$

where $V_{K_d} = \Omega_o r_o$ is the Keplerian rotation speed at the anchoring point of the field line, meaning the magnetic field surfaces closest to the polar axis are also the ones with the highest asymptotic poloidal speeds.

Blandford and Payne, 1982 also introduced the well-known κ parameter, constant in their solutions:

$$\kappa \equiv \eta \frac{\Omega_0 r_0}{B_0} \simeq \frac{4\pi \Omega_0 r_0}{B_0^2} \rho_0 u_{z_0} \tag{2.93}$$

This κ parameter measures the mass load by the disk on a specific magnetic surface.

Those two parameters λ and κ can be approximated via the ejection efficiency ξ, and thus the α parameter (see e.g. Ferreira, 1997):

$$\lambda \simeq 1 + \frac{1}{2\xi} \tag{2.94}$$

$$\kappa \simeq \xi \tag{2.95}$$

The magnetic lever arm can be expressed as $\lambda = 1 + q/\kappa$, where $q = |B_\varphi / B_z|$ is the magnetic shear at launch, found close to unity in self-similar jets. The exact link between α, λ and κ depends on the solution. Figure 2.3 displays those relations for the solutions of Blandford and Payne, 1982.

There are a few restrictions on what solutions are able to provide collimated super-Alfvénic flows. First, only in solutions with high enough $\kappa\lambda \left(2\lambda - 3\right)^{1/2}$ does the flow eventually become super-Alfvénic. Thus, the parameter $\beta \equiv \kappa \left(2\lambda - 3\right)^{3/2}$ should be larger than unity, but not to large, otherwise the centrifugal force would be too large for the magnetic field to collimate the flow. Then, for the flow to be magnetically dominated, at least at launch, the parameter κ needs to be smaller than unity. However, recently Jacquemin-Ide, Ferreira, and Lesur, 2019 showed that it is

possible to launch super-Alfvénic and lowly magnetized jets with κ up to ten (see their Figure 4).

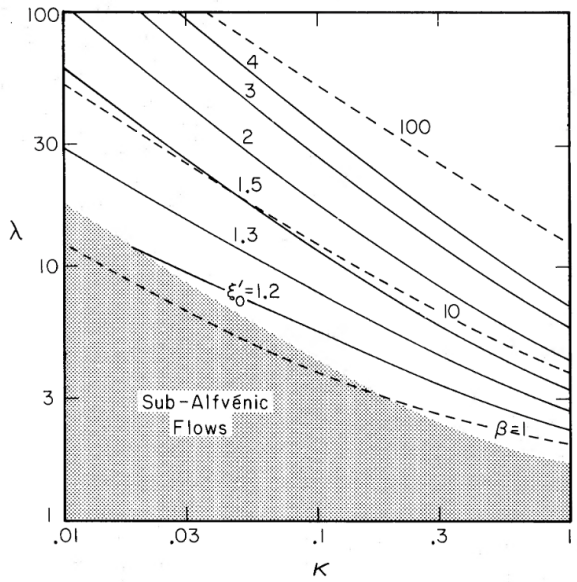

FIGURE 2.3: Values of λ and κ for the solutions of Blandford and Payne, 1982. The parameter $\xi_0' \equiv B_r/B_z$ is the inclination of the magnetic field lines on the disk surface. The parameter $\beta \equiv \kappa\,(2\lambda-3)^{3/2}$ relates to the asymptotic collimation of the solution.

2.6.6 Electric circuits and collimation

How can a magnetically-dominated jet be collimated ? In plasma physics, there are two complementary mechanisms can confine a flow towards its axis. In both mechanisms, the plasma is threaded by the associated magnetic field $\vec{B}$ and electric current $\vec{j}$. They are illustrated in Figure 2.4.

- In the z-pinch mechanism, the electric current $\vec{j}$ is axial and the magnetic field $\vec{B}$ is toroidal. This is the tension effect, or hoop-stress.
- In the θ-pinch mechanism, the magnetic field $\vec{B}$ is axial and the electric current $\vec{j}$ is toroidal. This is the radial gradient of the poloidal magnetic pressure.

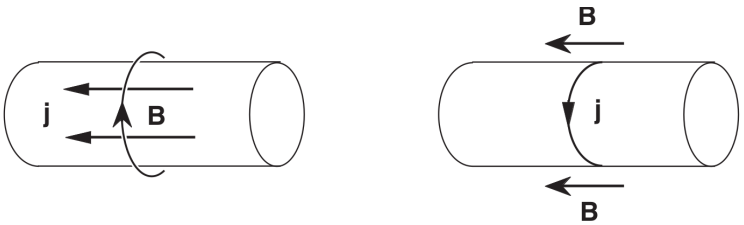

FIGURE 2.4: Illustration of the pinching mechanisms (Goedbloed and Poedts, 2004). Left: Z-pinch mechanism. Right: θ-pinch mechanism.

For both cases, the result is the same: a Laplace force $\vec{j} \times \vec{B}$ that is radial and directed towards the axis, thus achieving confinement. In fusion experiments, an

external electric current is applied, creating the associated magnetic field. In astrophysical jets, it is the opposite: the magnetic field emitted from the disk induces an electric circuit.

Is this circuit created by the poloidal or the toroidal magnetic field ? In steady state ideal MHD, both integrated intensity rB_φ and flux $\pi r^2 B_z$ are conserved along a flux tube. This leads to different power laws variations for the two components: $B_\varphi \propto 1/r$ and $B_z \propto 1/r^2$. As the amplitude of the poloidal magnetic field decreases with altitude much faster than the amplitude of the toroidal magnetic field, the toroidal field becomes dominant early in the jet. Moreover, the differential rotation induces a negative toroidal magnetic field, along $-\vec{u_\varphi}$. Thus, in order to create a confining z-pinch, the electric current needs to be along $-\vec{u_z}$, directed towards the central object or the disk. Here, I assume the presence of preexistent vertical magnetic field lines at the vicinity of the disk, as in situation A of Figure 1.14. This field is maintained by toroidal current in the disk.

How are the self-similar solutions confined ? A negative electric current $I_{axis} < 0$ is transported along the axis and enters the disk at its inner radius r_{int}. The total current emitted from the jet is

$$I_{jet} = \int_{r_{int}}^{r_{ext}} 2\pi r J_z dr = I_{axis}\left[1 - \left(\frac{r_{int}}{r_{ext}}\right)^{1-\alpha}\right] \tag{2.96}$$

We see that there are three possible cases, illustrated in Figure 2.5

- For $\alpha < 1$ (left handside of Figure 2.5), the disk-emitted jet transports a positive current. As the circuits close on $r = r_{int}$, only the innermost parts of the jet are confining.
- For $\alpha = 1$, the disk-emitted jet does not transport any current as $I_{jet} = 0$ and the jet is only confined by the current on the axis, that should close in an external cocoon beyond r_{ext}.
- For $\alpha > 1$ (right handside of Figure 2.5), the disk-emitted jet transports a negative current. As the circuits close on $r = r_{ext}$, the jet is self-confined in its entirety, the positive return current being transported by an external cocoon.

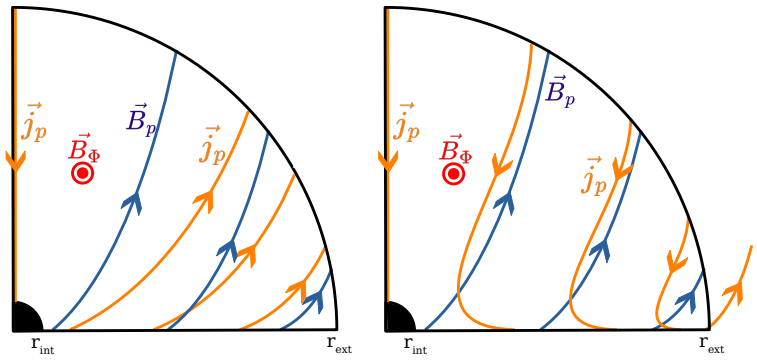

FIGURE 2.5: Electric circuits over a Jet-Emitting disk, for an α parameter lower than unity (left) and greater than unity (right).

In all cases, the current closure condition $\vec{\nabla} \cdot \vec{j}$ imposes the presence of an external anticollimated zone with a positive current. A globally collimated jet is beyond the reach of the self-similar solutions, as the two configurations of Figure 2.5 cannot be described by a single power law.

2.6.7 Jet transverse equilibrium

The force balance in the poloidal plane is described by the transfield equation (Hu and Low, 1989). Projected orthogonally to the field lines, it gives (Ferreira, 1997)

$$(1-m^2)\frac{B_p^2}{4\pi\mathcal{R}} - \nabla_\perp\left(P+\frac{B^2}{8\pi}\right) - \rho\nabla_\perp\Phi_G + \left(\rho\Omega^2 r - \frac{B_\varphi^2}{4\pi r}\right)\nabla_\perp r = 0 \qquad (2.97)$$

where $m^2 \equiv \frac{v_p}{V_{A_p}}$ is the poloidal Alfvénic mach number squared, $\nabla_\perp \equiv \frac{\vec{\nabla}\Psi\cdot\vec{\nabla}}{|\vec{\nabla}\Psi|}$ is the gradient perpendicular to a magnetic surface and $\mathcal{R}$ is the local curvature radius of the magnetic surface, positive when bent inwards and negative when bent outwards.

This equation provides the transverse equilibrium of the jet. The first term describes both the magnetic tension of the field lines and inertia, the other forces being the pressure gradient, gravity, and the competing centrifugal force and hoop stress. These last two terms are respectively the two main decollimating and collimating forces in the jet.

2.7 Discontinuities

Ultimately, the collimation of the jet at the largest scales is set by the value of the asymptotic current I_∞. For instance, we saw in section 1.3.5 that the absence of such a current ($I_\infty = 0$) could explain the conical shape of the M87 jet past the HST-1 knot. Whatever the value of the asymptotic current, it should be separated from the accelerating current connected to source by a recollimation shock, as sketched in Figure 1.17. According to the self-similar solutions (Ferreira, 1997; Jacquemin-Ide, Ferreira, and Lesur, 2019), this recollimation shock would occur at large distances, beyond 10^2 astronomical units for a YSO jet or 10^3 Schwarzchild radii for an AGN jet. The left panel of Figure 2.6 shows a specific configuration, prolongation of a self-similar solution with an asymptotically collimated jet, meaning $I_\infty \neq 0$. In blue is a magnetic surface, symmetrization of a poloidal magnetic field line around the jet axis. The jet initially widens, then recollimates. At the recollimation shock, the surface is refracted, then stays collimated in a cylinder because of the return current $I_\infty \neq 0$. The recollimation shock is displayed in orange. In the self-similar ansatz, this is a cone whose apex is the central object (black hole or star).

In the numerical simulations presented in this thesis, the recollimation shocks act as a separatrix between the accelerating current and the asymptotic current. Before delving into the simulations and seeing how the numerical shocks behave, let us see what is expected from the theory.

One of the applications of the MHD conservation equations is the derivation of shock conditions. In hydrodynamics, such a discontinuity is associated with a transition from a subsonic flow upstream to a supersonic flow downstream (Hugoniot, 1887, 1888; Rankine, 1870). The ideal MHD problem is much richer, as there are three characteristic speeds. The geometry of the jet and recollimation shock is described in the right panel of Figure 2.6. I consider a 2.5D jet, thus axisymmetrical around its Oz axis, and study a standing shock that remains stationary in the lab frame. Therefore, no system of coordinates is required to move with the shock front.

I write the Rankine-Hugoniot jump conditions valid for standing, adiabatic recollimation shocks. Contrary to Ouyed and Pudritz, 1993, I take account the toroidal magnetic field into account, as the shocks happen when that component is dominant.

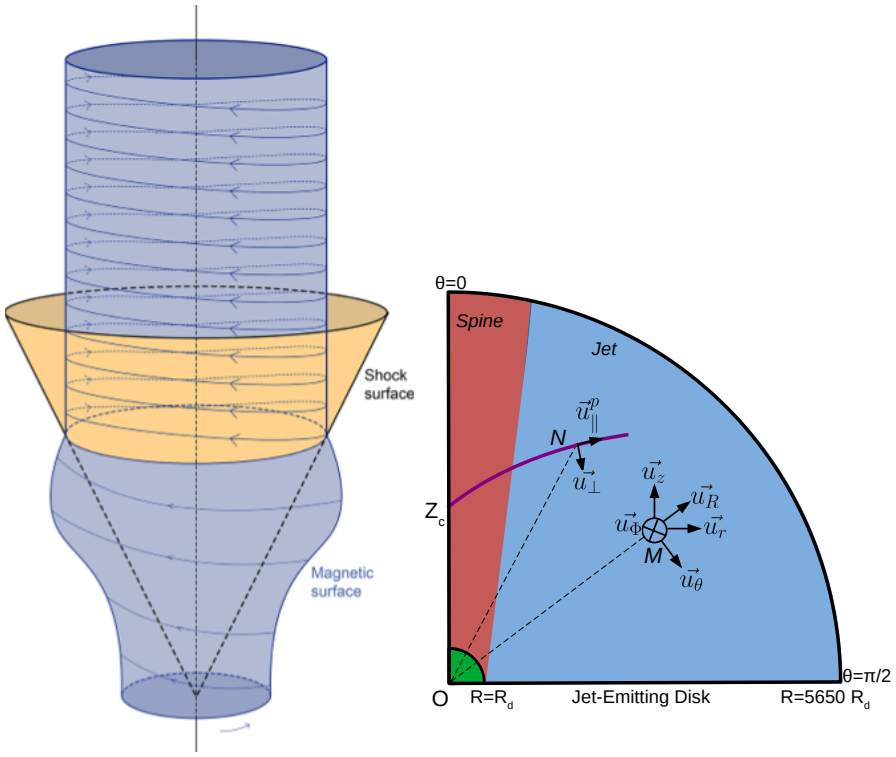

FIGURE 2.6: Structure of MHD recollimation shocks. Left: 3D structure in the self-similar approach. The shock is displayed in orange. It is a cone, whose apex is the central object (black hole or star). Right: Geometry of the 2.5D recollimation shocks. In green in the central object. It emits an axial spine, in red. The Jet-Emitting Disk is at the lower boundary, between R_d and R_{ext} at $\theta = \pi/2$. The solid purple line represents a recollimation shock surface starting on the axis at a height Z_c. For each point N lying on this surface, I use local poloidal unit vectors $(\vec{u}_\perp, \vec{u}^p_\parallel)$, respectively perpendicular and parallel to the shock surface. Also, at any point M inside the domain, I either use spherical $(\vec{u}_R, \vec{u}_\theta, \vec{u}_\varphi)$ or cylindrical $(\vec{u}_r, \vec{u}_\varphi, \vec{u}_z)$ coordinates.

The local jumps $[A] = A_2 - A_1$ between a pre-shock quantity A_1 and its post-shock value A_2 are expressed in the rest frame of the shock as

$$\begin{aligned}
[\rho v_\perp] &= 0 \\
[\rho v_\perp (\frac{v^2}{2} + H) + \frac{B^2}{4\pi} v_\perp - \frac{\vec{v}\cdot\vec{B}}{4\pi} B_\perp] &= 0 \\
[P + \rho v_\perp^2 + \frac{B_\parallel^2 - B_\perp^2}{8\pi}] &= 0 \\
[\rho v_\perp v_\parallel - \frac{B_\perp}{\mu_o} B_\parallel] &= 0 \\
[B_\perp] &= 0 \\
[B_\perp v_\parallel - v_\perp B_\parallel] &= 0,
\end{aligned} \tag{2.98}$$

where $H = V_s^2/(\Gamma - 1)$ is the enthalpy and $v_\perp, B_\perp$ (respectively $\vec{v}_\parallel, \vec{B}_\parallel$) are the normal (respectively tangential) components to the shock surface. The shock is axisymmetric, so that the tangential component (e.g. parallel to the shock) of the

magnetic field is $\vec{B}_\parallel = B^p_\parallel \vec{u}^p_\parallel + B_\varphi \vec{u}_\varphi$, whereas the poloidal component is $\vec{B}_p = B^p_\parallel \vec{u}^p_\parallel + B_\perp \vec{u}_\perp$, with the unit vectors $(\vec{u}_\perp, \vec{u}^p_\parallel, \vec{u}_\varphi)$ defining a local direct orthonormal coordinate system. As these jump conditions express the conservation of mass, angular momentum and energy in ideal MHD, the five MHD invariants along a given magnetic surface $(\eta, \Omega_*, L, E, S)$ are therefore also conserved.

A shock corresponds to $\rho u_\perp \neq 0$ with $B_\perp \neq 0$. The Rankine-Hugoniot conditions give

$$\vec{B}_{\parallel 2} = \frac{m^2 - 1}{m^2/\chi - 1} \vec{B}_{\parallel 1} \tag{2.99}$$

which shows that the two tangential magnetic field components remain parallel through the discontinuity. Three discontinuities can be derived from this equation:

- Oblique shock for $m^2 > \chi > 1$.
- Normal shock for $m^2 = \chi > 1$.
- Alfvén shear discontinuity for $m^2 = \chi = 1$.

In this section, I will only focus on the case $m^2 > \chi > 1$. After some algebra, all post-shock quantities (region 2) can be expressed as a function of the pre-shock ones (region 1). In particular

$$\begin{aligned}
\frac{B_{\varphi 2}}{B_{\varphi 1}} &= \frac{B^p_{\parallel_2}}{B^p_{\parallel_1}} = \chi \frac{m^2 - 1}{m^2 - \chi} \\
\frac{v_{\varphi 2}}{v_{\varphi 1}} &= \frac{m^2 - 1}{m^2 - \chi} \frac{m^2 r_A^2 - \chi r^2}{m^2 r_A^2 - r^2} \\
\frac{P_2}{P_1} &= 1 + \Gamma m_s^2 (\chi - 1) \left(\frac{1}{\chi} + \frac{b^2}{2} \frac{2\chi - m^2(1+\chi)}{(\chi - m^2)^2} \right) \\
\frac{T_2}{T_1} &= \frac{1}{\chi} \frac{P_2}{P_1},
\end{aligned} \tag{2.100}$$

where the sonic Mach number $m_s = v_\perp / V_s$ and magnetic shear $b^2 = (B_\parallel / B_\perp)^2$ are computed in the pre-shock region. Of particular interest are the relative variations of the toroidal magnetic field component $\delta B_\varphi = B_{\varphi_2}/B_{\varphi_1} - 1$ and the plasma angular velocity $\delta\Omega = \Omega_2/\Omega_1 - 1$, as well as the total deflection angle of the poloidal magnetic surface $\delta i = i_2 - i_1$ where $\tan i = B^p_\parallel / B_\perp$:

$$\begin{aligned}
\delta B_\varphi &= (\chi - 1) \frac{m^2}{m^2 - \chi} \\
-\delta\Omega &= \frac{\chi - 1}{m^2 - \chi} \frac{m^2 (r^2 - r_A^2)}{m^2 r_A^2 - r^2} \leq \frac{\chi - 1}{m^2 - \chi} \\
\tan \delta i &= \frac{m^2 (\chi - 1)}{m^2 - \chi} \frac{\tan i_1}{1 + \chi \tan^2 i_1 \frac{m^2 - 1}{m^2 - \chi}}.
\end{aligned} \tag{2.101}$$

Before delving further into the resolution, a few remarks can be made on the properties of the post-shock region. For a highly super-Alfvénic jet ($m^2 \gg 1$), we have $0 < -\delta\Omega \lesssim (\chi - 1)/m^2$ which is small. The shock should thus slow down the

jet rotation, but only slightly. Then, as a shock corresponds to $\chi > 1$, we have $\delta B_\varphi \simeq \chi - 1 > 0$. The shock should thus increase the current intensity $I = -rB_\varphi$. In the inner regions, the post-shock region should be more collimating than the pre shock region. Naturally, this has to be put in perspective with the outwards refraction of the poloidal magnetic field lines at the shock.

Let us now go back to the resolution. The compression rate χ is the solution of the cubic polynomial equation

$$-A\chi^3 + B\chi^2 - C\chi + D = 0 \tag{2.102}$$

with

$$\begin{aligned} A &= 1 + b^2 + \frac{1+\chi_o}{\Gamma m_s^2} \\ B &= \chi_o(1+b^2) + 2m^2\left(1 + \frac{1+\chi_o}{\Gamma m_s^2} - b^2\frac{\chi_o - 3}{4}\right) \\ C &= m^2\left(2\chi_o + b^2\frac{1+\chi_o}{2} + m^2\left(1 + \frac{1+\chi_o}{\Gamma m_s^2}\right)\right) \\ D &= \chi_o m^4, \end{aligned}$$

where $\chi_o = (\Gamma+1)/(\Gamma-1)$ is the maximal compression rate for a hydrodynamic shock. Equation 2.102 has one positive root only for an incoming super-FM flow, namely for $n_\perp = v_\perp / V_{FM_\perp}$ larger than unity.

This is a hefty equation that can be simplified for supersonic ($m_s \gg 1$) and super-Alfvénic ($m \gg 1$) cold jets, where the dominant magnetic field is the toroidal one ($b^2 \simeq (B_\varphi/B_\perp)^2 \gg 1$). The fast-magnetosonic Mach number in the normal direction therefore writes $n_\perp \simeq mV_{Ap,\perp}/V_{A\varphi} = m/b$, which leads to the simplified equation for χ

$$\frac{\chi_o - 3}{2}\chi^2 + \left(\frac{1+\chi_o}{2} + n_\perp^2\right)\chi - \chi_o n_\perp^2 = 0\,. \tag{2.103}$$

This shows that whenever the jets reach a very large fast-magnetosonic Mach number $n_\perp$, compression rates close to the hydrodynamical case χ_o are possible.

2.8 Summary

In this chapter, I have shown that the equations of non-relativistic ideal MHD are applicable to both black hole and protostellar jets, with a few reserves. Then, I defined and derived the MHD invariants, that, with the magnetic flux, can be followed along a field line from the launching conditions until the asymptotic regions. I also drew a few properties of the jet asymptotics and collimation, both generic and restricted to the self-similar approach. Finally, I derived the phase speeds of the three waves that can propagate in ideal MHD. I highlighted the requirements they bring to the formation of a steady state ideal MHD jet, and derived the Rankine-Hugoniot jump conditions for a fast-magnetosonic oblique shock.

The knowledge of these points was required to design the numerical setup used to produce the simulations. They will also be useful in understanding the simulation results. I will now move on to the bulk of the thesis. In the next chapter, I will describe the MHD code and the setup used to produce the simulated jets. The following chapters will then be dedicated to the description and analysis of the numerical simulations.

Chapter 3

Numerical framework

Contents

3.1 The PLUTO code 59
3.1.1 Finite volume methods 60
3.1.2 Constrained transport 60
3.1.3 Riemann solvers 62
3.1.4 Godunov scheme 63
3.1.5 CFL condition and acceleration scheme 64
3.1.6 Accounting 66
3.2 Numerical setups 67
3.2.1 Simulation domain and grid 67
3.2.2 Initial conditions 69
3.2.3 Boundary conditions 69
Causality and number of parameters 70
Jet-Emitting Disk: $\theta = \pi/2$ 70
Central object: $R = R_d$ 72
3.2.4 Normalization 73

"Poco portäi in là volta la testa,
che me parve veder molte alte torri;
ond'io : «Maestro, di', che terra è questa ? »
Ed elli a me : «Però che tu trascorri
per le tenebre troppo da la lungi,
avvien che poi nel maginare abborri.
Tu vedrai ben, se tu là ti congiungi,
quanto 'l senso s'inganna di lontano ;
però alquanto più te stesso pungi.»"

"À peine avais-je tourné la tête vers ce côté
que je crus voir plusieurs très hautes tours ;
et moi : «Maître, dis-moi, quelle est cette cité ? »
Il répondit : «Lorsque ta vue
veut pénétrer trop loin dans les ténèbres,
il advient qu'en imaginant tu t'égares.
Tu verras bien, si tu arrives jusque-là,
combien les sens y sont trompés par la distance ;
tâche de presser un peu le pas.»"

"No sooner had I turned my head this way
I thought I saw several very high towers ;
And I said, «Master, tell me, what is this city ? »
He answered: «When your sight
wants to penetrate too far into the darkness,
it happens that in imagining you go astray.
You will see, if you get there,
how much the senses are deceived by distance ;
try to quicken your pace a little. »"

Dante Alighieri

Au cours de la thèse, l'essentiel de mon travail à concevoir, produire et analyser des simulations numériques de jets astrophysiques. Comme nous le verrons, l'utilisation du code PLUTO (Mignone et al., 2007) s'est imposée naturellement comme une solution à ce problème. En général, l'exécution d'une simulation sur PLUTO est soumise à deux conditions préalables :

- *Adapter le code aux spécificités du problème : choisir les modules physiques et les schémas d'intégration.*
- *Créer une configuration numérique : définir le domaine d'intégration et sa grille, implémenter les conditions initiales et limites.*

Au cours de ce chapitre, je détaille les choix faits au cours de ces deux étapes et leurs motivations.

Dans la jungle des codes MHD, le code PLUTO (Mignone et al., 2007) est particulièrement adapté à la problématique de ma thèse, principalement pour trois raisons. Premièrement, il est très flexible, ce qui permet de réaliser des implémentations spécifiques. Deuxièmement, il fournit des schémas de capture des chocs à haute résolution, utiles pour étudier les grands chocs de recollimation attendus dans les jets collimatés. Enfin, Claudio Zanni étant l'un des rédacteurs du code, il a pu m'apporter une aide précieuse dans la création des configurations de simulation.

Il s'agit d'un code aux volumes finis. Pour s'assurer que la divergence du champ magnétique reste bien nulle tout au long de la simulation, j'utilise la méthode de transport contraint. Celle-ci permet que si le champ est initialement à divergence nulle, il le reste, à précision machine, jusqu'à la fin de la simulation.

Dans le domaine de calcul, deux solveurs de Riemann sont utilisés, HLL et HLLD. Tous deux permettent de résoudre les ondes magnétosoniques rapides, nécessaires à la présence des chocs de recollimation. Le solveur HLL, plus approché, n'est utilisé que dans une petite partie du domaine, proche de l'axe, afin de permettre une convergence plus rapide des simulations. En dehors de ce domaine, j'utilise le solveur HLLD, plus précis, et je reconstruis les grandeurs à l'intérieur des cellules entre chaque pas de temps.

Une des différences principales entre mon travail et les simulations précédentes est la conception et la mise en place d'une méthode d'accélération. Celle-ci repose sur le fait que dans les cellules les plus petites du domaine, le jet converge rapidement vers un état stationnaire. Cette méthode a permis une convergence des simulations plus d'un millier de fois plus rapidement que la méthode usuelle, et le projet n'aurait pu être mené à bien.

Les simulations menées au cours de cette thèse sont dites 2.5D. Cela signifie que la rotation et le champ magnétique toroidal sont bien calculés à chaque pas de temps, mais sont supposés axisymétriques. La grille de calcul est plus de 5000 fois plus grande que le rayon de troncation du disque, ce qui est bien plus grand que les simulations de type plateforme de la littérature.

Au cours de ma thèse, j'ai effectué trois types de simulations :

- *Premièrement, des simulations 2.5D dans lesquelles le jet est émis par l'ensemble du disque. Elles ont été réalisées pour vérifier si les simulations globales dépendantes du temps peuvent contenir des chocs de recollimation réguliers, comme le prévoient les solutions auto-similaires.*
- *Ensuite, des simulations 2.5D dans lesquelles le jet n'est émis que depuis les parties les plus internes du disque. Elles ont été réalisées pour étudier la présence et le comportement des chocs de recollimation dans un cadre plus réaliste.*
- *Enfin, des simulations 3D similaires aux simulations tronquées, mais symétrisées autour de l'axe $\theta = 0$, afin d'étudier la stabilité des chocs de recollimation.*

Les deux derniers types de simulations sont des raffinements du premier, d'abord en stoppant l'éjection dans les parties externes du disque, puis en symétrisant les simulations tronquées autour de l'axe. Dans cet chapitre, je décris la configuration numérique conçue pour le premier type de simulation.

La condition initiale est une simple solution potentielle auto-similaire. Elle assure qu'il n'y a initialement ni courant ni force dans le jet. Ainsi, il n'y a pas de jet collimaté présent ab initio dans la simulation. Celui-ci est bien lancé depuis le disque.

Les conditions limites délicates sont celles correspondant au disque et à l'objet central, car elles doivent modéliser les conditions d'éjection du jet (depuis le disque) et de la colonne interne (depuis l'objet central). On veut que le jet soit émis sub-FM et sub-Alfvénique, mais super-SM. Cela suppose de fixer six quantités à la surface du disque, deux étant laissées libres, le champ magnétique toroidal ainsi que celui perpendiculaire à la frontière.

Sur le disque, les conditions limites sont fixées comme dans les solutions autosimilaires Jet-Emitting Disk (Ferreira, 1997). De plus, on s'assure que les lignes de champ de vitesse soient colinéaires avec celles de champ magnétique, en cohérence avec la théorie des jets stationnaires en MHD idéale.

Sur l'objet central, les quantités sont interpolées entre leurs valeurs fixées au bord interne du disque et leurs valeurs sur l'axe. On veut réaliser des simulations de jets émis depuis un disque d'accrétion, les conditions sont donc fixées de sorte à limiter l'éjection autour de l'axe. Par exemple, la densité sur l'axe est fixée cent fois plus faible que celle sur le bord interne du disque.

Pour réaliser les simulations présentées dans ce manuscrit, j'ai bénéficié de temps de calcul sur GRICAD (Grenoble Alpes Recherche-Infrastructure de Calcul Intensif et de Données). Au cours de ma thèse, j'ai effectué 371 simulations, soit sur 256 CPU pour les simulations de production, soit sur un plus petit nombre d'unités pour les simulations de test parallélisées. La durée totale d'utilisation de l'unité centrale est de 25 ans (soit 219 000 heures d'utilisation), ce qui correspond à une tonne d'émissions de CO_2.

Ce chapitre ce termine sur quelques formules permettant de passer des valeurs en unités de code présentes dans le manuscrit à des unités physiques, pour un jet stellaire émis autour d'une étoile semblable au Soleil.

The gist of my work was setting up, producing and analyzing numerical simulations of astrophysical jets. As we will see, the use of the PLUTO code (Mignone et al., 2007) came naturally as a solution to this problem. Typically, running a simulation on PLUTO has two prerequisites:

- Adapting the code to the specificities of the problem: choosing the physical modules and integration schemes.
- Creating a numerical setup: defining the integration domain and its grid, implementing the initial and boundary conditions.

The two sections of this chapter will lay out the choices made in these two steps and their reasons. Results will be shown in the later chapters.

3.1 The PLUTO code

We have seen in chapter 2 that ideal MHD is suited for the study of astrophysical jets, with some reserves for jets emitted around compact objects. Moreover, my jets are launched via the magnetocentrifugal process[1] of Blandford and Payne, 1982 that works in an ideal MHD framework. There are many other methods in numerical astrophysics which are complementary to MHD, but they are not yet appropriate to study astrophysical jets, especially at large scales. Hydrodynamic methods, either with a fixed grid or grid-free (Smooth-Particle Hydrodynamics (SPH) for instance) seem ruled out because the absence of a magnetic field. Moreover, even though Smooth-Particle MagnetoHydroDynamics (SPMHD) codes exist (see e.g. Price, 2012), their computational cost is prohibitive for large scale simulations. Also, the absence of a collimating Lorentz force rules out force-free methods. Finally, Particle-In-Cell methods require collisionless plasmas, and astrophysical jets are collision-dominated in the acceleration zone.

I thus ran ideal MHD simulations, using the PLUTO (Mignone et al., 2007) code[2]. In the jungle of MHD codes, it is particularly suited for this problem for three main reasons. First, it is very flexible, enabling specific implementations to be made. Second, it provides high-resolution shock capturing schemes, useful to study the large recollimation shocks expected in collimated jets. Third, Claudio Zanni being one of the redactors of the code, he was able to provide me with some much needed help in creating the simulation setups.

[1] Here, "jet" only refers to the disk-ejected outflow. The central object (black hole or star) also ejects an outflow, called "spine", but not by the magnetocentrifugal process. Details are in section 3.2.3.

[2] I used the static grid version (Mignone et al., 2007) of PLUTO 4.3.

3.1.1 Finite volume methods

The PLUTO code uses a finite volume method to solve the equations of magnetohydrodynamics. It thus requires the equations in their conservative form:

$$\frac{\partial \rho}{\partial t} + \vec{\nabla} \cdot (\rho \vec{v}) = 0 \qquad \textit{Continuity} \tag{3.1}$$

$$\frac{\partial \rho \vec{v}}{\partial t} + \vec{\nabla} \cdot \left[\rho \vec{v} \otimes \vec{v} + \left(P + \frac{B^2}{8\pi} \right) \bar{\bar{I}} - \frac{1}{4\pi} \vec{B} \otimes \vec{B} \right] = -\rho \vec{\nabla} \Phi_G \qquad \text{where } \Phi_G = -\frac{GM}{R} \qquad \textit{Motion} \tag{3.2}$$

$$\frac{\partial S}{\partial t} + \vec{\nabla} \cdot (S \vec{v}) = 0 \qquad \text{where } S = \frac{P}{\rho^\Gamma} \qquad \textit{Energy} \tag{3.3}$$

$$\frac{\partial \vec{B}}{\partial t} + \vec{\nabla} \cdot (\vec{v} \otimes \vec{B} - \vec{B} \otimes \vec{v}) = \vec{0} \qquad \text{where } \vec{\nabla} \cdot \vec{B} = 0 \qquad \textit{Induction} \tag{3.4}$$

Let us take one of these equations, of the form

$$\frac{\partial u}{\partial t} + \vec{\nabla} \cdot \vec{f} = \sigma \tag{3.5}$$

where u is the density of the scalar unknown, $\vec{f}$ its associated flux and σ its associated source term. Integrating on an elementary volume $\mathcal{V}$ and using Stokes theorem on its closed surface $\mathcal{S}$ we get

$$\frac{\partial}{\partial t} \int_{\mathcal{V}} u dv + \oint_{\mathcal{S}} \vec{f} \cdot \vec{ds} = \int_S \sigma dv \tag{3.6}$$

In the case of a cubic cell of n faces, this simplifies to

$$\frac{\partial U}{\partial t} + \sum_{i=1}^{n} F_i S_i = \Sigma \tag{3.7}$$

where U is the unknown value integrated in the cell and Σ its source term. F_i and S_i are respectively the entering flux and the surface on the i^{th} face.

3.1.2 Constrained transport

The equation of Maxwell-Faraday depicts the evolution of the magnetic field. Taking its divergence, we derive that provided that $\vec{\nabla} \cdot \vec{B} = 0$ initially, $\vec{B}$ should remain divergence-free indefinitely. However, some discretizations do not conserve $\vec{\nabla} \cdot \vec{B} = 0$ at machine precision. In ideal MHD, such errors may significantly influence the equation of motion, creating an additional unphysical term:

$$\frac{\partial (\rho \vec{v})}{\partial t} = \frac{1}{4\pi} \vec{\nabla} \cdot (\vec{B} \otimes \vec{B}) + ... = \frac{1}{4\pi} \left[(\vec{\boldsymbol{\nabla}} \cdot \vec{\boldsymbol{B}}) \vec{\boldsymbol{B}} + (\vec{B} \cdot \vec{\nabla}) \vec{B} \right] + ... \tag{3.8}$$

Several techniques have been developed to guarantee that $\vec{\nabla} \cdot \vec{B} = 0$ at machine precision. One can rewrite the ideal MHD equations using the vector potential $\vec{A}$ such that $\vec{B} = \vec{\nabla} \times \vec{A}$, ensuring a divergence-free magnetic field. This is what I used to set up my initial conditions.

To evolve the induction equation over time, I used a different method: the constrained transport (Evans and Hawley, 1988), well suited for finite volume methods. It requires the magnetic field b_n to be defined at the face centers and the electric field E_n to be defined at the edge centers, (see Figure 3.1). For each face, we store the magnetic field perpendicular to that face. For each edge, we store the electric field colinear to that edge.

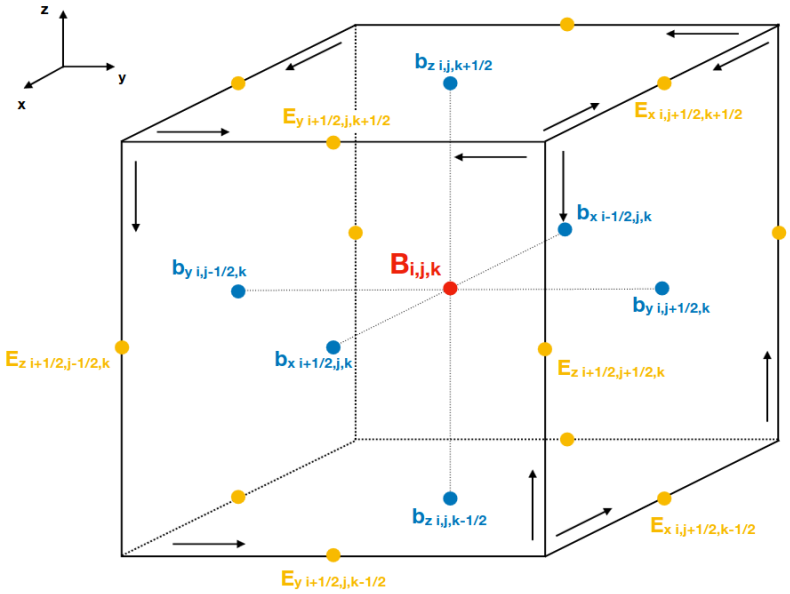

FIGURE 3.1: Representation of the magnetic field and the electric field components in a cell for constrained transport. In blue are the magnetic fields defined on the faces centers. In orange are the electric fields defined on the edge centers. In red is the mean magnetic field, computed at the center of the cell. The arrows indicate the direction in which the integral on each contour is made. The figure is taken from Nicolas Scepi's PhD thesis.

Integrating the Maxwell-Faraday equation over a face $\mathcal{F}$ of closed contour $\mathcal{C}$ and using Stokes theorem we obtain:

$$\frac{\partial}{\partial t}\left(\int_{\mathcal{F}} \vec{B}\cdot\vec{ds}\right) = -\frac{1}{c}\oint_{\mathcal{C}} \vec{E}\cdot\vec{dl} \tag{3.9}$$

To get the variation of the total flux entering the cell, this equation is then summed on all n cell faces and associated contours. Looking at Figure 3.1, one realizes this means each edge is considered twice, in opposite directions. This gives

$$\frac{\partial}{\partial t}\left(\oint_{\mathcal{S}} \vec{B}\cdot\vec{ds}\right) = \sum_{i=1}^{n}\left[\frac{\partial}{\partial t}\left(\int_{\mathcal{F}_i} \vec{B}\cdot\vec{ds}\right)\right] = -\frac{1}{c}\sum_{i=1}^{n}\left(\oint_{\mathcal{C}_i} \vec{E}\cdot\vec{dl}\right) = 0 \tag{3.10}$$

where $\mathcal{S}$ is the total closed surface of the cell. Consequently, as long as the magnetic field is initially divergence-free, it should then stay divergence-free at machine precision.

3.1.3 Riemann solvers

Riemann problem is the name for a type of initial value problem composed of a conservation equation and piecewise initial conditions with a single discontinuity. This is be used to study the evolution of a fluid between two neighbouring cells of a computational grid. To simplify the formalism, we consider a single conservative variable u and a one-dimensional problem along the direction x.

The evolution of u is dictated by the conservation equation

$$\frac{\partial u}{\partial t} + \frac{\partial f}{\partial x} = 0 \tag{3.11}$$

where f is the flux associated to the conservative variable u.

The initial conditions (at $t = 0$) are represented on Figure 3.2-left. The discontinuity is at $x = 0$, the constant value of u on the left state ($x < 0$) is u_L and the constant value of u on the right state ($x > 0$) is u_R.

We have seen in chapter 2 that a pair of fast-magnetosonic, alfvénic and slow-magnetosonic waves may propagate on both sides of the discontinuity, at respective speeds V_{FM}, V_A and V_{SM}. The discontinuity itself is comoving with the fluid at speed V. At $t > 0$, six new constant states may then be created, whose boundaries move at speeds $V - V_{FM}$, $V - V_A$, $V - V_{SM}$, V, $V + V_{SM}$, $V + V_A$ and $V + V_{FM}$. This is illustrated by the Riemann fan on Figure 3.2-right. Being able to estimate those speeds is crucial in computing the intercell fluxes. As exact solvers present a prohibitive numerical cost for my problem, I used approximate Riemann solvers: the HLL and HLLD solvers, based on the seminal work of Harten, Lax, and Leer, 1983. I will shortly describe how they function and their respective advantages. For a more exhaustive yet comprehensive explanation of these solvers, I recommend the read of chapter 2 of Massaglia et al., 2008, on which this section is based. This will be of particular interest to a reader curious about how the wave speeds and intercell fluxes are computed.

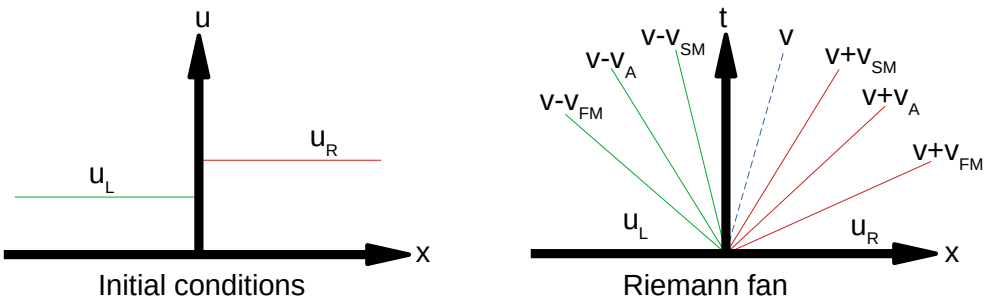

FIGURE 3.2: Left: Representation of the initial condtions for a variable u. Right: General structure of a Riemann fan generated by two constant states u_L and u_R.

Both the HLL and HLLD solvers only resolve some of the seven possible waves that can propagate in a MHD plasma, two for HLL and five for HLLD. The approximate structure of the Riemann fan used for both solvers is displayed on Figure 3.3.

- The HLL solver only computes an estimate of the leftmost (λ_L) and rightmost (λ_R) signal speeds, corresponding to fast-magnetosonic waves. It then averages the intermediate states into a single constant state between the two outermost waves. Because of its simplicity, it is computationally cheap, and preserves the positivity of density, pressure and energy. However, it cannot

resolve any intermediate structures (e.g. Alfvén, slow and contact modes) and is thus more diffusive than more complete algorithms.

- The HLLD solver (Miyoshi and Kusano, 2005) computes the two fast waves of speeds λ_L and λ_R, but also two rotational discontinuities of speeds λ_{LI} and λ_{RI} corresponding the Alfvén wave, and a contact wave of speed λ_C. Although more computationally expensive, it is particularly robust and less diffusive, allowing stronger discontinuities. It can also resolve all the possible MHD waves, with the exception of slow-magnetosonic waves.

Thanks to the high modularity of the PLUTO code, I used both the HLL and the HLLD solvers in all the simulations presented in this manuscript. I will explain in the rest of this chapter why and how this was done.

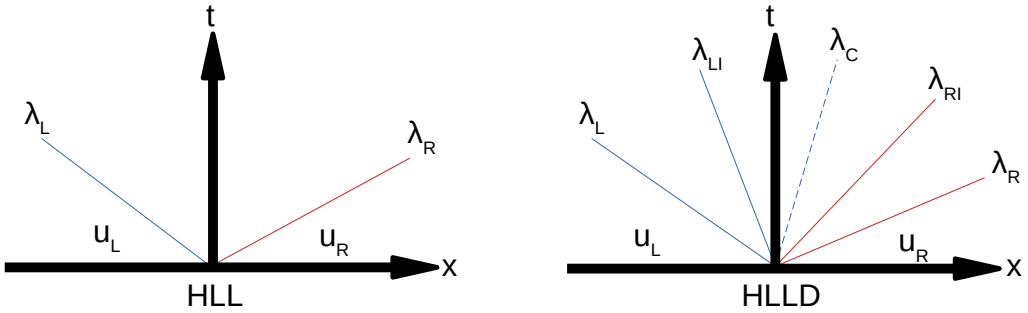

FIGURE 3.3: Left: Approximate structure of the Riemann fan used in the HLL solver. Right: Approximate structure of the Riemann fan used in the HLLC solver.

3.1.4 Godunov scheme

Solving a Riemann problem allows to compute the intercell fluxes in the equation 3.7 dictating the evolution of the cell-centered variable U. Integrating it over a time increment $\Delta t = t_2 - t_1$ we obtain:

$$U(t_2) - U(t_1) = \int_{t_1}^{t_2} \left(\Sigma(t) - \sum_{i=1}^{n} F_i(t) S_i \right) dt \tag{3.12}$$

We see that a correct estimation of these fluxes is critical to get a precise enough integration scheme. In a Godunov scheme they are estimated by solving a Riemann problem at each intercell face, whose initial conditions are set using the values of the conservative variables at t_1. While historically these initial values were constant in each cell and simply equal to the values of the variables in the cell at t_1 (flat reconstruction scheme), nowadays most codes use interpolation schemes to reconstruct the variation of the variables inside the cell.

In my simulations, I mainly used a second order in space piecewise reconstruction. To avoid spurious oscillations, I used it in conjunction with various slope limiters, listed from least diffusive to most diffusive:

- Monotonized Center (van Leer, 1977) for the density ρ.
- Van Leer (van Leer, 1974) for the velocity $\vec{v}$ and the magnetic field $\vec{B}$.
- Minmod (Roe, 1986) for the pressure P.

Such a reconstruction scheme (including the slope limiters) is the standard in PLUTO. The curious reader is referred to section 3.1 of Mignone, 2014 for an exhaustive description of the scheme and a comparison between solvers. For our problem, it has the big perk of being Total Variation Diminishing, meaning that the sum of all variations between neighbouring cells is decreasing with time (see Harten, 1983). It is well-suited to capture shocks as it avoids misleading oscillations and preserves monotonicity at the cell boundaries.

For all simulations, I also used a flat reconstruction scheme in conjunction with the Minmod solver in small parts of the domain. I will explain in the rest of this chapter why and how this was done.

3.1.5 CFL condition and acceleration scheme

We now know how to integrate the ideal MHD equations over time in our computational domain. A priori, all the cells should evolve at the same time, but how do we choose the time increment Δt ? When integrating differential equations, the maximal possible timestep is usually set by the Courant, Friedrichs, and Lewy, 1928 condition (hereafter CFL condition), prohibiting any wave to travel to an adjacent grid point during a time increment. Let us consider an integration domain $\mathcal{D}$ of dimension $N_{dim} \leq 3$, containing a certain numbers of cells $\mathcal{C}$. In ideal MHD without diffusion, the CFL condition is written:

$$\frac{\Delta t}{N_{dim}} \max_{\mathcal{C}\in\mathcal{D}} \left(\sum_{d=1}^{N_{dim}} \frac{|\lambda_d|}{\Delta l_d} \right) = C_a \tag{3.13}$$

where for a specific direction d and a cell $\mathcal{C}$, $|\lambda_d|$ is the maximum absolute signal speed and Δl_d is the cell size. C_a is an arbitrary constant, chosen such that $C_a \leq 1/N_{dim}$.

Because of its simplicity and generality, this condition is particularly reliable and easy to use. However, its issue is that it does not put any lower boundary on the amplitude of the wave propagating at speed λ_d. Thus, extremely weak modes of the MHD waves can cause prohibitively small time increments, if they arise in small cells. This is particularly harmful for computational domains that are very large, have big discrepancies in cell sizes, or for integrations that need to run for very long. To get rid of this issue, Claudio Zanni implemented in 2.5D, and we implemented in 3D, a special acceleration scheme. Let us describe how it works.

In our problem, it is expected that a portion $\mathcal{D}_1$ of the integration domain converges way faster than the rest, $\mathcal{D}_2$ [3]. At any time t, we take a relative variation of the density as a criterion for convergence:

$$\left(\frac{|\Delta\rho|}{\rho}(t) \right)_{\mathcal{C}} \leq 10^{-4} \Leftrightarrow \mathcal{C} \in \mathcal{D}_1(t) \tag{3.14}$$

where $\left(\frac{|\Delta\rho|}{\rho}(t) \right)_{\mathcal{C}}$ is the relative variation of density over the precedent timestep in the cell $\mathcal{C}$.

Then, we say that only the portion of the domain that has not converged, $\mathcal{D}_2$, contributes to setting the following timestep Δt_{acc}:

$$\frac{\Delta t_{acc}}{N_{dim}} \max_{\mathcal{C}\in\mathcal{D}_2} \left(\sum_{d=1}^{N_{dim}} \frac{|\lambda_d|}{\Delta l_d} \right) = C_a \tag{3.15}$$

[3] $\mathcal{D}_1 \cup \mathcal{D}_2 = \mathcal{D}$ and $\mathcal{D}_1 \cap \mathcal{D}_2 = \phi$.

This prevents cells in the converged domain $\mathcal{D}_1$ to lower the time increment because of extremely small variations. Here, it is important to note that the subdivision of the total domain $\mathcal{D}$ in a converged domain $\mathcal{D}_1$ and a non-converged domain $\mathcal{D}_2$ depends on time: the size of the converged domain $\mathcal{D}_1$ is expected to grow with time. However, converged cells are not frozen, they keep evolving at the time increment Δt_{acc} and perturbations can propagate from $\mathcal{D}_2$ to $\mathcal{D}_1$. Thus, if these perturbations are strong enough to break the convergence condition 3.15 in some specific cells, those cells would move from $\mathcal{D}_1$ to $\mathcal{D}_2$, and thus contribute in setting the global time increment.

Such an acceleration scheme was motivated by our rather niche requirements: a stationary state as the expected final outcome, a huge discrepancy in cell sizes with small cells converging faster than large cells, and a need to integrate over very large scales in space and time. Still, it proved extremely effective. For means of comparison, let us introduce two timescales, one using the acceleration algorithm, and one without using it. I consider a simulation which at time t, has already performed N timesteps. The effective accelerated timescale is

$$t(N) = \sum_{i=0}^{i=N} \Delta t_{acc}(i) \tag{3.16}$$

where $\Delta t_{acc}(i)$ is the accelerated time increment at the i^{th} timestep (see equation 3.15). In all the following, this timescale will simply be referred as time.

The timescale without acceleration is

$$t_{na}(N) = \sum_{i=0}^{i=N} \Delta t(i) \tag{3.17}$$

where $\Delta t(i)$ is the non-accelerated time increment at the i^{th} timestep (see equation 3.13).

This non-accelerated timescale is simply the one the simulation would have each at each timestep N, had the acceleration not been implemented. It helps quantifying the effectiveness of the acceleration. At each timestep N I define the acceleration parameter as the ratio between the two timescales $t(N)/t_{na}(N)$. Figure 3.4 illustrates the evolution of this acceleration parameter over time (equation 3.16). Three simulations are represented, K2 being the reference simulation of chapter 4 (see chapter 5 for information on the other simulations).

A clear acceleration is seen after t=10^3, as the simulations begin to converge: the size of the accelerated domain $\mathcal{D}_1$ is non-negligible. At the end of the simulation, the acceleration factor reaches three orders of magnitude. For instance, the reference simulation ran on the same CPU hours without the acceleration would have ended at a timescale 2500 times smaller (e.g. $t_{end} = 2.60 \times 10^2$ instead of $t_{end} = 6.51 \times 10^5$). Alternatively, this means that to reach the same physical timescales, the simulation would have had to run on approximately[4] 2500 times more CPU hours (e.g. around two million hours instead of 725 hours). The simulations performed in this manuscript could not have been done without this acceleration scheme. Chapter 5 delves a bit more in the specifics of the acceleration for each simulation in Figure 3.4 and Appendix C explains the differences between the 2D and 3D acceleration schemes.

[4]Contrary to the timescale comparison, this is only an approximation as: (a) For $t < t_{end}$ even the non-accelerated time increment changes with time (see equation 3.13), and thus is not a perfect proxy for the CPU cost. (b) For $t > t_{end}$ this is a prediction assuming the acceleration factor stays the same, but it could be slowly evolving.

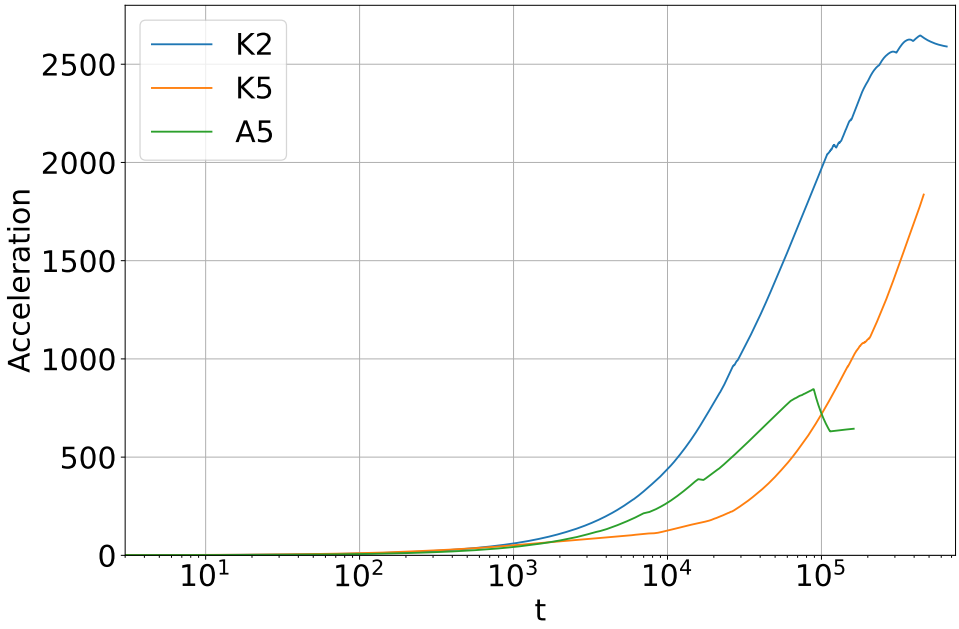

FIGURE 3.4: Evolution of the acceleration with time for the simulations K2, K5, and A5. See chapter 5 for details on the simulations.

3.1.6 Accounting

Before delving into the setups, let us open a short parenthesis about accounting. To perform the simulations presented in this manuscript, I was granted computing time on GRICAD (Grenoble Alpes Recherche-Infrastructure de Calcul Intensif et de Données), who provides some statistics. Over the course of the PhD I ran 371 simulations, either on 256 CPUs for production runs, or on a smaller number for parallelized test runs. The total CPU duration is 25 years (e.g. 219 000 CPU hours), which amounts to a ton of CO_2 emission. For means of comparison, Knödlseder et al., 2022 estimates the research-related carbon dioxide emission of an average astronomer at 36.6 ± 14.0 tons of CO_2 per year.

Additionally, I was granted 50 000 CPU hours of preparatory time on the Irene-Rome machine of the national computing center GENCI-TGCC (Grand Equipement National de Calcul Intensif-Très Grand Centre de Calcul). Out of these CPU hours, only 485.05 were used to run tests of 3D simulations. I will come back to these tests in Appendix C.

3.2 Numerical setups

The astrophysical problem at hand is the study of astrophysical jets emitted from Keplerian accretion disks surrounding a spine emitted from a central object. A sketch of the computational domain is presented on the left panel of Figure 3.5. I use two systems of coordinates: spherical (R, θ, φ) and cylindrical (r, φ, z), both originated on the same point O. At the origin lies the central object of mass M. The sphere of radius $R = R_d$ (green area in Figure 3.5-left) represents the central object, and its with the disk. The disk itself extends from $R = R_d$ to $R = 5650R_d$. It is not computed but is a boundary condition at $\theta = \pi/2$.

Over the course of my thesis, I ran three types of simulations:

- First, 2.5D simulations in which the jet is emitted from the whole disk ($\theta = \pi/2$), from $R = R_d$ to $R = 5650R_d$. They were performed to probe whether time-dependent global simulations can contain steady recollimation shocks, as predicted by the self-similar solutions. Hereafter, they will be referred to as **self-similar simulations**[5].
- Then, 2.5D simulations in which the jet is only emitted from the inner parts of the disk ($\theta = \pi/2$), from $R = R_d$ to $R = 10R_d$. They were performed to investigate the presence and behavior of the recollimation shocks in a more realistic setup. Hereafter, they will be referred to as **truncated simulations**.
- Finally, 3D simulations similar to the truncated simulations, but symmetrized around the axis $\theta = 0$, to probe the stability of the recollimation shocks.

The last two types of simulations are refinements of the self-similar simulations, first by stopping the ejection after $R = 10R_d$ on the lower $\theta = \pi/2$ axis, then by symmetrizing the truncated simulations around the $\theta = 0$ axis, along the toroidal direction $\vec{u_\varphi}$. In this section, I describe the numerical setup made for the self-similar simulations. The refinements made for truncated and 3D simulations will be described in the dedicated chapters, respectively chapters 5 and Appendix C.

The boundary conditions on the disk are consistent with those provided at the surface of a JED (Ferreira, 1997). In my setup, a large-scale magnetic field threads both the disk and the central object. This allows the production of two outflows, emitted from the disk (blue region in Figure 3.5-left) and from the central object (red region in Figure 3.5-left).

3.2.1 Simulation domain and grid

The 2.5D computational domain is discretized using spherical (R, θ) coordinates. It extends from the polar axis ($\theta = 0$) until the disk surface ($\theta = \pi/2$) [6].

The cell size in the θ direction is mostly uniform, but heavily decreases in the few cells near the axis (see Figure 3.5-right). This is essential to the setup, as the expected recollimation shocks should form first near the axis. Setting a too low resolution in this zone would prevent their formation.

In most of the computational domain, I use a HLLD solver and the default reconstruction scheme of PLUTO described in section 3.1.4 (Monotonized Center for

[5] The simulations themselves are not self-similar, only the boundary conditions. This is a misnomer to avoid long paraphrases.

[6] Consistently with the JED model, the surface of the disk is not exactly at $\theta = \pi/2$, but at $\theta = \pi/2 - \epsilon$, where ϵ is the disk sound speed relative to its the Keplerian speed. As for all simulations, $\epsilon = 10^{-2} \ll \pi/2$, to ease notations the disk boundary is called $\theta = \pi/2$.

ρ, Van Leer for $\vec{v}$ and $\vec{B}$, Minmod for P). In the regions closest to the axis, as well as in those of very low density and high Alfvén speed, I use a HLL solver with a flat reconstruction scheme and a flat limiter. This was done to avoid prohibitively high computational costs.

The cell spacing in the R direction is logarithmic: $\Delta R \propto R$. This ensures that apart from the region near the polar axis, the cells remain approximately squared ($\Delta R \simeq R\Delta\theta$).

Our computational domain is huge compared to previous jet simulations (see section 1.3.4). This is motivated by the self-similar solutions of Ferreira, 1997, where jets are emitted from a JED. According to their Figure 6, reproduced on the top panel of Figure 1.16, recollimation shocks are expected to occur at altitudes beyond a thousand times the jet launching radius. The first objective of my thesis being to produce these shocks using self-similar ejection conditions (as in the JED model), using a large enough grid is crucial. Simulations in a domain that large may be able to capture the expected shocks, but have a serious drawback: as the disk is Keplerian, it presents a huge contrast in time scales between the inner and outer edge. During the time the outer disk takes to complete an orbit, the inner disk completes half a million orbits. This constraint, in conjunction with the logarithmic cell spacing in the radial direction, is required for the development of the special acceleration scheme (see section 3.1.5). The innermost cells are the smallest and thus lower the global time increment the most, but also have the smallest time scale and converge the fastest.

In this manuscript, two different grid meshes are used: a high-resolution one with $N_R = 1408$ points in the radial direction and $N_\theta = 266$ points in the orthoradial direction, and a low-resolution one with $N_R = 704$ points in the radial direction and $N_\theta = 144$ points in the orthoradial direction. The low-resolution grid mesh is represented in Figure 3.5-right.

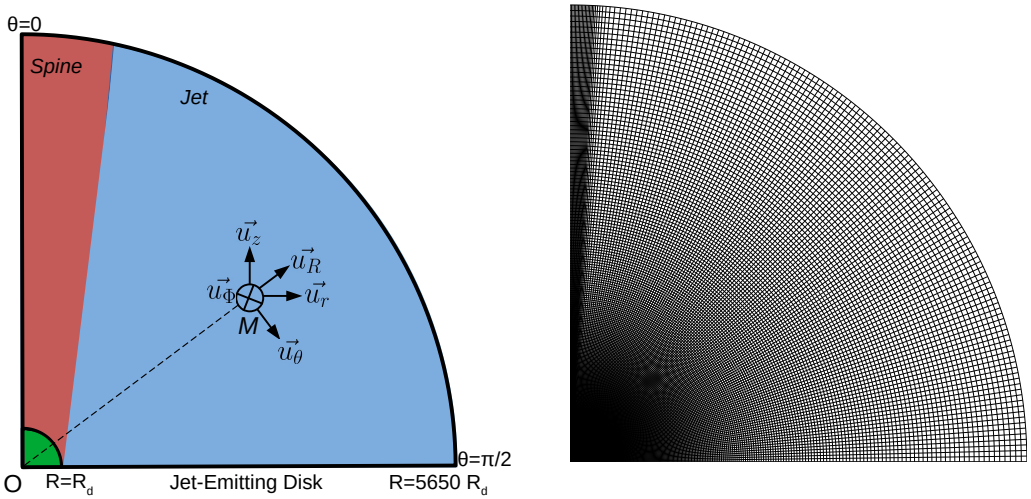

FIGURE 3.5: Left: Sketch of the computational domain for self-similar simulations. The central object and its interaction with the innermost disk are located below the inner boundary at $R = R_d$ (green region), the near-Keplerian jet-emitting disk (JED) being established from $R = R_d$ to the end of the domain $R = 5650R_d$. An axial outflow (the spine) is emitted from the central regions (in red) and the jet is emitted from the JED (in blue). At any point M inside the domain, I either use spherical ($\vec{u_R}$,$\vec{u_\theta}$,$\vec{u_\varphi}$) or cylindrical ($\vec{u_r}$,$\vec{u_\varphi}$,$\vec{u_z}$) coordinates. Right: Low resolution grid.

3.2.2 Initial conditions

The initial conditions are set following the radially self-similar ansatz (see sections 2.6.4 and 2.6.5). We assume a magnetic flux of the form

$$\Psi(R,\theta) = \Psi_d \left(\frac{R}{R_d}\right)^{\alpha} \Phi(\theta) \tag{3.18}$$

where the function $\Phi(\theta)$ is determined such that the initial magnetic field is potential, e.g. current-free and force-free ($J_\varphi = 0$).

This magnetic flux naturally describes the initial magnetic field in the jet, but also in the spine. This is a simplification, as the magnetic field near the axis $\theta = 0$ is different from a stellar magnetic field. Because of the force-free condition, there is initially no toroidal magnetic field, and a potential poloidal field is set by

$$\vec{B}_p = \frac{1}{2\pi r}\vec{\nabla}\Psi \times \vec{u}_\varphi \tag{3.19}$$

The exponent α is a parameter of the setup, fixed for each simulation. It naturally sets the topology of the initial magnetic field: $B_R \propto B_\theta \propto R^{\alpha-2}$ (see also table 2.3).

The initial magnetic field being potential, there is no magnetic force in the plasma. It is therefore assumed to be in a spherically symmetric hydrostatic equilibrium ($\vec{v} = \vec{0}$) with $dP/dR = -\rho GM/R^2$. We choose the following solution:

$$\rho = \rho_a \left(\frac{R}{R_d}\right)^{2\alpha-3} \tag{3.20}$$

$$P = \frac{1}{4-2\alpha}\frac{\rho_a GM}{R_d}\left(\frac{R}{R_d}\right)^{2\alpha-4} \left(= \rho\frac{V_S^2}{\Gamma} = \rho\frac{k_B T}{\frac{1}{2}m_p}\right) \tag{3.21}$$

where ρ_a is the density at $(R = R_d, \theta = 0)$.

In all the following, quantities with a subscript a refer the values on the axis directly over the central sphere $(R = R_d, \theta = 0)$, while quantities with a subscript d refer to the values at the inner edge of the disk $(R = R_d, \theta = \pi/2)$. The values of ρ_a and P_a are fixed in accordance with the boundary conditions.

3.2.3 Boundary conditions

There are four boundaries to the simulation domain:

- The polar axis ($\theta = 0$, $R \in [R_d; 5650R_d]$)
- The outer boundary ($R = 5650R_d$, $\theta \in [0; \pi/2]$)
- The Jet-Emitting Disk ($\theta = \pi/2$, $R \in [R_d; 5650R_d]$)
- The central object ($R = R_d$, $\theta \in [0; \pi/2]$)

At these four boundaries, conditions have to be set on the eight evolving quantities ρ, P, $\vec{v}$ and $\vec{B}$. On the first two boundaries, the conditions are rather straightforward. On the polar axis, usual reflecting conditions are applied on all quantities. At the outer boundary, "outflow" conditions are imposed: the gradient along $\vec{u_R}$ of ρ, P, B_R, B_θ, RB_φ, v_R, v_θ and v_φ is conserved. The Van Leer slope limiter is used to avoid spurious oscillations. Additionally, a positive Lorentz force is enforced on the subalfvénic parts of this boundary. It turned out that this last condition is not strictly

needed for the convergence of the simulation, but slightly decreases the computational cost. This boundary condition was carefully studied in the very specific case of time-dependent (oscillating) truncated simulations (see chapter 6).

The last two boundary conditions (the Jet-Emitting Disk and the central object) are particularly crucial as they set the ejection conditions of the two outflow components (the jet and the spine). All choices will be made with the intent of limiting the impact of the spine on global jet dynamics: the intent of this thesis is to investigate the collimation properties of a jet emitted from an accretion disk. In the rest of the section, I describe in detail how the ejection conditions were set. But first, let us determine how many quantities should be fixed and how many should be let free at these boundaries.[7].

Causality and number of parameters

In ideal MHD, there are three critical speeds (V_{SM}, V_A and V_{FM}). In a steady state, each time the flow passes through a critical point, it defines a regularity condition that fixes a quantity at its launching point. Thus, each crossing of a critical speed on the spine/jet leaves one free quantity at the central object/disk surface. I want to control the mass loss in the spine and the jet, to be capable of set $\dot{M}_{spine}/\dot{M}_{jet} \ll 1$. This requires the outflow to be super-SM (see section 2.6.2). Thus, there should be six quantities imposed on the injection boundaries, and two that are let free to adjust with time, the toroidal magnetic field B_φ and the poloidal magnetic field perpendicular to the boundary (B_R on the disk surface and B_θ on the central object). I make this choice in order to control the injected magnetic flux while allowing the magnetic field to bend in response to the jet dynamics.

Jet-Emitting Disk: $\theta = \pi/2$

Along the $\theta = \pi/2$ (so that $r = R$) boundary, I choose the following six conditions:

$$\begin{aligned}
\rho &= \rho_d \left(\frac{r}{R_d}\right)^{2\alpha-3} \\
P &= \rho_d \frac{V_{s_d}^2}{\Gamma} \left(\frac{r}{R_d}\right)^{2\alpha-4} \\
B_\theta &= -B_d \left(\frac{r}{R_d}\right)^{\alpha-2} \\
v_\theta &= -v_d \left(\frac{r}{R_d}\right)^{-1/2} \\
v_R &= v_\theta \frac{B_R}{B_\theta} \\
v_\varphi &= \Omega_* r + v_\theta \frac{B_\varphi}{B_\theta},
\end{aligned} \tag{3.22}$$

The disk being set as Keplerian, the angular velocity of the magnetic surfaces is $\Omega_* = \Omega_K = \sqrt{GM/r^3}$.

These boundary conditions are consistent with a self-similar JED (see section 2.6.4. In particular, they preserve the alignment of the velocity and magnetic field

[7] A quantity that is "let free" at a boundary here means that the value of the quantity at the edge a domain fixes the value of the quantity at the boundary, through gradient conservation (and use of Van Leer slope limiter). It is also an "outflow condition".

lines ($\vec{v_p} \parallel \vec{B_p}$), describing a steady ideal MHD flow. This sets the toroidal component of the electric field $\vec{E} = -\vec{v} \times \vec{B}$ to zero, and thus as seen in section 2.4, enforces that the injected magnetic flux distribution does not change with time.

These conditions let four dimensionless parameters to be specified at $r = R_d$: ρ_d, V_{S_d}, B_d and v_d, acting as normalizing quantities. They are set consistently with the self-similar solutions of Ferreira, 1997:

- The jet density ρ_d is fixed relative to the density at the polar axis with the parameter $\delta \equiv \rho_d/\rho_a$. This δ parameter defines the density contrast between the spine and the jet.
- The disk sound speed V_{S_d} is fixed relative to the Keplerian speed with the parameter $\epsilon = V_{S_d}/V_{K_d}$. This parameter is also the disk scale height, and the disk sound speed sets the jet temperature. Since $\epsilon \ll 1$, the jet is cold.
- The disk magnetic field strength B_d is fixed with the parameter $\mu \equiv V_{A_d}/V_{K_d} = B_d/\sqrt{4\pi\rho_d GM}$, vertical component of the Alfvén speed over the Keplerian speed.
- The vertical injection speed v_d is related to the mass-loading parameter κ introduced by Blandford and Payne, 1982[8]:

$$\kappa = \frac{4\pi\rho_d v_d V_{Kd}}{B_d^2} = \frac{v_d V_{Kd}}{V_{Ad}^2} = \frac{v_d}{V_{Kd}}\frac{1}{\mu^2}\,. \tag{3.23}$$

There are thus six conditions fixed at the disk boundary: the four parameters above, the Keplerian rotation of the magnetic field lines ($\Omega_* = \sqrt{GM/r^3}$) and $\vec{v}_p \parallel \vec{B}_p$ (with $v_R = v_\theta(B_R/B_\theta)$). As there are eight quantities, this lets two three parameters, B_φ and B_R. This way I avoid overconstraning the problem, as the inner jet is expected to cross the Alfvén and fast-magnetosonic critical surfaces. Freedom on the six profiles of equation 3.22 allows a wealth of possibilities, explaining while to this day, few generic results are known.

What are the values of the four parameters above ? As I want to impose the jet mass loss rate, I need a super-SM ejection: $M_{SM} > 1$. This places a constraint on v_d/V_{K_d}. I choose to impose v_d/V_{K_d} which in return sets the parameter μ as a function of κ.

In order to restrain the parameter space, some parameters are the same in all simulations. By fixing $v_d/V_{K_d} = 0.1$, I get the relation $\kappa = 0.1/\mu^2$. This relation leads to $B_d = 10V_{K_d}\sqrt{4\pi\rho_a}$ for all simulations. The goal being to produce cold outflows, I set $\epsilon = 10^{-2}$. This is consistent with a super-SM injection, as the vertical component of the sonic mach number is $M_{S_\theta} = v_d/V_{S_d} = v_d/(V_{K_d}\epsilon) = 10$. The poloidal speed being longer than v_d, the sonic mach number then gives $M_S = v_p/V_{S_d} > v_d/V_{S_d} = M_{S_\theta} = 10$. As the Alfvén speed is much greater than the sound speed ($\mu \gg \epsilon$), the sound speed is greater than the SM speed, and thus the injection is super-SM.

As the disk injection speed v_d and magnetic field strength B_d are the same for all simulations, the disk mass load and Alfvén speed are varied only by changing the disk density ρ_d. As a consequence, the density contrast δ can be expressed as a function of κ. In order to keep a high contrast in all simulations, the relation $\delta = 10^2/\mu^2 = 10^3\kappa$ is assumed.

[8]The expression of κ here slightly differs from that of Blandford and Payne, 1982 or Jannaud, Zanni, and Ferreira, 2023 as these papers were written in SI units, while this manuscript is written using Gaussian-cgs units.

The key feature of this parametrization is that it only depends on one dimensionless parameter, the mass load κ. Indeed, ϵ is fixed in all simulations, and μ and δ are defined as functions of κ. Table 3.1 serves as a reminder of the values taken for these parameters.

Parameter	δ	ϵ	μ	κ
Value or expression	$10^3\kappa$	10^{-2}	$\sqrt{0.1/\kappa}$	TBD

TABLE 3.1: Values or expressions of the disk parameters.

Naturally, apart from these normalization parameters, the self-similar parameter α setting the distributions on the disk has to be fixed.

Central object: $R = R_d$

On the boundary corresponding to the central object, six quantities need to be specified, so B_φ and B_θ are let free to evolve. In order to keep the magnetic field flowing into the spine constant with time, $B_R(\theta)$ is fixed to its initial value. Since B_R is fixed at $R = R_d$ and $\theta \in [0; \pi/2]$ and B_θ is fixed at $\theta = \pi/2$ and $R \in [R_d; 5650R_d]$, then at $R = R_d$ and $\theta = \pi/2$, B_R and B_θ are both fixed. Thus, the normalizing value of the magnetic field strength on the central object boundary is also fixed by the JED parameter μ.

Just like the JED conditions at $\theta = \pi/2$ were fixed consistently with an ideal MHD steady jet, the central object conditions at $R = R_d$ are fixed consistently with an ideal MHD steady spline. Thus velocity is set so that $\vec{v_p} \parallel \vec{B_p}$, and one has $v_\theta = v_R(B_\theta/B_R)$. Then, there stays the four θ-distributions of ρ, V_s, v_R and v_φ to be specified. This is done through a spline function $f(\theta)$ that smoothly connects the inner disk values ($\theta = \pi/2$) to the values set on the polar axis ($\theta = 0$). Its expression is:

$$f(\theta) = \left(3\sin^2\theta - 2\sin^3\theta\right)^{3/2} \tag{3.24}$$

so that $f(\theta = 0) = 0$ on the axis and $f(\theta = \pi/2) = 1$ on the disk.

Similarly to the JED boundary conditions, we set the plasma rotation as $v_\varphi = \Omega_* r + v_R(B_\varphi/B_R)$, the magnetic surfaces rotating at

$$\Omega_* = \Omega_{*_a}\left(1 - f(\theta)\right) + \Omega_{K_d} f(\theta) \tag{3.25}$$

where Ω_{*_a} is the central object rotation on the axis. It will be used as a free parameter, typically ranging from Ω_{K_d} (solid-body rotation on the central object) to zero. The choice of Ω_{*_a} is crucial in our problem. Sections 5.1.3 and 6.4.1 are dedicated to its study.

The radial speed v_R is set constant with θ, and fixed through the sonic Mach number by $v_R = M_{S_R} V_s$. The value of M_{S_R}, chosen constant with θ for simplicity, is fixed by continuity at $\theta = \pi/2$, with $M_{S_R} = M_{S_\theta}|B_R/B_\theta|_d = 10|B_R/B_\theta|_d > 1$. As the magnetic inclination at the inner disk boundary $|B_R/B_\theta|$ is constant, M_{S_R} does not change with time. However, it may change from simulation to simulation with the inclination of the field lines (in our parameter space with the value of α), while always staying higher than unity.

The sound speed on the central object is computed using

$$V_S = V_{S_a}(1 - f(\theta)) + V_{S_d} f(\theta) \tag{3.26}$$

The sound speed on the axis V_{S_a} is fixed thanks to the Bernoulli invariant on the axis E_a. The MHD term $\Omega_* r B_\varphi / \eta$ vanishing on the axis, one directly obtains

$$V_{s_a}^2 = \frac{GM}{R_d} \frac{1+e_a}{\frac{1}{2}M_{S_R}^2 + \frac{1}{\Gamma-1}} \tag{3.27}$$

and

$$v_{R_a}^2 = \frac{GM}{R_d} \frac{1+e_a}{\frac{1}{2} + \frac{1}{M_{S_R}^2(\Gamma-1)}}, \tag{3.28}$$

where v_{R_a} is the injection speed on the axis and $e_a = E_a R_d/(GM)$ is the Bernoulli invariant normalized to the gravitational energy at $R = R_d$. It is the parameter used to fix the axial spine temperature. The aim is to make a transition as smooth as possible, to avoid introducing discontinuities.

As our jets are cold, the energy is mostly determined by the magnetic lever arm λ and for the field line anchored at $r = R_d$, $e_d = \lambda_d - 3/2 + \epsilon^2/(\Gamma-1)$. The jet magnetic lever arm being expected to be $\lambda_d \simeq 10$ (see Figure 2.3), in order to get a spine of smaller energy than the jet, I fix $e_a = 2$. With these conditions, the two flows should reach the following poloidal asymptotic speeds:

- For the spine $v_{\infty_{spine}}^p \simeq 2\sqrt{E_a} = 2\sqrt{e_a} V_{K_d}$ (equation 2.88).
- For the jet $v_{\infty_{jet}}^p \simeq \sqrt{2\lambda_d - 3} V_{K_d}$ (equation 2.92).

This gives $v_{\infty_{spine}}^p / v_{\infty_{jet}}^p \simeq 0.7$. Asymptotically, the jet should be faster than the spine, but this small difference should avoid extreme shears.

The plasma density is connected from its value on the axis ρ_a to its much larger value on the disk $\rho_d = \delta \rho_a$ via the MHD invariant η, as $\rho(\theta) = \eta B_R/(4\pi v_R)$, and η follows:

$$\eta = \eta_a(1 - f(\theta)) + \eta_d f(\theta) \tag{3.29}$$

where η_a and η_d are determined with ρ_a and ρ_d. This method simply ensures that the mass flux to magnetic flux ratio has a smooth variation between the disk and the axis. Keep in mind that my goal is to study the outcome of the disk jet, not so much the spine-jet interaction.

3.2.4 Normalization

The MHD equations are solved with PLUTO and the results will be presented in dimensionless units. Unless otherwise specified, lengths are given in units of R_d, velocities in units of $V_{K_d} = \sqrt{GM/R_d}$, time in units of $T_d = R_d/V_{K_d}$, densities in units of ρ_a, magnetic fields in units of $B_0 = V_{K_d}\sqrt{4\pi\rho_a} = B_d/10$, mass fluxes in units of $\dot{M}_d = \rho_a R_d^2 V_{K_d}$ and powers in units of $P_d = \rho_a R_d^2 V_{K_d}^3$.

In order to be more specific, I translate these quantities for the case of a young star, assuming a star of one solar mass with an innermost disk radius $R_d = 0.1$au and a density on the axis $\rho_a = 10^{-15}$g.cm^{-3}, namely

$$\begin{aligned}
V_{Kd} &= 94.3 \left(\frac{M}{\mathrm{M}_\odot}\right)^{1/2} \left(\frac{R_d}{0.1\mathrm{au}}\right)^{-1/2} \mathrm{km.s}^{-1} \\
\dot{M}_d &= 3.35 \times 10^{-10} \left(\frac{\rho_a}{10^{-15}\mathrm{g.cm}^{-3}}\right) \left(\frac{M}{\mathrm{M}_\odot}\right)^{1/2} \left(\frac{R_d}{0.1\mathrm{au}}\right)^{3/2} \mathrm{M}_\odot.\mathrm{yr}^{-1} \\
P_{jet} &= 1.26 \times 10^{12} \left(\frac{\rho_a}{10^{-15}\mathrm{g.cm}^{-3}}\right) \left(\frac{M}{\mathrm{M}_\odot}\right)^{3/2} \left(\frac{R_d}{0.1\mathrm{au}}\right)^{1/2} \mathrm{ergs.s}^{-1} \\
B_0 &= 10.6 \left(\frac{\rho_a}{10^{-15}\mathrm{g.cm}^{-3}}\right)^{1/2} \left(\frac{M}{\mathrm{M}_\odot}\right)^{1/2} \left(\frac{R_d}{0.1\mathrm{au}}\right)^{-1/2} \mathrm{G} \\
T_d &= 1.8 \left(\frac{M}{\mathrm{M}_\odot}\right)^{-1/2} \left(\frac{R_d}{0.1\mathrm{au}}\right)^{3/2} \mathrm{days.}
\end{aligned} \tag{3.30}$$

Such a star is illustrated in Figure 3.6. This scheme shows that while the jet only corresponds to the disk emitted outflow, the spine corresponds to the stellar jet and the star-disk interaction jet.

Even though the choices of M and R_d are constrained by the observations, that of ρ_a is arbitrary. Ultimately, it is the choice of ρ_a that defines the normalizations of mass flux, pressure and magnetic field in the jet.

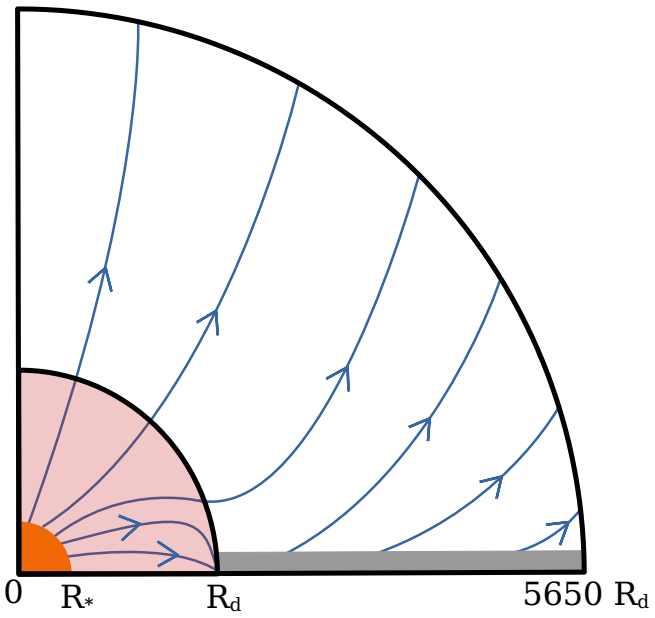

FIGURE 3.6: Scheme of young star and its magnetosphere, surrounded by an accretion disk. In blue are poloidal magnetic field lines. The star of radius R_* is in orange, and the magnetized accretion disk extends from R_d to 5650 R_d. Between R_* and R_d is the Star-Disk Interaction (SDI) in red.

Chapter 4

Self-similar simulations: The Blandford & Payne case

Contents

4.1 A standing collimated jet . . . 80
4.1.1 Description of the simulation . . . 80
4.1.2 Quasi steady state . . . 82
4.1.3 Radial layering . . . 84
A two-component outflow: spine+jet . . . 84
Layering inside the jet . . . 85
4.2 Steady recollimation shocks . . . 86
4.2.1 Rankine-Hugoniot conditions . . . 86
Numerical detection of shocks . . . 86
Compression factor and verification of the jump conditions 87
Physical characteristics of the main shock . . . 87
4.2.2 Two kinds of stationary shocks . . . 89
4.2.3 Shock spacing . . . 90
4.3 Electric circuits . . . 91
4.4 Time evolution . . . 92
4.5 Large scale collimation . . . 95
4.6 Summary . . . 98

"Half the charm of climbing mountains is born in visions preceding this experience - visions of what is mysterious, remote, inaccessible."

"La moitié du charme de l'ascension des montagnes naît des visions qui précèdent cette expérience - visions de ce qui est mystérieux, lointain, inaccessible."

George Mallory

Maintenant que nous avons vu les équations résolues, les méthodes numériques, la configuration et la plupart de ses paramètres, examinons les résultats. Comme nous l'avons vu au chapitre 3, tous les paramètres sont réglés pour les quatre conditions aux limites, sauf trois qui doivent encore être fixés pour les conditions d'injection :

- *Le paramètre de chargement en masse κ.*
- *Le paramètre d'autosimilarité et exposant du flux magnétique α.*
- *La rotation des surfaces magnétiques sur l'axe Ω_{*_a}.*

Le but du travail présenté dans ce chapitre était de produire des simulations à grande échelle de jets de type Blandford & Payne, afin d'observer leurs propriétés de collimation et de voir s'ils produiraient des chocs de recollimation. Ainsi, pour la simulation de référence, j'ai simplement pris les valeurs des paramètres figurant dans l'article fondateur Blandford and Payne, 1982, c'est-à-dire $\kappa = 0.1$ et $\alpha = 3/4$. J'ai aussi simplement décidé de fixer $\Omega_{*_a} = 0$ pour limiter l'éjection magnétocentrifuge depuis l'axe. Une étude paramétrique de κ, α et Ω_{*_a} est décrite dans le chapitre 5. Dans ce chapitre, je vais m'attacher à décrire la simulation de référence.

La simulation a été exécutée jusqu'à un temps $t_{end} = 6,5 \times 10^5$, ce qui correspond à 10^5 orbites à la limite interne du disque et à un quart d'orbite à la limite externe du disque. L'apparition de chocs de recollimation est la caractéristique la plus importante de la simulation, car à ma connaissance, c'est la première fois que des simulations "globales" de jets super-FM présentent les schémas prédits par les études analytiques. Ils commencent près de l'axe polaire, et deux d'entre eux suivent approximativement la forme attendue des caractéristiques des jets auto-similaires MHD. Cependant, l'image est plus complexe : il y a aussi des chocs plus petits qui semblent fusionner avec les plus grands.

Au dernier instant de la simulation, le jet a atteint un état stationnaire. Les grandeurs caractéristiques de l'éjection n'évoluent presque plus, et les invariants MHD sont bien quasiment constants le long des surfaces de champ magnétique. On peut alors vérifier si on y retrouve bien les propriétés des jets stationnaires en MHD idéale. S'étendant jusqu'aux chocs, le circuit accélérateur a bien la forme usuelle, ressemblant à un papillon. Au cours de la propagation, l'énergie magnétique du jet est transférée en énergie cinétique. Lorsqu'il atteint le bord externe de la grille de calcul, le jet a presque atteint sa vitesse asymptotique théorique, eu égard des conditions de lancement.

L'écoulement présent est cependant légèrement différent de l'image vue dans les solutions auto-similaires. Cela est du à deux raisons. La première est la présence d'une colonne axiale émise depuis l'objet central, qui rompt l'autosimilarité. Elle correspond à un flux de masse dix fois plus faible que celui du jet, mais à une puissance semblable. Par conséquent, le jet s'écarte de plus en plus de l'image théorique lorsque l'on se rapproche de l'axe.

La seconde raison est la présence des chocs de recollimation stationnaires. Ceux-ci étaient prédits mais pas observés par les solutions auto-similaires. Pour étudier ces chocs, j'ai développé des algorithmes me permettant de suivre précisément l'évolution du jet le long de chaque ligne de champ. Cela m'a permis de comparer l'état du jet juste après le choc à celui juste avant le choc. Ici, la quantité d'intérêt particulier est le taux de compression, augmentation relative de la densité au niveau du choc. Son calcul, ainsi que d'autres, m'a tout d'abord permis de confirmer que les chocs suivaient bien les conditions de Rankine-Hugoniot. Mais surtout, cela m'a permis de caractériser les chocs obtenus. Ils sont de deux types :

- *Les chocs de recollimation prédits par les solutions auto-similaires. Leur existence résulte de la collimation globale des surfaces magnétiques : lorsque le rayon du jet augmente, la contrainte de cerceau diminue plus lentement que le terme centrifuge, ce qui conduit inévitablement à une contrainte de cerceau dominante et à une collimation. Une focalisation magnétique vers l'axe est inévitable, et l'écoulement n'a alors d'autre choix que de rebondir, créant les chocs de recollimation de cette première classe. Il s'agit de chocs faibles, dont le taux de compression ne monte pas au delà de 1.5.*

- *Des chocs plus petits et plus faibles, limités à l'interface entre la colonne et le jet. Leur facteur de compression tombe rapidement à l'unité, et certains fusionnent même avec des chocs de recollimation plus puissants. Ils semblent également régulièrement espacés. Cette régularité pourrait être due à une propagation horizontale d'ondes entre l'axe et la frontière extérieure de la colonne. Ces plus petits chocs seraient alors la résultante d'ondes magnétosoniques rapides déclenchés par les plus grands chocs.*

La présence de ces chocs engendre de nombreuses différences dans la structure des circuits électriques, au delà du circuit accélérateur en forme de papillon décrit ci-dessus. On n'atteint pas la déconnexion espérée entre le circuit accélérateur et le circuit asymptotique, de nombreux circuits contournant le choc pour venir se refermer sur l'objet central en longeant l'axe. De plus, plusieurs circuits se referment hors de la grille de calcul, laissant perplexe quant à l'origine physique du courant post-choc.

Ces circuits électriques régissent la collimation du jet, que ce soit avant où après les chocs. Au cours de la simulation, comme attendu le jet interne se décollimate tandis que le jet externe se décollimate. Cette collimation est du au "hoop stress" créé aux forces de Laplace créées par le champ magnétique toroidal. Sur toute l'étendue du jet, ce "hoop stress" reste la force confinante dominante. Dans la partie interne du jet, la force déconfinante est la force centrifuge, tandis que dans la partie externe il s'agit du gradient de pression magnétique.

Dans ce chapitre, je me suis également intéressé à l'évolution temporelle du jet simulé. Qu'est-il arrivé avant que celui-ci converge ? D'abord, la colonne et les parties les plus internes du jet progressent de la frontière inférieure jusqu'à la frontière extérieure, pour l'atteindre après quelques milliers d'orbites au bord interne. Immédiatement après, les chocs commencent à se former, mais leur position n'est stabilisée qu'après une dizaine de milliers d'orbites. Puis, le jet se collimate petit à petit, jusqu'à une réorganisation massive après une centaine de milliers d'orbites. Cette réorganisation, créée par une forte accumulation de courant sur l'axe, entraîne la création d'un choc supplémentaire.

Now that we have seen the equations solved, the numerical methods, the setup and most of its parameters, let us look at the results. As seen in chapter 3, all parameters are set on all four boundary conditions, except three that still need to be fixed on the injection conditions:

- The mass loading parameter κ.
- The self-similar parameter α.
- The rotation of the magnetic surfaces on the axis Ω_{*_a}.

The aim of the work presented in this chapter was to produce large-scale simulations of Blandford & Payne jets, in order to observe their collimations properties and see whether they would produce recollimation shocks. Thus, for the reference simulation we simply took the parameter values as in the seminal Blandford and Payne, 1982 paper, that is $\kappa = 0.1$ (Figure 2.3) and $\alpha = 3/4$. We then simply decided to set $\Omega_{*_a} = 0$ to limit the magnetocentrifugal ejection from the axis. A parametric study in κ, α and Ω_{*_a} is described in chapter 5 and for now, I will discuss the reference simulation. Figure 4.1 shows several quantities just above the injection boundary at the final simulation time t_{end}. This boundary is almost self-similar: all parameters follow power laws on the JED ($r \geq 1$) and are smoothly interpolated to their finite axis values on the central object ($r \leq 1$). Note that B_φ, B_θ for $r < 1$ and B_R for $r > 1$ are determined by the simulation ("outflow" conditions). For all other quantities, the profiles are those described in section 3.2.3 with $\kappa = 0.1$, $\alpha = 3/4$ and $\Omega_{*_a} = 0$.

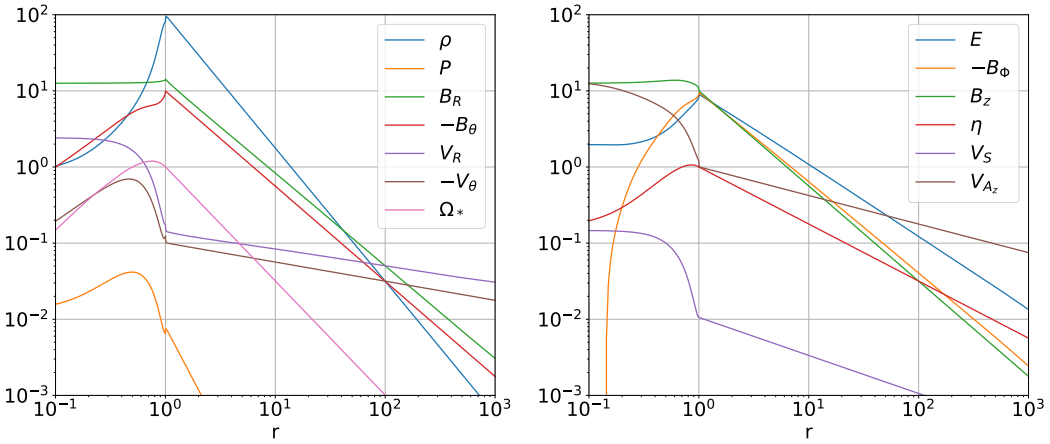

FIGURE 4.1: Boundary conditions on the lowermost cells of the reference simulations. The quantities are plotted on the first cell along the injection boundaries (e.g. central object $R = 1$ for $r \leq 1$ and JED $\theta = \pi/2$ for $r \geq 1$). On the left are shown the conditions that are directly set at the injection boundaries: the density ρ, the pressure P, the radial and orthoradial magnetic fields B_R and $-B_\theta$, the radial and orthoradial velocities v_R and $-v_\theta$ and the rotation speed of the magnetic surfaces Ω_*. On the right are quantities dependent on those set conditions: the Bernoulli invariant E, the toroidal and vertical magnetic field $-B_\varphi$ and B_z, the mass to magnetic flux ratio η, the sound speed V_s and the vertical Aflvén speed V_{A_z}.

4.1 A standing collimated jet

4.1.1 Description of the simulation

The simulation was run until a time $t_{end} = 6.5 \times 10^5 T_d$, corresponding to 10^5 orbits at the inner disk boundary ($r = 1$) and to a quarter of an orbit at the outer disk boundary ($r = 5650$). The final stage reached by the simulation is displayed on Figure 4.2. The black lines are poloidal magnetic field surfaces, the dotted red line is the Alfvén surface where $m \equiv v_p/V_{A_p} = 1$ and the dashed red line is the FM surface where $n \equiv v_p/V_{FM_p} = 1$. The left panel is a snapshot of the whole computational domain and the right panel is a zoom on the innermost outflow, corresponding to the scale used by Fendt, 2006. The background colors are the logarithm of the FM mach number on the left and the logarithm of the density on the right.

I define $r_{0,FM}$ as the anchoring radius of the outermost magnetic surface that reaches super-FM speeds. In all the following, I will only refer to the jet as the outflow ejected between the anchoring radii $r_0 = 1$ and $r_0 = r_{0,FM}$, and to the spine as the outlfow ejected between $r_0 = 0$ and $r_0 = 1$. For this simulation, $r_{0,FM} = 323$, meaning that the majority of the jet plasma eventually becomes super-FM: $\dot{M}_{jet+spine}(r_0 \leq r_{0,FM})/\dot{M}_{jet+spine}(r_0 \leq 5650) = 65\%$. The critical surfaces are conical in a large portion of the domain[1], characteristic of the steady state of self-similar solutions. In the same way, I define $r_{0,A}$ as the anchoring radius of the outermost magnetic surface that reaches super-Alfvénic speeds. Beyond $r_{0,A} = 1284$ the flow cannot become stationary.

The yellow lines are the electric circuits, isocontours of the poloidal electric current $I = rB_\varphi$, mostly oriented counterclockwise. These circuits showcase some features inside the jet:

- The usual butterfly shape of the initial accelerating circuit, extended until a spherical radius $R \simeq 3000$.
- Current-closure happening outside of the domain: Circuits leaving the JED at disk radii $r_0 \gtrsim 2000$ exit the domain via the outer boundary, mostly at high colatitudes in the sub-alfvénic regime, and re-enter it at smaller colatitudes, in the super-FM jet.
- The presence of several current sheets, in the form of an accumulation of current lines. Those are standing recollimation shocks.

Without the shocks, the electric circuits are quite similar to the theoretical picture presented on the left panel of Figure 2.5, as here $\alpha = 3/4 < 1$. The appearance of recollimation shocks is the most important feature in the simulation, as to my knowledge, this is the first time that "global" simulations of super-FM jets exhibit the patterns predicted by analytical studies. They start near the polar axis, and roughly follow the expected shape of MHD self-similar jets characteristics (see Figure 13 of Ferreira, 1997 or Figures 3 of Vlahakis et al., 2000 and Ferreira and Casse, 2004). One may see on Figure 4.3 two main recollimation shocks: a first one leaving the axis at an altitude $Z_1 = 1850$, fully enclosed in the domain and merging with the FM surface around $r = 2500$, $z = 3800$; a second one starting on the axis at an altitude $Z_5 = 2634$ and leaving the simulation domain at $r = 1800, z = 5200$. However, the picture is more complex: there are also smaller shocks emerging from the axis at altitudes between Z_1 and Z_5. The section 4.2 is dedicated to the study of the shocks. For now, I describe the jet in its globality.

[1] Except near the shock for the FM surface.

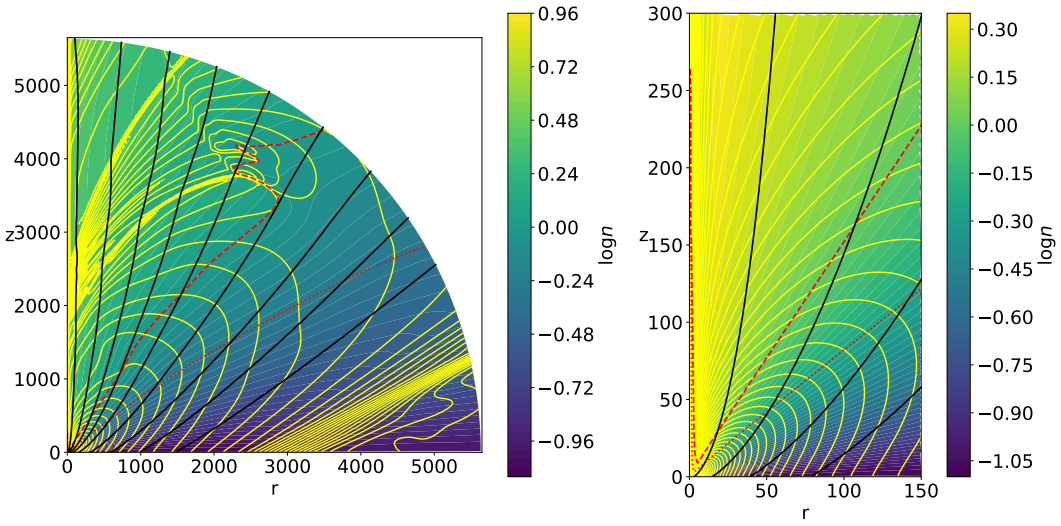

FIGURE 4.2: Snapshot of the simulation at t_{end}. Left: Global view with of the simulation domain. Right: Close-up view of the innermost regions. In both panels, black solid lines are the poloidal magnetic surfaces anchored on the disk at $r_o = 3; 15; 40; 80; 160; 320; 600; 1000; 1500$, the yellow solid lines are isocontours of the poloidal electrical current, and the red dashed (resp. dotted) line is the FM (resp. Alfvén) critical surface. In the background is the logarithm of the FM mach number n.

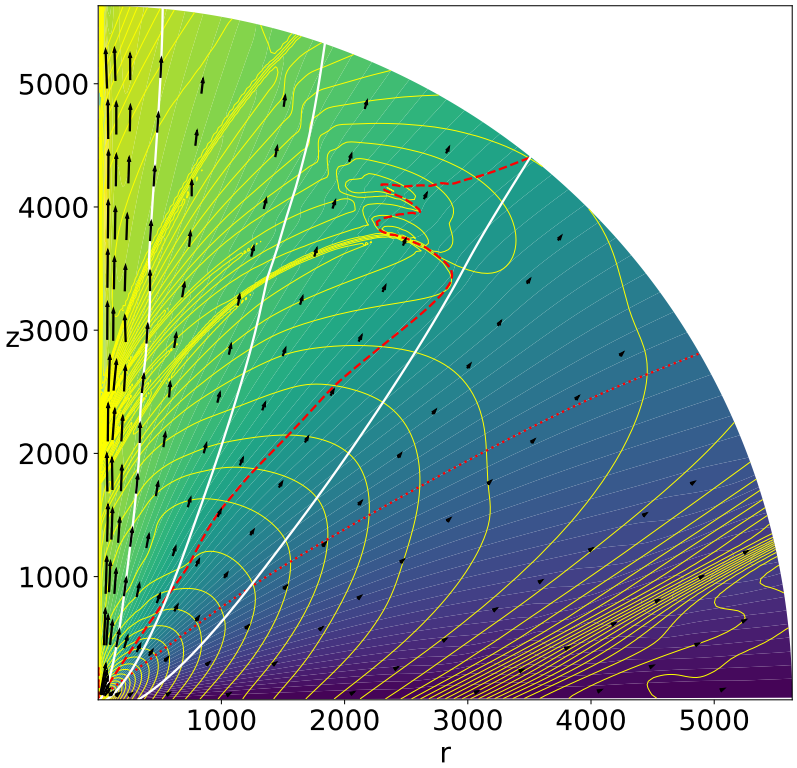

FIGURE 4.3: Snapshot of the simulation at t_{end}. I use the same color coding as in Figure 4.2, left for the background, critical surfaces and electric circuits. The black arrows show the poloidal velocity. The white lines are streamlines inside which (from left to right) 50%, 75%, and 100% of the super-FM (spine+jet) mass outflow rate is carried in.

4.1.2 Quasi steady state

I have pointed out that the simulated jet is stationary. In order to backup this assertion, I compute a few global jet quantities with time: the radius $r_{0,FM}$ of the outermost FM magnetic surface and the colatitudes θ_A^{ext} and θ_{FM}^{ext} of the intersection between the outer boundary and the critical surfaces (respectively Alfvén and FM). On Figure 4.4 I represent the evolution of these quantities from $t_0 = 5.1 \times 10^5$ until t_{end}, normalizing the quantities to their "initial" values at t_0. Their evolution is rather straightforward: $r_{0,FM}$ and $\dot{M}_{jet}$ increase as the jet gets larger, while θ_A^{ext} and θ_{FM}^{ext} get smaller as it gets more collimated. The relative variations of those quantities are however very small, i.e. less than 3% for $r_{0,FM}$ and 1% for the other quantities.

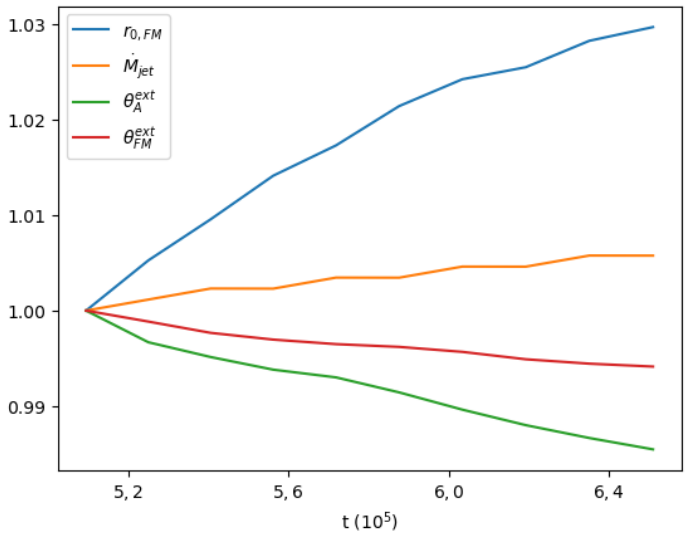

FIGURE 4.4: Late evolution of several global jet quantities: the radius $r_{0,FM}$ of the last super-FM surface, the jet mass-loss rate $\dot{M}_{jet}$, and the two colatitudes θ_A^{ext} and θ_{FM}^{ext} defined by the position of the two critical surfaces. A slight drift from their initial value is indeed observed.

Therefore, the jet has achieved a relative global steady state at t_{end}. Let us probe whether the properties of steady-state ideal MHD jets are retrieved.

Figure 4.5 details the energy contributions to the Bernoulli invariant E at t_{end} along a magnetic surface anchored at $r_0 = 100$. The total energy is indeed conserved, and the usual pattern (Casse and Ferreira, 2000a) is retrieved: the kinetic energy (green) increases thanks to the magnetic acceleration, leading to a decrease in the magnetic energy (magenta). The outflow being cold, enthalpy (red) is negligible, as well as gravity at high enough altitudes. The shock is also clearly seen around $z = 3800$; the flow is slowed down and the energy is transferred to the magnetic field, in agreement with the Rankine-Hugoniot jump conditions (see section 4.2). After the shock, the MHD acceleration is resumed, but the magnetic energy still holds around 45% of the total energy. The poloidal speed thus remains smaller than its asymptotic value $v_\infty = \sqrt{2\lambda - 3V_K}$ (although close, see Figure 4.7).

Figure 4.6 depicts the evolution of the five MHD invariants at t_{end} along two magnetic surfaces. Their evolution is normalized to their value on the disk surface, at anchoring radii $r_0 = 100$ (left) and $r_0 = 1000$ (right). As their name suggests, the MHD invariants are constant in a steady flow (see section 2.6.1). On the left panel, we see that along this surface the invariants only display a small drift from their values near the disk surface. They mostly vary at $z \simeq 3800$, as the magnetic field line

crosses the shock. This variation remains very small, of about 1%. It is of numerical origin, and after the shock the invariants quickly return to their pre-shock values. For the right panel, as $r_0 = 1000 > 323 = r_{0,FM}$, the flow remains sub-FM along the field line and no shock is crossed. The variations of the invariants are thus smaller, always less than 0.5 %. The reader may notice that thanks to our choice of energy equation, the entropy is conserved at machine precision.

This invariant evolution shows that my simulated jets are indeed steady, and also that the PLUTO code and the configuration used are efficient.

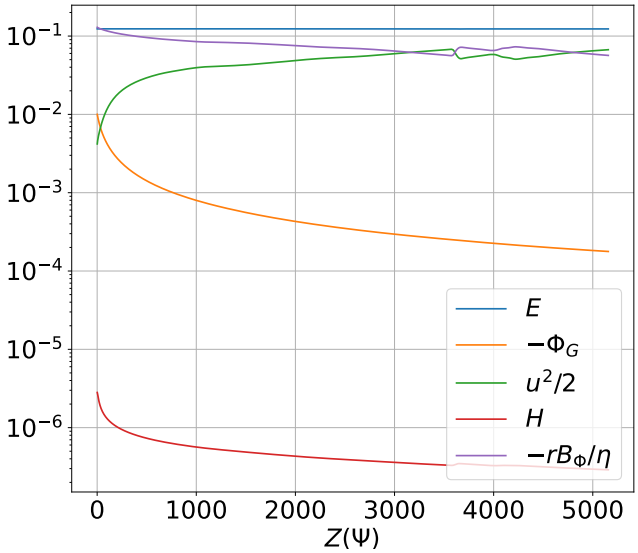

FIGURE 4.5: Evolution of the various energy contributions along a magnetic surface of anchoring radius $r_0 = 100$ at t_{end}: the Bernoulli invariant E, the gravitational potential Φ_G, the total specific kinetic energy $u^2/2$, the enthalpy H, and the magnetic energy $-\Omega_* r B_\varphi / \eta$. The abscissa is the altitude $Z(\Psi)$.

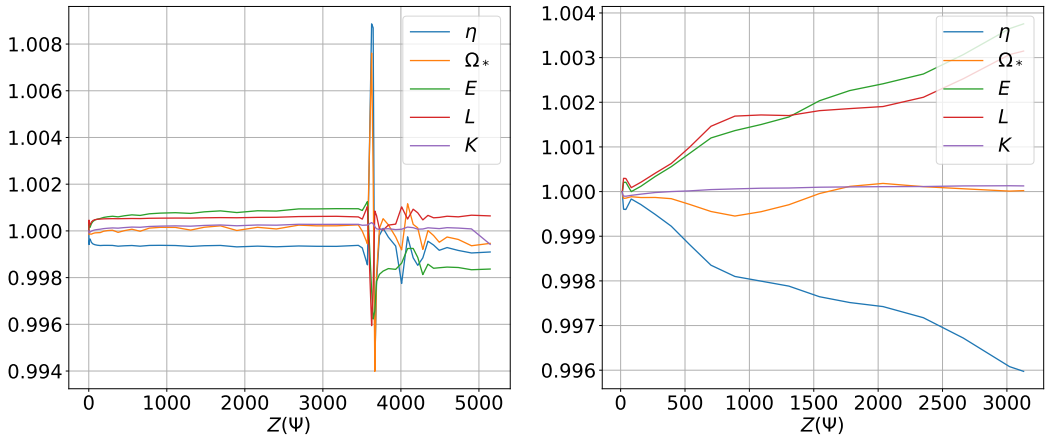

(A) Anchoring radius $r_0 = 100$.

(B) Anchoring radius $r_0 = 1000$.

FIGURE 4.6: Evolution of the MHD invariants along field lines of two different anchoring radii r_0 at t_{end}. All invariants have been normalized to their values at r_0. The abscissa is the altitude $Z(\Psi)$.

The steady-state jet looks a lot like the theoretical case described in section 2.6. On the left panel of Figure 4.7 I represent the evolution of the magnetic lever arm λ for field lines of anchoring radii r_0. It is smaller in the inner jet regions, as the energy of the spine is smaller than that of the jet (see section 3.2.3). The arm lever is 12 in the innermost regions then grows with r_0 until around 17. The two red vertical lines are $r_0 = r_{0,FM}$ (dashed) and $r_0 = r_{0,A}$ (dotted). Beyond $r_{0,A}$ the field lines cannot become stationary and λ is discontinuous. The right panel compares two poloidal speeds: the asymptotic speed of each field line $v_\infty = \sqrt{2\lambda - 3}V_K(r_0)$ and the actual speed on the field line at the edge of the domain $R = 5650$, named v_{max}. We see that the two values are close, and v_{max} mimics the decrease of v_∞ with the radius, caused by the disk Keplerian rotation.

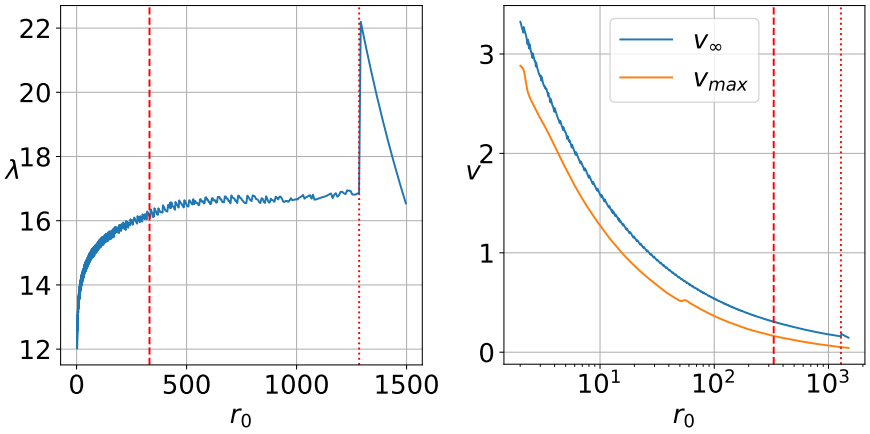

FIGURE 4.7: Left: Evolution of the field line magnetic lever arm λ over the anchoring radius r_0. Right: Evolution of the asymptotic speed $v_\infty = \sqrt{2\lambda - 3}V_K(r_0)$ in blue and the poloidal speed at the intersection between the field line and the outer boundary $R = 5650$ in orange, over the anchoring radius r_0. The vertical red lines are $r_0 = r_{0,FM}$ (dashed) and $r_0 = r_{0,A}$ (dotted).

4.1.3 Radial layering

A two-component outflow: spine+jet

The outflow is composed of a spine emitted from the central object, and a jet emitted from the Jet-Emitting Disk, as shown on Figure 3.5-left. In order to quantify the impact of each component on outflow dynamics, I compute the mass loss rate of the jet $\dot{M}_{jet} = \int_{R_d}^{r_{0,FM}} \rho\vec{u} \cdot \vec{dS}$ and the spine $\dot{M}_{spine} = \int_0^{\pi/2} \rho\vec{u} \cdot \vec{dS}$. I obtain a relative mass loss rate $\dot{M}_{spine}/\dot{M}_{jet} = 10\%$, showing that the outflow mass loss rate is controlled by the Jet-Emitting Disk. Figure 4.3 shows how this mass loss rate is spread across the jet. The three white lines are streamlines inside which 50%, 75% and 100% of the total super-FM outflow (spine+jet) mass is carried. These streamlines are anchored on the disk at respectively $r_0 = 10$, $r_0 = 66$ and $r_{0,FM} = 323$. As the JED mass loss rate falls off very rapidly ($d\dot{M}_{jet}/dr = 2\pi r\rho V_z \propto r^{2\alpha-5/2} = r^{-1}$), even in a very large domain the JED ejection is dominated by the innermost region of the disk. This radial layering may also be vizualized by the black arrows on Figure 4.3, that are poloidal velocity vectors, showing the swift radial decrease at the outer boundary, from $v_p = 3.5$ in the spine to $v_p = 0.2$ at the outer edge of the super-FM domain (see Figure 4.7). Note that at this outer boundary, the spine width ($r_{spine} \sim 20$) is around the cell width, as the grid resolutions decreases with altitude.

I also compute the power emanating from the jet $P_{jet} = \int_{R_d}^{r_{0,FM}} \rho E \vec{u} \cdot \vec{dS}$ and the spine $P_{spine} = \int_0^{\pi/2} \rho E \vec{u} \cdot \vec{dS}$. I obtain a relative power $P_{spine}/P_{jet} = 0.81$. This means that the central object, even though its area is roughly 10^{-7} that of the disk, has quite an influence on the topology of the electric circuits, and thus and the collimation of the outfow. The spine quickly reaches super-FM speeds, at $z \sim 260$. Because of the boundary conditions ($\Omega_{*_a} = 0$) there is no magnetocentrifugal acceleration near the polar axis, and the spine slows down with altitude: it becomes super-FM thanks to the vertical decrease of the magnetic field strength.

In physical units and considering the same solar mass star as in section 3.2.4, the jet mass loss rate is $1.2 \times 10^{-7} M_\odot.yr^{-1}$ and jet power 7.8×10^{14}ergs.s^{-1} with a magnetic field around 10 G at 0.1 au. As a reminder, jet here refers to what is ejected between $r_0 = 1$ and $r_0 = r_{0,FM} = 323$.

Layering inside the jet

How is this layering the jet itself ? Naturally, conditions resembling those set at the JED boundary are recovered. Figure 4.8 shows in dashed lines the rotation speed, the toroidal and vertical magnetic field along the horizontal $z = 1500$, upstream of the shocks. In full lines are various power laws. The exponents are chosen so that a full line power law is what is expected by the radially self-similar solutions for the quantities represented by dashed lines of the same color. Those exponents are simply computed by using $\alpha = 3/4$ in the expressions of Table 2.3. The quantities qualitatively follow the variations expected from the self-similar solutions. Differences can be explained by two factors. First, our solutions are not purely self-similar due to the presence of an axial spine ejected at $r_0 \leq 1$. Second, radially self-similar means following power laws in spherical radius R, and here quantities are represented along the cylindrical radius r. Still, the radial structure of the pre-shock jet retrieves the layering of the self-similar MHD jets, with the inner regions being denser, with higher velocities and magnetic fields. This is analogous to the "onion-like" structure seen in protostellar jets (see e.g. Agra-Amboage et al., 2011; Agra-Amboage et al., 2014).

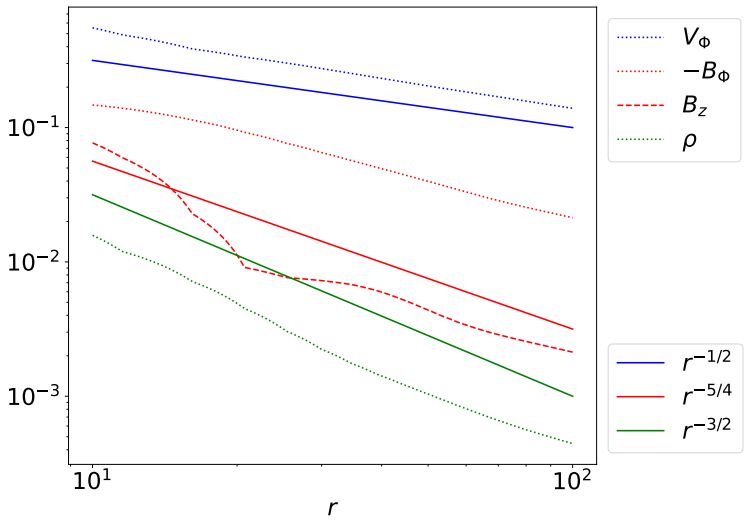

FIGURE 4.8: Dashed lines: radial distribution of various quantities at t_{end} along the horizontal $z = 1500$. Solid lines: Radial profiles of various monomials of r.

4.2 Steady recollimation shocks

The presence of large scale shocks is certainly the most interesting feature of the simulation. There are five shocks, highlighted in color on Figure 4.9, emerging from the polar axis at altitudes $Z_1 = 1850$, $Z_2 = 2000$, $Z_3 = 2160$, $Z_4 = 2372$ and $Z_5 = 2634$. They all occur occur when the magnetic field lines starts to bend towards the axis, and then give rise to an outward refraction of the field line; thus coinciding with a local minimum in the cylindrically radial magnetic field B_r. Combined with the fact that they are motionless with time (see section 4.4), the shocks may be called **standing recollimation shocks**. Of all the shocks, only the two mentioned on section 4.1.1 and starting at altitudes Z_1 and Z_5 span over a large portion of the simulation domain. And, as the shock starting at Z_5 is not fully enclosed in the domain, the shock starting at Z_1 (in red on Figure 4.9) is the only one that will be extensively studied. Hereafter, it is named main recollimation shock.

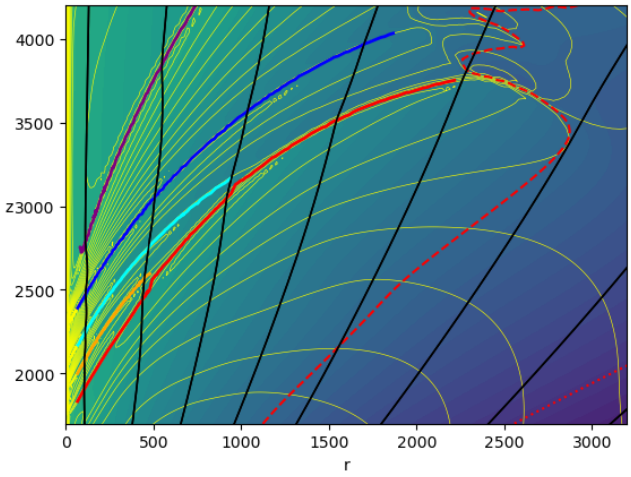

FIGURE 4.9: Close-up view of the simulation at t_{end} showing the shock forming region, with field lines anchored at $r_0 = 1.2; 2; 3; 4; 5; 7; 9$. The five shocks are highlighted in red, orange, cyan, blue, and purple. We use the same color coding as in the left panel of Fig. 4.2.

4.2.1 Rankine-Hugoniot conditions

Happening beyond the $n = 1$ fast-magnetosonic critical surface, the recollimation shocks are fast shocks, described in section 2.7. They correspond to a sudden jump in all flow quantities that naturally follow the Rankine-Hugoniot conditions, thanks to PLUTO's shock capturing scheme. In this section I first explain how I studied the shocks and confirm that the jump conditions are indeed retrieved. Then I detail the characteristics of the main recollimation shock, that could lead to observational consequences.

Numerical detection of shocks

Detecting a shock requires the ability to follow the evolution of various quantities along a magnetic field line. To this end, I used the standard Cash and Karp, 1990 method, that I adapted to my needs using the interpolation schemes of the Python library Scipy (Virtanen et al., 2020). The adaptative step of the Cash-Karp method

was particularly useful given the huge discrepancy in cell sizes in my numerical grid[2]. With this method, I followed all magnetic field lines looking for discontinuities. In a discrete grid, this is not so obvious. To do so, I computed the derivative of the toroidal magnetic field ($\partial B_\varphi / \partial s$) over the curvilinear absissa (s) along each field line, as shocks are best seen with the poloidal electric currents. Then, I explored the local extrema of $\partial B_\varphi / \partial s$, that would correspond to the shock centers. I checked the consistency using a different approach based on the magnetic field line refraction angle δi, that produced very similar results. I then implemented a few failsafes, most notably that the shock leads to outward refraction ($\delta i_{shock} > 0$) and density growth (compression factor $\chi > 1$). This gave me the shock locations (colored lines on Figure 4.9). Thanks to PLUTO's shock capturing scheme, each shock is resolved and has a finite width as both the HLL and HLLD solvers capture fast shocks. To determine the shock width, I started from the shock center (maximum of $\partial B_\varphi / \partial s$), and searched along the field line for the closest local minimum and maximum in density. These local extrema respectively correspond to the pre and post shock positions, that were used to compute the pre-shock and post-shock quantities. Later in the PhD, the existence of more robust methods (such as Lehmann, Federrath, and Wardle, 2016; Richard et al., 2022) came to my knowledge, but my homemade method managed to produce consistent results.

Compression factor and verification of the jump conditions

The use of this method enables to compute various jump quantities. On Figure 4.10 are represented the compression factor $\chi \equiv \rho_2/\rho_1$[3] along the main recollimation shock, as well as various quantities that should be equal to it. We see that the shocks are relatively weak, with the compression rate remaining lower than 1.3. On the top panel are represented the direct jumps in density ρ, Alfvén mach number m, toroidal magnetic field B_φ and poloidal magnetic field parallel to the shock $B^p_\parallel$. As at these altitudes the jet is very super-alfvénic ($m \sim 10^2 \gg \chi > 1$), the Rankine-Hugoniot conditions (equation 2.100) can be simplified and all these jumps should be equal to the compression factor. On the bottom panel are represented the compression factor χ and the theoretical compression factor χ_{th} expected from equation 2.102 given the pre-shock conditions. The top panel shows the efficiency of PLUTO's shock capturing scheme and my post-treatment shock detection algorithm, as curves are almost superimposed. The bottom panel shows a pretty good coincidence between the detected and theoretical compression factors, except near the axis where it is around 10%, and near the mergers with the smaller shocks. Note that the shocks the cell width is around 10.

Physical characteristics of the main shock

We have seen that the shocks remain relatively weak. This is due to two factors. First, the obliquity of the shocks near the polar axis is high, reducing the FM mach number normal to the shock $n_\perp \leq n$. Second, the total FM mach number itself is low. Jets with a high Alfvén mach number can have a low FM mach number if they are highly collimated ($r_A \ll r$, see Michel, 1969) and the magnetic field is mostly toroidal ($|B_p/B_\varphi| \ll 1$, see Pelletier and Pudritz, 1992). Figure 4.11 displays several quantities along the main shock surface (in red on Figure 4.9), including

[2] I used this same method every time I had to plot a field line.

[3] As in section 2.7, a quantity with a subscript 1 is computed pre-shock and a quantity with a subscript 2 is computed post-shock.

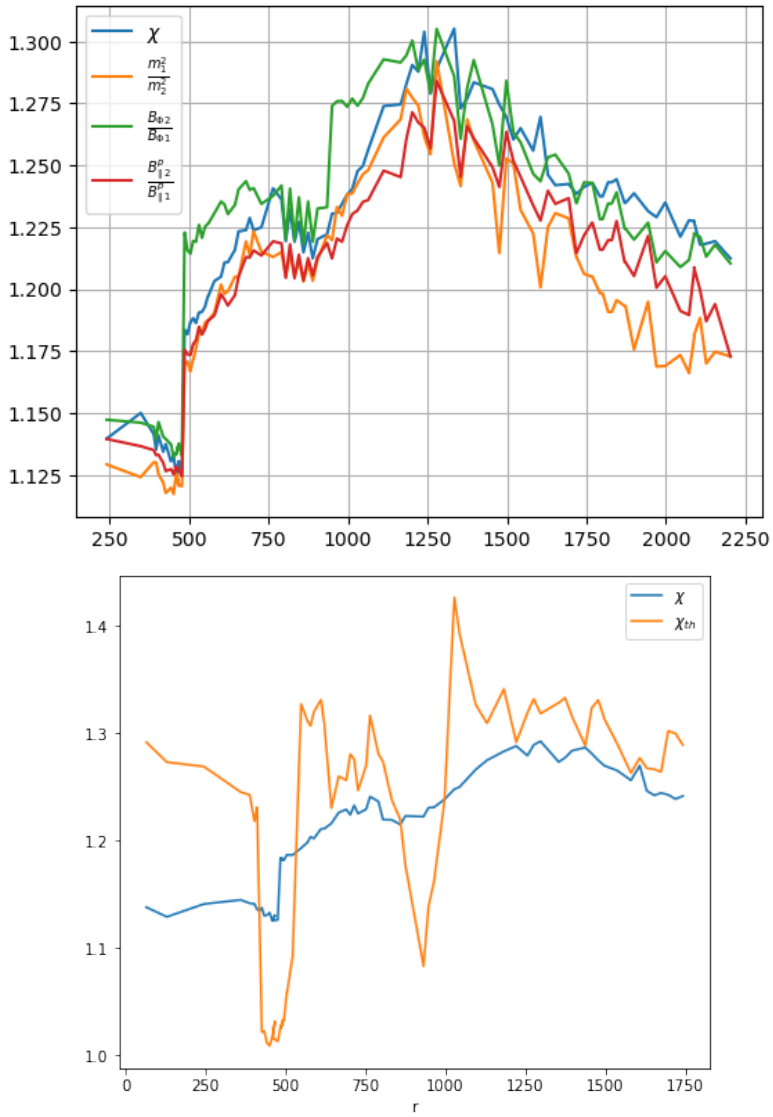

FIGURE 4.10: Distributions of several quantities equal to the compression factor χ along the main recollimation shock at t_{end}. Top: Direct jumps in various quantity: density ρ, Alfvén mach number m, toroidal magnetic field B_φ and poloidal magnetic field parallel to the shock $B^p_{||}$. Bottom: Theoretical solution χ_{th} of equation 2.102 computed using pre-shock quantities, and actual compression rate $\chi \equiv \rho_2/\rho_1$.

the compression rate χ, the Alfvén mach number m and the normal FM number $n_\perp$. We see that even with an Alfvén mach number $m \sim 10^2$, the normal FM mach number stays around unity. Following the shock front from the polar axis to the FM surface, the incident angle[4] decreases, the shock becoming normal at its outer edge ($z \sim 2500$), on the FM surface. Thus as the shock becomes normal $n_\perp \to n = 1$ and the shock vanishes with a compression rate $\chi \to 1$.

The three other curves on Figure 4.11 show the evolution along the shock of the relative jumps in toroidal magnetic field δB_φ, plasma angular velocity $\delta\Omega$ and of the

[4]Here and in all the following, the angles of incidence and refraction are defined as in Snell-Descartes law, i.e. measured from the normal to the shock front.

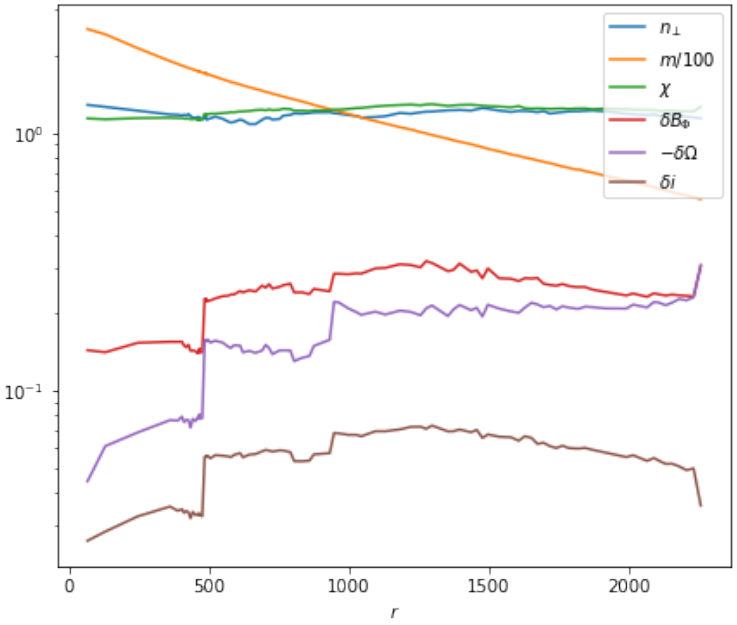

FIGURE 4.11: Distributions of several quantities along the main recollimation shock at t_{end}: Normal incident FM Mach number $n_\perp$, Alfvénic Mach number m, compression rate χ, relative variations of the toroidal magnetic field δB_φ and plasma angular velocity $-\delta\Omega$, and total deviation δi (in rad) of the poloidal magnetic field line.

field line deviation $\delta i = i_2 - i_1$, where i_2 is the angle of refraction and i_1 the angle of incidence. The maximal deviation is $\delta_i = 0.07\text{rad} = 4^o$ which is very small, in agreement with the small compression rate.

The purple curve depicts the relative variation of the flow rotation, $\delta\Omega = (\Omega_2 - \Omega_1)/\Omega_1$. As $\delta\Omega$ is always negative, the shock introduces a sudden decrease in azimuthal speed. Even though the detection of rotation signatures is an important tool for retrieving information on fundamental jet properties (see for instance Anderson et al., 2003; Fendt, 2006; Louvet et al., 2018; Tabone et al., 2020), the weak shocks observed here only create a rotation decrease of around 20% at the outer edge of the shock.

The angular momentum lost by the plasma in the rotation jump is compensated by an increase in toroidal magnetic field strength: the field lines twist is increased by the shock. This is illustrated by the red curve, showing that $\delta B_\varphi = (B_{\varphi_2} - B_{\varphi_1})/B_{\varphi_1} > 0$. This dictates that in the current sheet, the current density is flowing outwards, from the polar axis to the FM surface.

Naturally, as the shock follows the Rankine-Hugoniot conditions, the jumps described above are consistent with those laid out in section 2.7 with the approximations $r \ll r_A$ and $|B_\varphi / B_p| \ll 1$.

4.2.2 Two kinds of stationary shocks

On Figure 4.12 are shown the compression factors along all five shocks in the simulation, the color coding being the same as in Figure 4.9. All shocks but the red one studied before have a higher compression factor near the polar axis. The orange and purple shocks merge with the red one, respectively at $r \sim 500$ and $r \sim 900$, increasing its compression factor. The simulation exhibits two classes of recollimation shocks:

- The recollimation shocks predicted by the self-similar solutions: the red and purple shocks. Their existence results the global collimation of the magnetic surfaces described in section 4.5: as shown in Ferreira, 1997, as the jet radius increases, the hoop stress decreases slower than the centrifugal term, inevitably leading to a dominant hoop stress and collimation, (see also Figure 4.18). This is also consistent with Blandford and Payne, 1982 and Contopoulos and Lovelace, 1994. A magnetic focusing towards the axis is unavoidable, and the flow has then no choice but to bounce away, creating the recollimation shocks of this first class.
- Smaller and weaker shocks that are limited to the spine-jet interface: the orange, cyan and blue shocks. Their compression factor quickly drops to unity, and some even merge with stronger recollimation shocks. They also seem regularly spaced.

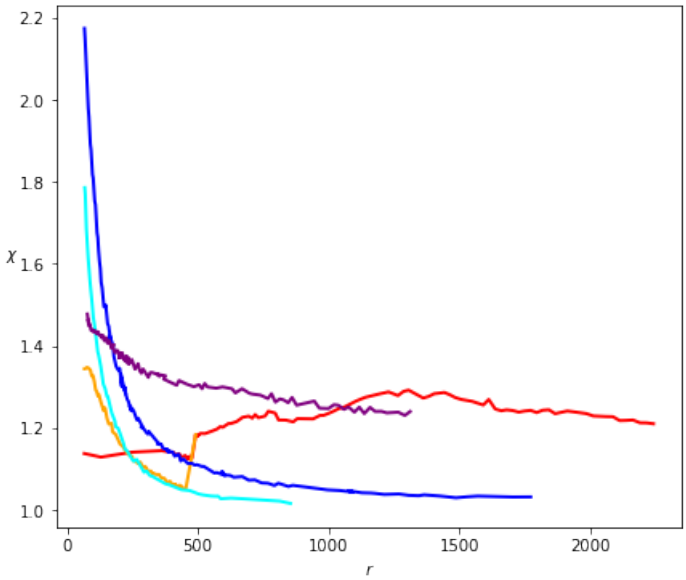

FIGURE 4.12: Bottom: Compression rates χ of all shocks appearing in Figure 4.9, using the same color code. The main shock corresponds to the red curve.

4.2.3 Shock spacing

One interesting feature of these shocks are their consistent spacing, the distance to the following shock is only slightly increasing with altitude: $\Delta Z_{12} = Z_2 - Z_1 = 150$, $\Delta Z_{23} = 160$, $\Delta Z_{34} = 212$ and $\Delta Z_{45} = 262$. This spacing may also be seen on Figure 4.14, representing the time evolution of the altitude of the various shocks. These smaller shocks at the spine-jet interface can thus be associated to steady oscillations, reminiscent to those seen in Vlahakis and Tsinganos, 1997. The stability of these shocks/oscillations is due to the scaling of the dominant forces at this interface (see section 4.5).

What causes this regular spacing ? When reaching a shock front, the flow should take a time $\Delta t_z = \Delta Z / u_z$ to reach the next shock front. In the meantime, if a stationary wave was to propagate horizontally because of a shock-induced radial imbalance, it would do so at the FM speed. Such a wave would go back and forth

on the interface via the polar axis in the timescale $\Delta t_r = 2r_{spine}/V_{FM}$, where r_{spine} is the spine width and V_{FM} the local FM speed. In a steady state the two times Δt_z and Δt_r should be equal, requiring $\Delta Z \simeq 2nr_{spine}$ where n is the local FM mach number. At the fourth shock we have $r_{spine} \simeq 40$ and $n \simeq 3$, which gives $\Delta Z \simeq 2nr_{spine} \simeq 240 \sim 262 = \Delta Z_{45}$. It also provides the correct order of magnitude for the smaller shocks. Such a correspondence indicates that these smaller shocks might be the outcome of stationary radial FM waves triggered by the steady large-scale recollimation shocks.

4.3 Electric circuits

The presence of these shocks make the electric circuits differ quite a lot from the theoretical picture of Figure 2.5-left. Figure 4.13 depicts the electric circuits in more detail. Four remarkable electric circuits have been highlighted in color. The left panel is the actual shape of the circuits in the simulation at t_{end}, and the right panel is a simplified sketch of this rather complicated picture.

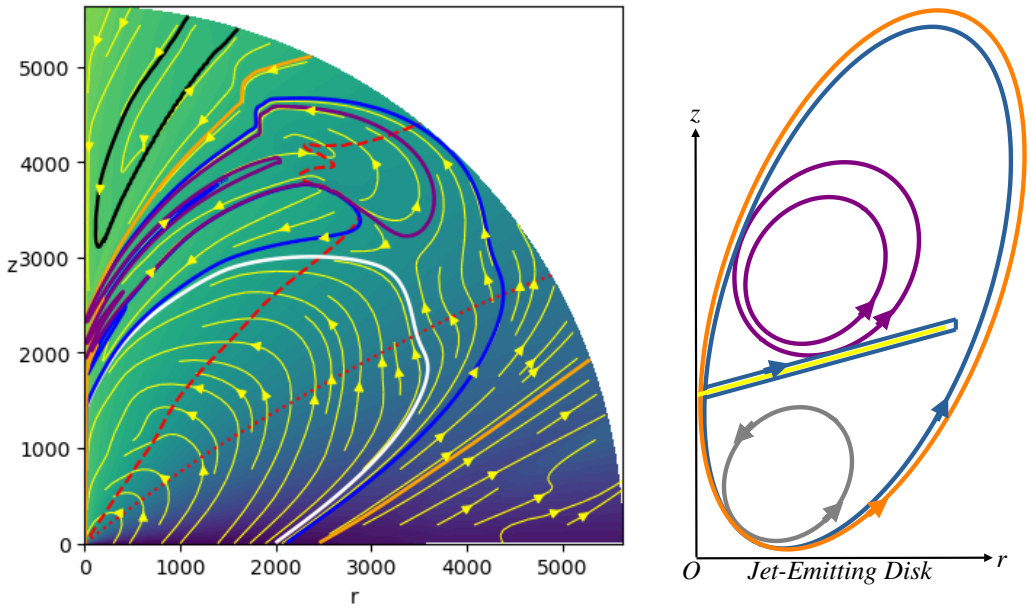

FIGURE 4.13: Left: Plot of the poloidal electric circuits at t_{end}. The two red curves are the critical surfaces, Alfvén (dotted) and FM (dashed). The yellow curves are the poloidal electric circuits, defined as isocontours of rB_φ, where the arrow indicates the direction of the poloidal current density $\vec{j_p}$. Four circuits are highlighted in particular: (1) the envelope of the inner accelerating current in white ($rB_\varphi = -2.06$), (2) the outermost circuit still fully enclosed within the domain in blue ($rB_\varphi = -2.005$), (3) a circuit closed outside the domain in orange ($rB_\varphi = -1.80$), and (4) a post-shock accelerating circuit in purple (also with $rB_\varphi = -2.06$). Right: Simplified sketch with the same color coding, also representing the current closure outside the box for the blue and orange circuits.

The white circuit is the outermost contour of the initial accelerating circuit, with its usual counter-clockwise butterfly shape. It loops from the disk to the central object, eventually flowing down along the axial spine. Right above it lies the first recollimation shock, inducing more complexity in the circuit topology.

The blue circuit is the outermost circuit which is still fully enclosed inside the computational domain. It flows downstream of the first recollimation shock, but stays below the other self-similar shock (in purple in Figure 4.9), flowing back to the polar axis at an altitude between Z_4 and Z_5. Each shock acts as its own electromotive force, with the current flowing clockwise around it. Thus, the blue current flows around the four shocks below Z_4. This is more visible for the larger shocks, emerging from the polar axis at altitudes Z_3 (in blue in Figure 4.9) and Z_1 (main shock, in red in Figure 4.9). After flowing around the main recollimation shock, it flows back to the polar axis then down to the central object along the axial spine, on a path similar to that of the white circuit.

The purple circuit is enclosed between the two self-similar recollimation shocks (in red and purple in Figure 4.9), while having the same rB_φ value as the white circuit. It highlights the reacceleration of the plasma after each shock. As the current density is flowing counter-clockwise in this circuit, it serves as an envelope to go from the main red shock to the second blue shock. The black circuit has the same purpose, but after the second recollimation shock.

These three (white, purple and blue) electric circuits are fully enclosed within the computational domain. It is clear that any electric current leaving the disk beyond $r_0 \sim 2000$ will exit the domain and re-enter it at small colatitudes. This is highlighted by the orange circuit on Figure 4.13. Those circuits that close outside the domain boundaries are the ones responsible for the jet asymptotic collimation, as they are the only circuits on the polar axis beyond the highest recollimation shock, at altitudes greater than $Z_5 = 2634$. But these outermost electric circuits cannot be fully self-consistent, as they are determined by the outer boundary conditions ($R = 5650R_d$), and are not necessarily consistent with the disk electromotive force. Even though it does not affect the main recollimation shock, it may impact the large scale collimation of the jet.

4.4 Time evolution

Such a current-closure issue is inherent to our self-similar ansatz. The jet launching conditions are are established up to the outer domain, as quantities follow power laws in the disk. It also requires to integrate the simulations over very long timescales. It was noted in section 4.1.2 that at $t_{end} = 6.5 \times 10^5$, the jet is stationary. What happened before ?

The time evolution of my simulated jet can be described by different physical timescales, some common to most MHD disk jets, some specific to this one. Figures 4.14 and 4.15 illustrate these many timescales. Figure 4.14 shows the time evolution of the shock altitude Z_{shock} for all shocks found in the simulation via the algorithm described in section 4.2.1. The vertical lines correspond to seven various representative jet times, at which the simulation is represented in Figure 4.15. These times are labeled from t_1 to t_6, the last one being $t_7 = t_{end}$.

The creation of the jet is a very quick process that scales with the local disk Keplerian timescale, the plasma quickly reaching its final speed, close to $v_\infty(r_0) = \sqrt{2\lambda - 3}V_K(r_0) = \sqrt{2\lambda - 3}V_{K_d}/\sqrt{r_0}$. Thus, in the matriochka of magnetic surfaces that is a MHD jet, the innermost regions (anchored at $r_0 \sim 1$) are built first. Then, it is an inside-out build-up until the outermost jet regions (anchored at $r_0 \sim r_{0,FM}$) are built. I compute the time for the innermost and outermost jet regions to cross the whole domain. In both cases, that time is $t_{ext}(r_0) \sim Z_{ext}/v_\infty$, where $v_\infty(r_0)$ is computed with $\lambda = 10$. As the innermost jet is very collimated, $Z_{ext}(r_0 = R_d) \simeq 5650R_d$,

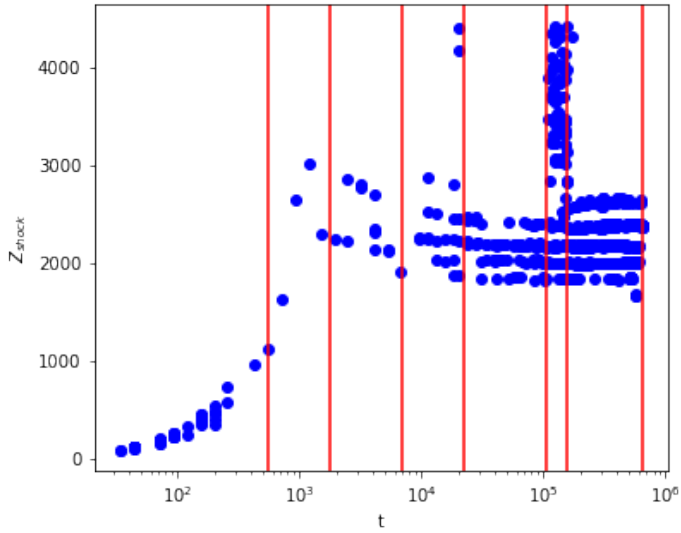

FIGURE 4.14: Altitude z of the different shocks (measured at the axis) as a function of time (in T_d units). The first sixvertical lines correspond to the six times t_i used in Fig. 4.15: $t_1 = 551, t_2 = 2.08\,10^3, t_3 = 8.51\,10^3, t_4 = 1.99\,10^4, t_5 = 1.05\,10^5$, and $t_6 = 1.58\,10^5$. The last vertical line is $t_{end} = 6.51\,10^5$.

which gives $t_{ext}(r_0 = R_d) \sim 10^3$. For the outermost jet, taking $Z_{ext}(r_0 = r_{0,FM}) = R_{ext}\cos\theta_{FM} = 4430R_d$ gives $t_{ext}(r_0 = r_{0,FM}) \sim 10^4$. We saw in section 3.2.3 that the asymptotic speeds in the spine and in the inner jet are similar, so both are created on the same timescale $t_{ext}(r_0 = R_d) \sim 10^3$.

The times $t_1 = 551$ and $t_2 = 2080$ have been chosen to enclose $t_{ext}(r_0 = R_d)$. At t_1, the inner bow shock is clearly seen (Figure 4.15). It is seen on Figure 4.14 until $t_{ext}(r_0 = R_d) \sim 10^3$, thus tracking its outward progression. At t_2, we see the creation of several shocks near $z \sim 2000$ on the axis (Figure 4.15), whose altitudes (Figure 4.14) are close to their final values. However, they are not settled yet, and new shocks are bound to appear. The jet is still far from being at equilibrium: $t_2 \ll t_{ext}(r_0 = r_{0,FM})$.

The times $t_3 = 8.51\,10^3$ and $t_4 = 1.99\,10^4$ have been chosen to enclose $t_{ext}(r_0 = r_{0,FM})$. Between those times, four standing recollimation shocks located between $z = 2000$ and $z = 2500$ appear to settle. Moreover, the transient shocks that are present at t_3 near the axis for $z > 4000$ are mostly gone at t_4 and have completely disappeared at t_5. But at t_4, the JED is still evolving: the disk has only done half an orbit at $r_{0,FM}$. This can be seen in the shape of the critical surfaces, that are not conical yet.

After t_4, the flow is slowly evolving, with four standing recollimation shocks. The outer jet regions converge, and the critical surfaces progressively approach a conical shape, without any obvious evolution in the shock positions. That is, until a dramatic reorganization that occurs between times $t_5 = 1.05\,10^5$ and $t_6 = 1.58\,10^5$, illustrated by the presence of many transient shocks beyond the four standing shocks ($z > 2500$). Figure 4.14 clearly shows the creation of an additional fifth shock beyond the first four during this reorganization. After t_6 the other four shocks are very similar to what they were before t_5, the altitude of the highest one (Z_4) being only slightly lowered.

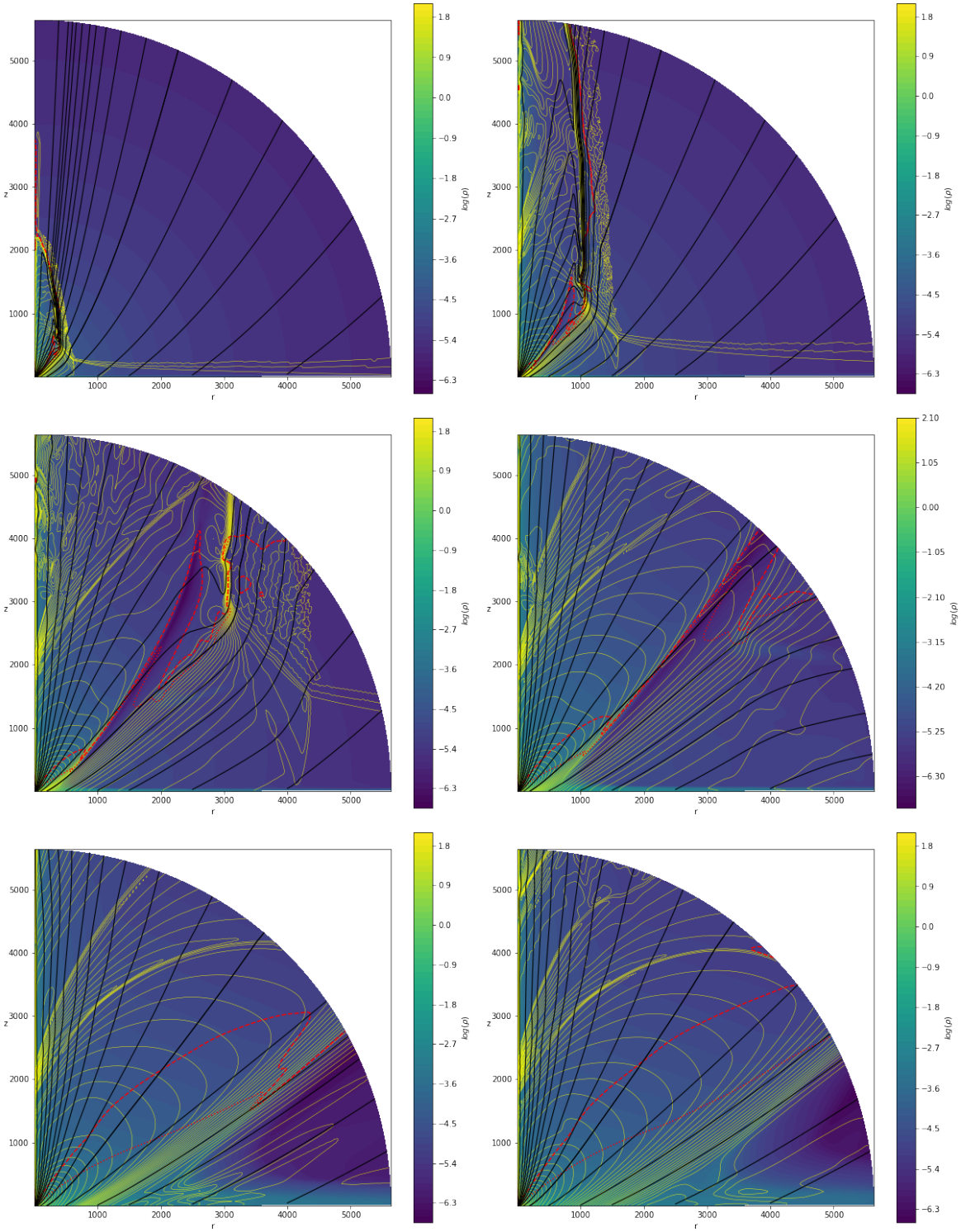

FIGURE 4.15: Snapshots of the simulation at different times (given in T_d units). From top to bottom, left to right: $t_1 = 551, t_2 = 2.08\,10^3, t_3 = 8.51\,10^3, t_4 = 1.99\,10^4, t_5 = 1.05\,10^5$, and $t_6 = 1.58\,10^5$. The background color is the logarithm of the density, black lines are the magnetic surfaces, red lines the Alfvén (dotted) and FM (dashed) surfaces, and yellow curves are isocontours of the poloidal electric current.

This dramatic transient phase leading to a new steady state jet/shocks configuration is illustrated on Figure 4.16. In blue is shown the evolution of the cylindrical radius of the field line anchored at $r_0 = 3$, measured at constant altitude $z = 3500$. It shows that before the transient phase, the inner jet is getting slowly more confined, with the field line radius dropping from $r \sim 150$ to $r \sim 135$ between t_4 and t_5. Then at t_5, the jet becomes too confined to remain stable, and magnetic field fluctuations are suddenly triggered. This oscillating phase ends at t_6, where a new stable configuration has been obtained, with the appearance of an additional shock.

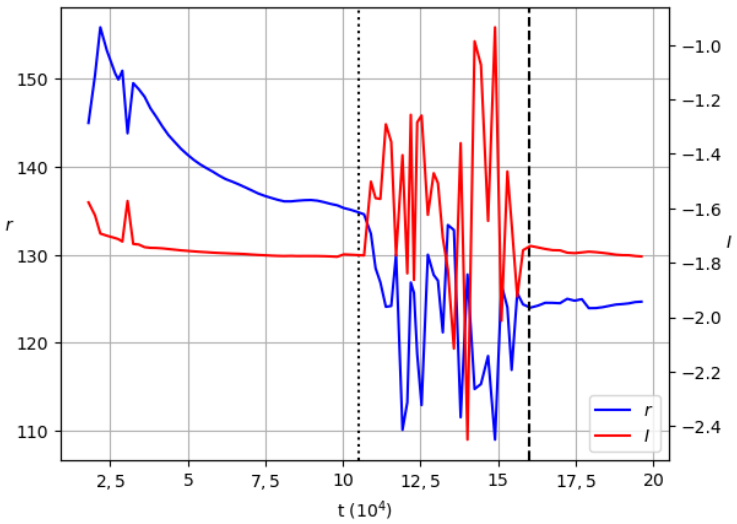

FIGURE 4.16: Time evolution of the cylindrical radius r measured at $z = 3500$ of the magnetic surface anchored at $r_0 = 3$ (blue curve) and the electric current $I = rB_\varphi$ (red) flowing within that surface. The two vertical dashed lines correspond to $t_5 = 1.05\,10^5$ and $t_6 = 1.58\,10^5$.

In red is shown the electric current $I = rB_\varphi$ at that point, whose strength slowly increases until reaching a steady state value. This is consistent with a slow confinement of the jet: the electromotive force of the outer disk regions slowly contributes to the current and the subsequent confinement as their associated field lines converge and their associated electric circuits flow back towards the polar axis. We know that the outermost magnetic field line that can become steady is the outermost field line that becomes super-Alfvénic, as passing the Alfvén critical surface fixes the outflowing angular momentum. For a cold jet, $E \simeq (\lambda - 3/2)\Omega_K^2 r^2$, so fixing λ fixes also E. Let us name the anchoring radius of this outermost super-Alfvénic field line $r_{0,A}$. In my simulation, this radius is $r_{0,A} \sim 10^3$, and the associated Keplerian timescale is thus roughly equal to $t_6 = 1.58 \times 10^5$: The fact that the simulation achieves a global steady state after t_6 should be due to the convergence of all super-Alfvénic magnetic field lines.

4.5 Large scale collimation

Now that we have looked at the particular case of recollimation shocks, let us look at the jet more globally. How is it collimated ? What are the forces driving the collimation ?

As explained in section 2.6.6, in a self-collimated jet the main confining mechanism is the Laplace force $\vec{j} \times \vec{B}$. In our case, the poloidal magnetic field is negligible

with regards to the toroidal field, and consequently the toroidal current is negligible with regards to the poloidal current. Any θ-pinch can thus be neglected, and the confining force is thus the z-pinching $\vec{j_p} \times \vec{B_\varphi}$. As $B_\varphi < 0$, the Laplace force is confining when $j_z < 0$ and deconfining when $j_z > 0$. Looking at the topology of $\vec{j}$ on the right panel of Figure 4.2, we see that the innermost field lines ($r_0 \lesssim 30$) have a mostly negative j_z while the outermost field lines ($r_0 \gtrsim 30$) have a mostly positive j_z. Figure 4.17 shows the initial field configuration (dotted lines) and the final field configuration (solid lines), where each color is associated with an anchoring radius r_0. We clearly see that the inner jet regions ($r_0 \lesssim 30$) are more collimated after the jet propagation while the outer regions ($r_0 \gtrsim 30$) are less collimated.

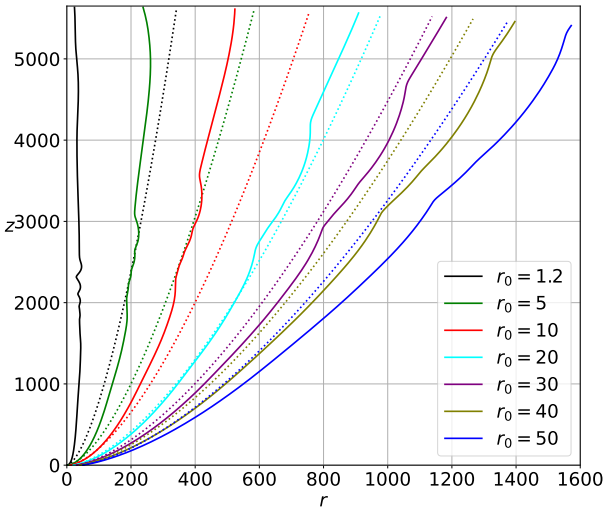

FIGURE 4.17: Evolution of several magnetic field lines during the simulation computation, for different anchoring radii r_0. The field lines at the first output of the simulation (initial conditions) are shown in dotted lines. The field lines at the last output of the simulation (final state) are shown as full lines.

How does this z-pinching force compare to the rest of the present forces ? What drives the radial equilibrium ? The radial balance of a MHD jet is described by the transfield equation 2.97. We consider the inner asymptotic jet, where the field lines are almost vertical and gravity is negligble. Equation 2.97 then reduces to

$$-\frac{\partial}{\partial r}\left(P + \frac{B^2}{8\pi}\right) + \rho\Omega^2 r - \frac{B_\varphi^2}{4\pi r} = 0 \tag{4.1}$$

On Figure 4.18 these forces[5] are plotted along the horizontal $z = 2400$. At this altitude, gravity is negligible (see Figure 4.5) and field lines may be considered vertical until $r \sim 100$.

The three dominant forces are:

- The centrifugal force $\rho\Omega^2 r\vec{u_r}$.
- The hoop stress $-\frac{B_\varphi^2}{4\pi r}\vec{u_r}$.
- The toroidal magnetic pressure $-\frac{\partial}{\partial r}\left(\frac{B_\varphi^2}{8\pi}\right)\vec{u_r}$.

[5] I do not exactly plot the forces but the acceleration (forces over the density ρ) for better visualisation. Of course, if a force is dominant over the other forces then the corresponding acceleration is dominant over the other accelerations and vice-versa.

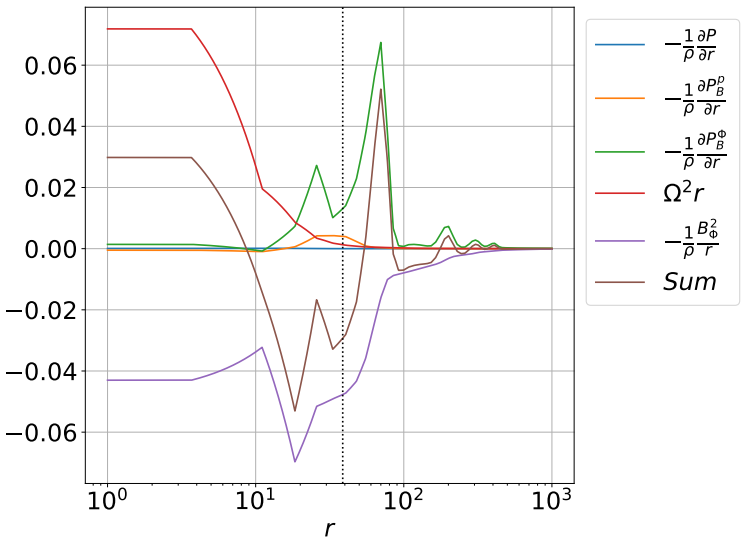

FIGURE 4.18: Radial distribution of the radial accelerations and their sum at the altitude $Z = 2400$ at t_{end}: thermal pressure gradient $-1/\rho(\partial P)/(\partial r)$, poloidal magnetic pressure gradient $-1/\rho(\partial P_B^p)/(\partial r)$, toroidal magnetic pressure gradient $-1/\rho(\partial P_B^\varphi)/(\partial r)$, centrifugal acceleration $\Omega^2 r$, hoop stress acceleration $-B_\varphi^2/(\rho r)$ and sum of all accelerations. The vertical dashed line corresponds to the spine–jet interface, namely the field line anchored at $r_o = R_d$. This figure replaces the incorrect Figure 10 of Jannaud, Zanni, and Ferreira, 2023.

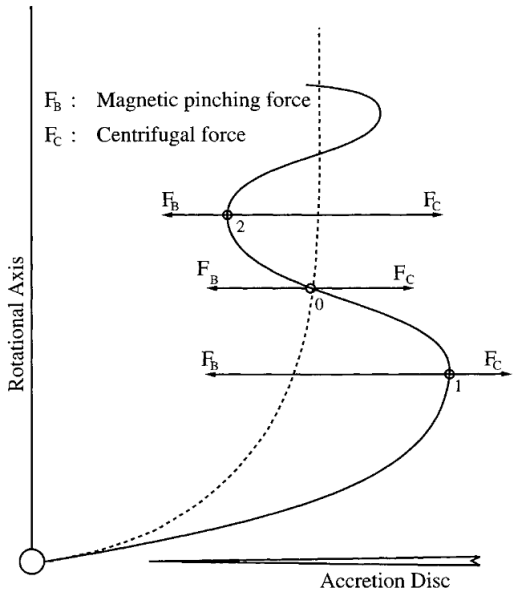

FIGURE 4.19: Sketch of an oscillating spine (Vlahakis and Tsinganos, 1997). Solid line: Oscillating streamline At position 0, the confining pinching force $\vec{F_B}$ is equal to the deconfining centrifugal force $\vec{F_C}$. At position 1 $\vec{F_B}$ is stronger than $\vec{F_C}$ and at position 2 $\vec{F_B}$ is weaker than $\vec{F_C}$. Dotted line: positions at which $\vec{F_B} + \vec{F_C} = \vec{0}$.

The hoop stress is a confining force, while the magnetic pressures and the centrifugal force are deconfining. We see that the sum of all forces is not strictly zero, meaning that the magnetic field lines are not strictly vertical. They are bended outwards in the innermost region ($r < 10$) where the decollimating centrifugal force dominates, and bended inwards in the adjacent region ($r \gtrsim 10$) where the collimating hoop stress dominates. Such a situation is reminiscent of the picture of Vlahakis and Tsinganos, 1997. In their self-similar solutions of a MHD jet, they find magnetic field lines with steady radial oscillations oscillations, due to a different scaling between the pinching force and the centrifugal force (see Figure 4.19). Those oscillations are damped in the z direction. At $z = 2400$ my simulation is in the midst of stationary oscillations, although more complex than those of their solutions. As these oscillations are located at the interface between two outflows (the jet and the spine), the mismatch creates a radial equilibrium that highly depends on the altitude and to the position relative to the shock. Note that these oscillations are not standing modes of an instability, as none where found in the simulation (see A).

4.6 Summary

In this chapter, I presented an axisymmetric simulation of a 2.5D MHD jet launched from a magnetized Keplerian disk. It is the first to showcase the formation of standing recollimation shocks, beyond a thousand times the innermost disk radius. Recollimation shocks are intrinsic to the process of MHD self-collimation. They were suggested as the eventual outcome of self-similar jet solutions (Ferreira, 1997; Polko, Meier, and Markoff, 2010). In my simulation there is not one single shock as presumed from the aforementioned solutions, but several. Two large recollimation shocks, extending from the jet axis to fast-magnetosonic surface or the domain boundary, enclose three smaller shocks that eventually merge with the bigger ones. The shocks are regularly spaced, and the appearance of the smaller ones could be due to a mismatch at the interface between two outflows: the axial spine emitted from the central object and the jet emitted from the disk.

This is an enticing result. As such shocks were not seen in earlier simulations, suspicions grew that they were not a consistent feature of the jets, but rather a biais of self-similarity. It seems that few of those works were performed on scales large enough to capture standing recollimation shocks, as those are bound to happen far away from the central object. Using unprecedented scales in space and time enabled to narrow the gap between analytical and numerical approaches.

There is however still work to do in order to bridge this gap. In chapter 5 I will present a parameter study in α, κ and Ω_{*_a} and carry out a quantitative analysis of the self-collimated jets and recollimation shocks. I will also compare my results to previous studies, both analytical and numerical.

Then, in chapters 6 and 7 I will present simulations in which the JED does not extend on the whole $\theta = \pi/2$ boundary, but is limited to the innermost disk regions, moving away from the self-similar approach. Among others, this will enable to confirm that standing recollimation shocks are a consistent feature of jets and not a biais of self-similarity.

Chapter 5

Self-similar simulations: Parameter dependence and discussions

Contents

5.1 Parameter dependence 103
5.1.1 Mass loading parameter κ 103
The simulations 104
Comparison with self-similar solutions 107
5.1.2 Magnetic field distribution α 109
The constraint $\alpha < 1$ 109
The simulations 110
Comparison with self-similar solutions 111
5.1.3 Influence of the central object 114
The parameters Ω_{*_a} and e_a 114
The simulation 116
5.2 Discussions 117
5.2.1 Setup limitations 117
5.2.2 Comparison with other numerical works 118
5.3 Summary 122

"People who hear of some extraordinary phenomenon start proposing to explain it with improbable hypotheses. First consider the simplest explanation: that it's all nonsense."

"Les gens qui entendent parler d'un phénomène extraordinaire commencent par proposer des hypothèses improbables pour l'expliquer. Considérons d'abord l'explication la plus simple : ça n'a aucun sens."

Lev Landau

Précédemment, on a laissé trois paramètres libres de varier aux conditions limites d'éjection : le chargement en masse κ, la distribution du champ magnétique via le paramètre autosimilaire α et la rotation des surfaces magnétiques sur l'axe Ω_{*_a}. Le chapitre 4 présente la simulation de référence, la plus proche des solutions de Blandford and Payne, 1982 (par exemple $\kappa = 0,1$, $\alpha = 3/4$ et $\Omega_{*_a} = 0$). Celle-ci a montré les chocs de recollimation permanents attendus, accompagnés d'un ensemble de chocs permanents plus petits près de l'axe polaire. Pour mieux comprendre le comportement de ces deux chocs et la façon dont ils dépendent des conditions de lancement, j'ai effectué une étude des paramètres dans κ, α et Ω_{*_a}. Dans ce chapitre, pour chaque paramètre, je fais une brève présentation de sa signification physique et de la manière dont sa plage de variation a été choisie. Ensuite, je présente les simulations où ce paramètre est varié.

Le paramètre κ mesure la charge de masse du disque sur une surface magnétique spécifique. Cinq simulations ont été produites, avec κ allant de $\kappa = 0,05$ à $\kappa = 1$. Cette gamme de valeurs est similaire à celle de Blandford and Payne, 1982, κ devant être inférieur à l'unité pour que le flux sortant (jet+spine) soit dominé par le champ magnétique au moment du lancement.

Les cinq simulations convergent vers un état stationnaire après quelques centaines de milliers d'orbites. A chaque fois on observe la présence de chocs de recollimation stationnaires étendus allant de l'axe jusqu'aux surfaces critiques, ainsi que de plus petits chocs fusionnant avec les plus grands. Ainsi, ces simulations sont semblables à la simulation de référence présentée dans le chapitre précédent. Quelles sont les différences ?

On remarque que le flux de masse du jet et de la colonne sont tous deux proportionnels à κ, la colonne éjectant dix fois moins de masse que le jet quelle que soit la valeur du paramètre. Les puissances suivent la même évolution, la puissance de la colonne étant comparable à celle du jet pour toutes les valeurs de κ. Ces variations découlent directement des conditions.

Comme attendu, les surfaces caractéristiques se rapprochent du disque lorsque le chargement en masse augmente. Cela entraîne une diminution de l'altitude des chocs de recollimation. Cette diminution était aussi présente dans les solutions autosimilaires. En augmentant κ d'un facteur 10, leur altitude de choc est diminuée de six ordres de grandeur. Lorsque j'augmente κ d'un facteur 10, l'altitude du choc est diminuée d'un facteur 3 seulement. Cette différence doit être principalement due à la différence des propriétés d'éjection. Les solutions étant radialement autosimilaires, toutes les quantités suivent des évolutions en loi de puissance, même à proximité de l'axe. Leur courant de retour, essentiel au confinement, peut croître de façon illimitée. De même, dans les solutions le champ magnétique toroidal et l'invariant de Bernoulli augmente lorsque l'on se rapproche de l'axe, tandis que pour mes simulations il diminue fortement. Ceci suggère que même s'il n'éjecte qu'une faible quantité de masse, l'objet central affecte considérablement les propriétés de collimation, et donc la localisation des chocs. Ceci est confirmé par l'étude paramétrique à venir en α, et de façon plus importante en Ω_{*_a}. Cela signifie également que les conditions aux limites du champ magnétique toroïdal sont critiques pour les propriétés de collimation.

Enfin, pour les simulations avec κ le plus élevé, un deuxième groupe de chocs apparaît lorsque les lignes de champ se recollimatent en aval du premier groupe de chocs. Comme aucune dissipation n'est introduite, il y a toujours un courant sur l'axe. Il n'y a aucune raison pour que de tels groupes de chocs cessent d'apparaître même plus en aval, tant que la limite du domaine de simulation n'est pas atteinte. Dans une boîte de taille infinie, les lignes de champ devraient se recollimater, être réfractées vers l'extérieur par un choc de recollimation, puis se recollimater et ainsi de suite indéfiniment.

La deuxième section traite de la variation de α, paramètre auto-similaire défini comme l'exposant du flux magnétique dans les conditions initiales et aux limites. J'ai essayé, sans succès, d'obtenir des solutions stables pour $\alpha \geq 1$. Ceci est dû aux différences de topologie du courant électrique entre $\alpha < 1$ et $\alpha > 1$.

- *Pour $\alpha < 1$, les circuits se referment sur l'objet central, où nous voyons les circuits électriques sortir du disque et se refermer sur l'objet central. Ainsi, seules les régions les plus internes du disque contribuent à la collimation du jet : Ces régions sont les seules à avoir un courant de retour descendant et donc une force de Lorentz collimatrice.*

- *Pour $\alpha > 1$, le courant électrique à la surface du disque croît avec la distance à la source, et les courants électriques descendent sur l'objet central et sur le disque. Comme il n'y a initialement pas de champ ou de courant magnétique toroïdal dans la simulation, il s'en crée constamment aux rayons convergents les plus extérieurs, qui croissent avec $r \propto t^{3/2}$. L'algorithme d'accélération ne peut jamais être activé sur un domaine suffisamment grand pour être significatif. Ainsi, ces simulations sont numériquement hors de portée car elles ne vont jamais à des échelles de temps physiques suffisamment grandes.*

J'ai donc réalisé six solutions pour α compris entre 10/16 et 15/16. Excepté celle avec la valeur de α la plus élevée, toutes ont convergé vers un état stationnaire. Toutes les simulations montrent également les chocs de recollimation stationnaires attendus. Le flux de masse et la puissance du jet augmentent avec α: les régions les plus externes du disque contribuent alors plus, la distribution du flux magnétique d'éjection étant plus plate. De plus, lorsque la valeur de α augmente, l'extension verticale des chocs diminue. Cela est une conséquence directe des conditions d'éjection: Quand α augmente, les lignes de champ magnétique deviennent plus verticales au lancement.

Compte tenu des solutions autosimilaires, la valeur du paramètre α devrait fortement modifier l'altitude des chocs. Mes simulations ne montrent pas un tel comportement, l'altitude du choc restant à peu près la même quelle que soit la valeur de α. Encore une fois, cela est probablement dû à la présence dans mes simulations d'une colonne axiale non auto-similaire jouant un rôle majeur dans le processus de collimation, alors que les solutions sont purement auto-similaires.

En plus des simulation décrites ci-dessus, ce chapitre présente une simulation où le profil d'éjection sur l'objet central a été modifié. Pour les simulations décrites précédemment, la rotation diminue rapidement sur l'objet central, pour être nulle sur l'axe. Dans celle-ci, la rotation sur l'axe est la même qu'au bord interne du disque. De plus, l'énergie sur l'axe a été doublée afin de limiter la collimation sur l'axe. Dans cette simulation, le choc de recollimation est deux fois plus proche du disque que dans celle de référence, à cause d'un accroissement de la collimation au niveau de la colonne, où les chocs se forment.

Ce chapitre ce termine sur quelques mots de mise en garde quant à l'applicabilité des résultats, et sur une comparaison de mon travail aux autres simulations de jets semblables. Les points de mise en garde à retenir sont: le cadre non-relativiste, l'impact non totalement compris de la colonne interne, l'absence de dissipation, le réglage fin du dispositif numérique afin d'obtenir des chocs, et la dépendance à la résolution numérique de la complexité des chocs.

Les résultats restent cependant bien solides. Les chocs de recollimation produits dans mes simulations étaient attendus des solutions auto-similaires, mais n'ont pas été observés dans les simulations "globales" précédentes. Cela est très probablement dû aux énormes échelles associées dans l'espace et le temps, qui n'ont pas pu être prises en compte par les travaux antérieurs. Ici, cela a notamment été rendu possible par la méthode d'accélération de la convergence développée spécifiquement pour ce problème.

5.1 Parameter dependence

The constraints leave three parameters free to vary at the boundary conditions: the mass loading parameter κ, the magnetic field distribution via the self-similar parameter α and the rotation of the magnetic surfaces on the axis Ω_{*_a}. Chapter 4 presented the reference simulation, closest to the solutions of Blandford and Payne, 1982 (e.g. $\kappa = 0.1$, $\alpha = 3/4$ and $\Omega_{*_a} = 0$). It showed the expected standing recollimation shocks, accompanied by a bunch of smaller standing shocks near the polar axis. To further understand the behavior of both these shocks and how they depend on the launching conditions, I ran parameter study in κ, α and Ω_{*_a}. All simulations are presented in Table 5.1, and the three parameters are described in section 3.2.3. When one parameter is varied, the other two stay fixed at their value in the reference simulation K2. For each parameter, I will give a brief presentation of its physical meaning and how its range of variation was chosen. Then, I will present the simulations related to the variation of this parameter.

Name	κ	α	μ	δ	$\frac{t_{end}}{10^5}$	Z_{shock}	θ^{ext}_{FM}	θ^{ext}_{A}	$r_{o,FM}$	$\dot{M}_{jet}$	$\frac{\dot{M}_{spine}}{\dot{M}_{jet}}$	P_{jet}	$\frac{P_{spine}}{P_{jet}}$
K1	0.05	12/16	1.41	50	7.34	2150	0.64	0.94	301	179	0.102	492	0.82
K2	0.1	12/16	1.00	100	6.51	1850	0.67	1.05	323	363	0.096	616	0.81
K2l	0.1	12/16	1.00	100	12.3	2490	0.65	1.02	289	357	0.094	620	0.81
K3	0.2	12/16	0.71	200	10.1	1810	0.69	1.09	368	743	0.093	768	0.80
K4	0.5	12/16	0.45	500	8.67	1150	0.90	1.26	655	2040	0.093	1024	0.81
K5	1.0	12/16	0.32	1000	4.62	700	0.99	1.34	670	4095	0.116	1264	0.96
A1	0.1	10/16	1.00	100	9.08	1900	0.96	1.23	234	195	0.206	551	1.21
A2	0.1	11/16	1.00	100	8.34	1800	0.87	1.15	349	272	0.137	578	0.99
A3	0.1	13/16	1.00	100	5.79	1920	0.59	0.95	566	690	0.047	668	0.66
A4	0.1	14/16	1.00	100	6.26	2050	0.64	0.94	398	1321	0.023	740	0.53
A5	0.1	15/16	1.00	100	1.62	2030	0.50	0.83	1046	3275	0.009	848	0.41
SP	0.1	12/16	1.00	100	3.93	1250	0.82	1.09	506	392	0.097	613	0.98

TABLE 5.1: List of the simulations presented in this chapter. The reference simulation of chapter 4 is called K2. All the simulations presented have been performed in the high resolution grid ($N_R = 1408$ and $N_\theta = 266$) except K2l, performed in a lower resolution grid ($N_R = 704$ and $N_\theta = 144$). The parameters κ and α are varied independently, allowing to compute μ and δ. The columns $Z_{shock}, \theta^{ext}_{FM}, \theta^{ext}_{A}, r_{0,FM}, \dot{M}_{jet}, \dot{M}_{spine}/\dot{M}_{jet}, P_{jet}$, and P_{spine}/P_{jet} are outputs of the simulation measured at the final time t_{end} (given in $10^5 T_d$ units). Simulations K1 to A5 were performed with a nonrotating spine, namely $\Omega_{*_a} = 0$ and $e_a = 2$. Simulation SP is preformed for $\Omega_{*_a} = \Omega_{K_d}$ and $e_a = 10$.

5.1.1 Mass loading parameter κ

This first section deals with the variation of the mass-loading parameter κ. It is defined by equation 2.93 and its expression using simulation parameters is equation 3.23. Five simulations were produced, with κ ranging from $\kappa = 0.05$ to $\kappa = 1$. This range of values is similar to that of Blandford and Payne, 1982, who took $\kappa \in [0.01; 1]$

(see Figure 2.3). As explained in section 2.6.5, κ should be lower than unity for the outlfow (jet+spine) to be magnetically dominated at launch.

The simulations

The five simulations are named K1 ($\kappa = 0.05$), K2 ($\kappa = 0.1$), K3 ($\kappa = 0.2$), K4 ($\kappa = 0.5$) and K5 ($\kappa = 1$). Four of them are displayed in Figure 5.2, the last one being the reference simulation K2, extensively described in chapter 4. The simulations are represented at their final state t_{end} shown in Table 5.1. They have all reached a steady state by t_{end}, and have structures similar to K2, with at least one group of standing recollimation shocks. The left column of Figure 5.2 shows the whole simulation domain, and the right column shows a zoom on the shock-forming region near the polar axis. Table 5.1 shows that for all simulations the spine mass loss rate is around 10% of the jet mass loss rate. As shown in the $\dot{M}_{jet}$ column, both mass loss rates are proportional to κ. The outflow powers follow the same behavior, with $P_{spine}/P_{jet} = 80\%$ for all simulations, and with P_{spine} and P_{jet} both proportional to κ. These variations follow directly from the expressions of $\dot{M}_{jet}$ and P_{jet}:

$$\begin{aligned} \dot{M}_{jet} &= \int \rho \vec{v}_p \cdot \vec{ds} = \frac{1}{4\pi} \int \eta \vec{B}_p \cdot \vec{ds} = \frac{1}{4\pi} \int \eta \, d\Psi \propto \kappa \\ P_{jet} &= \int \rho E \vec{v}_p \cdot \vec{ds} = \frac{1}{4\pi} \int \eta E \vec{B}_p \cdot \vec{ds} = \frac{1}{4\pi} \int \eta E \, d\Psi \propto \kappa \end{aligned} \tag{5.1}$$

where the last step comes from the definition of κ (equation 3.23), the MHD invariant η being the mass flux to magnetic flux ratio (equation 2.71). This has the caveat that the integration boundaries $r_0 \in [R_d, r_{0,FM}]$ depend on κ, but the outer regions contribute little to the mass loss rate and power of the jet.

When κ increases, the Alfvén and fast-magnetosonic surfaces get closer to the disk. This is expected as the Alfvén speed increases when κ increases:

$$V_{A_d} = \mu V_{K_d} = \sqrt{0.1/\kappa} V_{K_d} \tag{5.2}$$

In all simulations, the main recollimation shock is defined as the shock intersecting the FM surface. This intersection is defined as the tip of the shock. The shock altitude on the axis Z_{shock} is clearly decreasing with κ, as evidenced in Figure 5.3: it goes down from $Z_{shock} = 2500$ for $\kappa = 0.05$ to $Z_{shock} = 700$ for $\kappa = 1$. The shock geometry and opening angle are not perturbed, and the tip of the main shock Z_{tip} experiences a similar decrease. The whole jet structure is brought closer to the disk with the increase of κ.

A second interesting aspect is the appearance of a second group of standing recollimation shocks at higher altitudes. This happens only when the first group has gone to low enough altitudes, away from the domain outer boundary. This is for $\kappa \geq 0.5$. For $\kappa = 0.5$, this shock group is at $z > 3000$ and for $\kappa = 1$ it is at $z > 2000$. This second set of shocks has a structure very similar to that of the first one:

- Two large recollimation shocks. Apart from the multiplicity that was also seen in the other group, those are similar to the ones predicted from the self-similar solutions. Like the other shock group, the lower shock has a large opening angle while the higher shock has a much smaller one.
- Several smaller recollimation shocks, that are limited to the innermost jet radii. They correspond to the spine-jet interaction.

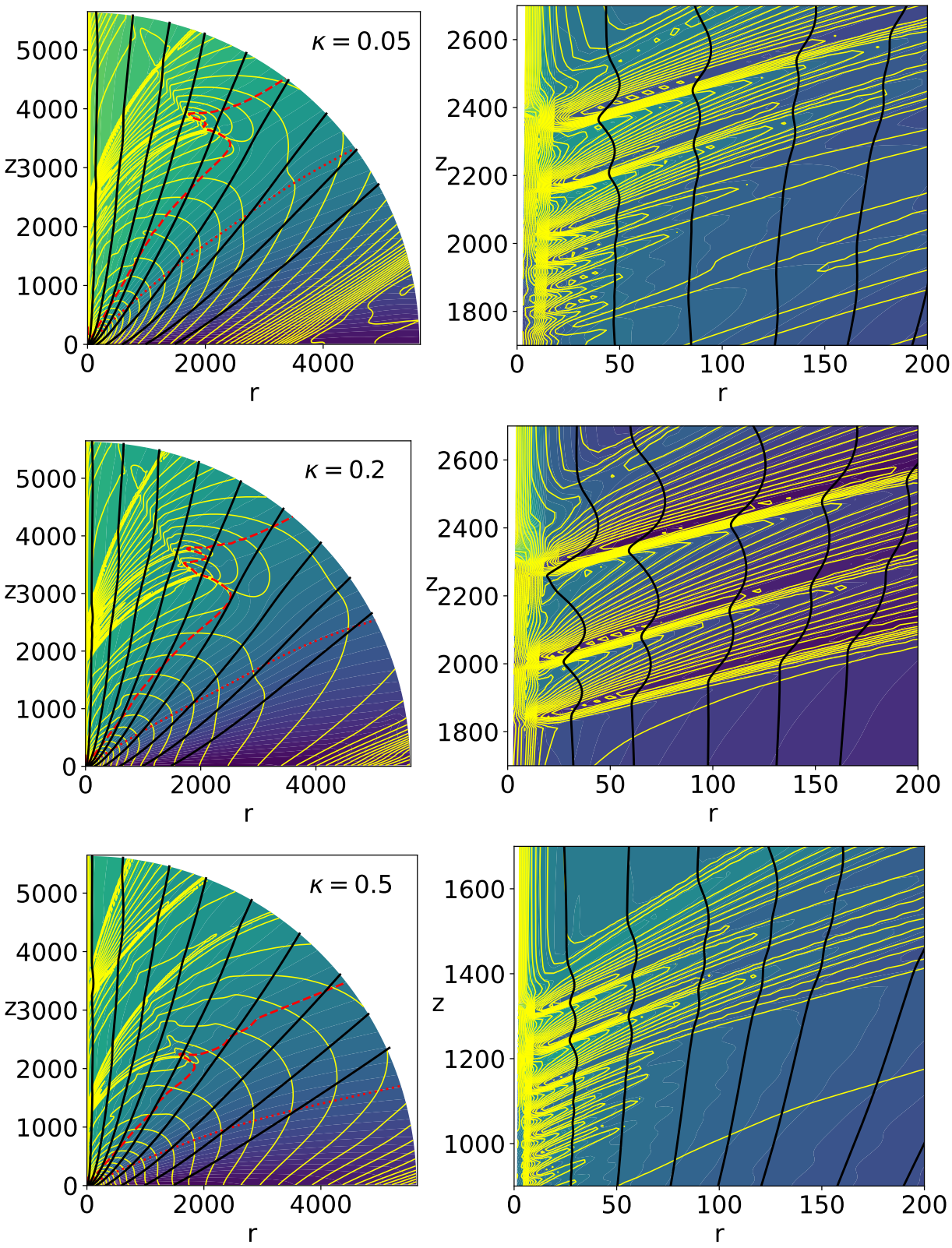
$\kappa = 0.05$
$\kappa = 0.2$
$\kappa = 0.5$
z
r
0
1000
2000
3000
4000
5000
1800
2000
2200
2400
2600
1000
1200
1400
1600
50
100
150
200

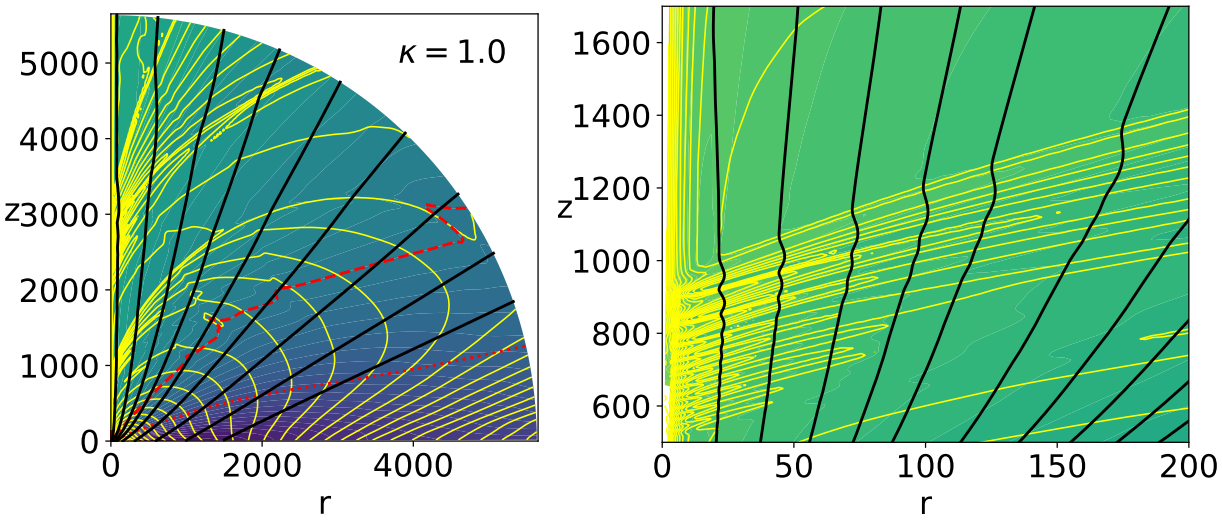

FIGURE 5.2: Influence of the mass-loading parameter κ on the final stage of jets obtained with $\alpha = 3/4$. The color background is the logarithm of the FM Mach number n, black solid lines are field lines, yellow lines are isocontours of the electric current rB_φ and the red dashed (resp. dotted) curve is the FM (resp. Alfvén) critical surface. The left panels show the whole domain and the right panels a close-up view around the shock-formation regions. In the left panels, the field lines anchoring radii are $r_0 = 3; 15; 40; 80; 160; 320; 600; 1000; 1500$. In the right panels, the field lines anchoring radii are $r_0 = 1.2; 2; 3; 4; 5; 7; 9; 11; 13; 15$ and the flow is super-FM everywhere. The shocks displayed in the right panels are the lowest in the simulation.

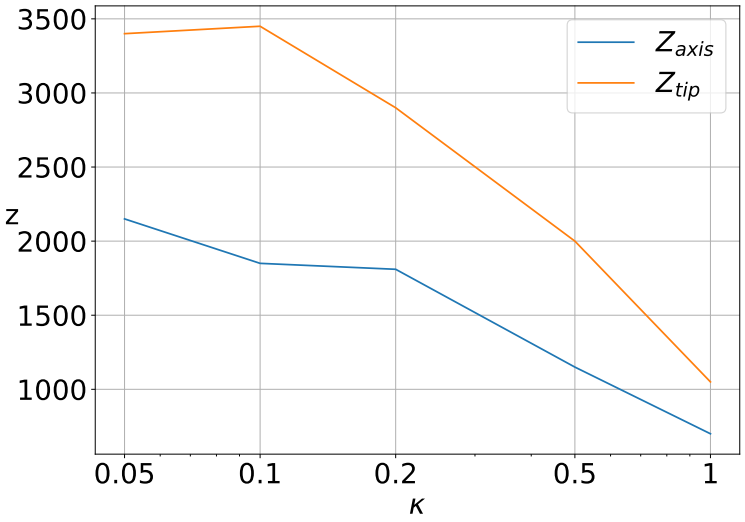

FIGURE 5.3: Influence of κ on the altitude of the main recollimation shock. This is done by measuring two altitudes for each shock: its height at the axis (Z_{axis}, blue) and the altitude of its outer edge (Z_{tip}, orange).

This second group of shocks appears as the field lines recollimate downstream of the first group of shocks. As no dissipation is introduced, there is still a current I_{axis} on the axis. There is no reason why such groups of shocks should stop appearing even further downstream, as long as the boundary of the simulation domain is not reached. In a box of infinite size, the field lines should recollimate, be refracted outwards by a recollimation shock, then recollimate and so on indefinitely.

Similarly to the small shocks (see section 4.2.3), one would expect the distance between the shock groups to be periodic. However, the distance between the two shocks H_R appears quite larger than the altitude of the main shock Z_{shock}. For the simulation K4 ($\kappa = 0.5$), $Z_{shock} = 1150$ while $H_R = 1650$. This is because the "launching" conditions at the recollimation shock are quite different from the actual launching conditions on the disk. The acceleration and collimation happen at much larger scales. At these large scales, even the collimated spine has become larger. Moreover, the grid is logarithmic in the spherical $\vec{u_R}$ direction: $\Delta R \propto R$. At higher altitudes gradients become weaker and structures are displaced upwards.

Now that we know what simulations K2 and K5 are, we can also take another look at Figure 3.4, showing the evolution of the acceleration factors of these two simulations over their computation. Table 5.1 shows that the simulations with a mass load closer to that of Blandford and Payne, 1982 ($\kappa = 0.1$) converge faster: they reach greater timescales t_{end}. This is also seen on Figure 3.4 where the acceleration factor for K5 lies under that of K2. In simulations with higher values of κ, the collimation is stronger and all structures, including the recollimation shocks, are displaced downwards. They now appear in smaller cells, which limit both the time increment and the size of the accelerated zone. However, it still reaches large acceleration factors at the end of the simulation, which is also the case for the three other simulations K1, K3 and K4.

Comparison with self-similar solutions

On Figure 5.4 I plot the magnetic lever arm λ as a function of the mass-loading κ. To compare my simulations with the seminal solutions of Blandford and Payne, 1982, I select the field lines with an inclination at launch $\xi'_0 \equiv B_r/B_z$ equal to 1.4, 1.5 and 1.65. This allows to draw the isocontours of ξ'_0 and facilitates the comparison with Figure 2.3, reproducing the Figure 2 of Blandford & Payne. Most works on similar solutions produced such figures, and the comparison can be extended to e.g. Figure 3 of Ferreira, 1997, Figure 5 of Casse and Ferreira, 2000b or Figure 4 of Jacquemin-Ide, Ferreira, and Lesur, 2019 that all show similar trends. Contrary to those solutions, my simulations are not strictly self-similar: the greater the anchoring radius, the greater the field line inclination ξ'_0 and thus the greater the magnetic lever arm λ. On Figure 5.4 I also represent for each simulation (each value of κ) the magnetic lever arm for $r_0 = 5$, 50 and 500. We see that the simulations are in good agreement with the analytical expectations. The intended values of the arm lever (see section 3.2.3) are retrieved. We learned in section 2.6.5 that $\lambda = 1 + q/\kappa$, with $q = |B_\varphi/B_z|$ being the magnetic shear at the disk surface. As shown in the right panel of Figure 4.1 for the reference simulation, my simulations have $q \sim 1$, thus $\lambda \sim 1 + 1/\kappa$. For the reference simulation K2 ($\kappa = 0.1$), the magnetic arm lever λ is in the 12 to 17 range (see Figure 4.7), similar to what is expected by this relation.

This relation also explains the decrease in shock altitude with the mass load illustrated in Figure 5.3. As the mass load increases and the magnetic lever arm decreases, the centrifugal acceleration is weaker and the shocks appear closer to the

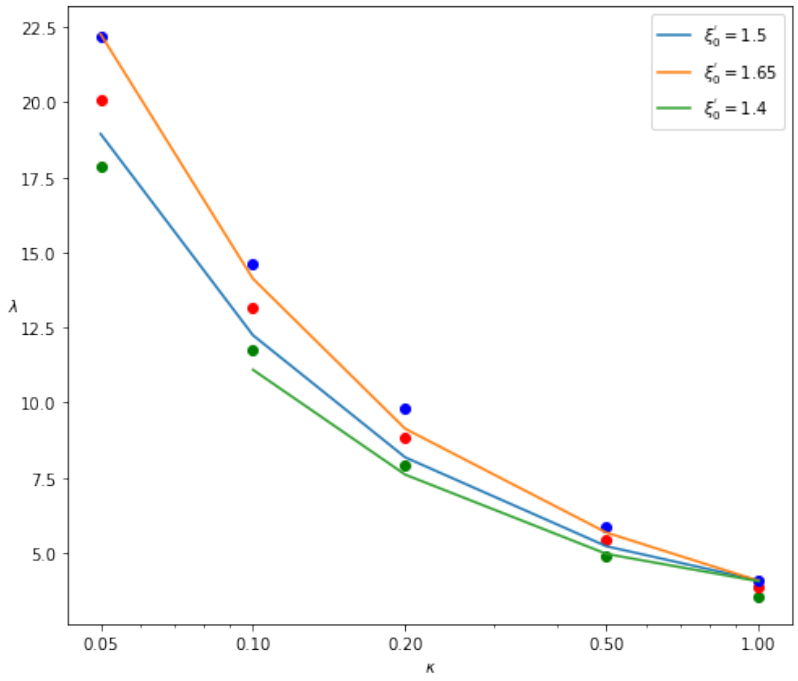

FIGURE 5.4: Jet parameter space $\lambda(\kappa)$ at the final stage of our simulations K1-K5 with $\alpha = 3/4$. Each simulation is obtained for a unique mass loading κ and gives rise to a distribution of the magnetic lever arm λ with the radius: green, red, and blue dots correspond to anchoring radii $r_o = 5, 50$, and 500, respectively. The solid curves are obtained for constant values (indicated in the panel) of the initial magnetic field inclination $\xi_0' = B_r/B_z$ at the disk surface and reproduce the Blandford & Payne scaling (Figure 2.3).

disk. This behavior was also seen in self-similar simulations such as the ones of Ferreira, 1997. The top panel of Figure 1.16 reproduces their Figure 6. It shows several field lines anchored at the same point in the disk, with $\xi \sim \kappa$ varying from 0.005 to 0.05, all other things being equal. As those solutions do not exhibit fast shocks, they cannot make precise predictions on their location. Indeed, they can occur at any super-FM point on the field line, which happens even before the recollimation. When extrapolating shock positions from these simulations, I will consider that they happen beyond the recollimation point: $Z_{shock} > Z_{recollimation}$. Here the recollimation point is where $B_r = 0$, and the field line is at it widest.

We see on Figure 1.16 that the expected location of the recollimation shock decreases in altitude with κ. However, their variation is much greater than mine. When increasing κ by a factor 10, their shock altitude is decreased by six orders of magnitude. When I increase κ by a factor 10, the shock altitude is decreased by a mere factor 3. This discrepancy should be mostly due to the difference in ejection properties. The solutions of Ferreira, 1997 and others are radially self-similar, meaning that all quantities follow power-law evolutions, even close to the axis where $r \to 0$. Their return current $\lim_{r\to 0}(rB_\varphi)$, essential to the collimating hoop stress $-B_\varphi^2/(4\pi r)\vec{u}_r$ can grow limitless. In self-similar solutions, following the central object ($r < 1$) from $r = 1$ to $r = 0.1$ leads to an increase in toroidal magnetic field by a factor 18 and in Bernoulli invariant e by a factor 10. In my simulations (see Figure 4.1 for the reference simulation K2), the toroidal magnetic field vanishes and the Bernoulli invariant is decreased by a factor 5. This suggests that even though it only ejects a small

amount of mass, the central object drastically affects the collimation properties, and thus the location of the shocks. This is confirmed by the upcoming parameter study in α, and more importantly in Ω_{*_a}. This also means that the boundary conditions on the toroidal magnetic field are critical for the collimation properties. Here, B_φ is a simple "outflow" condition at the ejection boundaries.

As a side note: even though the impact of κ on the shock altitude is smaller here than in self-similar solutions, it is sufficient to noticeably modify the shock physics. We see on Figure 5.2 the shocks becoming weaker with an increasing κ. This is directly due to their decrease in altitude, which leads to a decrease in pre-shock FM mach number n_1 and thus in compression factor χ, as shown by the Rankine-Hugoniot jump conditions of section 2.7.

5.1.2 Magnetic field distribution α

The constraint $\alpha < 1$

This second section deals with the variation of α, self-similar parameter defined as the exponent of the magnetic flux (see section 2.6.4) in the initial and boundary conditions. On the disk boundary, $B_z \propto r^{\alpha-2}$. A shown in section 2.6.5, in self-similar solutions the relation between α and the ejection index $\tilde{\zeta}$ limits the parameter space to $3/4 < \alpha < 5/4$ for super-SM outflow.

I have tried, without success, to obtain steady solutions for $\alpha \geq 1$. This is due to the differences in electric current topology between $\alpha < 1$ and $\alpha > 1$ described in section 2.6.6 and illustrated in Figure 2.5.

- For $\alpha < 1$, the circuits close on the central object. This is illustrated for the reference simulation K2 ($\alpha = 3/4$) on Figure 5.5[1], where we see the electric circuits flowing out of the disk and closing down into the central object ($R = 1$). Thus, only the innermost disk regions contribute to the jet collimation, as explained in section 4.5 and illustrated on Figure 4.17: Those regions are the only ones with a return current $j_z < 0$ and thus a collimating Lorentz force $\vec{j_p} \times \vec{B}_\varphi$, along $-\vec{u}_r$.
- For $\alpha > 1$ the electric current at the disk surface $I = rB_\varphi \propto r^{\alpha-1}$ grows with r, and the electric currents flow down on the central object and on the disk (see the right panel of Figure 2.5). As there is initially no toroidal magnetic field or current in the simulation, it is constantly being created at the outermost converged radii, that grows with $r \propto t^{3/2}$. The acceleration scheme (see section 3.1.5) can never be activated on a large enough domain to be significant. Thus, these simulations are numerically out of reach as they never go to large enough physical timescales.

For this reason I will only show simulations with $\alpha < 1$. Six simulations were produced, for α ranging from 10/16 to 15/16. For $\alpha = 1$ the current would be flowing out of the disk only at its outermost radius, so the numerical issue described above would still be present.Simulations with $\alpha \geq 1$ will be shown in section 6.4.3 in the case of a truncated JED.

[1]On this figure, we also see a peak in density (background color) at the intersection between the central object boundary and the disk boundary ($r = 1$, $z = 0$). The decrease in density is steep in both on the disk ($\rho = \rho_d (r/R_d)^{2\alpha-3}$ with $\alpha = 3/4$ for K2) and on the central object ($\rho_a = \rho_d/\delta$ with $\delta(\kappa) = 10^2$ for K2). See the left panel of Figure 4.1 for the variation of the density along the whole ejection boundary.

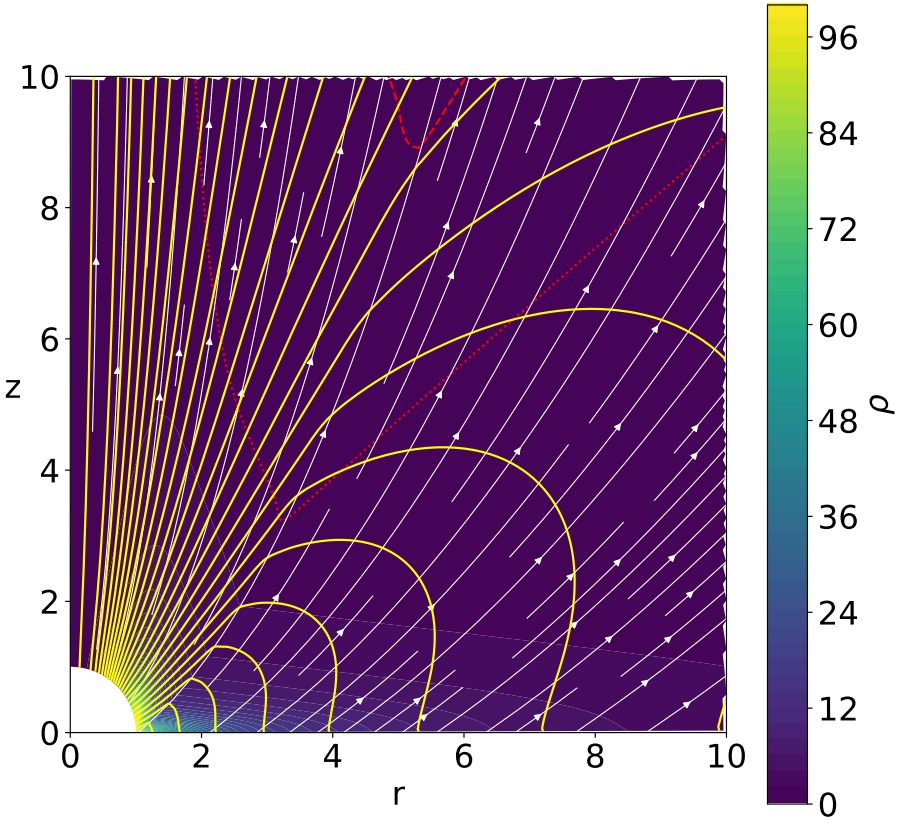

FIGURE 5.5: Snapshot of the reference simulation K2 at t_{end}, zoomed for $r < 10$ and $z < 10$. The white lines are poloidal magnetic field lines. The red lines are the two critical surfaces, Alfvén (dotted) and FM (dashed). The yellow lines are electric circuits. They are oriented counter-clockwise, flowing out of the disk with $j_z > 0$ ($z = 0$, $r \in [1;10]$) and closing into the central object with $j_z < 0$ ($R = \sqrt{r^2+z^2} = 1$). In the background is the plasma density ρ.

The simulations

The six solutions are named A1 ($\alpha = 10/16$), A2 ($\alpha = 11/16$), K2 ($\alpha = 12/16$), A3 ($\alpha = 13/16$), A4 ($\alpha = 14/16$) and A5 ($\alpha = 15/16$). Five of them are displayed on Figure 5.7, the last one being the reference simulation K2 extensively described in chapter 4. All of them were performed with $\kappa = 0.1$, same as K2. These simulations are displayed in their final state at t_{end}. Except the simulation A5, they have all reached a stationary state. All simulations have structures similar to K2, with one group of shocks. In the left column of Figure 5.7 is the whole simulation domain, and in the right column is a zoom on the shock-forming region near the polar axis. The final times t_{end} are shown in Table 5.1, with other global simulation characteristics. We see that the anchoring radius of the outermost FM surface $r_{0,FM}$ increases with α, while the colatitudes of the critical surfaces at the outer boundary θ^{ext}_{FM} and θ^{ext}_{A} decrease. This is a direct consequence of the magnetic surfaces becoming more vertical at launch as α increases.

We have seen in section 3.2.3 that at the intersection between the central object and disk boundaries ($R = R_d$, $\theta = \pi/2$), the inclination of the magnetic surfaces $|B_r/B_z|$ is fixed. It is roughly equal to $1/\alpha$, thus the magnetic field lines are more collimated at launch for higher values of α. As the jet mass loss rate $\dot{M}_{jet}$ and power

P_{jet} are computed until a $r_{0,FM}$ that increases with α, it is natural that they increase with α. Still, mass loss rate and power increase with α even when computed until a fixed radius. The distributions become flatter with a higher α ($\rho \propto r^{2\alpha-3}$ for instance) while the normalizations stay the same, and thus the outer disk regions contribute more to the jet mass loss rate and power for higher values of α.

There are some clear evolutions in shock behavior with the parameter α. As shown in Figure 5.8, the shock altitude on the axis barely changes, while the altitude at its outermost point z_{tip} decreases with α. This is also a direct consequence of a stronger jet collimation at launch for higher values of α. We see on the left column of Figure 5.7 the shock radial extent decreasing for an increasing α. The main shocks have an opening angle on the axis roughly equal to $\pi/4$, and more extended shocks naturally end up at higher altitudes z_{tip}. The simulations A1 ($\alpha = 10/16$) and A2 ($\alpha = 11/16$) have the lowest values of α. Their main shock stretches beyond the outer $R = 5650$ boundary, and the altitude of the outermost shock point z_{tip} cannot be computed. The critical surfaces are too horizontal for the size of our (already very large) simulation domain. For the simulations A4 and A5 with the largest values of α (respectively $\alpha = 14/15$ and $\alpha = 15/16$) the critical surfaces are much more vertical. The two large recollimation shocks as seen in K2 are now fully enclosed in the domain and merge with the FM surface[2]. In these simulations, one or two additional shocks also appear at higher altitudes.

Looking at the t_{end} column in Table 5.1 we see a clear decrease with α, especially for $\alpha = 15/16$. This is due to the difficulties in computing simulations with $\alpha \gtrsim 1$ described in section 5.1.2, as computing times were identical. We see also in Figure 3.4 the simulation A5 reaching acceleration factors smaller than those of the reference simulation K2. Still, at t_{end} the simulation A5 has reached timescales that would have been sufficient for the reference simulation K2 to reach a steady state. As we saw in section 4.4 the timescale at which the jet becomes stationary is $t_{ext}(r_{0,A})$, and $r_{0,A}$ is larger for A5. The simulation A5 should be run until $t_{ext}(r_{0,A}) \sim 2 \times 10^5$ to reach a stationary state.

Comparison with self-similar solutions

Which of my simulations can be compared to the self-similar solutions ? A self-similar parameter $\alpha < 12/16$ would correspond to an inflowing solution with a negative ejection index ξ. The comparison will thus be restrained to simulations with $\alpha \geq 3/4$. Of those, only the reference solution $\alpha = 3/4$ could be considered a cold jet as it corresponds to low ejection indexes similar to those displayed on the top panel of Figure 1.16 ($\xi \sim 10^{-2}$). Having higher ejection indexes would require either additional disk heating (Casse and Ferreira, 2000a) or much lower disk magnetization (Jacquemin-Ide, Ferreira, and Lesur, 2019).

The simulations with $\alpha > 3/4$ should thus not be compared to the cold jet solutions of Ferreira, 1997 but rather to those of Contopoulos and Lovelace, 1994. Some of their solutions are represented on Figure 5.9, exhibiting the three classes they obtain:

- Recollimating solutions that cross the FM point for $\alpha \leq 0.856$: Figure 5.9-(a).
- Non-recollimating sub-FM solutions for $0.856 < \alpha < 1$: Figure 5.9-(b).
- Vertically damped oscillating sub-FM solutions for $\alpha > 1$: Figure 5.9-(c).

[2]For the reference simulation K2 the highest large scale shock was too big to be fully featured in the domain and reached the outer boundary.

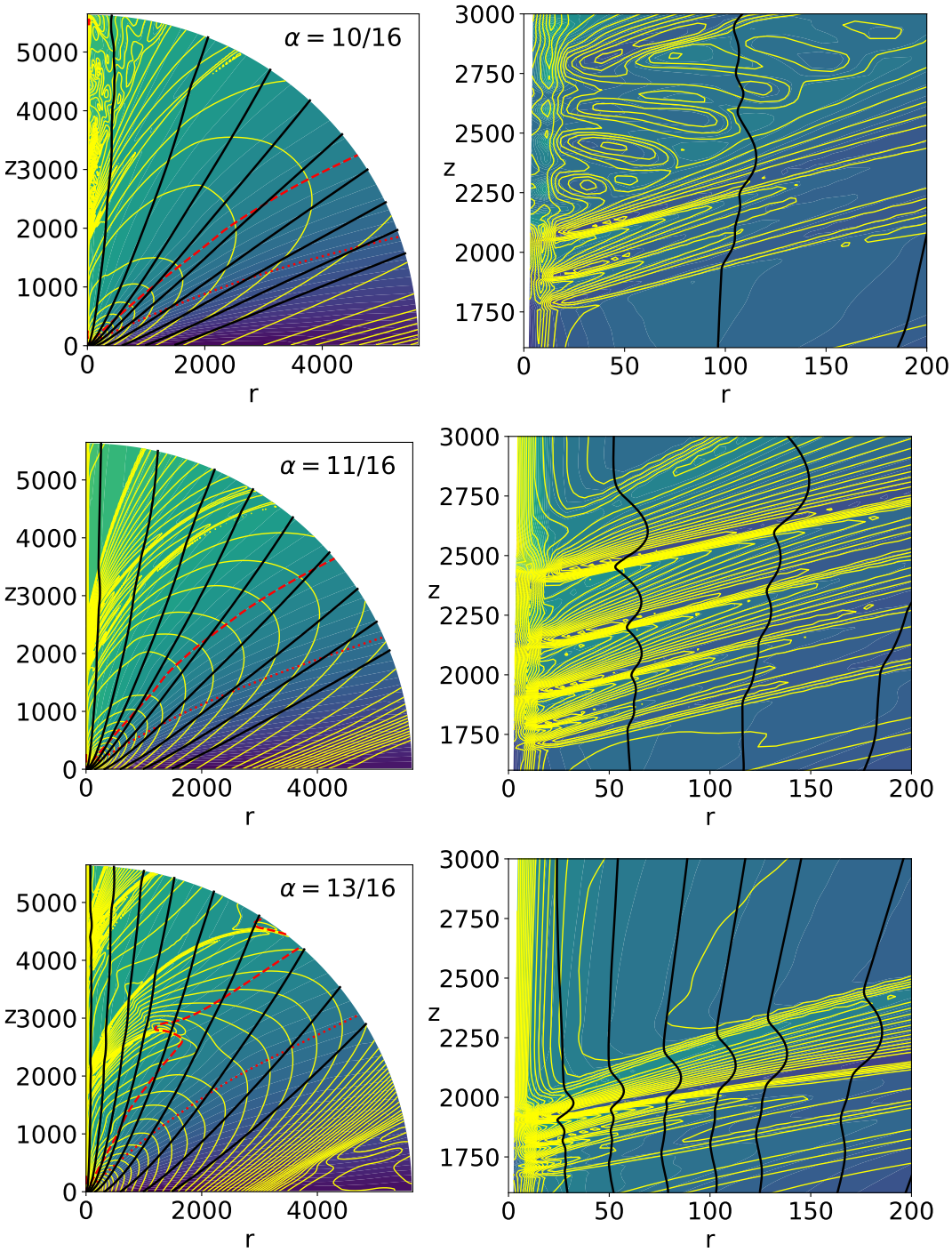
α = 10/16
α = 11/16
α = 13/16
z
r
0
1000
2000
3000
4000
5000
1750
2250
2500
2750
50
100
150
200

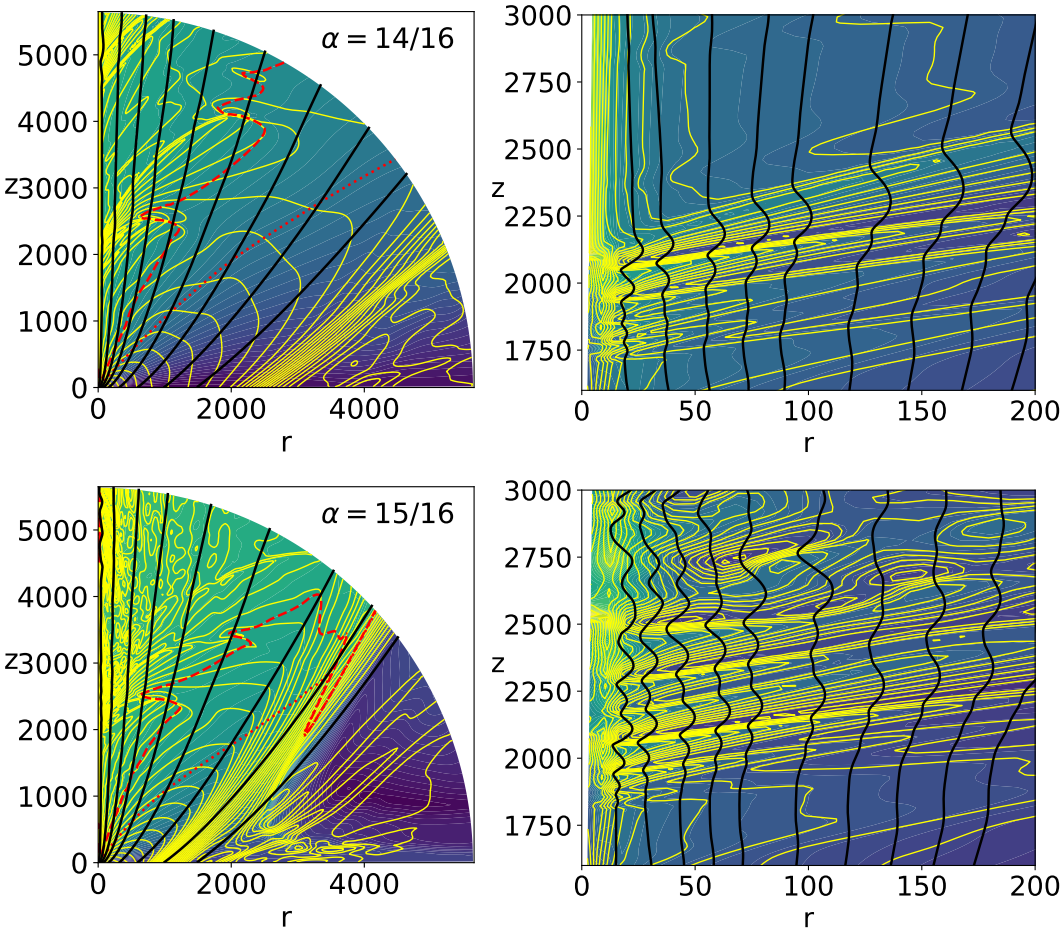

FIGURE 5.7: Influence of the magnetic field distribution α on the final stage of jets obtained with $\kappa = 0.1$. I use the same notations, colors, and field lines anchoring radii as in Figure 5.2.

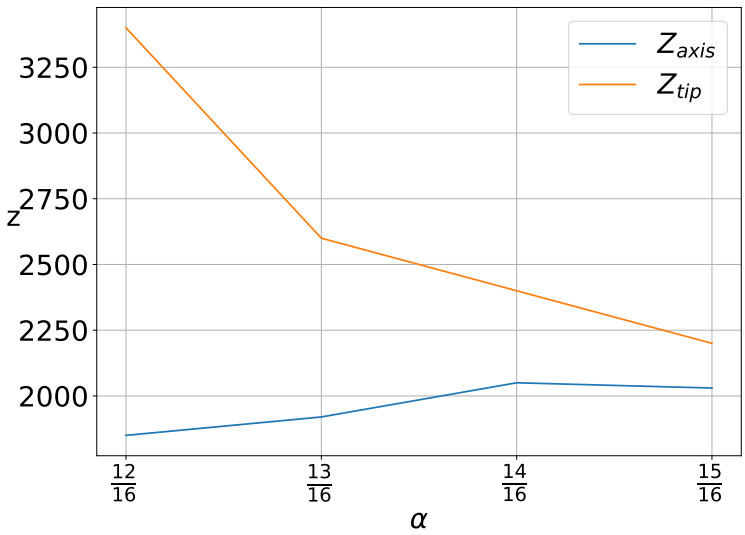

FIGURE 5.8: Influence of α on the altitude of the main recollimation shock. This is done by measuring two altitudes for each shock: its height at the axis (Z_{axis}, blue) and the altitude of its outer edge (Z_{tip}, orange).

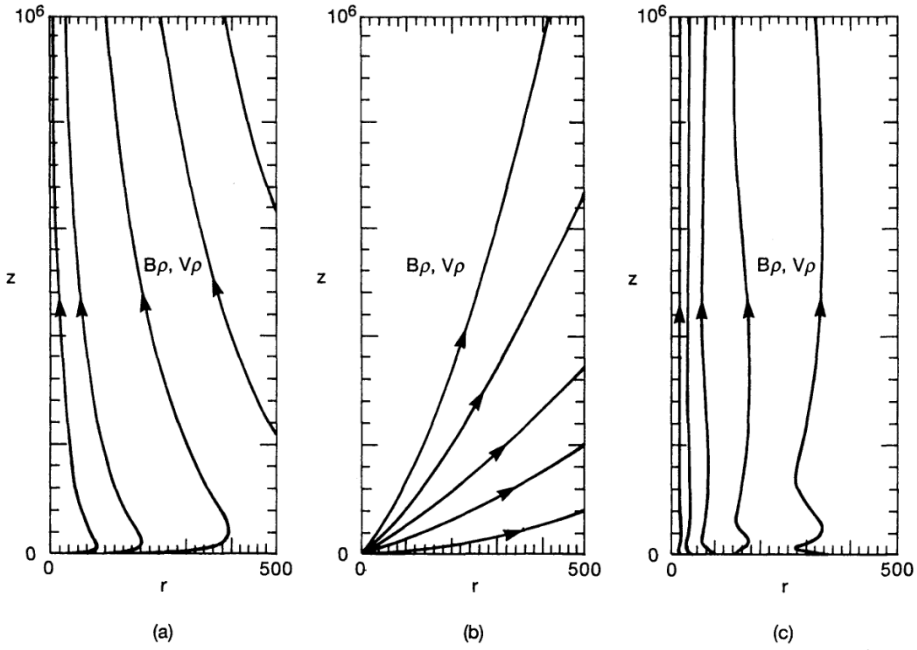

FIGURE 5.9: Figure 2 of Contopoulos and Lovelace, 1994. Solutions for various magnetic field distributions: (a) recollimating solution with $\alpha = 0.8$ (b) non-recollimating solution with $\alpha = 0.9$ (c) oscillating solution with $\alpha = 1.02$.

Should my simulations behave similarly to their solutions, I would observe a dichotomy between the simulations A1, A2, K2 and A3 and the simulations A4 and A5, as $13/16 < 0.856 < 14/16$. In the first class of solutions, they also observe a increase with α of collimation altitude by several decades. My simulations do not display such a behavior, the shock altitude staying roughly the same no matter the value of α. Again, this is probably caused by the presence in my simulations of a non self-similar axial spine playing a major role in the collimation process, while the solutions of Contopoulos and Lovelace, 1994 are purely self-similar.

5.1.3 Influence of the central object

The parameters Ω_{*_a} and e_a

This third section deals with the influence of the spine emitted from the central object on the surrounding jet emitte by the disk. To do so, I mostly play with the axis rotation Ω_{*_a}, although sometimes also with its energy e_a. The Ω_{*_a} parameter measures rotation speed of the magnetic surfaces on the axis in units of Ω_{K_d}, keplerian rotation in the inner disk ($r = 1; z = 0$). The central object could be either a star or a black hole, producing different kinds of axial spines. Possible rotation profiles for both cases are represented on Figure 5.10.

- If the central object is a star (A), then the radius R_d corresponds to the disk truncation radius r_t. Inside the central object boundary are hidden the star and its magnetosphere, launching the stellar wind and the star-disk interaction wind. Setting the rotation on the axis fixes the value of this truncation radius with respect to the disk corotation radius with the star $r_{co} = (GM/\Omega_{*_a}^2)^{1/3}$. As the case $\Omega_{*_a} > 1$ or $r_{co} < r_t$ corresponds to the "propeller" regime where accretion is inhibited (see e.g. Illarionov and Sunyaev, 1975), this manuscript

will be restricted to the case $\Omega_{*_a} \leq 1$. If $\Omega_{*_a} = 1$ the corotation and truncation radii are confounded (in blue on Figure 5.10-(A)). If $\Omega_{*_a} < 1$ the corotation radius is pushed further into the disk (in red on Figure 5.10-(A)). In both cases, the two radii are linked by $r_{co}/r_t = \Omega_{*_a}^{-2/3}$.

- If the central object is a black hole (B), then the radius R_d would correspond to the innermost stable circular orbit r_{ISCO}, neglecting all GR effects. Setting the rotation on the axis then fixes the spin of the black hole, and thus r_{ISCO} with respect to the Schwarzchild radius r_S. The case $\Omega_{*_a} = 0$ would model a Schwarzchild black hole of spin parameter $a = 0$ with $r_{ISCO}/r_S = 3$. It is represented in red on Figure 5.10-(B). The case $\Omega_{*_a} > 0$ would model a Kerr black hole of spin parameter $a \in]0;1]$, in prograde rotation at the speed $\Omega_H(a) = ac/(2r_H)$, where $r_H = r_g(1 + \sqrt{1 - a^2})$ is the radius of its event horizon. Assuming a Keplerian disk starting in r_{ISCO}, the black hole rotation over the disk rotation at the ISCO would reach a maximum $\Omega_H(a = a_{max})/\Omega_{K_d} \simeq 1.5$ for $a_{max} \in]0;1[$. This case is represented in blue on Figure 5.10-(B). For higher spin parameters, the black hole rotation speed compared to that of the disk at ISCO gets lower, until reaching $\Omega_H(a = 1)/\Omega_{K_d} = 1/2$ for a maximal spin parameter $a = 1$. Naturally, the higher the spin parameter, the stronger the non-relativistic and Keplerian disk at ISCO approximations. For $a \lesssim 1$, the $r = R_d$ JED boundary is rejected far beyond the ISCO, where the disk becomes quasi-Keplerian. And anyway, in the case of black hole jets the non-relativistic framework forces us to draw only qualitative conclusions for the simulations.

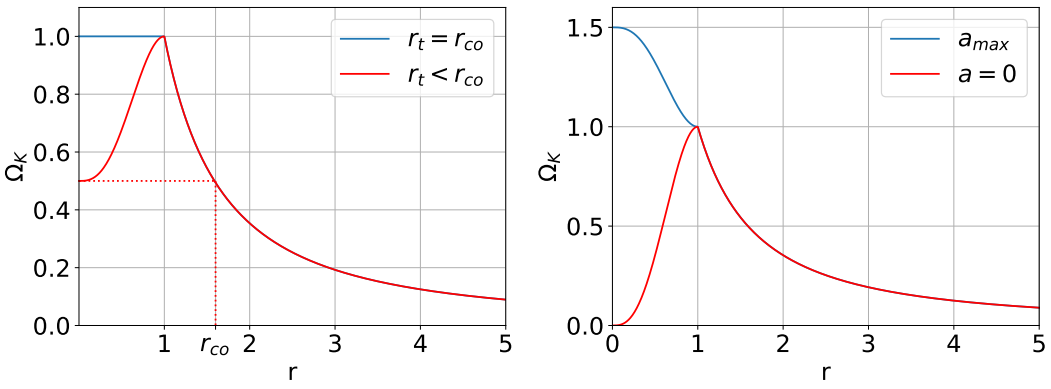

(A) Protostar (B) Black hole

FIGURE 5.10: Schemes of the rotation profiles along the central object and JED boundaries, normalized to Ω_{K_d}. (A) Protostar: Either $\Omega_{*_a} < \Omega_{K_d}$ (red) and the truncation radius is smaller than the corotation radius or $\Omega_{*_a} = \Omega_{K_d}$ (blue) and the truncation radius is equal to the corotation radius. (B) Black hole: Either $a = 0$ and the black hole does not spin ($\Omega_{*_a} = 0$, Kerr black hole, red) or $a \in]0;1]$ and the black hole spins ($\Omega_{*_a} > 0$, Schwarzchild black hole, blue).

Therefore, Ω_{*_a} may be varied from 0 to around 1, which bears some physical meaning for both YSO and prograde black hole jets. The aim of this work is to produce and study jets emitted from the disk via the Blandford & Payne process. Therefore, the influence of the axial spine was minimized as much as possible, by setting $\Omega_{*_a} = 0$ for all previous simulations[3]. However even in this case the spine has a clear influence on parameter dependence and jet dynamics.

[3]But not only, see section 3.2.3.

The simulation

To further probe the impact of the axial spine I ran the simulation SP with solid-body rotation on the central object: $\Omega_{*_a} = 1$. To produce this simulation I made another change from the reference simulation K2: the normalized Bernoulli invariant on the axis is increased from $e_a = 2$ to $e_a = 10$. It was done to limit the overgrowth of the radial pinch on the axis and consequential imbalances, and therefore allows faster convergence of the simulations.

Its final state is displayed on Figure 5.11 and some of its global characteristics are written in Table 5.1. It achieves a steady state and exhibits the same features as the reference simulation K2. As expected, the main shock is closer to the disk: here $Z_{shock} = 1300$, while for the reference simulation $Z_{shock} = 1850$. The spine and jet power both depend on the available electromotive force (emf) $e = \int \vec{E}_m \cdot \vec{dl} = \int (\vec{v} \times \vec{B}_p) \cdot \vec{dl}$. For the disk this emf is $e_{disk} \simeq \int_{r=1}^{5650} \Omega_K r B_z dr$ and for the central object $e_{obj} \simeq \int_{\theta=0}^{\pi/2} \Omega r B_R d\theta$. Going from K2 where $\Omega_{*_a} = 0$ to SP where $\Omega_{*_a} = 1$ the rotation on the central object and therefore the emf e_{obj} are greatly increased. The collimating hoop stress in the spine becomes stronger, leading to lower shocks.

Further study on the influence of Ω_{*_a} on jet collimation in the context of jets emitted from truncated disks (see section 6.4.1) showed the modification of e_a has little influence on shock altitude. Note that other quasi self-similar simulations with smaller changes in Ω_{*_a} and e_a were performed. They also led to a lowering of the shock compared to K2, although naturally smaller.

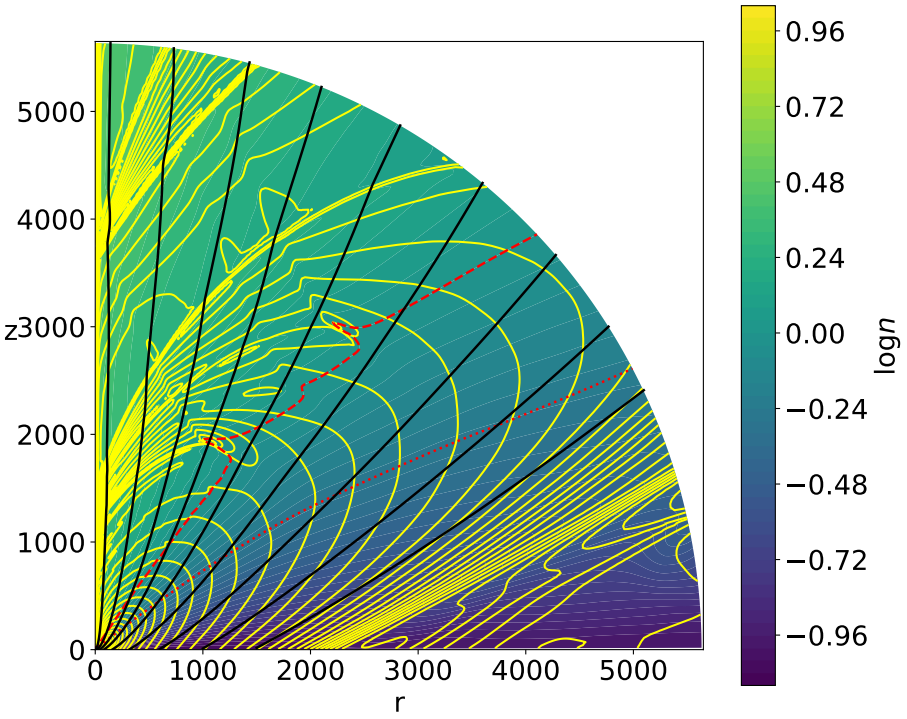

FIGURE 5.11: Snapshot at t_{end} of the SP simulation with a rotating spine, $\alpha = 3/4$ and $\kappa = 0.1$. I use the same color coding as in Figure 4.2. The magnetic field lines (black solid lines) are anchored at the same disk radii.

5.2 Discussions

In this chapter and the previous one, I made some observations and drew a few conclusions on my simulations of jets emitted from quasi self-similar disks. This section aims to provide a step back from these simulations and place them in a broader context.

- First, by putting the emphasis on a few caveats of the numerical setup, highlighting what can and cannot be deduced from my simulations.
- Then, by comparing my methods and results to other published works, highlighting why we believe the steady recollimation shocks presented here are the first of their kind.
- Finally, by summing up the conclusions that could be drawn from these quasi self-similar simulations.

5.2.1 Setup limitations

As for all numerical works, a few words of caution are necessary to avoid overgeneralising the results obtained. The reader should also keep in mind that this work was done in the framework of ideal non-relativistic MHD.

First, these simulations show jets emitted from a keplerian disk. The impact of the axial spine has been reduced at maximum, for instance via setting the axis rotation Ω_{*_a} to zero and fixing a constant sonic mach number M_S on the whole ejection boundary, including the central object. Nevertheless, this axial spine proved to have a strong impact on the jet structure. Its role in flow dynamics has yet to be explored in the case of a more physical spine-jet outflow.

Second, these isentropic simulations prohibit energy dissipation, including in the shocks. Therefore, the jet could recollimate, experience another shock, recollimate again, etc. indefinitely. In this chapter, we saw this happening when the first group of shocks is at low enough altitudes, for simulations K4, K5 (see Figure 5.2) and SP (see Figure 5.11). On top of not being realistic, this prevents the simulations from containing a true asymptotic circuit, extending from the shock until "infinite" altitudes. Instead, there is a succession of circuits along the polar axis, located between the consecutive shocks.

Third, the numerical setup has been fine tuned to capture the shocks. Different Riemann solvers and reconstruction schemes were employed near the axis and in regions of extremely low density and high Alfvén speed. The grid cells are also smaller near the axis. As all other simulations, mine depend on those conditions, although convergence tests were performed to test the validity of the acceleration scheme and the solidity of the results. Figure 5.12 shows the simulation K2l that has the same parameters as the reference simulation K2 but was performed in the low-resolution grid that has roughly four times fewer cells (see the right panel of Figure 3.5 for a representation of the grid). It attains a stationary state, and naturally manages to reach a greater final time t_{end} (see Table 5.1) in less computing time[4]. It has a structure similar to that of K2, most notably containing two recollimation shocks with a large radial extent: the lower main one with a large opening angle ending on the FM surface, and higher one with a smaller opening angle ending at the outer boundary. There are a few differences. Naturally, this simulation shows less

[4]In the same computing time, one would expect a factor 8 between the two final times t_{end}: a factor 4 as there are 4 times fewer cells and a factor 2 because of the timestep (see equations 3.13 and 3.15).

complexity: while in the simulation K2 there were two shock mergers along the main shock (see Figure 4.9) in the simulation K2l there is only one, at ($r \sim 700$, $z \sim 3100$). This is also why the shocks at lower altitudes in simulations K4 and K5 (see the right column of Figure 5.2) showed higher complexity: as $\Delta R \propto R$ the resolution decreases with altitude. Also, the shocks appear at higher altitudes: $Z_{shock} = 1850$ for K2 and $Z_{shock} = 2490$ for K2l. This was also expected, a lower-resolution grid inducing lower gradients and thus weaker recollimation. Still, the shocks have the same impact on the jet morphology, and remain rather weak ($\chi \sim 2$ in the spine and $\chi \sim 1.4$ in the jet, similar to K2). Therefore, the collimation and shock properties are globally conserved in this simulation, and the resolution seems to only have a small impact on the simulations.

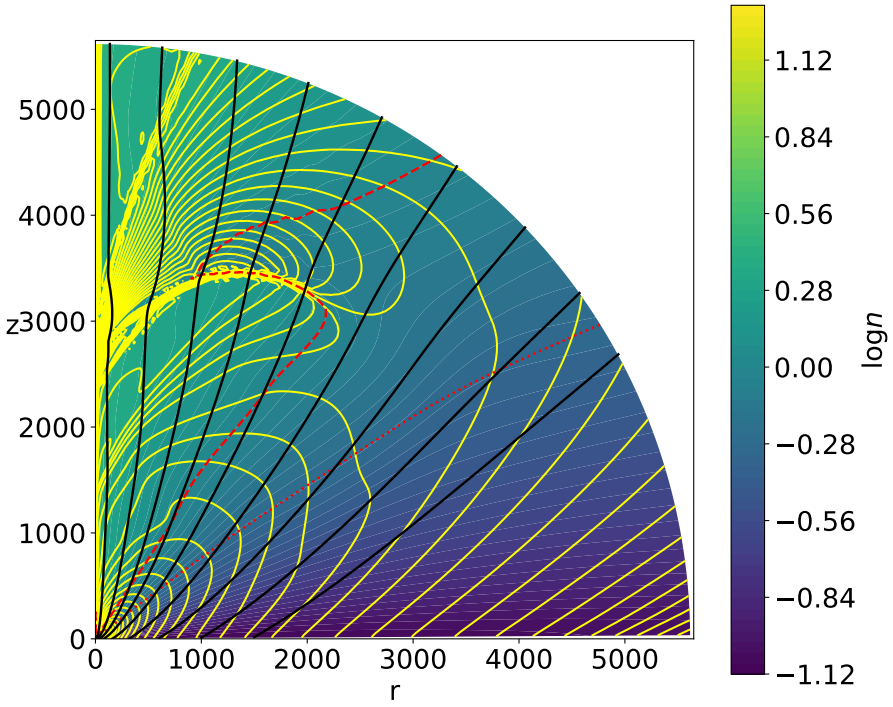

FIGURE 5.12: Snapshot of the low-resolution simulation K2l at t_{end}. The color coding is the same as the left panel of Figure 4.2, snapshot of the high-resolution simulation K2.

5.2.2 Comparison with other numerical works

In this section, I compare my results to those found in the litterature, restraining it to 2D nonrelativistic simulations. Relativistic jets develop displacement currents and an electric field modifying jet collimation, and 3D jets are susceptible to many additional instabilities, mostly interface or current-driven. Those additional processes forbid direct comparison to my simulations. As mentioned in the introduction, I will also only deal with "global" simulations. In those, the jet is launched in a "bottom-up" approach: there is no collimated jet ab initio in the domain. Some stationary 2D jet simulations relying on self-similar solutions have been shown to contain standing recollimation shocks. The domain of those works starts high above the disk, allowing to be initially filled by either a Blandford & Payne-type jet (Gracia, Vlahakis, and Tsinganos, 2006; Stute et al., 2008) or a combination of a Blandford & Payne jet dominant in the outer regions and a meridionally self-similar solution dominant in the inner regions (Matsakos et al., 2008, 2009). Naturally, the boundary conditions are

set consistently with these initial conditions. After short timescales of a few tens to a few thousands T_d, their simulations converge to a steady state, with a collimated jet containing recollimation shocks of properties similar to those in my simulations (see section 4.1.2. of Matsakos et al., 2008 for instance). However, these shocks were bound to appear because of the boundary conditions: In Matsakos et al., 2008 the inner regions are set super-FM with magnetic field lines already bent inwards. Their intent was to prove the numerical stability of the self-similar solutions, thus they naturally reproduced such solutions.

The intent of my "global" platform simulations and those presented in this section is different. The aim is to study which launching conditions, sub-FM, sub-Alfvénic and consistent with disk models, would lead to the formation of collimated jets, and maybe of additional substructures, steady or not. This section is not an exhaustive review, and some other simulations performed with a different intent are mentioned in the introduction.

Ouyed, Clarke, and Pudritz, 2003; Ouyed and Pudritz, 1997a,b performed simulations in a small cylindrical domain $(r, z) = (20R_d, 80R_d)$ with 200×500 cells. Their parameter space is quite different from mine: the magnetic field distribution is set with $\alpha = 1$ or $\alpha = 2$, the inner jet regions are highly super-Alfvénic ($\mu_d = 10^{-2}$) with a mass load κ steeply decreasing radially ($\kappa \propto r^{3/2-2\alpha}$). They do not reach a stationary state, but see unsteady knots caused by jet collimation towards the axis. Those shocks, only happening for small mass loads ($\kappa_d \sim 10^{-2}$) could be due to overconstrained boundary conditions at the jet launch. Pudritz, Rogers, and Ouyed, 2006 continued their work using the same grid and Alfvénic mach number at launch, but explored magnetic field configurations closer to mine, with $\alpha \in [1/4, 1]$, and thus had a flatter $\kappa \propto r^{3/2-2\alpha}$ distribution. Their simulations showed a dichotomy between parabolic field lines for $\alpha = 1/4$ and $\alpha = 1/2$ and cylindrical field lines for $\alpha = 3/4$ and $\alpha = 1$. I suspect it is a direct geometric consequence of the boundary conditions, as the magnetic field lines become more collimated at launch when α increases.

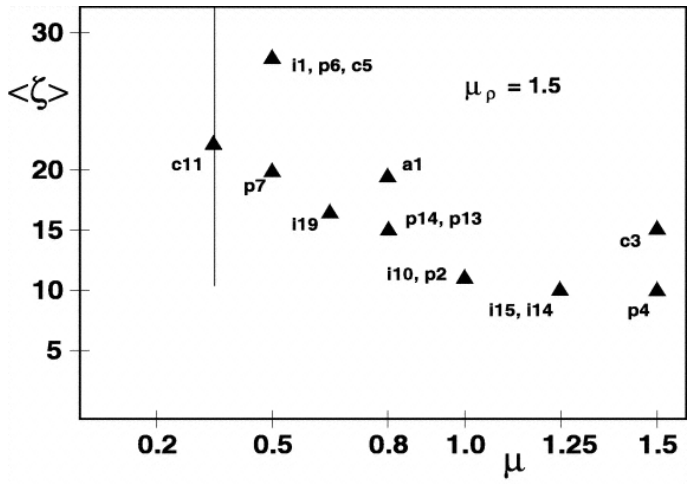

FIGURE 5.13: Adapted from Figure 6 of Fendt, 2006. Variation of the averaged jet collimation degree $\zeta \equiv \dot{M}_z/\dot{M}_r = (\int_0^{r_{max}} r\rho v_z dr)/(r_{max}\int_0^{z_{max}} \rho v_r dz)$ with the disk radial distribution of the magnetic field ($B_p \propto r^{-\mu}$ i.e. $\mu \equiv 2 - \alpha$). $(r_{max}, z_{max}) = (150R_d, 300R_d)$ is his grid size. All simulations presented here have a disk density radial distribution similar to my reference simulation K2 ($\rho \propto r^{-\mu_\rho} = r^{-3/2}$).

Fendt, 2006 performed forty simulations in a bigger grid $(r, z) = (150R_d, 300R_d)$ with 256×256 cells. His simulations are run for longer timescales, up to a few thousand times T_d, allowing some of the simulations to reach a steady state. He had a vast parameter space, exploring at launch the radial distributions in density and magnetic field. He also explored the impact of the boundary Alfvén mach number with $\mu_d \in [0.1, 2.67]$, thus having some simulations with fully sub-Alfvénic launch conditions. Like Pudritz, Rogers, and Ouyed, 2006 he saw an increasing jet collimation for flatter magnetic field configuration (higher α), and showed that this holds true whatever the disk density distribution. For instance, 5.13 shows the evolution of $< \zeta >$ quantifying jet collimation with $\mu \equiv 2 - \alpha$[5] for a disk density distribution $\rho \propto r^{-3/2}$ as in our reference simulation K2. This tends to confirm that as mentioned in the paragraph above and in section 5.1.2, the stronger collimation may simply be a consequence of more vertical magnetic field, as in the potential solutions.

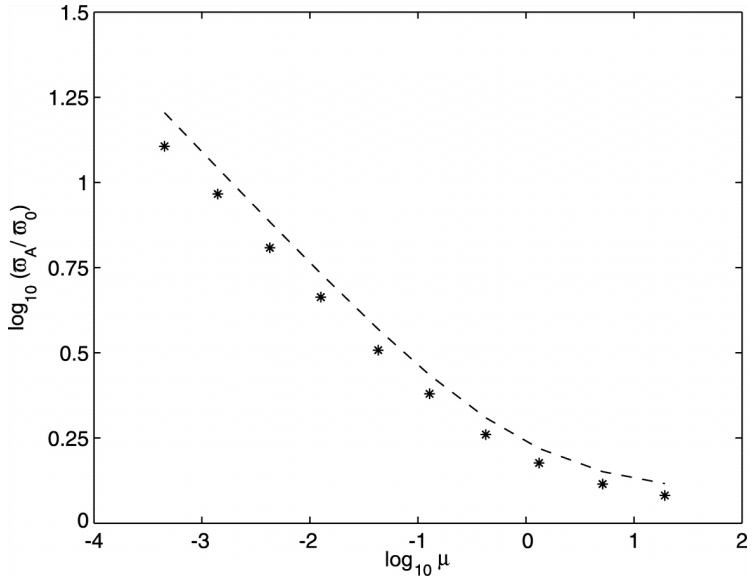

FIGURE 5.14: Figure 7 of Anderson et al., 2005. Evolution of the Alfvén radius over anchoring radius r_A/r_0 with the mass loading $\mu \equiv \kappa$. The asterisks show their simulation values and the dashed line are the values expected from the fit of Spruit, 1996: $(r_A/r_0) = \sqrt{3/2}(1+\kappa)^{-2/3}$.

Krasnopolsky, Li, and Blandford, 2003 continued the work of Krasnopolsky, Li, and Blandford, 1999 on a much larger domain: $(r, z) = (1000R_d, 1000R_d)$ with 210×190 cells. As Pudritz, Rogers, and Ouyed, 2006 they saw an increase in jet collimation degree for a steeper disk density distribution, with a dichotomy between configurations with a mass load κ radially increasing and decreasing. They did not reach a steady state, that they attribute to their non self-similar scaling. Anderson et al., 2005 used the same numerical setup and grid and made simulations with a parameter space similar to the simulations of section 5.1.1. They have a Blandford & Payne disk with $\alpha = 3/4$, $\rho \propto r^{-3/2}$ and a constant mass load κ. They performed simulations with $\kappa \in \left[6.3 \times 10^{-4}, 19\right]$, and found a jet collimation growing with the mass load, as expected by analytical (Spruit, 1996) and semi-analytical (Ferreira,

[5]This $\mu \equiv 2 - \alpha$ parameter has nothing to do with my $\mu \equiv V_{A_d}/V_{K_d}$ parameter.

1997) works. Figure 5.14 shows in asterisks their observed evolution of the normalized Alfvén radius (r_A/r_0) over the mass load $\mu \equiv \kappa$[6]. They did not reach a steady state for mass loads $\kappa \gtrsim 1$, and did not see any recollimation shock. My simulations (see section 5.1.1) indicate that the only case where standing recollimation shocks would appear in their simulation domain, that is when $Z_{shock} < 1000$, is for $\kappa \sim 1$, where they do not reach a steady state.

The earlier works mentioned above were the first to be interested in the influence of launching conditions on jet collimation. Due to numerical constraints, they were performed on relatively small scales in space and time. As a reminder, my simulations were performed in a spherical grid $(R, \theta) = (5650R_d, [0; \pi/2])$ with 1408×266 cells and run up to roughly a million T_d. This discrepancy, especially on time scales, forbids direct comparisons between these earlier works and my simulations.

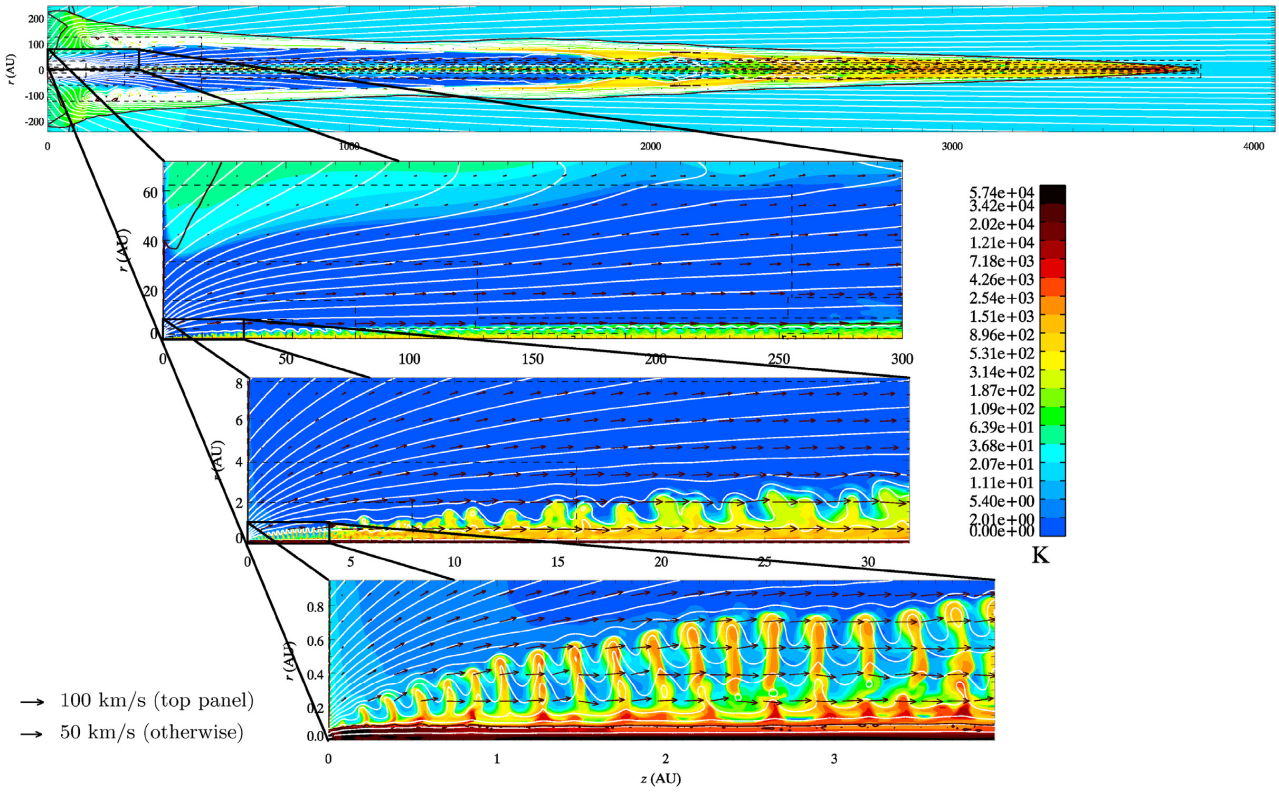

FIGURE 5.15: Figure 6 of Ramsey and Clarke, 2019, simulation F with $\kappa_d = 2$. The background is the temperature, the black arrows indicate the poloidal velocity, the white contours are poloidal magnetic field lines and the black contour is the SM critical surface. The inner jet core and sheath reach super-FM speeds (see their Figure 3).

Ramsey and Clarke, 2011, 2019 are to my knowledge the first to perform simulations on a grid large enough to capture standing recollimation shocks: $(r, z) = (5 \times 10^3 R_d, 8 \times 10^4 R_d)$ with nine levels of AMR, their coarsest resolution being 160×2548. Their magnetic field profile is the critical flat distribution $\alpha = 1$ (see section 5.1.2). They also use the standard $\rho \propto r^{-3/2}$ density distribution and have a mass load slowly decreasing radially with $\kappa \propto 1/\sqrt{r}$. Despite this decrease, only the innermost regions ($r_0 \lesssim 10R_d$) reach a relative steady state. They also explore the impact of the mass loading parameter κ. Its value on the disk is explored on a large range:

[6]This $\mu \equiv \kappa$ parameter has nothing to do with my $\mu \equiv V_{A_d}/V_{K_d}$ parameter.

$\kappa_d \in \left[5 \times 10^{-2}, 32\right]$. Knots appear near the polar axis in their $\kappa_d = 0.5$ simulation E, and become stronger and periodic in their $\kappa_d = 2$ simulation F. This simulation F is presented on Figure 5.15, where the periodic knots are clearly seen in the bottom panel. These knots are quite different from the steady recollimation shocks of my simulations, as their radial extent is small, and the MHD invariants are not constant through them (see the discussion in their section 4.3). Compared to my simulations, their grid is ten times larger and the integration is made on a time t_{end} ten times smaller. Moreover, as explained in section 5.1.2 their vertical magnetic field configuration should prevent them from reaching a steady state out of the innermost jet regions in reasonable timescales, which was not their intention anyway.

5.3 Summary

The simulations presented in this chapter and the previous one are the first to show standing recollimation shocks in a jet emitted from emitted from a magnetized keplerian disk. Such shocks were expected from the self-similar solutions, but were not seen in previous "global" simulations. This most likely due to the huge associated scales in space and time, that could not be captured by the earlier works.

In this chapter, I analyzed the influence of the launch conditions on those shocks. I showed that they qualitatively follow the behavior demonstrated by the self-similar studies, i.e. that they get closer to the disk as the mass load κ increases. I confirmed that the magnetic field distribution in the disk ($B_z \propto r^{\alpha-2}$) is the key quantity shaping the collimation of the jet. In this quasi self-similar setup, the collimation follows the trend of potential fields: the greater α, the stronger the collimation. In addition, no steady-state simulations are obtained for $\alpha \geq 1$: at those large scales, it is difficult to establish a consistent and stationary electrical circuit along the outer regions.

Although qualitatively in line with the self-similar studies, my results show an undeniable impact of the axial spine on the jet asymptotics. This inner spine is not ejected from the Keplerian disk, but from the central object and its interaction with the surrounding disk. It carries a return current responsible for the collimation of the innermost flow.

Chapter 6

Steady simulations of jets emitted from a truncated JED

Contents

6.1 Introduction . . . 127
6.1.1 Reproducing the observations . . . 127
6.1.2 Disconnecting accelerating and asymptotic circuits . . . 128
6.2 Numerical setup . . . 129
6.2.1 A setup resembling the quasi self-similar one . . . 129
6.2.2 Different boundary conditions on the disk . . . 130
Density and pressure . . . 130
Velocities . . . 131
A transition between the ejecting and non-ejecting regions . 131
Magnetic fields . . . 132
6.3 The reference simulation . . . 133
6.3.1 A two/three-component outflow . . . 133
6.3.2 Outflow properties . . . 137
6.3.3 Radial balance . . . 139
6.4 Parameter dependence . . . 141
6.4.1 Rotation on the axis . . . 142
6.4.2 External magnetic field . . . 145
6.4.3 Radial distribution of the vertical magnetic field . . . 148
6.5 Comparison with other numerical works . . . 151
6.6 Summary . . . 154

"Les montagnes ne vivent que de l'amour des hommes. Là où les habitations, puis les arbres, puis l'herbe s'épuisent, naît le royaume stérile, sauvage, minéral ; cependant, dans sa pauvreté extrême, dans sa nudité totale, il dispense une richesse qui n'a pas de prix: le bonheur que l'on découvre dans les yeux de ceux qui le fréquentent."

"The mountains live only on the love of man. Where houses, then trees, then grass are exhausted, a barren, wild, mineral kingdom is born ; yet, in its extreme poverty, in its total bareness, it dispenses a priceless treasure: the happiness you discover in the eyes of those who frequent it."

Gaston Rébuffat

Les résultats présentés dans les chapitres précédents ont été obtenus dans une configuration quasi auto-similaire, l'ensemble de la frontière inférieure étant un disque d'émission de jets (JED). Les jets émis à partir d'un disque aussi grand peuvent être comparés à des solutions auto-similaires et à des simulations numériques avec une frontière d'éjection semblable. Cependant, ces jets simulés sont très différents de ceux observés autour des YSOs, des AGNs ou des binaires à rayons X. Pour cette raison, dans ce chapitre nous verrons des jets simulés où l'éjection ne se fait que depuis la partie interne du disque, à la manière du modèle JED-SAD. Ce modèle a été développé dans le contexte des binaires à rayons X, mais il est également valable pour les jets protostellaires. Il s'agit d'un disque hybride, avec à l'intérieur un disque d'émission de jets (JED, Ferreira, 1997) fortement magnétisé, entouré d'un disque d'accrétion standard (SAD, Shakura and Sunyaev, 1973) à l'extérieur. La transition entre le JED qui lance des jets et le SAD qui n'en lance pas se produit à un rayon fini. Dans le cas d'une binaire à rayons X, la valeur de ce rayon de transition devrait varier au cours du cycle de fonctionnement, mais ne jamais dépasser quelques dizaines de rayons de Schwarzchild.

Une autre raison de réaliser des simulations utilisant ce type de dispositif est de déconnecter le circuit accélérateur, lié au disque, du circuit asymptotique, qui dicte la forme observée du jet. Cela implique que la valeur du courant post-choc est fixée par la valeur du courant sortant du disque. Par conséquent, un certain nombre de morphologies de jets ne sont pas atteignables. Par exemple, le jet de M87 est parabolique avant de rencontrer les chocs de recollimation, puis devient conique. Dans mes simulations, la présence d'un courant poloidal avant et après le choc force le jet à rester parabolique. Mais, si le choc permet une déconnexion entre le circuit accélérateur et le circuit asymptotique, alors l'allure du jet de M87 pourrait être reproduite.

Dans la région interne du disque, les variables sont fixés conformément aux solutions JED, comme dans la simulation de référence. De même, sur l'objet central on interpole les grandeurs de leur valeur au bord interne du disque jusqu'à la condition voulue sur l'axe. Dans la partie externe, l'éjection est arrêtée en diminuant fortement la densité et en arrêtant la rotation. L'éjection étant alors sub-SM, la vitesse d'éjection est laissée libre. Afin de limiter la force électromotrice du SAD, son champ magnétique toroidal est petit à petit diminué au cours de la simulation.

Cette fois, il y a un écoulement interne super-FM et un écoulement externe sub-Alfvénique, à cause de la nature des conditions d'éjection. Dans la partie super-FM, on observe des chocs de recollimation similaires à ceux observés dans les simulations précédentes. La présence de ces chocs est un résultat fort, montrant que leur formation n'est pas un biais d'auto-similarité, mais une conséquence des conditions d'éjection du disque. Dans ce cas, les chocs façonnent également l'interface entre les flux super et sub FM : une réfraction de la surface FM peut être observée sur à chaque croisement de choc. Partout, l'interface est grossièrement parabolique. Cette situation est inévitable en raison de la présence d'une nappe de courant externe le long de l'interface. Celle-ci se referme sur l'axe, menant à de la collimation, avant et après le choc. L'interface est confondue avec la surface FM. Dans son équilibre, les deux forces dominantes sont les deux pressions magnétiques. La chute du champ magnétique toroïdal à l'interface créant la nappe de courant induit une forte force dirigée vers l'intérieur. Elle est ensuite compensée par une forte augmentation du champ magnétique poloïdal, créant une force tout aussi forte dirigée vers l'extérieur.

Pour ce type de jets à l'éjection tronquée, j'ai également réalisé une étude paramétrique. Les trois paramètres modifiés furent la rotation sur l'axe, la pression magnétique externe, et la distribution du flux magnétique, via le paramètre α.

Concernant la rotation sur l'axe, je me suis limité à des étoiles ou trous noirs tournant moins vite que leur disque. Le cas contraire correspondrait à correspond à des trous noirs en rotation rapide qui développeraient des jets relativistes puissants, ou à des étoiles en rotation rapide dans le "propeller regime" (voir Romanova et al., 2009; Zanni and Ferreira, 2009). Tous deux sont hors de portée de ce travail. Ici il n'a pas été nécessaire de modifier l'énergie sur l'axe, et il est clair que la rotation de l'objet central affecte la collimation. Un jet dont l'objet central est en rotation est plus confiné que son homologue dont l'objet central n'est pas en rotation. Mais surtout, ses chocs de recollimation se produisent à des altitudes plus basses, ce qui pourrait conduire, dans les observations, à des noeuds stationnaires plus proches du disque. Cependant, la rotation sur l'axe ne modifie ni la puissance du jet, ni son bras de levier magnétique.

Concernant la pression magnétique externe, j'ai réalisé cinq simulations différentes, en partant d'une pression nulle. Dans le cas d'une pression nulle, l'interface est conique, maisla collimation du jet par rapport à la solution potentielle initiale est bien présente. Puis, plus la pression magnétique extérieure est forte, plus l'interface est collimatée, donc plus le jet lui-même est collimaté. Il semble que les pressions nécessaires pour produire la collimation coincident avec ce qu'on observe dans les jets protostellaires, mais il est difficile de conclure sans image synthétique du jet simulé.

Concernant la distribution du flux magnétique sur le disque, j'ai à nouveau tenté de réaliser des simulations avec $\alpha \geq 1$, mais cela n'a à nouveau pas fonctionné, j'ai par contre pu observer que pour celles-ci ont obtenait bien un jet plus collimaté (du moins proche du disque), ainsi qu'un bras de levier magnétique plus faible.

Enfin, je compare mes résultats à ceux de la littérature. A ma connaissance, la dynamique et l'influence réciproque entre un jet MHD émis par un disque de taille finie et une atmosphère statique n'ont pas encore été étudiées, et ces simulations sont les premières à le faire.

6.1 Introduction

6.1.1 Reproducing the observations

The results presented in the previous chapters were obtained in a quasi self-similar setup, the whole lower boundary ($r \in [R_d; 5650R_d]$) being a Jet-Emitting Disk (JED). Jets emitted from such a large disk can be compared to self-similar solutions and to numerical simulations with a similar ejection boundary. However, such simulated jets are very different from those observed around YSOs, AGNs or X-ray binaries.

Let us take the case of Young Stellar jets as an example. As my disk inner radius R_d is considered to be the disk truncation $r_t = 0.1$au, the JED would extend until 565au. Such a large emission zone is inconsistent with outflow observations (Ferreira, Dougados, and Cabrit, 2006; Lee, 2020; Tabone et al., 2020 and references therein) that derive from jet kinematics an ejection no further than a few au from the star. In the case of AGNs, radio-emitting regions seem limited to a maximum of a thousand Schwarzchild radii from the source (see e.g. Anderson and Ulvestad, 2005). Ejection from a limited disk would also be consistent with black hole X-ray binariy observations. The JED-SAD model (Ferreira et al., 2006; Marcel et al., 2018; Marcel et al., 2018) manages to fit X-ray and radio spectra during the jetted hard states of GX 339-4 (Barnier et al., 2022; Marcel et al., 2019, 2022).

The JED-SAD model was developed in the context of X-ray binaries, but also holds for protostellar jets/winds. In that case, the structure is that of Figure 6.1. It consists in a hybrid disk, with an inner highly magnetized Jet-Emitting Disk (JED, Ferreira, 1997) surrounded by an outer Standard Accretion Disk (SAD, Shakura and Sunyaev, 1973). The transition from the jet-launching JED to the non jet-launching SAD happens at a finite radius r_J. In the case of an X-ray binary, the value of this transition radius is expected to vary during the duty cycle, but never exceeds a few tens of r_{ISCO}.

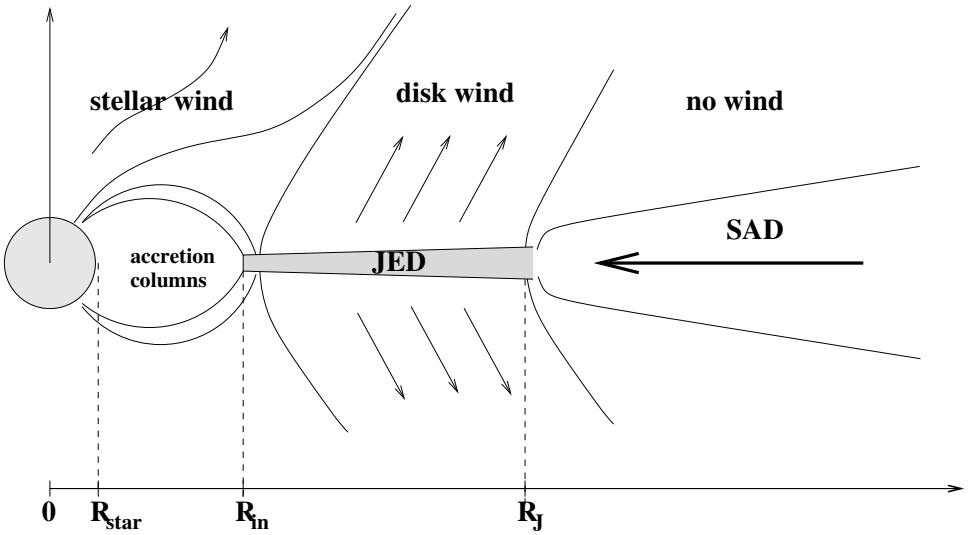

FIGURE 6.1: Scheme of the JED-SAD model in the case of a protostar (Combet and Ferreira, 2008). With my notations, $R_{in} = R_d$. The Jet-Emitting Disk (JED) is limited to $[R_d; r_J]$. Beyond r_J lies a non-ejecting Standard Accretion Disk (SAD).

6.1.2 Disconnecting accelerating and asymptotic circuits

Stopping the jet production beyond a finite disk radius is thus required to produce jets more consistent with the observations, most notably for young stars and X-ray binaries. But such a restriction could also be useful for another intent. One of the objectives of producing jet simulations on such a large grid was to capture recollimation shocks. Those recollimation shocks, observed in YSO (Bonito et al., 2011) and AGN (Cheung, Harris, and Stawarz, 2007) jets and predicted by self-similar solutions (Ferreira, 1997; Polko, Meier, and Markoff, 2010) were expected to create a disconnection between the accelerating and asymptotic circuits. Figure 6.2a presents this situation, assuming a single recollimation shock, in yellow. It acts as a separatrix between the accelerating circuit in green and the asymptotic circuit in red. In this simple case, the value of the post-shock current is directly determined by the ejection conditions. But the situation recovered in my simulations is more complex.

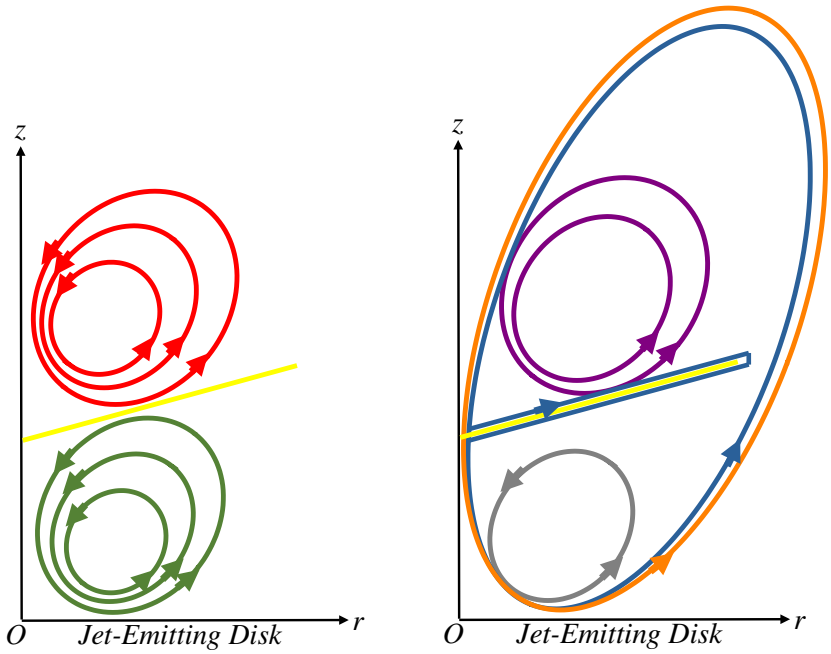

(A) Expected circuits (B) Actual circuits

FIGURE 6.2: Schemes of the circuits for a steady state jet with one recollimation shock in yellow, acting as a current sheet. (a) Expected behavior, with disconnected acceleration and asymptotic electric circuits. (b) Obtained behavior: sketch of the circuits for the reference simulation K2, right panel of Figure 4.13.

Figure 6.2b presents a simplified scheme of the circuits obtained in the reference simulation K2, still assuming only one shock. There are still circuits fully enclosed before the shock (such as the one in grey) or fully enclosed after the shock (such as the one in purple). But there are also circuits going around the shock before flowing back onto the central object, either by circumventing the shock (such as the one in blue) or by directly flowing along the axis (such as the one in orange). The circuits induce a direct link between the pre-shock and the post-shock regions, and thus prevent the creation of a "true" asymptotic circuit: the intensity in the post-shock region is dictated by the ejection conditions at the disk surface. This prevents the simulations from showcasing all the possible jet topologies seen by the analytical

work of Heyvaerts and Norman, 1989 mentioned in the introduction. In particular, Asada and Nakamura, 2012 showed that the M87 jet shape presents a dichotomy on the two sides of the recollimation shock at the HST-1 knot. This is illustrated on their Figure 2, reproduced in this manuscript on Figure 1.11.

- Between the black hole and the shock, the jet is "parabolic" with $z_{jet} \propto r_{jet}^{1.73\pm0.05}$.
- After the recollimation shock, the jet is conical with $z_{jet} \propto r_{jet}^{0.96\pm0.1}$.

According to Heyvaerts and Norman, 1989, this observation may be interpreted as an electric current vanishing in the shock: they showed that jets threaded by an asymptotic current appear parabolic, while jets without an asymptotic current appear conical. My simulated jets do not provide such a dichotomy, and the shocks induce a transition from parabolic field lines to parabolic field lines.

But stopping the ejection at a finite disk could force all the emitted plasma to go through the shock, and create the dreaded disconnection between the accelerating and asymptotic circuits. Naturally, this relies on the strong assumption that the general behavior of the inner jet would be the same as in the quasi self-similar simulations, namely still undergoing recollimation. Thus, I decided to produce simulations in which the ejection is gradually stopped on the disk beyond $r_0 = r_J \equiv 10$. Depending on the central objects, the size of the the emitting zone thus extends to:

- For a stellar jet: $r_J = 1$au considering a disk truncation radius $r_t = R_d = 0.1$au.
- For an AGN or a black hole X-ray binary jet: $r_J = 10 r_{ISCO}$, with $R_d = r_{ISCO}$.

Those values are consistent with the size of the ejecting disk inferred by observations, and the field line anchored in $r_J = 10\,R_d$ is well within the last field line crossing the main shock. As shown by Figure 4.2, such a field line is anchored at $r_0 \simeq 320$. The value $r_J = 10\,R_d$ meets this requirement while keeping a JED much larger than the spine. Additionally, this factor ten between R_d and r_J makes it possible to consider a power-law in the JED (see equation 1.5), but one should not expect the jet to behave in a self-similar way within this truncated approach.

6.2 Numerical setup

For the sake of clarity, I will hereafter refer to the region of finite radial extent launching jets according to JED values as JED. Thirteen simulations with a truncated JED until $r_J = 10$ were performed. In this section, I will describe the numerical setup used to produce the truncated simulation of reference, called O1. To produce the other simulations I varied one parameter, all else being equal. They are presented in Table 6.1.

6.2.1 A setup resembling the quasi self-similar one

The simulation was performed in the Low-Resolution grid, i.e. $N_R = 704$ and $N_\theta = 144$ for computing time constraints. The combination of Riemann solvers and the reconstruction schemes used are those used in all the simulations presented previously. Naturally, the same usual set of ideal MHD are solved, and they are integrated using the accelerated CFL condition (equation 3.15) with great success.

The conditions at all boundaries but the disk remain the same:

- On the polar axis ($\theta = 0$, $R \in [R_d; 5650 R_d]$): usual reflecting conditions.

- On the outer boundary ($R = 5650 R_d$, $\theta \in [0; \pi/2]$): conservation of the spherical gradient in ρ, P, B_R, B_θ, RB_φ, v_R, v_θ and v_φ.
- On the central object ($R = R_d$, $\theta \in [0; \pi/2]$): conditions on P, ρ, $\vec{v}$ and B_R described in section 3.2.3, set to limit the influence of the axial spine: For the reference simulation O1 the rotation on the axis is set to zero: $\Omega_{*_a} = 0$.

6.2.2 Different boundary conditions on the disk

On the disk, the boundary conditions remain the same JED conditions as in the previous setup until $r_J = 10\, R_d$. There, the conditions on P, ρ, $\vec{v}$ and B_θ are the power law distributions described in section 3.2.3, with exponents depending on the self-similar parameter α and normalizations depending on the mass loading κ. The initial conditions are fixed with a potential solution created with those parameters, same as for the self-similar setup. For the truncated simulation of reference O1, the values of those parameters are the same as in the self-similar simulation of reference K2, i.e. $\alpha = 3/4$ and $\kappa = 0.1$.

I first describe the boundary conditions on the density, pressure and velocities. They follow different distributions in the ejecting JED and in the non-ejecting SAD. Then, I present how the transition between the two regions is done. Finally, I describe the boundary conditions on the magnetic field, which is set differently. All boundary conditions are illustrated in Figure 6.3. In all the following, distributions in the inner ejecting region ($r_0 \leq r_J$) are indicated by the subscript JED and distributions in the outer non ejecting region ($r_0 \geq r_S$)[1] are indicated by the subscript SAD.

Density and pressure

Same as in the self-similar setup, the density and profiles in the ejecting zone are:

$$\begin{aligned} \rho_{JED} &= \rho_d \left(\frac{r}{R_d}\right)^{2\alpha-3} \\ P_{JED} &= \rho_d \frac{V_{S_d}^2}{\Gamma} \left(\frac{r}{R_d}\right)^{2\alpha-4} \end{aligned} \tag{6.1}$$

In the non-ejecting zone, the distributions are set as:

$$\begin{aligned} \rho_{SAD} &= \rho_a \left(\frac{r}{R_d}\right)^{2\alpha-3} \\ P_{SAD} &= \frac{1}{4-2\alpha} \frac{\rho_a GM}{R_d} \left(\frac{r}{R_d}\right)^{2\alpha-4} \end{aligned} \tag{6.2}$$

The density distribution follows the same power law as in the inner ejecting zone, normalized at the axis density ρ_a instead of ρ_d. The two normalizations are linked by the parameter $\delta \equiv \rho_d/\rho_a = 10^3\kappa$. All truncated simulations are set with $\kappa = 0.1$ thus $\delta = 100$. This sets the same strong contrast between the ejecting JED and the non-ejecting SAD as the one between the ejecting JED and the axis. The pressure distribution is chosen to be consistent with the initial condition, that was normalized to the boundary conditions on the axis ($R = R_d, \theta = 0$). The ejection in the SAD is thus already limited by a density drop of two orders of magnitude at r_J.

[1] For the sake of simplicity, this outer region is called non-ejecting, even though there is still some remaining mass loss, although much smaller than in the inner region.

Velocities

The rotation of the magnetic surfaces simply transitions from keplerian rotation ($\Omega_{*_{JED}} = \sqrt{GM/r^3}$) in the ejecting zone to no rotation ($\Omega_{*_{SAD}} = 0$) in the non-ejecting zone. The intent is to suppress the MHD Poynting flux in this non-ejecting region, as it is $\vec{S}_{MHD} = -1/(4\pi)\Omega_* r B_\varphi \vec{B}_p$ in steady state. The vanishing of Ω_* greatly reduces the plasma rotation $v_\varphi = \Omega_* r + v_\theta B_\varphi / B_\theta$ and consequently any magnetocentrifugal ejection. However, we still observe a little rotation due to a remaining toroidal magnetic field (see section on magnetic fields).

The distributions of poloidal velocities in the ejecting part are naturally those of the self-similar setup:

$$\begin{aligned} v_{\theta_{JED}} &= -v_d \left(\frac{r}{R_d}\right)^{\alpha-2} \\ v_{R_{JED}} &= v_\theta \frac{B_R}{B_\theta} \end{aligned} \tag{6.3}$$

In the first tests, the poloidal velocity was set to zero in the outer non-ejecting region: $\vec{v}_{p_{SAD}} = \vec{0}$. While obviously preventing ejection by $v_{\theta_{SAD}} = 0$, this simple condition had two drawbacks, most likely related. First, the simulations converged quite slowly, as the acceleration scheme took time to get started. Second, the ejection was now sub-SM in the non-ejecting SAD: The slow-magnetosonic speed increases by two orders of magnitude due to the decrease in density, and the vertical speed is dropped to zero. One condition had to be relaxed: when $M_{SM} < 1$, the injection speed v_θ is now an outflow condition, meaning that its value in the domain fixes the value at the boundary, with gradient conservation and the use of slope limiters.

As a summary:

$$v_{\theta_{SAD}} = \begin{cases} v_\theta(\theta_{-1}) + \frac{\partial v_\theta}{\partial \theta}(\theta_{-1})(\frac{\pi}{2} - \theta_{-1}) & \text{if } M_{SM} < 1 \\ 0 & \text{if } M_{SM} \geq 1 \end{cases} \tag{6.4}$$

$$v_{R_{SAD}} = 0$$

The first line describes in a very simplified way an "outflow" condition for v_θ at the $\theta = \pi/2$ boundary. The value at the boundary $v_{\theta_{SAD}}$ is set by gradient conservation from the cell just above the boundary and thus in the domain, at $\theta = \theta_{-1}$.

This simple fix produces faster converging solutions. However, one caveat remains: these conditions are not compatible with steady state ideal MHD, as $\vec{v}_{p_{SAD}} \nparallel \vec{B}_{p_{SAD}}$. The left panel of Figure 6.3 shows that in the non-ejecting region the radial speed is not equal to zero, even in the lowermost cell: there is a discontinuity in v_R just below $\theta = \pi/2$. This is not redhibitory as the field lines anchored in the outer region remain subAlfvénic and thus non-stationnary. Still, future tests with the radial speed set as $v_{R_{SAD}} = v_{\theta_{SAD}}(B_{R_{SAD}}/B_{\theta_{SAD}})$ would be interesting, and will be done in the near future.

A transition between the ejecting and non-ejecting regions

The disk boundary conditions are modified only for $r_0 > r_J \equiv 10R_d$. The ejection is stopped for $r_0 > r_S \equiv 12\,R_d$, and the region $r \in [r_J; r_S]$ consists in a transition zone. Let us define a parameter x giving the position on this transition:

$$x \equiv \begin{cases} 0 & \text{if } R_d \leq r < r_J \\ \frac{r-r_J}{r_S-r_J} & \text{if } r_J \leq r \leq r_S \\ 1 & \text{if } r_S < r \leq 5650 R_d \end{cases} \tag{6.5}$$

For $n \in \mathbb{N}$, I define the spline function f_n:

$$\begin{aligned} f_n \colon x &\longrightarrow \left(1 - 3x^2 + 2x^3\right)^n \\ [0;1] &\longmapsto [0;1] \end{aligned} \tag{6.6}$$

This function varies from $f_n(x=0) = 1$ in the inner ejecting zone to $f_n(x=1) = 0$ in the outer non-ejecting zone. The density, pressure and velocities are set with such a spline, and increasing the integer n allows the production of coarser transitions for certain quantities. Naming $\mathcal{U}$ one of those quantities, their distributions in the whole disk are fixed by the spline function as:

$$\mathcal{U}(r) = \mathcal{U}_{JED}(r) f_n\left(x(r)\right) + \mathcal{U}_{SAD}(r)\left[1 - f_n\left(x(r)\right)\right] \tag{6.7}$$

Density and pressure are linked by the steep spline function f_{20} while the velocities are linked by the smoother function f_1. As the transition region $[r_J = 10; r_S = 12]$ is small, this doesn't change much. Naturally, the distributions in the ejecting zone are set as in the self-similar simulations, and the distributions in the non-ejecting are set to minimize the ejection from the SAD region. Those distributions are shown in the left panel of Figure 6.3. Those are plots on the lowermost cells of the computing domain, thus quantities not set at the boundary (e.g. B_θ for $r < 1$ and B_R for $r > 1$) are also plotted, and differences with what is set can be observed.

Magnetic fields

In simulation B1 (see Table 6.1), the vertical magnetic field is set the same as in the self-similar reference simulation K2. To probe the impact of external pressure, a constant vertical magnetic field B_{ext} is added, which provides additional collimation. This gives a vertical magnetic field disk distribution on the disk boundary:

$$B_\theta = -B_d \left(\frac{r}{R_d}\right)^{\alpha-2} - B_{ext} \tag{6.8}$$

For the truncated reference simulation O1, $B_{ext} = 2 \times 10^{-4}\, B_d = 2 \times 10^{-3}$. This external magnetic field is naturally more dominant in the outer disk regions ($r \gtrsim 10^3\, R_d$) where the power law drops off, as is visible in both panels of Figure 6.3.

In order to reduce rotation in the non-ejecting region as much as possible, the toroidal magnetic field is limited. However, this cannot be done by simply setting $B_{\varphi_{SAD}} = 0$, are the appropriate number of disk ejection conditions are already fixed:

- Six in the super-SM part: ρ, P, v_R, v_θ, v_φ and B_θ.
- Five in the sub-SM part: ρ, P, v_R, v_φ and B_θ.

To avoid setting overconstrained boundary conditions, I gradually limit the toroidal magnetic field for $r > r_S$, with

$$B_\varphi(r, t+dt) = B_\varphi(r,t) e^{-\frac{dt}{\mathcal{T} T_K(r)}} \tag{6.9}$$

where $T_K(r) = \sqrt{r^3/(GM)}$ is the local keplerian timescale at radius r and $\mathcal{T} = 10^{-6}$ is an adimensioned number quantifying how fast the toroidal magnetic field decreases with time. This condition is not applied in the transition zone ($r \in [r_J; r_S]$) to prevent the creation of too high magnetic field gradients. While the simulations with $B_{\varphi_{SAD}} = 0$ do not converge, the simulations produced with this technique converged fast, even faster than with a simple outflow condition on B_φ. The impact of this condition on the jet radial structure was carefully studied. Various tests are shown in appendix B, as well as the reasons behind the choices of $r_S = 12R_d$ and $\mathcal{T} = 10^{-6}$.

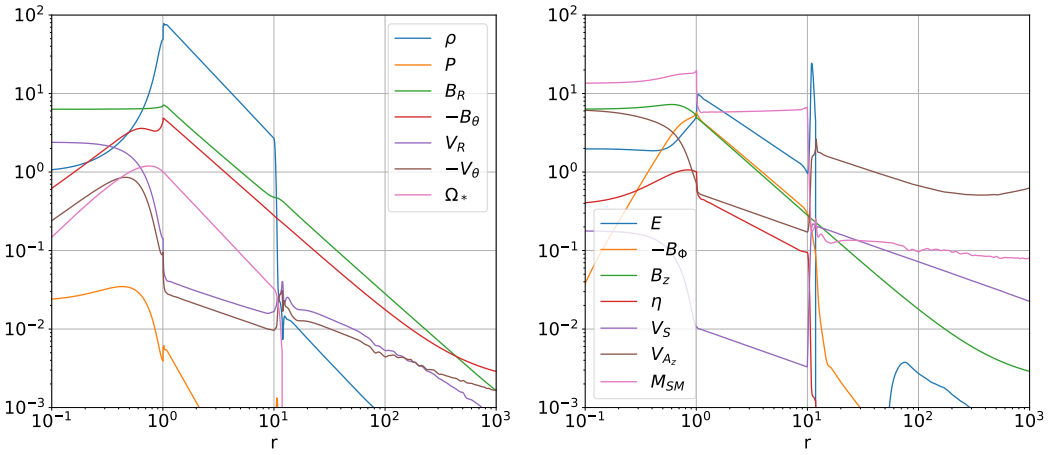

FIGURE 6.3: Boundary conditions on the lowermost cells of the reference truncated simulation. The quantities are plotted on the first cell along the injection boundaries (e.g. central object $R = 1$ for $r \leq 1$ and JED $\theta = \pi/2$ for $r \geq 1$). On the left are shown the conditions that directly set on the injection boundaries: the density ρ, the pressure P, the radial and orthoradial magnetic fields B_R and $-B_\theta$, the radial and orthoradial velocities v_R and $-v_\theta$ and the rotation speed of the magnetic surfaces Ω_*. On the right are quantities dependent on those set conditions: the Bernoulli invariant E, the toroidal and vertical magnetic field $-B_\varphi$ and B_z, the mass to magnetic flux ratio η, the sound speed V_s, the vertical Aflvén speed V_{A_z} and the SM mach number M_{SM}. This is a reproduction of Figure 4.1, which was for a quasi self-similar simulation.

6.3 The reference simulation

Thirteen simulations where the jet is emitted from a truncated disk were run. In this section I present the reference simulation O1. It was obtained without axis rotation Ω_{*_a}, with the Blandford & Payne magnetic field configuration $\alpha = 3/4$ and an additional magnetic field $B_{ext} = 2 \times 10^{-3}$.

6.3.1 A two/three-component outflow

A snapshot of this simulation is presented on Figure 6.4. It clearly shows two outflows:

- A super-FM and and super-Alfvénic inner outflow, containing the axial spine.
- A sub-FM and sub-Alfvénic outer outflow.

The two flows are separated by the confounded FM and Alfvén surfaces. This interface is collimated to a radius $500 \lesssim r_I \lesssim 1000$ at large distances from the source ($z > 1500$). We will see later that this due to the external magnetic field B_{ext}.

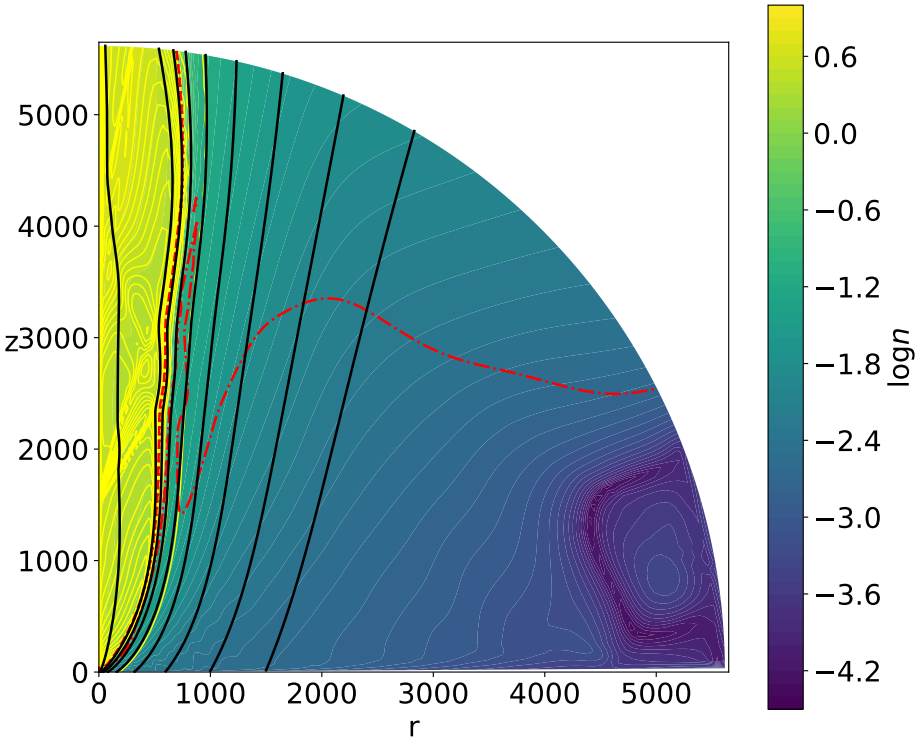

FIGURE 6.4: Snapshot of the truncated reference simulation O1 at t_{end}. The color coding is the same as the left panel of Figure 4.2, snapshot of the self-similar reference simulation K2, with the addition of the SM critical surface (dash-dotted, red).

As shown in Table 6.1, the outermost magnetic field line that ultimately becomes super-FM is anchored on the disk at $r_{0,FM} = 58$. This means the interface is slightly less collimated than the magnetic field lines. There is some spreading, and the interface between the super-FM and sub-FM flows does not exactly follow the field line anchored in $r_0 = r_J$. This is due to a lateral numerical diffusion at high altitudes, where the cells are large. As set by the boundary conditions, the SAD region beyond r_S ejects very little. The mass flux emitted from the $r_J < r_0 < r_{0,FM}$ disk region is forty times smaller than the one emitted from the $R_d < r_0 < r_J$.

For the sake of clarity, I will unfortunately have to use a different definition of jet from what I used in the quasi-self-similar simulations. As a reminder, jet used to refer to everything ejected between R_d and $r_{0,FM}$. Now, throughout the rest of this thesis and for all truncated simulations:

- The jet is the outflow ejected from the JED, between R_d and r_J.
- The wind is the sparse outflow ejected from the SAD, between r_S and $5650R_d$.

The spine remains the plasma ejected from the central object ($r \leq 1$). The super-FM inner flow and the sub-FM outer flow will be referred as such. The cocoon is defined as the part of the wind that eventually reaches super-FM speeds, i.e. ejected between r_S and $r_{0,FM}$.

The wind is injected at sub-SM speeds, as the slow-magnetosonic mach number becomes lower than unity in the $r_J < r_0 < r_S$ transition zone. It becomes super-SM at large distances from the disk, $z \sim 3000$ in the outer regions.

The most notable feature of the jet is the presence of two large recollimation shocks, leaving the polar axis at $Z_{shock} = 1550$, and extending until the interface. These shocks have a structure similar to those observed in the self-similar simulation of reference, K2, having different opening angles while being ejected at the same point on the axis. These are weak shocks, introducing a small refraction of the magnetic field lines, before the eventual recollimation due to the post-shock circuits. The simulation O1 shows little complexity: there are no smaller shocks at the spine-jet interface that would merge with these larger ones. It was done in the low-resolution grid, the same that was used to produce the simulation K2l that also showed less complexity.

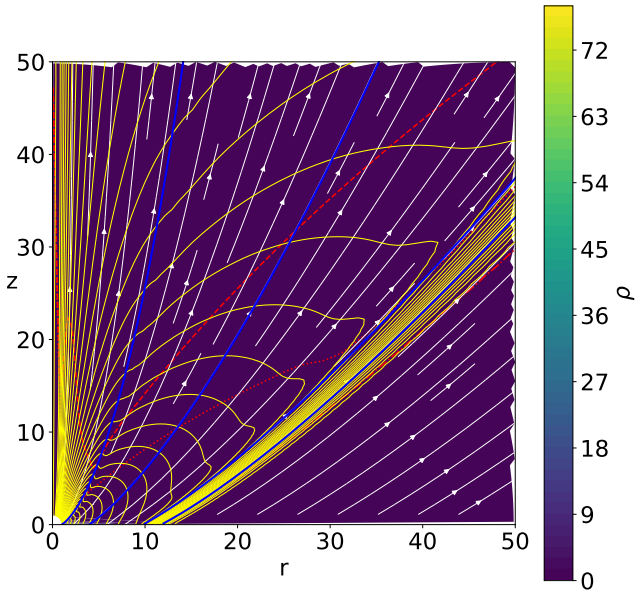

FIGURE 6.5: Snapshot of the reference simulation O1 at t_{end}, zoomed for $r < 50$ and $z < 50$. The white and blue lines are poloidal magnetic field lines, the blue ones being anchored on the disk at $r_0 \in [1.02; 4; 10; 12]$. The red lines are the three critical surfaces, SM (dashdot) Alfvén (dotted) and FM (dashed). The yellow lines are electric circuits, flowing out of the ejecting ($z = 0$, $r \in [1; 10]$) and transition ($z = 0$, $r \in [10; 12]$) regions, and closing into the central object ($R = \sqrt{r^2 + z^2} = 1$). The background is the plasma density ρ.

The presence of these shocks is quite a strong result, showing that their formation is not a bias of self-similarity, but a consequence of the disk ejection conditions. In this case, the shocks also shape the interface between the super and sub FM flows: a refraction of the FM surface may be seen on Figure 6.4 at each shock crossing, at the altitudes $z \simeq 2200$ and $z \simeq 3050$. The interface has three sections: 1) before the first recollimation shock, 2) between the two shocks, and 3) after the second one. In each of these sections, its shape is roughly parabolic. Such a situation is unavoidable, because of an outer current sheet flowing along the interface. This current sheet is reminiscent of the orange circuit drawn on Figure 6.2b: when it eventually flows down into the central object, it creates a post-shock circuit, either between the two shocks, or after the second shock for circuits of smaller intensities $|I| = -rB_\varphi$. There is thus no disconnection between the accelerating circuit and

those post-shock, and the intensities in the post-shock regions depend directly on the ejecting conditions. We see on Figure 6.5 this yellow sheath flowing out of the transition zone $r_J = 10 \leq r_0 \leq 12 = r_S$. The vanishing of the toroidal magnetic field in the $r_0 > r_S$ region due to the procedure described by equation 6.9 (and seen in the right panel of Figure 6.3) creates a steep gradient in intensity $I = rB_\varphi$ in the transition. This then gives rise to the current sheet, each circuit being an isocontour of intensity.

The evolution of the global outflow from its initial potential solution until the final state is described in Figure 6.6. For magnetic field lines anchored in the disk at various radii r_0, the initial state is plotted in dotted lines and the final state in full lines. One can see that at high altitudes, the super-FM outflow contains field lines anchored further than r_J and up to $r_{0,FM}$. For instance, the shocks are clearly visible on the field line anchored at $r_0 = 50$. We also see that only the innermost field lines ($r_0 \lesssim 4$) end up more collimated, while the others ($r_0 \gtrsim 4$) are decollimated. This a direct consequence of the shape of the electric circuits. As seen on Figure 6.5, the presence of the current sheet constrains the distribution of the current density $\vec{j}$. Its vertical component j_z is mostly negative only along the magnetic field anchored at $r_0 \lesssim 4$, whereas for those anchored at $r_0 \gtrsim 4$ it is positive, inducing a Laplace force $\vec{j_p} \times \vec{B_\varphi}$ directed outwards. As a consequence, the overall jet radial balance depends on outer pressure.

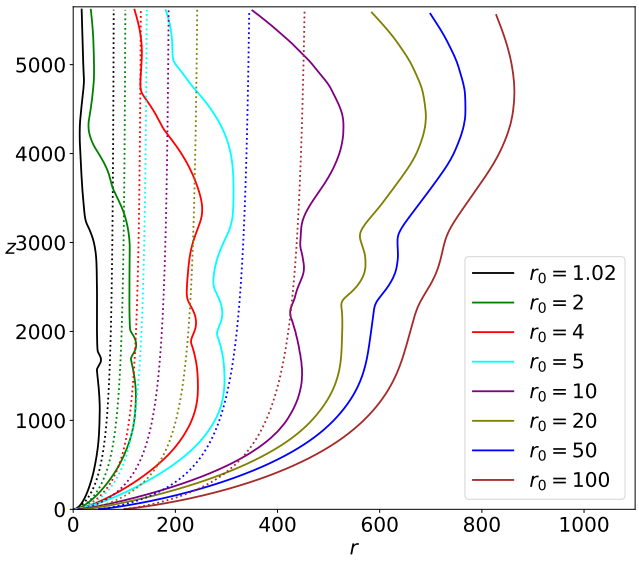

FIGURE 6.6: Evolution of several magnetic field lines during the simulation computation, for different anchoring radii r_0. The field lines at the first output of the simulation (initial conditions) are shown in dotted lines. The field lines at the last output of the simulation (final state) are shown as full lines.

One should also keep in mind that while the two most visible outflows are the jet emitted from $R_d \leq r_0 < r_J \sim r_S$ and the wind emitted from $r_J \sim r_S < r_0 \leq 5650 R_d$, the axial spine emitted from $0 < r_0 \leq R_d$ is still present and has an impact on the collimation of the other two outflows. Its interface with the jet can be seen in Figure 6.5 by turning points in the electric circuits near the field line anchored in the disk at $r_0 \simeq R_d$, while the interface between the jet and the wind can be seen by turning points in the electric circuits near the field line anchored at $r_0 = r_J$.

6.3.2 Outflow properties

At the time $t_{end} = 2.26 \times 10^6$ the jet has reached a steady state, as its mass loss rate $\dot{M}_{jet}$ barely evolves with time and the observed shocks are stationary. Table 6.1 describes a few properties of the reference simulation O1. Here, the jet mass loss rate is defined by $\dot{M}_{jet} = 2\pi \int_{r_0=R_d}^{r_0=r_J} \rho v_z r dr$ and the jet power by $P_{jet} = 2\pi \int_{r_0=R_d}^{r_0=r_J} \rho E v_z r dr$. The mass loss rate is $\dot{M}_{jet} = 37.8$, considerably smaller than that of the self-similar simulations with the same κ, α and Ω_{*_a} parameters: $\dot{M}_{jet} = 363$ for K2 and $\dot{M}_{jet} = 357$ for K2l. That was expected as the $r > r_J$ region now does not contribute. The same trend is seen in the jet power: $P_{jet} = 148$ for the truncated simulation O1, while the self-similar simulations have $P_{jet} = 616$ for K2 and $P_{jet} = 620$ for K2l, although this decrease is much smaller. The energy varying on the disk as $E \propto 1/r$ in the self-similar ansatz, the outer regions contribute more to the jet mass flux than to the jet power.

Naturally, as the disk has been amputated of a large part compared to the self-similar simulations, the axial spine now has a much greater influence on the kinematics of the global outflow. In the simulation O1, it represents half of the jet mass flux, thus a third of the total outflow mass flux: $\dot{M}_{spine}/\dot{M}_{jet} = 0.51$. The jet and spine powers are now similar despite $\Omega_{*_a} = 0$: $P_{spine}/P_{jet} = 1.05$.

It is interesting to look at how the magnetic field lines in this three-component outflow behave compared to what is expected from steady state ideal MHD. The global evolution pattern of the various energy contributions is retrieved at the middle of the jet. Figure 6.7 details the energy contributions to the Bernoulli invariant E along the magnetic surface anchored at $r_0 = 4$.

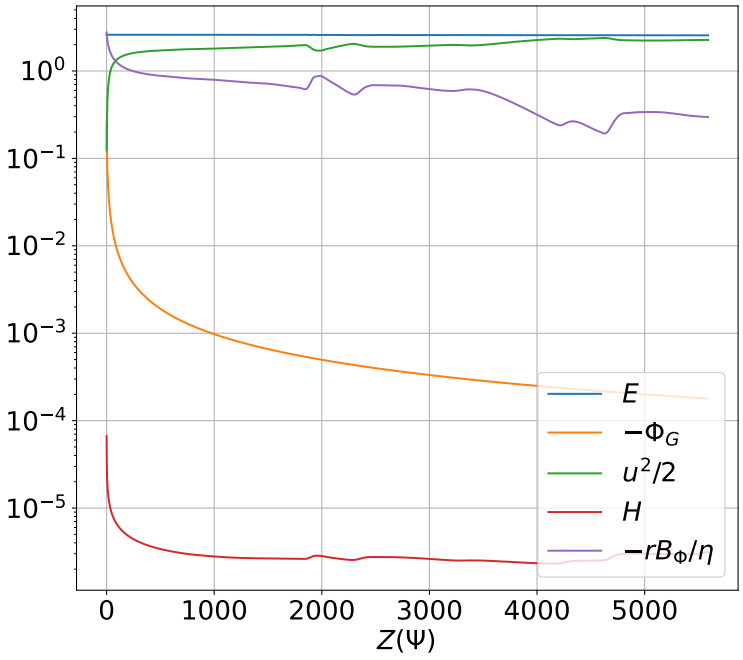

FIGURE 6.7: Evolution of the various energy contributions along a magnetic surface of anchoring radius $r_o = 4$ at t_{end}: Bernoulli invariant E, gravitational potential Φ_G, total specific kinetic energy $u^2/2$, enthalpy H and magnetic energy $-\Omega_* r B_\varphi/\eta$. The abscissa is the altitude $Z(\Psi)$.

The enthalpy is negligible, as well as gravity beyond altitudes of a few hundreds. As in the quasi self-similar simulations, the total energy is conserved and is composed of two major components. The magnetic term is dominant near the disk, and as the flow accelerates the kinetic term rises, composing the vast majority of the energy at the outer boundary. The presence of the shocks can be seen at altitudes $z \simeq 1800$ and $z \simeq 2200$. They induce a slow-down of the plasma and a localized increase of magnetic energy.

On Figure 6.8 I plot the evolution of the five MHD invariants along the magnetic field lines anchored in the disk at $r_0 \in [2; 4; 6; 8]$. The invariants are normalized to their values at the anchoring point. We see that the field lines anchored near the middle of the ejecting region ($r_0 = 4$ and $r_0 = 6$) conserve their invariants almost as well as those in the self-similar simulations (see Figure 4.6). Their variation over the whole domain is only of a few percents. The shock crossing can also be clearly seen at $z \simeq 1900$ for the field line of anchoring radius $r_0 = 4$ and at $z \simeq 2050$ for the field line of anchoring radius $r_0 = 6$. The behavior changes when going away from the center of the ejecting region.

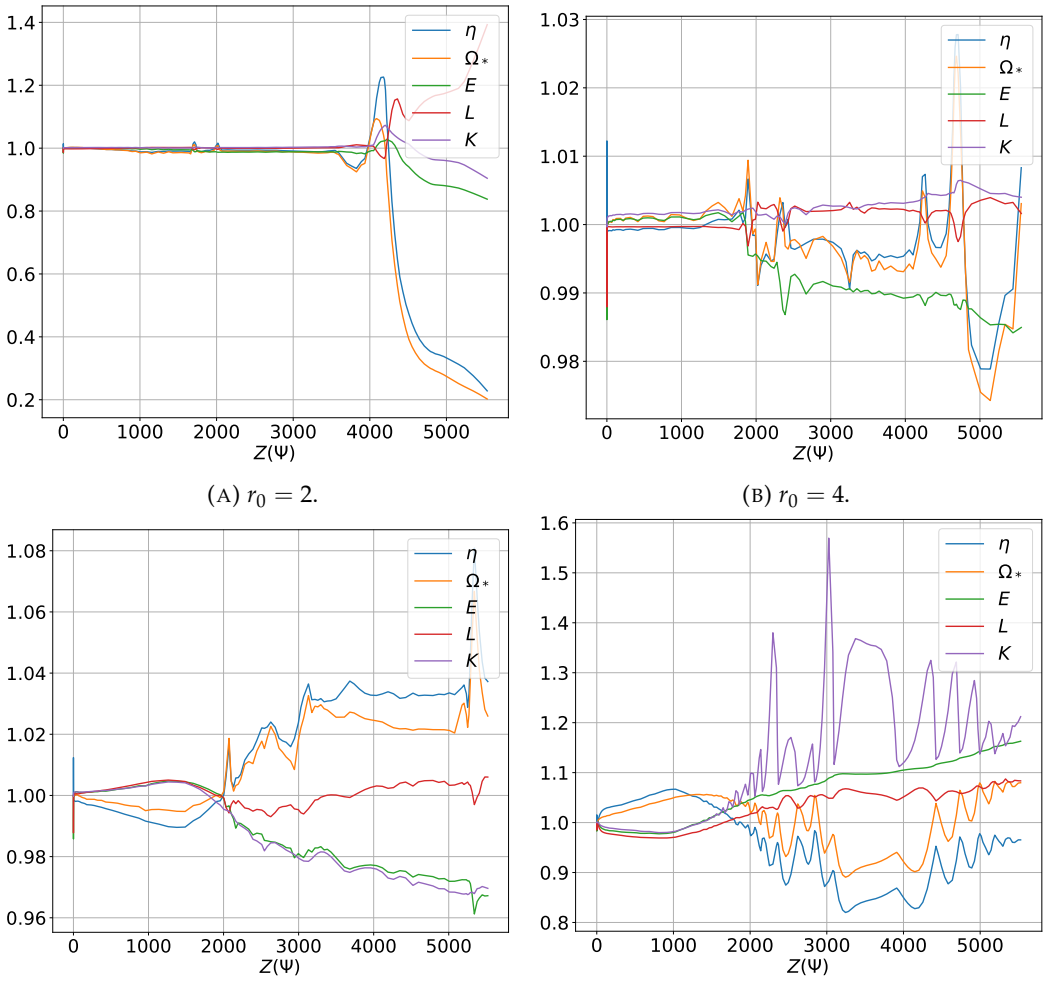

(A) $r_0 = 2$.

(B) $r_0 = 4$.

(C) $r_0 = 6$.

(D) $r_0 = 8$.

FIGURE 6.8: Evolution of the MHD invariants along field lines of four different anchoring radii r_0 at t_{end}. All invariants have been normalized to their values at r_0. The absicssa is the altitude $Z(\Psi)$.

Closer to the axial spine, the field line anchored at $r_0 = 2$ keeps a small invariant variation until $z \simeq 3500$. Small perturbations can be seen at the two shock crossings ($z \simeq 1700$ and $z \simeq 2000$). But the behavior is heavily modified beyond $z \simeq 3500$, and large invariant variations are observed, especially for the rotation of the magnetic surfaces Ω_* and the mass flux to magnetic flux ratio η. This is due to a contamination of the axial spine, as at these altitudes the resolution is small and there is lateral numerical diffusion. For instance, we see on Figure 6.4 that the innermost field line anchored at $r_0 = 3$ becomes extremely collimated at higher altitudes. The axial spine being non-rotating ($\Omega_{*_a} = 0$) and low in density ($\delta = \rho_d/\rho_a = 10^2$), the contamination lowers the inner jet rotation Ω_* and thus the mass flux to magnetic flux ratio $\eta = 4\pi\rho v_p/B_p$.

Similarly, along the field line anchored on the disk at $r_0 = 8$ the invariants vary by a few tens of percents. This time, this is due to a contamination by the wind: the boundary conditions in the non-ejecting regions are not compatible with steady-state ideal MHD, as $\vec{v}_{p_{SAD}} \nparallel \vec{B}_{p_{SAD}}$.

6.3.3 Radial balance

At the final time t_{end}, the outflow is at equilibrium, with a stable mass loss rate and steady shocks and boundaries. What are the forces driving the radial balance ? Neglecting gravity and cylindrically radial magnetic field ($|B_r/B_z| \ll 1$), we have seen that the radial equilibrium equation reduces to:

$$-\frac{\partial}{\partial r}\left(P + \frac{B^2}{8\pi}\right) + \rho\Omega^2 r - \frac{B_\varphi^2}{4\pi r} = 0 \tag{4.1}$$

On Figure 6.9 I plot all these terms along the horizontal $z = 500$, both on the whole domain (left panel) and zoomed on the jet/wind interface (right panel).

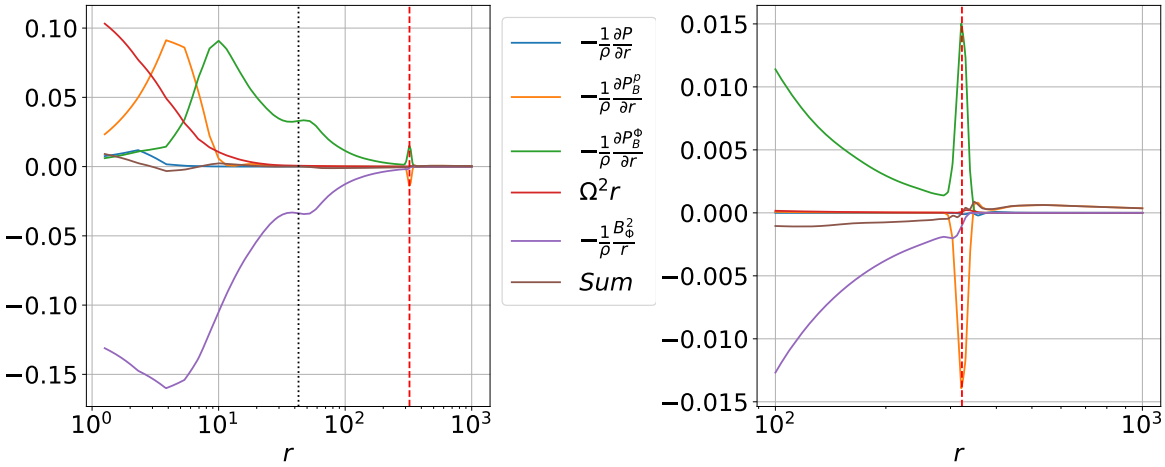

FIGURE 6.9: Radial distributions of the radial accelerations and their sum at the altitude $Z = 500$ at t_{end}: thermal pressure gradient $-1/\rho(\partial P)/(\partial r)$, poloidal magnetic pressure gradient $-1/\rho(\partial P_B^p)/(\partial r)$, toroidal magnetic pressure gradient $-1/\rho(\partial P_B^\varphi)/(\partial r)$, centrifugal acceleration $\Omega^2 r$, hoop stress acceleration $-B_\varphi^2/(\rho r)$ and sum of all accelerations. The vertical black dotted line corresponds to the spine–jet interface, namely the field line anchored at $r_o = R_d$. The vertical red dashed line corresponds to the FM surface. The right panel is a zoom of the left one between $r = 10^2$ and $r = 10^3$.

For simplicity, this altitude was chosen below the shocks. The spine-jet interface anchored at $r_0 = 1$ is highlighted by the dotted vertical line. Inside it, we see the same three dominant terms as in the self-similar simulations:

- The outward centrifugal force $\rho\Omega^2 r\vec{u}_r$.
- The inward hoop stress $-\frac{B_\varphi^2}{4\pi r}\vec{u}_r$.
- The outward total magnetic pressure $-\frac{\partial}{\partial r}\left(\frac{B^2}{8\pi}\right)\vec{u}_r$.

In this simulation of lower complexity there are no oscillations. The magnetic field lines are indeed vertical and the sum of all forces is zero: The collimating hoop stress compensates the decollimating centrifugal and magnetic pressure terms.

On the right panel are shown the forces at the interface between the inner dense super-FM flow and the outer sparse sub-FM flow. This interface is naturally confounded with the FM surface (vertical red line). The two dominant forces are the two magnetic pressures. The drop in toroidal magnetic field at the interface creating the current sheet induces a strong force directed inwards. It is then compensated by a steep increase in poloidal magnetic field, creating an equally strong force directed outwards.

6.4 Parameter dependence

This truncated simulation of reference O1 shows stationary recollimation shocks resembling those in the self-similar simulation of reference K2. To further understand the impact of jet launching conditions on collimation and shock behavior, I explore the physical parameter space. I ran four simulations varying each parameter, all others being equal to that of the reference. I vary three parameters:

- The rotation of magnetic surfaces on the axis Ω_{*_a}: Simulations O2 to O5.
- The external vertical magnetic field on the disk B_{ext}: Simulations B1 to B4.
- The exponent of the self-similar ansatz α: Simulations AT1 to AT4.

All simulations are presented in Table 6.1. They were all performed in the low-resolution grid ($N_R = 704$ and $N_\theta = 144$). The first three columns describe the modified parameters, and the others show various global properties of the jet. For the simulations where Ω_{*_a} was modified (O2 to O5) and the simulations where B_{ext} was modified (B1 to B4) the time t_{end} at which the jet is studied is the same: $t_{end} = 2.26 \times 10^6$. This was done to accurately compare collimation properties from simulation to simulation. It was impossible to do so with $\alpha \geq 1$ (AT2 to AT4) as will be discussed later.

In each subsection I will describe and interpret the simulations retrieved when varying one parameter.

Name	Ω_{*_a}	$\frac{B_{ext}}{10^3}$	α	$\frac{t_{end}}{10^5}$	Z_{shock}	θ^{ext}_{FM}	θ^{ext}_{A}	$r_{o,FM}$	$\dot{M}_{jet}$	$\frac{\dot{M}_s}{\dot{M}_j}$	P_{jet}	$\frac{P_s}{P_j}$
O1	0	2	3/4	22.6	1550	0.129	0.129	58	37.8	0.51	148	1.05
O2	1/4	2	3/4	22.6	1600	0.083	0.083	44	37.7	0.51	148	1.09
O3	1/2	2	3/4	22.6	1150	0.035	0.035	54	37.7	0.52	147	1.12
O4	3/4	2	3/4	22.6	1050	0.117	0.117	62	37.8	0.51	148	1.15
O5	1	2	3/4	22.6	1100	0.075	0.075	51	37.7	0.51	148	1.18
B1	0	0	3/4	22.6	1250	0.78	0.78	64	37.6	0.51	147	1.06
B2	0	1	3/4	22.6	1500	0.34	0.34	80	37.7	0.51	148	1.06
B3	0	4	3/4	22.6	1450	0.075	0.075	51	37.9	0.51	148	1.05
B4	0	8	3/4	22.6	1550	0.029	0.029	31	38	0.51	149	1.05
AT1	0	2	15/16	66.4	1500	0.075	0.075	34	61	0.25	174	0.63
AT2	0	2	1	0.012	DNE	DNE	DNE	DNE	69	0.54	172	0.02
AT3	0	2	17/16	0.014	DNE	DNE	DNE	DNE	82	0.29	187	0.02
AT4	0	2	18/16	0.016	DNE	DNE	DNE	DNE	99	0.22	203	0.03

TABLE 6.1: List of the simulations presented in this chapter. The reference simulation of section 6.3 is called O1. The parameters Ω_{*_a}, B_{ext} and α are defined above and the results are defined in chapter 4. For all simulations the jet mass flux and power are computed until $r_J = 10$.

6.4.1 Rotation on the axis

I run four simulations varying the rotation of the magnetic surfaces on the axis Ω_{*_a}. Contrary to the self-similar simulation SP, here the energy on the axis is not modified: $e_a = 4$ as in the reference simulation. The parameter is modified from $\Omega_{*_a} = 0$ (Schwarzchild black hole, or young star whose corotation radius on the disk is casted to infinity) to $\Omega_{*_a} = 1$ (Kerr black hole, or young star whith coinciding truncation and corotation radii). The case $\Omega_{*_a} > 1$ corresponds to highly rotating black holes that would develop strong relativistic Blandford and Znajek, 1977 jets, or to rapidly rotating stars in the "propeller regime" (see Romanova et al., 2009; Zanni and Ferreira, 2009). Both are out of reach of this work.

On Figure 6.10 are represented the rotation profiles at the ejection boundary for the five simulations O1 to O5. Four regions are clearly seen. On the outer disk ($r \geq 10$), the conditions are the same for all simulations. In the ejecting region ($1 \leq r \leq 10$) the rotation is keplerian: $\Omega_* = \sqrt{GM/r^3}$. In the transition region (JED, $10 \leq r \leq 12$) it quickly drops to zero and in the non-ejecting region (SAD, $12 \leq r \leq 5650$) there is no rotation: $\Omega_* = 0$. It is only at the central object boundary ($r \leq 1$) that the rotation varies from simulation to simulation, in order to reach its value on the axis as set by equations 3.24 and 3.25.

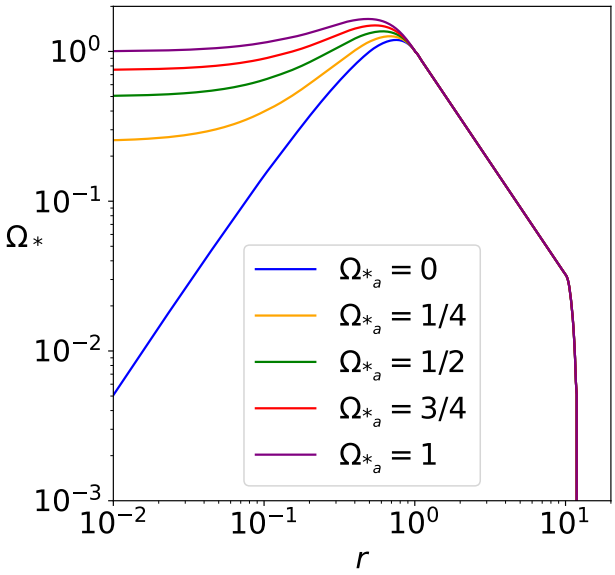

FIGURE 6.10: Rotation profiles at the ejection boundary (on the central object for $r \leq 1$ and on the disk for $r \geq 1$) for the different values of rotation on the central object Ω_{*_a}.

The four simulations O2 to O5 are presented at the same time t_{end} in Figure 6.11, and some of their general properties are highlighted in Table 6.1. As in the reference O1 they present two visible components, the inner dense and super-FM flow and the outer sparse and sub-FM flow. The spine whose rotation I am varying is contained in the inner component. The shocks are always present, with a structure similar those in the reference O1. As for the self-similar setup their altitude decreases with Ω_{*_a}, from $Z_{shock} = 1550$ for $\Omega_{*_a} = 0$ to $Z_{shock} = 1100$ for $\Omega_{*_a} = 1$. For $\Omega_{*_a} \geq 1/2$ a second set of shocks appears at higher altitudes, as in the simulation SP. This renders drawing conclusions on the influence of Ω_{*_a} on global jet collimation difficult. For instance there is no clear trend in the variations of $\theta^{ext}_{FM} = \theta^{ext}_{A}$ with Ω_{*_a}.

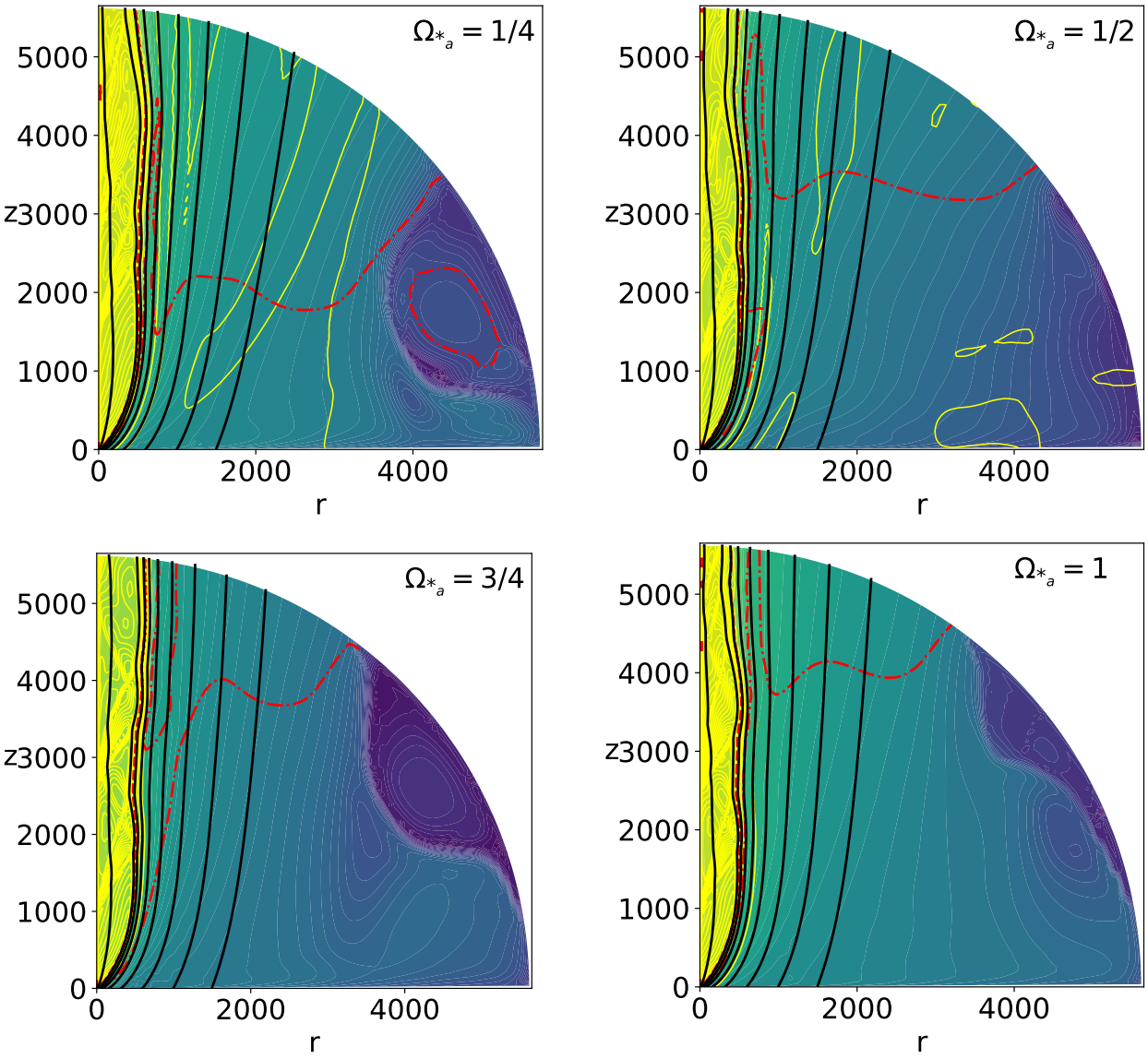

FIGURE 6.11: Influence of the axis rotation Ω_{*_a} of jets obtained with $B_{ext} = 2 \times 10^{-3}$, at the same time $t_{end} = 2.26 \times 10^6$. I use the same notations, colors, and field lines anchoring radii as in Figure 5.2.

However, axis rotation still has a small impact on jet collimation below the shocks. Figure 6.12 shows on the left panel the magnetic field line anchored at $r_0 = 10$ for all five simulations, and on the right panel the evolution of the turning radius r_t with Ω_{*_a} for those field lines. It is defined as the maximal field line radius before recollimation, where $B_r = 0$. This is the radius of the collimation point defined in the previous chapter. We see a small decrease in r_t with the axis rotation. This is a direct consequence of a more collimated (i.e. more cylindrical) spine, that allows for higher collimation in the outer jet. As seen in section 5.1.3, this increase in collimation with the central object rotation is due to the growing emf $e_{obj} \simeq \int_{\theta=0}^{\pi/2} \Omega r B_R d\theta$. On the left panel we see that beyond the turning point, this order is disrupted by the presence of the shocks.

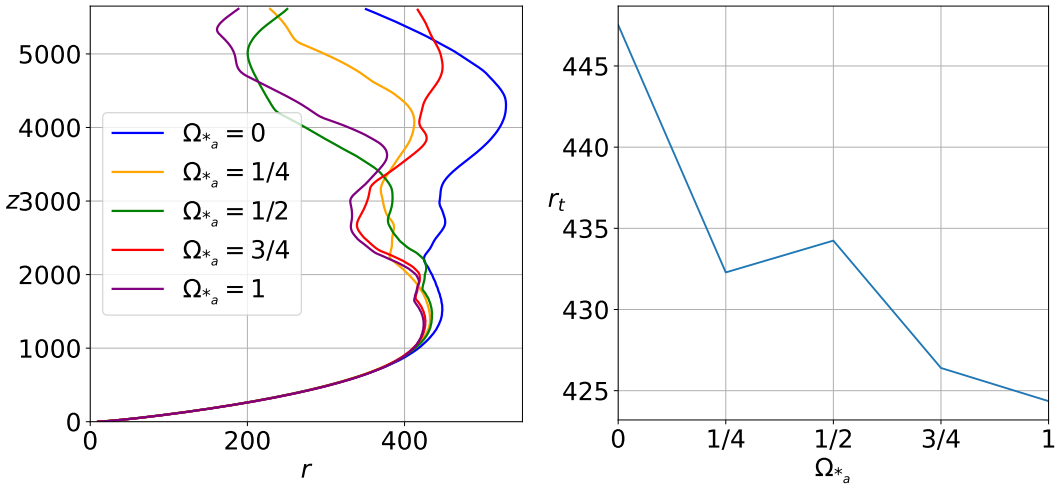

FIGURE 6.12: Collimation properties for different rotations on the axis Ω_{*_a}. Left: Poloidal magnetic field lines anchored in the disk at $r_0 = 10$ for all five simulations. Right: Turning radius r_t of the field anchored at $r_0 = 10$ as a function of the rotation on the axis Ω_{*_a}.

We have seen that shock altitude is lowered by an increased rotation due to a stronger Z-pinch. This strong result proves that for the self-similar simulation SP the decrease in shock altitude is not due to an increase in the energy on the axis e_a, but rather to the increased rotation on the axis. Figure 6.13 compares this decrease to that of the self-similar simulations. We see that passing from no-rotation to solid-body rotation has the same impact on both cases: the reduction of shock altitude by a factor of roughly one third.

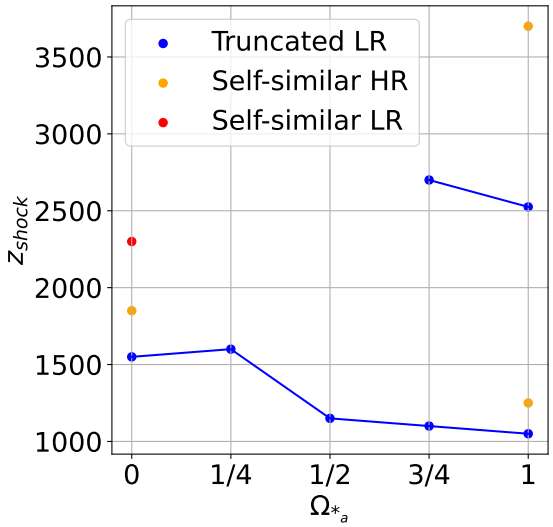

FIGURE 6.13: Evolution of the shock altitude with the rotation on the central object. Truncated ejection in blue, self-similar ejection in orange (high resolution) and red (low resolution).

These simulations could be useful in interpreting the radio-Xray correlations of black hole X-ray binaries. When plotting the radio power tracing the ejection as a function of the X-ray luminosity tracing the accretion, we observe a strong correlation that was one of the motivations of this work. However, it appears that neutron star X-ray binaries lie under this correlation (see for instance Figure 5 of Coriat et al.,

2011, reproduced in Figure 1.7). This means that a slower rotating neutron star emits a jet of lower power than a highly spinning black hole of similar accretion power. Moreover Table 6.1 shows that the spine power increases with the axis rotation Ω_{*_a}. This is naturally still work in progress and deserves further investigation.

As a conclusion, it is clear that the central object rotation affects the collimation. A jet with a rotating central object is more confined than its counterpart with a non-rotating central object. But more importantly, its recollimation shocks occur at lower altitudes, which could lead in the observations to standing knots closer to the disk. However, the axis rotation does not change the jet power, nor its magnetic lever arm λ. We have $\lambda \simeq 12$ in the jet for all simulations, as in the inner regions of the quasi self-similar jet (see Figure 4.7 for the reference simulation K2). As a consequence, the asymptotic speeds of the jets are very similar, and in my simulation domain, they almost attain these speeds: $v_{max} \simeq 0.9 v_\infty$ for the simulations O1 to O5.

6.4.2 External magnetic field

I ran four simulations varying the constant external magnetic field B_{ext} added on top of the power law variation of the vertical magnetic field set on the disk surface. Because the power law is steep ($B_\theta \propto r^{\alpha-2} = r^{-5/4}$) and the grid is large, only a small variation was needed: at maximum $8 \times 10^{-4} B_d$ for the simulation B4. Figure 6.14 presents these boundary conditions, showing the profile of the vertical magnetic field over the whole injection boundary. We see that this constant field starts being dominant beyond a few hundreds, far into the non-ejecting region. It barely modifies the jet launching conditions, and can be seen as a way to add an external pressure, magnetic in this case. This limited effect on the inner ejecting disk can be seen in the variations of $\dot{M}_{jet}$ on Table 6.1. As in the JED, the poloidal velocity is set such that $\vec{v_p} \parallel \vec{B_p}$, increasing the vertical magnetic field increases v_z and with it the jet mass loss rate. However this variation is extremely marginal, with a relative mass flux rate variation of only one percent between the two extremes. Naturally, the effect is the same on jet power.

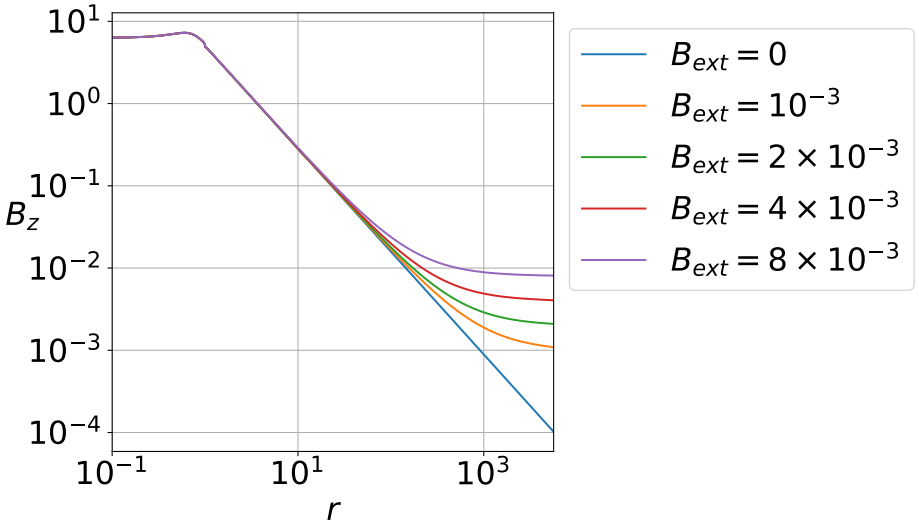

FIGURE 6.14: Vertical magnetic field radial profiles at the ejection boundary (on the central object for $r \leq 1$ and on the disk for $r \geq 1$) for the different values of the imposed external magnetic field B_{ext}. This is in code units, with $B_d = 10$.

The four simulations are shown on Figure 6.15. All simulations contain the usual set of steady recollimation shocks, leaving the axis at comparable altitudes. The direct effect of the change in boundary conditions is clearly seen. The higher B_{ext}, the more vertical the outermost field lines (anchored at r_0 =320, 600, 1000 and 1500). Here, this has a direct impact on global outflow collimation. The interface between the jet and the wind, confounded with the Alfvén and FM critical surfaces, is increasingly more vertical for higher values of the external magnetic field. The colatitude of this interface, seen in Table 6.1 with $\theta^{ext}_{FM} = \theta^{ext}_{A}$, decreases with B_{ext}, going from 0.78 in the absence of an external field to 0.029 when the external field is maximal. The increase of B_{ext} also induces a decrease in lateral diffusion, seen by the decrease of $r_{0,FM}$ with B_{ext} in Table 6.1.

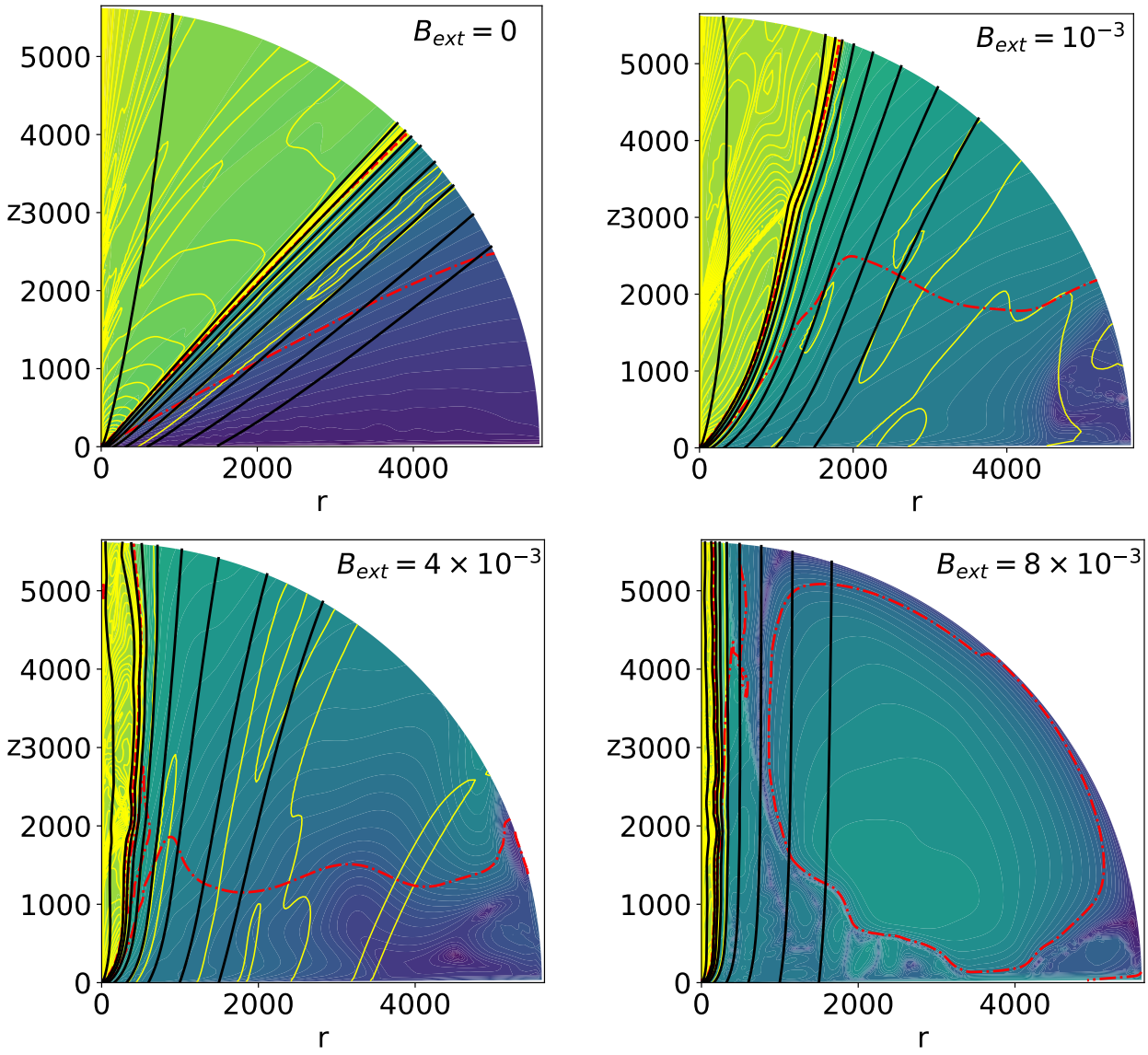

FIGURE 6.15: Influence of the external magnetic field B_{ext} on the final stage of jets obtained with $\Omega_{*_a} = 0$, at the same time $t_{end} = 2.26 \times 10^6$. I use the same notations, colors, and field lines anchoring radii as in Figure 5.2.

Such an impact on collimation is also visible on Figure 6.16. It represents the total magnetic field $B = \sqrt{\vec{B} \cdot \vec{B}}$ along the horizontal $z = 500$ for all five simulations. In the same color is also represented the fast-magnetosonic surface, corresponding to the interface between the two visible components. This interface gets closer to the axis with increasing values of the external magnetic field. We see that this interface corresponds with a change of regime, from the self-similar profile in the super-FM flow to a flatter one in the sub-FM flow. This behavior is very natural, and is expected from analytical works (see e.g. Figure 3 of Beskin and Nokhrina, 2009).

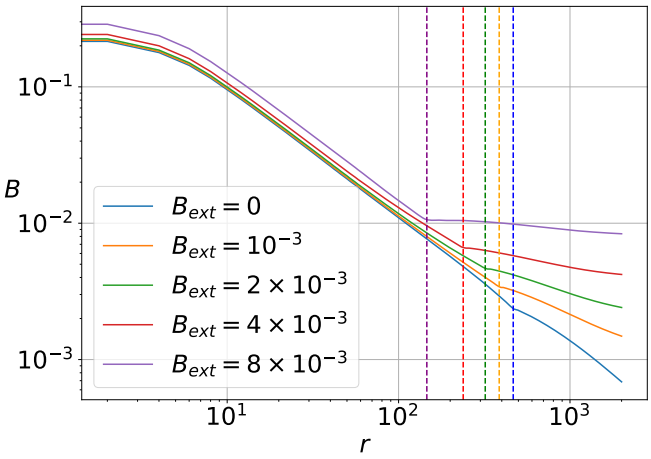

FIGURE 6.16: Radial distribution of the total magnetic field B over the horizontal $z = 500$ for the five simulations. Each color corresponds to a simulation (see legend). The vertical dashed lines indicate the position of the FM surface for this simulation.

Figure 6.16 tells us about jet collimation in another way. The value of the magnetic field on the axis is seen to be increasing with the external magnetic field. This is not a direct consequence of the boundary conditions, as the external field B_{ext} is negligible compared to that in the innermost disk regions. The axis field increase is due to the growing collimation. On the axis the toroidal magnetic field vanishes. As along a magnetic field line the poloidal field varies in $B_p \propto 1/r^2$, the magnetic field on the axis is less diluted for more collimated jets, that is for higher values of B_{ext}.

Let us get back to equation 1.2, prescribing the magnetic pressure $B_{coll}^2/2$ to collimate a jet of mass loss rate $\dot{M}_{jet}$ and speed v_{jet} at a distance z_{jet}:

$$B_{coll} \simeq 10 \left(\frac{\dot{M}_{jet}}{10^{-8} \mathrm{M}_\odot.\mathrm{yr}^{-1}} \right)^{1/2} \left(\frac{v_{jet}}{300\,\mathrm{km.s}^{-1}} \right)^{1/2} \left(\frac{z_{coll}}{50\,\mathrm{au}} \right)^{-1} \mathrm{mG} \qquad (1.2)$$

Taking into account the normalizations of section 3.2.4, the simulation B4 collimates the jet to $r_{jet} = 15\,\mathrm{au}$ at $r_{jet} = 50\,\mathrm{au}$, the external magnetic field is roughly 100 mG, inducing a field of 10 mG at $z = 500$ on the interface. Equation 1.2 then gives

$$B_{coll} \simeq 10 \left(\frac{38 \times 3.35 \times 10^{-10}}{10^{-8}} \right)^{1/2} \left(\frac{1.8 \times 94.3}{300} \right)^{1/2} \left(\frac{50}{50} \right)^{-1} \mathrm{mG} = 9\,\mathrm{mG}. \qquad (6.10)$$

This means that according to analytical calculations (Cabrit, 2007), an external magnetic field of 9 mG would provide the collimation occurring in B4. In this simulation I applied an external magnetic field of 10 mG, so this seems consistent.

How can this collimation be quantified ? The left panel of Figure 6.17 shows the magnetic field line anchored at $r_0 = 10$ for all five simulations. Naturally, the higher the external magnetic field, the more vertical this field line. The jet topology is thus modified by this external magnetic field. The magnetic field lines below $z = 500$ and thus below any shocks can be fitted reasonably well by the monome $z \propto r^{\tilde{n}}$. The right panel shows the evolution of the exponent $\tilde{n}$ with the external field. It swiftly increases with the external field, from 1.2 for B1 to 3.2 for B4.

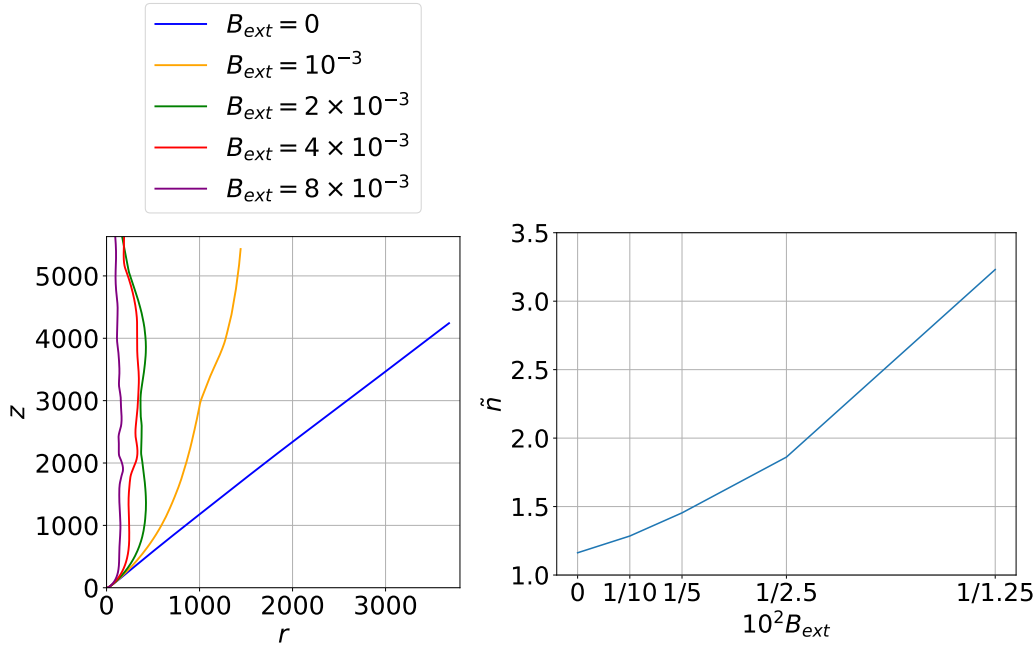

FIGURE 6.17: Collimation properties for different external magnetic fields B_{ext}. Left: Poloidal magnetic field lines anchored in the disk at $r_0 = 10$ for all five simulations. Right: Value of the exponent $\tilde{n}$ in $z \propto r^{\tilde{n}}$ for all the field lines on the left. The fit is limited to $z < 500$.

The case of simulation B1 ($B_{ext} = 0$) is particularly interesting. In the right panel of Figure 6.17 its exponent is not exactly equal to one because below $z = 500$ it is still very much affected by the launching conditions. This fit on the whole field line gives an exponent much closer to unity. On the top left panel of Figure 6.15 we see that the interface between the inner super-FM and the outer sub-FM components is also conical. Nevertheless, the interface should not be considered as ballistic: in a bigger computational domain, the current sheath would eventually close out, thus at those altitudes the return current could induce a shape of the interface different from a simple cone. Note that this only the case for the interface. Figure 6.18, is same as Figure 6.6 but for the simulation without constant outer magnetic field B1. The SAD field lines anchored at $r_0 \geq 10$ appear ballistic, but the JED field lines follow the expected pattern. The innermost ones ($r_0 \leq 3$) are self-collimated because the negative return current ($j_z > 0$) while the outermost ones ($3 < r_0 < 10$) are decollimated because of the positive current flowing out of the disk ($j_z > 0$).

6.4.3 Radial distribution of the vertical magnetic field

Finally I modified the disk distribution of the magnetic field via the self-similar radial exponent α. This parameter modifies the poloidal magnetic field in the ejecting

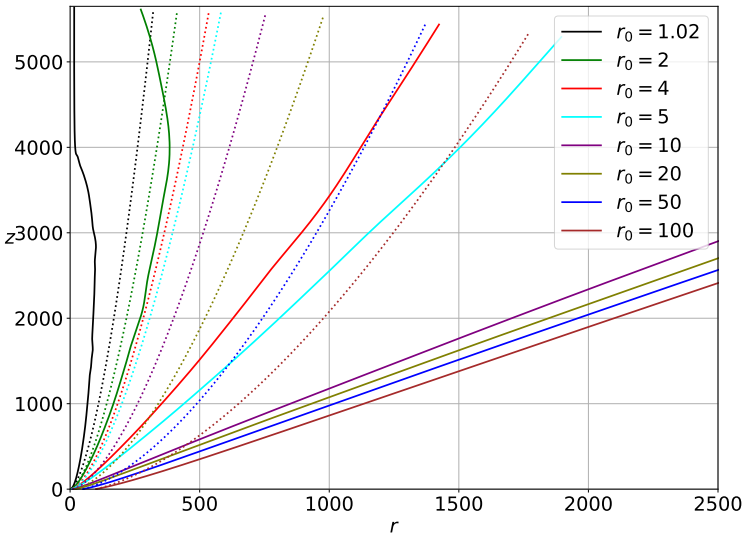

FIGURE 6.18: Evolution of several magnetic field lines during the computation of the simulation B1, for different anchoring radii r_0. The field lines at the first output of the simulation (initial conditions) are shown in dotted lines. The field lines at the last output of the simulation (final state) are shown as full lines.

JED ($1 < r < 10$) and non-ejecting SAD ($12 < r < 5650$) regions, both regions having the same profile in $B_\theta \propto r^{\alpha-2}$ (equation 6.8). I ran four simulations: one with $\alpha = 15/16$ to probe whether the results obtained with the self-similar setup would be retrieved in the truncated one, and three with $\alpha \geq 1$ to explore different electric circuit topologies. The four simulations are presented on Figure 6.19, both on the whole domain (left column) and zoomed near the central object (right column).

We have seen in section 5.1.2 that as long as $\alpha < 1$, its modification does not significantly change the shocks altitude, only its radial extent. The simulation AT1 with $\alpha = 15/16$ produces the expected results. The usual shocks are present in the jet, leaving the axis at $Z_{shock} = 1500$. This altitude is close to that observed in the reference simulation O1 ($Z_{shock} = 1550$). Here also, the change in α modifies the shocks radial extent: the FM interface is much closer to the axis in AT1 than it was in the reference simulation O1. We see in Table 6.1 that on $\theta_{FM}^{ext} = \theta_A^{ext}$ this field distribution change has the same impact as an additional $B_{ext} = 2 \times 10^{-3}$[2].

For the simulations with $\alpha \geq 1$, the situation is more complex. One would expect that since the current is only ejected from the inner zone ($1 < r_0 < 10$), we would avoid the numerical troubles described in section 5.1.2. It is not the case. Those simulations do not reach any steady state, and converge way slower that those with $\alpha < 1$. They reach final times t_{end} three orders of magnitude smaller, even though they are done using more computing time.

To check whether this is due to the presence of the current sheath that prevents circuits from closing beyond the transition zone, the same simulations were done without the condition set by equation 6.9 to supress the toroidal magnetic field beyond the transition zone. It lead to similar results. And, in the simulations AT2, AT3 and AT4 this condition has not had time to take effect, as there is still current flowing beyond $r_0 = 12$ at t_{end}. For those simulations, the point on the disk where the vertical current j_z changes sign is no longer $r = 1$ but now $r = 12$. The keplerian

[2]The values of $\theta_{FM}^{ext} = \theta_A^{ext}$ are the same for simulations AT1 and B3, and the difference in B_{ext} between the two is $(4-2) \times 10^{-3} = 2 \times 10^{-3}$.

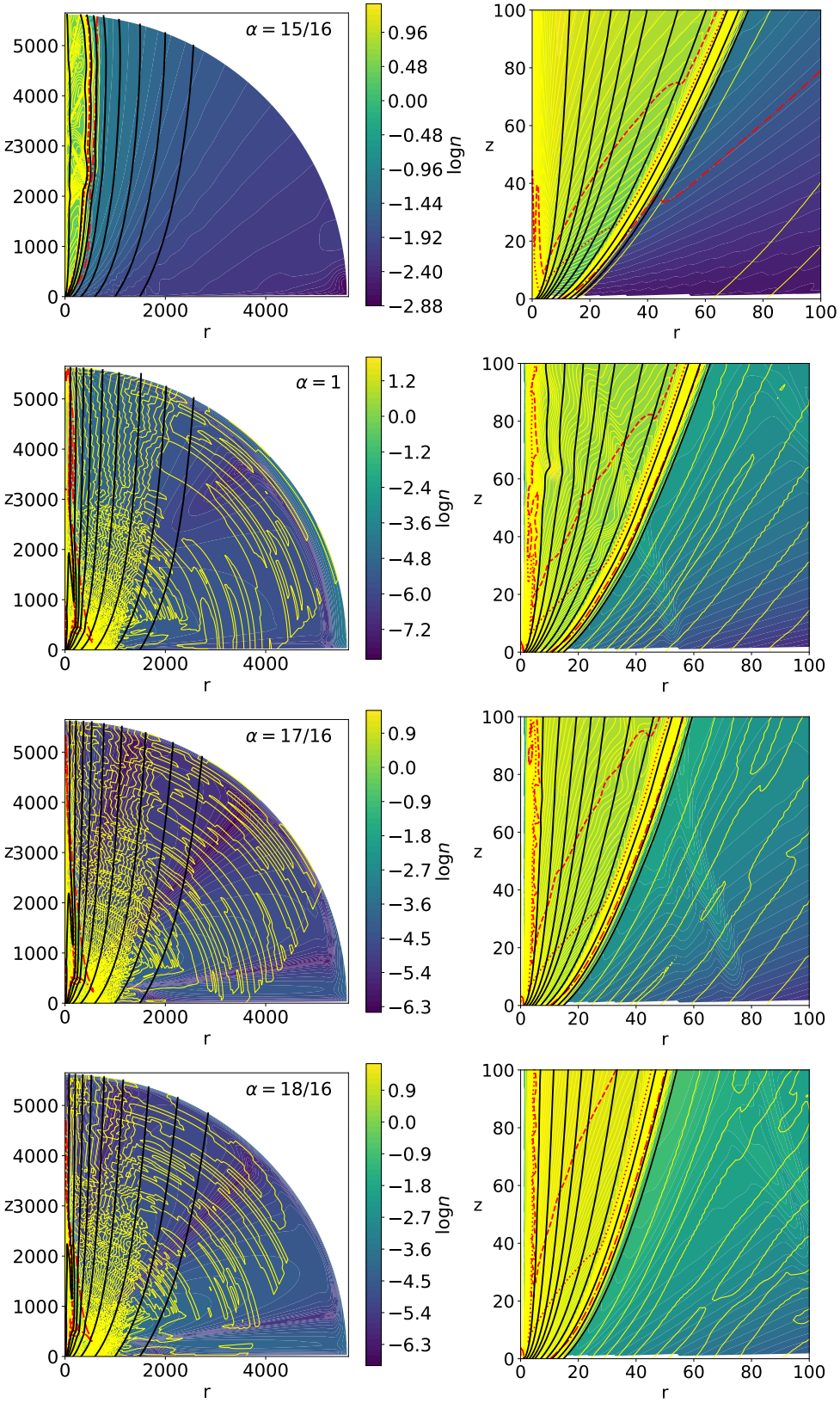

FIGURE 6.19: Influence of the magnetic field distribution α on the final stage of jets. We use the same notations, colors, and field lines anchoring radii as in Figure 5.2. The yellow stripes (circuits) seen for $\alpha \geq 1$ reveal an unsteady situtation at t_{end}.

timescales at this radius are still too long to provide global jet convergence in the whole grid.

However, in the innermost zones represented in the right column of Figure 6.19, a jet has formed by t_{end}. The left panel of Figure 6.20 shows the field line anchored at $r_0 = 5$ for all five simulations. They are more collimated for higher values of α. At $r = 1$ the inclination of the magnetic surfaces is fixed to roughly $1/\alpha$. This creates a more collimated jet with smaller magnetic lever arms λ, as illustrated in the right panel of Figure 6.19.

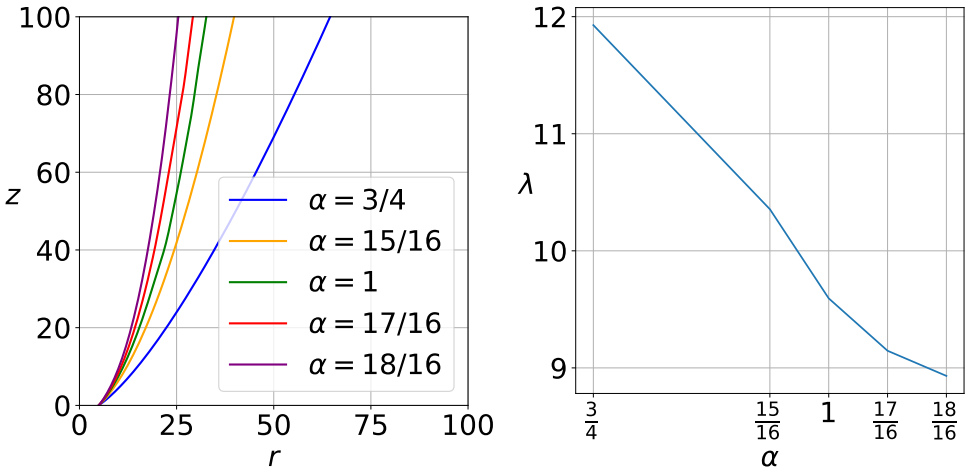

FIGURE 6.20: Jet properties for different magnetic field distributions. Left: Poloidal magnetic field lines anchored in the disk at $r_0 = 5$ for all five simulations. Right: Value of the magnetic lever arm λ for all the field lines on the left.

6.5 Comparison with other numerical works

In chapter 5 I compared the results of my self-similar simulations to those found in the literature. Here, I will compare the results of this chapter to other works simulating a two-component outflow. To my knowledge, there is yet no published simulations of jets accelerating and propagating in an outer atmosphere, à la JED-SAD. Either the interaction with the ambient is studied far away from the central object, in the propagation zone (see Figure 1.15 and references below). Or, the simulations contain an inner strong jet surrounded by a sparser but similar wind, as will be detailed in this section. Komissarov et al., 2007 proposed relativistic simulations in which the jet interface with the ambient medium is a boundary condition. And, as relativistic effects are expected to alter the jet collimation, I will also restrain the comparison to non-relativistic simulations.

Murphy, Ferreira, and Zanni, 2010 produced short-scale 2.5D simulations, extending up to $(r, z) = (40R_d, 120R_d)$ with 512×1536 cells. In these simulations, both the jet and the accretion disk are computed. In the viscous disk, a Shakura and Sunyaev, 1973 alpha prescription is assumed. It extends up to $\epsilon \equiv h/r = V_S/V_K = 0.1$ and is weakly magnetized, with $B^2/(4\pi P)$ initially set varying as R^{-1}, starting from $\left(B^2/(4\pi P)\right)(R = R_d) = 2 \times 10^{-3}$. Because of this decreasing magnetization, the ejection only occurs from a finite zone in the disk. The outflow stratification is represented on Figure 6.21. In their stationary state there are three zones:

- Zone I, between the field lines anchored at $r_0 = R_d$ and $r_0 = 5R_d$. In this inner region the jet becomes super-FM.
- Zone II, between the field lines anchored at $r_0 = 5R_d$ and $r_0 = 13R_d$. In this intermediate region the outflow is always sub-FM but becomes super-Alfvénic.
- Zone III, beyond the field line anchored at $r_0 = 13R_d$. In this outer region there is little outflowing material, that always remains sub-Alfvénic.

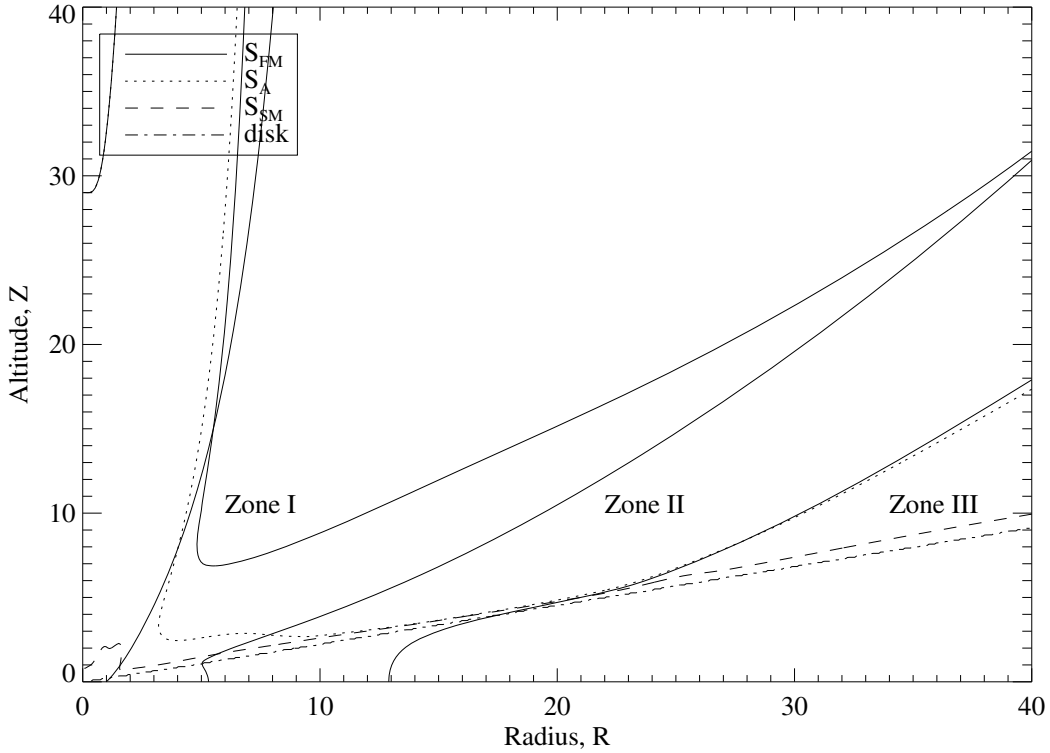

FIGURE 6.21: Figure 2 of Murphy, Ferreira, and Zanni, 2010. The three zones are demarcated by the field lines anchored in $r_0 \in \{1;5;13\}$. The critical surfaces and disk boundary ($\epsilon \equiv h/r = 0.1$) are also represented.

The super-FM jet of zone I is self-confined. Additionnaly they show that an increased resolution strengthens the collimation (see their Figure 13), as I saw in my self-similar simulations (see section 5.2).

In Murphy, Ferreira, and Zanni, 2010, just like in Ramsey and Clarke, 2011, 2019 the super-FM jet is limited to the region close to the axis is not because of a hybrid disk, but because their self-similar ejection quickly drops with r. They observe that their simulated disks behaves like a SAD. However, some works have produced simulations of two-component outflows, ejected from a hybrid disk.

Stute et al., 2008 produced truncated simulations on a cartesian grid $(r,z) \in [0;50] \times [5;100]$ with 200×400 cells. They use the super-FM solution of Vlahakis et al., 2000 as their initial solution. Beyond a field line anchored in the disk at a certain radius r_J, this solution is damped. This is illustrated on Figure 6.22. The field line anchored at r_J is shown in black. The white lines are the electric circuits, that I show in yellow for all my simulations. The bottom right plot corresponds to a non-truncated simulation.

At the final time $t = 2\pi \times 50T_d$ at which those snapshots were produced, the jet has reached a stationary state. The electric circuits (in white) we see that these

maps resemble those produced using my simulations. The usual counterclockwise butterfly-shaped accelerating electric circuit is retrieved. In the non truncated simulation (bottom right panel), it is emitted from the whole lower boundary; in the truncated simulations, there is either two accelerating circuits on both sides of the separatrix (black line), or just one on the inside. Additionally, they retrieve a recollimation shock, shown as an accumulation of electric circuits leaving the axis at $z \simeq 20$ for all simulations. Matsakos et al., 2008 showed that a comparable non-truncated setup produces recollimation shocks, and Stute et al., 2008 extended those results to truncated setups. I emphasize that such works have a different intent as mine. They study the stability of a jet that is already present and super-FM in the domain, starting relatively far away from the disk.

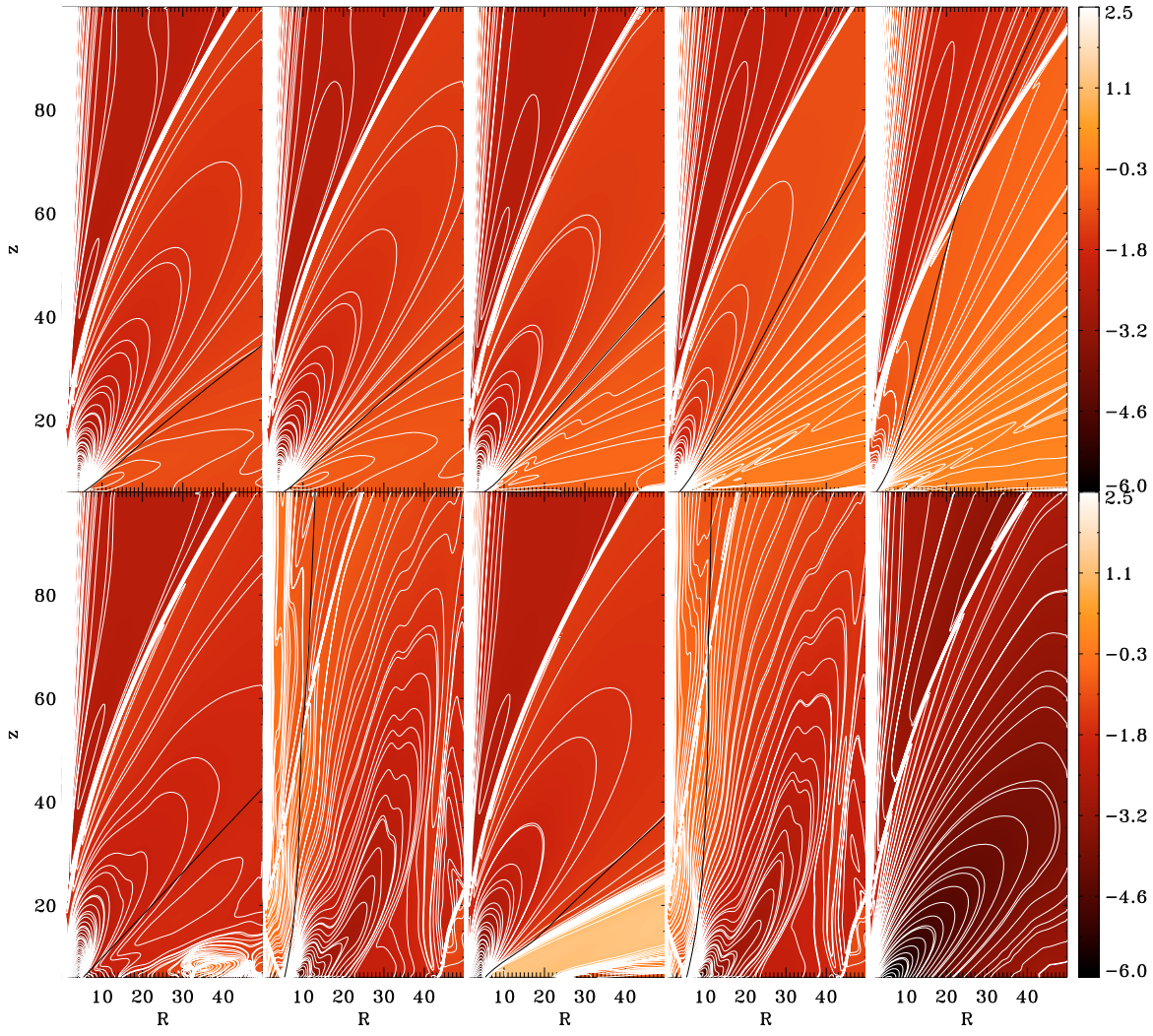

FIGURE 6.22: Figure 15 of Stute et al., 2008. Background: Logarithm of the density. White lines: Electric circuits, isocontours of rB_φ. Black line: Magnetic field line anchored at the truncation. **Top**: From left to right, $[R/(R_* G)]^2 \in \{0.4; 0.2; 0.1; 0.01; 0.001\}$. **Bottom**: In the odd columns the outer region is scaled down, in the even columns the inner region is scaled down; In columns 1 and 2, the scaling factor is 10^3, in columns 3 and 4 it is 10 (see their Table 2 for details). The bottom right plot corresponds to their analytical solution.

The first row of Figure 6.22 shows the impact of the truncation radius r_J, which decreases from left to right. In the outer regions, the magnetic field and density are damped by a factor 10^3, the thermal pressure by a factor 10^6 and the velocity by a factor $10^{3/2}$. The increase of collimation we see from left to right is directly caused by the decreasing influence of the overpressured inner region as its size decreases.

The second row of Figure 6.22 shows the impact of the damping strength on the jet structure. In the first four panels, the truncation radius r_J is the same as in the top left panel. In panel 1 the damping strength is decreased, and in panel 3 it is decreased even more. This seems to have little impact on the global jet structure. The inside regions seems freely expanding into the outside one. Panels 2 and 4 are similar to respectively panels 1 and 3, but the damped down region is not outside but inside. Naturally, the jet appears much more collimated.

The outputs of such simulations were compared to observations of protostellar jets by Teşileanu et al., 2014. They find temperature, velocities and densities in the range of what is expected for such jets ($n \sim 10^4$ to $10^5 \mathrm{cm}^{-3}$, $T \sim 10^4 \mathrm{K}$ and $v \sim 400 \mathrm{km.s}^{-1}$). They follow ionization and recombination of various ions and produce synthetic maps. They retrieve several non-standing knots at a few hundreds of astronomical units from the source, and have a jet radius around 50au. This is in the same ballpark of what I see in my simulations, as well as what observers see in Herbig-Haro jets.

The 2.5D results of Stute et al., 2008 were expanded to 3D by Stute et al., 2014, on a grid $(x, y, z) \in [-100; 100] \times [-100; 100] \times [10; 210]$ with 256^3 or 1024^3 cells. These 3D jets behave in a way comparable to the 2.5D ones. In particular, there still is a standing recollimation shock beyond the super-FM critical surface. There are some instabilities: In the sub-FM region, the poloidal magnetic field and toroidal velocity are very different from the 2.5D simulations, showing large oscillations in the toroidal direction. However, these instabilities are absent beyond the FM surface. The crossing of this critical surface provides stability to the jet, forbidding perturbations to propagate to the larger scales.

To my knowledge, the dynamics and reciprocal influence between a MHD jet emitted from a disk of finite size and a static atmosphere has not been studied yet, and these simulations are the first to do so.

6.6 Summary

In this chapter I presented simulations in which the Jet-Emitting Disk (JED) only extends to a finite radius r_J. Beyond this radius the disk is non-ejecting, and the boundary conditions can be likened to a Standard Accretion Disk (SAD). Using this more realistic setup, the standing recollimation shocks seen in simulations with quasi self-similar boundary conditions are retrieved. This confirms that the shocks are not a bias of self-similarity, but a feature of collimated jets launched by such magnetized keplerian accretion disks.

The interface between the dense super-FM outflow and the sparse sub-FM atmosphere does not exactly follow the field line anchored at r_J in the disk. It is broader, due to numerical lateral diffusion. This widening may be reminiscent of the mixing at an interface caused by Kelvin-Helmholtz shear instabilities in dedicated numerical experiments. Additionally, in this case either there is no disconnection between the accelerating circuit linked to the source and the asymptotic circuit at observable

scales. A current sheet at the interface circumvents the shock and links the two circuits, ultimately creating a collimating post-shock return current that is connected to the disk.

The parameter study confirms the conclusions drawn in the precedent chapter with a quasi self-similar setup. The rotation of the central object slightly reinforces the jet confinement, but more notably reduces the altitude of the recollimation shock. More vertical magnetic profiles lead to more collimated jets, and in this case a more vertical interface between the super and sub-FM flows. Again, the cases $\alpha \geq 1$ are numerically out of reach because the return current is then not only located on the central object but extends until r_J, leading to larger time increments. As expected, an external (magnetic) pressure leads to a more confined jet, but does not modify the shock altitude. The magnetic fields needed for such a collimation are on the same scale as those predicted by analytical works.

Chapter 7

Time-dependent simulations of jets emitted from a truncated JED

Contents

7.1 Quasi-periodic oscillations in X-ray binaries 161
7.1.1 Ubiquitous in the observations 161
7.1.2 Secular oscillations on the disk time scales 164
7.2 Oscillating simulations 167
7.2.1 Ejection properties 167
7.2.2 Periodic oscillations 169
7.2.3 Origin of the oscillations 172
Inconsistent boundary conditions 172
The impact of boundary conditions in the literature 174
Instabilites and forcing 177
7.2.4 Vertical propagation 177
Cross-correlation 177
Space-time diagram 179
7.2.5 Radial propagation 182
7.3 Summary 184

"At midnight I was at the tiller and suddenly noticed a line of clear sky between the south and southwest. I called to the other men that the sky was clearing, and then a moment later I realized that what I had seen was not a rift in the clouds but the white crest of an enormous wave."

"À minuit, j'étais au gouvernail. Soudain, vers le sud, m'apparut une ligne claire dans le ciel. J'en prévins les autres ; puis, après un instant, je compris que la clarté en question n'était pas un reflet dans les nuages, mais la crête blanche d'une énorme vague."

Ernest Shackleton

En effectuant divers tests afin de produire les simulations présentées dans le chapitre précédent, j'ai découvert qu'un ensemble particulier de simulations avait un comportement particulier. Ces simulations n'étaient pas stationnaires, car les jets simulés subissaient une succession d'oscillations radiales presque périodiques. Il s'agit d'une découverte fortuite, car elle a été obtenue en essayant d'obtenir des jets stationnaires dans une configuration avec éjection tronquée. Il s'agit néanmoins d'une découverte bienvenue. Les oscillations quasi-périodiques (QPO) sont omniprésentes dans les observations des binaires à rayons X. Ces oscillations rappellent les oscillations de l'espace. Ces oscillations rappellent un scénario récent (Ferreira et al., 2022) suggérant que les QPOs pourraient être la réponse du disque à une instabilité dans le jet. Dans ce chapitre, je présente d'abord les QPOs et leurs propriétés pertinentes pour cette étude, puis je décris le scénario susmentionné. Puis, je présente mes simulations oscillantes, en explorant en particulier l'origine, la propagation et l'amplitude des oscillations.

Le scénario d'origine des QPOs

Les binaires à rayons X sont des systèmes composés d'un objet compact (trou noir ou étoile à neutrons) qui accrète la matière d'un compagnon stellaire. Leur taille angulaire étant inférieure à une nano-arcseconde, ils ne peuvent pas être directement imagés, mais leur variabilité en rayons X fournit de nombreuses informations. Une composante spécifique de la variabilité est le QPO, une observation très courante dans les binaires à rayons X, qu'il s'agisse de trous noirs ou d'étoiles à neutrons. Dans les binaires d'étoiles à neutrons, la phénoménologie est plus riche et les QPOs sont donc plus difficiles à classer. Par conséquent, je me concentre sur les binaires à trous noirs. Les QPOs sont mieux visibles dans les spectres de puissance, qui mesurent la puissance d'un signal en fonction de sa fréquence. Ils apparaissent sous forme de pics, entre 0,1 et 10 Hertz pour les QPO à basse fréquence qui nous intéressent ici. Une de leur proriétés intéressantes est qu'ils sont d'abord détectés dans l'état soft de basse énergie, puis seulement après dans l'état hard. Cela indiquerait que l'oscillation touche en premier les parties externes du disque, puis seulement après les parties internes.

Les oscillations de ces QPOs basse fréquence sont particulièrement lentes comparées aux temps caractéristique du disque d'accrétion, et les deux sont proportionnelles. Des instabilités haut dans le jet pourraient être la source de ces oscillations. A haute altitude, les échelles de temps des instabilités du jet sont proportionnelles à sa largeur, qui est elle-même proportionnelle au rayon de transition JED-SAD. Et ce rayon de transition est proportionnel aux échelles de temps des QPO. Enfin, les échelles de temps de ces instabilités de jet sont proportionnelles aux échelles de temps des QPOs. Le scénario de Ferreira et al., 2022 contient donc deux étapes. 1) Une instabilité est créée dans le jet, à haute altitude. 2) Cette instabilité se propage en aval du jet, donc dans la partie sub-FM, perturbant le disque lorsqu'elle l'atteint. Cette perturbation peut conduire aux signatures QPO communément observées dans les spectres des binaires à rayons X.

Simulations dépendant du temps

La deuxième partie du chapitre a pour but d'explorer cette deuxième étape, la propagation, dans le cadre de simulations 2.5D. J'y montre que les simulations de jets bidimensionnels fournissent des informations utiles sur le scénario QPO basé sur l'instabilité du jet de Ferreira et al., 2022. Elles mettent en évidence la propagation en amont d'une perturbation depuis les régions asymptotiques du jet jusqu'au disque. Cela montre la possibilité réelle d'obtenir une rétroaction le long de l'interface entre un jet super-FM et le milieu ambiant, à l'intérieur d'une gaine sub-FM. Les ondes sont canalisées à travers cette gaine, arrivent sur le disque (dans la zone entre JED et SAD) et se propagent vers l'intérieur. Elles produisent des variations du champ magnétique toroïdal conduisant à des variations de couple et donc de flux de masse. Ces variations s'affaiblissent au cours de leur propagation vers l'intérieur, à cause des réfractions vers le jet.

Cependant, ces perturbations n'ont pas été créées par une instabilité MHD, mais par des conditions aux limites incompatibles avec un jet collimaté. Sans cette incohérence, les simulations de jet tronqué en 2D sont stables, comme le montre le chapitre 7. Les instabilités susceptibles de créer ces effondrements sont tridimensionnelles, car elles reposent sur des variations de la direction toroïdale. Par exemple, ces instabilités pourraient être :

- *Le mode "kink" de l'instabilité de pincement de Bennett (Bromberg and Tchekhovskoy, 2016; Tchekhovskoy and Bromberg, 2016).*
- *L'instabilité de "recollimation" (Gourgouliatos and Komissarov, 2018; Matsumoto, Komissarov, and Gourgouliatos, 2020).*

Afin d'étudier la stabilité en trois dimensions des jets collimatés et des chocs de recollimation, mais aussi d'avoir une source cohérente pour les perturbations des jets, Claudio Zanni et moi-même avons développé une configuration numérique pour produire des simulations de jets en 3D. Cette configuration est présentée dans l'annexe C.

When making various tests in order to produce the simulations shown in the precedent chapter, I found out that one particular set of simulations had a peculiar behavior. Those simulations were not stationary, as the simulated jets experienced a succession of almost periodical radial oscillations. This was serendipitous, because obtained while attempting to get stationary jets in a setup with truncated ejection.

However, this was a welcome discovery. The Quasi-Periodic Oscillations (QPOs) omnipresent in the observations of X-ray binaries. These oscillations are reminiscent of a recent scenario (Ferreira et al., 2022) suggesting that the QPOs could be the disk response to an instability in the jet.

In a first section, I present the QPOs and their properties relevant to this study, then describe the aforementioned scenario. In a second section, I present my oscillating simulations, exploring in particular the origin, spread and amplitude of the oscillations.

7.1 Quasi-periodic oscillations in X-ray binaries

In astrophysics, many topics are described as rich or complex. QPOs are no exception, but in this case it is not an exaggeration. They happen at many frequencies and at all phases of X-ray binaries outburst cycles. A large number of physical scenarios and models have been proposed to understand them. This section is only an introduction to the subject, and a description of the scenario relevant for my work. The curious reader is referred to Ingram and Motta, 2019; Motta, 2016 for recent and comprehensive reviews of QPOs.

7.1.1 Ubiquitous in the observations

X-ray binaries are systems composed of a compact object (black hole or neutron star) accreting matter from a stellar companion. Their angular size being less than a nanoarcsecond, they cannot be directly imaged, but their X-ray variability provides a lot of information. One specific variability component is the QPO, a very common observation in both black hole and neutron star X-ray binaries. In neutron star binaries, their phenomenology is richer and QPOs are thus harder to classify. As a consequence, I focus on black hole binaries.

QPOs are best seen in power spectra, that measure a signal power versus its frequency. They are obtained by computing the Fourier transform of a light curve. What is most often represented is the Leahy power, modulus squared of the Fourier transform (see Leahy et al., 1983; van der Klis, 1989 for the methodology). Examples of power spectra for the archetypal black hole X-ray binary GX 339-4 are represented on Figure 7.1. The QPOs appear as peaks, here seen between four and ten Hertz.

Why are there three power spectra for a single object ? Most black hole binaries are transient. While being in quiescence majority of the time, they occasionally experience bright outbursts. These outbursts last weeks to months, and are spaced by months to decades. Those are commonly studied using Hardness Intensity Diagrams (HID), sketched in Figure 1.6 or Figure 7.2. They represent the X-ray luminosity as a function of the spectrum hardness. The hardness is the ratio of the hard X-ray emission of high energy over the total X-ray emission. This hardness ratio can thus be roughly understood as a proxy for the energy[1] or the outburst state. When

[1] I will only write energy (and not frequency) when discussing the energy/frequency of the detected photons. This is to avoid any confusion with the frequencies in the power spectra that lie in the Fourier space.

the ratio is close to unity, the object is in a hard state, and when it is close to zero, it is in a soft state.

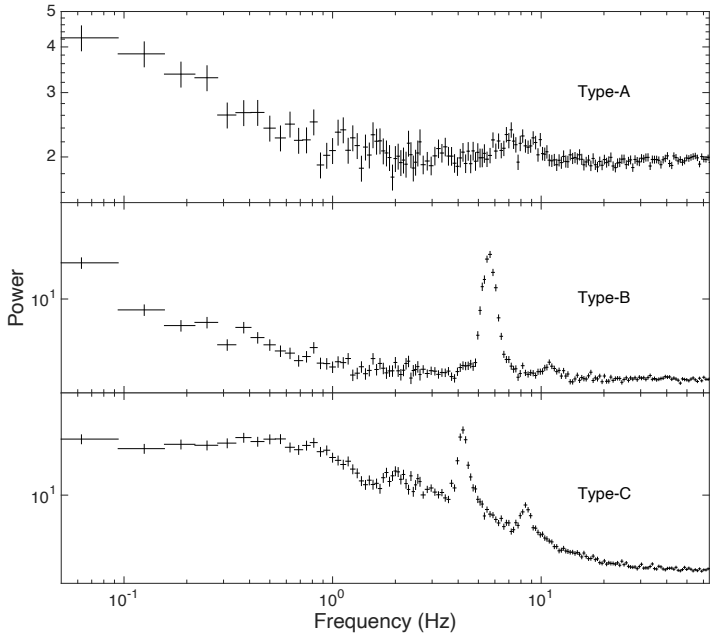

FIGURE 7.1: Examples of type A, B and C QPOs. PDS from the observations of GX 339-4 (Motta et al., 2011)

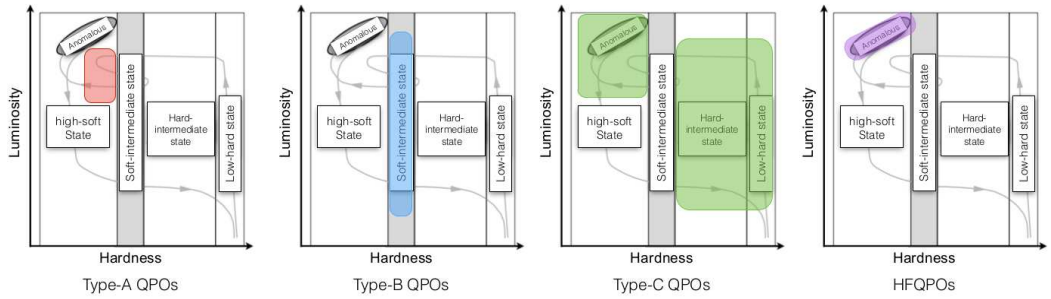

FIGURE 7.2: Repartition of the QPO types among the phases of a X-ray binary outburst. Type C QPOs are the only ones present during the hard states. Figure taken from Motta, 2016.

As noted in the introduction, typical X-ray binary outbursts follow a counter-clockwise q-shaped path in the HID. During this path the source can be either in a hard state, in a soft state or in an intermediate state. The different types QPOs shown Figure 7.1 are observed in different states. What we need to know for the following is that steady radio jets are only observed in the hard state (Fender, Belloni, and Gallo, 2004), and Figure 7.2 shows that type C QPOs are the only ones present in the hard state. As we are interested in jet-induced QPOs, we will focus on the type C.

These are by far the most common type of QPOs in black hole X-rays binaries. They are mostly observed in the hard states, at Fourier frequencies ranging from a few mHz to around 10 Hz. They show narrow peaks, with quality factors $Q = \nu_{QPO}/\Delta\nu_{QPO} \gtrsim 8$ where $\Delta\nu_{QPO}$ is the full width at half-maximum. They also have a high amplitude compared to the other types. This allows for distinguishable

harmonics in the power spectra, as seen on Figure 7.1. Still, even type C QPOs remain epiphenomena of the global binary system physics. As seen on Figure 7.3, the QPO represents at maximum a quarter of the total rms power, Leahy power of the QPO normalized to the total Leahy power.

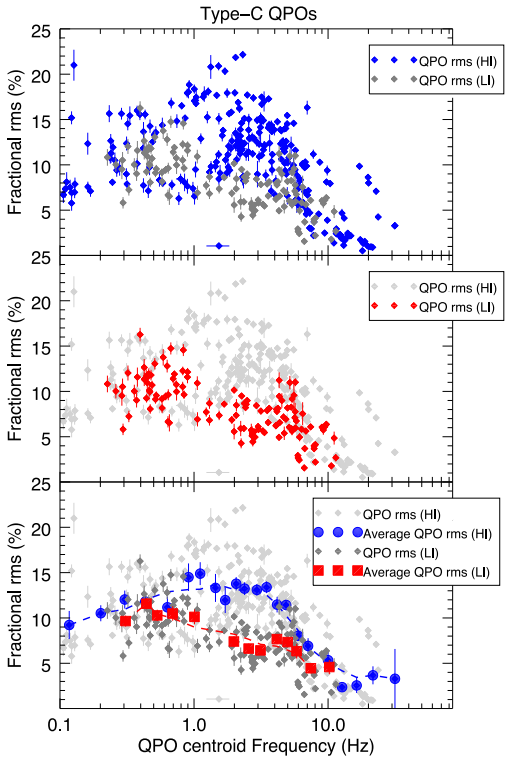

FIGURE 7.3: QPO rms for various sources of high-inclination (HI, blue) or low-inclination (LI, red) (Motta et al., 2015).

While one QPO is localized at a specific Fourier frequency, it is detected in the whole hard state. One important property is that their frequency ν_{QPO} does not depend on the energy or source inclination (see van den Eijnden et al., 2017 for instance). However, harder and softer photons are not always detected at the same time, and one can be lagging the other. There are thus two possibilities:

- The harder photons are lagging the softer photons: a hard lag.
- The softer photons are lagging the harder photons: a soft lag.

Figure 7.4 presents the phase lags as a function of the QPO frequency for type C QPOs in various sources. They count hard lags as positive and soft lags as negative. The lags are slightly positive at lower frequencies ($\nu_{QPO} \lesssim 2$Hz). Then, at higher frequencies ($\nu_{QPO} \gtrsim 2$Hz) there is a change of behavior between high and low-inclination sources. Low inclination sources (in red) acquire a greater hard lag, while the lag of low inclination sources (in blue) becomes negative. Here, a low-inclination source means the binary orbital plane is close to perpendicular to the line of sight (face-on accretion disk). This lag behavior has been consistently observed in many objects (de Ruiter et al., 2019; Motta et al., 2015; van den Eijnden et al., 2017; Zhang et al., 2020).

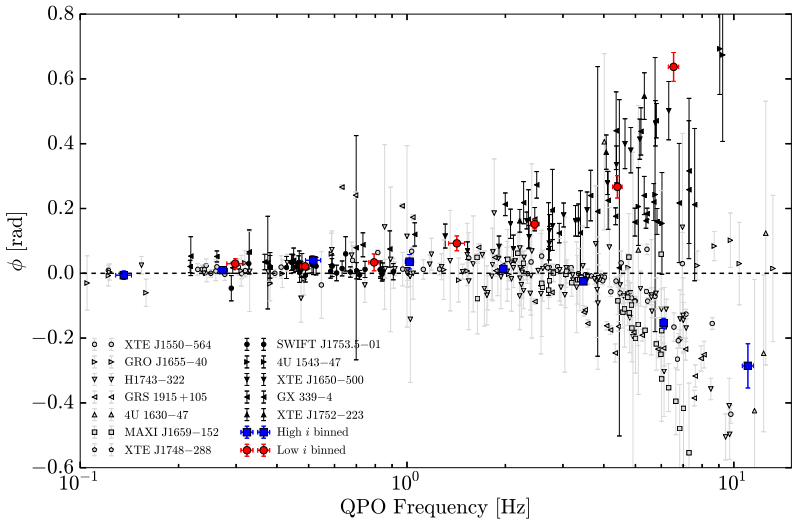

FIGURE 7.4: Hard-to-soft phase lags of type C QPOs versus centroid frequency, for both high-inclination (blue) and low-inclination (red) sources. Figure taken from van den Eijnden et al., 2017.

7.1.2 Secular oscillations on the disk time scales

One property that is hard to explain is their frequency range. Type C QPOs are low-frequency, mainly between 0.1 Hz and 10 Hz. This would correspond to variations extremely slow compared to timescales of the inner highly magnetized disk (Marcel et al., 2020; Markwardt, Swank, and Taam, 1999; Muno, Morgan, and Remillard, 1999; Rodriguez et al., 2002, 2004; Sobczak et al., 2000; Vignarca et al., 2003). Let us quantify this discrepancy using the JED-SAD framework. The boundary between the inner ejecting JED and the outer non-ejecting SAD happens at a radius r_J. In GRMHD simulations this inner zone would correspond to the Magnetically Arrested Disk (MAD, see McKinney, Tchekhovskoy, and Blandford, 2012 for instance). Fitting the accretion rate $\dot{m}$ and the transition radius r_J independently with time, Marcel et al., 2020 managed to reproduce both the spectra and the HID of four outburst cycles of GX 339-4. During those outbursts, many QPOs are observed, mostly of type C. They observed a correlation between the keplerian frequency at the transition radius and the QPO frequency:

$$\nu_{QPO} = \nu_K(r_J)/\mathcal{F} \tag{7.1}$$

where the factor $\mathcal{F}$ is a constant that varies between 70 and 130 depending on the outburst cycle. This correlation is illustrated on Figure 7.5, where the dark blue dots are the type C QPOs and the black line is $\nu_{QPO} = \nu_K(r_J)/100$. This correlation was realized on all periods accessible to type C QPOs, from 0.1 to 10 Hz. Below 2 Hz the uncertainty on r_J (deduced from the spectral fits) disables any strong constraint on this radius, and make it impossible to verify the correlation. But nevertheless, we see on Figure 7.5 that the observations are still compatible with $\nu_{QPO} \sim \nu_K(r_J)/100$ at these lower frequencies.

Thus, the physical phenomenon at the origin of the QPOs should be particularly slow, pointing to some secular evolution within the disk at the transition radius. For this reason, instabilities at this interface such as the magnetic Rayleigh-Taylor instability or the Accretion-Ejection instability (Tagger and Pellat, 1999) seem ruled out (see section 2 of Ferreira et al., 2022). The frequency ν_{QPO} being the same across the

whole energy band also rules out some local instability being triggered on the whole disk. The physical phenomenon at the origin of type C QPOs can be global, such as the solid-body Lense-Thirring disk precession (see Bardeen and Petterson, 1975; Ingram, Done, and Fragile, 2009; Ingram and Motta, 2019 and references therein). But it can also be a local phenomenon at large timescales that propagates into the disk and perturbs it.

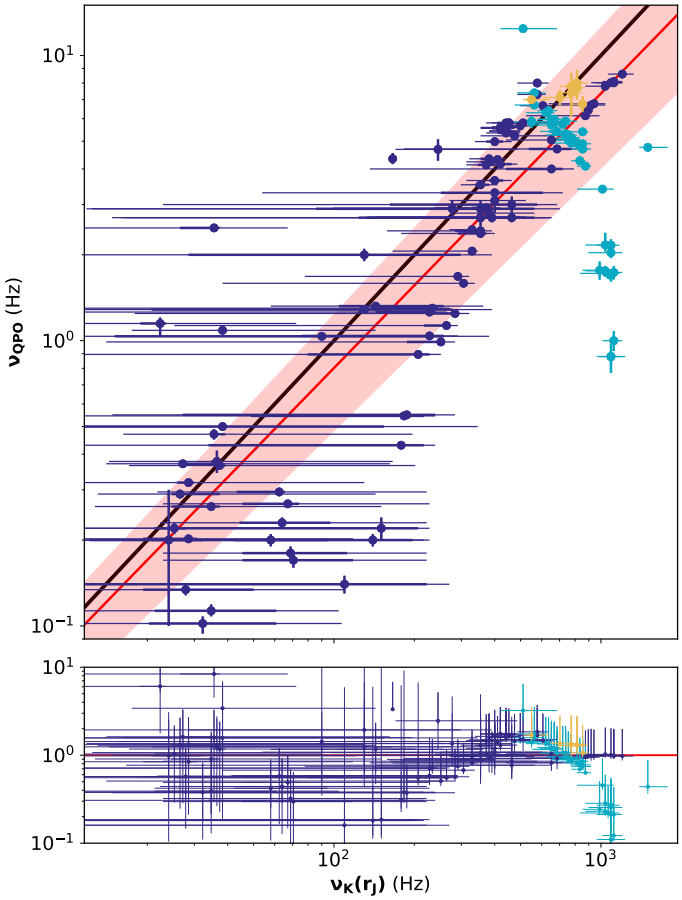

FIGURE 7.5: Correlation between the keplerian frequency at r_J and the QPO frequency ν_{QPO}(Marcel et al., 2020). The dark blue points are type C. The black line is $\nu_{QPOS} = \nu_K(r_J)/10^2$. In red is a weighed linear fit on type C QPOs $\nu_{QPO} = (10 \pm 3) \times 10^{-3} \nu_K(r_J)^{0.96 \pm 0.04}$.

One such phenomenon could be instabilities in the jet. The timescales of theses instabilities are proportional to the jet width. And we see in Figure 7.6 that this jet width is proportional to the transition radius r_J. This Figure illustrates the JED-SAD framework, and looks eerily similar to my truncated simulations of the precedent chapter. At launch, the spine width is $r_{in} = R_d$ and the jet width is r_J. High above the disk at altitude $z_2 > z_{FM}$, the jet has a radius $r_{jet}(z_2) \gg r_J$ with $r_{jet} \propto r_J$.

As a summary, at high altitudes $z_2 > z_{FM}$ the timescales of jet instabilities are proportional to its width $r_{jet}(z_2)$, which in turn is proportional to the JED-SAD transition radius r_J. And, this transition radius is proportional to the QPO timescales (equation 7.1). Finally, the timescales of those jet instabilities are proportional to the QPO timescales.

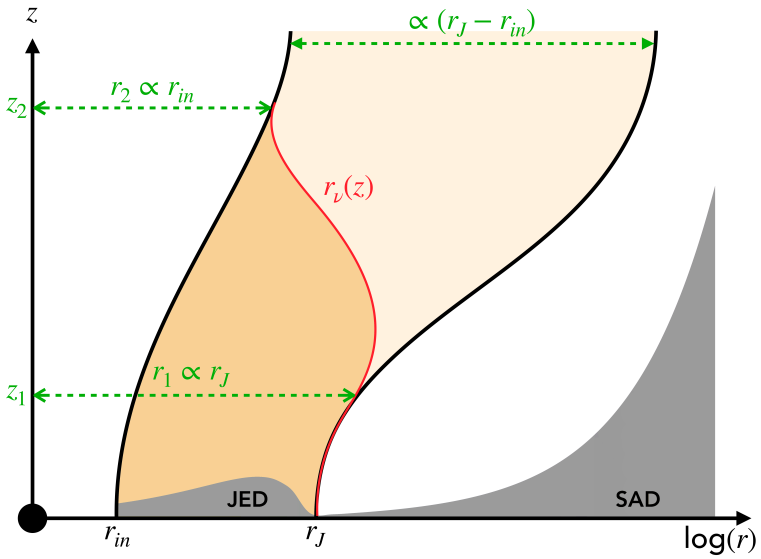

FIGURE 7.6: Scheme of the JED-SAD model (Marcel et al., 2019).

The large jet width compared to the JED width could then be the answer to the secularity of the QPOs compared to the disk timescales. Does this work in quantitative terms ? Similarly to what was discussed for the spine-jet interface in section 4.2.3, there may be long wavelength oscillations starting at the outer edge of the jet. For the jet to perform global instabilities, this wavelength should be tied with the jet radial size $r_{jet}(z_2) = r_2$. The instability frequency is then:

$$\nu_I = \left(\frac{V_{FM}}{2r_{jet}}\right)(z_2) \tag{7.2}$$

In cold jets with a dominant toroidal magnetic field, the fast-magnetosonic speed at z_2 can be simplified as

$$V_{FM} \simeq V_{A_\varphi} = \frac{B_\varphi}{\sqrt{4\pi\rho}} = \frac{m}{m^2-1}\left(1 - \frac{r_A^2}{r_2^2}\right)\Omega_* r_2 \simeq \frac{\Omega_* r_2}{m} \tag{7.3}$$

as in Pelletier and Pudritz, 1992: at z_2 the jet is assumed to be highly super-Alfvénic and $m^2 \gg 1$ and $r_2^2 \gg r_A^2$.

As seen in section 2.6.3, on the disk $g \simeq 0$ and $\Omega_* \simeq \Omega_K$. The invariant Ω_* being conserved along the field line anchored at r_J, the fast-magnetosonic speed becomes $V_{FM} \simeq \Omega_K(r_J) r_2/m$. This then simplifies equation 7.2:

$$\nu_I(z_2) = \left(\frac{V_{FM}}{2r_{jet}}\right)(z_2) \simeq \frac{\Omega_K(r_J)}{2m} = \frac{\pi}{m}\nu_K(r_J) \tag{7.4}$$

For this instability to be in the same frequency range as those of the type C LFQPOs, one would require $m = \pi\mathcal{F}$, where m is the jet Alfvénic mach number high above the disk and $\mathcal{F} \sim 100$ is the constant of equation 7.1. We have seen that our simulated jets can reach asymptotic Alfvénic mach numbers of a few hundreds (see Figure 4.11 for instance), so this frequency range is attainable.

Thus, jet instabilities would be a reliable way to produce perturbations with variabilities in the same frequency-range as the QPOs. Those could be current-driven instabilities such as the kink instability (Figure 7.7) or instabilities at the interface between the jet and the ambient medium such as the centrifugal instability (Figure 7.8). Those 3D jet instabilities and others are quickly presented in section C.1.

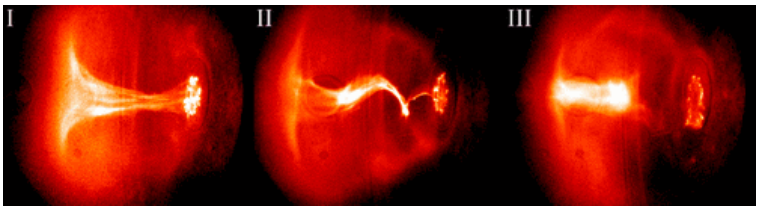

FIGURE 7.7: Destructive kink instability in a laboratory experiment (Hsu and Bellan, 2003).

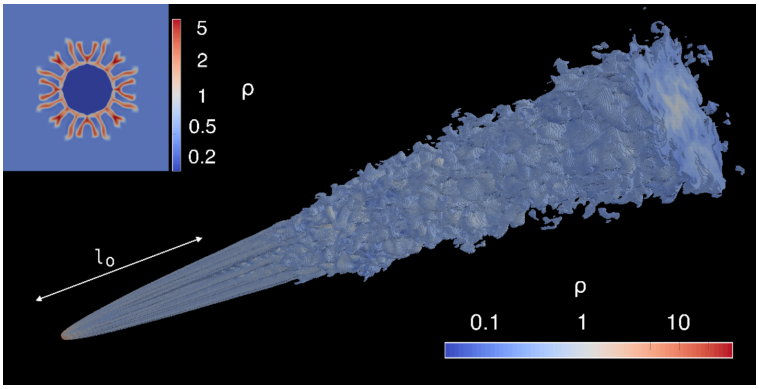

FIGURE 7.8: Centrifugal instability in an AGN jet simulation (Gourgouliatos and Komissarov, 2018).

As a summary, this scenario contains two steps. 1) An instability is created in the jet, at large altitudes. 2) This instability propagates downstream in the jet, thus in the sub-FM part, disrupting the disk when it reaches it. This disruption may lead to the QPO signatures commonly observed in X-ray binary spectra. The next section is aimed at exploring this second step, the propagation, within 2.5D simulations. The first step should be explored with full 3D simulations, whose setup is detailed in appendix C.

7.2 Oscillating simulations

Some simulations I performed during my PhD were very interesting in that context: they exhibit jets that wiggle in an almost periodic manner. As mentioned above, this discovery was serendipitous, the simulations being performed while making numerical tests to produce the stationary jets emitted from a truncated disk.

In the follwing, I mostly focus on an oscillating simulation of reference, hereafter called Q1, on which the behavior was discovered. First, I describe the ejection conditions of these simulations, showing the changes from the stationary simulations of chapter 6. Then, I discuss the origin of the oscillations, showing simulations other than Q1 for which the outer boundary condition has been changed. Finally, I describe the oscillations and their period. After that, my interest will be on the vertical (upstream) and radial (inwards) propagation of the perturbations.

7.2.1 Ejection properties

The conditions used to produce the oscillating simulation of reference Q1 are almost the same as those used to produce the truncated simulation of reference O1. There are only three differences.

First, the condition that causes the vanishing of the toroidal current on the non-ejecting disk regions ($r_0 > r_S$) is not implemented. For the record, this condition is

$$B_\varphi(r, t + dt) = B_\varphi(r, t) e^{-\frac{dt}{\mathcal{T} T_K(r)}} \tag{6.9}$$

For Q1 the toroidal magnetic field was simply let as an "outflow" condition. It is thus freely varying on the whole lower boundary.

Second, the end of the transition zone is now at $r_S = 20$, while it was at $r_S = 12$ for the simulations of chapter 6. The conditions described in this chapter work the same way in this now longer zone (e.g. $r_0 \in [r_J = 10; r_S = 20]$).

Third, the vertical speed is fixed on the whole disk. On the ejecting boundary ($r_0 \in [R_d; r_J]$), v_z is set as in the Jet-Emitting Disk, and thus as in all simulations presented in this thesis. On the non-ejecting boundary ($r_0 \in [r_S; R_{ext}]$), it is simply set at zero, with no distinction on slow-magnetosonic mach values as in the precedent chapter.

Other than these three points, everything remains the same: the other boundary conditions, the initial conditions, the grid size and resolution, the Riemann solvers and reconstruction schemes. These ejection conditions are represented on Figure 7.9. It is a zoom on the innermost regions of the simulation Q1, at a time t_b chosen before the oscillations. This map is very similar to the one showing the simulation O1, Figure 6.5. The only visible difference is beyond $r_J = 10$. For O1 there was no current in this region because of the condition of equation 6.9. For Q1 there is little current because of the drop in Ω_*, but we can still see that there are a few electric circuits in the non-ejecting region.

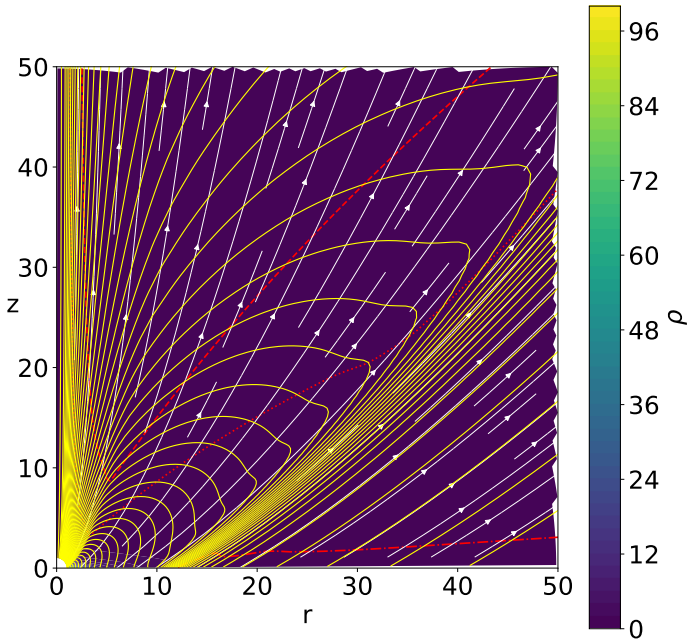

FIGURE 7.9: Snapshot of the simulation at $t_b = 1.8317 \times 10^6$ (top left panel of Figure 7.10), zoomed for $r < 50$ and $z < 50$. The yellow contours are the poloidal electric circuits, the white lines are velocity field lines and the red lines the critical surfaces: FM (dashed), Alfvén (dotted) and SM (dash-dotted). In the background is the plasma density.

What kind of jet do these conditions produce ? The top left panel of Figure 7.10 present a simulation snapshot taken at $t_b = 1.8317 \times 10^6$, before the oscillations. Naturally, the simulation Q1 is very similar to the truncated simulation of reference O1. It still contains two visible flows, in addition to the axial spine: an inner super-FM dense flow and an outer sub-FM sparse flow. The jet exhibits the usual recollimation shocks, but they are now located at higher altitudes: $Z_{shock} = 2350$, against $Z_{shock} = 1550$ for O1.

Same as for O1, the wind emitted beyond $r_J = 10$ has a negligible impact on the outflow dynamics: its mass loss rate is 0.4 % that of the jet, and its power is 1.2 % that of the jet. The outermost super-FM field line is ejected at $r_{0,FM} = 39$ and as a reminder:

- The mass loss rates are $\dot{M}_{jet} = 2\pi \int_{R_d}^{r_J} \rho v_z r dr$ and $\dot{M}_{wind} = 2\pi \int_{r_J}^{r_{0,FM}} \rho v_z r dr$.
- The powers are $P_{jet} = 2\pi \int_{R_d}^{r_J} \rho E v_z r dr$ and $P_{wind} = 2\pi \int_{r_J}^{r_{0,FM}} \rho E v_z r dr$.

7.2.2 Periodic oscillations

The most notable feature of this simulation is its time-dependence: it exhibits a succession of radial oscillations. One of these oscillations is represented on Figure 7.10. The top left snapshot is at time t_b before the oscillation, and the bottom right snapshot is taken after the oscillation at a time t_e, when the jet has again reached a quasi-stationary state. The state of the jet at t_e resembles that at t_b, although less collimated.

This oscillation is a body mode, the whole interface is wobbling, radially drifting inwards, then outwards. Note that the term body mode is usually used to describe instabilities, and as we will see later this is no instability. We see on Figure 7.11 that the oscillations are quasi-periodic. It represents the variation of B_φ / B_z with time along the field line anchored on the disk at $r_S = 20$. Each color represents the field line inclination B_φ / B_z at a specific altitude on the field line. Those altitudes range from $z = 100$, close to the disk, to $z = 5000$, close to the outer boundary. We see that the oscillations perturb the whole field line, although this perturbation increases with altitude. It is greatest at $z \sim 5000$, near the outer boundary. This is where the oscillation probably starts, since the amplitude is greater there.

On Figure 7.11 we see five oscillations, all separated by a similar timescales Δt_{osc} ranging from 2×10^5 to 5×10^5. What can this timescale be related to ? After each oscillation, the jet is set in a decollimated state. We have seen in section 4.4 that for the jet to reach its final state, all the plasma that eventually becomes super-FM should have time to reach the outer boundary. Thus, calling $\mathscr{L}_{r_{0,FM}}$ the field line anchored in $r_{0,FM} = 39$, that time is

$$t_{ext}(r_{0,FM}) = \int_{\mathscr{L}_{r_{0,FM}}} \frac{ds}{v_p(s)} = 1.82 \times 10^5 \tag{7.5}$$

where v_p is the poloidal speed and s is the curvilinear abscissa along the field line. This was computed at t_b, just before the oscillation. Thus, the jet experiences quasi-periodic collapses on jet formation timescales.

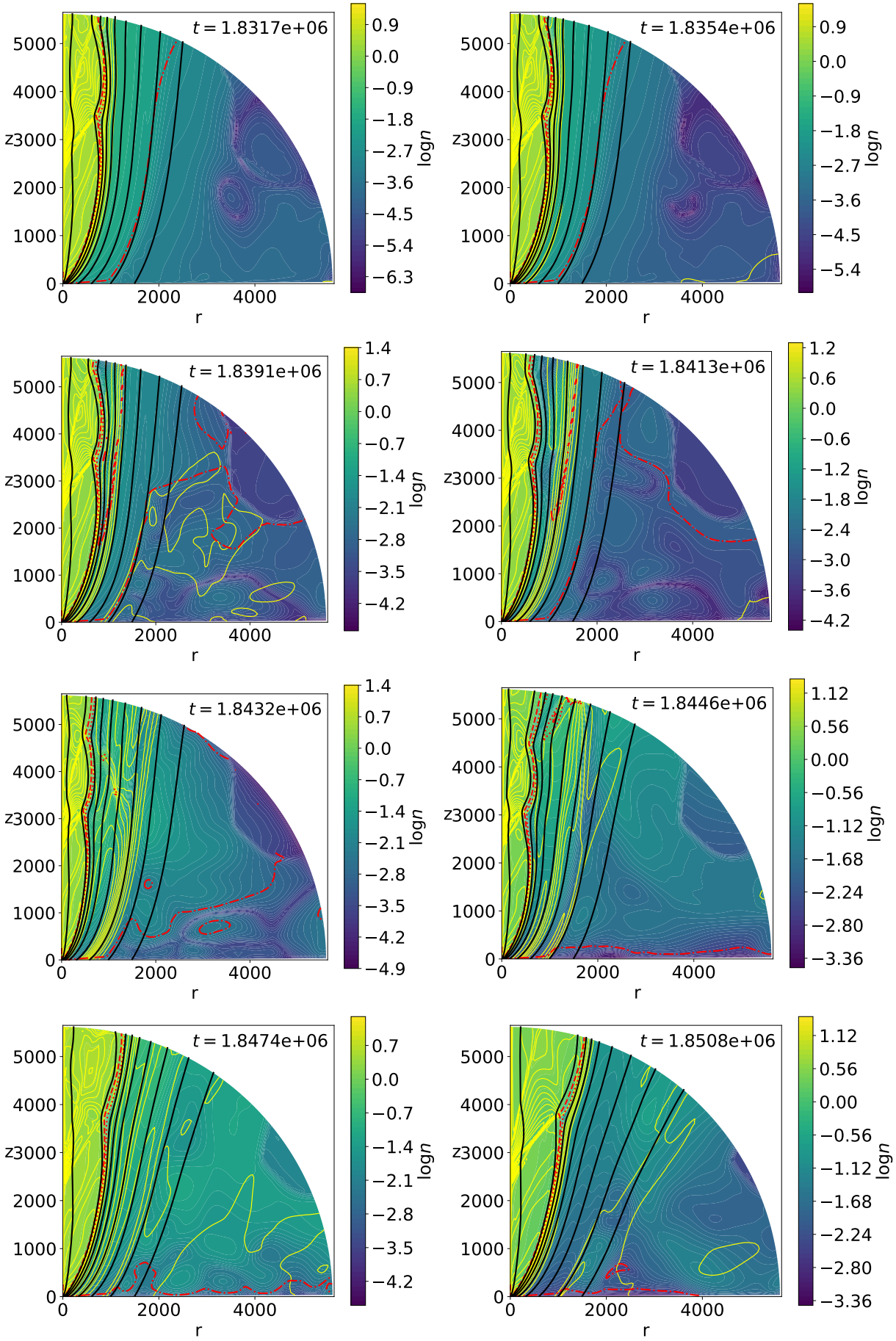

FIGURE 7.10: Evolution of the reference simulation with time during the first oscillation. We use the same notations, colors, and field lines anchoring radii as in Figure 5.2.

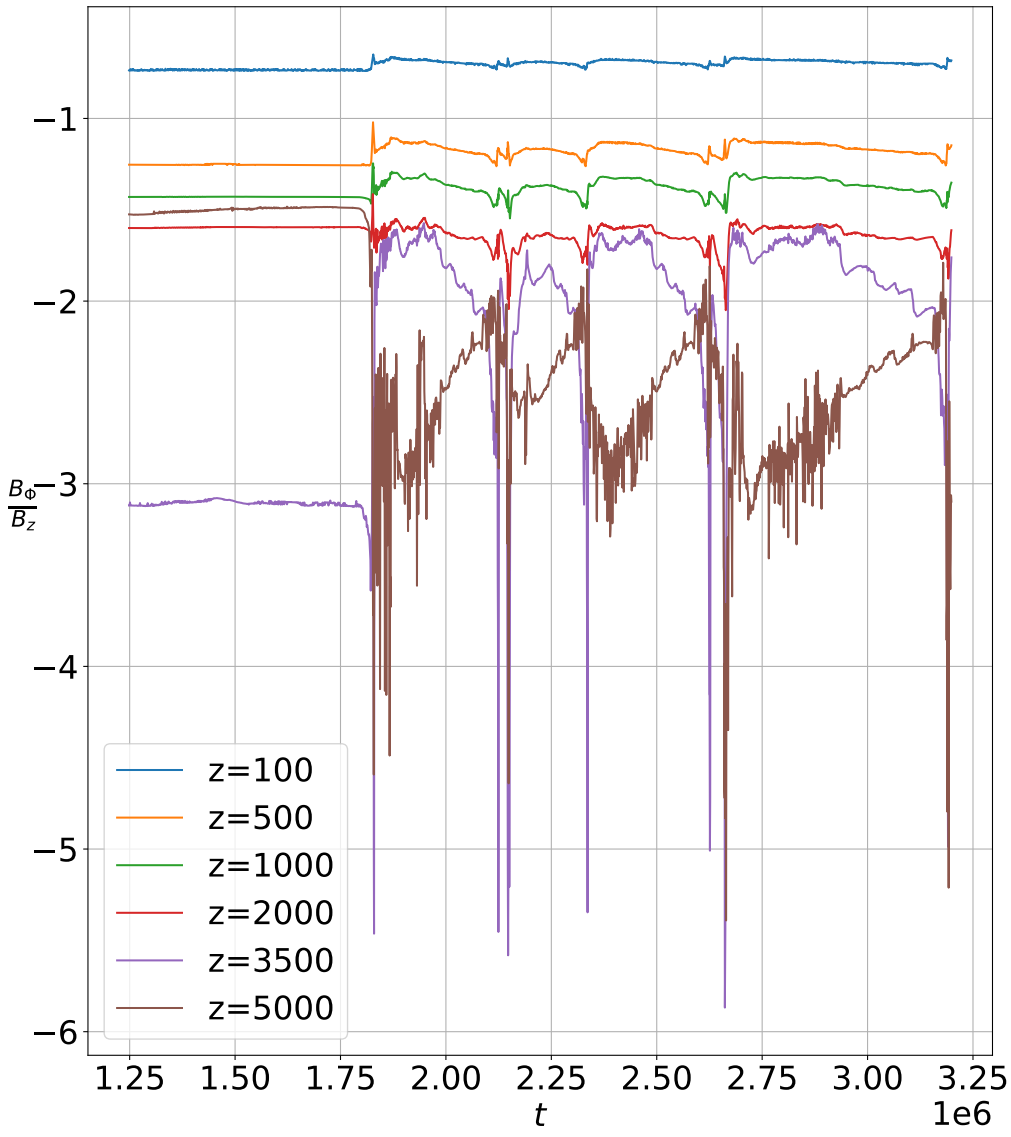

FIGURE 7.11: Evolution with time of B_φ / B_z at the intersection between the field line anchored at $r_0 = 20$ (in the sheath) and at various altitudes z.

7.2.3 Origin of the oscillations

What causes these oscillations ? The fact that it starts at the outer boundary (see Figure 7.10) is rather suspicious. To see if this is a coincidence, I ran another simulation where the outer boundary was moved from $R_{ext} = 5650$ to $R_{ext} = 9936$. This simulation is named Q2, and its characteristics and parameters are described in Table 7.1. All other things are the same as in the reference Q1. In particular, the resolution for $R < 5650$ is unchanged. As the grid size along $\vec{u_R}$ is logarithmic ($\Delta R \propto R$), performing this simulation was not much more computationally expensive. There is not a lot more cells, as we go from $N_R = 704$ to $N_R = 750$. Moreover, these additional cells are large, so they do not modify the time increment (cf CFL equation 3.15).

Name	R_{ext}	Boundary condition at $R = R_{ext}$	$\frac{t_b}{10^5}$	Z_{shock}	θ_{FM}^{ext}	θ_{A}^{ext}	$r_{o,FM}$	Oscillations
Q1	5650	$\partial^2(RB_\varphi)/\partial R^2 = 0$ and $F_{B_\varphi}^{sub-A} > 0$	18.32	2350	0.14	0.14	39	Yes
Q2	9936	$\partial^2(RB_\varphi)/\partial R^2 = 0$ and $F_{B_\varphi}^{sub-A} > 0$	21.02	2400	0.063	0.063	59	No
Q3	5650	$\partial^2(RB_\varphi)/\partial R^2 = 0$	16.10	2000	0.15	0.16	37	Yes
Q4	5650	$\partial(RB_\varphi)/\partial R = 0$ and $F_{B_\varphi}^{sub-A} > 0$	17.20	2350	0.10	0.12	25	Yes

TABLE 7.1: List of the simulations presented in this chapter. Values are computed at t_b, before any oscillation. For simulation Q1, this corresponds to the top left snapshot of Figure 7.10. For simulations Q2 to Q4, this corresponds to the snapshots of Figure 7.12.

This simulation is presented in the first row of Figure 7.12. The left panel is a snapshot of the simulation at time $t_b = 2.1018 \times 10^6$. We see that in the inner regions ($R < 5650$), the simulation is very close to Q1. The FM outer interface is at the same place, the two shocks are at the same altitude (see also Table 7.1). The only difference is that the highest point of the highest shock, at $R \sim 5650$, is now far away from the outer boundary condition. This causes the change observed in the right panel. This plot is the analogue to Figure 7.11 as it presents the time evolution of B_φ / B_z along the field line anchored at $r_0 = 40$, here only at altitude $z = 5000$. There is no oscillation, only a steady growth over time. This growth is directly caused by an increase the jet collimation, that induces a greater vertical magnetic field. This is due to a drift in the axial electric current (as in self-similar studies) whose origin is certainly numerical. The small oscillations are caused by the point of intersection between the field line and $z = 5000$ moving from one cell to its neighbour, as the resolution is already quite low at this point.

Inconsistent boundary conditions

This is direct evidence that the oscillations seen in the simulation Q1 are caused by the boundary conditions, and not a local instability. As in the precedent chapters, the boundary conditions in the inner ejecting zone ($1 < r_0 < 10, \theta = \pi/2$) are consistent with steady-state ideal MHD. Thus the simulation is trying to converge to a stationary state, as described in section 4.4 for the self-similar simulations. But here, the outer boundary conditions ($R = R_{ext}$) are not consistent with this stationary state. Thus, each time the jet is collimated enough, it experiences a forcing caused by the boundary conditions. That forcing disrupts the jet equilibrium, and it experiences a collapse. After this collapse, the jet ends in an uncollimated state, as in the bottom

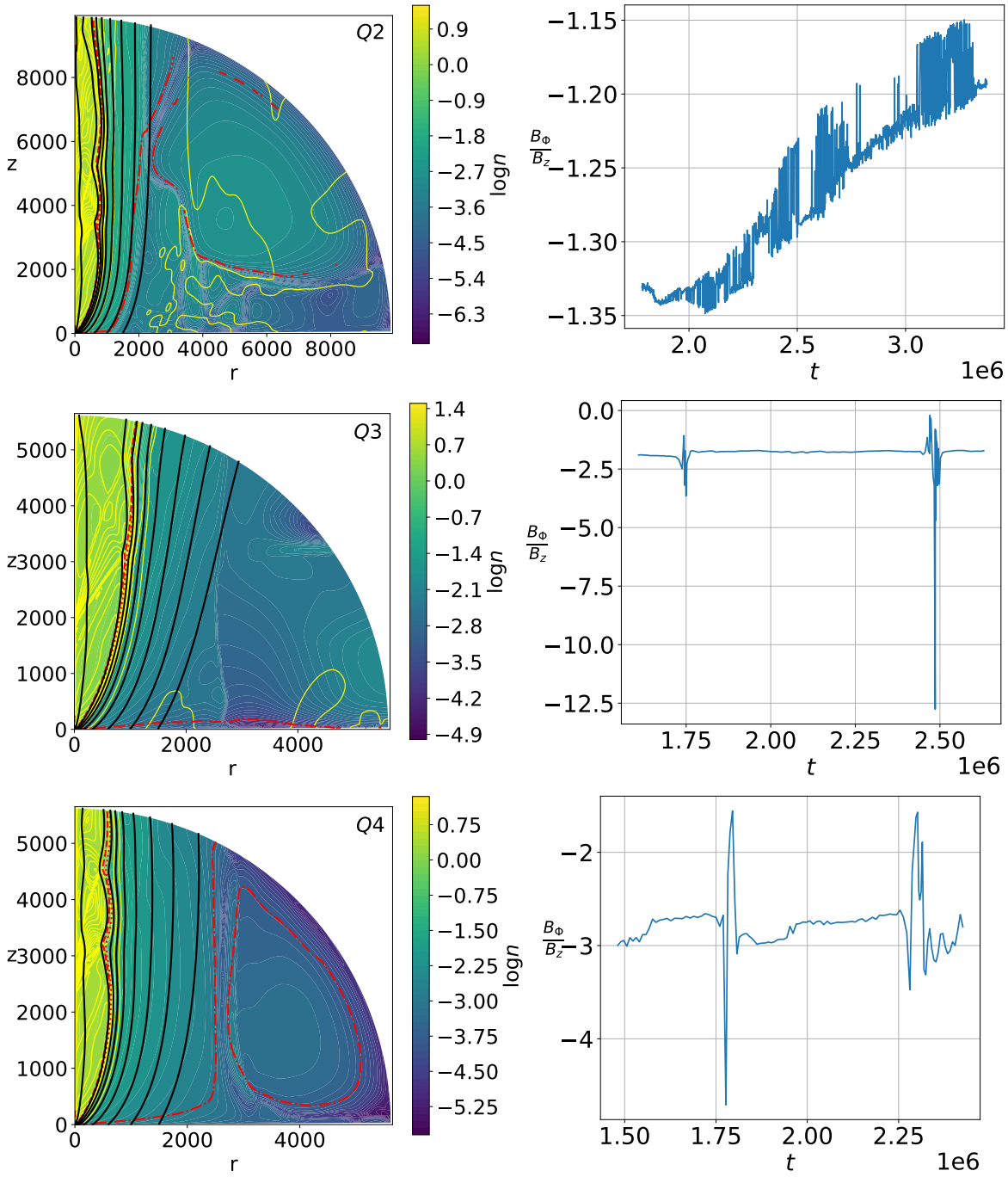

FIGURE 7.12: Impact of the outer boundary conditions change. For each simulation: In the left column, a snapshot at t_b, before any oscillation; In the right column the time evolution after t_b of B_φ / B_z at the intersection between the field line anchored at $r_0 = 40$ and $z = 5000$. I use the same notations, colors, and field lines anchoring radii as in Figure 5.2.

right panel of Figure 7.10. It then takes a time $t_{ext}(r_{0,FM}) \simeq 2 \times 10^5$ to get collimated again. At that time, the forcing is triggered again, and the jet experiences another collapse. After that collapse, it takes another $t_{ext}(r_{0,FM})$ for the jet to be rebuilt from the launching zone, get collimated again, and experience yet another collapse. As the boundary conditions do not change with time, this succession of collimations and collapses should continue indefinitely, causing the apparent quasi-periodicity.

What makes the boundary conditions inconsistent in the specific case of the simulation Q1 ? As seen in the top left panel of Figure 7.10, the point ($r \simeq 800, z \simeq 5000$) where the perturbation seems to rise is at the intersection of three lines:

- The intersection between the super-FM and sub-FM outflows, naturally confounded with the fast-magnetosonic but also the Alfvén critical surfaces.
- The highest recollimation shock, in a stationary state inside the jet. It extends from the axis at $z \simeq 2000$ uo to this point.
- The outer boundary, at $R = R_{ext}$.

Let us place ourselves on this point, on the shock and at the very last grid cell, at $R_{ext} = 5650$. As the next cell along $\vec{u_R}$ is a "ghost" cell in the boundary, its values of P, ρ, $\vec{v}$ and $\vec{B}$ are set as in the "outflow" condition. The gradients along $\vec{u_R}$ of ρ, P, B_R, B_θ, RB_φ, v_R, v_θ and v_φ are conserved, and the Van Leer slope limiter is used. At any other point in the boundary this would not be an issue. But here, due to the presence of either the shock or the interface, these gradients are strong. This outflow condition weakens the shock, making the compression factor weaker that what is expected from the Rankine-Hugoniot jump conditions (equations 2.100). The density in the ghost zone after the shock is smaller than what it would be without the boundary.

That accentuates the mismatch at the interface, illustrated for example in the right panel of Figure 6.9. The inwards acceleration in the super-FM side of the interface and the outwards acceleration in the sub-FM side of the interface are increased. The natural consequence is an emptying and widening of this zone, leading to lower densities, and thus even stronger accelerations. This reinforcing cycle of perturbation leads to the jet collapses seen in Figure 7.10. We will see in the next sections that the location of the perturbation at the interface is also important for the propagation.

The impact of boundary conditions in the literature

A similar but less dramatic influence of the boundary conditions has already been noticed by Ustyugova et al., 1999. They ran simulations in both cartesian and spherical grids, looking at the impact of the toroidal magnetic field boundary condition on jet collimation. They used three different "outflow" boundary conditions, expressed here on a spherical boundary $R = R_{ext}$:

- The "free" boundary condition, enforcing $\frac{\partial B_\varphi}{\partial R} = 0$.
- The "force-free" boundary condition, enforcing $\vec{B_p} \cdot \vec{\nabla}(RB_\varphi) = 0$.
- The "force-balance" boundary condition, enforcing $\vec{B_p} \cdot \vec{\nabla}(RB_\varphi) \propto B_R B_\varphi$.

The "force-balance" condition relies on the Ω_* invariant to impose the toroidal magnetic field. It is therefore better than the "force-free" condition that imposes $\vec{j_p} \parallel \vec{B_p}$ and thus removes the decollimating force $\vec{j_p} \times \vec{B_p}$. But on the other side,

the "force-balance condition is cumbersome, as it requires additional simulations to compute the proportionality coefficient between $\vec{B_p} \cdot \vec{\nabla}(RB_\varphi)$ and $B_R B_\varphi$. Both give more consistent results than the "free" condition that impose an artificial $\vec{j_p} \times \vec{B_p}$ collimating force (see Figure 7.13).

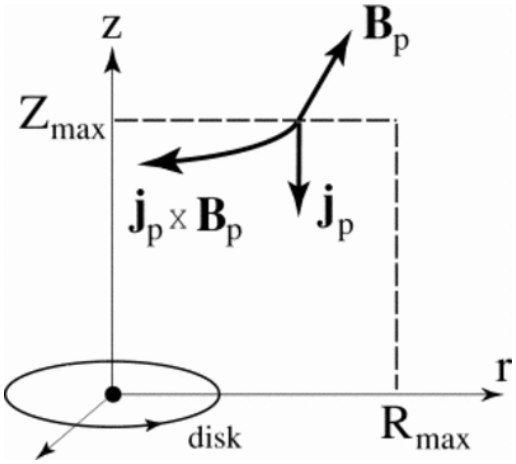

FIGURE 7.13: Figure 5 of Ustyugova et al., 1999. Artificial collimating $\vec{j_p} \times \vec{B_p}$ force for a "free" condition at the boundary of a cartesian grid.

Ustyugova et al., 1999 found that simulations with a "free" boundary condition experience a collapse and never reach a steady state:

"These "boundary" forces act such way that the flow never reaches a stationary state. To check this fact and to be sure that this is not an effect of nonstationarity of our initial configuration, we did simulations for cases that went to a stationary state with other outer boundary conditions. After establishing stationarity, we substituted the outer boundary conditions on B_φ to a "free" boundary condition. We observed that the stationary state was destroyed for the reasons mentioned above." Ustyugova et al., 1999 (section 4.1.1.).

They also observe that simulations with a "force-free" condition are much more collimated than those with the "force-balance" condition, where there is no suppressed collimation. Later, Zanni et al., 2007 remarked that "outflow" boundary conditions similar to those of my simulations (e.g. gradient conservation) give results very similar to "force-free" conditions.

Using a "free" outer boundary condition, Stute et al., 2008 saw a jet collapse in their test simulations. Those were made on a cartesian grid $(r; z) \in [0; 50] \times [5; 100]$. It is represented on Figure 7.14. Their setup is similar to that of Matsakos et al., 2008, but truncated at a field line anchored at a certain r_J (white line in Figure 7.14). Inside this field line, the initial values are taken as in the super-FM solution of Vlahakis et al., 2000. Based on the seminal work of Blandford and Payne, 1982, it also features refocusing towards the axis. Outside this field line, the initial values are also taken from this solution, but with damped density and vertical speed. The boundary conditions are set consistently to these initial conditions, without overspecification.

They observe a collapse similar to the one seen in my simulations, and also propose the collapse is triggered by the boundary conditions. Since their initial conditions fill the computational domain with an already super-FM collimated flow, the collapse happens immediately. At the $z = 100$ upper boundary, they use "free"

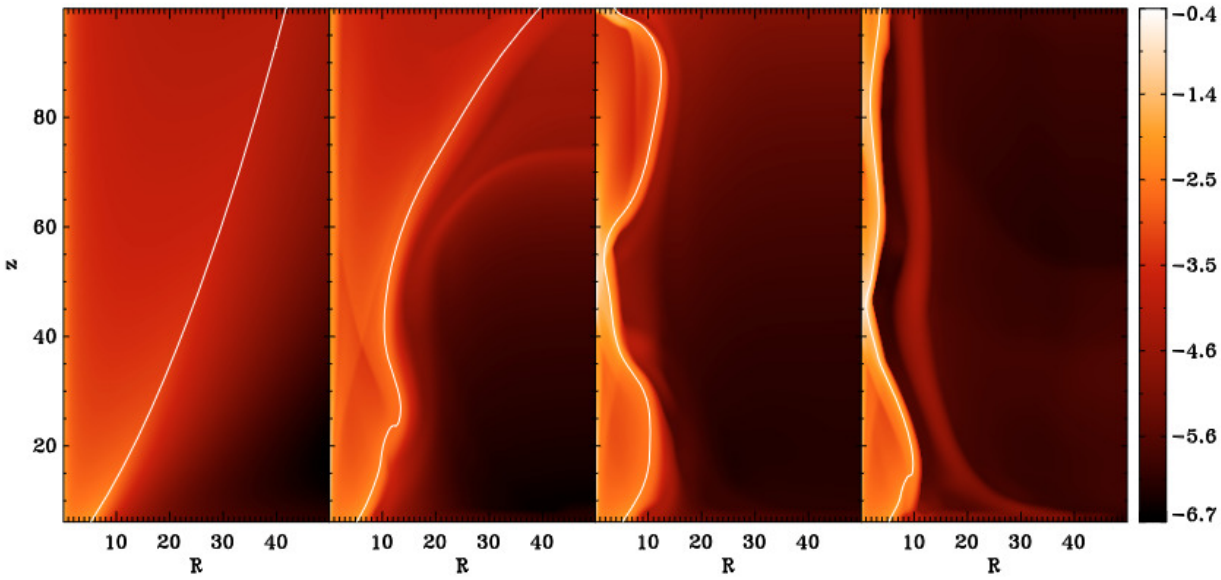

FIGURE 7.14: Figure 1 of Stute et al., 2008. From left to right, snapshots of their test simulations at times $0; 2; 3; 6 \times 2\pi\, T_d$ where T_d is defined at $R = 1$. In the background is the density logarithm, and the white line is the field line anchored at r_J.

boundary conditions. All quantities (ρ, P, $\vec{v}$ and $\vec{B}$) are constant, meaning their gradient along $\vec{u_z}$ is zero. As they state, this affects the radial[2] component of the Laplace force:

$$F_r = -\frac{1}{2}\frac{\partial B_\varphi^2}{\partial r} - \frac{B_\varphi^2}{r} - \frac{1}{2}\frac{\partial B_z^2}{\partial r} + B_z\frac{\partial B_r}{\partial z} \tag{7.6}$$

their "free" boundary condition suppressing the last term. Since that term is positive, suppressing it creates an artificial collimation, leading to the collapse. They also produce simulations for which B_φ is also damped in the outer region where they do not see this collapse: in those, the z-pinching $-B_\varphi^2/r$ is greatly reduced.

To see whether these conclusions still hold in my setup, I ran two additional simulations varying the boundary conditions at the outer edge:

- In the simulation Q3, I dropped the requirement of the toroidal Lorentz force to be positive in the sub-Alfvénic wind.
- In the simulation Q4, I used a "free" condition on the toroidal magnetic field: $\partial(RB_\varphi)/\partial R = 0$.

They are also represented in Figure 7.12 As seen in the left column, the simulation Q3 is very similar to the reference Q1, while the simulation Q4 is more collimated. This is also evidenced by the values of θ_{FM}^{ext} in Table 6.1. This evolution is consistent with Stute et al., 2008; Ustyugova et al., 1999, the "free" condition adding an artificial $\vec{j_p} \times \vec{B_p}$ at the outer boundary. As a consequence, the upper shock in simulation Q4 does not reach the outer boundary.

The right column of Figure 7.12 shows the evolution of B_φ/B_z over time at the intersection between the field line anchored on the disk at $r_0 = 20$ and $z = 5000$.

[2] As Stute et al., 2008 used a cylindrical grid, "radial" here refers to the cylindrically radial component of the force, along $\vec{u}_r$.

The oscillations are present in both Q3 and Q4. They appear at similar times as in the reference simulation Q1: $t \sim 1.75 \times 10^6$. As the shock does not reach the outer boundary in Q4, this means that the presence of a shock is not required to trigger the perturbations. They simply require a collimated jet, inconsistent boundary conditions, and a sub-FM sheath where they can propagate.

Instabilites and forcing

Here, it is important to state that the jet radial oscillations are not caused by a physical instability. The perturbation does not arise from the integration of the MHD equations but from inconsistent boundary conditions. A more appropriate term would be forcing. It is akin to what happens when you compress a wooden plank by putting two opposite forces at the extremities: if the forces are large enough, it breaks. In addition, I searched for two-dimensional (axisymmetric) MHD instabilities. I looked for instability criteria in all simulation outputs, and found out that they were never verified in zones more than a few cells wide. This is described in Appendix A. Nevertheless, it is of great interest to study the upstream propagation of the perturbation, to see if the jet perturbation caused by a physical instability could perturb the disk in a manner similar to type-C LFQPOs.

7.2.4 Vertical propagation

Let us now focus on the top-down propagation of the perturbation. For this study to be relevant to the QPO scenario, the perturbation, no matter its cause, should propagate upstream, from high in the jet down to the disk. On Figure 7.11 it is clear that the field line is perturbed at all altitudes, but it is unclear which ones oscillate first, and how such a propagation can be accomplished.

Cross-correlation

At first, I investigated this anteriority problem using methods inspired from observations. Figure 7.11 is very reminiscent of multi-wavelength studies, used to extrapolate jet properties from timing analysis (see for instance Tetarenko et al., 2019, 2021). Different wavelengths probing different jet regions, in this analogy each altitude of Figure 7.11 would correspond to a different wavelength. The method the observers used is called cross-correlation It is rather intuitive. To illustrate it, let us define a quantity $\mathcal{U}$, of which we know the time evolution at altitudes Z_1 and Z_2, called respectively $\mathcal{U}_1(t)$ and $\mathcal{U}_2(t)$. These could also be light curves at wavelengths λ_1 and λ_2. The correlation function is defined as

$$CF(\tau) = \frac{COV(\mathcal{U}_1(t), \mathcal{U}_2(t+\tau))}{\sigma_{\mathcal{U}_1}\sigma_{\mathcal{U}_2}} \tag{7.7}$$

For each function $\mathcal{U}$, $E(\mathcal{U})$ is the mean and $\sigma_U \equiv \sqrt{E[\mathcal{U}^2] - (E[\mathcal{U}])^2}$ the standard deviation. Defining U_2^τ by $\forall\, t, \mathcal{U}_2^\tau(t) = \mathcal{U}_2(t+\tau)$, the covariance of the two functions is $COV(\mathcal{U}_1(t), \mathcal{U}_2(t+\tau)) = COV(\mathcal{U}_1, \mathcal{U}_2^\tau) = E\left[(\mathcal{U}_1 - E[\mathcal{U}_1])\,(\mathcal{U}_2^\tau - E[\mathcal{U}_2^\tau])\right]$.

The correlation function quantifies how much $\mathcal{U}_1(t)$ and $\mathcal{U}_2(t+\tau)$ are correlated. If they are equal, $CF(\tau) = 1$. If they are in phase opposition, $CF(\tau) = -1$. If they are uncorellated (a sine and a cosine for instance), $CF(\tau) = 0$. The lag between the two functions $\mathcal{U}_1$ and $\mathcal{U}_2$ is then simply defined as the value of τ for which this correlation function is maximal. As light curves are not continuous but discrete

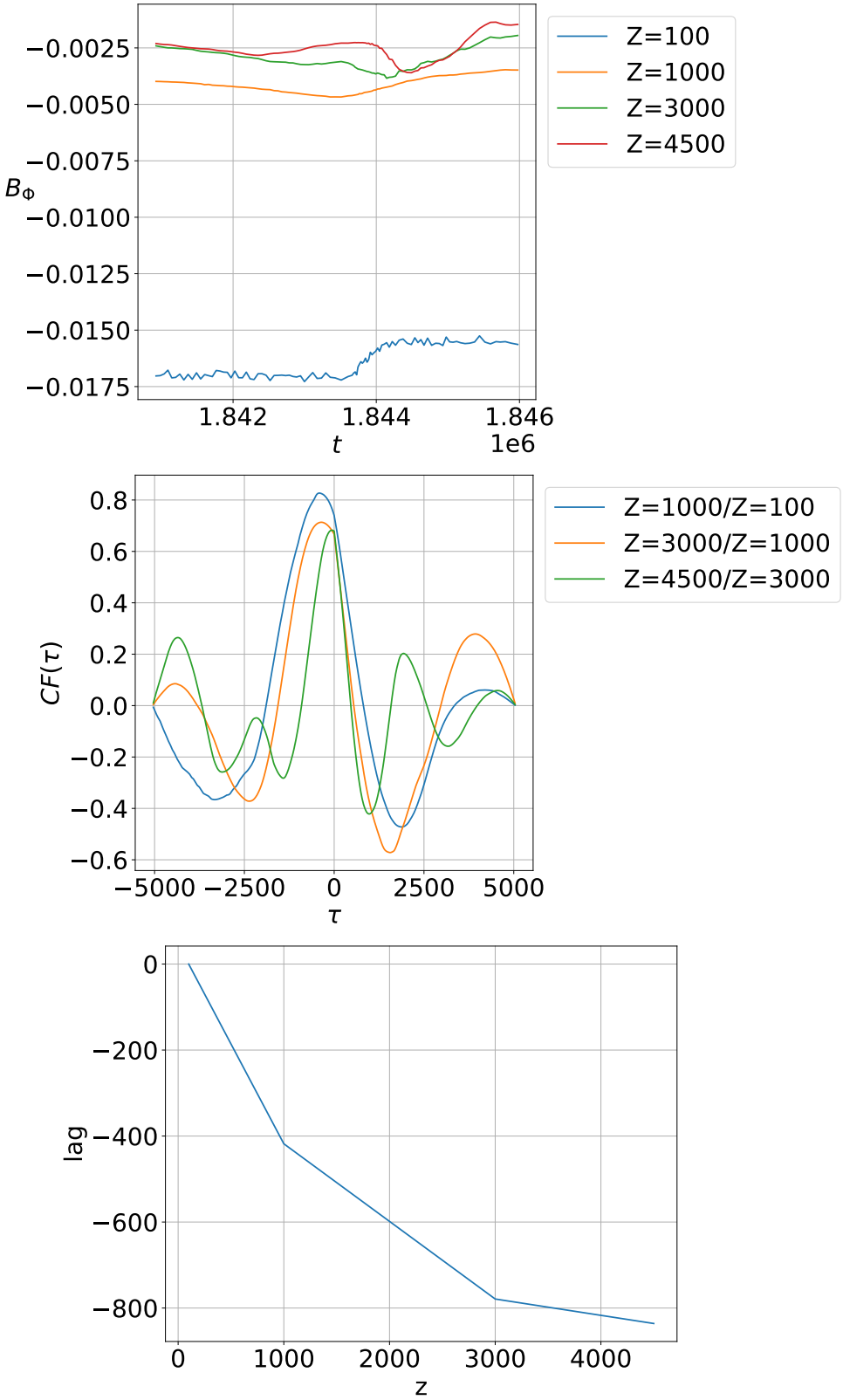

FIGURE 7.15: Cross-correlations during the first oscillation of the reference simulation Q1. Top: Evolution of the toroidal magnetic field at the intersection between the field line anchored at $r_0 = 20$ and various altitudes ($Z \in \{100; 1000; 3000; 4500\}$). Middle: Cross-correlation functions between the neighbouring altitudes of the signals in the top panel. Bottom: Cumulative lag as a function of the altitude. All times are in T_d units.

functions, several techniques have been developed to avoid binning issues (see for instance Edelson and Krolik, 1988).

I used this method at first, and it provided encouraging results. I retrieved apparent upstream propagation with reliable correlation factors, in the 0.7 to 0.9 range. An example is shown on Figure 7.15. The top panel represents the variation of the toroidal magnetic field B_φ at the intersection between the field line anchored at $r_0 = 20$ and several horizontals $Z \in \{100; 1000; 3000; 4500\}$. They are analogous to the light curves of multi-wavelength observations. The middle panel represents the correlation function between the neighbouring altitudes Z_1 and Z_2. I simply compute equation 7.7 with $\mathcal{U}_1 = B_\varphi(Z_1)$ and $\mathcal{U}_2 = B_\varphi(Z_2)$. We see that the point where the correlation function is maximal, where the lag is defined, always corresponds to negative values of the delay τ. This means that the lower altitudes lag the higher altitudes, hinting towards upstream propagation. The bottom panel shows the cumulative lag, taking $Z = 100$ close to the disk as the reference point. We retrieve the negative delays (i.e. upstream propagation). This plot also shows a propagation speed increasing with altitude, as the lag drops with altitude.

The further apart two altitudes Z_1 and Z_2 are, the easier it is to compute the average propagation velocity between them. This is simply because further apart altitudes means higher lag. But the further apart the altitudes, the more different the two signals: the wave may be refracted or reflected along the way. This can make the cross-correlation study inconclusive. But here, I could only use the cross-correlation between relatively distant altitudes. Indeed, while for multi-wavelength observations, the limiting factor is the number of light curves, for me it is the number of outputs during the oscillation. The oscillation lasting only one hundredth of the simulation duration, this method could only calculate time lags between distant altitudes, i.e. between only four altitudes between the simulations. Moreover, computing lags between far apart altitudes means averaging the propagation speed over a large distance. For all these reasons, cross-correlation is not adapted to measure varying propagation speeds along the jet.

Space-time diagram

Thus, I relied on another method, more common to the time-dependence analysis of numerical simulations: the use of space-time diagrams. Figure 7.16 is such a diagram. It represents the evolution of the perturbation in both space and time. The abscissa is time, starting before the perturbation at $t_b = 1.8317 \times 10^6$, and stopping after the perturbation has reached the disk. The ordinate is the altitude of the field line anchored at $r_0 = 40 \gtrsim r_{0,FM}(t_b)$. The background is the relative variation of the squared toroidal magnetic field, for each altitude and along the field line anchored at $r_0 = 40$. This means that for each point of coordinates (t, z) is plotted:

$$\frac{\delta B_\varphi^2}{B_\varphi^2} = \frac{|B_\varphi^2(r_0, t) - B_\varphi^2(r_0, t_b)|}{B_\varphi^2(r_0, t_b)} \tag{7.8}$$

Here, we can see an apparent upstream propagation (negative slope), from the regions close to the outer boundary ($z > 5000$) down to the disk ($z \gtrsim 0$). At each altitude, I define the start of the oscillation as a variation of squared toroidal field of more than 5%, first colored contour in Figure 7.18. Looking closely at the diagram, we can see two propagation zones, above and below $z \simeq 3000$. As seen in Figure 7.10, this altitude corresponds to the intersection between the lower shock with the jet/wind interface.

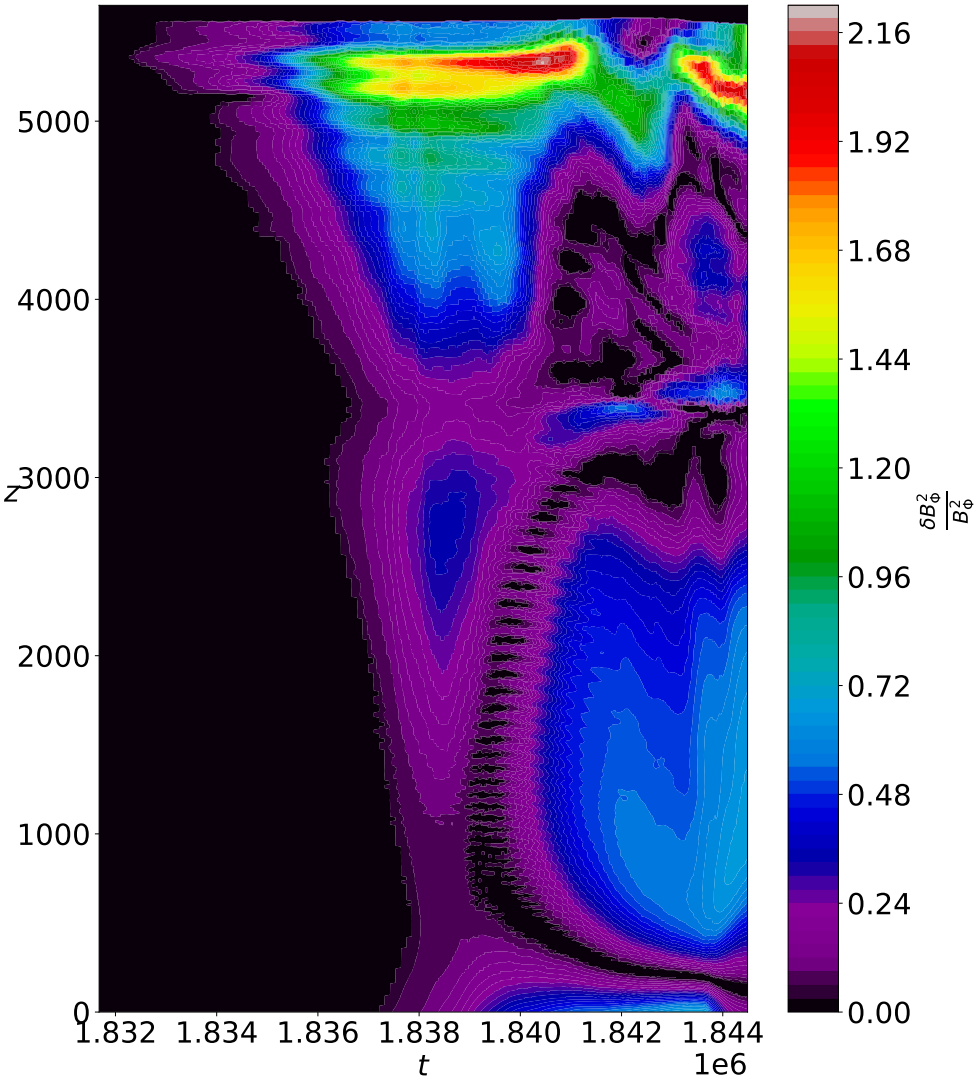

FIGURE 7.16: Space-time diagram of the relative variation of B_φ^2 for the first oscillation along the field line anchored at $r_0 = 40$. For each pixel the abscissa is time, the ordinate is the altitude z, and the color is the relative variation of B_φ^2 compared to its value at the start of the oscillation, $t_b = 1.8317 \times 10^6$ (top left panel of Figure 7.10). It is computed at the point of altitude z on the field line anchored at $r_0 = 40$.

What causes this division ? The study of space-time diagrams with smaller thresholds show that small perturbations coming from the outer boundary trigger stronger perturbations at the shock. But let us focus on this diagram. The perturbation takes a time $T_P^u = 3000$ to reach the shock from the outer boundary, and a time $T_P^l = 1800$ to reach the disk from the shock. Here the exponents u and l respectively stand for upper ($z \geq 3000$, downstream of the shock) and lower ($z \leq 3000$, upstream of the shock).

These timescales should be compared to the timescales of critical waves, that would propagate along the field line anchored at $r_0 = 40$, here named $\mathscr{L}_{r_0}$. The timescales of such waves are:

$$T_C(r_0) = \int_{\mathscr{L}_{r_0}} \frac{dz}{V_C - v_p} = \underbrace{\int_{\mathscr{L}_{r_0} \cap (z \leq 3000)} \frac{dz}{V_C - v_p}}_{T_C^l} + \underbrace{\int_{\mathscr{L}_{r_0} \cap (z \geq 3000)} \frac{dz}{V_C - v_p}}_{T_C^u} \tag{7.9}$$

with the critical speed V_c being either the fast-magnetosonic speed V_{FM} or the Alfvén speed V_A. In both zones, the timescales of critical waves are smaller than that of the perturbation:

- Between the boundary and the shock, $T_{FM}^u = 1603 < T_A^u = 2006 < T_P^u = 3000$.
- Between the shock and the disk, $T_{FM}^l = 845 < T_A^l = 1137 < T_P^u = 1800$.

This order is expected. As the field line anchored at $r_0 = 40$ is located in the sub-FM and sub-Alfvénic wind, no perturbation can propagate through it at speeds faster than the critical speeds.

The perturbation thus takes a time $T_P^{u+l} = T_P^u + T_P^l = 4800$ to propagate from the outer boundary down into the disk. The perturbation is born at the intersection between the field line anchored at $r_0 = 40$ and the outer boundary $R = R_{ext}$. This point is also where the field line is the most likely to be disturbed by a fast-magnetosonic wave, being the closest to the FM surface: As $r_0 = 40 \gtrsim 39 = r_{0,FM}(t_b)$, that point is located at the interface between the inner super-FM dense flow and the outer sub-FM sparse flow.

The fact that the perturbation leads to waves emerging from the intersection between the interface and the outer boundary was confirmed by studying space-time diagrams performed on more inner field lines, well inside the jet. In those, the perturbations are weaker, happen later and do not have a clear sense of propagation.

The rising phase of the oscillations is the upstream propagation of a perturbation in the sub-FM zone that surrounds the super-FM jet and cocoon. But all perturbations do not reach the disk. Refraction occurs, mostly close to the disk. Figure 7.17 represents the evolution of the fast-magnetosonic speed V_{FM} with the altitude z along the magnetic field line anchored in the disk at $r_0 = 40$.

As the perturbation propagates downwards, the fast-magnetosonic speed increases. At $z \sim 100$ there is a change of slope in V_{FM}. As the pulsation of the perturbation $\omega = V_{FM}k$ is constant, its wavenumber $k = 2\pi/\lambda$ decreases suddenly. Therefore, this abrupt jump in magnetosonic speed acts as a low-pass filter. Only the perturbations of lowest wavelengths λ can pass through, and then reach the disk, the others being reflected back.

Moreover, because of the jet radial stratification, at a fixed altitude V_{FM} decreases with the cylindrical radius r, which induces a refraction of the waves towards the interface. This provides the conditions for a perturbed sheath lying just outside the

fast-magnetosonic interface. As a consequence, in the disk everything happens as if all the perturbation arrives in r_J.

As a conclusion, the information emanating from the jet collapses can propagate from the outer boundary down to to the disk, at $r_{0,FM} \simeq 39$ and $r_J = 10$.

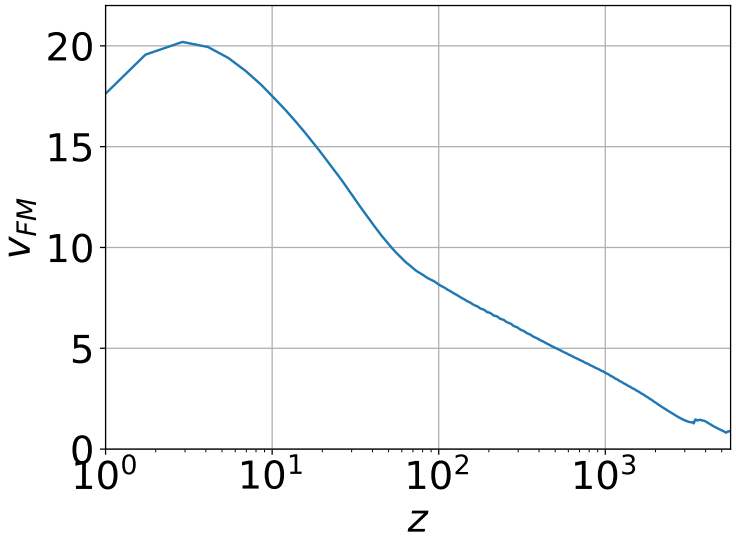

FIGURE 7.17: Variation of the FM speed with the altitude along the field line anchored in $r_0 = 40$, at a time t_b before the oscillation.

7.2.5 Radial propagation

I then used the same method to study radial propagation. This is interesting to see if the perturbation can reach the inner disk regions ($r \gtrsim 1$) emitting the harder photons. This could also show if the scenario is compatible with the hard lags observed in QPOs (see Figure 7.4), meaning that the information first arrives in the outer disk regions ($r_0 \gtrsim r_J$) and only later in the inner regions ($r_0 \gtrsim 1$).

Figure 7.18 is a similar space-time diagram, but here the ordinate is the anchoring radius of the field line. The fixed value is the altitude on the field line, $z = 1$. At each time t, I plot the relative variation of the squared toroidal magnetic field at $z = 1$ for all field lines anchored in the disk at $r_0 \in [1; 40]$.

We see that the propagation is clearly inwards. The perturbation first hits the disk at $r_0 \simeq 40$, and is then detected at smaller radii. However, this radial propagation is too quick to be resolved: the fast-magnetosonic speed being around unity at r_J, the timescale of the radial propagation would be smaller than $10\,T_d$. This requires a time resolution too high for the available outputs. The timescale seen in Figure 7.18 is the rising time of the outburst, roughly 5×10^3. Note that this rising time is roughly that of the downwards propagation $T_P^{u+l} = 4800$.

As it did with distance to the outer boundary, the perturbation fades as the radius gets smaller. This is especially visible in Figure 7.19 that follows the square rooted relative evolution with the radius of the squared toroidal magnetic field, again at altitude $z = 1$. This distribution is shown at different times, from the beginning of the perturbation ($t = 1.8322 \times 10^6$) to near its apex ($t = 1.8409 \times 10^6$). It shows the strong increase of the perturbation with time, but also a strong decrease with the radius. The perturbation is quite small in the transition zone ($r_0 \in [r_J = 10; r_S = 20]$), being always lower than 20%.

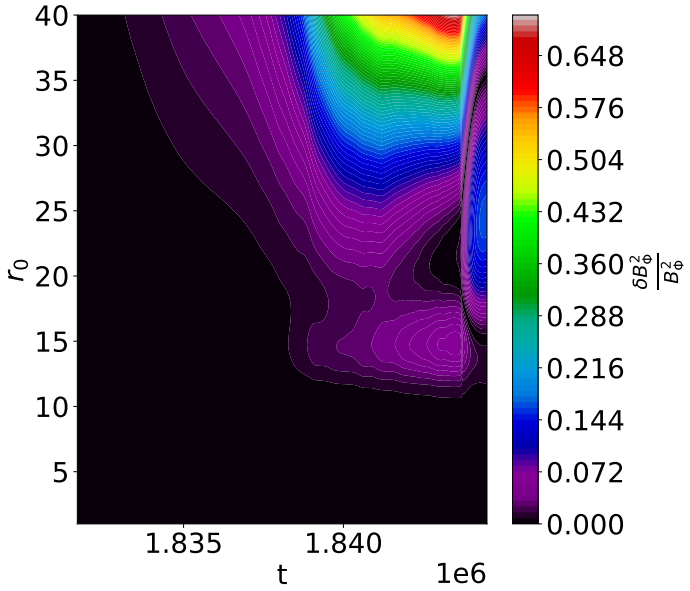

FIGURE 7.18: Space-time diagram of the relative variation of B_φ^2 for the first oscillation along the horizontal $z = 1$. For each pixel the abscissa is time, the ordinate is the anchoring radius r_0, and the color is the relative variation of B_φ^2 compared to its value at the start of the oscillation, $t = 1.8317 \times 10^6$ (top left panel of Figure 7.10). It is computed at $z = 1$ on the field line anchored at r_0.

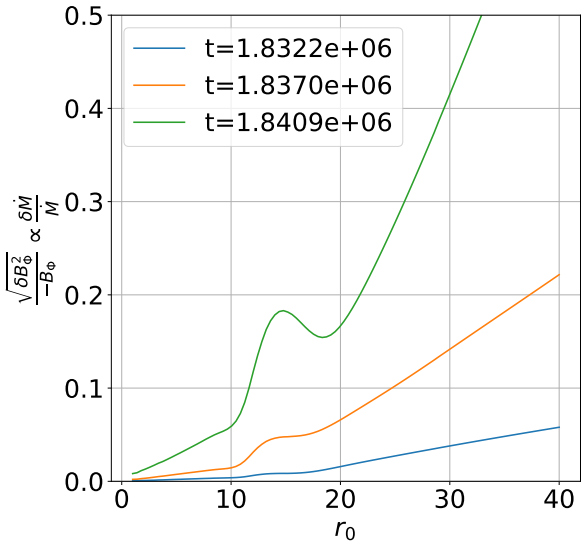

FIGURE 7.19: Square rooted relative evolution of B_φ^2 along the horizontal $z = 1$, for various three times during the rising phase of the first oscillation.

How can we translate this variation in terms of luminosity ? As the jet is cold and the magnetic field is mainly toroidal, it can be related to a variation of mass loss rate: $\dot{M} \propto B_z B_\varphi$. Then, for simplicity, I relate the mass loss rate to luminosity: $\dot{M} \propto L_\nu$. This gives

$$\sqrt{\frac{\delta B_\varphi^2}{B_\varphi^2}} \simeq \frac{\delta \dot{M}}{\dot{M}} \sim \frac{\delta L_\nu}{L_\nu} \tag{7.10}$$

This means that those perturbations would only have a small impact on the light curve emitted from the black hole accretion disk. It is consistent with the QPOs, as those are an epiphenomenon with a fractional rms that is less than 20% (see Figure 7.3). Note that here in ideal MHD there is no dissipation, and the perturbation decrease in only due do upwards refraction. In a more realistic setup, such dissipation might reduce the amplitude. But as accretion and ejection are interdependent (see Figure 1.14), the variation in jet mass flux might also foster additional accretion, leading to a perturbation of greater intensity. Thus it too early to estimate the strength of the perturbation, especially as its origin is unphysical.

Moreover, this perturbation in this simulation is consistent with the consistently hard lag of lower frequency QPOs (see Figure 7.4). In my simulation, the outer regions that produce softer photons are hit first, while it is only at the later stages the inner regions that produce harder photons experience a visible perturbation. However, such a pertubation propagation does not explain the difference between high and low inclination sources for the QPOs of highest frequencies (frequencies over 2 Hz in Figure 7.4).

7.3 Summary

In this chapter, I have shown two-dimensional jet simulations provide useful insights on the QPO scenario based on jet instability of Ferreira et al., 2022. It features the upstream propagation of a perturbation from the asymptotic jet regions down to the disk. This shows the true possibility to get a feedback along the interface between a super-FM jet and the ambient medium, within a sub-FM sheath. The waves are channeled through this sheath, arrive on the disk (in the zone between JED and SAD, $r_0 \gtrsim 10$) then propagate inwards. They produce variations of the toroidal magnetic field leading to torque and thus mass flux variations. These variations weaken during their inwards propagation, because of refractions towards the jet.

However, these perturbations were not created by any MHD instability, but by boundary conditions inconsistent with a collimated jet. Without this inconsistency, the 2D truncated jet simulations are steady, as shown in chapter 6. The instabilities that could create those collapses are three-dimensional, as they rely on variations in the toroidal direction. For instance, these instabilities could be:

- The "kink" $m = 1$ mode of the Bennett pinch instability (Bromberg and Tchekhovskoy, 2016; Tchekhovskoy and Bromberg, 2016).
- The "recollimation" instability (Gourgouliatos and Komissarov, 2018; Matsumoto, Komissarov, and Gourgouliatos, 2020).

In order to investigate the stability in three dimensions of collimated jets and recollimation shocks, but also to have a consistent source for the jet perturbations, Claudio Zanni and I developed a numerical setup to produce 3D jet simulations. This setup is presented in Appendix C.

Chapter 8

Conclusions and perspectives

Contents

8.1 Summary of the main results 189

8.2 Perspectives 189

8.2.1 3D simulations: collimation stability 189

8.2.2 Towards a realistic ejection from the central object 190

More realistic magnetic field and rotation profiles on the central object 190

Black hole and neutron star radio/Xray correlations 191

8.2.3 Time-dependent features in jets 191

AGN jet flares 191

Periodic knots in protostellar jets 193

"Je laisse Sisyphe au bas de la montagne ! On retrouve toujours son fardeau. Mais Sisyphe enseigne la fidélité supérieure qui nie les dieux et soulève les rochers. Lui aussi juge que tout est bien. Cet univers désormais sans maître ne lui paraît ni stérile, ni futile. Chacun des grains de cette pierre, chaque éclat minéral de cette montagne pleine de nuit, à lui seul forme un monde. La lutte elle-même vers les sommets suffit à remplir un cœur d'homme. Il faut imaginer Sisyphe heureux."

"I'm leaving Sisyphus at the bottom of the mountain ! We always find our burden. But Sisyphus teaches the higher fidelity that denies the gods and lifts the rocks. He too believes that all is well. This universe, now masterless, seems to him neither sterile nor futile. Each grain of this stone, each mineral shard of this mountain full of night, alone forms a world. The struggle to reach the summit is enough to fill a man's heart. We have to imagine Sisyphus happy."

Albert Camus

Conclusions

Dans cette thèse, j'ai présenté plusieurs simulations "globales" 2.5D de jets. Ces simulations ont été réalisées à des échelles de temps sans précédent, grâce à un algorithme d'accélération spécial (voir la section 3.1.5). Les jets simulés ont été éjectés à partir d'une condition limite cohérente avec le modèle Jet-Emitting Disk (JED), qui permet le lancement, à partir d'un disque d'accrétion magnétisé, d'un jet puissant traversant toutes les surfaces critiques. Dans les chapitres 4 et 5, ce JED a été étendu à l'ensemble de la frontière inférieure, tandis que dans les chapitres 6 et 7, il a été limité aux régions les plus internes du disque.

Ces travaux ont confirmé l'existence de chocs de recollimation stationnaires. Ceux-ci avaient été prédits par des études analytiques, mais n'avaient jamais été reproduits dans des simulations de jets "globaux". Leur présence dans les simulations où le JED a une taille finie (chapitre 6) montre qu'ils ne sont pas un biais de l'auto-similarité, mais une caractéristique des jets magnétisés auto-collimatés. Ces chocs de recollimation ne fournissent pas la déconnexion attendue entre le circuit électrique accélérateur connecté au disque et le circuit asymptotique définissant la forme asymptotique du jet. Il existe toujours une nappe de courant dans le cocon entourant le jet qui contourne le choc et relie les zones d'accélération et de propagation. L'étude paramétrique a montré un accord qualitatif avec la solution autosimilaire pour les jets autosimilaires (chapitre 5) et tronqués (section 6.4).

Enfin, des effondrements quasi-périodiques du jet se sont produits dans certaines simulations (chapitre 7). Ces effondrements pourraient être un mécanisme concret pour créer des oscillations quasi-périodiques à basse fréquence (LFQPO) en tant que réponse du disque aux instabilités du jet. Mes simulations montrent qu'une perturbation dans le jet peut se propager sur le disque, à condition qu'il y ait un mécanisme physique créant la perturbation.

Perspectives

Les simulations 3D de jets collimatés sont connues pour être sujettes à diverses instabilités, telles que l'instabilité "kink" (Bromberg and Tchekhovskoy, 2016; Tchekhovskoy and Bromberg, 2016) ou l'instabilité de "recollimation" (Gourgouliatos and Komissarov, 2018; Matsumoto, Komissarov, and Gourgouliatos, 2020). Ces instabilités pourraient être le mécanisme de départ des LFQPOs susmentionnés. Dans ce but, et aussi pour explorer la stabilité générale des jets à grande échelle et les chocs de recollimation qu'ils contiennent, j'ai développé avec Claudio Zanni une configuration numérique pour propager les simulations 2.5D en 3D. Afin d'atteindre des temps de calcul raisonnables, nous avons codé plusieurs nouvelles méthodes numériques dans PLUTO, y compris la version de transport contraint de la méthode de la moyenne des anneaux (Zhang et al., 2019). Cela me permettra de réaliser des simulations de jets en 3D.

Les simulations de cette thèse sont censées modéliser un écoulement émis par un disque, à la Blandford & Payne. En conséquence, les profils sur la frontière centrale de l'objet ont été maintenus très simples, et choisis afin de minimiser l'influence de la colonne axiale. Cependant, il est clair que même une colonne axiale avec un faible taux de perte de masse a un impact énorme sur la collimation du jet de disque environnant. Par conséquent, les conditions d'éjection de l'objet central doivent être affinées pour mieux modéliser l'éjection et l'accélération de la colonne vertébrale. Des conditions plus réalistes pourraient être appliquées en mettant en place une éjection subsonique près de l'axe.

Dans le cas d'un jet de trou noir comme dans celui d'une étoile, il serait intéressant de modéliser correctement le jet émis par l'objet central avec une configuration de champ magnétique plus réaliste. De plus en plus d'observations sont interprétées comme des conséquences de la juxtaposition d'une colonne interne et d'un jet de disque externe. Barnier et al., 2022 interprète les observations radio de GX 339-4 comme le mélange d'une épine de Blandford

& Znajek interne avec un jet de Blandford & Payne externe. Récemment, l'interférométrie radio a fourni des images détaillées des régions de lancement des jets de M87. Par exemple, les observations de Lu et al., 2023 ont montré qu'autour de la colonne axiale se trouve un flux externe qui n'est pas ancré dans le trou noir central, mais dans le disque d'accrétion qui l'entoure. Dans le cas des jets protostellaires, ceux-ci devraient être le mélange d'un jet stellaire et d'un vent de disque en forme d'oignon (Bacciotti et al., 2000; Lavalley-Fouquet, Cabrit, and Dougados, 2000).

En particulier, il serait intéressant d'étudier le degré plus élevé de collimation du jet pour un objet central à rotation plus rapide, comme montré par mes simulations. Cela pourrait expliquer pourquoi les étoiles à neutrons sont aberrantes dans la corrélation radio/rayons X, étant donné que les étoiles à neutrons à rotation lente émettent moins en radio que les AGN à rotation rapide d'une puissance en X similaire. Il serait très intéressant de produire des simulations de jet GRMHD à grande échelle pour les rotateurs rapides et lents, et de créer des cartes de flux synthétiques du jet en rayons radio/X/γ, en commençant relativement près de l'objet central (étoile à neutrons ou trou noir) jusqu'à la zone asymptotique, au-delà du rayon de Bondi. Ceci pourrait également être intéressant pour les observations Gravity/ngEHT ou X-ray des AGNs.

De telles cartes synthétiques issues de simulations à grande échelle de jets AGN collimatés permettraient également de prédire la variabilité observée du flux à plusieurs longueurs d'onde. Certains travaux tels que Clairfontaine et al., 2021; Clairfontaine, Meliani, and Zech, 2022 expliquent les éruptions de jets d'AGN par l'accélération de particules sur des chocs de recollimation permanents. Lorsque des noeuds en mouvement passent à travers un noeud stationnaire, une éruption est détectée. Cet éruption est observée à la fois dans le jet et dans les noeuds mobiles. Les auteurs combinent des simulations hydrodynamiques de jets pré-collimatés avec le transfert radiatif. Dans un jet précollimaté et en surpression avec des chocs de recollimation permanents similaires aux miens agissant comme des noeuds permanents, ils lancent des éjectas du bas vers le haut, à une vitesse supérieure à celle de l'écoulement. Ces éjecta modèlent les noeuds en mouvement. Lorsque ces éjectas en mouvement traversent un choc de recollimation permanent, les auteurs observent une éruption dans leurs courbes de lumière et leurs images synthétiques qui permet de retrouver qualitativement les propriétés des éruptions des blazars à haute énergie.

Je pourrais utiliser des simulations de plateforme MHD ou GRMHD de jets autocollimatés à grande échelle et de transfert radiatif pour sonder un tel scénario afin de trouver des structures de jet fiables. Plutôt que d'injecter des chocs ad hoc dans le jet, le cadre de la MHD me permettra de lancer, par exemple, des inversions de polarité dans le jet (Giannios and Uzdensky, 2019), en sondant comment ces régions peuvent interagir avec les structures de recollimation pour fournir une reconnexion magnétique. L'éruption potentielle induite par une telle configuration doit être comparée à la dissipation sans doute plus intrinsèque résultant des instabilités de kink dans la zone de recollimation (Bromberg and Tchekhovskoy, 2016; Tchekhovskoy and Bromberg, 2016). Ceci est particulièrement intéressant dans le contexte du jet M87, dont le choc de recollimation au niveau du nœud HST-1 est une source d'éruption au TeV (Giannios, Uzdensky, and Begelman, 2010).

Ces méthodes pourraient également être étendues aux jets protostellaires. Des noeuds périodiques sont observés dans de nombreux jets protostellaires. Cette périodicité pourrait être due à une éjection périodique de l'étoile, créant des chocs périodiques le long de l'axe du jet stellaire. C'est ce que préconisent la remarquable symétrie jet/contre-jet et les simulations hydrodynamiques simples de Tabone et al., 2018. Il serait intéressant de réaliser des simulations MHD d'un jet stellaire variable entouré d'un vent de disque stationnaire, et de produire des images synthétiques de ces simulations. Une façon simple de commencer cette investigation serait de lancer une simulation dans laquelle la vitesse d'éjection de l'objet central est temporellement périodique, et d'étudier comment cette variabilité affecte le jet environnant.

8.1 Summary of the main results

In this thesis, I presented various 2.5D "global" simulations of jets. These simulations were performed on scales unprecedented in time, thanks to a special acceleration algorithm (see section 3.1.5). The simulated jets were ejected from a boundary condition consistent with the Jet-Emitting Disk (JED) model, that enables the launching from a magnetized accretion disk of a powerful jet crossing all critical surfaces. In chapters 4 and 5 this JED was extended on the whole lower boundary, while in chapters 6 and 7 it was limited to innermost disk regions.

These works confirmed the existence of steady recollimation shocks. Those were predicted by analytical studies, but had never been reproduced in "global" jet simulations. Their presence in simulations were the JED has a finite size (chapter 6) shows they are not a bias of self-similarity, but a feature of self-collimated magnetized jets. These recollimation shocks do not provide the expected disconnection between the accelerating electric circuit connected to the disk and the asymptotic circuit setting the asymptotic shape of the jet. There is always a current sheet in the cocoon surrounding the jet that bypasses the shock and links the acceleration and propagation zones. The parameteric study showed qualitative agreement with the self-similar solution for both the self-similar (chapter 5) and truncated (section 6.4) jets.

A second strong result is the non-negligible influence of the central object (black hole or star). Even when a vast majority of the matter is emitted from the disk, the spine ejected from the central object has a strong influence on the collimation of the jet emitted from the disk. It may explain why my simulations showed a relative apathy when exploring the parameter space when compared to the self-similar solutions where such a spine is missing. This spine can be a Blandford & Znajek flow emanating from the surroundings of black hole or a stellar wind. My simulations show that even if it is weak, it greatly diminishes the altitude of the recollimation shocks by increasing the jet collimation.

Finally, quasi-periodic jet collapses occurred in specific simulations (chapter 7). These collapses could be a concrete mechanism to create Low-Frequency Quasi-Periodic Oscillations (LFQPOs) as the disk response to instabilities in the jet. My simulations show that a perturbation in the jet can propagate onto the disk, provided there is a physical mechanism creating the perturbation.

8.2 Perspectives

The work described in chapters 4 and 5 has lead to a publication (Jannaud, Zanni, and Ferreira, 2023, reproduced in Appendix D). The results shown in chapters 6 and 7 will each lead to the submission of a paper. However, the subject of jet collimation is very rich, and there are many pending questions. Below are a few perspectives, sorted by stage of development. For the first point, the setup has been done and what remains is to run and analyze the simulations. For the second point, a few test simulations and calculations were performed. The third point is a long-term plan, still at the discussion stage.

8.2.1 3D simulations: collimation stability

3D simulations of collimated jets are known to be prone to various instabilities, such as the kink instability (Bromberg and Tchekhovskoy, 2016; Tchekhovskoy and Bromberg, 2016) or the "recollimation" instability (Gourgouliatos and Komissarov, 2018; Matsumoto, Komissarov, and Gourgouliatos, 2020). Those instabilities could

be the starting mechanism of the aforementioned LFQPOs. For this purpose, and also to explore the general stability of the large-scale jets and the recollimation shocks their contain, I developed with Claudio Zanni a numerical setup to propagate 2.5D simulations into 3D. In order to reach reasonable computing times, we have coded several new numerical methods into PLUTO, including the constrained transport version of the ring-average method (Zhang et al., 2019). This will enable me to run 3D jet simulations. I do not expand on this topic here as this is the subject of Appendix C.

8.2.2 Towards a realistic ejection from the central object

The simulations of this thesis are supposed to model a disk-emitted outflow, à la Blandford & Payne. As a consequence, the profiles on the central object boundary were kept very simple, and chosen in order to minimize the influence of the axial spine. However, it is clear that even an axial spine with a small mass loss rate has huge impact on the collimation of the surrounding disk jet. Therefore, the ejection conditions from the central object should be refined to better model the ejection and acceleration of the spine. More realistic conditions could be applied by setting a subsonic ejection near the axis. In the simulation presented in this thesis, the initial acceleration of the spine is not taken into account, as at launch $v_p > c_S$. This approcimation could be relaxed.

More realistic magnetic field and rotation profiles on the central object

It would be also interesting to explore different magnetic field or rotation configurations near the axis. Let us do a few back of the envelope calculations to see what profiles could be expected from astrophysical objects.

In the case of a star, the innermost disk radius R_d is inevitably smaller than the corotation radius r_{co}. The ratio $R_d = r_{co}/4$ is often assumed for T Tauri stars (see e.g. Bessolaz et al., 2008), which lead to $\Omega_{*_a}/\Omega_{K_d} = 1/8$. Such simulations were already performed (see section 6.4.1). However, one should also modify the vertical magnetic field profile. Assuming continuity of the magnetic field at R_d and a dipolar magnetic field, $B_d = B_a(R_d/R_*)^{-3}$, where B_d is the vertical magnetic field in the disk ($R = R_d; \theta = \pi/2$), B_a is the vertical magnetic field on the axis ($R = R_d; \theta = 0$) and R_* is the stellar radius. Assuming $R_* = R_d/2$ this leads to $B_a = 8B_d$. This is not the case in my simulations, that have $B_a \simeq B_d$.

The case of a black hole is a bit more complicated. The innermost disk radius R_d corresponds to the Innermost Stable Circular Orbit (ISCO). The value of r_{ISCO}, and thus the rotation at that point (Ω_{ISCO}) highly depends on the black hole spin parameter a (see e.g. Bardeen, Press, and Teukolsky, 1972). The event horizon is located at radius $r_H = r_g(1+\sqrt{1-a^2})$, and it rotates at speed $\Omega_H = ac/(2r_H)$. Assuming a Keplerian disk, differences in the spin parameter only induce relatively small variations on the rotation profile. Naturally, a Schwarzchild black hole ($a = 0$) is non-rotating ($\Omega_H = 0$). And at maximum ($a = a_{max} \simeq 3/4$) we only have $\Omega_H/\Omega_{ISCO} = 3/2$. Both these extreme cases are in the same ballpark as my simulations of section 6.4.1. But as for a star, it is the vertical magnetic field whose profile should be modified. Simple extrapolations from the fits of Narayan et al., 2021 make us lean towards a magnetic field on the axis B_a much higher than that in the disk B_d, with $B_a \gg 100B_d$ whatever the spin parameter a. This would increase the magnetic pressure in the inner regions and thus lower the collimation.

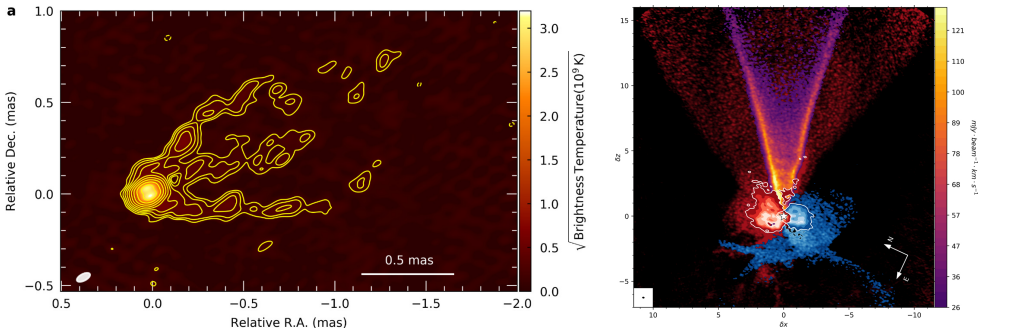

FIGURE 8.1: Radial layering of the jets. Left: Launching region of the M87 jet (Lu et al., 2023). VLBI radio observations (GMVA, ALMA, GLT). Right: Launching region of the DG Tauri B jet (de Valon et al., 2020). Radio observations in CO (ALMA)

In both cases it would be interesting to properly model the jet emitted by the central object with a more realistic magnetic field configuration on the $R = R_d$ boundary. More and more observations are interpreted as consequences of the juxtaposition of an inner axial spine and an outer disk jet. Barnier et al., 2022 interpret the radio observations of GX 339-4 as the mixing of an inner Blandford & Znajek spine with an outer Blandford & Payne jet. And recently, radio interferometry provided detailed images of the jet launching regions of M87. For instance, the observations of Lu et al., 2023 showed that surrounding the axial spine is an outer flow not anchored in the central black hole, but in the surrounding accretion disk (see Figure 8.1). In the case of protostellar jets, those should be the mixing of a stellar jet and an onion-like disk wind (Bacciotti et al., 2000; Lavalley-Fouquet, Cabrit, and Dougados, 2000).

Black hole and neutron star radio/Xray correlations

In particular, it would be interesting to investigate the higher degree of jet collimation for a faster-spinning central object shown by my simulations. This hints towards an explanation as to why neutron stars are outliers in the Radio/X-ray correlation, as slow-rotating neutron stars emit less in radio than fast-rotating AGNs of similar X-ray power (see the top panel of Figure 1.7, from Coriat et al., 2011). It would be of great interest to produce large-scale GRMHD jet simulations for both fast and slow rotators, and to create synthetic flux maps of the jet in radio/X-ray/γ-ray, starting from relatively close to the central object (neutron star or black hole) until the asymptotic zone, beyond the Bondi radius. This could also be of interest for Gravity/ngEHT or X-ray observations of AGNs.

This involves tools different from those I used during this thesis (special or general MHD simulations) but is also a natural next step. Verifying if the asymptotic behavior of the jet varies a lot with the central object may be a way to understand the differences between black hole and neutron star jets.

8.2.3 Time-dependent features in jets

AGN jet flares

Such synthetic maps from large-scale simulations of collimated AGN jets would also help predict observed multi-wavelength flux variability. Some works such as Clairfontaine et al., 2021; Clairfontaine, Meliani, and Zech, 2022 explain AGN jet flares via

particle acceleration on standing recollimation shocks. Figure 8.2 shows radio observations of the blazar 3C 273. In the top panel are the positions of the blazar knots, either quasi-stationary (k32 and k35) or drifiting away from the core. We see that when the moving knots pass through the standing k32 knot, a flare is detected (vertical lines). This flaring is seen in both the jet (middle panel) and the moving knots (bottom panel). The authors combine hydrodynamic simulations of pre-collimated jets with radiative transfer. In a pre-collimated and overpressured jet with standing recollimation shocks similar to mine acting as the standing knots, they launch ejecta from the bottom up, at a speed higher than that of the flow. These ejecta model the moving knots. When these moving ejecta cross a standing recollimation shock, the authors observe a flare in their light curves and synthetic images that qualitatively retrieves the properties of the high-energy blazar flares.

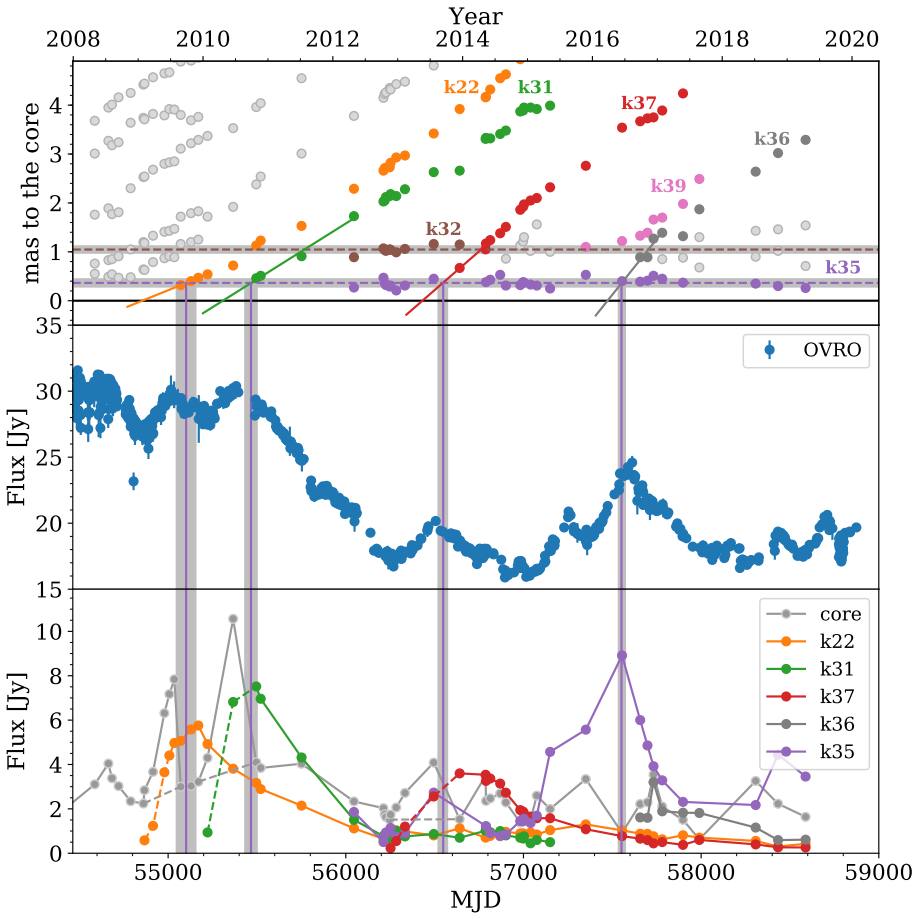

FIGURE 8.2: Radio observations of the blazar 3C 273 (Clairfontaine et al., 2021). Top: Distance of the knots to the core. Straight lines are linear extrapolations of the moving knots position. Horizontal dashed lines are the mean position of the quasi-stationary knots k32 and k35. Middle: Radio jet light curve. Bottom: Flux of the radio core and moving knots. The vertical lines show the most likely time for when the moving knots pass through the quasi-stationary k35 knot (purple dashed line).

One could use MHD or GRMHD platform simulations of large-scale self-collimated jets and radiative transfer to probe such a scenario for reliable jet structures. Rather than injecting had hoc shocks into the jet, the framework of MHD will enable me to launch, for example, polarity reversals into the jet (Giannios and Uzdensky, 2019),

probing how these regions may interact with recollimation structures to provide magnetic reconnection. The potential flaring induced by such a setup should be compared to the arguably more intrinsic dissipation resulting from kink instabilities in the recollimation zone (Bromberg and Tchekhovskoy, 2016; Tchekhovskoy and Bromberg, 2016). This is particularly interesting in the context of the M87 jet, whose recollimation shock at the HST-1 knot is source of TeV flaring (Giannios, Uzdensky, and Begelman, 2010).

Periodic knots in protostellar jets

These methods could also be expanded to protostellar jets. Periodic knotty features are seen in many protostellar jets, such as HH212 (see Figure 1.9) or the jet from the source C7 in the protostellar cluster Serpens South (see Figure 8.3 below). This periodicity could be caused vy periodic ejection from the star, creating periodic bow shocks along the stellar jet axis. This is advocated by the remarkable jet/counter-jet symmetry, and by the simple hydrodynamic simulations of Tabone et al., 2018. It would be interesting to perform MHD simulations of variable a stellar jet surrounded by a steady disk wind, and to produce synthetic images of these simulations. One simple way to start this investigation would be to launch a simulation in which the ejection velocity from the central object is time-periodic, and study how this variability affects the surrounding jet.

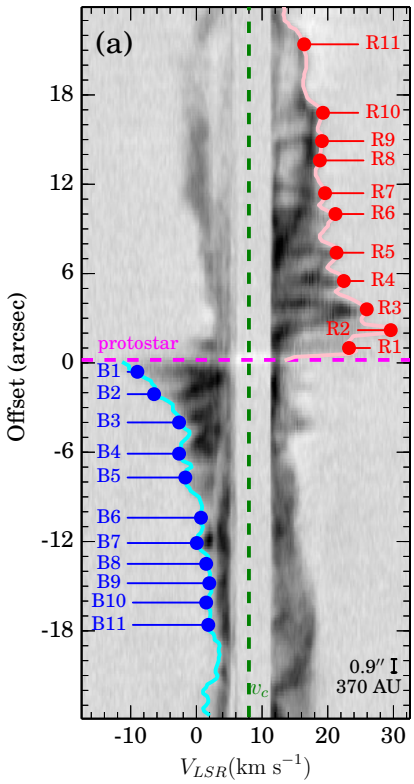

FIGURE 8.3: Outflow ejecta from the C7 source of the protostellar cluster Serpens South (Plunkett et al., 2015). Position-velocity diagram along the axis of the flow. The points correspond to velocity maxima that were identified as outflow knots. The redshifted knots of the northern jet are shown in red, and the blueshifted knots of the southern jet are shown in blue.

Appendix A

2.5D MHD instabilities

Contents

A.1 Axisymmetric instability criteria 195
A.1.1 Z-pinch 196
A.1.2 Screw-pinch 196
A.2 Application to the simulations 197
A.3 Conclusion 197

Accross the simulations described in this manuscript I saw two outflow behaviors that could be associated to plasma instabilities:

- The standing oscillations seen at the spine-jet interface of the self-similar simulation of reference K2 (see sections 4.2.3 and 4.5).
- The jet oscillations seen in the time-dependant simulations of chapter 7.

In this Appendix I will say a few words on MHD instabilities to explain why they are not the cause of these oscillations. I will only consider instabilities that can develop in axisymmetric ideal MHD plasmas. For exhaustive overviews the curious reader is referred to Chandrasekhar, 1961 or Freidberg, 1982.

A.1 Axisymmetric instability criteria

Let us consider a confined column of magnetized plasma. We saw in section 2.6.6 that the confinement can be created via a toroidal magnetic field and axial current (z-pinch); or via an axial magnetic field and toroidal current (θ-pinch). In addition, the screw-pinch is a combination of both z-pinch and θ-pinch.

In this section I will not make any demonstration[1], only show a few results. I assume the column to be of constant velocity, without any rotation or gravity. Those are strong assumptions, but reasonable far away from the disk. While the θ-pinch has be shown to remain stable, both the pure z-pinch and the general screw-pinch are susceptible to some ideal MHD instabilities.

[1] They can be found in Kadomtsev, 1966 or in section 9.4 of Goedbloed and Poedts, 2004.

A.1.1 Z-pinch

In the z-pinch configuration the magnetic field is only toroidal. Only considering the $m = 0$ mode because of axisymmetry, the stability condition is

$$-\frac{d\ln P}{d\ln r} < 2\gamma + \frac{8\pi P}{B^2} \tag{A.1}$$

where γ is the adiabaticity index and $B = B_\varphi$ is the toroidal magnetic field.

Highly magnetized jets ($8\pi P \ll B^2$) are more prone to this instability. It is called the "sausage" instability, characterized by regular oscillations along the axis (see Figure A.1). This is a a sufficient and necessary condition for stability, but it only works in the case of a pure z-pinch.

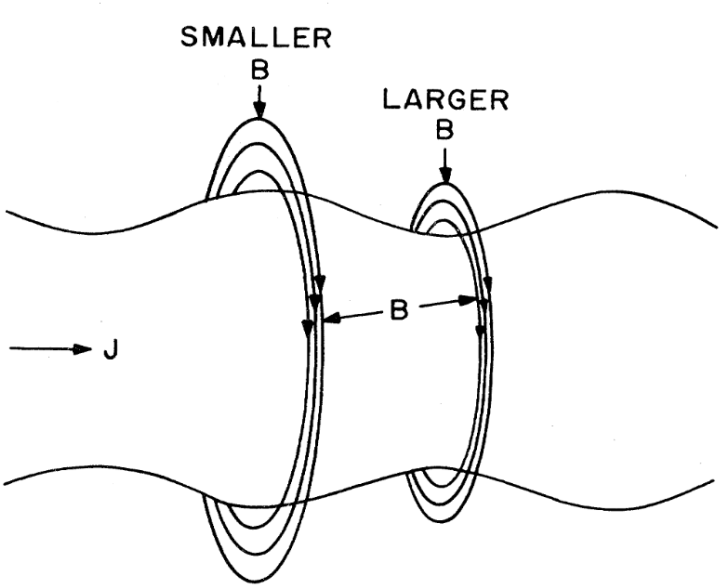

FIGURE A.1: Mechanism of the $m = 0$ sausage instability in a pure z-pinch configuration (Freidberg, 1982).

A.1.2 Screw-pinch

In the screw-pinch configuration there is both an axial and a toroidal component of the magnetic field. This case is more complex, and here I will only deal with the Suydam, 1958 criterion for localized interchange. It relies on the pitch of the plasma column $\mathcal{P}$, defined along a magnetic field line as

$$\mathcal{P} = \frac{B_\varphi}{rB_z} = \frac{d\varphi}{dz} \tag{A.2}$$

The stability condition is then

$$8\frac{dP}{dr} + rB_z^2\left(\frac{1}{\mathcal{P}}\frac{d\mathcal{P}}{dr}\right)^2 > 0 \tag{A.3}$$

A negative pressure gradient combined with a small magnetic shear $d\mathcal{P}/dr$ drives the instability, while a strong axial magnetic field stabilizes the flow. This is only a sufficient condition for stability: if equation A.3 is verified the flow stable, but if it is not verified it is not necessarily unstable.

A.2 Application to the simulations

I searched for both instabilities in the simulation K2. How applicable are the criteria ? We see on Figure 4.18 that the centrifugal force is negligible compared to other forces at the spine-jet interface, tus rotation is negligible. The Suydam criterion (equation A.3) is better suited than the Kadomtsev criterion (equation A.1): As $-B_\varphi/B_z \sim 2$ in the spine and 4 in the jet we are not in a pure z-pinch configuration. For this reason, on Figure A.2 I only show the evolution of the Suydam criterion along several horizontals. We see that this criterion remains relatively small, for both negative and positive values. In particular, it is positive at the spine-jet interface, located at $r \simeq 8$ for $z = 1200$. Thus, this instability is not the cause of the standing oscillations. Note that even inside the spine, the invalidity of the criterion does not mean the flow is unstable, especially as this zone is only a few cells wide.

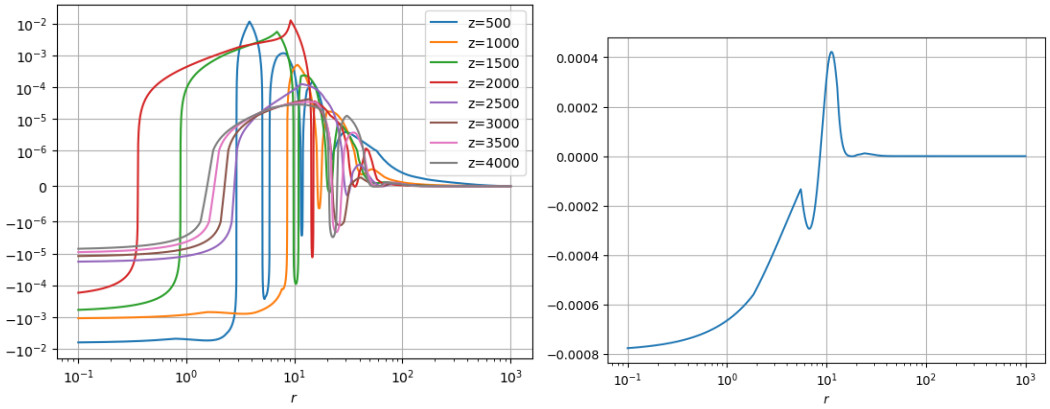

FIGURE A.2: Evolution of the Suydam stability criterion (equation A.3) for the self-similar simulation of reference K2, along various horizontals (left) or only $z = 1200$ (right).

I also looked for the satisfaction of the criteria during the oscillations of the time-dependant simulations of chapter 7. I adopted a straightforward technique: Produce videos of the oscillations where the cells appear in one color if the criterion is satisfied, and in another color if it is unsatisfied. I saw that the stability criterion was never unsatisfied in zones larger than one or two cells. As a consequence, these instabilities is not the cause of the jet collapses.

A.3 Conclusion

In this Appendix, we saw that the described MHD instabilities are not the cause of the standing or moving oscillations present in my simulations. This an additionnal argument in favor of the causes given in the manuscript:

- For the simulation K2, a standing imbalance at the interface between the inner spine and the outer jet (see section 4.5).
- For the time-dependant truncated simulations of chapter 7, a perturbation created by the boundary condition at the outer edge of the simulation domain (see section 7.2.3).

Appendix B

Limiting the disk toroidal magnetic field

Contents

B.1 Context 199
B.2 Tests 200
B.3 Conclusion 200

B.1 Context

In this appendix I describe the process performed to get to two parameters of the truncated simulation of reference of chapter 6:

- The size of the transition region $[r_J; r_S]$. This region is located between the inner ejecting JED $[R_d; r_J]$, and the outer SAD ($r > r_S$) where the ejection has vanished. I play on the size of this regions by varying r_S, while r_J is fixed to 10.
- The parameter $\mathcal{T}$, quantifying the characteristic time of reduction of the toroidal magnetic field beyond r_S (equation 6.9).

As a reminder, in the SAD ($r > r_S$) is diminished at each timestep via

$$B_\varphi(r, t + dt) = B_\varphi(r, t) e^{-\frac{dt}{\mathcal{T} T_K(r)}} \tag{6.9}$$

where $T_K(r) = \sqrt{r^3/(GM)}$ is the local keplerian timescale.

B.2 Tests

To study the impact of these two parameters on jet collimation and toroidal magnetic field, I ran the tests R1, R2 and R3 described in table B.1. Those simulations were then analyzed by a first year Masters student, Victorien Mouton, in the context of his two-month internship. In table B.1 is also the simulation Q1, reference of chapter 7, without the reduction of B_φ, and thus $\mathcal{T}$ is not defined (ND).

Name	r_S	$\mathcal{T}$	t_{end}
R1	12	10^{-4}	1.71×10^6
R2	15	10^{-4}	4.73×10^4
R3	20	10^{-4}	4.29×10^4
Q1	20	ND	3.20×10^6

TABLE B.1: Simulations performed in the search of optimal r_S and $\mathcal{T}$.

On Figure B.1 I show the radial distribution of the electric current $-rB_\varphi$ along the disk surface, on the first cell above the boundary. The left panel shows the variation of the current with the disk transition radius r_S. We naturally see that for lower values of r_S the plateau corresponding to the SAD ($\theta = \pi/2, r > r_S$) happens sooner, but also that its current $-rB_\varphi(r > r_S)$ is lower. The right panel shows the reduction of the toroidal magnetic field via equation 6.9. In Q1 it was not implemented, and B_φ is one order of magnitude higher than in R3 where it is implemented. The impact of this reduction of B_φ can also be seen by comparing Figures 6.5 and 7.9. As Q1 was done without the reduction, and we can see on Figure 7.9 a current sheet leaving the disk at $r > r_S = 20$ which is missing in Figure 6.5.

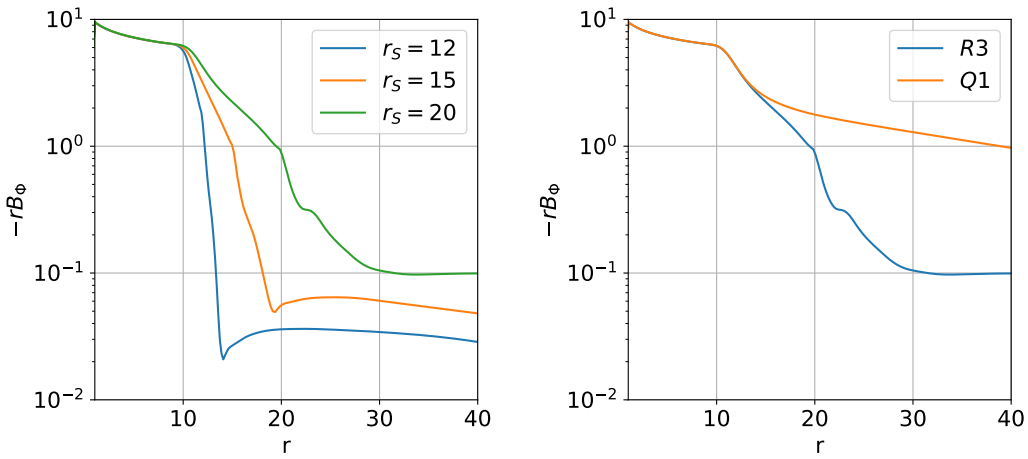

FIGURE B.1: Evolution of the current $-rB_\varphi$ at the disk surface for several values of the transition radius r_S (left) and for several values of the parameter $\mathcal{T}$ (right).

B.3 Conclusion

The conclusion of these tests is straightforward: The lower r_S and $\mathcal{T}$, the lower the electric current in the SAD ($\theta = \pi/2$, $r > r_S$). As our goal was to limit current sheet ejected from this region, I set low values of both r_S (12) and $\mathcal{T}$ (10^{-6}) for the truncated simulation of reference O1.

Appendix C

3D jet simulations

Contents

C.1 Motivations and constraints **202**
C.2 Numerical setup **204**
C.2.1 Initial conditions 204
C.2.2 Boundary conditions 205
Polar axis: $\theta = 0$ 206
Lower boundaries: $R = R_{min}$ and $\theta = \pi/2$ 206
C.3 Ring-Average method **207**
C.4 Scaling tests **208**
C.5 Summary **209**

C.1 Motivations and constraints

The simulations presented in this thesis were all in 2.5D. This means that they are axisymmetric, but compute and depend on quantities in the toroidal direction (B_φ and v_φ). A natural follow-up is to produce full 3D simulations. In those, the jet would be free to evolve in the φ-direction. This would be interesting for two reasons.

First, such simulations could be used to investigate the general stability of the collimated jets and recollimation shocks. The recollimation shocks presented in this thesis are intrinsically axisymmetric. They rely on all magnetic field lines ejected from the disk at the same radius to hit the axis at the same altitude. It would be interesting to see if the shocks are conserved if some asymmetry is introduced.

Second, 3D collimated jets are known to be prone to several instabilities. These can be current-driven such as the kink (see e.g. Appl, 1996; Barniol Duran, Tchekhovskoy, and Giannios, 2017; McKinney, 2006; Mizuno, Hardee, and Nishikawa, 2014; Moll, Spruit, and Obergaulinger, 2008) that may play role in the FRI/FRII dichotomy of AGN jets (see e.g. Bromberg and Tchekhovskoy, 2016; Tchekhovskoy and Bromberg, 2016). These instabilities can also happen at the interface between the jet and the outer medium such as the Kelvin-Helmholtz (KH, see Baty and Keppens, 2002, 2006; Bodo et al., 1994) or Rayleigh-Taylor (RTI, see Hassam, 1992; Matsumoto and Masada, 2013; Meliani and Keppens, 2009; Rayleigh, 1882; Taylor, 1950) or centrifugal (CFI, see Rayleigh, 1917) instabilities. The last two are at the origin of the non-destructive recollimation instability seen in 3D jet simulations (see Matsumoto, Komissarov, and Gourgouliatos, 2020 and references therein).

Third, the expected 3D instabilities could be the cause of the type-C LFQPOs ubiquitous in X-ray binary observations. This could especially be the case of the aforementioned recollimation instability. It happens beyond the recollimation point, and could thus provide the large timescales yet unexplained by accretion disk physics (see Ferreira et al., 2022). Indeed, the simulations described in chapter 7 show that provided there is a physical instability creating an oscillation or wobbling, a perturbation could propagate along the sub-FM sheath from beyond the recollimation point down to the disk. Making 3D simulations could provide a consistent origin to these oscillations, instead of a forcing caused by the boundary conditions.

Thus, performing 3D jet simulations is of great interest. The most obvious way to do this would be to take the final output of a 2.5D simulation as an initial condition by symmetrizing it in the toroidal direction around the polar axis Oz. Figure C.1 illustrates what these initial conditions could look like. It is a 3D rendering of the 2.5D self-similar simulation of reference K2. We see several magnetic surfaces of equal values of magnetic flux Ψ. The outer surfaces look very similar to the theoretical picture (Figure 2.1). The inner surfaces are slightly different because of the pre-shock recollimation and the post-shock refraction.

Performing such a simulation could in principle be relatively simple. One would mostly need to adapt the boundary conditions to 3D. Unfortunately, it would also be very computionally expensive. Let us do a back-of-the-enveloppe calculation to see how much. I start from the low-resolution 2D grid with $N_R = 704$ cells in the radial direction and $N_\theta = 144$ cells in the orthoradial direction, to which I add $N_\varphi = 128$ cells in the toroidal direction. Naturally, each timestep should cost around 10^2 times more, as there is 10^2 times more cells. But the timestep itself is also changed. The non-accelerated timestep Δt is computed by the CFL condition:

$$\frac{\Delta t}{N_{dim}} \max_{\mathcal{C}\in\mathcal{D}} \left(\sum_{d=1}^{N_{dim}} \frac{|\lambda_d|}{\Delta l_d} \right) = C_a \tag{3.13}$$

It is set by the smallest cell, or by a cell nearby. In the 2.5D grid, the smallest cell is in the bottom left corner, near the $(R = 1, \theta = 0)$ boundary. Its sizes are $dr \simeq 10^{-2}$ and $rd\theta \simeq 3 \times 10^{-3}$. But in 3D, it also has the size $r \sin\theta d\varphi \simeq 10^{-4}$. Thus, passing from 2.5D to 3D reduces the minimum cell size and thus the timestep by a factor 30. Additionnaly, as 3D simulations are expected to be unstable, the acceleration algorithm should not work, or at least not as well. This amounts to reducing the timestep by a factor up to 10^3, as this was the acceleration factor reached in the 2.5D simulations (see Figure 3.4).

Thus, to run as long as the 2.5D simulations, the 3D ones would require around 10^6 times more computing time. As a typical 2.5D simulation runs for 10^3 HCPU, it would take nearly a billion HCPU to run 3D simulations on the same physical timescales. That is way too much, and the numerical technique detailed in section C.3 does not compensate for this nearly enough. For this reason, I decided to limit the simulation domain to right under the shock location, at $z \sim 10^3$. I set a minimal spherical radius $R_{min} \sim 10^3$, and all cells with $R < R_{min}$ are removed from the domain. Between the decrease in cell numbers and the increase in cell size, it saves a factor 10^4 in computing time. A run would then take 10^4 to 10^5 HCPU, putting us back in reasonable territory. While 10^9 HCPU is unreachable for any supercomputer, computations of 10^4 to 10^5 can be made on national supercomputers, but even at local ones such as GRICAD in Grenoble. Naturally, such a setup prevents to showcase the propagation of an eventual instability born near the shock, or at least its upstream propagation below R_{min}. However there shouldn't be much difference in the propagation of information through the sub-FM sheath between the 3D simulations and the 2.5D ones of 7 .

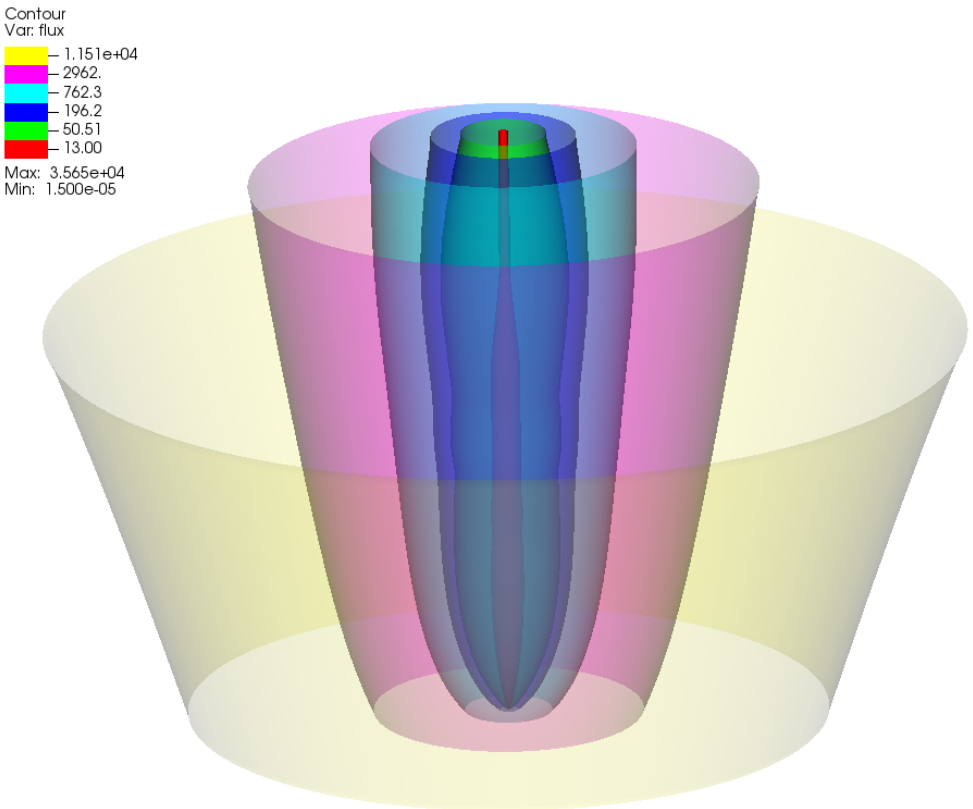

FIGURE C.1: Magnetic surfaces (surfaces of iso-magnetic flux Ψ) for K2, self-similar simulation of reference.

C.2 Numerical setup

C.2.1 Initial conditions

Let us now see how the initial conditions and the value of R_{min} were set. As a 3D initial condition, the self-similar simulations of chapters 4 and 5 are discarded: the absence of an interface forbids the development of the KH, RTI and CFI instabilities described above. And obviously, the time-dependant simulations of chapter 7 are ruled out: as they are already unstable in 2.5D, it would be hard to disentangle the 3D effects from the perturbations caused by the boundary conditions. Therefore, to initialize the 3D jet I use the 2.5D simulation of reference of the steady-state simulations of chapter 6, named O1.

I consider all the variables ($\vec{B}$, $\vec{v}$, P, ρ) of the simulation O1 at its final output, $t_f = 2.26 \times 10^6$ beyond $R_{min} = 1403$. It is represented on Figure C.2, with the boundary $R = R_{min}$ highlighted in purple. Its value was chosen to be below the lowest recollimation shock ($Z_{shock} = 1550$), but also at the exact position of a cell in the 2.5D grid. It allows the 3D cells to be in the exact same positions in each poloidal (R, θ) plane as they were in the 2.5D simulation. This is of particular importance to ensure that the initial 3D conditions are divergence-free. We have seen in section 3.1.2 that provided the initial magnetic field is divergence-free, it should stay divergence-free at machine precision during the computation. Thus O1 is divergence-free at $t_f = 2.26 \times 10^6$; and if the 3D magnetic field is initally set divergence-free, it should stay so at machine precision along the computation. Equation C.1 is the expression of the 3D divergence of the magnetic field in spherical coordinates:

$$\vec{\nabla} \cdot \vec{B} = \frac{1}{R^2}\frac{\partial(R^2 B_R)}{\partial R} + \frac{1}{R\sin\theta}\frac{\partial(B_\theta \sin\theta)}{\partial\theta} + \boldsymbol{\frac{1}{R\sin\theta}\frac{\partial B_\varphi}{\partial\varphi}} \tag{C.1}$$

In PLUTO, its computation relies on the use of face-centered magnetic fields. The sum of the first two terms is the 2.5D divergence and depends on B_R and B_θ which were already face-centered in 2D. Thus as the 3D cells are in the exact same (R, θ) positions as their 2.5D counterparts, the sum of the first two terms in the initial 3D conditions is zero. In the 2.5D simulations, the toroidal magnetic field is cell-centered while in 3D it is face-centered. However, simply setting the 3D face-centered B_φ as equal to the 2.5D cell-centered B_φ is enough to ensure that the last term in equation C.1 is zero, as it sets $\partial B_\varphi / \partial\varphi = 0$ inside the cell.

Let us make a quick recap on how the initial 3D conditions are set. I consider a cell $\mathcal{C}$ centered in $(R_\mathcal{C}, \theta_\mathcal{C}, \varphi_\mathcal{C})$ of half-widths $(\Delta R_\mathcal{C}, \Delta\theta_\mathcal{C}, \Delta\varphi_\mathcal{C})$. The values of $\vec{v}$, P and ρ were cell-centered (i.e. defined in $(R_\mathcal{C}, \theta_\mathcal{C}, \varphi_\mathcal{C})$) in 2.5D; and in 3D they remain cell-centered, and are thus set to the same value in the same position. Similarly, B_R and B_θ are face-centered in both 2.5D and 3D, i.e. respectively defined in $(R_\mathcal{C} \pm \Delta R_\mathcal{C}, \theta_\mathcal{C}, \varphi_\mathcal{C})$ and $(R_\mathcal{C}, \theta_\mathcal{C} \pm \Delta\theta_\mathcal{C}, \varphi_\mathcal{C})$; they are also set to the same value in the same position. For B_φ, the 2.5D cell-centered value is translated to the cell faces in $(R_\mathcal{C}, \theta_\mathcal{C}, \varphi_\mathcal{C} \pm \Delta\varphi_\mathcal{C})$ to set the initial 3D conditions. Naturally this is done N_φ times, with N_φ being the number of cells in the toroidal direction.

These simple conditions provide two crucial characteristics to the initial 3D state. First, it is the exact same as the final state of the 2.5D simulation O1, simply limited to $R > R_{min} = 1403$, and symmetrized around the polar axis Oz. Second, its magnetic field is divergence-free.

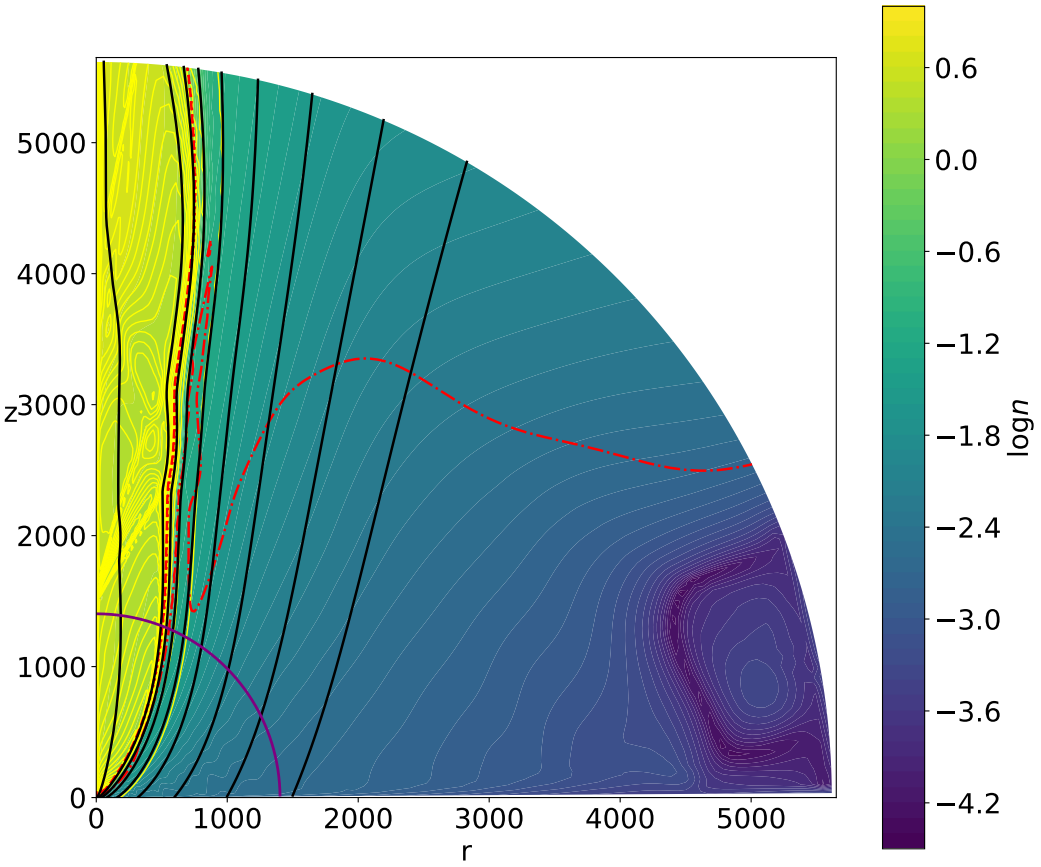

FIGURE C.2: Final state at $t_f = 2.26 \times 10^6$ of the 2.5D reference simulation O1. The legend is the same as in Figure 6.4, with $R_{min} = 1403$ highlighted in purple.

C.2.2 Boundary conditions

Naturally, as the simulations go from 2.5D to 3D, the boundary conditions need to be adapted. There are still four boundaries to the computational domain:

- The polar axis ($\theta = 0$, $R \in [R_{min}; 5650R_d]$)
- The outer boundary ($R = 5650R_d$, $\theta \in [0; \pi/2]$, $\varphi \in [0; 2\pi]$)
- The disk ($\theta = \pi/2$, $R \in [R_{min}; 5650R_d]$, $\varphi \in [0; 2\pi]$)
- The $R = R_{min}$ boundary ($R = R_{min}$, $\theta \in [0; \pi/2]$, $\varphi \in [0; 2\pi]$)

The outer boundary ($R = 5650R_d$) is kept unchanged from the 2.5D setup. "Outflow" conditions are imposed: the gradient along $\vec{u}_R$ of ρ, P, B_R, B_θ, RB_φ, v_R, v_θ and v_φ is conserved. Same as in the 2.5D setup, I use the Van Leer slope limiter to avoid spurious oscillations, and enforce a positive Lorentz force on the subalfvénic parts of the boundary.

The three other boundaries are however different from their 2.5D counterparts.

Polar axis: $\theta = 0$

As a reminder, in PLUTO the boundary conditions are set using "ghost" cells, enclosing the actual computational domain. On the outer boundary they are located at $R > 5650R_d$, on the disk at $\theta > \pi/2$ [1] and on the $R = R_{min}$ boundary at $R < R_{min}$. In these ghost zones, the variables can be set via a fixed condition, or by their values inside the domain, for example via gradient conservation ("outflow" condition).

The way the boundary conditions are handled near the polar axis is illustrated on Figure C.3. For each cell near the boundary located at φ_C, the corresponding ghost cell is also in the domain, at $\varphi_C + \pi$. For the cell-centered variables (ρ, $\vec{v}$, P), as well as the face-centered B_R and B_φ we can use standard outflow conditions described above. However, B_θ is defined at $\theta = 0$ which is degenerate, and a shift in θ accross the axis is necessary to get to the corresponding ghost face. Naturally, the $\theta = 0$ "face" is not taken into account when computing $\vec{\nabla} \cdot \vec{B}$.

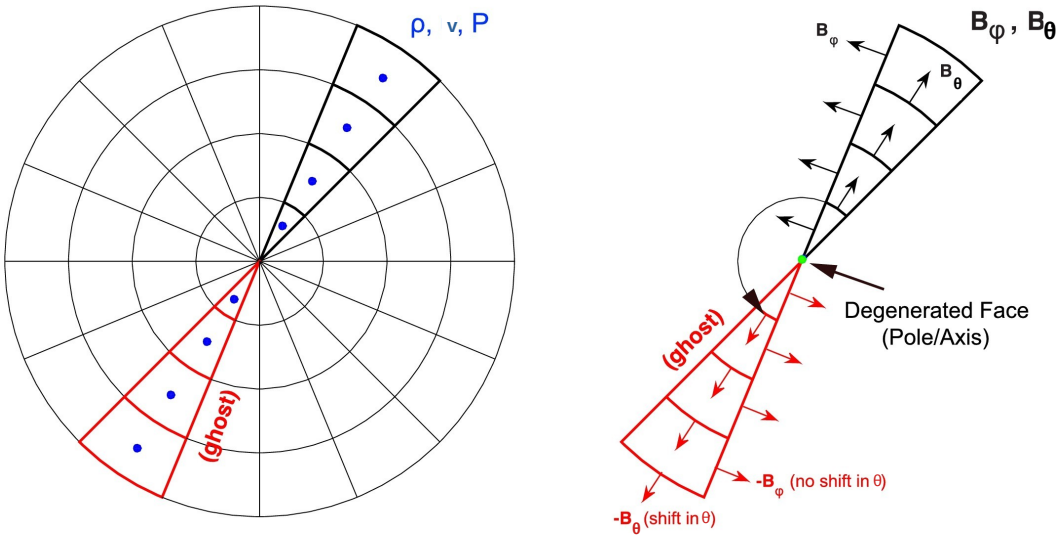

FIGURE C.3: Boundary conditions on the $\theta = 0$ polar axis of a 3D spherical grid, face-on view adapted from Figure 4 of Zhang et al., 2019. Left: Cell-centered variables (ρ, $\vec{v}$, P). Right: Face-centered variables ($\vec{B}$).

Lower boundaries: $R = R_{min}$ **and** $\theta = \pi/2$

In this 3D setup, the lower boundaries are quite different from the 2.5D setup. While in the 2.5D setup the ejection was always sub-FM and sub-Alfvénic, we see in Figure C.2 that in O1, at $R = R_{min}$ there is a significant super-FM zone at the lowest colatitudes. Then, as θ increases, the flow becomes sub-FM, then sub-Alfvénic, then sub-SM. The crossing of these critical surfaces increases the number of degrees of freedom at the $R = R_{min}$ boundary from zero to three. A simple solution is to set all variables at the boundary equal to their initial values if $v_p > V_{FM}$; then relax the B_R condition and set it as an outflow condition if $V_{FM} > v_p > V_A$; then relax B_φ if $V_A > v_p > V_{SM}$; then relax v_z if $V_{SM} > v_p$.

[1] Well not exactly because the boundary is not at $\theta = \pi/2$ but at $\theta = \pi/2 - \epsilon$ with $\epsilon = 10^{-2}$. For the sake of clarity we forget about ϵ here.

At the $\theta = \pi/2$ boundary the same conditions as in the 2.5D simulations can be used, as they are consistent with the initial conditions and the $R = R_{min}$ boundary conditions.

C.3 Ring-Average method

We have seen in section C.1 that one of the reasons of the high computing cost of 3D spherical simulations is the small cell size in the φ-direction: $\Delta\varphi_{\mathcal{C}} = r \sin\theta d\varphi$. This is problematic for the cells close to the axis, especially when they have a small size in θ. We see on the left panel of Figure C.4 that even in a grid with a regular spacing in θ, the cell size in the φ-direction can become prohibitively small. People doing disk simulations usually solve this problem by enlarging the θ-cell size close to the axis. But my jets and recollimation shocks happen close to the axis, and the cell size in the θ-direction is smaller near the axis (see Figure 3.5).

To increase $\Delta\varphi_{\mathcal{C}} = r \sin\theta d\varphi$ without changing the cell size in the θ-direction, we can increase $d\varphi$ for the cells closest to the axis. One way to do this is to use the Ring-Average method, illustrated on the right panel of Figure C.4. In a first ring, closest to the axis, the cells are clumped by groups of eight. In the next ring, the cells are clumped by groups of four and in the next two rings, they are grouped by clumps of two. The number of cells merged in each clump of the innermost ring is the Ring-Average Parameter N_{RA}, here equal to 8. It naturally has to be a power of 2, starting from $2^0 = 1$ (i.e. no Ring-Average). We see on Figure C.4 that the clumping also limits the aspect ratio, the clumps being squarer than the associated cells.

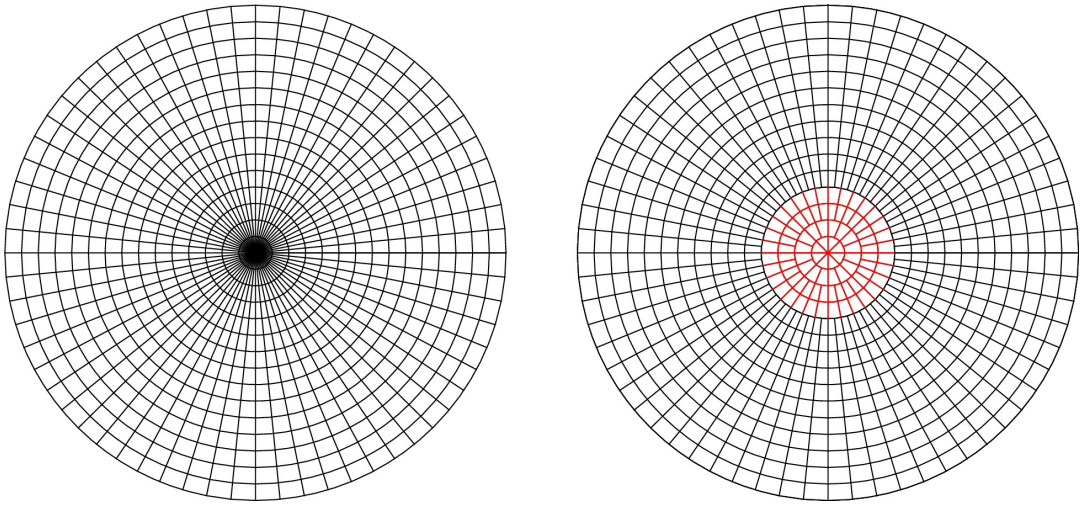

FIGURE C.4: Scheme of the Ring-Average method, adapted from Figure 1 of Zhang et al., 2019. Left: Spherical grid in the $(\vec{u}_\theta,\vec{u}_\varphi)$ plane with $N_\theta \times N_\varphi = 15 \times 64$ regularly spaced cells. Right: Same grid using the Ring-Average method with $N_{RA} = 8$.

This method is intuitive but its implementation can be tricky, especially in constrained transport. We saw in section 3.1.2 that it relies on the computation of the electric field along the edges of each face to enforce $\vec{\nabla} \cdot \vec{B} = 0$; but with the Ring-Average method $\vec{B}$ and $\vec{E}$ are not defined on the same place at the inner and outer sides of the clump.

Claudio Zanni and I had the unpleasant surprise to find out that the Ring-Average method was not implemented in the constrained transport version of PLUTO, right

in the middle of the PhD. Given the importance of the 3D simulations in the project, we decided to implement it. As in Zhang et al., 2019, we reconstruct the magnetic flux inside each clump using a piecewise reconstruction scheme. With this reconstructed magnetic flux we compute the variation of the electric field along each edge within the clump. Again, when summing all the variations to compute the total flux flowing in the cell (equation 3.10), each edge is considered twice, in opposite senses. The curious reader is referred to section 2 of Zhang et al., 2019 for details. As described in the next section, this method is now working, and could be implemented into the public constrained transport version of PLUTO, so that it benefits the community.

C.4 Scaling tests

The initial and boundary conditions, as well as the Ring-Average method, were implemented in a 3D setup. CLaudio Zani adapted the acceleration algorithm (see section 3.1.5) to 3D, but as expected it did not modify the timestep much.

To estimate the computing costs of such 3D simulations, we asked and obtained 5×10^5 HCPU of preparatory time on Irene-Rome, one of the supercomputers of TGCC (Très Grand Centre de Calcul), one of France's national CPU computing centers. With around 3×10^5 cores it is suited to very high performance computing. As my simulations are performed on $N_R \times N_\theta \times N_\varphi = 114 \times 144 \times 128$ cells the parallelization is quite high: the subdomain affected to each core can be down to a dozen cells. In practice it was down to 128 cells as the acceleration algorithm was not parallelized in the φ-direction.

Some of the performed 3D tests are described in Table C.1. The test T1 was performed with the grid on which the science simulations are expected to be run. Each timestep took 4×10^{-3} HCPU. Thus, assuming the timestep stays constant, running a simulation up to a physical time t_{end} in T_d units would take $0.30 t_{end}$ HCPU. For $t_{end} = 10^6$ as in the 2.5D runs it gives 3×10^5 HCPU, well within the range of usual 3D MHD simulations.

Name	R_{min}	N_φ	N_{RA}	dt
T1	1403	128	8	1.38×10^{-2}
T2	1	128	8	3.10×10^{-5}
T3	1	64	8	5.24×10^{-5}
T4	1	128	16	3.75×10^{-5}

TABLE C.1: Scaling of the 3D simulations. For all tests, there is $N_R \times N_\theta = 114 \times 144$ cells in a poloidal plane. R_{min}: Minimal value of the spherical radius, at the lower boundary. N_φ: Number of cells in the φ-direction. N_{RA}: Number of cells in each clump of the first ring. dt: Timestep in T_d units.

The tests T2 to T4 were performed with $R_{min} = 1$, in order to investigate the effectiveness of the Ring-Average method. From T2 to T3, the number of cells in the φ-direction is halved. From T2 to T4, the Ring-Average parameter N_{RA} is doubled: each clump is composed of twice as many cells. We see that the Ring-Average represents a significant improvement in timestep and thus computing time, but not as big as reducing the resolution. This is certainly because of the reconstruction in the φ-direction mentioned in section C.3. These tests also tell us how much we have

gained in computing time moving R_{min} from 1 to 1403. A science simulation with $R_{min} = 1$ run until $t_{end} = 10^6$ would have taken 2×10^8 HCPU and is thus fully out of reach of any supercomputer.

C.5 Summary

In this appendix, I described a 3D simulation setup made to investigate the stability of the collimated jets and the associated recollimation shocks. This setup took half a year to do, as it required the writing of the initial and boundary conditions, the implementation of various numerical methods (Ring-Average and acceleration), as well as running various tests. Unfortunately, there was no time left in the PhD to run simulations, but the now working setup should be used to run science simulations in the near future.

Appendix D

Article published in A&A

This appendix is the article that I published in Astronomy & Astrophysics with Claudio Zanni and Jonathan Ferreira (Jannaud, Zanni, and Ferreira, 2023). It corresponds to the results of chapters 4 and 5.

A&A 669, A159 (2023)
https://doi.org/10.1051/0004-6361/202244311

Astronomy & Astrophysics

Numerical simulations of MHD jets from Keplerian accretion disks

I. Recollimation shocks

T. Jannaud[1], C. Zanni[2], and J. Ferreira[1]

[1] Univ. Grenoble Alpes, CNRS, IPAG, 414 rue de la Piscine, 38400 Saint-Martin d'Hères, France
e-mail: thomas.jannaud@univ-grenoble-alpes.fr
[2] INAF – Osservatorio Astrofisico di Torino, Strada Osservatorio 20, Pino Torinese 10025, Italy

Received 20 June 2022 / Accepted 23 October 2022

ABSTRACT

Context. The most successful scenario for the origin of astrophysical jets requires a large-scale magnetic field anchored in a rotating object (black hole or star) and/or its surrounding accretion disk. Platform jet simulations, where the mass load onto the magnetic field is not computed by solving the vertical equilibrium of the disk but is imposed as a boundary condition, are very useful for probing the jet acceleration and collimation mechanisms. The drawback of such simulations is the very large parameter space: despite many previous attempts, it is very difficult to determine the generic results that can be derived from them.
Aims. We wish to establish a firm link between jet simulations and analytical studies of magnetically driven steady-state jets from Keplerian accretion disks. In particular, the latter have predicted the existence of recollimation shocks – due to the dominant hoop stress –, which have so far never been observed in platform simulations.
Methods. We performed a set of axisymmetric magnetohydrodynamics (MHD) simulations of nonrelativistic jets using the PLUTO code. The simulations are designed to reproduce the boundary conditions generally expected in analytical studies. We vary two parameters: the magnetic flux radial exponent α and the jet mass load κ. In order to reach the huge unprecedented spatial scales implied by the analytical solutions, we used a new method allowing us to boost the temporal evolution.
Results. We confirm the existence of standing recollimation shocks at large distances. As in self-similar studies, their altitude evolves with the mass load κ. The shocks are weak and correspond to oblique shocks in a moderately high, fast magnetosonic flow. The jet emitted from the disk is focused toward the inner axial spine, which is the outflow connected to the central object. The presence of this spine is shown to have a strong influence on jet asymptotics. We also argue that steady-state solutions with $\alpha \geq 1$ are numerically out of range.
Conclusions. Internal recollimation shocks may produce observable features such as standing knots of enhanced emission and a decrease in the flow rotation rate. However, more realistic simulations (e.g. fully three-dimensional) must be carried out in order to investigate nonaxisymmetric instabilities and with ejection only from a finite zone in the disk, so as to to verify whether these MHD recollimation shocks and their properties are maintained.

Key words. magnetohydrodynamics (MHD) – methods: numerical – ISM: jets and outflows – galaxies: active

1. Introduction

Astrophysical jets are commonly observed in most, if not all, types of accreting sources. They are emitted from young stellar objects (YSOs; Bally et al. 2007; Ray et al. 2007; Ray & Ferreira 2021), active galactic nuclei (AGNs) and quasars (Boccardi et al. 2017), close interacting binary systems (Fender & Gallo 2014; Tudor et al. 2017), and even post-AGB stars (Bollen et al. 2017). Despite the different central objects (be it a black hole, a protostar, a white dwarf, or a neutron star), these jets share several properties: (i) they are supersonic collimated outflows with small opening angles, (ii) the asymptotic speeds scale with the escape speed from the potential well of the central object, and (iii) they carry away a sizeable fraction of the power released in the accretion disk. As the only common feature shared by all these different astrophysical objects is the existence of an accretion disk, it is natural to seek a jet model that is related to the disk and not to the central engine. This universal approach is further consistent with the accretion–ejection correlations observed in these objects (see e.g., Merloni & Fabian 2003; Corbel et al. 2003; Gallo et al. 2004; Coriat et al. 2011; Ferreira et al. 2006; Cabrit 2007 and references therein).

Despite these general common trends, astrophysical jets do show some differences in their collimation properties. For instance, the core-brightened extragalactic jets, classified as FRI jets after Fanaroff & Riley (1974), appear conical and show large-scale wiggles (see e.g., Laing & Bridle 2013, 2014 and references therein). On the contrary, the edge-brightened FRII jets appear nearly cylindrical, with a terminal hotspot (Laing et al. 1994; Boccardi et al. 2017). Most of the jets imaged with very long baseline interferometry do not appear as continuous flows, but can be modeled as a sum of discrete features, known as blobs or knots, usually associated with shocks (Zensus 1997). Those shocks are assumed to originate either from pressure mismatches at the jet boundary with the external medium or from major changes at the base of the flow (e.g., new plasma ejections or directional changes), with some of these knots being stationary features (e.g., Lister et al. 2009, 2013; Walker et al. 2018; Doi et al. 2018; Park et al. 2019).

On the other hand, jets from young forming stars do not seem to have such a clear FRI/FRII dichotomy and often display evidence of a conflictual interaction (shocks) with the ambient cloud medium (Reipurth & Bally 2001). This might be consistent with the suspicion that the FR dichotomy would only be a consequence of the jet interaction with its environment, with low-power jets remaining undisrupted and forming hotspots in lower mass hosts (Mingo et al. 2019). However, protostellar jets might also have intrinsic collimation properties different from those of extragalactic jets, possibly because they are nonrelativistic outflows. This is an open question.

Since the seminal model of Blandford & Payne (1982; hereafter BP82), it is known that a large-scale vertical magnetic field threading an accretion disk is capable of accelerating the loaded disk material up to super-fast magnetosonic speeds. This acceleration, usually termed magneto-centrifugal, goes along with an asymptotic collimation of the ejected plasma thanks to the magnetic tension associated with the toroidal magnetic field (hoop stress). In this semi-analytical model, a self-similar ansatz has been used allowing the full set of stationary ideal magnetohydrodynamic (MHD) equations to be solved. Later, this self-similar jet model was generalized in different ways by altering the magnetic field distribution (Contopoulos & Lovelace 1994; Ostriker 1997), thermal effects (Vlahakis et al. 2000; Ceccobello et al. 2018) and was even extended to the relativistic regime (Li et al. 1992; Vlahakis & Königl 2003; Polko et al. 2010, 2014). However, it is unclear whether or not self-similarity affects the overall jet collimation properties. Not only are both the axis and the jet-ambient medium region not taken into account, but the final outcome of the jets (i.e., acceleration efficiency, jet kinematics and opening angle, presence of radial oscillations, or even shocks) may well also be impacted by the imposed geometry.

Using the only class of self-similar jet models smoothly connected to a quasi-Keplerian accretion disk, Ferreira (1997; hereafter F97) showed that these super-fast magnetosonic jets systematically undergo a refocusing toward the axis (see also Polko et al. 2010). Such a recollimation is due to the dominant effect of the internal hoop stress and has nothing to do with a pressure mismatch at the jet–ambient medium interface proposed to explain knotty features in extragalactic jets (Komissarov & Falle 1998; Perucho & Martí 2007; Perucho 2020). According to F97, recollimation would be generic to MHD jets anchored over a large range of Keplerian accretion disks. This is indeed verified for warm outflows (Casse & Ferreira 2000a) and weak magnetic fields (Jacquemin-Ide et al. 2019).

While MHD recollimation is also seen in nonself-similar works (e.g., Pelletier & Pudritz 1992), other strong assumptions are usually made, leaving the question of the jet asymptotics open. Heyvaerts & Norman (1989) used another approach based on the electric poloidal current (or Poynting flux) still present at infinity. These authors showed that any stationary axisymmetric magnetized jet will collimate at large distances from the source to paraboloids or cylinders, depending on whether or not the asymptotic electric current vanishes. This important theorem was later generalized (Heyvaerts & Norman 2003a) by taking into account the issue of current closure and its effect on the geometry of the solution (Okamoto 2001, 2003). However, the theorem only addresses the asymptotic electric current, and it is unclear how much of this current is actually left as no simple connection with the source can be made.

Connecting the asymptotic electric current to the source is naturally done with time-dependent MHD simulations. Those reaching the largest spatial scales treat the accretion disk as a boundary condition, allowing the jet dynamics to be studied independently of the disk (Ustyugova et al. 1995, 1999; Ouyed & Pudritz 1997a,b, 1999; Krasnopolsky et al. 1999, 2003; Ouyed et al. 2003; Anderson et al. 2005, 2006; Fendt 2006; Pudritz et al. 2006; Porth & Fendt 2010; Porth & Komissarov 2015; Staff et al. 2010, 2015; Stute et al. 2014; Barniol Duran et al. 2017; Tesileanu et al. 2014; Tchekhovskoy & Bromberg 2016; Ramsey & Clarke 2019). The drawback of these platform jet simulations is their huge degree of freedom, which is attributable to the fact that several distributions must be specified at the lower injection boundary. It has therefore been very difficult to determine the exact generic results on jet collimation that can be derived from them.

In summary, despite many theoretical and numerical studies, no connection has been firmly established between the jet-launching conditions and the jet-collimation properties at observable scales. This work is the first of a series designed to bridge this gap. Our approach here is to assess whether the general results obtained within the self-similar framework still hold in full 2D time-dependent simulations. We will address in particular whether the existence of recollimation shocks is indeed unavoidable for the physical conditions expected in Keplerian accretion disks, as proposed by F97.

As a consequence of this approach, we focus only on steady-state jets, allowing us to directly confront our simulations with MHD jet theory. It is clear that most if not all astrophysical jets exhibit time-dependant features; see for example Cheung et al. (2007) for M87 or Bally et al. (2007) for young stars. However, our goal is not to reproduce a specific astrophysical jet, but instead to deduce the generic behaviors of MHD jets emitted from Keplerian accretion disks.

The paper is organized as follows. Section 2 describes our numerical setup and boundary conditions, which mimic an axial spine (related to the central object) surrounded by a self-similar cold jet. As analytical studies require huge spatial and temporal scales, a special temporal numerical scheme has been designed. Our reference simulation, which corresponds to a typical BP82 jet, is described in length in Sect. 3. We show that recollimation shocks are indeed obtained in agreement with the analytical theory. This is the first time that such shocks are obtained self-consistently, showing that these are not artificial biases due to the mathematical ansatz used, but consequences of the jet-launching conditions. A parametric study is presented in Sect. 4, where we vary the magnetic flux exponent α and the jet mass load κ, confirming the striking qualitative correspondance between our numerical simulations and analytical solutions. In particular, we show that the asymptotic jet collimation depends mostly on the exponent α. However, the existence of an axial spine introduces quantitative differences hinting at a possible role of the central object in affecting the collimation properties of the jets emitted by the surrounding disk. Our results are finally confronted to the wealth of previous 2D numerical simulations in Sect. 5 and we conclude in Sect. 6.

2. MHD simulations of jets from Keplerian disks

2.1. Physical framework and governing equations

We intend to study the collimation properties of magnetically driven jets emitted from Keplerian accretion disks, as depicted in Fig. 1. The disk is settled from an inner radius R_d to an outer radius $R_{\rm ext} = 5650.4R_d$ and is assumed to be orbiting around a central object of mass M located at the center of our coordinate system. The disk itself is not computed and we assume that it behaves like a JED, with consistent prescribed boundary conditions. As we use a spherical grid, the central object as well as its interaction with the disk are assumed to occur inside a sphere

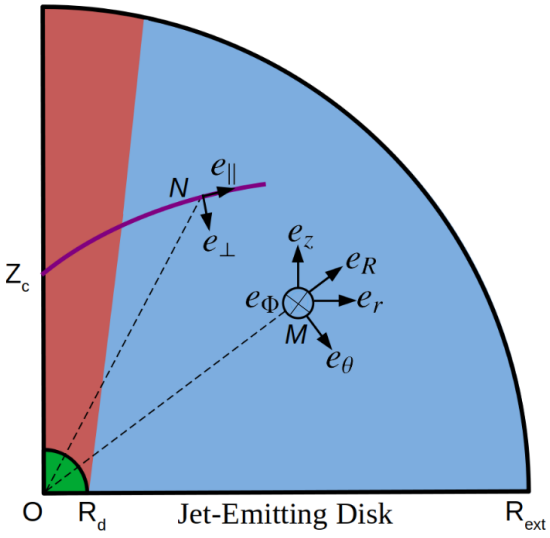

Fig. 1. Sketch of our computational domain. The central object and its interaction with the innermost disk are located below the inner boundary at R_d (green region), the near-Keplerian jet-emitting disk (JED) being established from R_d to the end of the domain $R_{\rm ext}$. An axial outflow (the spine) is emitted from the central regions (in red) and the jet is emitted from the JED (in blue). The solid purple line represents a recollimation shock surface starting on the axis at a height Z_c. For each point N lying on this surface, we use local poloidal unit vectors $(\boldsymbol{e}_\perp, \boldsymbol{e}_\parallel)$, respectively perpendicular and parallel to the shock surface. Also, at any point M inside the domain, we either use spherical $(\boldsymbol{e_R}, \boldsymbol{e_\theta}, \boldsymbol{e_\phi})$ or cylindrical $(\boldsymbol{e_r}, \boldsymbol{e_\phi}, \boldsymbol{e_z})$ coordinates.

of radius R_d (the green zone in Fig. 1). This sphere defines the inner boundary discussed below.

We further assume that a large-scale magnetic field is threading both the disk and the central object. The existence of this field allows the production of two outflows, one from the disk (blue region in Fig. 1) and one from the central spherical region (red region in Fig. 1). Hereafter, we always refer to the disk-emitted outflow as the "jet", and to the outflow emitted from the spherical region (green zone in Fig. 1) as the "spine". As our goal is to focus on the dynamics of the jet itself, we try to limit the influence of the spine as much as possible.

Two systems of coordinates centered on the mass M are used, spherical (R, θ, ϕ) and cylindrical (r, ϕ, z). Both the spine and the jet are assumed to be in ideal MHD and we numerically solve the usual set of MHD equations. This includes mass conservation

$$\frac{\partial \rho}{\partial t} + \nabla \cdot (\rho \boldsymbol{u}) = 0, \tag{1}$$

where ρ is the density and $\boldsymbol{u}$ the flow velocity, and the momentum equation is

$$\frac{\partial \rho \boldsymbol{u}}{\partial t} + \nabla \cdot \left[\rho \boldsymbol{u}\boldsymbol{u} + \left(P + \frac{\boldsymbol{B}\cdot\boldsymbol{B}}{2\mu_o} \right) - \frac{\boldsymbol{B}\boldsymbol{B}}{\mu_o} \right] = -\rho \nabla \Phi_G, \tag{2}$$

where P is the thermal pressure, $\boldsymbol{B}$ the magnetic field, and $\Phi_G = -GM/R$ the gravitational potential due to the central mass.

The evolution of the magnetic field is determined by the induction equation,

$$\frac{\partial \boldsymbol{B}}{\partial t} + \nabla \times (\boldsymbol{B} \times \boldsymbol{u}) = 0. \tag{3}$$

As we focus on highly supersonic flows, we decided to derive the pressure P and internal energy by solving the entropy equation,

$$\frac{\partial \rho S}{\partial t} + \nabla \cdot (\rho S \boldsymbol{u}) = 0, \tag{4}$$

where $S = P/\rho^\Gamma$ is the specific entropy and $\Gamma = 1.25$ is the polytropic index (the same for all our simulations). This simple advection equation guarantees that the pressure does not assume nonphysical (e.g., negative) values. But on the other hand, it does fail to provide the correct entropy jump in the shocks. However, as long as the thermal energy of the flow remains negligible compared to the kinetic and magnetic energy, this should not present a problem.

Thanks to axisymmetry, the poloidal magnetic field can be computed using the magnetic flux function Ψ (which corresponds to $R \sin\theta A_\phi$, where $\boldsymbol{A}$ is the vector potential),

$$B_R = \frac{1}{R^2 \sin\theta} \frac{\partial \Psi}{\partial \theta} \qquad B_\theta = -\frac{1}{R \sin\theta} \frac{\partial \Psi}{\partial R}, \tag{5}$$

which already verifies $\nabla \cdot \boldsymbol{B} = 0$. An axisymmetric magnetized jet can therefore be seen as a bunch of poloidal magnetic surfaces defined by $\Psi(R, \theta) = $ constant, nested around each other and anchored on the disk for the jet and in the central object for the spine.

In steady state, Eqs. (1) to (4) lead to the existence of the following five MHD invariants, namely quantities that remain constant along each magnetic surface (Weber & Davis 1967):

- the mass flux to magnetic flux ratio $\eta(\Psi) = \mu_o \rho u_p / B_p$,
- the rotation rate of the magnetic surface $\Omega_*(\Psi) = \Omega - \eta B_\phi / (\mu_0 \rho r)$,
- the total specific angular momentum carried away by that surface $L(\Psi) = \Omega r^2 - r B_\phi / \eta$,
- the Bernoulli invariant $E(\Psi) = \frac{u^2}{2} + H + \Phi_G - \Omega_* r B_\phi / \eta$,
- the specific entropy $S(\Psi) = P/\rho^\Gamma$,

where $\Omega = u_\phi / r$ and $H = \frac{\Gamma}{\Gamma - 1} \frac{P}{\rho}$ is the specific enthalpy. We make use of these relations when designing boundary conditions.

2.2. Numerical setup

We solve the above set of equations using the MHD code PLUTO[1] (Mignone et al. 2007). We configured PLUTO to use a second-order linear spatial reconstruction with a monotonized-centered limiter on all the variables. This method provides the steeper linear reconstruction compatible with the stability requirements of the scheme. A flatter and more diffusive linear reconstruction is employed in a few cells around the rotation axis to dampen numerical spurious effects that typically appear in these zones due to the discretization of the equations around the geometrical singularity of the axis. The HLLD Riemann solver of Miyoshi & Kusano (2005) is employed to compute the intercell fluxes. This solver is one of the best suited to properly capture Alfvén waves, a crucial element in properly modeling trans-Alfvénic flows. So as to match the order of the spatial reconstruction, we chose a second-order Runge-Kutta scheme to advance the equations in time. The $\nabla \cdot \boldsymbol{B} = 0$ condition is ensured by employing a constrained transport (CT) scheme, enforcing that constraint at machine accuracy.

The two-dimensional computational domain is discretized using spherical coordinates (R, θ) assuming axisymmetry around the rotation axis of the disk. The domain encompasses a spherical sector going from the polar axis ($\theta = 0$) to the surface of the disk that is assumed to be $\theta = \pi/2$ for simplicity, and is resolved with $N_\theta = 266$ points in the θ direction. The cell size in the θ direction is mostly uniform, but decreases on a few cells near the axis. This is essential to our setup, as the expected collimation shocks are formed near the axis: an overly low resolution in

[1] PLUTO is freely available at http://plutocode.ph.unito.it

this zone would prevent their formation. In the radial direction, the grid goes from R_d to $R_{\rm ext} = 5650.4R_d$ with $N_R = 1408$ points in a logarithmic spacing ($\Delta R \propto R$) so as to make sure the cells remain approximately square ($\Delta R \approx R\Delta\theta$) far from the axis.

We choose such a huge numerical domain because our goal is to capture the recollimation shocks predicted in the self-similar solutions of F97. According to their Fig. 6, those shocks may occur at altitudes spanning from several hundred to a thousand times the jet launching radius. Our spherical grid with a ratio of 5650.4 therefore provides a suitable range to observe such shocks. The drawback of these huge spatial scales is of course the terrible contrast in timescales. The Keplerian time scaling in $r^{3/2}$ means that in order to compute a full orbit at the outer disk edge, the inner one should have completed over 4×10^5 orbits. This would be barely affordable if we were to use a standard evolutionary scheme. In order to achieve such long timescales, we designed a specific method that accelerates the numerical integration using larger and larger time steps to evolve the equations as the solution starts to converge towards a steady-state. This method is very successful and allowed us to significantly boost the evolution of our jets (see Appendix A).

2.3. Initial conditions

Our initial magnetic field is assumed to be potential, which leads to a second-order partial differential equation on $\Psi(R, \theta)$. In order to represent suitable self-similar solutions, we solve this equation by assuming

$$\Psi = \Psi_d (R/R_d)^\alpha \Phi(\theta)\,, \tag{6}$$

where the function $\Phi(\theta)$ has been determined assuming that the initial field is potential, that is, current-free and force-free ($J_\phi = 0$).

The exponent α is a free parameter of the model leading to $B_R \propto B_\theta \propto R^{\alpha-2}$. For $\alpha = 0$, field lines are conical, for $\alpha = 1$ they are parabolic, and $\alpha = 2$ describes a constant (straight) vertical field. The seminal BP82 solution is for $\alpha = 3/4$.

As the magnetic field is potential, no magnetic force is initially imposed on the plasma. It is therefore assumed to be in spherically symmetric hydrostatic equilibrium ($\boldsymbol{u} = 0$) with $\mathrm{d}P/\mathrm{d}R = -\rho GM/R^2$. We choose the following trivial solution:

$$\begin{aligned} \rho &= \rho_a \left(\frac{R}{R_d}\right)^{2\alpha-3} \\ P &= \frac{1}{4-2\alpha}\frac{\rho_a GM}{R_d}\left(\frac{R}{R_d}\right)^{2\alpha-4}\,. \end{aligned} \tag{7}$$

The sound speed C_s is defined as $C_s^2 = \partial P/\partial\rho = \Gamma P/\rho$. In the following, ρ_a refers to the density at the axis immediately above the central sphere.

2.4. Boundary conditions

Boundary conditions must be imposed at the polar axis ($\theta = 0$, R from R_d to $R_{\rm ext}$), at the outer frontier ($R = R_{\rm ext}$, θ from 0 to $\pi/2$), at the JED surface ($\theta = \pi/2$, R from R_d to $R_{\rm ext}$), and at the spine boundary ($R = R_d$, θ from 0 to $\pi/2$). On the polar axis, usual proper reflecting boundary conditions are imposed on all quantities. The special treatment done for the other three boundaries is described, especially for the JED and spine boundaries where mass is being injected.

2.4.1. Outer boundary ($R = R_{\rm ext}$)

"Outflow" conditions are imposed at the outer frontier: for ρ, P, B_R, B_θ, RB_ϕ, u_R, u_θ and u_ϕ, the gradient along the radial direction is conserved, and we use the Van Leer slope limiter to avoid spurious oscillations. Additionally, we enforce a positive toroidal Lorentz force on the subalfvénic part of this boundary.

2.4.2. Jet generation: the jet-emitting disk ($\theta = \pi/2$)

We need to specify eight quantities $(\rho, \boldsymbol{u}, \boldsymbol{B}, P)$ that must be representative of the fields expected at the surface of a JED. As the lifted material gets accelerated along a field line, its poloidal velocity will become larger than the slow magnetosonic $V_{\rm sm}$, poloidal Alfvén $V_{\rm Ap}$, and fast magnetosonic $V_{\rm fm}$ phase speeds. Crossing each of these critical speeds defines a regularity condition that determines one quantity at the jet basis, therefore leaving five free functions to be specified. However, we wish to control the mass loss from the JED, which requires that the injected outflow be already super-slow magnetosonic (hereafter super-SM). We therefore have to impose six functions at the JED boundary, leaving two free to adjust over time, B_ϕ and B_R, the latter controlling the magnetic field bending.

Our choice of boundary conditions at $\theta = \pi/2$ (so that $R = r$) is therefore as follows:

$$\begin{aligned} \rho &= \rho_d \left(\frac{R}{R_d}\right)^{2\alpha-3} \\ P &= \rho_d \frac{C_{s_d}^2}{\Gamma}\left(\frac{R}{R_d}\right)^{2\alpha-4} \\ B_\theta &= -B_d \left(\frac{R}{R_d}\right)^{\alpha-2} \\ u_\theta &= -u_d \left(\frac{R}{R_d}\right)^{-1/2} \\ u_R &= u_\theta \frac{B_R}{B_\theta} \\ u_\phi &= \Omega_* r + u_\theta \frac{B_\phi}{B_\theta}, \end{aligned} \tag{8}$$

where Ω_* is the angular velocity of the magnetic surfaces (an MHD invariant in steady-state). We assume $\Omega_* = \Omega_K = \sqrt{GM/r^3}$, in agreement with a near Keplerian accretion disk, leaving four normalizing quantities, ρ_d, C_{s_d}, B_d, and u_d, to be specified at R_d. These distributions are consistent with a self-similar JED and describe an ideal steady MHD flow with $\boldsymbol{u}_p \parallel \boldsymbol{B}_p$[2], anchored on a disk that imposes magnetic field lines rotating at the Keplerian angular velocity Ω_K. We note that the fixed component of the magnetic field threading the disk (B_θ) is actually the initial condition to conserve the magnetic flux injected into the computational domain, and only B_R is allowed to vary in response to the jet dynamics.

In order to pick up values at R_d that are consistent with the jet calculations performed by BP82 or F97, we express the JED boundary conditions as a function of four dimensionless parameters: (1) the jet density ρ_d is fixed with respect to the density at the polar axis using $\rho_d = \delta\rho_a$; (2) the disk sound speed (temperature) is defined relative to the Keplerian speed with $\epsilon = C_{sd}/V_{Kd}$; (3) the magnetic field strength B_d is controlled by measuring the θ component of the poloidal Aflvén speed with respect to the

[2] With this condition, the ϕ component of the electric field $\boldsymbol{E} = -\boldsymbol{u}\times\boldsymbol{B}$ is zero and the magnetic flux distribution does not change in time.

Keplerian speed, namely $\mu = V_{Ad}/V_{Kd} = B_d\sqrt{R_d/(\mu_o\rho_d GM)}$; and (4) the (vertical) injection velocity u_d can be determined with the well-known mass-loading parameter κ introduced by BP82 using

$$\kappa = \frac{\mu_o\rho_d u_d V_{Kd}}{B_d^2} = \frac{u_d V_{Kd}}{V_{Ad}^2} = \frac{u_d}{V_{Kd}}\frac{1}{\mu^2}\,. \tag{9}$$

By fixing $u_d/V_{Kd} = 0.1$ for all the simulations, we obtain $\kappa = 0.1/\mu^2$. In order to be able to fix the value of the injection speed u_d and therefore the JED mass flux, we must require that $u_p > V_{sm}$. As we are mostly interested in producing cold MHD outflows, we assume $\epsilon = 0.01$ so that the θ component of the sonic Mach number is $M_{s\theta} = u_d/C_s = u_d/V_{Kd}\epsilon = 10$. As the total poloidal speed at the jet boundary is larger than u_d, the sonic Mach number $M_s = u_p/C_s > 10$. As the poloidal Alfvén speed at the disk surface is much larger than the sound speed, $C_s > V_{sm}$ and $M_s > 1$ is enough to warrant a super-SM condition.

We decided to vary the mass load and the disk Alfvén speed by only changing the disk density ρ_d (and keeping the injection speed u_d and the disk magnetic field B_d constant for all the simulations). As a consequence, the density contrast δ can be expressed as a function of μ (or κ). We assume the relation $\delta = 100/\mu^2 = 1000\kappa$. We highlight the fact that with our parametrization the JED boundary conditions are determined by only one dimensionless parameter, typically κ, while the other two free parameters μ and δ are determined as a function of κ, and ϵ is fixed for all the simulations.

2.4.3. Spine generation: the central object ($R = R_d$)

In the spine, we follow a similar methodology to that in the JED and specify six quantities along the inner spherical boundary at R_d. This again leaves two quantities that are free to evolve, B_ϕ and B_θ. In order to conserve the magnetic flux injected into the computational domain, we fix $B_R(\theta)$ to its initial value. We note that, as the $B_\theta(R)$ profile is fixed along the JED boundary ($\theta = \pi/2$) and $B_R(\theta)$ is kept constant in time along the spine boundary ($R = R_d$), the total poloidal field and its inclination B_R/B_θ do not change with time at the inner radius of the disk ($R = R_d, \theta = \pi/2$). The strength of the magnetic field is already determined by the value of μ chosen in the JED. As the outflowing material leaving the central region is in ideal MHD and we are looking for a steady jet, one has $u_\theta = u_R B_\theta/B_R$. This leaves us with the four distributions ρ, C_s, u_R, and u_ϕ to be specified along θ.

If the central object possesses its own magnetosphere, then R_d might be considered as the disk truncation radius. What would be encapsulated within R_d could then be a complex combination of a stellar wind plus any type of magnetospheric wind (steady or not; see for instance Zanni & Ferreira 2013 and references therein). If the central object is instead a black hole, then R_d might be considered as the innermost stable circular orbit and what is hidden inside R_d would highly depend on the black hole spin. While a nonrotating black hole would provide no outflow, a rather strong magnetic flux concentration is seen to occur in GRMHD simulations of spinning black holes, leading to the generation of powerful outflows through the Blandford-Znajek process (see e.g., Blandford & Znajek 1977; Tchekhovskoy et al. 2010; Liska et al. 2018 and references therein).

However, our goal is to study the outcome of the jet emitted from the disk. We therefore decided to minimize the influence of the spine as much as possible. This was found to be an almost impossible task; details are given below. As pointed out in early works on magnetized rotating objects (e.g., Ferreira & Pelletier 1995), the jet power depends on the available electromotive force (emf) $e = \int \boldsymbol{E}_m \cdot \mathbf{d}\boldsymbol{l} = \int(\boldsymbol{u}\times\boldsymbol{B}_p)\cdot\mathbf{d}\boldsymbol{l}$. While the disk provides an emf $e_{\rm disk} \simeq \int \Omega_K r B_z \mathrm{d}r$, the central region provides $e_{\rm obj} \simeq \int \Omega r B_R R_d \mathrm{d}\theta$. An obvious way to decrease $e_{\rm obj}$ is therefore to allow Ω to decrease as one goes from the disk to the pole. We therefore use (in agreement with steady-state ideal MHD) $u_\phi = \Omega_* r + u_R B_\phi/B_R$, with magnetic surfaces rotating as

$$\Omega_* = \Omega_a(1 - f(\theta)) + \Omega_{Kd} f(\theta), \tag{10}$$

where $f(\theta)$ is a spline function varying smoothly from zero at $\theta = 0$ to unity $\theta = \pi/2$ (see Appendix B). Most of the simulations presented in this paper were done with $\Omega_a = 0$ (but not all, see Sect. 4.3). This choice is consistent with a nonrotating black hole but also with an innermost disk radius (our R_d) well below the co-rotation radius in the case of a star.

The fixed radial speed is defined through the sonic Mach number M_{sR}, by $u_R = M_{sR}C_s$. For M_{sR} we assume a constant value along θ that can be derived from the JED boundary conditions by assuming its continuity at the inner disk radius R_d, $M_{sR} = M_{s\theta}|B_R/B_\theta|_d = 10|B_R/B_\theta|_d > 1$. As the field inclination at the inner disk radius $|B_R/B_\theta|_d$ is constant, also M_{sR} does not change with time. The sound speed at the base of the spine is computed as

$$C_s = C_{sa}(1 - f(\theta)) + C_{sd} f(\theta), \tag{11}$$

where the sound speed on the axis C_{sa} is computed so as to verify the Bernoulli integral $E_a = E(\theta = 0)$ at the axis. As the MHD contribution vanishes on the axis, one directly obtains

$$C_{sa}^2 = \frac{GM}{R_d}\frac{1 + e_a}{\frac{1}{2}M_{sR}^2 + \frac{1}{\Gamma - 1}} \tag{12}$$

and

$$u_{Ra}^2 = \frac{GM}{R_d}\frac{1 + e_a}{\frac{1}{2} + \frac{1}{M_{sR}^2(\Gamma - 1)}}\,, \tag{13}$$

where u_{Ra} is the injection radial speed on the axis and $e_a = E_a R_d/GM$ is the Bernoulli integral normalized to the gravitational energy at R_d and will be used as a parameter to fix the axial spine temperature. We note that the normalized Bernoulli integral for the jet at R_d writes $e_d = \lambda_d - 3/2 + \epsilon^2/(\Gamma - 1)$, where $\lambda = L(\Psi)/\sqrt{GMr_o}$ is the magnetic lever arm parameter, measured here at the anchoring radius $r_o = R_d$. As our jets are cold, enthalpy plays no role and e_d is mostly determined by λ (which is known only once the simulation has converged to a steady state). For our simulations, we expect a λ of around 10 (see our parameter space Fig. 15). We therefore fix $e_a = 2$ in order to obtain a spine with a smaller energetic content than the surrounding jet. We note that, with our choice of parameters, the injection speed along the axis, set in Eq. (13), is higher than the escape speed. As the flow is cold and there is no magneto-centrifugal acceleration along the symmetry axis, the flow will gradually slow down along R in the spine from this very high speed in its core. The spine flow can cross the Alfvén and fast-magnetosonic critical points due to a decrease of the magnetic field intensity, not thanks to a flow acceleration.

Finally, for the density, we need to smoothly connect its axial value ρ_a to the much larger value injected at the disk surface ρ_d. We choose to do this by computing $\rho(\theta) = \eta B_R/(\mu_o u_R)$, with the MHD invariant η following

$$\eta = \eta_a(1 - f(\theta)) + \eta_d f(\theta), \tag{14}$$

with η_a and η_d being fully determined (see Appendix B). This method ensures that the mass flux to magnetic flux ratio has a smooth variation from the disk to the axis. For numerical stability reasons, as the strongest magnetic field is on the axis, the density in the code is normalized to ρ_a, providing a dimensionless density at the axis of 1.

2.5. Summary of parameters and normalization

Each simulation is entirely determined by the following dimensionless parameters and quantities: the radial exponent of the magnetic field α; the Bernoulli parameter e_a (equal to 2 for most cases) and the spine angular frequency on the axis Ω_a (equal to 0 in most simulations); and the cold jet parameters: $\kappa, \mu = \sqrt{0.1/\kappa}$, $\delta = 1000\kappa$, $\epsilon = 0.01$.

With our choices, we ensure that the injected flow is everywhere super-SM and that the main emf is due the JED, which is magnetically launching a cold jet. The profiles of several quantities along the magnetic flux near the lower boundary (inner spherical boundary and disk) reached by our reference simulation K2 at the final time can be seen in Fig. B.1.

This leaves us with only two free parameters, α and κ. We do not explore their whole range here but keep them within the parameter space of jets from JEDs as obtained by F97 but also by the solutions of Contopoulos & Lovelace (1994) and the simulations of Ouyed & Pudritz (1997a). The radial exponent α is varied from 10/16 to 15/16. In a strict self-similarity, this exponent must be consistent with the underlying disk, namely $\alpha = (12+8\xi)/16$, where ξ is the disk ejection efficiency defined with the disk accretion rate as $\dot{M}_a(r) \propto r^{\xi}$ (Ferreira & Pelletier 1995). However, our simulations are not strictly self-similar because of the presence of the axis and its spine, and so we also explore a slightly smaller α than the fiducial BP82 value $\alpha = 12/16$. As discussed further below, values of $\alpha \geq 1$ are numerically problematic. The mass load parameter κ is varied between 0.05 and 1, which is a range globally consistent with BP82 and F97 jets, both solutions leading to a flow recollimation toward the axis.

The MHD equations have been solved with PLUTO and the results will be presented in dimensionless units. Unless otherwise specified, lengths are given in units of R_d, velocities in units of $V_{Kd} = \sqrt{GM/R_d}$, time in units of $T_d = R_d/V_{Kd}$, densities in units of ρ_a, magnetic fields in units of $B_d = V_{Kd}\sqrt{\mu_o \rho_a}$, mass fluxes in units of $\dot{M}_d = \rho_a R_d^2 V_{Kd}$ and powers in units of $P_d = \rho_a R_d^2 V_{Kd}^3$. In order to be more specific, we translate these quantities for the case of a young star, assuming a star of one solar mass with an innermost disk radius $R_d = 0.1$ au, namely

$$
\begin{aligned}
V_{Kd} &= 94.3 \left(\frac{M}{M_\odot}\right)^{1/2} \left(\frac{R_d}{0.1\times \mathrm{au}}\right)^{-1/2} \ \mathrm{km\,s^{-1}} \\
\dot{M}_d &= 3.3\times 10^{-10} \left(\frac{\rho_a}{10^{-15}\mathrm{g\,cm^{-3}}}\right) \left(\frac{M}{M_\odot}\right)^{1/2} \left(\frac{R_d}{0.1\,\mathrm{au}}\right)^{3/2} M_\odot\,\mathrm{yr^{-1}} \\
P_{\rm jet} &= 6.7\times 10^{41} \left(\frac{\rho_a}{10^{-15}\mathrm{g\,cm^{-3}}}\right) \left(\frac{M}{M_\odot}\right)^{3/2} \left(\frac{R_d}{0.1\,\mathrm{au}}\right)^{1/2} W \\
B_d &= 10.6 \left(\frac{\rho_a}{10^{-15}\mathrm{g\,cm^{-3}}}\right)^{1/2} \left(\frac{M}{M_\odot}\right)^{1/2} \left(\frac{R_d}{0.1\,\mathrm{au}}\right)^{-1/2} \mathrm{G} \\
T_d &= 1.8 \left(\frac{M}{M_\odot}\right)^{-1/2} \left(\frac{R_d}{0.1\,\mathrm{au}}\right)^{3/2} \mathrm{days}. \qquad (15)
\end{aligned}
$$

The list of all the simulations performed in this paper is provided in Table 1, with their input parameters α and κ and several quantities that are measured at the final stage $t_{\rm end}$ of the simulation. As explained in Sect. 2.4.1, the values of μ and δ are dictated by the values of κ. As discussed below, all our simulations display several recollimation shocks. In the table, we provide only the altitude (measured at the axis) of the first main recollimation shock $Z_{\rm shock}$. As stationary jets require them to become super-Afvénic and super-fast magnetosonic (hereafter super-A and super-FM, respectively), we also display the colatitudes $\theta_A^{\rm ext}$ and $\theta_{\rm FM}^{\rm ext}$ of the intersection of the outer boundary $R_{\rm ext}$ and the Alfvén and FM surfaces, respectively. The last super-FM magnetic surface (defining the jet) can then be followed down to the disk, allowing us to identify the largest anchoring radius $r_{o,\rm FM}$ that we consider in the JED. This allows us to measure the mass flux emitted from the JED as $\dot{M}_{\rm jet} = \int_{R_d}^{r_{o,\rm FM}} \rho \boldsymbol{u}\cdot\mathbf{d}\boldsymbol{S}$ and compare it with the mass loss emitted from the spine only $\dot{M}_{\rm spine} = \int_0^{\pi/2} \rho \boldsymbol{u}\cdot\mathbf{d}\boldsymbol{S}$. We also compute the power emanating from the jet $P_{\rm jet} = \int_{R_d}^{r_{o,\rm FM}} \rho E \boldsymbol{u}\cdot\mathbf{d}\boldsymbol{S}$ and compare it to the power emanating from the spine $P_{\rm spine} = \int_0^{\pi/2} \rho E \boldsymbol{u}\cdot\mathbf{d}\boldsymbol{S}$.

Simulations K1 to A5 were performed with a nonrotating spine, namely $\Omega_a = 0$ and $e_a = 2$. Our reference simulation K2 is extensively analyzed in the following section. This reference was repeated with a lower resolution in K2l –all other things being equal– to verify numerical convergence. Section 4 addresses the influence of κ (simulations K1 to K5) and α (simulations A1 to A5). In Sect. 4.3, the effect of a rotating spine (simulation SP) is briefly addressed.

3. The Blandford & Payne case

3.1. Overview

In this section, we discuss our reference simulation K2 performed for the BP82 $\alpha = 3/4$ magnetic field distribution and a mass-loading parameter $\kappa = 0.1$. It was run up to $t_{\rm end} = 6.5\,10^5\,T_d$ and has reached a steady-state in a sizable fraction of our computational domain (a quarter of an orbit has been done at $r_o = R_{\rm ext}$).

Figure 2 displays the final stage reached by K2 at $t_{\rm end}$. The black solid lines are the poloidal field lines, the dotted red line is the Alfvén surface (where the Alfvénic Mach number $m = u_p/V_{\rm Ap}$ is equal to unity) and the dashed red line is the FM surface (where the FM Mach number $n = u_p/V_{\rm fm} = 1$). The left panel shows our simulation on the full computational domain, with a close-up view on the scale used by (Fendt 2006) in the right panel. The background color is the logarithm of n on the left and the logarithm of the density on the right. The last magnetic surface characterizing the super-FM jet is anchored at $r_{\rm o,FM} = 323$ in the JED, and the critical surfaces (A and FM) both achieve a conical shape over a sizable fraction of the domain, which is characteristic of a self-similar steady-state situation. Our spine also achieves super-FM speed at an altitude of $z \sim 260$.

The poloidal velocity vectors can be seen in Fig. 3. The velocity decreases radially very rapidly, mirroring the injection conditions, going from 3.5 at the spine to 0.2 at the edge of the super-FM zone (in $V_{\rm Kd}$ units). The white lines show streamlines inside which 50%, 75%, and 100% (from left to right) of the total super-FM mass outflow (spine + jet) rate is being carried in. These lines are anchored in the disk at $r_0 = 10$, $r_o = 66$, and $r_{o,\rm FM} = 323$, respectively. As $\mathrm{d}\dot{M}/\mathrm{d}R = 2\pi R V_z$ falls off very rapidly, this plot shows that even ejection from a very large radial domain may be observationally dominated by the innermost, highly collimated regions up to $r_o \sim 10$, with the outer "wide angle wind" probably remaining barely detectable.

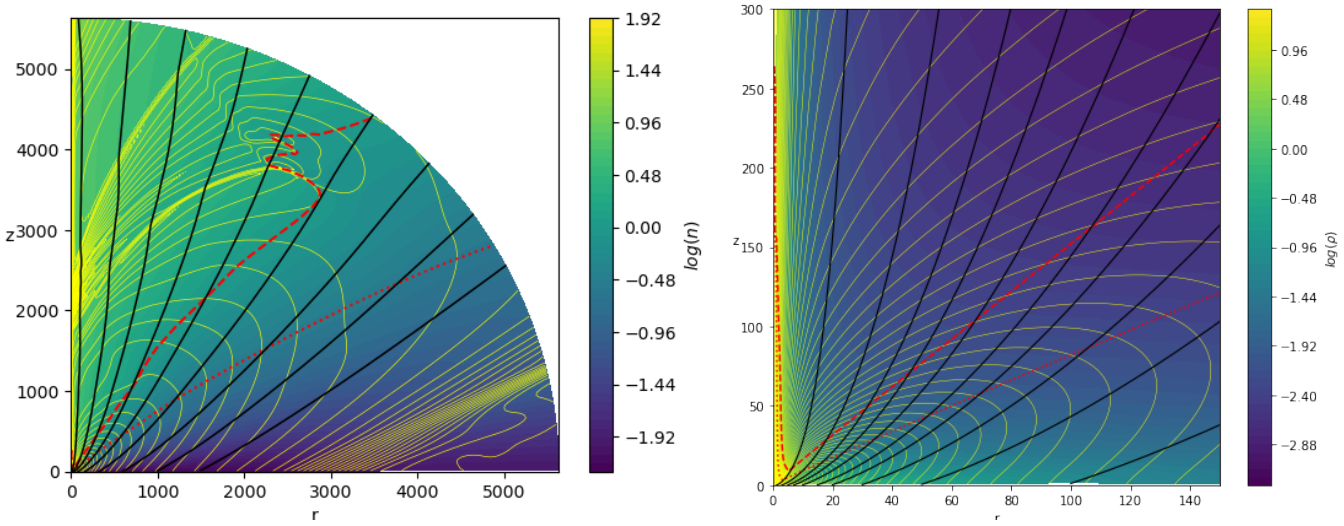

Fig. 2. Snapshot at $t_{\rm end}$ of our Blandford & Payne simulation K2. *Left*: global view with field lines anchored on the disk at $r_o = 3; 15; 40; 80; 160; 320; 600; 1000; 1500$, where the background is the logarithm of the FM mach number n. *Right*: close-up view of the innermost regions, where the background is the logarithm of the density. In *both panels*, black solid lines are the poloidal magnetic surfaces, the yellow solid lines are isocontours of the poloidal electrical current, and the red dashed (resp. dotted) line is the FM (resp. Alfvén) critical surface.

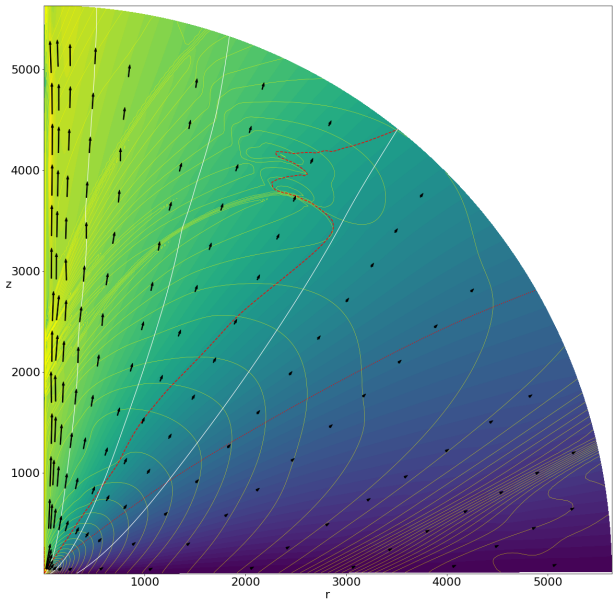

Fig. 3. Snapshot of our reference simulation K2 at $t_{\rm end}$. We use the same color coding as in Fig. 2, left. The black arrows show the poloidal velocity. The white lines are streamlines inside which (from left to right) 50%, 75%, and 100% of the super-FM (spine+jet) mass outflow rate is carried in.

The yellow solid lines are isocontours of the poloidal electric current $I = 2\pi r B_\phi/\mu_o$. These contours are very useful as they allow us to grasp several important features of the simulation: (1) The typical butterfly shape of the initial accelerating closed electric circuit can be seen up to a spherical radius $R \sim 3000$. (2) For disk radii $r_o \gtrsim 2000$, the electric current flowing out of the disk reaches the outer boundary (most of it in the sub-A regime at high colatitudes) and re-enters in the jet at smaller colatitudes, in the super-FM regime. (3) More importantly, several current sheets can be clearly seen (as an accumulation of current lines), highlighting the existence of several standing (stationary) recollimation shocks. To our knowledge, this is the first time that simulations of super-FM jets exhibit the patterns predicted in analytical jet studies. Justifications for this assessment are provided in Sect. 5.2.

These shocks are best seen in Fig. 4, which presents a zoom onto the region of interest. Five shocks (highlighted in colors) can be seen starting near the polar axis, following approximately the expected shape of the MHD characteristics in self-similar jets (see Figs. 3 in Vlahakis et al. 2000; Ferreira & Casse 2004). They are located at $Z_1 = 1850, Z_2 = 2000, Z_3 = 2160, Z_4 = 2372$, and $Z_5 = 2634$. Only two of these shocks span a significant lateral portion of the jet (those best seen also in the left panel in Fig. 2). The first one (in red) leaves the axis at an altitude $Z_1 = 1850$ (labeled $Z_{\rm shock}$ in Table 1) and stays within our domain, finally merging with the FM surface (red dashed curve) around ($r = 2500, z = 3800$). The second shock starts at Z_5 and leaves the simulation domain at ($r = 1800, z = 5200$), and is therefore not fully captured by our simulation. For this reason, only the first shock is extensively described here.

It can be seen that all shocks do occur only after the magnetic surface has started to bend toward the axis (with a decreasing cylindrical component B_r), and give rise to a sudden outward refraction of the surface with its ouflowing material. This, plus the fact that their positions remain steady in time (see below), justifies our use of the name "standing recollimation shocks" to describe them. While these standing recollimation shocks appear quite generic for our set of simulations, we stress that fantastically large spatial and temporal scales are required to see them.

This simulation was also performed with a two-times-smaller resolution (see K2l in Table 1). We also observed standing recollimation shocks that are similar, although with less complexity.

3.2. Quasi steady-state jet and spine

Jet production is a very rapid process that scales with the local Keplerian timescale (especially As μ is constant with the radius). It is therefore an inside-out build-up of the jet with its associated electric circuit, until the innermost jet regions (including the spine) reach the outer boundary. This will take a time of typically $t_{\rm ext}(r_o = 1) \sim R_{\rm ext}/V_z$, with the maximal jet speed

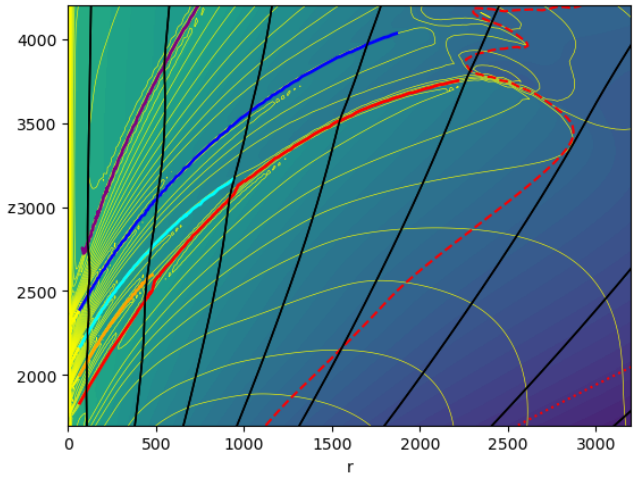

Fig. 4. Close-up view of our reference simulation K2 at $t_{\rm end}$ showing the shock forming region, with field lines anchored at r_o = 1.2; 2; 3; 4; 5; 7; 9. The five shocks are highlighted in red, orange, cyan, blue, and purple. We use the same color coding as in the left panel of Fig. 2.

$V_z \simeq \sqrt{2\lambda - 3}V_K$. According to BP82, cold outflows with moderate inclinations and $\kappa = 0.1$ reach $\lambda \sim 10$ (see their Fig. 2), which is exactly what we also obtain (see Fig. 15, with a minimum value $\lambda = 11$). This leads to a dynamical time $t_{\rm ext} \sim 1.3 \times 10^3$ (in T_d units) and so the innermost jet regions achieve an asymptotic state very early. However, the transverse (radial) equilibrium of the outflowing plasma is still slowly adjusting, because, as time increases, more and more of the outer magnetic surfaces achieve their asymptotic state, providing an outer pressure and modifying the global jet transverse equilibrium. This, in turn, necessarily modifies the shape of the magnetic surfaces as well as the associated poloidal electric circuit.

This means that the MHD invariants along each magnetic surface can always be defined (each surface is quasi-steady), but that they are also slowly evolving in time as the global magnetic structure evolves. For our simulation K2, the last super-FM magnetic surface is anchored at $r_{o,\rm FM} = 323$, defining a local Keplerian time $T_K = 5.8 \times 10^3$. At that distance, the boundary is located at $Z_{\rm ext} \sim R_{\rm ext} \cos\theta_{\rm FM} \sim 4430$, leading to a dynamical time $t_{\rm ext}(r_{o,\rm FM}) \sim Z_{\rm ext}/V_z(r_{o,\rm FM}) \sim 1.6 \times 10^4$ (with $\lambda = 14$) as the speed distribution on the disk is Keplerian. We can therefore expect MHD invariants within our jet to evolve much less only after a time $\sim 10^4$.

This slight evolution of the jet quantities over time is illustrated in Fig. 5. We chose to look at global quantities, such as the radius $r_{o,\rm FM}$ of the last super-FM surface, the jet mass-loss rate $\dot{M}_{\rm jet}$, and the two colatitudes $\theta_A^{\rm ext}$ and $\theta_{\rm FM}^{\rm ext}$ that define the position of the two critical surfaces. We pick up their values at $t = 5.1 \times 10^5$ and plot their evolution by normalizing them to this "initial" value. It can be seen from Fig. 5 that their evolution is quite obvious: $r_{o,\rm FM}$ keeps on increasing, leading to an increase in $\dot{M}_{\rm jet}$ and a decrease in both $\theta_A^{\rm ext}$ and $\theta_{\rm FM}^{\rm ext}$. But the relative variations are less than 3% for $r_{o,\rm FM}$ and 1% for the other quantities.

We therefore consider that our simulation K2 has achieved a relatively global steady-state. In physical units (and for our choice of axial density ρ_a), the jet mass loss is about $2 \times 10^{-7}\, M_\odot\, {\rm yr}^{-1}$ with a magnetic field around 10 G at 0.1 au. The spine mass loss is only $\sim$10% of the jet mass loss, and so we can safely presume that the dynamics are mostly controlled by the JED, as expected. However, as the spine power is comparable to the jet power ($P_{\rm spine}/P_{\rm jet} = 0.81$), the impact of the spine on the collimation and topology of the electric field cannot be neglected. The influence of the spine is detailed in Sect. 4.3.

Figure 6 shows the various contributions to the Bernoulli integral $E(\psi)$ along a magnetic surface anchored at $r_o = 100$ at the final stage $t_{\rm end}$. It can be seen that E is indeed conserved and that jet acceleration follows the classical pattern (Casse & Ferreira 2000a): the kinetic energy (green) increases thanks to the magnetic acceleration, leading to a decrease in the magnetic contribution (magenta). Enthalpy (red) is negligible in this cold outflow. The presence of the shock is clearly seen around $Z = 3800$: the flow is suddenly slowed down and the energy is transferred back to the magnetic field, in agreement with the Rankine-Hugoniot jump conditions (see Appendix C). Beyond the shock, MHD acceleration is resumed but, at the edge of our domain, the magnetic field still maintains around 45% of the initial available energy.

The evolution along a magnetic surface of the five MHD invariants is shown in Fig. 7 for two surfaces, one anchored at $r_o = 100$ (left) and the other at $r_o = 1000$ (right). In order to plot η, Ω_*, L, E, and S on the same figure, we normalize each quantity by its initial (at the disk surface) value at $t_{\rm end}$. On the left, variations of the invariants can indeed be seen but only at the shock located at $Z = 3800$; they remain very small, much less than 1% for all but the entropy (which is conserved to machine accuracy). On the right plot, the field line is anchored beyond $r_{o,\rm FM}$ and the flow remains sub-FM while crossing no shock. Variations of the invariants are again observed, but always less than 0.3%. This shows that the PLUTO code is quite efficient and the MHD solution is indeed steady.

3.3. Jet collimation

Before analyzing the shocks in the following section, let us briefly discuss jet collimation. Figure 8 shows the initial magnetic field configuration (in dotted lines) along with the final configuration (solid lines) obtained at $t_{\rm end}$. Each color is associated with a different anchoring radius r_o, allowing us to see the evolution from the initial potential field and the final full MHD solution. This plot clearly illustrates how magnetic collimation works. As the poloidal electric circuit responsible for the collimation must be closed, its sense of circulation must change within the whole outflow (defined as both the jet and its spine). The poloidal current density $\boldsymbol{J}_p$ is therefore downward in the inner regions and outward in the outer jet regions. As a consequence, field lines anchored up to $r_o \sim 25$ are focused to the polar axis (Z-pinch due a pole-ward $\boldsymbol{J}_p \times \boldsymbol{B}_\phi$ force as $J_z < 0$), while field lines anchored beyond $r_o \sim 30$ are de-collimated and pulled out (because of the outward action of the same $\boldsymbol{J}_p \times \boldsymbol{B}_\phi$ force as $J_z > 0$). See the right panel of Fig. 2 for the topology of $\boldsymbol{J}$.

The inner self-collimated jet region can only exist thanks to the existence of these outer jet regions that are pulled back and out. The final state of the jet collimation, namely the asymptotic jet radius achieved by these inner regions (the densest ones, possibly responsible for the observed astrophysical jets), is therefore also a consequence of the transverse equilibrium achieved by the outflow outskirts with the ambient medium. This balance is mathematically described by the Grad-Shafranov equation and expresses the action of the poloidal electric currents – how they are flowing and how electric circuits are closed within the jet – on the shape of the magnetic surfaces (Heyvaerts & Norman 1989, 2003a,b; F97; Okamoto 2001). We return to this point below.

Table 1. Simulations presented in this paper.

Name	κ	α	μ	δ	$\frac{t_{\rm end}}{10^5}$	$Z_{\rm shock}$	$\theta^{\rm ext}_{\rm FM}$(rad)	$\theta^{\rm ext}_{A}$(rad)	$r_{\rm o,FM}$	$\dot{M}_{\rm jet}$	$\frac{\dot{M}_{\rm spine}}{\dot{M}_{\rm jet}}$	$P_{\rm jet}$	$\frac{P_{\rm spine}}{P_{\rm jet}}$
K1	0.05	12/16	1.41	50	7.34	2150	0.64	0.94	301	179	0.102	492	0.82
K2	0.1	12/16	1.00	100	6.51	1850	0.67	1.05	323	363	0.096	616	0.81
K2l	0.1	12/16	1.00	100	12.3	2490	0.65	1.02	289	357	0.094	620	0.81
K3	0.2	12/16	0.71	200	10.1	1810	0.69	1.09	368	743	0.093	768	0.80
K4	0.5	12/16	0.45	500	8.67	1150	0.90	1.26	655	2040	0.093	1024	0.81
K5	1.0	12/16	0.32	1000	4.62	700	0.99	1.34	670	4095	0.116	1264	0.96
A1	0.1	10/16	1.00	100	9.08	1900	0.96	1.23	234	195	0.206	551	1.21
A2	0.1	11/16	1.00	100	8.34	1800	0.87	1.15	349	272	0.137	578	0.99
A3	0.1	13/16	1.00	100	5.79	1920	0.59	0.95	566	690	0.047	668	0.66
A4	0.1	14/16	1.00	100	6.26	2050	0.64	0.94	398	1321	0.023	740	0.53
A5	0.1	15/16	1.00	100	1.62	2030	0.50	0.83	1046	3275	0.009	848	0.41
SP	0.1	12/16	1.00	100	3.93	1250	0.82	1.09	506	392	0.097	613	0.98

Notes. All the simulations presented have been performed in the grid described in Sect. 2.2 (e.g., $N_R = 1408$ and $N_\theta = 266$) except K2l, performed in a lower resolution grid (e.g., $N_R = 704$ and $N_\theta = 144$) The parameters κ and α are varied independently, allowing us to compute μ, δ, and M_S. The columns $Z_{\rm shock}$, $\theta^{\rm ext}_{\rm FM}$, $\theta^{\rm ext}_{A}$, $r_{o,\rm FM}$, $\dot{M}_{\rm jet}$, $\dot{M}_{\rm spine}/\dot{M}_{\rm jet}$, $P_{\rm jet}$, and $P_{\rm spine}/P_{\rm jet}$ are outputs of the simulation measured at the final time $t_{\rm end}$ (given in $10^5 T_d$ units). Simulations K1 to A5 were done with a nonrotating spine, namely $\Omega_a = 0$ and $e_a = 2$. Simulation SP is done for $\Omega_a = \Omega_{Kd}$ and $e_a = 10$ and is discussed in Sect. 4.3. See Sect. 2.5 for the definition of all these quantities.

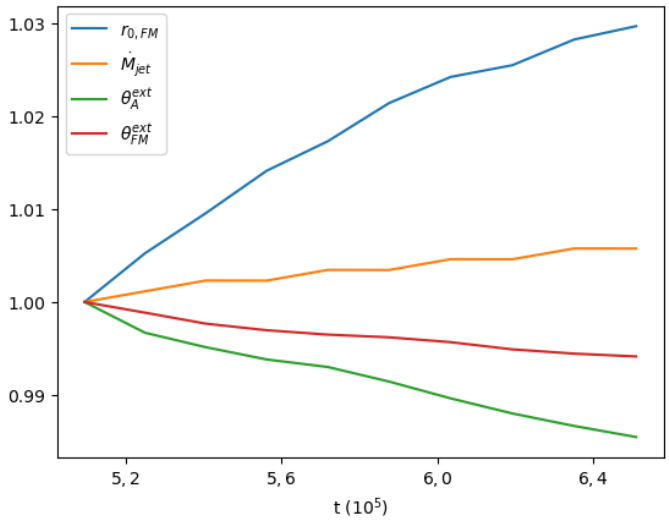

Fig. 5. Late evolution of several global jet quantities for the simulation K2: the radius $r_{o,\rm FM}$ of the last super-FM surface, the jet mass-loss rate $\dot{M}_{\rm jet}$, and the two colatitudes $\theta^{\rm ext}_{A}$ and $\theta^{\rm ext}_{\rm FM}$ that define the position of the two critical surfaces. A slight drift from their initial value is indeed observed. The values provided in Table 1 are those achieved at the final time.

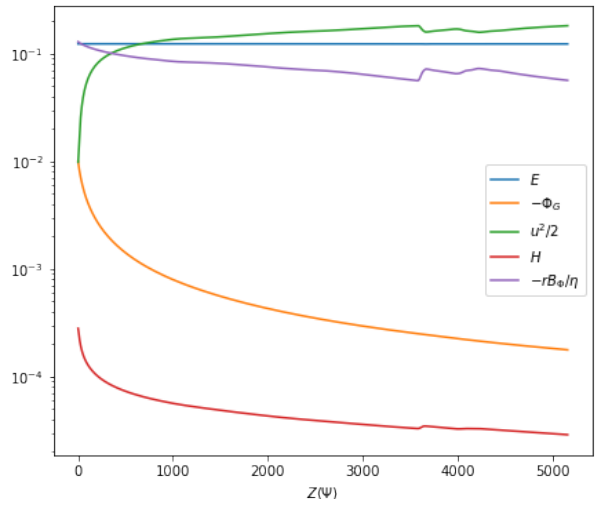

Fig. 6. Evolution of the various energy contributions along a magnetic surface of anchoring radius $r_0 = 100$ for the simulation K2 at $t_{\rm end}$: the Bernoulli invariant E, the gravitational potential Φ_G, the total specific kinetic energy $u^2/2$, the enthalpy H, and the magnetic energy $-\Omega_* r B_\Phi/\eta$. The absicssa is the altitude $Z(\Psi)$.

3.4. Standing recollimation shocks

Our reference simulation K2 ends with five standing shocks, of which only the first (red in Fig. 4), starting on the axis around $Z_1 = 1850$, is studied hereafter. This is for two reasons: (1) Contrary to the orange and cyan shocks, the red shock surface covers a large extension in the jet itself. It is therefore most probably related to the dynamics of our quasi self-similar jet, whereas these smaller shocks may be related to the spine–jet interaction. (2) It remains far away from the outer boundary (it ends up at the FM surface at a point $r = 2500, z = 3800$), which is clearly not the case for the purple shock and also probably not for the blue one.

3.4.1. Rankine-Hugoniot conditions

All shocks are due to the flow heading toward the axis (with decreasing, usually negative B_r and u_r components) at a super-FM velocity, resulting in a sudden jump in all flow quantities with an outward refraction of the magnetic surface (this can be seen in Fig. 8). The Rankine-Hugoniot jump conditions (see Appendix C for more details) are of course satisfied with the shock-capturing scheme of PLUTO and MHD invariants are conserved (up to some accuracy, as discussed above).

The left panel of Fig. 9 displays the evolution of several quantities along the red shock surface. It can be seen that the compression rate χ (green curve), defined as the ratio of the post-shock to the pre-shock densities, is larger than unity while remaining small ($\lesssim$1.3, see red curve in the right panel), despite a very large Alfvénic Mach number $m \sim 100$ (orange). This is probably because the shock is oblique and the incoming jet

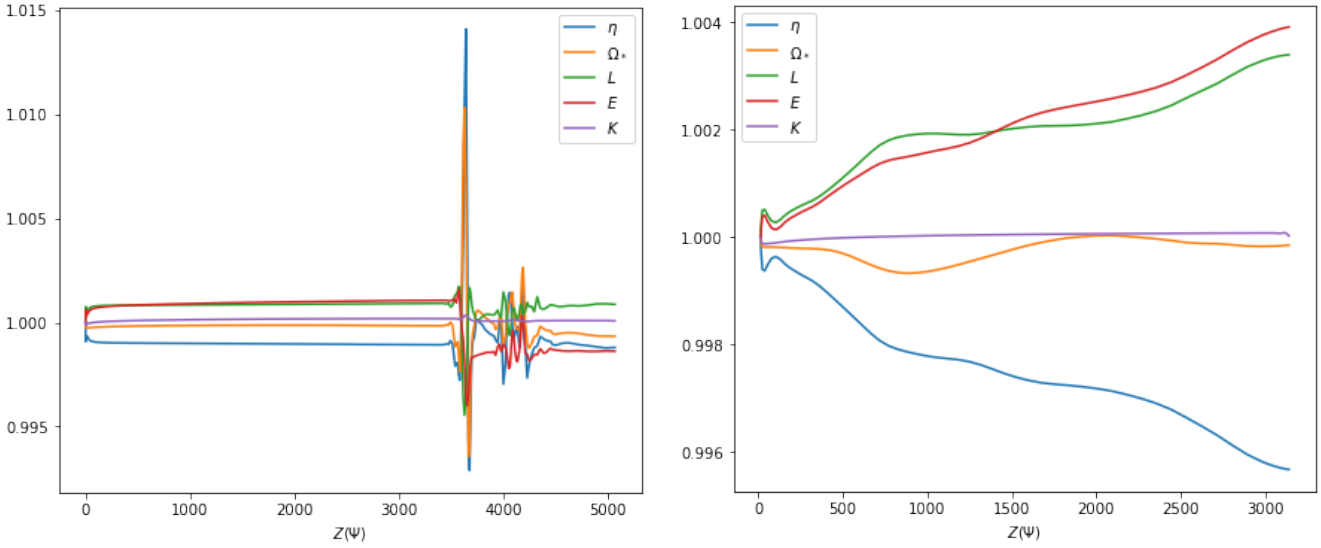

(a) (b)

Fig. 7. Evolution of the MHD invariants along field lines of two different anchoring radii r_o at $t_{\rm end}$ for simulation K2. All invariants have been normalized to their values at r_o. The absicssa is the altitude $Z(\Psi)$.

material does not reach very large super-FM Mach numbers $n_\perp$ (defined as the ratio of the flow velocity normal to the shock surface to the FM phase speed in that same direction; blue curve). In fact, $n_\perp \leq n = u_p/V_{fm}$, and at these distances the jet has reached its asymptotic state with a maximum velocity of $u_p \sim \sqrt{2\lambda - 3}V_{Ko}$ ($V_{Ko} = \Omega_* r_o$ the Keplerian speed at the anchoring radius). Assuming $B_p \ll |B_\phi|$, $m \gg 1$ and a jet widening such that $r \gg r_A$ where r_A is the Alfvén cylindrical radius along a flow line where $m = 1$, leads to

$$n \simeq \frac{u_p}{V_{A\phi}} = \frac{u_p}{\Omega_* r}\frac{m}{1 - r_A^2/r^2} \simeq m\frac{r_o}{r}\sqrt{2\lambda - 3} \sim m\frac{r_A}{r}, \qquad (16)$$

which shows that the asymptotic FM Mach number critically depends on how much the jet widens (see Pelletier & Pudritz 1992 and Sect. 5 in F97). In our case, $n \sim 4$ at the outer edge of the spine–jet interface, in agreement with self-similar studies. Following the main red shock along growing r, the incident angle[3] of the magnetic field lines on the shock front decreases until turning into a normal shock on its external edge ($r \sim 2000$). Hence, on this edge, the shock front coincides with the FM critical surface $n = 1$. As the shock becomes normal, $n_\perp \to n = 1$ and the shock vanishes, with a compression rate χ going to 1.

The three other curves in the left panel of Fig. 9 describe other modifications in jet dynamics. The brown curve is the magnetic field line deviation at the shock front, $\delta i = i_2 - i_1$, where i is the flow incidence angle to the normal to the shock surface (subscripts 1 and 2 refer to the pre- and post-shock zones, respectively). The maximum deviation of 0.07 rad = 4° is very small, in agreement with the small compression rate.

The purple curve describes the relative variation of the flow rotation $\delta\Omega = (\Omega_2 - \Omega_1)/\Omega_1$, which is always negative. The shock introduces a sudden brake in the azimuthal speed, meaning that the compressed shocked material is always rotating less. As t.e detection of rotation signatures in YSO jets is an important tool for retrieving fundamental jet properties (see e.g., Anderson et al. 2003; Ferreira et al. 2006; Louvet et al. 2018; Tabone et al. 2020), recollimation shocks appear to be a very interesting means to lower the jet apparent rotation. However, the rather weak shock found here only introduces a decrease of ∼20% at the outer edge of the shock.

The plasma loss of its angular momentum at the shock is of course compensated for by a gain of magnetic field (the angular moment is a MHD invariant). This means that the magnetic field lines are more twisted after the shock than before, as illustrated in the red curve showing $\delta B_\phi = (B_{\phi_2} - B_{\phi_1})/B_{\phi_1} > 0$. The shock surface acts therefore as a current sheet with an electric current density flowing outwardly (in the spherical R direction).

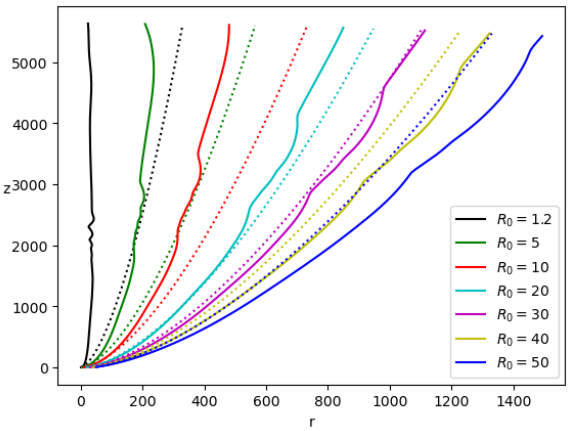

Fig. 8. Evolution of several magnetic field lines during the simulation computation, for different anchoring radii R_0 and for the reference simulation K2. The field lines at the first output of the simulation (initial conditions) are shown in dotted lines. The field lines at the last output of the simulation (final state) are shown as full lines.

3.4.2. Two families of shocks

The right panel of Fig. 9 displays the compression rate χ for the five shocks seen in Fig. 2, using the same color code. All

[3] Here and throughout the following, the angles of incidence and refraction are defined as in Snell-Descartes law, e.g., measured from the normal to the shock front.

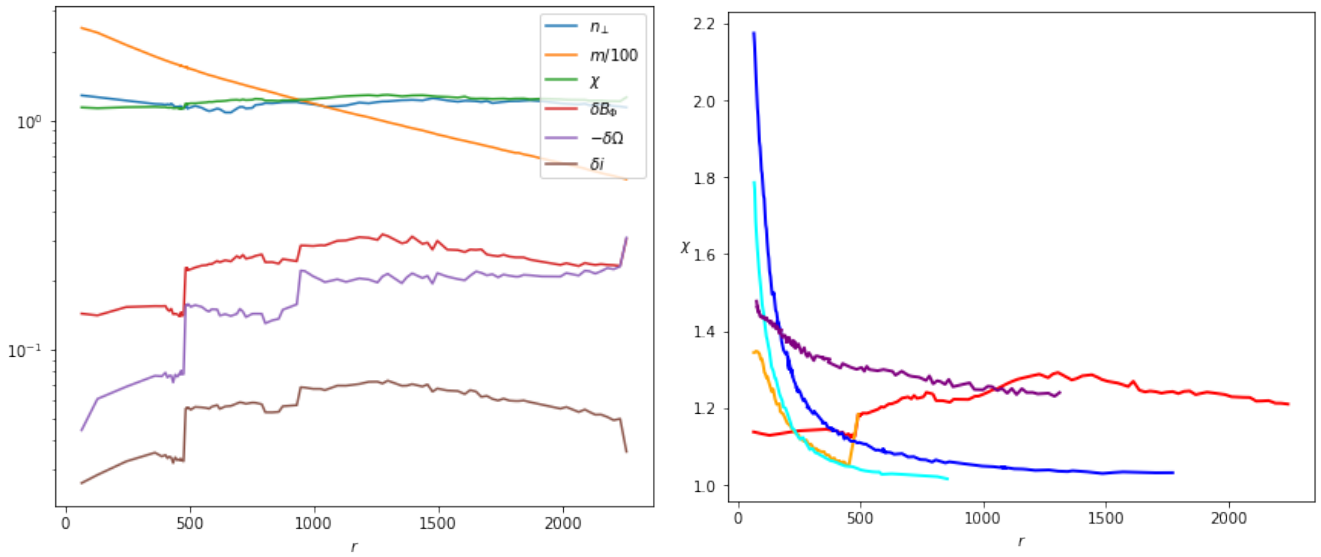

Fig. 9. Distributions along the shock of several quantities for K2 at $t_{\rm end}$. *Left*: normal incident FM Mach number $n_\perp$, Alfvénic Mach number m, compression rate χ, relative variations of the toroidal magnetic field δB_ϕ and plasma angular velocity $-\delta\Omega$, and total deviation δi (in rad) of the poloidal magnetic field line for the main recollimation shock. *Right*: compression rates χ of all shocks appearing in Fig. 4, using the same color code. The main shock corresponds to the red curve. See Appendix C for more details on this figure.

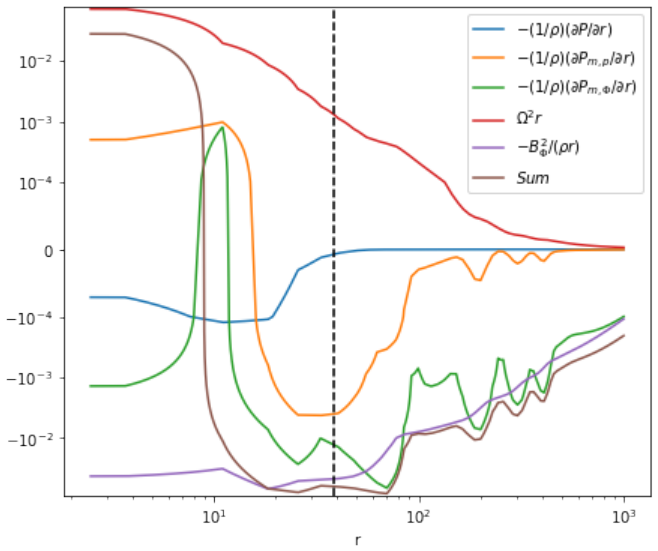

Fig. 10. Radial distribution of the radial accelerations and their sum at the altitude $Z = 2400$ for the simulation K2 at $t_{\rm end}$. The vertical dashed line corresponds to the spine–jet interface, namely the field line anchored at $r_o = R_d$.

shocks but the red one have larger compression factors near the axis. The orange and cyan shocks merge with the main red one (respectively at $r \sim 500$ and $r \sim 900$), leading to an increase in its compression rate χ. The large blue shock has the same behavior as the orange and cyan but remains alone (i.e., not merging with the red) with χ converging to 1, while the purple shock seems to have a similar behavior to the red one, maintaining a larger value for χ. Although these last two shocks are probably affected by their proximity with the outer boundary, it seems that two classes of recollimation shocks are at stake.

The first class (represented by the red and purple shocks) corresponds to the recollimation shock predicted in self-similar studies (FP97, Polko et al. 2010). The reason for their existence is the hoop-stress that becomes dominant as the jet widens, leading to a magnetic focusing toward the axis. As shown in FP97, such a situation always arises in the super-FM regime, meaning that a shock is the only possibility for the converging flow to bounce away. However, as long as no dissipation is introduced, such a situation will repeat. Indeed, after the flow refraction due to the shock, the magnetic field starts to accelerate the plasma again, the magnetic surface widens and the same situation repeats. One would therefore expect periodic oscillations and shocks on a vertical scale H_R (measured on the axis). Figure 8 provides some evidence of this pattern for the field lines anchored at $r_o = 20, 30$ or 40. The first recollimation shock (red) is quite far away from the disk ($Z_{\rm shock} = 1850$), but the second shock (purple) occurs at $Z_5 \simeq 2634$. A much larger computational domain would be necessary in order to clearly assess a periodic pattern.

The second class of recollimation shocks (represented by the orange, cyan, and blue shocks) are limited to the vicinity of the spine–jet interface and are thereby a consequence of a radial equilibrium mismatch between these two super-FM outflows. The transverse equilibrium of a magnetic surface is provided by projecting the stationary momentum equation in the direction perpendicular to that surface, leading to the equation (FP97)

$$(1-m^2)\frac{B_p^2}{\mu_0\mathcal{R}} - \nabla_\perp\left(P+\frac{B^2}{2\mu_0}\right) - \rho\nabla_\perp\Phi_G + \left(\rho\Omega^2 r - \frac{B_\phi^2}{\mu_0 r}\right)\nabla_\perp r = 0. \quad (17)$$

Here, $\nabla_\perp = \boldsymbol{e}_\perp \cdot \nabla$ provides the gradient perpendicular to a magnetic surface with $\boldsymbol{e}_\perp = \nabla\Psi/|\nabla\Psi|$ and $B_p^2/\mathcal{R} = \boldsymbol{e}_\perp \cdot (\boldsymbol{B}_p \cdot \nabla \boldsymbol{B}_p)$, measures the local curvature radius $\mathcal{R}$ of the magnetic surface. In the asymptotic region where these small recollimation shocks are observed, the field lines are almost vertical and gravity is negligible. The above equation therefore reduces to

$$-\frac{\partial}{\partial r}\left(P + \frac{B^2}{2\mu_0}\right) + \rho\Omega^2 r - \frac{B_\phi^2}{\mu_0 r} = 0. \quad (18)$$

Looking at Fig. 10, where the various forces are plotted as a function of the cylindrical radius at a constant height $Z = 2400$,

it can be clearly seen that the dominant force is the hoop stress $-B_\phi^2/(\mu_o r)$ (purple curve) near the spine-jet interface (dashed vertical line), defined as the magnetic field line anchored at $r_o = R_d$. That pinching force overcomes the others (the above sum is actually nonzero and negative), indicating that the field lines do have a curvature and are actually converging toward the axis (therefore Eq. (18) is too simplistic). Nevertheless, this behavior of the forces is consistent with the stationary shape of the magnetic surfaces seen at $Z = 2400$ at those radii. Further out, downstream, the fifth (purple) shock will make the field lines bounce back again. This tells us that we are witnessing radial oscillations of the radius of the spine driven by a mismatch between the dominant forces (hoop stress, magnetic pressure, and centrifugal term).

This oscillatory behavior may be a generic feature of MHD outflows from a central rotator as shown by Vlahakis & Tsinganos (1997), because of the different scaling with the radius of the pinching force and the centrifugal force (as in the self-similar jet; F97). But it may also be triggered by the pinching due to the outer jet recollimation, namely the spine–jet interface response to the global jet recollimation. Indeed, no spine–jet shock is seen before the onset of the main recollimation shock. We further note that the five shocks are located at a slightly increasing distance from each other. Indeed, $\Delta Z_{12} = Z_2 - Z_1 = 150, \Delta Z_{23} = 160, \Delta Z_{34} = 212$, and $\Delta Z_{45} = 262$, which is the sign of some damping of the spatial oscillations at the spine–jet interface (see e.g., Vlahakis & Tsinganos 1997). This corresponds to three spine–jet shocks (orange, cyan, and blue) located between the two large jet recollimation shocks (red and purple), as can be seen in Fig. 4.

Despite the fact that the magnetic surfaces are in a steady state, it is useful to look at this spatial oscillatory pattern as the nonlinear outcome of transverse waves. Immediately after a shock, the flow is again outwardly accelerated leading to a widening of the magnetic surface and its refocusing toward the axis with the unavoidable shock. It will therefore take a time $\Delta t_z = \Delta Z/u_z$ to reach the next shock. On the other hand, any radial unbalance triggered immediately after the shock gives rise to a transverse (radial) FM wave that bounces back on a timescale of $\Delta t_r = 2r/V_{fm}$ measured at the spine–jet interface. In steady-state, these two times must be the same, which requires $\Delta Z \sim 2nr$, where n is the FM Mach number measured at the spine–jet interface. At $Z = 2400$, the width of the spine is $r \simeq 40$, and $n \simeq 3$, providing the correct order of magnitude for $\Delta Z \sim 240$. This is also verified for all other shocks. This correspondence strengthens the idea that these small shocks are actually triggered by the first large recollimation shock.

3.5. Electric circuits

The existence of these shocks drastically affects the poloidal electric circuits that go along with MHD acceleration (and of course collimation). This can be seen in Fig. 11, where several interesting circuits are shown in color. Each poloidal circuit corresponds to an isocontour of rB_ϕ, the arrows indicating their flowing direction.

The white contour marks the last electric circuit that flows below the first recollimation shock and defines the envelope of the initial accelerating current. It links the disk emf with the accelerated jet plasma and flows back to the disk along the spine. This is due to the fact that the largest electric potential difference is with the axis.

The blue circuit is the last electric circuit fully enclosed within the computational domain. The current flows out of the disk (further away than the previous circuit) and makes a large loop that goes beyond (downstream) the main recollimation shock, flowing back on the axis below Z_5 until it encounters the smaller shock at Z_4 (blue curve in Fig. 4). As a shock behaves as an emf, with an outwardly (positive J_r) electric current flowing along its surface, the blue electric current gets around it and goes back to the axis where it meets the next shock surface at Z_3 (cyan in Fig. 4). As that shock merges with the main recollimation shock, the blue electric current flows along these two surfaces, gets around the main shock (near the point $r \sim z \sim 3000$ in Fig. 11) and returns back to the disk via the spine, where it joins the white circuit below Z_1.

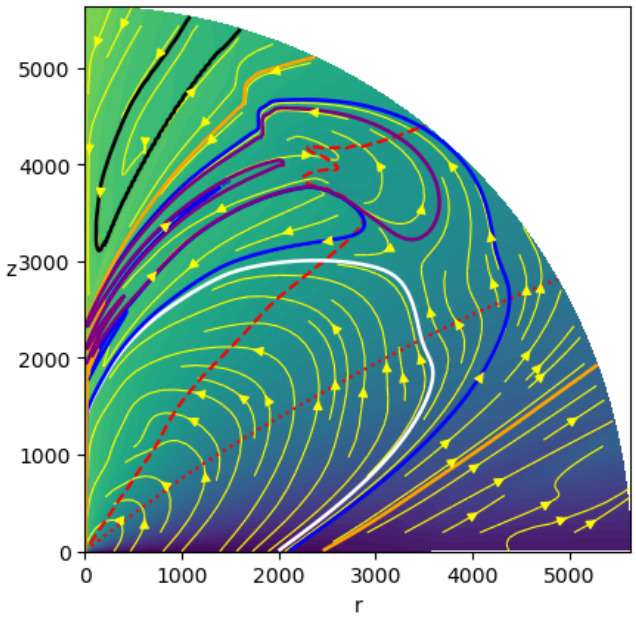

Fig. 11. Plot of the poloidal electric circuits at $t_{\rm end}$ for simulation K2. The two red curves are the critical surfaces, Alfvén (dotted) and FM (dashed). The yellow curves are the poloidal electric circuits, defined as isocontours of rB_ϕ, where the arrow indicate the direction of the poloidal current density $\boldsymbol{J}_p$. Four circuits are highlighted in particular: (1) the envelope of the inner accelerating current in white ($rB_\phi = -2.06$), (2) the outermost circuit still fully enclosed within the domain in blue ($B_\phi = -2.005$), (3) a circuit closed outside the domain in orange ($rB_\phi = -1.80$), and (4) a post-shock accelerating circuit in purple (also with $rB_\phi = -2.06$).

As mentioned above, the outflowing plasma gets re-accelerated after each shock. This requires a local accelerating electric circuit, which is naturally enclosed within two recollimation shocks. One such circuit is exemplified by the purple contour in Fig. 11. It actually has the same rB_ϕ value as the white one, but is enclosed between the two large recollimation shocks. As the small shocks (orange and cyan in Fig. 4) merge with the main one, the purple accelerating circuit is the envelope of the current used to go from the first main shock to the second one flowing back to the spine just before Z_5 (and getting around the shock starting at Z_4 near the point $r \sim 2000, z \sim 4000$, like the previous blue electric circuit).

These three examples of electric circuits (white, purple, and even blue) are fully closed within the computational domain and therefore do not contribute to any further asymptotic collimation. However, it can be seen that the electric current outflowing from the disk beyond $r_o \sim 2000$ leaves the computational domain and is supposedly closed by the inflowing current that enters the computational domain at small colatitudes. One example of such

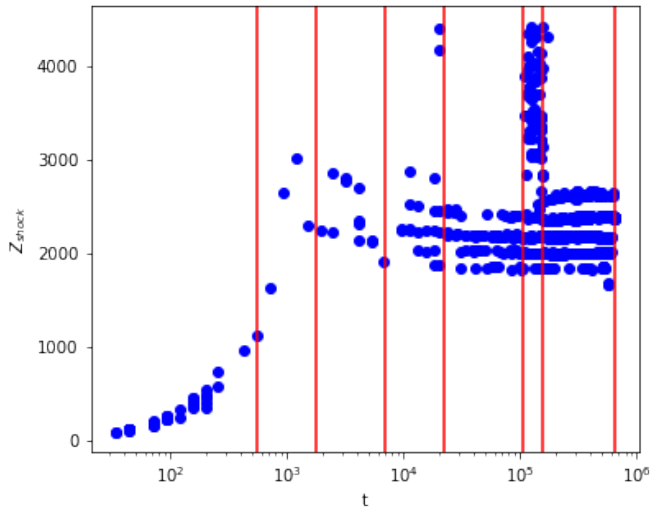

Fig. 12. Altitude Z of the different shocks (measured at the axis) as a function of time (in T_d units) for simulation K2. The vertical lines correspond to the six times t_i used in Fig. 13: $t_1 = 551, t_2 = 2.08 \times 10^3, t_3 = 8.51 \times 10^3, t_4 = 1.99 \times 10^4, t_5 = 1.05 \times 10^5$, and $t_6 = 1.58 \times 10^5$. The last vertical line is $t_{\rm end} = 6.51 \times 10^5$.

an electric circuit is shown by the orange curve in Fig. 11. This inward electric current is responsible for the inner jet collimation at large distances, say at $Z \gtrsim 3000$, and is seen to flow back to the disk along the spine, which acts as a conductor. This implies that the asymptotic jet collimation is here somewhat controlled by an electric circuit that is not fully self-consistent. Indeed, this electric circuit is actually determined by the boundary conditions at $R_{\rm ext}$ and there is no guarantee that its evolution is consistent with the disk emf. This is of course unavoidable but it may have an impact on the collimation properties of numerical jets (see discussion in Sect. 5). Moreover, as this current embraces very large spatial scales, very long timescales are consistently implied and may lead to evolution of the jet transverse equilibrium on those scales.

3.6. Time evolution

Figure 12 shows the evolution in time of the vertical height Z (measured at the axis) of all shocks found in the simulation. As discussed previously, it takes a time $t_{\rm ext}(1) \sim 10^3$ for the innermost jet (anchored at $r_o = R_d$) to reach the boundary of our computational box. During this early evolution with $t < t_{\rm ext}(1)$, the detected shocks correspond to the first bow shock where the jet front meets the initial unperturbed ambient medium. Once the jet has reached the boundary, the spine is in a steady-state while the jet transverse equilibrium continues to evolve due to the self-similar increase in its width. Indeed, the time to reach the outer boundary for a magnetic surface anchored at r_o in the disk grows as $t_{\rm ext}(r_o) \propto r_o^{1/2}$. It therefore takes a time $\sim 10^4$ to achieve a steady ejection from $r_o = r_{o,\rm FM} = 323$, where $r_{o,\rm FM}$ is the maximum radius of the field lines that achieve a super-FM flow speed. The global jet structure is only expected to have a steady state beyond that time.

The vertical lines in Fig. 12 trace six times $t_1 = 551, t_2 = 2.08 \times 10^3, t_3 = 8.51 \times 10^3, t_4 = 1.99 \times 10^4, t_5 = 1.05 \times 10^5$, and $t_6 = 1.58 \times 10^5$. The snapshots corresponding to each of these times are shown in Fig. 13, allowing us to see the global jet evolution. The times t_1 and t_2 have been chosen to enclose $t_{\rm ext}(1)$. The bow shock with the ambient medium is clearly seen, as is the outward (radial) evolution of the jet width. At t_2, several shocks near $Z \sim 2000$ can be seen in both figures. The jet radial equilibrium is clearly not yet steady. However, Fig. 12 shows that while the positions of the shocks (as measured on the axis) are already close to their final values, their final number is not yet settled.

Four standing recollimation shocks seem to settle somewhere between $t_3 = 8.51 \times 10^3$ and $t_4 = 1.99 \times 10^4$, in agreement with our previous estimate; they can be clearly seen in Fig. 13, where some transient shocks located further up at $Z > 4000$ at t_3 have disappeared at t_4. Also, given the huge spatial scales involved, most of our JED is still evolving. For instance, while there have already been 3183 orbital periods at R_d at t_4, the disk has done only half of an orbit at $r_o = 323$. This can be seen in the shape of the FM surface, which has not yet reached its steady-state configuration (conical).

Beyond t_4, the global flow is slowly evolving in time in some adiabatic way, with four standing recollimation shocks. The evolution of the jet outer regions and the progressive evolution of the A and FM surfaces to their conical shapes seems to produce no obvious evolution in the shocks until t_5. At that time, a dramatic evolution is triggered with the appearance of shocks beyond Z_4. Figure 12 clearly shows this pattern with the appearance of a fifth shock; its altitude Z_5 evolves in time, consistently with Z_4 until a steady-state is finally reached approximately near t_6. Our final state $t_{\rm end}$ shows no relevant difference in the positions of the five shocks. This evolution of the distribution of the shocks has only slightly affected the position of the farthest shock Z_4, leading to the final regular distance ΔZ discussed above.

The appearance of a fifth shock at t_5 leading – after a transient phase ending at t_6 – to a new steady state jet configuration is illustrated in Fig. 14. The time evolution of the cylindrical radius of the field line anchored at $r_o = 3$ (in blue) is measured at a constant height $Z = 3500$. It can be seen that this radius is steadily slowly decreasing in time, going from $r \sim 150$ near t_4 down to $r \sim 135$ at t_5 where some fluctuations are suddenly triggered. These oscillations describe a time-dependent behavior which ends at t_6, with a new radial balance found at a smaller radius $r \simeq 125$. Globally, this evolution describes a magnetic surface that is first slowly getting more and more confined, and then enters an unstable situation until the formation of another (tighter) equilibrium. This behavior is consistent with the evolution of the electric current (red curve) that flows within that magnetic surface, which is seen to first steadily (although very slowly) increase until achieving a final value.

In these inner regions, transverse equilibrium of the cold jet is mostly achieved by the poloidal magnetic pressure balancing the toroidal pressure and hoop stress (see Eq. (18) and Fig. 10). In this Bennett relation, one gets

$$(rB_\phi)^2 = (rB_z)^2 + \int_0^r 2B_z^2 r{\rm d}r \,. \tag{19}$$

This relation shows that the toroidal field B_ϕ is compelled to follow the same scaling as B_z in order to maintain the jet transverse equilibrium. If we assume that the self-similar radial scaling for the vertical field B_z is recovered at large distances, we get $(rB_\phi)^2 \propto r^{2(\alpha-1)}$. As a consequence, for $\alpha < 1$ (which is the case here), whenever the electric current is increasing, the radius of the magnetic surface decreases (as in a Z-pinch). This scaling provides $\Delta I/I = (\alpha - 1)\Delta r/r = -0.25\Delta r/r$, which is consistent with the evolution seen in Fig. 14.

This slow increase in time of the electric current flowing near the axis is a natural consequence of the increase of the disk emf $e_{\rm disk}$ as the outer disk regions achieve a steady state.

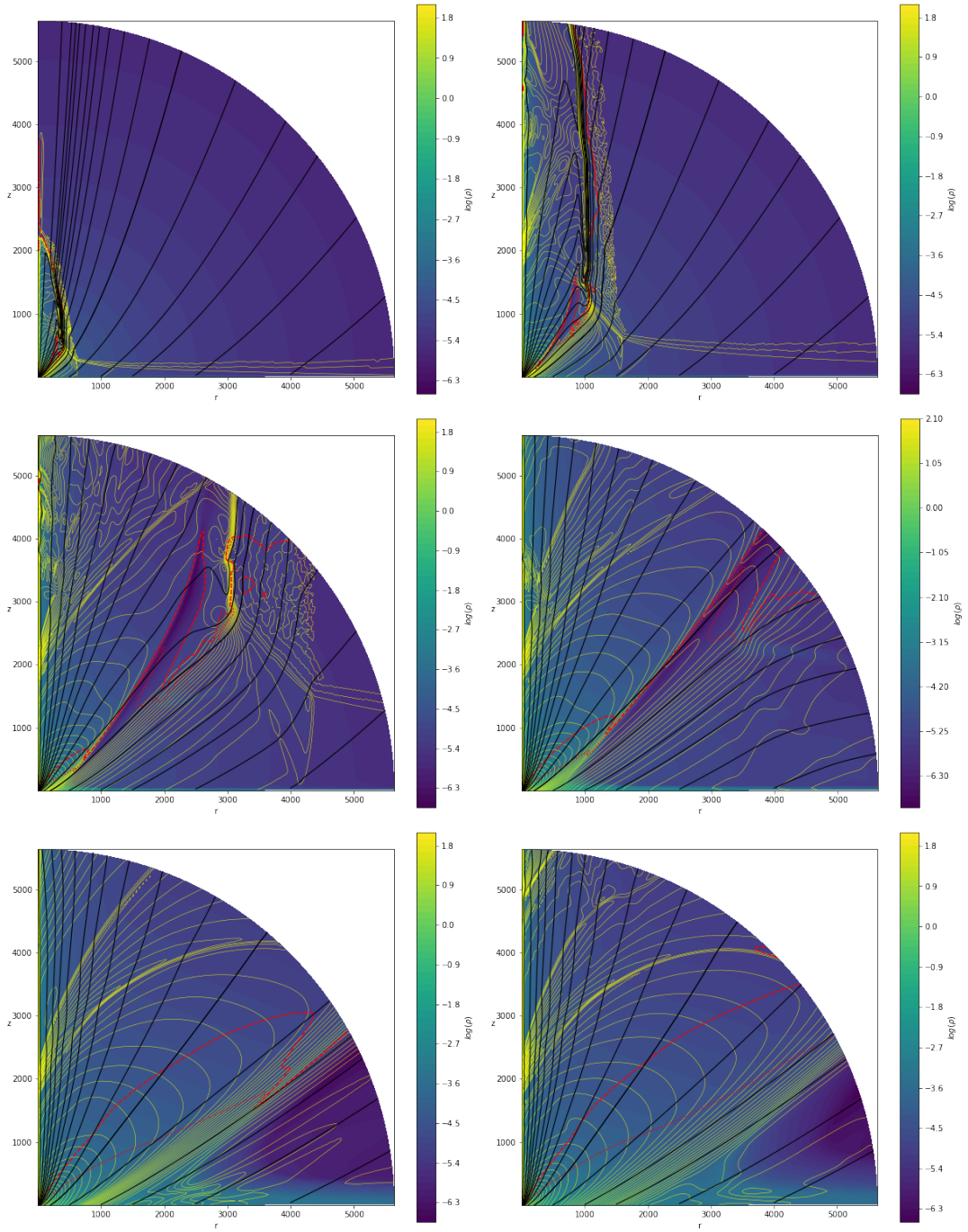

Fig. 13. Snapshots of our reference simulation K2 at different times (given in T_d units). From top to bottom, left to right: $t_1 = 551, t_2 = 2.08 \times 10^3, t_3 = 8.51 \times 10^3, t_4 = 1.99 \times 10^4, t_5 = 1.05 \times 10^5$, and $t_6 = 1.58 \times 10^5$. The background color is the logarithm of the density, black lines are the magnetic surfaces, red lines the Alfvén (dotted) and FM (dashed) surfaces, and yellow curves are isocontours of the poloidal electric current.

Indeed, $e_{\rm disk} \simeq \int_{R_d}^{r_{\rm max}} \Omega_K r B_z {\rm d}r$ increases with $r_{\rm max}$, which is the maximal radius in the disk that achieved a steady state. This increase in the available current is expected to stop when no further relevant emf is added. The available current is determined at the disk surface by the crossing of the Alfvén critical point, because it is that point that fixes the available total specific angular momentum carried away. One can therefore estimate the time where the current should level off as the time when the outermost magnetic field line reached the Alfvén point. Figure 14 shows that this is achieved approximatively around t_6 with $r_{\rm max} \sim 10^3$, corresponding to a full orbital period at $r_{\rm max}$ equal to $t = 2\pi r_{\rm max}^{3/2} = 2 \times 10^5$ (we note that the time for the flow ejected at $r_{\rm max}$ to reach the outer boundary is comparable). After a time of a few $10^5\ T_d$, our simulation has finally achieved a global steady state.

4. Parameter dependence

In the previous section, we showed that our reference simulation K2 behaves qualitatively like the self-similar analytical calculations of Blandford & Payne (1982) and F97, with a refocusing toward the axis and the formation of a recollimation

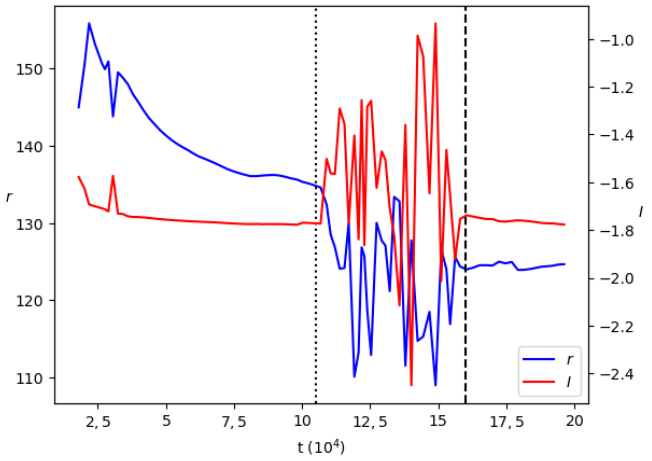

Fig. 14. Time evolution of the cylindrical radius r measured at $Z = 3500$ of the magnetic surface anchored at $r_o = 3$ (blue curve) and the electric current $I = rB_\phi$ (red) flowing within that surface for simulation K2. The two vertical dashed lines correspond to $t_5 = 1.05 \times 10^5$ and $t_6 = 1.58 \times 10^5$.

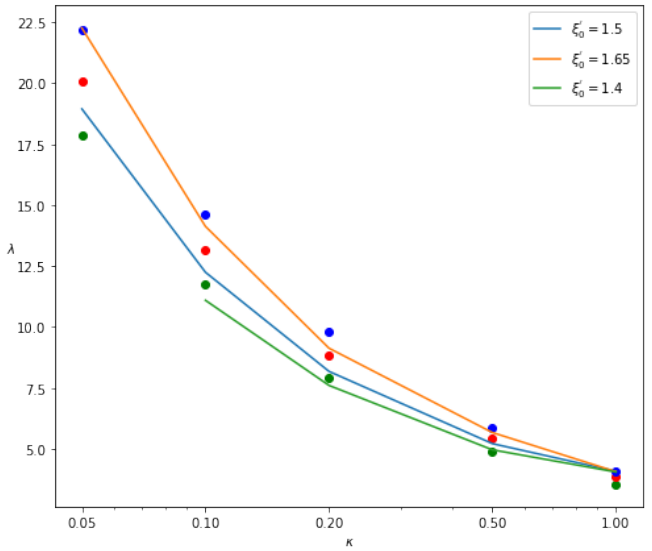

Fig. 15. Jet parameter space $\lambda(\kappa)$ at the final stage of our simulations K1–K5 with $\alpha = 3/4$. Each simulation is obtained for a unique mass loading κ and gives rise to a distribution of the magnetic lever arm λ with the radius: green, red, and blue dots correspond to anchoring radii $r_o = 5, 50$, and 500, respectively. The solid curves are obtained for constant values (indicated in the panel) of the initial magnetic field inclination $\xi'_0 = B_r/B_z$ at the disk surface.

shock. However, the presence of the axial spine breaks down the self-similarity and introduces additional shocks localized at the spine–jet interface.

To further understand the behavior of these shocks, we conducted a parameter study in κ and α, the jet mass load and the radial exponent of the disk magnetic flux, respectively. We finally ran one simulation with the same JED parameters as in our reference simulation K2, but with a rotating spine. All our simulations are presented in Table 1.

4.1. Influence of the mass loading parameter κ

In this section, we present our simulations K1 to K5, obtained with the same parameters as K2 except for the mass load κ which is varied from $\kappa = 0.05$ to $\kappa = 1$. Our parameter range in κ is slightly smaller than the one achieved by Blandford & Payne (1982) which goes down to $\kappa = 0.01$. It can be seen in Fig. 15, which represents the magnetic lever arm λ as a function of the mass-loading parameter κ. Each simulation is obtained for a unique value of κ but as the simulation is not strictly self-similar, we obtain a range in λ: the larger the anchoring radius, the larger the field line inclination at the disk surface and the larger the magnetic lever arm λ. To ease the comparison with Fig. 2 of Blandford & Payne (1982), for each simulation, we computed the anchoring radius r_o at which the field line inclination $\xi'_0 = B_r/B_z$ at the disk surface is equal to 1.4, 1.5, and 1.65. This allowed us to draw in our Fig. 15 iso-contours of ξ'_0, which are in agreement with the above expectations and analytical self-similar calculations (see also Fig. 3 in F97).

All simulations achieve a steady-state and exhibit roughly the same behavior as K2, as can be seen in Fig. 16. From top to bottom, κ increases from 0.05 to 1, the left panels showing the whole computational domain with the two critical surfaces in red (A, dotted and FM dashed) and the right panels providing a close up view around the shock-forming regions near the axis. Table 1 provides the value of several jet quantities: the spine mass-loss rate stays around 10% of the jet mass-loss rate, despite the net increase in $\dot{M}_{\rm jet}$ ($\propto\kappa$, factor 20 increase). Similarly, while the jet power $P_{\rm jet}$ scales in κ, the spine power stays around 80% of the jet power.

The first observation is that the altitude of the main recollimation shock (the one merging with the FM surface) decreases globally with κ. This is quantitatively shown in Fig. 17, where $Z_{\rm shock}$ moves from 2150 down to 700. The same evolution occurs for the altitude $Z_{\rm tip}$ where the main shock merges with the FM surface. Globally, as κ increases, the whole jet structure decreases toward the disk.

Such behavior is consistent with the self-similar calculations obtained by F97. Indeed, as evidenced in his Fig. 6, the denser the jet (larger κ), the sooner (smaller altitudes) recollimation takes place. This can be understood qualitatively by the fact that $\lambda = 1 + q/\kappa$, where $q = |B_\phi/B_z|$ is the magnetic shear at the disk surface (F97). Now, as the mass load κ increases, the magnetic lever arm λ must decrease (see also Fig. 15). This translates into magnetic surfaces that open less, a less efficient magneto-centrifugal acceleration, and recollimation shocks that are not only closer to the disk but also show a smaller compression rate χ due to a smaller FM Mach number n.

However, the physical scales implied are very different. Here, a factor 20 difference in κ leads to a decrease in $Z_{\rm shock}$ by a mere factor 3, with a minimum value of 700. In F97, the mass-loading parameter $\kappa \sim \xi$ varies from 0.01 to 0.05 only (for a constant disk aspect ratio, see his Fig. 3) but leads to variations in recollimation altitudes that span six decades. Our lowest $Z_{\rm shock}$ obtained for $\kappa = 1$ is still much farther away than the minimum height of $\sim$10 found for $\kappa \sim 0.05$ in F97.

This discrepancy can of course be attributed to the very different injection properties. Indeed, our numerical simulations assume a supersonic flow while the self-similar calculations compute the disk structure and outflows are found to only be super-SM (and still subsonic) at the disk surface. However, our guess is that the huge difference in the shock position is probably due to the existence of the spine, which breaks down the self-similarity. Indeed, recollimation is due to the dominant hoop stress, and while in our case all quantities are leveling off on the axis, strictly self-similar solutions have an axial electric current that grows without limits. For instance, at a cylindrical distance $r = 0.1$ from the axis at the spine basis, our

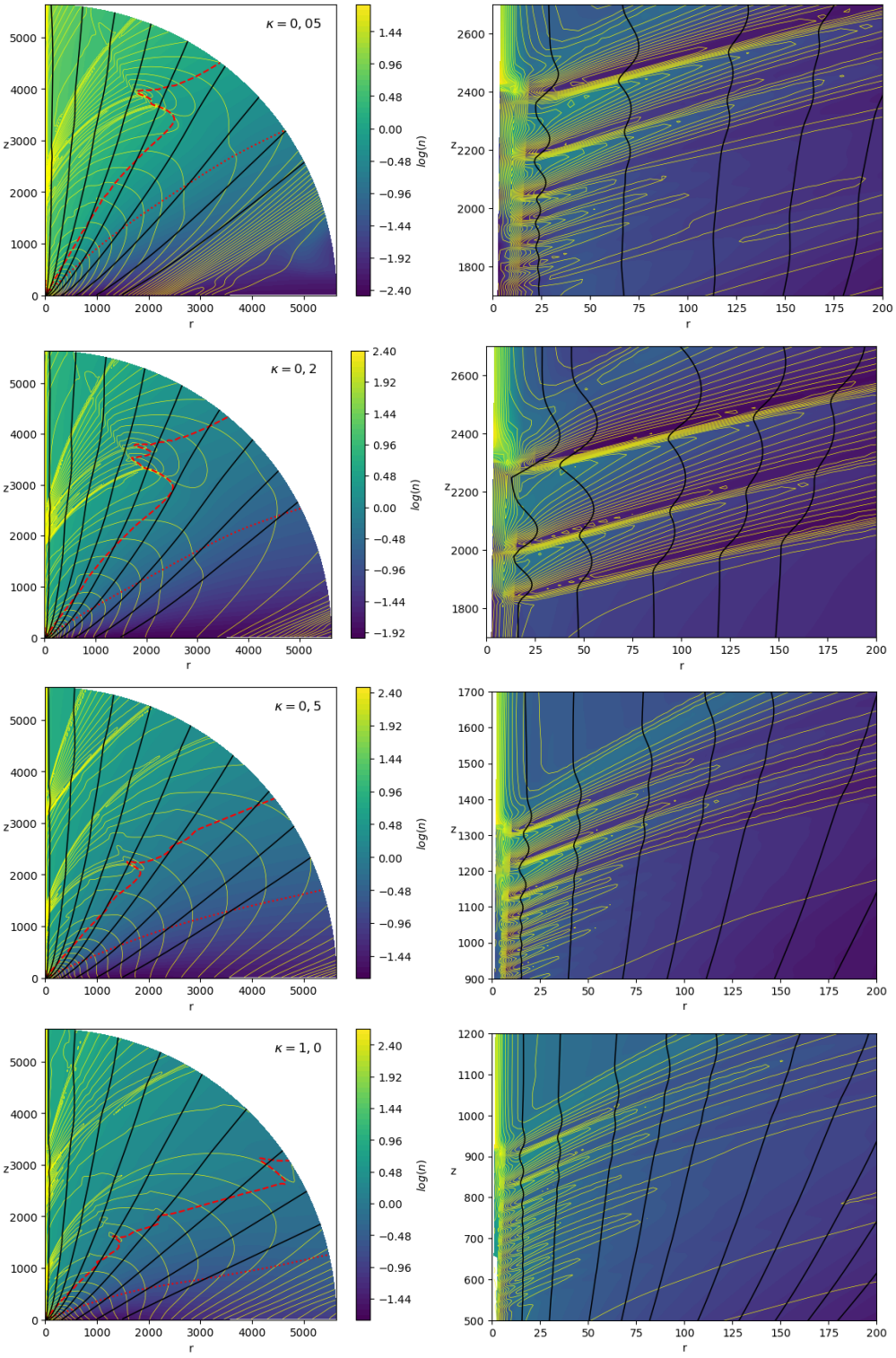

Fig. 16. Influence of the mass-loading parameter κ on the final stage of jets obtained with $\alpha = 3/4$. The color background is the logarithm of the FM Mach number n, black solid lines are field lines, yellow lines are isocontours of the electric current rB_ϕ and the red dashed (resp. dotted) curve is the FM (resp. Alfvén) critical surface. The *left panels* show the whole domain and the *right panels* a close-up view around the shock-formation regions. In the *left panel*, the field lines anchoring radii are $r_o = 3; 15; 40; 80; 160; 320; 600; 1000; 1500$. In the *right panel*, the field lines anchoring radii are $r_o = 1.2; 2; 3; 4; 5; 7; 9; 11; 13; 15$.

B_z remains comparable to the disk field, B_ϕ goes to zero, and the normalized Bernoulli integral e has decreased by a factor 5 (see Fig. B.1). Self-similar solutions, on the contrary, have fields and a Bernoulli integral increasing respectively by a factor $10^{5/4} = 17.8$ and 10. This suggests that the conditions assumed on the axis most certainly affect the overall jet collimation properties. We return to this aspect later on by changing the spine properties.

A second interesting aspect is the appearance of a second ensemble of shocks arriving at higher altitudes, namely

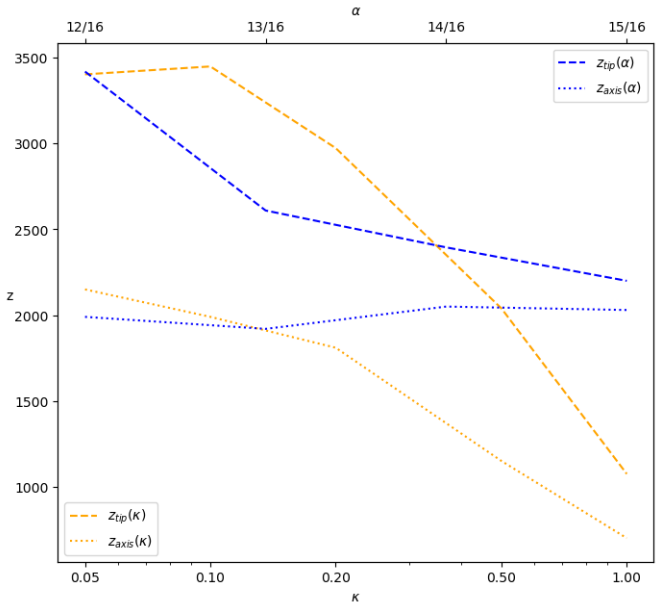

Fig. 17. Influence of κ (orange lines) and α (blue lines) on the altitude of the main recollimation shock. This is done by measuring two altitudes for each shock: its height at the axis ($Z_{\rm shock}$, solid lines) and the altitude of its outer edge ($Z_{\rm tip}$, dashed lines). The scale for κ is indicated below, while the scale for α is above.

$Z > 3000$ for $\kappa = 0.5$ and $Z > 2000$ for $\kappa = 1$. This second group of shocks is also composed of two large recollimation shocks separated by smaller ones. The distance (measured at the axis) between the two large shocks is comparable to the width of the first group of shocks. As discussed in Sect. 3.3, this hints to the fact that each group is caused by the global jet recollimation dynamics, which should be periodic in the Z-direction on a scale H_R. Looking at the simulation K4 with $\kappa = 0.5$, this would give $H_R \sim 1650$, while the width of each group is around $W \sim 300$ (the first group of shocks being located between 1150 and 1450, and the second between 3100 and 3400). As long as no dissipation is introduced, such a periodic behavior should continue in a box of infinite size.

4.2. Influence of the magnetic field distribution α

In this section, we vary the magnetic flux distribution exponent α in our simulations A1 to A5, keeping all other parameters (see Table 1) constant. A strict mathematical self-similarity links the magnetic field distribution α with the disk density in such a way that $\alpha = (12 + 8\xi)/16$, where ξ is the disk ejection efficiency and is related to the disk accretion rate $\dot{M}_a(r) \propto r^{\xi}$ (Ferreira & Pelletier 1995). As long as material is only outflowing from the disk (namely $\xi > 0$) and jet power is only released from accretion (namely $\xi < 1$, F97), this leads to the unavoidable constraint $12/16 < \alpha < 20/16$.

Only $\alpha = 12/16$ can be compared to the cold jet solutions of F97, assuming an ejection efficiency $\xi < 0.1$. Larger values of $\alpha > 12/16$ would require a disk ejection efficiency of $\xi = 0.125$ up to 0.5. These values are only achievable in analytical studies by introducing an additional heat deposition at the disk surface (magneto-thermal flows, Casse & Ferreira 2000b) and/or a much smaller magnetic field strength (Jacquemin-Ide et al. 2019). However, the physical processes required to get these solutions are missing in our simulation setup. We nevertheless vary α in order to allow a comparison with the self-similar jet solutions found by Contopoulos & Lovelace (1994), who tested the effects of α ranging from 0.5 to 1.02. We did not succeed to numerically obtain steady-state solutions for $\alpha \geq 1$ for reasons that are discussed below, and show only simulations with α ranging from $10/16 = 0.625$ to $15/16 = 0.937$.

All our A1 to A5 simulations reach a steady state with the same overall behavior as K2, namely the existence of two main recollimation shocks within the computational domain, separated by several smaller standing shocks located at the spine–jet interface. This can be clearly seen in Fig. 18 where, on the other hand, a trend with α can be observed. Indeed, the radial extension of the shocks decreases with α. This can also be seen in Fig. 17 which shows that the altitude $Z_{\rm tip}$ of the main recollimation shock decreases with α, while its altitude $Z_{\rm shock}$ at the axis barely changes. For simulations A1 ($\alpha = 10/16$) and A2 ($\alpha = 11/16$), the main recollimation shock ends out of the box, and therefore $Z_{\rm tip}$ cannot be defined. However, the value of $Z_{\rm shock}$ remains similar (see Table 1). This is a geometrical effect due to the fact that, as α increases, the magnetic field configuration goes from a highly inclined magnetic configuration ($\alpha = 0$ corresponds to a monopole) to one that is much less inclined ($\alpha = 2$ is a purely vertical field). This can be seen in the shape of the magnetic field lines (black solid lines) in Fig. 18. This geometrical effect translates into a smaller incidence angle near the axis and therefore to weaker shocks (the incidence becomes normal and $n_\perp$ decreases to unity).

For $\alpha = 10/16$ and $11/16$, the shocks still exist but the MHD characteristics are much more vertical than in K2. A larger box would probably be necessary to recover the K2 behavior. The opposite trend can be seen for $\alpha = 14/16$, with less vertical MHD characteristics allowing now the second main recollimation shock to merge with the FM surface within the domain.

Table 1 also shows that as α increases, the last radius on the disk giving rise to a super-FM flow increases and the colatitudes (measured at the outer boundary) $\theta_{\rm FM}^{\rm ext}$ and $\theta_{A}^{\rm ext}$ of the critical FM and A surfaces decrease. These results are a natural consequence of the magnetic field distribution becoming more vertical as α increases. As the jet mass loss $\dot{M}_{\rm jet}$ and jet power $P_{\rm jet}$ are computed up to $r_{0,\rm FM}$ which increases with α, $\dot{M}_{\rm jet}$ and $P_{\rm jet}$ increase with α. Still, the mass loss increases even when computing up to a fixed radius. Indeed, the density decreases less with an increasing α ($\rho \propto r^{2\alpha-3}$) and the outer disk regions contribute more to the mass flux and jet power. Moreover, as the distribution in density is flatter with an increasing α, it is only natural that $\dot{M}_{\rm spine}/\dot{M}_{\rm jet}$ and $P_{\rm spine}/P_{\rm jet}$ decrease when α increases.

In summary, we find that the altitude of the shocks barely changes with α, which is in strong contrast with Contopoulos & Lovelace (1994). Indeed, their Table 1 shows that as α increases from 0.5 to a critical value 0.856, their self-similar jet becomes super-FM and undergoes a recollimation at a distance that increases by several decades (as in F97). As discussed above, we believe that this discrepancy is due to our non-strict self-similar scaling (which forbids the unlimited growth of the inner electric current and the subsequential Z-pinch in self-similar solutions) and the presence of the spine. Contopoulos & Lovelace (1994) also report that their solutions with $\alpha > 0.856$ remain sub-FM, while we clearly achieve super-FM flows up to $\alpha = 0.937 = 15/16$. This is again probably a difference in our jet radial balance, leading to a slightly different jet acceleration efficiency. Finally, their solutions with $\alpha = 1$, 1.01, and 1.02 remain sub-FM but evolve through a series of radial oscillations at logarithmically equal distances in Z.

Our simulation A5 is the simulation with the largest value $\alpha = 15/16$, of close to unity. Although the final integration time

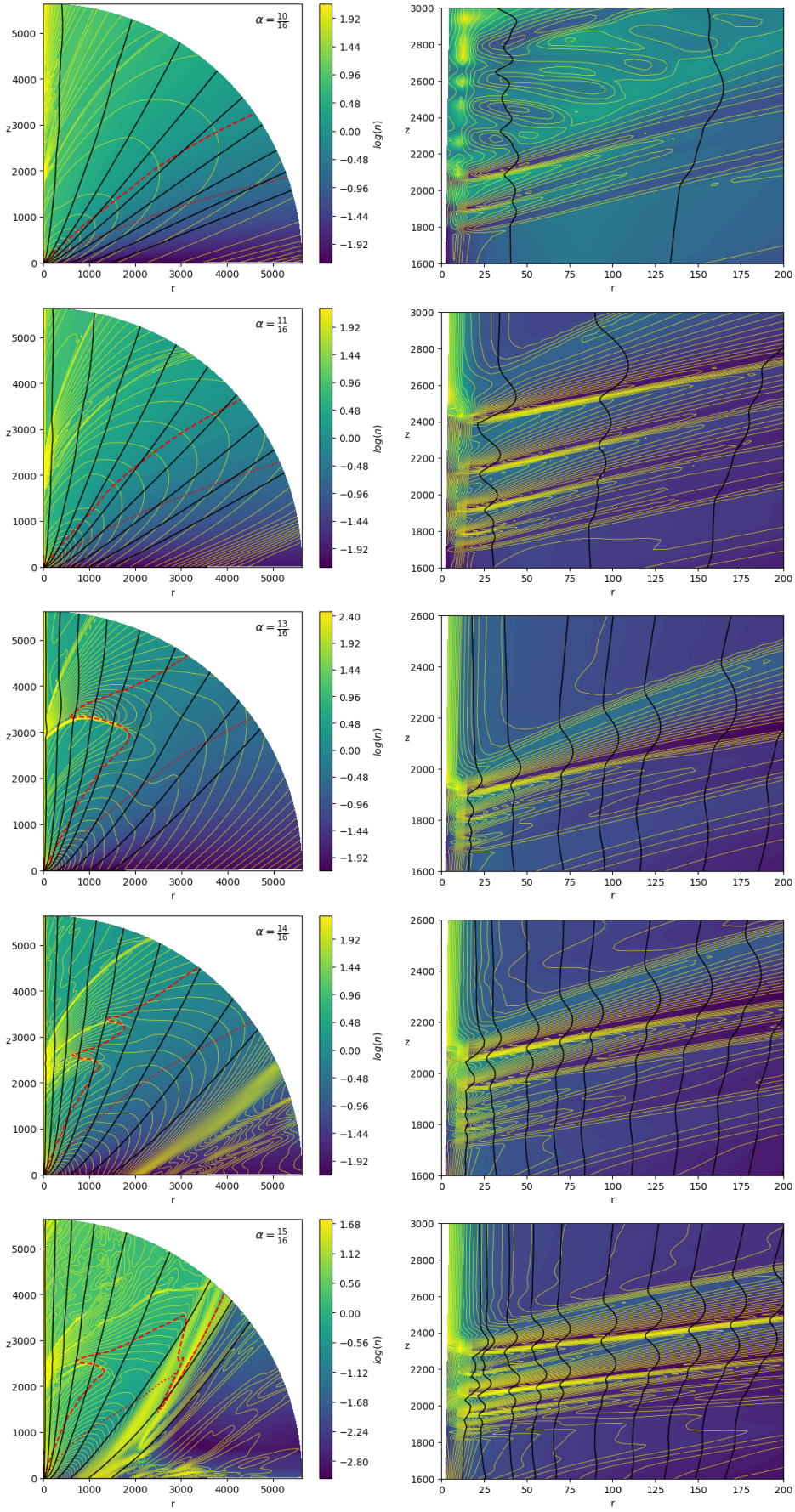

Fig. 18. Influence of the magnetic field distribution α on the final stage of jets obtained with $\kappa = 0.1$. We use the same notations, colors, and field lines anchoring radii as in Fig. 13.

$t_{\rm end}$ is quite comparable with the other simulations, its appearance clearly shows that the global configuration is still far from achieving a steady state like K2. This can be seen in Fig. 18, in the shape of the critical surfaces but also on the isocontours of the poloidal electric circuit (yellow curves) that are still struggling to find their final state. This is normal and points to a numerical difficulty in computing MHD codes when the magnetic configuration is such that $\alpha \geq 1$.

Indeed, it has been argued above that for self-similar boundary conditions, the jet transverse balance imposes a toroidal magnetic field scaling with the vertical magnetic field. This leads to an electric current at the disk surface behaving as $I = rB_\phi \propto r^{\alpha-1}$. Magnetic configurations with $\alpha < 1$ correspond to a poloidal current density leaving the disk surface and closing along or near the spine (where it flows back to the disk), whereas configurations with $\alpha > 1$ correspond to an inward poloidal current density, with current closure being done only at the outskirts of the outflow (F97). As div $\boldsymbol{J} = 0$ in ideal MHD, all electric circuits must be closed. Let us define a radius in the disk r_I such that for $r < r_I$, the electric current flows down into the disk whereas it flows out of it for $r > r_I$. For $\alpha < 1$, r_I is always larger but close to R_d implying very short timescales. As discussed in Sect. 3.6, as time is evolved, the outer disk regions provide more current that struggles to reach the innermost disk radius. But a global radial balance can be achieved consistently with the electric current closure condition because the local time near r_I is small. On the contrary, configurations with $\alpha > 1$ have r_I that is constantly increasing in time (as $t^{2/3}$), leading to an electric circuit that freezes in time and therefore to a transverse MHD balance that takes a much longer time to achieve steady state. We observe this behavior for all values of $\alpha > 1$ and none of these simulations has achieved a steady state.

The limiting value $\alpha = 1$ (close to our A5 simulation) would correspond to $r_I = R_d$ and absolutely no electric current flowing out of the disk until some outer radius. Current closure could only be done through the spine and the outer jet interface with the ambient medium. But then, no magnetic acceleration would be possible as no electric current could be used along the magnetic surfaces. This would correspond to an exact force-free field configuration fully determined by the chosen boundary conditions. To compute such a situation, boundary conditions must be designed where the jet launching region has a finite extent. However, we doubt that the outcome would be a force-free field unless explicitly enforced. This is beyond the scope of this paper.

4.3. Influence of a rotating central object

In this section, we do not intend to fully explore the physical parameters of the spine but instead wish to probe whether the spine, despite its small spatial extent, has indeed a profound influence on the overall jet dynamics. All simulations K1-K5 and A1-A5 were done with the same nonrotating central object in order to minimize its emf and numerically follow the outcome of a jet emitted from an outer self-similar disk (see Sect. 2.4.2). Our choice of parameters gives rise to a spine carrying typically 10% of the mass flux, and therefore providing only a small contribution to the overall outflow. Nevertheless, this spine carries a large fraction of the emitted power, even superior to that of the disk for the simulation A1. The spine plays an important role in introducing extra standing shocks at its interface with the jet, but is probably also determining the altitude where the first large recollimation shock occurs. Indeed, as discussed in the previous sections, the amount of electric current that is flowing along the innermost axial regions (along the spine and the inner jet) is

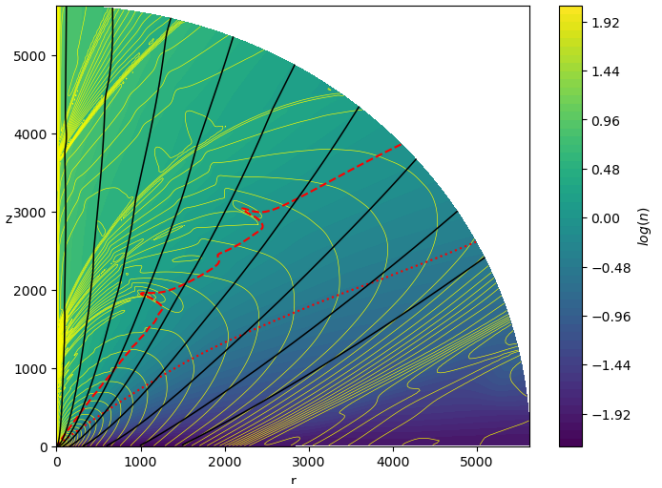

Fig. 19. Snapshot at $t_{\rm end}$ of our SP simulation with a rotating spine, $\alpha = 3/4$ and $\kappa = 0.1$. We use the same color coding as in Fig. 2. The magnetic field lines (black solid lines) are anchored at the same disk radii.

what determines the strength of the Z-pinch acting upon the jet and thereby the altitude $Z_{\rm shock}$.

In order to probe this idea, we ran another simulation with a rotating object (simulation SP in Table 1). We chose an object rotating at the same angular velocity as the innermost disk radius R_d, namely $\Omega_a = \Omega_{Kd}$. This is for instance representative of a star–disk interaction where the disk truncation radius is located at the co-rotation radius. By doing so, the emf due to the central object becomes non-negligible and we expect a stronger poloidal electric current. However, care must be taken as enhancing the hoop stress may also lead to an overwhelming radial pinch. To prevent this and get somewhat closer to the self-similar conditions, we also increase the value of the Bernoulli integral on the axis and use $e_a = 10$ ($e_a = 2$ for the other simulations). We note that the Bernoulli invariant from the innermost disk region is $e_d \simeq \lambda_d - 3/2 \sim 10$. This translates mostly into a thermal pressure that is five times larger than previously. Thus, our new conditions for the spine provide a rotation and a specific energy that are only comparable to those at the inner jet, not much larger as in a self-similar situation.

Figure 19 shows the final outcome of this new simulation. It achieves a global steady state with the same features as in our reference simulation K2. However, the shocks are, as expected, localized at lower altitudes, allowing a second set of large recollimation shocks to appear near $Z \sim 3700$. The first large recollimation shock appears at $Z_{\rm shock} = 1300$, which is significantly smaller than $Z_{\rm shock} = 1850$ obtained for a nonrotating central object. This result confirms the role of the central object in shaping, through its spine, the collimation properties of the jets emitted by the surrounding disk. This is very promising and deserves further investigation.

5. Discussion

5.1. Caveats

This paper provides some novel information on the collimation of jets emitted from self-similar magnetized disks. However, we would like the reader to pay attention to several caveats:

As we tried to replicate a Blandford & Payne process, we mostly explored the ejection conditions on the disk and not on

the source, with the exception of the rotation (see Sect. 4.3). For instance, we kept a value of sonic mach number $M_S = 10$ on the whole ejection zone, thus only creating cold jets. It would be interesting to provide a real exploration of the spine parameters to better understand the role of the central object in the collimation.

The shocks displayed in our simulations are rather weak ($\chi \sim 2$ near the axis, $\chi \sim 1.3$ in the jet). This is probably due to our isentropic scheme, but as the simulations only reach small values of n, the compression rates are intrinsically low (see Appendix C). Moreover, as shown in Eq. (C.4) the impact of those shocks on jet angular velocity in YSOs is probably weak, at least for jets achieving $m^2 \gg 1$.

Our adiabatic solutions do not allow energy dissipation, and so the shocks should go on, one above the other, with each shock producing its own local accelerating circuit. This is showcased by the presence of a second subset of shocks in simulations K4, K5 (see Fig. 16), and SP (see Fig. 19). Thus, this setup does not allow the presence of a "true" asymptotic circuit that would extend up to infinity on the jet axis.

These simulations are highly dependent on the numerical setup. In order to capture the expected shocks, we used an HLLD solver, switching to a more diffusive HLL solver and MINMOD linear spatial reconstruction in regions of extremely low density and very high Alfvén speed. For the same reason, we used a higher resolution in θ around the axis to resolve the shocks. Still, we were only able to reach very long timescales thanks to a novel method that boosts the numerical integration (see Appendix A).

5.2. Comparison with other numerical works

In this section, we only compare our findings with previous 2D platform simulations of nonrelativistic jets. Indeed, relativistic jets develop an electric force that deeply affects the asymptotic collimation, forbidding a direct comparison with our nonrelativistic setup. We also disregard 3D jet simulations as they usually introduce a whole new phenomenology related to jet instabilities that are not present in our work. Making 3D simulations of our jets is planned for future work.

Platform simulations of jets have a great many degrees of freedom and it is therefore very difficult to determine the exact generic results on jet collimation that can be derived from them. Even if the whole injection domain is chosen to be sub-SM, three free distributions must be chosen at the boundary (assumed to be the disk surface), usually $B_z(r), \rho(r)$, and $u_z(r)$. The disk being assumed to be Keplerian, most previous works used field lines rotating at Keplerian speeds and $u_z = V_{\rm inj} V_K$, where $V_{\rm inj}$ is a small dimensionless number. We use the following notations $B_z \propto r^{\alpha-2}$ and $\rho \propto r^{-\alpha_\rho}$ leading to

$$\kappa = \frac{V_{\rm inj}}{\mu^2} = \kappa_d r^{\alpha_\kappa}, \quad \mu = \frac{V_{Az}}{V_K} = \mu_d r^{\alpha_\mu}, \tag{20}$$

with $\alpha_\kappa = -2\alpha_\mu = -2\alpha + \alpha_\rho + 3$ and the cylindrical radius is normalized to the inner radius R_d. For a given magnetic field distribution, the way the mass is injected in the outflow (or how the magnetic energy must vary within the disk) is an important quantity allowing to compare the various jet models. Our injection conditions (Eq. (8)) have $\alpha_\rho = 2\alpha - 3$, and therefore $\alpha_\mu = \alpha_\kappa = 0$, which is in agreement with self-similar studies (BP82; F97). For our explored range in $\alpha < 1$, our jets are always dominated by the mass flux emitted from the innermost disk regions. As discussed previously, the spatial and temporal scales are also very important in order to obtain recollimation shocks. We recall that our spherical domain goes up to $R_{\rm ext} = 5650 R_d$ covered with 266×1408 zones and lasts $T_f \gtrsim 10^5\, T_d$.

The box size and timescales achieved in the pioneering works of Ouyed & Pudritz (1997a,b, 1999) were of course quite small, with a cylindrical domain $(z, r) = (80, 20)$ in R_d units and a resolution of $(500, 200)$ cells, with the simulations lasting up to $T_f \sim 500$. These authors studied mostly $\alpha = 1$ and $\alpha = 2$ magnetic configurations, assuming $\alpha_\rho = 3/2, \mu_d = 0.01$ and with no injected spine. Their jets have therefore a steeply decreasing κ (or increasing μ) with $\alpha_\kappa = 3/2 - 2\alpha$, providing situations very different from ours. The authors argued that the nature of the outflow (steady or not) is mostly determined by the mass load κ, with unsteady jets containing shocks and associated knots arising at small values of $\kappa_d \sim 10^{-2}$. While these shocks are indeed due to jet material being focused toward the axis, Ouyed & Pudritz (1997a,b, 1999) did not report any steady-state situation. Our own simulations show that their timescales were still too short to warrant a transverse jet balance, especially for $\alpha \geq 1$. Moreover, it remains unclear as to whether these knots were indeed a consequence of a small mass load κ_d or due to the boundary conditions used at the jet basis, which were too numerous and therefore over-determined the outflow dynamics (see discussions in e.g., Bogovalov 1997; Krasnopolsky et al. 1999; Ramsey & Clarke 2019).

Ustyugova et al. (1999) showed that if the simulation region is elongated in the z-direction, then Mach cones may be partially directed inside the domain, leading to an artificial influence (usually collimation) on the flow. Using a domain $(z, r) = (200, 170)$ with 100×100 cells, these authors showed that this effect can be reduced with a square or spherical grid.

Pudritz et al. (2006) extended their work by exploring a larger range in $\alpha = 1, 3/4, 1/2, 1/4$, using $\kappa = 5 r^{3/2-2\alpha}, \mu_d = 0.01$ and no spine. These latter authors argued that the collimation of a jet depends on its radial current distribution, which in turn is prescribed by the mass load. Simulations with $\alpha = 1, 3/4$ would collimate to cylinders due to a decreasing κ leading to a large B_ϕ, whereas simulations with $\alpha = 1/2, 1/4$ with an increasing κ would produce a smaller B_ϕ and jets closer to wide-range outflows with parabolic collimation. However, our simulations show that the physical scales needed to observe the correct asymptotic state are much larger than those achieved in these early simulations. Moreover, it is indeed correct that self-collimation depends on B_ϕ, which, in a magnetic jet that carries away the disk angular momentum, namely $-rB_\phi/\eta \propto \Omega r^2$, varies as $B_\phi \propto \kappa(r) B_z$ at the disk surface. In their case, this expression leads to $B_\phi \propto r^{-1/2-\alpha}$, which is indeed more steeply decreasing with α. (However, our guess is that the collimation observed within the box of Pudritz et al. 2006 is mostly a consequence of the potential magnetic field configuration used as the initial condition, as also illustrated in Fig. 8.) Therefore, the smaller α, the wider (less collimated at a fixed distance) the jet.

The influence of the magnetic field profile α on the asymptotic jet collimation has also been investigated: Fendt (2006) performed 40 simulations in a larger cylindrical grid $(z, r) = (300, 150)$ with 256×256 cells, with the simulations lasting up to $T_f \sim 300$ to $5\,10^3$ (for those achieving a steady state over at least 50% of the grid). He explored a wide range in α_ρ from 0.3 to 2 and in α from 0.5 to 1.8, using the same boundary conditions as Ouyed & Pudritz (1997b), with $V_{\rm inj} = 10^{-3}, \kappa_d = 5$, no spine, and μ_d varying between 0.1 and 2.67. Fendt (2006) confirmed that the degree of collimation is decreasing for a decreasing α regardless of α_ρ, in agreement with our suspicion that the overall MHD collimation trivially follows the potential field configuration (see also Sect. 3.2). For $\alpha > 1.6$, no steady-state jet is

actually found, with a wavy radial pattern evolving along the outflow. This is consistent with our finding that for $\alpha \geq 1$ the timescales for reaching stationarity become overwhelmingly long and also with the existence of radially oscillating, sub-FM analytical solutions for $\alpha \geq 1$ (Contopoulos & Lovelace 1994). Fendt (2006) also reports a degree of jet collimation increasing with the jet magnetization exponent, namely with $\mu_\sigma = -\alpha_\kappa - 3/2$ (see his Eq. 10). Now, of the 40 simulations, only 6 have $\alpha_\kappa = \alpha_\mu = 0$ and 8 have $\alpha_\kappa > 0$, meaning that most simulations describe a mass loading decreasing with the radius. None of the simulations show standing recollimation shocks, even in the BP82 case obtained with $\mu_d = 0.177$ (we use $\mu_d = 1$). Putting aside this difference, our Fig. 12 shows that around their final time $T_f = 5000$, we observed shocks only around $Z \sim 1900$, far beyond their computational domain.

Krasnopolsky et al. (1999) used a cylindrical grid $(z, r) = (80, 40)$ with 256×128 cells, with the simulations lasting up to $T_f \sim 170$, introducing a ballistic axial flow below R_d (the spine), injected close to the escape speed and surrounded by a disk wind. These authors used the correct number of boundary conditions and, by testing the effects of adjusting the size of the box, they showed the drastic importance of the amount of magnetic flux becoming super-A within the box on the overall flow collimation. They studied mostly $\alpha = 1/2$ and 3/4 with $\mu_d = 4$ and rather flat density distributions leading to $\alpha_\kappa > 0$, from 2 to 3/2. The authors do not report any time-dependent behavior seen in previous studies, which they attribute to both the existence of their sub-FM inner spine (where magneto-centrifugal acceleration is inefficient) and the correct treatment of boundary conditions. This latter work was extended by Krasnopolsky et al. (2003) on a much larger box $(z, r) = (10^3, 10^3)$ with 190×210 zones, with the simulations lasting an unspecified time T_f. They only studied the case $\alpha = 1/2$, with ejection from a finite zone $r_o = R_d$ and $r_o = 10R_d$, yielding $\alpha_\rho = 1$ ($\alpha_\kappa = 1$) or $\alpha_\rho = 3$ ($\alpha_\kappa = -1$). The authors found that the collimation degree of this finite jet is improved for a steeper density profile, namely with a decreasing mass load with the radius, as discussed above. Krasnopolsky et al. (2003) report neither recollimation toward the jet axis nor radial oscillations, and attributed this behavior to their nonself-similar scaling. Our own results show instead that recollimation should be seen farther out (beyond their box) and that radial oscillations are expected only for $\alpha > 1$.

Using the same grid and numerical setup as Krasnopolsky et al. (2003), Anderson et al. (2005) studied the effect of κ_d on the collimation of a cold BP82 jet model with $\alpha = 3/4$ and $\alpha_\rho = 3/2$ (thus $\alpha_\kappa = 0$). These authors varied κ_d from $6.3\,10^{-3}$ to 19 assuming that ejection takes place only from $r_o = R_d$ and $r_o = 10\,R_d$ (but enforcing B_z to zero at the edge of the launching region), while we assumed ejection from the whole disk and varied κ_d only from 5×10^{-2} to 1. Despite the truncation due to the limited ejection range and the (almost) purely radial magnetic field at the edge of the launching region, Anderson et al. (2005) recover the same results as in steady-state jet theory (FP97): jets become increasingly open as κ_d decreases (see discussion in Sect. 4.1). Anderson et al. (2005) do not report any recollimation shock (although wiggles can be seen in their Fig. 4) but again, our shocks fall below $Z = 1000$ (within their box) only for $\kappa_d \sim 1$ (see Fig. 17). We conclude that their box was too small to observe any standing recollimation shock. The authors report the inability to reach steady state (the timescale T_f is unspecified) for κ_d larger than unity, when field lines start to oscillate and produce ripples that propagate outward. This behavior is consistent with analytical studies and is related to the capability to produce super-A flows when they are heavily loaded (or have a weak magnetic field). Indeed, magnetically driven cold flows are possible only up to $\kappa \sim 1$, leading to a magnetic lever arm $\lambda \sim 2$. For larger mass loads (and smaller λ), gravity plays an important role, with the Alfvén surface getting closer to the disk, requiring the field lines to be bent by much more than the fiducial 30° at the disk surface[4] (see Fig. 4 and discussion around the Grad-Shafranov equation in Jacquemin-Ide et al. 2019).

The largest axisymmetric simulations have been provided by Ramsey & Clarke (2011, 2019), using nine levels of AMR in a cylindrical grid $(z, r) = (8\times10^4, 5\times10^3)R_d$ with simulations lasting up to $T_f \sim 6 \times 10^4$. These authors computed the propagation and evolution of eight jets up to observable scales, defined with varying mass loads κ_d from 5×10^{-2} to 32 and $\alpha_\rho = 3/2, \alpha = 1$ (thus a decreasing mass load with $\alpha_\kappa = -1/2$). In the simulations of these latter authors, mass is injected with $V_{\rm inj} = 10^{-3}$ and there is no injected spine as in Ouyed & Pudritz (1997a), although a spine naturally emerges. In all simulations, Ramsey & Clarke (2011, 2019) observe that regions beyond $r_o \sim 10\,R_d$ fail to displace the hot atmosphere and that the outflow is stifled, despite the decrease in κ. This is actually consistent with our previous discussion for simulations with $\alpha \geq 1$, which take a much longer timescale to reach steady state. Nevertheless, as the inner parts of the outflow evolve on much shorter timescales, some quasi-stationary situation can settle (see their Sect. 5.3). With no surprise, this is the case for small mass loads, while knots appear for $\kappa_d = 0.5$ (simulation E) and are recurrent (quasi-periodic) for $\kappa_d = 2$. These knots are not to be compared with our standing recollimation shocks, as none of the MHD invariants are constant along field lines passing through them. They are made of plasmoids launched from $R_d \lesssim r_o \lesssim 2R_d$, where gas is both dense and hot. The knot formation mechanism is here directly related to the jet-launching process from this innermost disk region. Indeed, in this region, the field line bending is insufficient to drive the massive injected material, until a sufficiently strong toroidal field builds up and lifts the matter, in agreement with steady-state theory of massive outflows (F97; Jacquemin-Ide et al. 2019). The regularity of knot spacing is indicative of a simple oscillator related to the necessary build up of a strong toroidal field. These plasmoids are magnetically confined by the surrounding poloidal magnetic field, follow the path of the jet, and eventually merge together. For larger mass loads ($\kappa_d = 8$ and 32, simulations G and H), the outflows are fully unsteady while keeping their global structure (probably because of their 2D nature, as destroying instabilities such as kink or Kelvin-Helmholtz require 3D, as argued by the authors).

To our knowledge, no previous jet simulation has shown the existence of standing recollimation shocks, either because the computational domain was too small and/or the simulation timescales were too short. These limitations are even worse of course for simulations that do take into account the disk physics, as they must also struggle to follow the disk and the mass-loading process.

The first of these simulations computed an accretion–ejection configuration with $\alpha = 3/4$ and $\alpha_\rho = 3/2$ (the BP82 case) within a cylindrical grid $(z, r) = (80, 40)$ on a time $T_f = 251$ only (Casse & Keppens 2002, 2004). On these timescales, the mass-loading process is computed, leading to the inside-out establishment of self-similar conditions with $\alpha_\kappa = 0$. Further simulations, carried out with the same initial configuration but exploring various disk parameters, were computed on slightly extended scales, a grid $(z, r) = (120, 40)$ on a timescale

[4] This is why we could not reach steady-state solutions with $\kappa > 1$ with our setup.

of $T_f = 400$ (Zanni et al. 2007; Tzeferacos et al. 2009, 2013) and a grid $(z, r) = (180, 50)$ on a timescale of $T_f = 5.6 \times 10^3$ (Sheikhnezami et al. 2012). As most of these works were focused on the disk physics and less on the jet dynamics, they provided little information about the latter. The simulations of Stepanovs & Fendt (2016) were done on a spherical grid up to $R_{\rm ext} = 1500$ with $(N_R \times N_\theta) = (600 \times 128)$ zones and up to $T_f = 10^4$, for the same BP82 initial configuration. Such scales would be relevant for the appearance of recollimation shocks but they only show close-up views below $R = 30$ and focus instead on the accretion–ejection correlations. However, the long timescales allow us to see a radial redistribution of both the vertical magnetic field and the disk density (as both evolve on accretion timescales; Jacquemin-Ide et al. 2019), thereby modifying the initial strict self-similar conditions.

The time evolution of the disk magnetic field distribution has been reported previously (Murphy et al. 2009). These simulations were done in a cylindrical grid $(z, r) = (120, 40)$ up to a time $T_f \simeq 6 \times 10^3$, and using $\alpha = 1/4$ with $\alpha_\rho = 3/2$. Such an initial magnetic field distribution leads to a magnetic energy density on the disk midplane that decreases very rapidly ($\propto r^{-1}$), meaning that a super-FM ejection (with proper MHD invariants) only takes place up to a certain radius $r_o \sim 5$ (Murphy et al. 2010). This latter study focused on this ejection from a limited zone within the disk and little was mentioned about the jets. However, we report that on the long timescale of the simulation, the magnetic field is seen to slowly evolve within the disk, leading to some readjustments also in the jet. How such a modification affects the jet transverse balance and possible standing recollimation shocks is an open issue that deserves further investigation.

We note that standing recollimation shocks have already been discussed in steady-state 2D jet simulations built upon analytical self-similar solutions. In these works, a cylindrical box is used, which starts at a z_o well above the disk (say z from $z_o = 10$ to 210 and r from 0 to 100 in units of R_d). This allows the whole domain to be filled with either only a self-similar BP82 jet model (Gracia et al. 2006; Stute et al. 2008) or a combination of an axial (meridionally self-similar) stellar wind surrounded by a BP82 jet model (Matsakos et al. 2008, 2009). The numerical procedure, which evolves the MHD equations over time for a set of boundary conditions, allows a stationary solution to be rapidly obtained on timescales of $T_f \sim 40$ to 10^3. A weak recollimation shock is always found between the axial flow and the BP82 jet, which fulfills most properties discussed in our paper. However, in strong contrast with our own work, the existence of this shock is unavoidable in these works and is directly imposed by the boundary conditions. Indeed, the outflow is already super-FM at the injection altitude z_o for all radii below $r_o \sim 6$ (see for instance Fig. 1 in Matsakos et al. 2008), while field lines are already being focused toward the axis.

5.3. Astrophysical consequences

In this paper, we showcase one mechanism enabling the creation of a recollimating jet and its subsequent shocks. There are other models explaining the creation of such shocks. They could be triggered for instance by a sudden mismatch between the jet and the ambient medium pressure. Studying FRII jets such as those from the radio galaxy Cygnus A, Komissarov & Falle (1998) proposed that the jet confinement and its consequential shocks are caused by the thermal pressure of an external cocoon. For the case of FRI jets, in Perucho & Martí (2007) the jet expands until it becomes under-pressured with respect to the ambient medium, and then recollimates and generates shocks, unless a turbulent mixing layer at its interface with the ambient medium forbids its formation (Perucho 2020). In any case, such shocks happen much farther away than in our case and depend critically on the ambient pressure distribution.

On the contrary, the jets in our simulations are intrinsically collimated by the self-induced hoop stress (see Fig. 10). As shown in FP97 for self-similar cold models and proven here in full 2D time-dependent simulations, this force will lead the cold jets toward the axis, leading to the formation of standing recollimation shocks. Such a mechanism should therefore apply regardless of the external medium and around various astrophysical objects.

Extragalactic jets imaged by VLBI display knots of enhanced emission that could be associated with shocks (as they play an important role for the production of nonthermal emission). While most of these features are moving, some of them appear stationary (Lister et al. 2009, 2013; Doi et al. 2018 and Boccardi et al. 2017 for a review). The closely studied M87 jet is a particularly interesting case. It contains several moving and stationary bright features near the HST-1 complex (Asada & Nakamura 2012; Walker et al. 2018; Park et al. 2019), whose origin may be due to pressure imbalance when the jet reaches the Bondi radius. This distance is actually larger than the scales reached by our simulations. However, these are Newtonian and it is unclear whether or not relativistic effects (in particular the decollimating force due to the electric field) would push the recollimation scale farther out. In any case, we note that our nonrelativistic simulations provide shocks that are located on the same scale as the closest features in the M87 jet (see Fig. 2 of Asada & Nakamura 2012).

Protostellar jets also present some interesting features along the flow usually interpreted as being bow shocks, as in HH212 (Lee et al. 2017) or HH30 (Louvet et al. 2018). Their origin remains highly debated, either instabilities triggered during jet propagation or variability induced by a time-dependent jet production mechanism (as advocated for instance in HH212 by the remarkable jet–counter-jet symmetry; see Tabone et al. 2018). However, we suspect that whenever a jet undergoes an MHD recollimation shock that refracts the jet away from the axis, more shocks are to be expected downstream (and probably affected by the external pressure distribution). MHD recollimation may therefore provide an intrinsic means to trigger jet variability on observable scales. Stationary emission features are sometimes indeed detected, as in HH154 (Bonito et al. 2011). These features are located from a few tens to a few hundreds of astronomical units from the source, a distance comparable to the altitude of the first standing recollimation MHD shock. This is worthy of further investigation.

6. Conclusion

We present axisymmetric simulations of nonrelativistic MHD jets launched from a Keplerian platform. These are the first to show the formation of standing recollimation shocks, at large distances from the source. These recollimation shocks are intrinsic to the MHD collimation process and have been proposed as a natural outcome of self-similar jet-launching conditions (F97; Polko et al. 2010). Because they were never seen in previous MHD simulations of jets, the suspicion grew that recollimation would be a bias due to the self-similar ansatz. It turns out that the physical scales required to capture these shocks are much larger than those used in previous works. Using unprecedentedly large

space and temporal scales allowed us to firmly demonstrate the existence of such internal standing shocks and thereby bridge the gap between analytical and numerical approaches.

We analyzed the conditions of formation of these recollimation shocks and show that they qualitatively follow the behavior demonstrated in analytical studies, namely that they get closer to the source as the mass load increases. We also confirm that the magnetic field distribution in the disk ($B_z \propto r^{\alpha-2}$) is the key quantity shaping the asymptotic jet collimation. For our self-similar ejection setup, this MHD collimation closely follows the trend satisfied by the potential field: the larger the α the stronger the collimation. However, no steady-state solution is obtained for $\alpha \geq 1$, because of the difficulty in establishing a stationary self-consistent poloidal electric circuit along the outer jet regions. As the magnetic field distribution is very likely to evolve on the accretion time scale, we expect jet signatures to vary as well (see e.g., discussion in Barnier et al. 2022).

Despite their qualitative agreement with analytical studies, our results reveal an undeniable impact of the central axial flow on the jet asymptotics. This inner spine is not related to the Keplerian disk but instead to the central object and its interaction with the surrounding disk. Indeed, the spine carries a poloidal electric current responsible for the innermost jet collimation. However, it may also introduce extra localized spine–jet interactions, leading potentially to disruptive instabilities (like kink and/or Kelvin-Helmholtz) or, on the contrary, to global jet stabilization in 3D. Going to 3D is therefore necessary in order to assess the role of the inner spine and the possible persistence of recollimation shocks. In any case, our results confirm the role of the central object in shaping, through its spine, the collimation properties of the jets emitted by the surrounding disk. This is a very interesting topic that merits further investigation.

These internal recollimation shocks introduce several interesting features: (i) an enhanced emission likely seen as stationary knots in astrophysical jets; (ii) a sudden decrease in the rotation rate of the ejected material, and (iii) a possible electric decoupling between the pre-shock and the post-shock regions. This is of especially great interest as these shocks occur at observable distances, typically ∼150−200 au in the case of a YSO. However, our setup also assumes ejection up to several hundreds of astronomical units, which is clearly inconsistent with derived jet kinematics (see e.g., Ferreira et al. 2006; Tabone et al. 2020 and references therein). Simulations with ejection from only a finite zone within the disk (the JED) must therefore be carried out in order to verify whether MHD recollimation shocks are indeed maintained. This is a work in progress.

Acknowledgements. We thank the referee for providing thoughtful comments on the manuscript. The authors acknowledge financial support from the CNES French space agency and PNHE program of French CNRS. All the computations presented in this paper were performed using the GRICAD infrastructure (`https://gricad.univ-grenoble-alpes.fr`), which is supported by Grenoble research communities.

References

Anderson, J. M., Li, Z.-Y., Krasnopolsky, R., & Blandford, R. D. 2003, ApJ, 590, L107
Anderson, J. M., Li, Z.-Y., Krasnopolsky, R., & Blandford, R. D. 2005, ApJ, 630, 945
Anderson, J. M., Li, Z.-Y., Krasnopolsky, R., & Blandford, R. D. 2006, ApJ, 653, L33
Asada, K., & Nakamura, M. 2012, ApJ, 745, L28
Bally, J., Reipurth, B., & Davis, C. J. 2007, Protostars and Planets V, 215
Barnier, S., Petrucci, P.-O., Ferreira, J., et al. 2022, A&A, 657, A11
Barniol Duran, R., Tchekhovskoy, A., & Giannios, D. 2017, MNRAS, 469, 4957
Blandford, R. D., & Payne, D. G. 1982, MNRAS, 199, 883
Blandford, R. D., & Znajek, R. L. 1977, MNRAS, 179, 433
Boccardi, B., Krichbaum, T. P., Ros, E., & Zensus, J. A. 2017, A&ARv, 25, 4
Bogovalov, S. V. 1997, A&A, 323, 634
Bollen, D., Van Winckel, H., & Kamath, D. 2017, A&A, 607, A60
Bonito, R., Orlando, S., Miceli, M., et al. 2011, ApJ, 737, 54
Cabrit, S. 2007, Star-Disk Interaction in Young Stars, 243, 203
Casse, F., & Ferreira, J. 2000a, A&A, 353, 1115
Casse, F., & Ferreira, J. 2000b, A&A, 361, 1178
Casse, F., & Keppens, R. 2002, ApJ, 581, 988
Casse, F., & Keppens, R. 2004, ApJ, 601, 90
Ceccobello, C., Cavecchi, Y., Heemskerk, M. H. M., et al. 2018, MNRAS, 473, 4417
Cheung, C. C., Harris, D. E., & Stawarz, L. 2007, ApJ, 663, L65
Contopoulos, J., & Lovelace, R. V. E. 1994, ApJ, 429, 139
Corbel, S., Nowak, M. A., Fender, R. P., Tzioumis, A. K., & Markoff, S. 2003, A&A, 400, 1007
Coriat, M., Corbel, S., Prat, L., et al. 2011, MNRAS, 414, 677
Doi, A., Hada, K., Kino, M., Wajima, K., & Nakahara, S. 2018, ApJ, 857, L6
Fanaroff, B. L., & Riley, J. M. 1974, MNRAS, 167, 31P
Fender, R., & Gallo, E. 2014, Space Sci. Rev., 183, 323
Fendt, C. 2006, ApJ, 651, 272
Ferreira, J. 1997, A&A, 319, 340
Ferreira, J., & Casse, F. 2004, ApJ, 601, L139
Ferreira, J., & Pelletier, G. 1995, A&A, 295, 807
Ferreira, J., Dougados, C., & Cabrit, S. 2006, A&A, 453, 785
Gallo, E., Corbel, S., Fender, R. P., Maccarone, T. J., & Tzioumis, A. K. 2004, MNRAS, 347, L52
Gracia, J., Vlahakis, N., & Tsinganos, K. 2006, MNRAS, 367, 201
Heyvaerts, J., & Norman, C. 1989, ApJ, 347, 1055
Heyvaerts, J., & Norman, C. 2003a, ApJ, 596, 1270
Heyvaerts, J., & Norman, C. 2003b, ApJ, 596, 1256
Jacquemin-Ide, J., Ferreira, J., & Lesur, G. 2019, MNRAS, 490, 3112
Komissarov, S. S., & Falle, S. A. E. G. 1998, MNRAS, 297, 1087
Krasnopolsky, R., Li, Z.-Y., & Blandford, R. 1999, ApJ, 526, 631
Krasnopolsky, R., Li, Z.-Y., & Blandford, R. D. 2003, ApJ, 595, 631
Laing, R. A., & Bridle, A. H. 2013, MNRAS, 432, 1114
Laing, R. A., & Bridle, A. H. 2014, MNRAS, 437, 3405
Laing, R. A., Jenkins, C. R., Wall, J. V., & Unger, S. W. 1994, ASP Conf. Ser., 54, 201
Lee, C.-F., Ho, P. T. P., Li, Z.-Y., et al. 2017, Nat. Astron., 1, 0152
Li, Z.-Y., Chiueh, T., & Begelman, M. C. 1992, ApJ, 394, 459
Lister, M. L., Aller, M. F., Aller, H. D., et al. 2013, AJ, 146, 120
Liska, M., Hesp, C., Tchekhovskoy, A., et al. 2018, MNRAS, 474, L81
Lister, M. L., Cohen, M. H., Homan, D. C., et al. 2009, AJ, 138, 1874
Louvet, F., Dougados, C., Cabrit, S., et al. 2018, A&A, 618, A120
Matsakos, T., Tsinganos, K., Vlahakis, N., et al. 2008, A&A, 477, 521
Matsakos, T., Massaglia, S., Trussoni, E., et al. 2009, A&A, 502, 217
Merloni, A., & Fabian, A. C. 2003, MNRAS, 342, 951
Mignone, A., Bodo, G., Massaglia, S., et al. 2007, ApJS, 170, 228
Mingo, B., Croston, J. H., Hardcastle, M. J., et al. 2019, MNRAS, 488, 2701
Miyoshi, T., & Kusano, K. 2005, J. Comput. Phys., 208, 315
Murphy, G. C., Zanni, C., & Ferreira, J. 2009, Astrophys. Space Sci. Proc. Ser., 13, 117
Murphy, G. C., Ferreira, J., & Zanni, C. 2010, A&A, 512, A82
Okamoto, I. 2001, MNRAS, 327, 55
Okamoto, I. 2003, ApJ, 589, 671
Ostriker, E. C. 1997, ApJ, 486, 291
Ouyed, R., & Pudritz, R. E. 1993, ApJ, 419, 255
Ouyed, R., & Pudritz, R. E. 1997a, ApJ, 482, 712
Ouyed, R., & Pudritz, R. E. 1997b, ApJ, 484, 794
Ouyed, R., & Pudritz, R. E. 1999, MNRAS, 309, 233
Ouyed, R., Clarke, D. A., & Pudritz, R. E. 2003, ApJ, 582, 292
Park, J., Hada, K., Kino, M., et al. 2019, ApJ, 887, 147
Pelletier, G., & Pudritz, R. E. 1992, ApJ, 394, 117
Perucho, M. 2020, MNRAS, 494, L22
Perucho, M., & Martí, J. M. 2007, MNRAS, 382, 526
Polko, P., Meier, D. L., & Markoff, S. 2010, ApJ, 723, 1343
Polko, P., Meier, D. L., & Markoff, S. 2014, MNRAS, 438, 959
Porth, O., & Fendt, C. 2010, ApJ, 709, 1100
Porth, O., & Komissarov, S. S. 2015, MNRAS, 452, 1089
Pudritz, R. E., Rogers, C. S., & Ouyed, R. 2006, MNRAS, 365, 1131
Ramsey, J. P., & Clarke, D. A. 2011, ApJ, 728, L11
Ramsey, J. P., & Clarke, D. A. 2019, MNRAS, 484, 2364
Ray, T. P., & Ferreira, J. 2021, New Astron. Rev., 93
Ray, T., Dougados, C., Bacciotti, F., Eislöffel, J., & Chrysostomou, A. 2007, Protostars and Planets V, 231
Reipurth, B., & Bally, J. 2001, ARA&A, 39, 403

Sheikhnezami, S., Fendt, C., Porth, O., Vaidya, B., & Ghanbari, J. 2012, ApJ, 757, 65
Staff, J. E., Niebergal, B. P., Ouyed, R., Pudritz, R. E., & Cai, K. 2010, ApJ, 722, 1325
Staff, J. E., Koning, N., Ouyed, R., Thompson, A., & Pudritz, R. E. 2015, MNRAS, 446, 3975
Stepanovs, D., & Fendt, C. 2016, ApJ, 825, 14
Stute, M., Tsinganos, K., Vlahakis, N., Matsakos, T., & Gracia, J. 2008, A&A, 491, 339
Stute, M., Gracia, J., Vlahakis, N., et al. 2014, MNRAS, 439, 3641
Tabone, B., Raga, A., Cabrit, S., & Pineau des Forêts, G. 2018, A&A, 614, A119
Tabone, B., Cabrit, S., Pineau des Forêts, G., et al. 2020, A&A, 640, A82
Tchekhovskoy, A., & Bromberg, O. 2016, MNRAS, 461, L46
Tchekhovskoy, A., Narayan, R., & McKinney, J. C. 2010, New Astron., 15, 749
Tesileanu, O., Matsakos, T., Massaglia, S., et al. 2014, A&A, 562, A117
Tudor, V., Miller-Jones, J. C. A., Patruno, A., et al. 2017, MNRAS, 470, 324
Tzeferacos, P., Ferrari, A., Mignone, A., et al. 2009, MNRAS, 400, 820
Tzeferacos, P., Ferrari, A., Mignone, A., et al. 2013, MNRAS, 428, 3151
Ustyugova, G. V., Koldoba, A. V., Romanova, M. M., Chechetkin, V. M., & Lovelace, R. V. E. 1995, ApJ, 439, L39
Ustyugova, G. V., Koldoba, A. V., Romanova, M. M., Chechetkin, V. M., & Lovelace, R. V. E. 1999, ApJ, 516, 221
Vlahakis, N., & Königl, A. 2003, ApJ, 596, 1080
Vlahakis, N., & Tsinganos, K. 1997, MNRAS, 292, 591
Vlahakis, N., Tsinganos, K., Sauty, C., & Trussoni, E. 2000, MNRAS, 318, 417
Walker, R. C., Hardee, P. E., Davies, F. B., Ly, C., & Junor, W. 2018, ApJ, 855, 128
Weber, E. J., & Davis, L., Jr 1967, ApJ, 148, 217
Zanni, C., & Ferreira, J. 2013, A&A, 550, A99
Zanni, C., Ferrari, A., Rosner, R., Bodo, G., & Massaglia, S. 2007, A&A, 469, 811
Zensus, J. A. 1997, ARA&A, 35, 607

Appendix A: Evolution on long timescales

In numerical simulations, the time increment is fixed by the–Friedrichs–Lewy condition $\Delta t < \Delta x/C_{max}$, where C_{max} is the maximal wave speed in the cell (in our case $u + v_{FM}$) and Δx is the cell size. In a standard simulation, the time increment of all cells is chosen by taking the absolute minimum of all the time increments in the full computational domain. In our simulations, this time step is set by the smallest cells around the inner spherical boundary at R_d, which also happen to have the strongest field and the highest Alfvén speed. However, these cells near the source are also the ones that converge the fastest to a stationary solution. Thus, the cells that we consider are converging to a steady state (meaning the relative variation of the density in one integration step is smaller than an arbitrarily small parameter) and are not used to determine the time increment of the cells that are still evolving in time. The time increment used to evolve the evolving cells is computed by taking a minimum over only the cells that have not converged yet. The cells that have converged to a steady state are still integrated in time using their own local time increment so as to ensure the stability of the integration and to be able to capture any perturbation that could possibly alter their steady condition. As the cells that converge the fastest are those characterized by the shortest time increment, the time increments used to evolve the cells that are still evolving in time and have not converged yet to a steady state become larger and larger.

It is important to point out that the stationary solutions obtained with this time boost are also a solution of the standard nonaccelerated algorithm.

Figure A.1 shows the gain in computing time obtained thanks to the time boost. The acceleration factor, defined as the ratio between the physical time reached using the time boost and the physical time that would have been achieved using the standard CFL condition, is plotted versus the progressive numbering of the outputted files.

Without the acceleration due to our handling of the CFL condition, the time interval between two outputs would have been constant, and the physical time of the solution would have been proportional to the output number. Any increase in the acceleration factor means that another batch of cells has converged. This means the time increment of the cells that are still evolving in time becomes larger, thus increasing the timescales reached.

This increase is clearly visible after the 300th output. Using the output number as a proxy for the computational cost of a simulation, this figure clearly shows that, at the end of the integration, the time boost enables us to reach timescales at least two or three orders of magnitude larger than using a standard CFL condition, without increasing the computational cost of the simulation. Analogously, without employing the time boost, we would have required two or three orders of magnitude more CPU hours to reach the same timescales. Our approach enabled us to produce simulations that would have consumed much more computing time otherwise. The reference simulation K2 consumed 725 CPU hours, but without the time boost it would have required almost two million CPU hours. This enabled us to work on simply 64 processors kindly provided by GRICAD (Grenoble Alpes Recherche - Infrastructure de Calcul Intensif et de Données).

For the evolution of the acceleration factor with the mass load, we can see in Table 1 that the simulations with κ closest to that of Blandford & Payne (1982) converge the fastest, reaching larger timescales at the end of the computation. Nevertheless, all seem to reach comparable convergence speeds: in Figure A.1 we see that the simulation K5 reaches an acceleration factor similar to that of K2 at the final output. For the evolution with the magnetic field, we can clearly see that the higher the α and thus the flatter the profile of the vertical magnetic field, the slower the simulation converges. For higher values of α, the jet is initially more collimated as B_r/B_z is higher on the disk. Therefore, the field lines further on the disk have a higher impact, retarding the global convergence. That is why the simulation A5 with $\alpha = 15/16$ has not yet converged. As an instability develops, some cells that were previously stable become unstable, hence the decrease in acceleration.

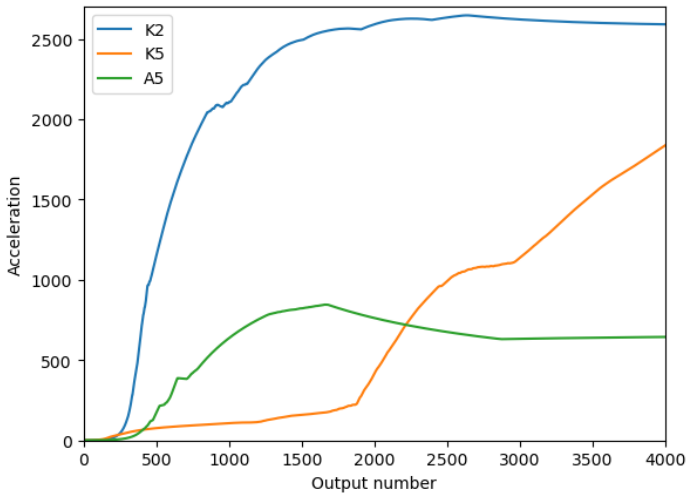

Fig. A.1. Evolution of the acceleration for the simulations K2, K5, and A5.

Appendix B: Boundary conditions

The plots represented in Figure B.1 illustrate the injection boundary conditions we have chosen for the reference simulation K2. The Bernouillli invariant E, the poloidal magnetic field B_Φ, the vertical magnetic field B_z, the mass to magnetic flux ratio $\eta = \mu_0 \rho v_p / B_p$, the rotation speed of the magnetic surfaces $\Omega_\star = \Omega - \eta B_\Phi/(\mu_0 \rho r)$, the speed of sound $C_s = \sqrt{\gamma P/\rho}$, and vertical Alfvénic speed $V_{A_z} = B_z/\sqrt{\mu_0 \rho}$ are plotted on the first cell over the injection boundary. The toroidal magnetic field goes to zero on the axis for symmetry reasons, and $|B_\Phi/B_z| \gtrsim 1$ on the disk : The JED magnetic field is weakly toroidal. The launching conditions are very cold as $V_{A_z}/C_s \sim 10^2$ on both the source and the disk.

The reader may observe the power-law dependency with the magnetic flux on the whole disk ($\Psi > 10$, after the black vertical line) for all parameters but the electric current. This is directly induced by the self-similar ansatz. However, the torroidal magnetic field B_Φ breaks the power-law dependency and shows a swift decrease for $\Psi > 2.10^6$. Of all eight variables, only B_R and B_Φ are free at the injection boundary (see Equation (8)), and need to cross a characteristic surface to be fixed. For the toroidal current, it is the Alfvénic surface. As all magnetic surfaces over $\Psi \gtrsim 10^9$ never cross the Alfvénic surface, the current can never be fixed. Thus, the simulation cannot ever be stationary in this region.

As the disk is a self-similar jet-emitting disk, all dimensionless parameters are assumed to be independent of the radius (Blandford & Payne (1982)). All these parameters are regrouped in section 2.4.

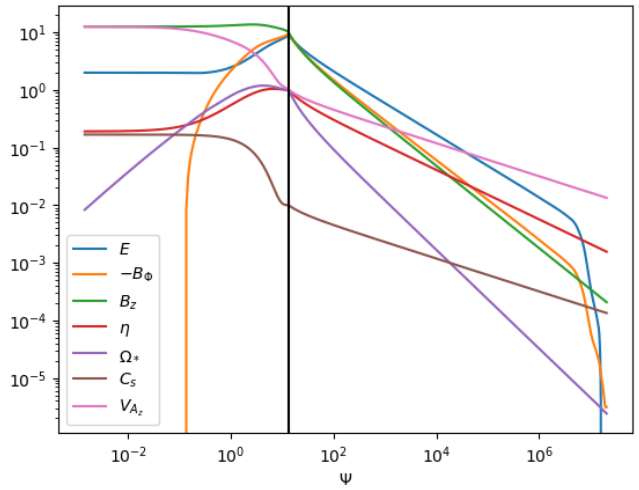

Fig. B.1. Conditions on the lowermost cells of the reference simulation K2. Here all parameters are traced along the first cell above the lower boundary : $R = 1$ and $\theta \in [0;\pi/2]$ on the source and then $\theta = \pi/2$ and $R \in [0; R_{\rm ext}]$ on the disk. Shown are the Bernouilli invariant E, the toroidal and vertical magnetic field B_Φ and B_z, the mass to magnetic flux ratio η, the rotation speed of magnetic surfaces Ω_*, the speed of sound C_s and the vertical Alfvénic speed V_{A_z}, over the magnetic flux Ψ. The black vertical line corresponds to the flux anchored at ($R = 1$,$\theta = \pi/2$), at the source/disk interface.

As explained in section 2.3.2.2, we defined a spline function $f(\theta)$ equal to zero on axis ($\theta = 0$) and one at the inner disk radius ($\theta = \pi/2$) to smoothly connect the axis values with the inner disk ones: $f(\theta) \equiv (3\sin^2\theta - 2\sin^3\theta)^{3/2}$.

The injection speed (V_R on the source, $-V_\theta$ on the disk) is fixed at $\kappa\mu^2 = 0.1$ even when varying κ. However, even though the injection Mach number $M_s = u_p/C_s$ is assumed to be the same all along the boundary, in order to account for the varying inclination of the magnetic surfaces, its value is modified with the parameter α from simulation to simulation. Its variation with α is shown in Table 1.

Appendix C: Rankine-Hugoniot jump conditions

In this section, we write the Rankine-Hugoniot jump conditions valid for standing, adiabatic recollimation shocks. Contrary to Ouyed & Pudritz (1993), we take into account the toroidal magnetic field as the shocks arise when that component is dominant. The local jump $[A] = A_2 - A_1$ between a pre-shock quantity A_1 and its post-shock value A_2 are expressed in the rest frame as

$$\begin{aligned}
[\rho u_\perp] &= 0\\
[\rho u_\perp(\frac{u^2}{2} + H) + \frac{B^2}{\mu_o}u_\perp - \frac{\boldsymbol{u}\cdot\boldsymbol{B}}{\mu_o}B_\perp] &= 0\\
[P + \rho u_\perp^2 + \frac{B_\parallel^2 - B_\perp^2}{2\mu_o}] &= 0\\
[\rho u_\perp \boldsymbol{u}_\parallel - \frac{B_\perp}{\mu_o}\boldsymbol{B}_\parallel] &= 0\\
[B_\perp] &= 0\\
[B_\perp \boldsymbol{u}_\parallel - u_\perp \boldsymbol{B}_\parallel] &= 0,
\end{aligned} \tag{C.1}$$

where $H = C_s^2/(\Gamma - 1)$ is the enthalpy and $u_\perp, B_\perp$ (respectively $\boldsymbol{u}_\parallel, \boldsymbol{B}_\parallel$) are the normal (respectively tangential) components to the shock surface. The shock is axisymmetric, and so the tangential component of the magnetic field $\boldsymbol{B}_\parallel = B_t\boldsymbol{e}_t + B_\phi\boldsymbol{e}_\phi$, whereas the poloidal component is $\boldsymbol{B}_p = B_t\boldsymbol{e}_t + B_\perp\boldsymbol{e}_\perp$, with the unit vectors $(\boldsymbol{e}_\perp, \boldsymbol{e}_t, \boldsymbol{e}_\phi)$ defining a local orthonormal coordinate system. As these jump conditions express the conservation of mass, angular momentum, and energy in ideal MHD, the five MHD invariants along a given magnetic surface $(\eta, \Omega_*, L, E, S)$ are therefore also conserved (see Fig.7).

In the case of a shock, the mass flux through the surface is nonzero, which requires $B_{\perp 2} = B_{\perp 1} \neq 0$ and leads to

$$\boldsymbol{B}_{\parallel 2} = \frac{m^2 - 1}{m^2/\chi - 1}\boldsymbol{B}_{\parallel 1}, \tag{C.2}$$

where $m = u_\perp/V_{Ap,\perp} = u_p/V_{Ap}$ is the Alfvénic Mach number of the incoming (pre-shock) flow and $\chi = \rho_2/\rho_1 = u_{\perp 1}/u_{\perp 2}$ is the shock compression rate. This equation shows that there are three nontrivial discontinuities with $\chi \geq 1$: (1) an oblique shock with $m^2 > \chi > 1$, (2) a normal shock with $m^2 = \chi > 1$ (requiring $\boldsymbol{B}_{\parallel 1} = 0$), and (3) an Alfvén shear discontinuity with $m^2 = \chi = 1$ (allowing an arbitrary jump between the two tangential field components). The oblique shock is the only case studied here.

After some algebra all post-shock quantities can be expressed as function of the pre-shock ones, in particular

$$\begin{aligned}
\frac{B_{\phi 2}}{B_{\phi 1}} &= \frac{B_{t2}}{B_{t1}} = \chi\frac{m^2 - 1}{m^2 - \chi}\\
\frac{u_{\phi 2}}{u_{\phi 1}} &= \frac{m^2 - 1}{m^2 - \chi}\frac{m^2 r_A^2 - \chi r^2}{m^2 r_A^2 - r^2}\\
\frac{P_2}{P_1} &= 1 + \Gamma m_s^2(\chi - 1)\left(\frac{1}{\chi} + \frac{b^2}{2}\frac{2\chi - m^2(1+\chi)}{(\chi - m^2)^2}\right)\\
\frac{T_2}{T_1} &= \frac{1}{\chi}\frac{P_2}{P_1},
\end{aligned} \tag{C.3}$$

where the sonic Mach number $m_s = u_\perp/C_s$ and magnetic shear $b^2 = (B_\parallel/B_\perp)^2$ are computed in the pre-shock region. Of particular interest are the relative variations of the toroidal magnetic field component $\delta B_\phi = B_{\phi 2}/B_{\phi 1} - 1$ and the plasma angular velocity $\delta\Omega = \Omega_2/\Omega_1 - 1$, as well as the total deflection angle of the poloidal magnetic surface $\delta i = i_2 - i_1$ where $\tan i = B_t/B_\perp$, which read

$$\begin{aligned}
\delta B_\phi &= (\chi - 1)\frac{m^2}{m^2 - \chi}\\
-\delta\Omega &= \frac{\chi - 1}{m^2 - \chi}\frac{m^2(r^2 - r_A^2)}{m^2 r_A^2 - r^2} \leq \frac{\chi - 1}{m^2 - \chi}\\
\tan\delta i &= \frac{m^2(\chi - 1)}{m^2 - \chi}\frac{\tan i_1}{1 + \chi\tan^2 i_1\frac{m^2 - 1}{m^2 - \chi}}.
\end{aligned} \tag{C.4}$$

These quantities are plotted in Fig. 9. The compression rate χ is the solution of the cubic polynomial equation

$$-A\chi^3 + B\chi^2 - C\chi + D = 0 \tag{C.5}$$

with

$$\begin{aligned}
A &= 1 + b^2 + \frac{1 + \chi_o}{\Gamma m_s^2}\\
B &= \chi_o(1 + b^2) + 2m^2\left(1 + \frac{1 + \chi_o}{\Gamma m_s^2} - b^2\frac{\chi_o - 3}{4}\right)\\
C &= m^2\left(2\chi_o + b^2\frac{1 + \chi_o}{2} + m^2\left(1 + \frac{1 + \chi_o}{\Gamma m_s^2}\right)\right)\\
D &= \chi_o m^4,
\end{aligned}$$

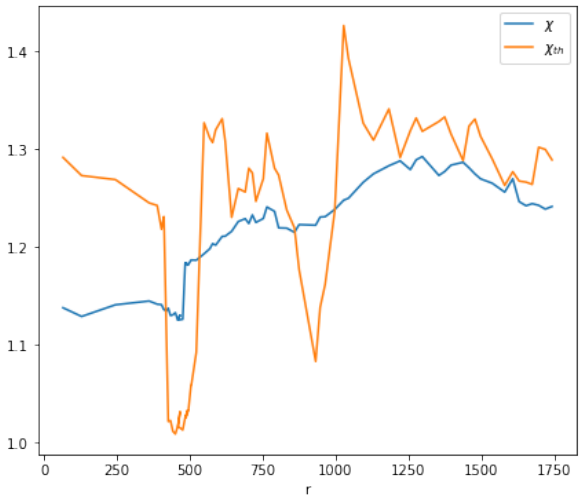

Fig. C.1. Distribution at t_{end} along the main recollimation shock of the compression ratio for simulation K2. The yellow curve is the theoretical solution χ_{th} of Eq. C.5, computed using the pre-shock quantities, while the blue curve is the ratio $\chi = \rho_2/\rho_1$.

where $\chi_o = (\Gamma + 1)/(\Gamma - 1)$ is the maximal compression ratio for a hydrodynamic shock. Equation C.5 has one positive root only for an incoming super-FM flow, namely for $n_\perp = u_\perp/V_{fm,\perp}$ larger than unity.

We are dealing here with supersonic ($m_s >> 1$) and super-A ($m >> 1$) cold jets, where the dominant magnetic field is the toroidal one ($b^2 \simeq (B_\phi/B_\perp)^2 >> 1$). The FM Mach number in the normal direction therefore writes $n_\perp \simeq mV_{Ap,\perp}/V_{A\phi} = m/b$, which leads to the simplified equation for χ

$$\frac{\chi_o - 3}{2}\chi^2 + \left(\frac{1+\chi_o}{2} + n_\perp^2\right)\chi - \chi_o n_\perp^2 = 0\,. \tag{C.6}$$

This shows that whenever jets reach a very large FM Mach number $n_\perp$, a large compression rate $\chi \simeq \chi_o$ is possible. But this is never achieved in our case. Indeed, the poloidal FM Mach number $n = u_p/V_{FM,p}$ ($> n_\perp$) writes

$$n^2 = \omega_A \frac{B_{pA} r_A^2}{B_p r^2} \frac{1 - 1/m^2}{1 - r_A^2/r^2} \left(\frac{u_p}{\Omega_* r_A}\right)^3 \sim \omega_A \left(\frac{u_p}{\Omega_* r_A}\right)^3, \tag{C.7}$$

where $\omega_A = \Omega_* r_A/V_{Ap,A}$ is the fastness parameter introduced in F97 (ratio at the Alfvén point of the speed of the magnetic rotator to the poloidal Alfvén speed). For magneto-centrifugal jets like ours, with $m^2 >> 1, r >> r_A$ and achieving their maximal velocity $u_p \sim \sqrt{2}\Omega_* r_A$, the FM Mach number is $n^2 \sim \omega_A$, which is larger than but of the order of unity (see also Krasnopolsky et al. 2003). As a consequence, we expect rather weak shocks as illustrated by the small values of χ achieved along the various shocks (see Fig. 9).

Figure C.1 plots the theoretical solution χ_{th} of Eq. C.5 (in yellow) computed along the main recollimation shock of our simulation K2 and compares it with the ratio $\chi = \rho_2/\rho_1$ (in blue) directly measured (see Fig. 4). The correspondence is very good, with discrepancies remaining below a few percent. The two regions where larger differences are obtained correspond to the positions where the two smaller shocks (triggered at the spine-jet interface) merge with the main shock: the orange one near $r \sim 500$ and the cyan one near $r \sim 900$.

The shocks were detected by following all magnetic field lines anchored on the disk and looking for discontinuities. This is not obvious in a discrete grid. To do so, we computed the derivative of the toroidal magnetic field (δB_ϕ) over the curvilinear abscissa along the field line, as shocks are best seen with the electric poloidal current and explored its local extrema. We checked that a different approach, based on the calculation of the refraction angle δi of the poloidal magnetic surface, produces very similar results. This gave us the shock locations used to produce the plots in Figures 2 and 17. As PLUTO has a shock capturing scheme, each shock is resolved and has a finite width. To determine the shock width, we checked that the density was growing within the shock as expected. Then, still following the field line, we looked for the closest local minimum and maximum in density. The positions of these extrema allowed us to compute the values of the pre-shock and the post-shock quantities, respectively. These were finally used to compute the parameters leading to the Figures 9 and C.1.

Bibliography

Agra-Amboage, V. et al. (Aug. 2011). "Sub-arcsecond [Fe ii] spectro-imaging of the DG Tauri jet. Periodic bubbles and a dusty disk wind?" en. In: *Astronomy & Astrophysics, Volume 532, id.A59, <NUMPAGES>15</NUMPAGES> pp.* 532, A59. ISSN: 0004-6361. DOI: 10.1051/0004-6361/201015886 (cit. on p. 85).

Agra-Amboage, V. et al. (Apr. 2014). "Origin of the wide-angle hot H_2 in DG Tauri. New insight from SINFONI spectro-imaging". In: *Astronomy and Astrophysics* 564, A11, A11. DOI: 10.1051/0004-6361/201220488. arXiv: 1402.1160 [astro-ph.SR] (cit. on p. 85).

Allen, S. W. et al. (Oct. 2006). "The relation between accretion rate and jet power in X-ray luminous elliptical galaxies". In: *Monthly Notices of the Royal Astronomical Society* 372. ADS Bibcode: 2006MNRAS.372...21A, pp. 21–30. ISSN: 0035-8711. DOI: 10.1111/j.1365-2966.2006.10778.x (cit. on p. 31).

Anderson, James M. and James S. Ulvestad (July 2005). "The Size of the Radio-Emitting Region in Low-Luminosity Active Galactic Nuclei". In: *the Astrophysical Journal* 627.2, pp. 674–700. DOI: 10.1086/430463. arXiv: astro-ph/0504066 [astro-ph] (cit. on p. 127).

Anderson, Jeffrey M. et al. (June 2003). "Locating the Launching Region of T Tauri Winds: The Case of DG Tauri". In: *The Astrophysical Journal* 590. ADS Bibcode: 2003ApJ...590L.107A, pp. L107–L110. ISSN: 0004-637X. DOI: 10.1086/376824 (cit. on p. 89).

— (Sept. 2005). "The Structure of Magnetocentrifugal Winds. I. Steady Mass Loading". In: *The Astrophysical Journal* 630, pp. 945–957. ISSN: 0004-637X. DOI: 10.1086/432040 (cit. on pp. 21, 120).

— (Dec. 2006). "Magnetocentrifugal Winds in Three Dimensions: A Nonaxisymmetric Steady State". In: *The Astrophysical Journal Letters* 653, pp. L33–L36. ISSN: 0004-637X. DOI: 10.1086/510307 (cit. on p. 21).

Appl, S. (Oct. 1996). "Instabilities in transmagnetosonic jets." In: *Astronomy and Astrophysics* 314, pp. 995–1002 (cit. on p. 202).

Araudo, Anabella T. et al. (Jan. 2018). "On the maximum energy of non-thermal particles in the primary hotspot of Cygnus A". In: *Monthly Notices of the Royal Astronomical Society* 473. ADS Bibcode: 2018MNRAS.473.3500A, pp. 3500–3506. ISSN: 0035-8711. DOI: 10.1093/mnras/stx2552 (cit. on p. 33).

Asada, Keiichi and Masanori Nakamura (Feb. 2012). "The Structure of the M87 Jet: A Transition from Parabolic to Conical Streamlines". In: *The Astrophysical Journal* 745, p. L28. ISSN: 0004-637X. DOI: 10.1088/2041-8205/745/2/L28 (cit. on pp. 14, 31, 36, 129).

Bacciotti, Francesca et al. (July 2000). "Hubble Space Telescope STIS Spectroscopy of the Optical Outflow from DG Tauri: Structure and Kinematics on Subarcsecond Scales". In: *the Astrophysical Journal Letters* 537.1, pp. L49–L52. DOI: 10.1086/312745. arXiv: astro-ph/0005463 [astro-ph] (cit. on pp. 188, 191).

Bally, J., B. Reipurth, and C. J. Davis (Jan. 2007). *Observations of Jets and Outflows from Young Stars*. Conference Name: Protostars and Planets V Pages: 215 ADS Bibcode: 2007prpl.conf..215B (cit. on pp. 5, 31).

Bardeen, James M. and Jacobus A. Petterson (Jan. 1975). "The Lense-Thirring Effect and Accretion Disks around Kerr Black Holes". In: *The Astrophysical Journal Letters* 195, p. L65. DOI: 10.1086/181711 (cit. on p. 165).

Bardeen, James M., William H. Press, and Saul A. Teukolsky (Dec. 1972). "Rotating Black Holes: Locally Nonrotating Frames, Energy Extraction, and Scalar Synchrotron Radiation". In: *the Astrophysical Journal* 178, pp. 347–370. DOI: 10.1086/151796 (cit. on pp. 23, 190).

Barnier, S. et al. (Jan. 2022). "Clues on jet behavior from simultaneous radio-X-ray fits of GX 339-4". en. In: *Astronomy & Astrophysics, Volume 657, id.A11, <NUMPAGES>19</NUMPA pp.* 657, A11. ISSN: 0004-6361. DOI: 10.1051/0004-6361/202141182 (cit. on pp. 127, 187, 191).

Barniol Duran, Rodolfo, Alexander Tchekhovskoy, and Dimitrios Giannios (Aug. 2017). "Simulations of AGN jets: magnetic kink instability versus conical shocks". In: *Monthly Notices of the Royal Astronomical Society* 469, pp. 4957–4978. DOI: 10.1093/mnras/stx1165 (cit. on pp. 21, 202).

Barral, J. F. and J. Canto (June 1981). "A stellar wind for model for bipolar nebulae." In: *Revista Mexicana de Astronomía y Astrofísica* 5, pp. 101–108 (cit. on p. 15).

Baty, H. and R. Keppens (Dec. 2002). "Interplay between Kelvin-Helmholtz and Current-driven Instabilities in Jets". In: *the Astrophysical Journal* 580.2, pp. 800–814. DOI: 10.1086/343893 (cit. on p. 202).

— (Feb. 2006). "Kelvin-Helmholtz disruptions in extended magnetized jet flows". In: *the Astrophysical Journal* 447.1, pp. 9–22. DOI: 10.1051/0004-6361:20053969 (cit. on p. 202).

Beskin, V. S. and E. E. Nokhrina (Aug. 2009). "On the central core in MHD winds and jets". In: *Monthly Notices of the Royal Astronomical Society* 397.3, pp. 1486–1497. DOI: 10.1111/j.1365-2966.2009.14964.x. arXiv: 0810.4307 [astro-ph] (cit. on p. 147).

Bessolaz, N. et al. (Jan. 2008). "Accretion funnels onto weakly magnetized young stars". In: *Astronomy and Astrophysics* 478.1, pp. 155–162. DOI: 10.1051/0004-6361:20078328. arXiv: 0712.2921 [astro-ph] (cit. on p. 190).

Biretta, J. A., W. B. Sparks, and F. Macchetto (Aug. 1999). "Hubble Space Telescope Observations of Superluminal Motion in the M87 Jet". In: *the Astrophysical Journal* 520.2, pp. 621–626. DOI: 10.1086/307499 (cit. on p. 5).

Biretta, J. A., C. P. Stern, and D. E. Harris (May 1991). "The Radio to X-ray Spectrum of the M87 Jet and Nucleus". In: *The Astronomical Journal* 101. ADS Bibcode: 1991AJ....101.1632B, p. 1632. ISSN: 0004-6256. DOI: 10.1086/115793 (cit. on p. 31).

Blandford, R. D. and D. G. Payne (June 1982). "Hydromagnetic flows from accretion discs and the production of radio jets". In: *Monthly Notices of the Royal Astronomical Society* 199, pp. 883–903. ISSN: 0035-8711. DOI: 10.1093/mnras/199.4.883 (cit. on pp. iii, v, 17–18, 22, 30, 46–48, 59, 71, 77, 79, 90, 101, 103, 107, 175).

Blandford, R. D. and M. J. Rees (Dec. 1974). "A 'twin-exhaust' model for double radio sources". In: *Monthly Notices of the Royal Astronomical Society* 169, pp. 395–415. ISSN: 0035-8711. DOI: 10.1093/mnras/169.3.395 (cit. on p. 15).

Blandford, R. D. and R. L. Znajek (May 1977). "Electromagnetic extraction of energy from Kerr black holes". In: *Monthly Notices of the Royal Astronomical Society* 179, pp. 433–456. DOI: 10.1093/mnras/179.3.433 (cit. on pp. 10, 142).

Blandford, Roger, David Meier, and Anthony Readhead (Aug. 2019). "Relativistic Jets from Active Galactic Nuclei". In: *Annual Review of Astronomy and Astrophysics* 57, pp. 467–509. DOI: 10.1146/annurev-astro-081817-051948. arXiv: 1812.06025 [astro-ph.HE] (cit. on p. 5).

Boccardi, B. et al. (Nov. 2017). "Radio observations of active galactic nuclei with mm-VLBI". In: *Astronomy and Astrophysics Review* 25, p. 4. ISSN: 0935-4956. DOI: 10.1007/s00159-017-0105-6 (cit. on p. 5).

Bodo, G. et al. (Mar. 1994). "Kelvin-Helmholtz instability of hydrodynamic supersonic jets." In: *Astronomy and Astrophysics* 283, pp. 655–676 (cit. on p. 202).

Bollen, Dylan, Hans Van Winckel, and Devika Kamath (Nov. 2017). "Jet creation in post-AGB binaries: the circum-companion accretion disk around BD+46°442". en. In: *Astronomy & Astrophysics, Volume 607, id.A60, <NUMPAGES>17</NUMPAGES> pp.* 607, A60. ISSN: 0004-6361. DOI: 10.1051/0004-6361/201731493 (cit. on p. 6).

Bonito, R. et al. (Aug. 2011). "X-Ray Emission from Protostellar Jet HH 154: The First Evidence of a Diamond Shock?" In: *The Astrophysical Journal* 737. ADS Bibcode: 2011ApJ...737...54B, p. 54. ISSN: 0004-637X. DOI: 10.1088/0004-637X/737/2/54 (cit. on p. 128).

Bromberg, Omer and Alexander Tchekhovskoy (Feb. 2016). "Relativistic MHD simulations of core-collapse GRB jets: 3D instabilities and magnetic dissipation". In: *Monthly Notices of the Royal Astronomical Society* 456. ADS Bibcode: 2016MNRAS.456.1739B, pp. 1739–1760. ISSN: 0035-8711. DOI: 10.1093/mnras/stv2591 (cit. on pp. 12, 21, 160, 184, 187–189, 193, 202).

Cabrit, S. (May 2007). "The accretion-ejection connexion in T Tauri stars: jet models vs. observations". In: 243. Conference Name: Star-Disk Interaction in Young Stars, pp. 203–214. DOI: 10.1017/S1743921307009568 (cit. on p. 147).

Cabrit, Sylvie (2007). "Jets from Young Stars: The Need for MHD Collimation and Acceleration Processes". In: *Lecture Notes in Physics, Berlin Springer Verlag*. Ed. by Jonathan Ferreira, Catherine Dougados, and Emma Whelan. Vol. 723, p. 21 (cit. on p. 16).

Camenzind, M. (July 1986). "Hydromagnetic flows from rapidly rotating compact objects. I - Cold relativistic flows from rapid rotators". In: *Astronomy and Astrophysics* 162. ADS Bibcode: 1986A&A...162...32C, pp. 32–44. ISSN: 0004-6361 (cit. on p. 45).

Carotenuto, F. et al. (June 2021). "The black hole transient MAXI J1348-630: evolution of the compact and transient jets during its 2019/2020 outburst". In: *Monthly Notices of the Royal Astronomical Society* 504.1, pp. 444–468. DOI: 10.1093/mnras/stab864. arXiv: 2103.12190 [astro-ph.HE] (cit. on p. 9).

Carrasco-González, Carlos et al. (Nov. 2010). "A Magnetized Jet from a Massive Protostar". In: *Science* 330. ADS Bibcode: 2010Sci...330.1209C, p. 1209. ISSN: 0036-8075. DOI: 10.1126/science.1195589 (cit. on p. 33).

Cash, J. R. and Alan H. Karp (1990). "A Variable Order Runge-Kutta Method for Initial Value Problems with Rapidly Varying Right-Hand Sides". In: *ACM Trans. Math. Softw.* 16.3, 201–222. ISSN: 0098-3500. DOI: 10.1145/79505.79507 (cit. on p. 86).

Casse, F. and J. Ferreira (Sept. 2000a). "Magnetized accretion-ejection structures. V. Effects of entropy generation inside the disc". en. In: *Astronomy and Astrophysics, v.361, p.1178-1190 (2000)* 361, p. 1178. ISSN: 0004-6361 (cit. on pp. 22, 82, 111).

Casse, Fabien and Jonathan Ferreira (Jan. 2000b). "Magnetized accretion-ejection structures. IV. Magnetically-driven jets from resistive, viscous, Keplerian discs". en. In: *Astronomy and Astrophysics, v.353, p.1115-1128 (2000)* 353, p. 1115. ISSN: 0004-6361 (cit. on p. 107).

Casse, Fabien and Rony Keppens (Dec. 2002). "Magnetized Accretion-Ejection Structures: 2.5-dimensional Magnetohydrodynamic Simulations of Continuous Ideal Jet Launching from Resistive Accretion Disks". In: *The Astrophysical Journal* 581.

ADS Bibcode: 2002ApJ...581..988C, pp. 988–1001. ISSN: 0004-637X. DOI: 10.1086/344340 (cit. on p. 21).

Casse, Fabien and Rony Keppens (Jan. 2004). "Radiatively Inefficient Magnetohydrodynamic Accretion-Ejection Structures". In: *The Astrophysical Journal* 601. ADS Bibcode: 2004ApJ...601...90C, pp. 90–103. ISSN: 0004-637X. DOI: 10.1086/380441 (cit. on p. 21).

Ceccobello, C. et al. (Feb. 2018). "A new method for extending solutions to the self-similar relativistic magnetohydrodynamic equations for black hole outflows". In: *Monthly Notices of the Royal Astronomical Society* 473. ADS Bibcode: 2018MNRAS.473.4417C, pp. 4417–4435. ISSN: 0035-8711. DOI: 10.1093/mnras/stx2567 (cit. on p. 22).

Chan, K. L. and R. N. Henriksen (Oct. 1980). "On the supersonic dynamics of magnetized jets of thermal gas in radio galaxies". In: *the Astrophysical Journal* 241, pp. 534–551. DOI: 10.1086/158368 (cit. on p. 17).

Chandrasekhar, Subrahmanyan (1961). *Hydrodynamic and hydromagnetic stability* (cit. on p. 195).

Chatterjee, K. et al. (Dec. 2019). "Accelerating AGN jets to parsec scales using general relativistic MHD simulations". In: *Monthly Notices of the Royal Astronomical Society* 490, pp. 2200–2218. DOI: 10.1093/mnras/stz2626 (cit. on p. 21).

Chen, Francis F. (Jan. 1974). *Introduction to plasma physics*. Publication Title: New York: Plenum Press ADS Bibcode: 1974itpp.book.....C (cit. on p. 31).

Cheung, C. C., D. E. Harris, and Ł. Stawarz (July 2007). "Superluminal Radio Features in the M87 Jet and the Site of Flaring TeV Gamma-Ray Emission". In: *The Astrophysical Journal* 663, pp. L65–L68. ISSN: 0004-637X. DOI: 10.1086/520510 (cit. on pp. 14, 128).

Clairfontaine, G. Fichet de et al. (Mar. 2021). "Flux variability from ejecta in structured relativistic jets with large-scale magnetic fields". en. In: *Astronomy & Astrophysics, Volume 647, id.A77, <NUMPAGES>18</NUMPAGES> pp.* 647, A77. ISSN: 0004-6361. DOI: 10.1051/0004-6361/202039654 (cit. on pp. 188, 191–192).

Clairfontaine, Gaëtan Fichet de, Zakaria Meliani, and Andreas Zech (Mar. 2022). *Flare echos from relaxation shocks in perturbed relativistic jets*. Tech. rep. Publication Title: arXiv e-prints ADS Bibcode: 2022arXiv220302765F Type: article (cit. on pp. 188, 191).

Combet, C. and J. Ferreira (Feb. 2008). "The radial structure of protostellar accretion disks: influence of jets". In: *Astronomy and Astrophysics* 479.2, pp. 481–491. DOI: 10.1051/0004-6361:20078734. arXiv: 0712.0913 [astro-ph] (cit. on p. 127).

Contopoulos, J. and R. V. E. Lovelace (July 1994). "Magnetically driven jets and winds: Exact solutions". In: *The Astrophysical Journal* 429, pp. 139–152. DOI: 10.1086/174307 (cit. on pp. 22, 90, 111, 114).

Coriat, M. et al. (June 2011). "Radiatively efficient accreting black holes in the hard state: the case study of H1743-322". In: *Monthly Notices of the Royal Astronomical Society* 414. ADS Bibcode: 2011MNRAS.414..677C, pp. 677–690. ISSN: 0035-8711. DOI: 10.1111/j.1365-2966.2011.18433.x (cit. on pp. 11, 144, 191).

Courant, R., K. Friedrichs, and H. Lewy (Jan. 1928). "Über die partiellen Differenzengleichungen der mathematischen Physik". In: *Mathematische Annalen* 100, pp. 32–74. DOI: 10.1007/BF01448839 (cit. on p. 64).

Curtis, H. D. (Jan. 1918). "Descriptions of 762 Nebulae and Clusters Photographed with the Crossley Reflector". In: *Publications of Lick Observatory* 13, pp. 9–42 (cit. on p. 5).

Davis, C. J. et al. (Apr. 2011). "VLT integral field spectroscopy of embedded protostars: using near-infrared emission lines as tracers of accretion and outflow". In:

Astronomy and Astrophysics 528, A3, A3. DOI: 10.1051/0004-6361/201015897 (cit. on p. 13).

de Ruiter, Iris et al. (May 2019). "A systematic study of the phase difference between QPO harmonics in black hole X-ray binaries". In: *Monthly Notices of the Royal Astronomical Society* 485.3, pp. 3834–3844. DOI: 10.1093/mnras/stz665. arXiv: 1903.03135 [astro-ph.HE] (cit. on p. 163).

de Valon, A. et al. (Feb. 2020). "ALMA reveals a large structured disk and nested rotating outflows in DG Tauri B". In: *Astronomy and Astrophysics* 634, L12, p. L12. DOI: 10.1051/0004-6361/201936950. arXiv: 2001.09776 [astro-ph.SR] (cit. on p. 191).

Done, Chris, Marek Gierliński, and Aya Kubota (Dec. 2007). "Modelling the behaviour of accretion flows in X-ray binaries. Everything you always wanted to know about accretion but were afraid to ask". In: *The Astronomy and Astrophysics Review* 15.1, pp. 1–66. DOI: 10.1007/s00159-007-0006-1. arXiv: 0708.0148 [astro-ph] (cit. on p. 8).

Dunn, R. J. H. et al. (Mar. 2010). "A global spectral study of black hole X-ray binaries". In: *Monthly Notices of the Royal Astronomical Society* 403.1, pp. 61–82. DOI: 10.1111/j.1365-2966.2010.16114.x. arXiv: 0912.0142 [astro-ph.HE] (cit. on p. 9).

Edelson, R. A. and J. H. Krolik (Oct. 1988). "The Discrete Correlation Function: A New Method for Analyzing Unevenly Sampled Variability Data". In: *The Astrophysical Journal* 333, p. 646. DOI: 10.1086/166773 (cit. on p. 179).

EHT et al. (Apr. 2019). "First M87 Event Horizon Telescope Results. VI. The Shadow and Mass of the Central Black Hole". In: *The Astrophysical Journal* 875. ADS Bibcode: 2019ApJ...875L...6E, p. L6. ISSN: 0004-637X. DOI: 10.3847/2041-8213/ab1141 (cit. on p. 36).

EHT et al. (Mar. 2021a). "First M87 Event Horizon Telescope Results. VII. Polarization of the Ring". In: *The Astrophysical Journal Letters* 910.1, L12, p. L12. DOI: 10.3847/2041-8213/abe71d. arXiv: 2105.01169 [astro-ph.HE] (cit. on pp. 5, 33).

EHT et al. (Mar. 2021b). "First M87 Event Horizon Telescope Results. VIII. Magnetic Field Structure near The Event Horizon". In: *The Astrophysical Journal* 910. ADS Bibcode: 2021ApJ...910L..13E, p. L13. ISSN: 0004-637X. DOI: 10.3847/2041-8213/abe4de (cit. on p. 5).

Ellerbroek, L. E. et al. (Mar. 2013). "The outflow history of two Herbig-Haro jets in RCW 36: HH 1042 and HH 1043". In: *Astronomy and Astrophysics* 551, A5, A5. DOI: 10.1051/0004-6361/201220635. arXiv: 1212.4144 [astro-ph.SR] (cit. on p. 11).

Espinasse, Mathilde et al. (June 2020). "Relativistic X-Ray Jets from the Black Hole X-Ray Binary MAXI J1820+070". In: *the Astrophysical Journal Letters* 895.2, L31, p. L31. DOI: 10.3847/2041-8213/ab88b6. arXiv: 2004.06416 [astro-ph.HE] (cit. on p. 8).

Evans, Charles R. and John F. Hawley (Sept. 1988). "Simulation of Magnetohydrodynamic Flows: A Constrained Transport Model". In: *The Astrophysical Journal* 332, p. 659. DOI: 10.1086/166684 (cit. on p. 61).

Fanaroff, B. L. and J. M. Riley (May 1974). "The morphology of extragalactic radio sources of high and low luminosity". In: *Monthly Notices of the Royal Astronomical Society* 167. ADS Bibcode: 1974MNRAS.167P..31F, 31P–36P. ISSN: 0035-8711. DOI: 10.1093/mnras/167.1.31P (cit. on p. 12).

Fender, R. P., T. M. Belloni, and E. Gallo (Dec. 2004). "Towards a unified model for black hole X-ray binary jets". In: *Monthly Notices of the Royal Astronomical Society*

355.4, pp. 1105–1118. DOI: 10.1111/j.1365-2966.2004.08384.x. arXiv: astro-ph/0409360 [astro-ph] (cit. on p. 162).

Fender, Rob and Tomaso Belloni (Aug. 2012). "Stellar-Mass Black Holes and Ultraluminous X-ray Sources". In: *Science* 337.6094, p. 540. DOI: 10.1126/science.1221790. arXiv: 1208.1138 [astro-ph.HE] (cit. on p. 10).

Fender, Rob and Elena Gallo (Sept. 2014). "An Overview of Jets and Outflows in Stellar Mass Black Holes". In: *Space Science Reviews* 183. ADS Bibcode: 2014SSRv..183..323F, pp. 323–337. ISSN: 0038-6308. DOI: 10.1007/s11214-014-0069-z (cit. on p. 6).

Fendt, Christian (Nov. 2006). "Collimation of Astrophysical Jets: The Role of the Accretion Disk Magnetic Field Distribution". In: *The Astrophysical Journal* 651, pp. 272–287. DOI: 10.1086/507976 (cit. on pp. 21, 80, 89, 119–120).

Ferreira, J. (Mar. 1997). "Magnetically-driven jets from Keplerian accretion discs." In: *Astronomy and Astrophysics* 319, pp. 340–359. ISSN: 0004-6361 (cit. on pp. iii, v, 4, 17, 22–23, 25, 30, 47, 50, 58, 67–68, 71, 80, 90, 98, 107–108, 111, 120, 125, 127–128).

Ferreira, J., C. Dougados, and S. Cabrit (July 2006). "Which jet launching mechanism(s) in T Tauri stars?" en. In: *Astronomy and Astrophysics, Volume 453, Issue 3, July III 2006, pp.785-796* 453.3, p. 785. ISSN: 0004-6361. DOI: 10.1051/0004-6361:20054231 (cit. on p. 127).

Ferreira, J. and G. Pelletier (Sept. 1993a). "Magnetized accretion-ejection structures. 1. General statements". In: *Astronomy and Astrophysics* 276, p. 625 (cit. on p. 20).

— (Sept. 1993b). "Magnetized accretion-ejection structures. II. Magnetic channeling around compact objects". In: *Astronomy and Astrophysics* 276, p. 637 (cit. on p. 20).

Ferreira, J. and G. Pelletier (Mar. 1995). "Magnetized accretion-ejection structures. III. Stellar and extragalactic jets as weakly dissipative disk outflows." en. In: *Astronomy and Astrophysics, v.295, p.807* 295, p. 807. ISSN: 0004-6361 (cit. on pp. 16, 18, 20, 46).

Ferreira, J. et al. (Mar. 2006). "A unified accretion-ejection paradigm for black hole X-ray binaries. I. The dynamical constituents". In: *Astronomy and Astrophysics* 447.3, pp. 813–825. DOI: 10.1051/0004-6361:20052689. arXiv: astro-ph/0511123 [astro-ph] (cit. on p. 127).

Ferreira, J. et al. (Apr. 2022). "Are low-frequency quasi-periodic oscillations in accretion flows the disk response to jet instability?" en. In: *Astronomy & Astrophysics, Volume 660, id.A66, <NUMPAGES>11</NUMPAGES> pp.* 660, A66. ISSN: 0004-6361. DOI: 10.1051/0004-6361/202040165 (cit. on pp. 4, 26, 159–161, 164, 184, 202).

Ferreira, Jonathan and Fabien Casse (Feb. 2004). "Stationary Accretion Disks Launching Super-fast-magnetosonic Magnetohydrodynamic Jets". In: *The Astrophysical Journal Letters* 601, pp. L139–L142. DOI: 10.1086/381804 (cit. on p. 80).

Frank, A. et al. (Jan. 2014). *Jets and Outflows from Star to Cloud: Observations Confront Theory*. Conference Name: Protostars and Planets VI Pages: 451 ADS Bibcode: 2014prpl.conf..451F. eprint: arXiv:1402.3553. DOI: 10.2458/azu_uapress_9780816531240-ch020 (cit. on p. 5).

Freidberg, J. P. (July 1982). "Ideal magnetohydrodynamic theory of magnetic fusion systems". In: *Reviews of Modern Physics* 54.3, pp. 801–902. DOI: 10.1103/RevModPhys.54.801 (cit. on pp. 195–196).

Frisch, Uriel (Jan. 1995). *Turbulence. The legacy of A.N. Kolmogorov*. Publication Title: Turbulence. The legacy of A. N. Kolmogorov ADS Bibcode: 1995tlan.book.....F (cit. on p. 36).

Garofalo, David and Chandra B. Singh (Feb. 2019). "FR0 Radio Galaxies and Their Place in the Radio Morphology Classification". In: *the Astrophysical Journal* 871.2,

259, p. 259. DOI: 10.3847/1538-4357/aaf056. arXiv: 1811.05383 [astro-ph.HE] (cit. on p. 12).

Ghisellini, G. and A. Celotti (Nov. 2001). "The dividing line between FR I and FR II radio-galaxies". In: *Astronomy and Astrophysics* 379, pp. L1–L4. DOI: 10.1051/0004-6361:20011338. arXiv: astro-ph/0106570 [astro-ph] (cit. on p. 12).

Ghisellini, G. et al. (Nov. 2014). "The power of relativistic jets is larger than the luminosity of their accretion disks". In: *Nature* 515.7527, pp. 376–378. DOI: 10.1038/nature13856. arXiv: 1411.5368 [astro-ph.HE] (cit. on pp. 10–11).

Giannios, D. and D. A. Uzdensky (Mar. 2019). "GRB and blazar jets shining through their stripes". In: *Monthly Notices of the Royal Astronomical Society* 484.1, pp. 1378–1389. DOI: 10.1093/mnras/stz082. arXiv: 1805.09343 [astro-ph.HE] (cit. on pp. 188, 192).

Giannios, Dimitrios, Dmitri A. Uzdensky, and Mitchell C. Begelman (Mar. 2010). "Fast TeV variability from misaligned minijets in the jet of M87". In: *Monthly Notices of the Royal Astronomical Society* 402.3, pp. 1649–1656. DOI: 10.1111/j.1365-2966.2009.16045.x. arXiv: 0907.5005 [astro-ph.HE] (cit. on pp. 188, 193).

Goedbloed, J. P., Rony Keppens, and Stefaan Poedts (Apr. 2010). *Advanced Magnetohydrodynamics*. Publication Title: Advanced Magnetohydrodynamics ADS Bibcode: 2010adma.book.....G (cit. on p. 31).

Goedbloed, J. P. Hans and Stefaan Poedts (Aug. 2004). *Principles of Magnetohydrodynamics*. Publication Title: Principles of Magnetohydrodynamics ADS Bibcode: 2004prma.book.....G (cit. on pp. 31, 48, 195).

Gourgouliatos, Konstantinos N. and Serguei S. Komissarov (Dec. 2018). "Reconfinement and loss of stability in jets from active galactic nuclei". In: *Nature Astronomy* 2, pp. 167–171. DOI: 10.1038/s41550-017-0338-3. arXiv: 1806.05683 [astro-ph.HE] (cit. on pp. 160, 167, 184, 187, 189).

Gracia, J., N. Vlahakis, and K. Tsinganos (Mar. 2006). "Jet simulations extending radially self-similar magnetohydrodynamics models". In: *Monthly Notices of the Royal Astronomical Society* 367. ADS Bibcode: 2006MNRAS.367..201G, pp. 201–210. ISSN: 0035-8711. DOI: 10.1111/j.1365-2966.2005.09945.x (cit. on p. 118).

Haro, Guillermo (May 1952). "Herbig's Nebulous Objects Near NGC 1999." In: *the Astrophysical Journal* 115, p. 572. DOI: 10.1086/145576 (cit. on p. 6).

— (Jan. 1953). "Hα Emission Stars and Peculiar Objects in the Orion Nebula." In: *the Astrophysical Journal* 117, p. 73. DOI: 10.1086/145669 (cit. on p. 6).

Harris, D. E. and Henric Krawczynski (Sept. 2006). "X-Ray Emission from Extragalactic Jets". In: *Annual Review of Astronomy and Astrophysics* 44. ADS Bibcode: 2006ARA&A..44..463H, pp. 463–506. ISSN: 0066-4146. DOI: 10.1146/annurev.astro.44.051905.092446 (cit. on p. 33).

Harten, Ami (Mar. 1983). "High Resolution Schemes for Hyperbolic Conservation Laws". In: *Journal of Computational Physics* 49.3, pp. 357–393. DOI: 10.1016/0021-9991(83)90136-5 (cit. on p. 64).

Harten, Amiram, Peter D. Lax, and Bram van Leer (1983). "On Upstream Differencing and Godunov-Type Schemes for Hyperbolic Conservation Laws". In: *SIAM Review* 25.1, pp. 35–61. DOI: 10.1137/1025002. eprint: https://doi.org/10.1137/1025002 (cit. on p. 62).

Hartigan, Patrick, Suzan Edwards, and Louma Ghandour (Oct. 1995). "Disk Accretion and Mass Loss from Young Stars". In: *the Astrophysical Journal* 452, p. 736. DOI: 10.1086/176344 (cit. on p. 16).

Hassam, A. B. (Nov. 1992). "Reconnection of Stressed Magnetic Fields". In: *the Astrophysical Journal* 399, p. 159. DOI: 10.1086/171911 (cit. on p. 202).

Heaviside, Oliver (1892). "Xi. on the forces, stresses, and fluxes of energy in the electromagnetic field". In: *Philosophical Transactions of the Royal Society of London.(A.)* 183, pp. 423–480 (cit. on p. 34).

Henri, Gilles and Guy Pelletier (Dec. 1991). "Relativistic Electron-Positron Beam Formation in the Framework of the Two-Flow Model for Active Galactic Nuclei". In: *The Astrophysical Journal Letters* 383, p. L7. DOI: 10.1086/186228 (cit. on p. 34).

Herbig, George H. (Jan. 1950). "The Spectrum of the Nebulosity Surrounding T Tauri." In: *the Astrophysical Journal* 111, p. 11. DOI: 10.1086/145232 (cit. on p. 6).

— (May 1951). "The Spectra of Two Nebulous Objects Near NGC 1999." In: *the Astrophysical Journal* 113, pp. 697–699. DOI: 10.1086/145440 (cit. on p. 6).

Heyvaerts, Jean and Colin Norman (Dec. 1989). "The collimation of magnetized winds". In: *The Astrophysical Journal* 347, pp. 1055–1081. ISSN: 0004-637X. DOI: 10.1086/168195 (cit. on pp. 25, 129).

— (Oct. 2003). "Kinetic Energy Flux versus Poynting Flux in Magnetohydrodynamic Winds and Jets: The Intermediate Regime". In: *The Astrophysical Journal* 596. ADS Bibcode: 2003ApJ...596.1256H, pp. 1256–1269. ISSN: 0004-637X. DOI: 10.1086/378222 (cit. on p. 25).

Homan, D. C. et al. (Dec. 2021). "MOJAVE. XIX. Brightness Temperatures and Intrinsic Properties of Blazar Jets". In: *The Astrophysical Journal* 923. ADS Bibcode: 2021ApJ...923...67H, p. 67. ISSN: 0004-637X. DOI: 10.3847/1538-4357/ac27af (cit. on p. 31).

Hsu, S. C. and P. M. Bellan (May 2003). "Experimental Identification of the Kink Instability as a Poloidal Flux Amplification Mechanism for Coaxial Gun Spheromak Formation". In: *Physical Review Letters* 90.21, 215002, p. 215002. DOI: 10.1103/PhysRevLett.90.215002. arXiv: physics/0304104 [physics.plasm-ph] (cit. on p. 167).

Hu, Y. Q. and B. C. Low (July 1989). "Steady Hydromagnetic Flows in Open Magnetic Fields. III. Allowing for Variations of Density with Latitude and Nonalignment of Velocity with Magnetic Field". In: *the Astrophysical Journal* 342, p. 1049. DOI: 10.1086/167661 (cit. on p. 50).

Hugoniot, H (1887). "Mémoire sur la propagation du mouvement dans un fluide indéfini (Première partie)". In: *Journal de Mathématiques Pures et Appliquées* 3, pp. 477–492 (cit. on p. 50).

— (1888). "Mémoire sur la propagation du mouvement dans un fluide indéfini (seconde Partie)". In: *Journal de Mathématiques Pures et Appliquées* 4, pp. 153–167 (cit. on p. 50).

Illarionov, A. F. and R. A. Sunyaev (Feb. 1975). "Why the Number of Galactic X-ray Stars Is so Small?" In: *Astronomy and Astrophysics* 39, p. 185 (cit. on p. 114).

Ingram, Adam, Chris Done, and P. Chris Fragile (July 2009). "Low-frequency quasi-periodic oscillations spectra and Lense-Thirring precession". In: *Monthly Notices of the Royal Astronomical Society* 397.1, pp. L101–L105. DOI: 10.1111/j.1745-3933.2009.00693.x. arXiv: 0901.1238 [astro-ph.SR] (cit. on p. 165).

Ingram, Adam R. and Sara E. Motta (Sept. 2019). "A review of quasi-periodic oscillations from black hole X-ray binaries: Observation and theory". In: *New Astronomy Reviews* 85. ADS Bibcode: 2019NewAR..8501524I, p. 101524. ISSN: 1387-6473. DOI: 10.1016/j.newar.2020.101524 (cit. on pp. 161, 165).

Jacquemin-Ide, J., J. Ferreira, and G. Lesur (Dec. 2019). "Magnetically driven jets and winds from weakly magnetized accretion discs". In: *Monthly Notices of the Royal Astronomical Society* 490, pp. 3112–3133. DOI: 10.1093/mnras/stz2749 (cit. on pp. 22–23, 47, 50, 107, 111).

Jannaud, T., C. Zanni, and J. Ferreira (Jan. 2023). "Numerical simulations of MHD jets from Keplerian accretion disks. I. Recollimation shocks". In: *Astronomy and Astrophysics* 669, A159, A159. DOI: 10.1051/0004-6361/202244311. arXiv: 2210.14809 [astro-ph.HE] (cit. on pp. 71, 97, 189, 211).

Kadomtsev, B. B. (Jan. 1966). "Hydromagnetic Stability of a Plasma". In: *Reviews of Plasma Physics* 2, p. 153 (cit. on p. 195).

Knödlseder, Jürgen et al. (Mar. 2022). "Estimate of the carbon footprint of astronomical research infrastructures". In: *Nature Astronomy* 6, pp. 503–513. DOI: 10.1038/s41550-022-01612-3. arXiv: 2201.08748 [astro-ph.IM] (cit. on p. 66).

Komissarov, S. S. and S. A. E. G. Falle (July 1998). "The large-scale structure of FR-II radio sources". In: *Monthly Notices of the Royal Astronomical Society* 297, pp. 1087–1108. ISSN: 0035-8711. DOI: 10.1046/j.1365-8711.1998.01547.x (cit. on pp. 21, 24).

Komissarov, Serguei S. et al. (Sept. 2007). "Magnetic acceleration of relativistic active galactic nucleus jets". In: *Monthly Notices of the Royal Astronomical Society* 380, pp. 51–70. DOI: 10.1111/j.1365-2966.2007.12050.x (cit. on p. 151).

Konigl, A. (Oct. 1982). "On the nature of bipolar sources in dense molecular clouds." In: *the Astrophysical Journal* 261, pp. 115–134. DOI: 10.1086/160324 (cit. on p. 15).

Krasnopolsky, Ruben, Zhi-Yun Li, and Roger Blandford (Dec. 1999). "Magnetocentrifugal Launching of Jets from Accretion Disks. I. Cold Axisymmetric Flows". In: *The Astrophysical Journal* 526, pp. 631–642. DOI: 10.1086/308023 (cit. on pp. 21, 120).

Krasnopolsky, Ruben, Zhi-Yun Li, and Roger D. Blandford (Oct. 2003). "Magnetocentrifugal Launching of Jets from Accretion Disks. II. Inner Disk-driven Winds". In: *The Astrophysical Journal* 595, pp. 631–642. ISSN: 0004-637X. DOI: 10.1086/377494 (cit. on pp. 21, 120).

Lavalley-Fouquet, C., S. Cabrit, and C. Dougados (Apr. 2000). "DG Tau: A shocking jet". In: *Astronomy and Astrophysics* 356, pp. L41–L44 (cit. on pp. 188, 191).

Leahy, D. A. et al. (Mar. 1983). "On searches for pulsed emission with application to four globular cluster X-ray sources : NGC 1851, 6441, 6624 and 6712." In: *The Astrophysical Journal* 266, pp. 160–170. DOI: 10.1086/160766 (cit. on p. 161).

Ledlow, Michael J. and Frazer N. Owen (July 1996). "20 CM VLA Survey of Abell Clusters of Galaxies. VI. Radio/Optical Luminosity Functions". In: *the Astronomical Journal* 112, p. 9. DOI: 10.1086/117985. arXiv: astro-ph/9607014 [astro-ph] (cit. on p. 12).

Lee, Chin-Fei (Mar. 2020). "Molecular jets from low-mass young protostellar objects". In: *The Astronomy and Astrophysics Review* 28.1, 1, p. 1. DOI: 10.1007/s00159-020-0123-7. arXiv: 2002.05823 [astro-ph.GA] (cit. on pp. 13, 127).

Lee, Chin-Fei et al. (June 2015). "Jet Motion, Internal Working Surfaces, and Nested Shells in the Protostellar System HH 212". In: *the Astrophysical Journal* 805.2, 186, p. 186. DOI: 10.1088/0004-637X/805/2/186. arXiv: 1503.07362 [astro-ph.GA] (cit. on p. 13).

Lee, Chin-Fei et al. (July 2017). "A rotating protostellar jet launched from the innermost disk of HH 212". In: *Nature Astronomy* 1. ADS Bibcode: 2017NatAs...1E.152L, p. 0152. ISSN: 2397-3366. DOI: 10.1038/s41550-017-0152 (cit. on p. 13).

Lee, Joyce W. Y., Charles L. H. Hull, and Stella S. R. Offner (Jan. 2017). "Synthetic Observations of Magnetic Fields in Protostellar Cores". In: *the Astrophysical Journal* 834.2, 201, p. 201. DOI: 10.3847/1538-4357/834/2/201. arXiv: 1611.08530 [astro-ph.GA] (cit. on p. 16).

Lehmann, Andrew, Christoph Federrath, and Mark Wardle (Nov. 2016). "SHOCKFIND - an algorithm to identify magnetohydrodynamic shock waves in turbulent

clouds". In: *Monthly Notices of the Royal Astronomical Society* 463.1, pp. 1026–1039. DOI: 10.1093/mnras/stw2015. arXiv: 1608.02050 [astro-ph.GA] (cit. on p. 87).

Li, Zhi-Yun, Tzihong Chiueh, and Mitchell C. Begelman (Aug. 1992). "Electromagnetically Driven Relativistic Jets: A Class of Self-similar Solutions". In: *The Astrophysical Journal* 394. ADS Bibcode: 1992ApJ...394..459L, p. 459. ISSN: 0004-637X. DOI: 10.1086/171597 (cit. on p. 22).

Louvet, F. et al. (Oct. 2018). "The HH30 edge-on T Tauri star. A rotating and precessing monopolar outflow scrutinized by ALMA". en. In: *Astronomy & Astrophysics, Volume 618, id.A120, <NUMPAGES>28</NUMPAGES> pp.* 618, A120. ISSN: 0004-6361. DOI: 10.1051/0004-6361/201731733 (cit. on pp. 31, 36, 89).

Lu, Ru-Sen et al. (Apr. 2023). "A ring-like accretion structure in M87 connecting its black hole and jet". In: *Nature* 616.7958, pp. 686–690. DOI: 10.1038/s41586-023-05843-w. arXiv: 2304.13252 [astro-ph.HE] (cit. on pp. 188, 191).

Lynden-Bell, D. (Aug. 1969). "Galactic Nuclei as Collapsed Old Quasars". In: *Nature* 223.5207, pp. 690–694. DOI: 10.1038/223690a0 (cit. on p. 5).

Marcel, G. et al. (July 2018). "A unified accretion-ejection paradigm for black hole X-ray binaries. II. Observational signatures of jet-emitting disks". In: *Astronomy and Astrophysics* 615, A57. ISSN: 0004-6361. DOI: 10.1051/0004-6361/201732069 (cit. on p. 127).

Marcel, G. et al. (Sept. 2018). "A unified accretion-ejection paradigm for black hole X-ray binaries. III. Spectral signatures of hybrid disk configurations". In: *Astronomy and Astrophysics* 617, A46, A46. DOI: 10.1051/0004-6361/201833124. arXiv: 1805.12407 [astro-ph.HE] (cit. on p. 127).

Marcel, G. et al. (June 2019). "A unified accretion-ejection paradigm for black hole X-ray binaries. IV. Replication of the 2010-2011 activity cycle of GX 339-4". In: *Astronomy and Astrophysics* 626, A115, A115. DOI: 10.1051/0004-6361/201935060. arXiv: 1905.05057 [astro-ph.HE] (cit. on pp. 127, 166).

Marcel, G. et al. (Aug. 2020). "A unified accretion-ejection paradigm for black hole X-ray binaries. V. Low-frequency quasi-periodic oscillations". en. In: *Astronomy & Astrophysics, Volume 640, id.A18, <NUMPAGES>19</NUMPAGES> pp.* 640, A18. ISSN: 0004-6361. DOI: 10.1051/0004-6361/202037539 (cit. on pp. 164–165).

Marcel, G. et al. (Mar. 2022). "A unified accretion-ejection paradigm for black hole X-ray binaries. VI. Radiative efficiency and radio-X-ray correlation during four outbursts from GX 339-4". In: *Astronomy and Astrophysics* 659, A194, A194. DOI: 10.1051/0004-6361/202141375. arXiv: 2109.13592 [astro-ph.HE] (cit. on p. 127).

Markwardt, Craig B., Jean H. Swank, and Ronald E. Taam (Mar. 1999). "Variable-Frequency Quasi-periodic Oscillations from the Galactic Microquasar GRS 1915+105". In: *The Astrophysical Journal* 513.1, pp. L37–L40. DOI: 10.1086/311899. arXiv: astro-ph/9901050 [astro-ph] (cit. on p. 164).

Massaglia, S. et al. (2008). *Jets From Young Stars III*. Vol. 754. DOI: 10.1007/978-3-540-76967-5 (cit. on p. 62).

Matsakos, T. et al. (Jan. 2008). "Two-component jet simulations. I. Topological stability of analytical MHD outflow solutions". In: *Astronomy and Astrophysics* 477, pp. 521–533. ISSN: 0004-6361. DOI: 10.1051/0004-6361:20077907 (cit. on pp. 21, 24, 118–119, 153, 175).

Matsakos, T. et al. (July 2009). "Two-component jet simulations. II. Combining analytical disk and stellar MHD outflow solutions". en. In: *Astronomy and Astrophysics, Volume 502, Issue 1, 2009, pp.217-229* 502.1, p. 217. ISSN: 0004-6361. DOI: 10.1051/0004-6361/200811046 (cit. on pp. 21, 24, 118).

Matsumoto, Jin, Serguei S. Komissarov, and Konstantinos N. Gourgouliatos (Oct. 2020). "Magnetic inhibition of the recollimation instability in relativistic jets". In: *arXiv e-prints* 2010, arXiv:2010.11012 (cit. on pp. 160, 184, 187, 189, 202).

Matsumoto, Jin and Youhei Masada (July 2013). "Two-dimensional Numerical Study for Rayleigh-Taylor and Richtmyer-Meshkov Instabilities in Relativistic Jets". In: *The Astrophysical Journal Letters* 772, p. L1. ISSN: 0004-637X. DOI: 10.1088/2041-8205/772/1/L1 (cit. on p. 202).

Matt, Sean and Ralph E. Pudritz (Oct. 2005). "Accretion-powered Stellar Winds as a Solution to the Stellar Angular Momentum Problem". In: *the Astrophysical Journal Letters* 632.2, pp. L135–L138. DOI: 10.1086/498066. arXiv: astro-ph/0510060 [astro-ph] (cit. on p. 10).

Maxwell, James Clerk (1873). *A treatise on electricity and magnetism*. Vol. 1. Clarendon press (cit. on p. 34).

McCaughrean, M. et al. (Sept. 2002). "Standing on the shoulder of a giant: ISAAC, Antu, and star formation". In: *The Messenger* 109, pp. 28–36 (cit. on p. 13).

McKinney, Jonathan C. (June 2006). "General relativistic magnetohydrodynamic simulations of the jet formation and large-scale propagation from black hole accretion systems". In: *Monthly Notices of the Royal Astronomical Society* 368.4, pp. 1561–1582. DOI: 10.1111/j.1365-2966.2006.10256.x. arXiv: astro-ph/0603045 [astro-ph] (cit. on p. 202).

McKinney, Jonathan C., Alexander Tchekhovskoy, and Roger D. Blandford (July 2012). "General relativistic magnetohydrodynamic simulations of magnetically choked accretion flows around black holes". In: *Monthly Notices of the Royal Astronomical Society* 423. ADS Bibcode: 2012MNRAS.423.3083M, pp. 3083–3117. ISSN: 0035-8711. DOI: 10.1111/j.1365-2966.2012.21074.x (cit. on p. 164).

McLure, R. J. and J. S. Dunlop (Oct. 2001). "The black hole masses of Seyfert galaxies and quasars". In: *Monthly Notices of the Royal Astronomical Society* 327.1, pp. 199–207. DOI: 10.1046/j.1365-8711.2001.04709.x. arXiv: astro-ph/0009406 [astro-ph] (cit. on p. 12).

Meliani, Z. and R. Keppens (Nov. 2009). "Decelerating Relativistic Two-Component Jets". In: *The Astrophysical Journal* 705, pp. 1594–1606. ISSN: 0004-637X. DOI: 10.1088/0004-637X/705/2/1594 (cit. on p. 202).

Michel, F. C. (Nov. 1969). "Relativistic Stellar-Wind Torques". In: *The Astrophysical Journal* 158, p. 727. DOI: 10.1086/150233 (cit. on p. 87).

Mignone, A. (Aug. 2014). "High-order conservative reconstruction schemes for finite volume methods in cylindrical and spherical coordinates". In: *Journal of Computational Physics* 270, pp. 784–814. DOI: 10.1016/j.jcp.2014.04.001. arXiv: 1404.0537 [physics.comp-ph] (cit. on p. 64).

Mignone, A. et al. (May 2007). "PLUTO: A Numerical Code for Computational Astrophysics". In: *The Astrophysical Journal Supplement Series* 170. ADS Bibcode: 2007ApJS..170..228M, pp. 228–242. ISSN: 0067-0049. DOI: 10.1086/513316 (cit. on pp. iii, v, 4, 25, 57, 59).

Mingo, B. et al. (Sept. 2019). "Revisiting the Fanaroff-Riley dichotomy and radio-galaxy morphology with the LOFAR Two-Metre Sky Survey (LoTSS)". In: *Monthly Notices of the Royal Astronomical Society* 488. ADS Bibcode: 2019MNRAS.488.2701M, pp. 2701–2721. ISSN: 0035-8711. DOI: 10.1093/mnras/stz1901 (cit. on p. 12).

Mirabel, I. F. and L. F. Rodríguez (Sept. 1994). "A superluminal source in the Galaxy". In: *Nature* 371.6492, pp. 46–48. DOI: 10.1038/371046a0 (cit. on p. 8).

Miyoshi, Takahiro and Kanya Kusano (Sept. 2005). "A multi-state HLL approximate Riemann solver for ideal magnetohydrodynamics". In: *Journal of Computational Physics* 208, pp. 315–344. DOI: 10.1016/j.jcp.2005.02.017 (cit. on p. 63).

Mizuno, Yosuke, Philip E. Hardee, and Ken-Ichi Nishikawa (Apr. 2014). "Spatial Growth of the Current-driven Instability in Relativistic Jets". In: *the Astrophysical Journal* 784.2, 167, p. 167. DOI: 10.1088/0004-637X/784/2/167. arXiv: 1402.2370 [astro-ph.HE] (cit. on p. 202).

Moll, R., H. C. Spruit, and M. Obergaulinger (Dec. 2008). "Kink instabilities in jets from rotating magnetic fields". In: *Astronomy and Astrophysics* 492.3, pp. 621–630. DOI: 10.1051/0004-6361:200810523. arXiv: 0809.3165 [astro-ph] (cit. on p. 202).

Motta, S. et al. (Dec. 2011). "Low-frequency oscillations in black holes: a spectral-timing approach to the case of GX 339-4". In: *Monthly Notices of the Royal Astronomical Society* 418.4, pp. 2292–2307. DOI: 10.1111/j.1365-2966.2011.19566.x. arXiv: 1108.0540 [astro-ph.HE] (cit. on p. 162).

Motta, S. E. (May 2016). "Quasi periodic oscillations in black hole binaries". In: *Astronomische Nachrichten* 337.4-5, p. 398. DOI: 10.1002/asna.201612320. arXiv: 1603.07885 [astro-ph.HE] (cit. on pp. 161–162).

Motta, S. E. et al. (Feb. 2015). "Geometrical constraints on the origin of timing signals from black holes". In: *Monthly Notices of the Royal Astronomical Society* 447.2, pp. 2059–2072. DOI: 10.1093/mnras/stu2579. arXiv: 1404.7293 [astro-ph.HE] (cit. on p. 163).

Muno, Michael P., Edward H. Morgan, and Ronald A. Remillard (Dec. 1999). "Quasi-periodic Oscillations and Spectral States in GRS 1915+105". In: *The Astrophysical Journal* 527.1, pp. 321–340. DOI: 10.1086/308063 (cit. on p. 164).

Murphy, G. C., J. Ferreira, and C. Zanni (Mar. 2010). "Large scale magnetic fields in viscous resistive accretion disks. I. Ejection from weakly magnetized disks". en. In: *Astronomy and Astrophysics, Volume 512, id.A82, <NUMPAGES>14</NUMPAGES> pp.* 512, A82. ISSN: 0004-6361. DOI: 10.1051/0004-6361/200912633 (cit. on pp. 21, 151–152).

Murphy, Gareth C., Claudio Zanni, and Jonathan Ferreira (Jan. 2009). "Magnetic Field Advection in Weakly Magnetised Viscous Resistive Accretion Disks: Numerical Simulations". In: 13. Conference Name: Protostellar Jets in Context ADS Bibcode: 2009ASSP...13..117M, pp. 117–122. DOI: 10.1007/978-3-642-00576-3_14 (cit. on p. 21).

Narayan, Ramesh et al. (May 2021). "The Polarized Image of a Synchrotron-emitting Ring of Gas Orbiting a Black Hole". In: *the Astrophysical Journal* 912.1, 35, p. 35. DOI: 10.3847/1538-4357/abf117. arXiv: 2105.01804 [astro-ph.HE] (cit. on p. 190).

Okamoto, I. (May 2003). "Global Asymptotic Solutions for Magnetohydrodynamic Jets and Winds". In: *The Astrophysical Journal* 589. ADS Bibcode: 2003ApJ...589..671O, pp. 671–676. ISSN: 0004-637X. DOI: 10.1086/374356 (cit. on p. 25).

Okamoto, Isao (Oct. 2001). "Magnetized centrifugal winds". In: *Monthly Notices of the Royal Astronomical Society* 327. ADS Bibcode: 2001MNRAS.327...55O, pp. 55–68. ISSN: 0035-8711. DOI: 10.1046/j.1365-8711.2001.04598.x (cit. on p. 25).

Ostriker, Eve C. (Sept. 1997). "Self-similar Magnetocentrifugal Disk Winds with Cylindrical Asymptotics". In: *The Astrophysical Journal* 486. ADS Bibcode: 1997ApJ...486..291O, pp. 291–306. ISSN: 0004-637X. DOI: 10.1086/304513 (cit. on p. 22).

Ouyed, Rachid, David A. Clarke, and Ralph E. Pudritz (Jan. 2003). "Three-dimensional Simulations of Jets from Keplerian Disks: Self-regulatory Stability". In: *The Astrophysical Journal* 582, pp. 292–319. ISSN: 0004-637X. DOI: 10.1086/344507 (cit. on pp. 21, 119).

Ouyed, Rachid and Ralph E. Pudritz (Dec. 1993). "Forbidden Line Formation in Hydromagnetic Disk Winds. I. Oblique Shocks". In: *The Astrophysical Journal* 419.

ADS Bibcode: 1993ApJ...419..255O, p. 255. ISSN: 0004-637X. DOI: 10.1086/173479 (cit. on p. 50).

— (June 1997a). "Numerical Simulations of Astrophysical Jets from Keplerian Disks. I. Stationary Models". In: *The Astrophysical Journal* 482, pp. 712–732. DOI: 10.1086/304170 (cit. on pp. 21, 119).

— (July 1997b). "Numerical Simulations of Astrophysical Jets from Keplerian Disks. II. Episodic Outflows". In: *The Astrophysical Journal* 484, pp. 794–809. ISSN: 0004-637X. DOI: 10.1086/304355 (cit. on pp. 21, 119).

— (Oct. 1999). "Numerical simulations of astrophysical jets from Keplerian discs - III. The effects of mass loading". In: *Monthly Notices of the Royal Astronomical Society* 309, pp. 233–244. ISSN: 0035-8711. DOI: 10.1046/j.1365-8711.1999.02828.x (cit. on p. 21).

Owen, F. N. and M. J. Ledlow (Jan. 1994). "The FRI/II Break and the Bivariate Luminosity Function in Abell Clusters of Galaxies". In: *The Physics of Active Galaxies*. Ed. by Geoffrey V. Bicknell, Michael A. Dopita, and Peter J. Quinn. Vol. 54. Astronomical Society of the Pacific Conference Series, p. 319 (cit. on p. 12).

Owen, Frazer N., Jean A. Eilek, and Namir E. Kassim (Nov. 2000). "M87 at 90 Centimeters: A Different Picture". In: *The Astrophysical Journal* 543. ADS Bibcode: 2000ApJ...543..611O, pp. 611–619. ISSN: 0004-637X. DOI: 10.1086/317151 (cit. on p. 32).

Pelletier, Guy and Ralph E. Pudritz (July 1992). "Hydromagnetic Disk Winds in Young Stellar Objects and Active Galactic Nuclei". In: *The Astrophysical Journal* 394, p. 117. ISSN: 0004-637X. DOI: 10.1086/171565 (cit. on pp. 45, 87, 166).

Perlman, Eric S. et al. (Dec. 2003). "Month-Timescale Optical Variability in the M87 Jet". In: *The Astrophysical Journal* 599. ADS Bibcode: 2003ApJ...599L..65P, pp. L65–L68. ISSN: 0004-637X. DOI: 10.1086/381191 (cit. on p. 33).

Perucho, M. and J. M. Martí (Dec. 2007). "A numerical simulation of the evolution and fate of a Fanaroff-Riley type I jet. The case of 3C 31". In: *Monthly Notices of the Royal Astronomical Society* 382, pp. 526–542. ISSN: 0035-8711. DOI: 10.1111/j.1365-2966.2007.12454.x (cit. on pp. 21, 24).

Perucho, M. et al. (Sept. 2010). "Stability of three-dimensional relativistic jets: implications for jet collimation". In: *Astronomy and Astrophysics* 519, A41, A41. DOI: 10.1051/0004-6361/200913012. arXiv: 1005.4332 [astro-ph.HE] (cit. on p. 21).

Perucho, Manel (May 2020). "Triggering mixing and deceleration in FRI jets: a solution". In: *Monthly Notices of the Royal Astronomical Society* 494, pp. L22–L26. ISSN: 0035-8711. DOI: 10.1093/mnrasl/slaa031 (cit. on p. 24).

Piner, B. Glenn and Philip G. Edwards (Dec. 2014). "First-epoch VLBA Imaging of 20 New TeV Blazars". In: *The Astrophysical Journal* 797. ADS Bibcode: 2014ApJ...797...25P, p. 25. ISSN: 0004-637X. DOI: 10.1088/0004-637X/797/1/25 (cit. on p. 31).

Plunkett, Adele L. et al. (Nov. 2015). "Episodic molecular outflow in the very young protostellar cluster Serpens South". In: *Nature* 527.7576, pp. 70–73. DOI: 10.1038/nature15702. arXiv: 1511.01100 [astro-ph.SR] (cit. on p. 193).

Polko, Peter, David L. Meier, and Sera Markoff (Nov. 2010). "Determining the Optimal Locations for Shock Acceleration in Magnetohydrodynamical Jets". In: *The Astrophysical Journal* 723, pp. 1343–1350. ISSN: 0004-637X. DOI: 10.1088/0004-637X/723/2/1343 (cit. on pp. 22, 98, 128).

— (Feb. 2014). "Linking accretion flow and particle acceleration in jets - II. Self-similar jet models with full relativistic MHD gravitational mass". In: *Monthly Notices of the Royal Astronomical Society* 438, pp. 959–970. ISSN: 0035-8711. DOI: 10.1093/mnras/stt2155 (cit. on p. 22).

Porth, Oliver and Christian Fendt (Feb. 2010). "Acceleration and Collimation of Relativistic Magnetohydrodynamic Disk Winds". In: *The Astrophysical Journal* 709. ADS Bibcode: 2010ApJ...709.1100P, pp. 1100–1118. ISSN: 0004-637X. DOI: 10.1088/0004-637X/709/2/1100 (cit. on p. 21).

Porth, Oliver and Serguei S. Komissarov (Sept. 2015). "Causality and stability of cosmic jets". In: *Monthly Notices of the Royal Astronomical Society* 452, pp. 1089–1104. ISSN: 0035-8711. DOI: 10.1093/mnras/stv1295 (cit. on p. 21).

Price, Daniel J. (Feb. 2012). "Smoothed particle hydrodynamics and magnetohydrodynamics". In: *Journal of Computational Physics* 231.3, pp. 759–794. DOI: 10.1016/j.jcp.2010.12.011. arXiv: 1012.1885 [astro-ph.IM] (cit. on p. 59).

Prieto, M. A. et al. (Apr. 2016). "The central parsecs of M87: jet emission and an elusive accretion disc". In: *Monthly Notices of the Royal Astronomical Society* 457. ADS Bibcode: 2016MNRAS.457.3801P, pp. 3801–3816. ISSN: 0035-8711. DOI: 10.1093/mnras/stw166 (cit. on p. 32).

Pudritz, Ralph E., Conrad S. Rogers, and Rachid Ouyed (Feb. 2006). "Controlling the collimation and rotation of hydromagnetic disc winds". In: *Monthly Notices of the Royal Astronomical Society* 365, pp. 1131–1148. DOI: 10.1111/j.1365-2966.2005.09766.x (cit. on pp. 21, 119–120).

Ramsey, Jon P. and David A. Clarke (Feb. 2011). "Simulating Protostellar Jets Simultaneously at Launching and Observational Scales". In: *The Astrophysical Journal Letters* 728, p. L11. ISSN: 0004-637X. DOI: 10.1088/2041-8205/728/1/L11 (cit. on pp. 21, 121, 152).

— (Apr. 2019). "MHD simulations of the formation and propagation of protostellar jets to observational length-scales". In: *Monthly Notices of the Royal Astronomical Society* 484, pp. 2364–2387. ISSN: 0035-8711. DOI: 10.1093/mnras/stz116 (cit. on pp. 21, 121, 152).

Rankine, William John Macquorn (1870). "XV. On the thermodynamic theory of waves of finite longitudinal disturbance". In: *Philosophical Transactions of the Royal Society of London* 160, pp. 277–288 (cit. on p. 50).

Ray, T. et al. (Jan. 2007). *Toward Resolving the Outflow Engine: An Observational Perspective*. Conference Name: Protostars and Planets V Pages: 231 ADS Bibcode: 2007prpl.conf..231R. eprint: arXiv:astro-ph/0605597 (cit. on pp. 6, 13).

Ray, T. P. and J. Ferreira (Dec. 2021). "Jets from young stars". In: *New Astronomy Reviews* 93. ADS Bibcode: 2021NewAR..9301615R, p. 101615. ISSN: 1387-6473. DOI: 10.1016/j.newar.2021.101615 (cit. on p. 6).

Rayleigh (1882). "Investigation of the Character of the Equilibrium of an Incompressible Heavy Fluid of Variable Density". In: *Proceedings of the London Mathematical Society* s1-14.1, pp. 170–177. DOI: https://doi.org/10.1112/plms/s1-14.1.170. eprint: https://londmathsoc.onlinelibrary.wiley.com/doi/pdf/10.1112/plms/s1-14.1.170 (cit. on p. 202).

Rayleigh, Lord (Mar. 1917). "On the Dynamics of Revolving Fluids". In: *Proceedings of the Royal Society of London Series A* 93.648, pp. 148–154. DOI: 10.1098/rspa.1917.0010 (cit. on p. 202).

Reipurth, Bo and John Bally (2001). "Herbig-Haro Flows: Probes of Early Stellar Evolution". en. In: *Annual Review of Astronomy and Astrophysics, Vol. 39, p. 403-455 (2001).* 39, p. 403. ISSN: 0066-4146. DOI: 10.1146/annurev.astro.39.1.403 (cit. on p. 13).

Reipurth, Bo et al. (Sept. 2019). "The Giant Herbig-Haro Flow HH 212 and Associated Star Formation". In: *the Astronomical Journal* 158.3, 107, p. 107. DOI: 10.3847/1538-3881/ab2d25. arXiv: 1911.05877 [astro-ph.SR] (cit. on p. 13).

Richard, Thibaud et al. (Aug. 2022). "Probing the nature of dissipation in compressible MHD turbulence". In: *Astronomy and Astrophysics* 664, A193, A193. DOI: 10.1051/0004-6361/202142531. arXiv: 2206.03045 [astro-ph.GA] (cit. on p. 87).

Rodriguez, J. et al. (May 2002). "Accretion-ejection instability and QPO in black hole binaries I. Observations". In: *Astronomy and Astrophysics* 387, pp. 487–496. DOI: 10.1051/0004-6361:20000524. arXiv: astro-ph/0203324 [astro-ph] (cit. on p. 164).

Rodriguez, J. et al. (Nov. 2004). "Spectral Properties of Low-Frequency Quasi-periodic Oscillations in GRS 1915+105". In: *The Astrophysical Journal* 615.1, pp. 416–421. DOI: 10.1086/423978. arXiv: astro-ph/0407076 [astro-ph] (cit. on p. 164).

Roe, P. L. (Jan. 1986). "Characteristic-based schemes for the euler equations". In: *Annual Review of Fluid Mechanics* 18, pp. 337–365. DOI: 10.1146/annurev.fl.18.010186.002005 (cit. on p. 63).

Romanova, M. M. et al. (Nov. 2009). "Launching of conical winds and axial jets from the disc-magnetosphere boundary: axisymmetric and 3D simulations". In: *Monthly Notices of the Royal Astronomical Society* 399.4, pp. 1802–1828. DOI: 10.1111/j.1365-2966.2009.15413.x. arXiv: 0907.3394 [astro-ph.SR] (cit. on pp. 126, 142).

Shakura, N. I. and R. A. Sunyaev (Jan. 1973). "Black holes in binary systems. Observational appearance." In: *Astronomy and Astrophysics* 24, pp. 337–355 (cit. on pp. 125, 127, 151).

Sheikhnezami, Somayeh et al. (Sept. 2012). "Bipolar Jets Launched from Magnetically Diffusive Accretion Disks. I. Ejection Efficiency versus Field Strength and Diffusivity". In: *The Astrophysical Journal* 757. ADS Bibcode: 2012ApJ...757...65S, p. 65. ISSN: 0004-637X. DOI: 10.1088/0004-637X/757/1/65 (cit. on p. 21).

Snell, R. L., R. B. Loren, and R. L. Plambeck (July 1980). "Observations of CO in L 1551 : evidence for stellar wind driven shocks." In: *the Astrophysical Journal Letters* 239, pp. L17–L22. DOI: 10.1086/183283 (cit. on p. 6).

Sobczak, Gregory J. et al. (Mar. 2000). "Correlations between Low-Frequency Quasi-periodic Oscillations and Spectral Parameters in XTE J1550-564 and GRO J1655-40". In: *The Astrophysical Journal* 531.1, pp. 537–545. DOI: 10.1086/308463. arXiv: astro-ph/9910519 [astro-ph] (cit. on p. 164).

Spitzer, L. (Jan. 1962). *Physics of Fully Ionized Gases*. Publication Title: Physics of Fully Ionized Gases ADS Bibcode: 1962pfig.book.....S (cit. on pp. 32, 35).

Spruit, H. C. (Jan. 1996). "Magnetohydrodynamic jets and winds from accretion disks". In: *Evolutionary Processes in Binary Stars*. Ed. by Ralph A. M. J. Wijers, Melvyn B. Davies, and Christopher A. Tout. Vol. 477. NATO Advanced Study Institute (ASI) Series C, pp. 249–286 (cit. on p. 120).

Staff, J. E. et al. (Feb. 2015). "Hubble Space Telescope scale 3D simulations of MHD disc winds: a rotating two-component jet structure". In: *Monthly Notices of the Royal Astronomical Society* 446, pp. 3975–3991. ISSN: 0035-8711. DOI: 10.1093/mnras/stu2392 (cit. on p. 21).

Staff, Jan E. et al. (Oct. 2010). "Confronting Three-dimensional Time-dependent Jet Simulations with Hubble Space Telescope Observations". In: *The Astrophysical Journal* 722, pp. 1325–1332. ISSN: 0004-637X. DOI: 10.1088/0004-637X/722/2/1325 (cit. on p. 21).

Stepanovs, Deniss and Christian Fendt (July 2016). "An Extensive Numerical Survey of the Correlation Between Outflow Dynamics and Accretion Disk Magnetization". In: *The Astrophysical Journal* 825. ADS Bibcode: 2016ApJ...825...14S, p. 14. ISSN: 0004-637X. DOI: 10.3847/0004-637X/825/1/14 (cit. on p. 21).

Stute, M. et al. (Nov. 2008). "Stability and structure of analytical MHD jet formation models with a finite outer disk radius". In: *Astronomy and Astrophysics* 491, pp. 339–351. ISSN: 0004-6361. DOI: 10.1051/0004-6361:200810499 (cit. on pp. 21, 24, 118, 152–154, 175–176).

Stute, Matthias et al. (Apr. 2014). "3D simulations of disc winds extending radially self-similar MHD models". In: *Monthly Notices of the Royal Astronomical Society* 439. ADS Bibcode: 2014MNRAS.439.3641S, pp. 3641–3648. ISSN: 0035-8711. DOI: 10.1093/mnras/stu214 (cit. on pp. 21, 154).

Suydam, Bergen R (1958). "Stability of a linear pinch". In: *Journal of Nuclear Energy (1954)* 7.3-4, pp. 275–276 (cit. on p. 196).

Tabone, B. et al. (June 2018). "Interaction between a pulsating jet and a surrounding disk wind. A hydrodynamical perspective". en. In: *Astronomy & Astrophysics, Volume 614, id.A119, <NUMPAGES>13</NUMPAGES> pp.* 614, A119. ISSN: 0004-6361. DOI: 10.1051/0004-6361/201732031 (cit. on pp. 188, 193).

Tabone, B. et al. (Aug. 2020). "Constraining MHD disk winds with ALMA. Apparent rotation signatures and application to HH212". In: *Astronomy and Astrophysics* 640, A82. ISSN: 0004-6361. DOI: 10.1051/0004-6361/201834377 (cit. on pp. 89, 127).

Tagger, M. and R. Pellat (Sept. 1999). "An accretion-ejection instability in magnetized disks". In: *Astronomy and Astrophysics* 349, pp. 1003–1016. DOI: 10.48550/arXiv.astro-ph/9907267. arXiv: astro-ph/9907267 [astro-ph] (cit. on p. 164).

Taylor, Geoffrey Ingram (1950). "The instability of liquid surfaces when accelerated in a direction perpendicular to their planes. I". In: *Proceedings of the Royal Society of London. Series A. Mathematical and Physical Sciences* 201.1065, pp. 192–196. DOI: 10.1098/rspa.1950.0052. eprint: https://royalsocietypublishing.org/doi/pdf/10.1098/rspa.1950.0052 (cit. on p. 202).

Tchekhovskoy, Alexander and Omer Bromberg (Sept. 2016). "Three-dimensional relativistic MHD simulations of active galactic nuclei jets: magnetic kink instability and Fanaroff-Riley dichotomy". In: *Monthly Notices of the Royal Astronomical Society* 461. ADS Bibcode: 2016MNRAS.461L..46T, pp. L46–L50. ISSN: 0035-8711. DOI: 10.1093/mnrasl/slw064 (cit. on pp. 12, 21, 160, 184, 187–189, 193, 202).

Tetarenko, A. J. et al. (Apr. 2019). "Radio frequency timing analysis of the compact jet in the black hole X-ray binary Cygnus X-1". In: *Monthly Notices of the Royal Astronomical Society* 484. ADS Bibcode: 2019MNRAS.484.2987T, pp. 2987–3003. ISSN: 0035-8711. DOI: 10.1093/mnras/stz165 (cit. on p. 177).

Tetarenko, A. J. et al. (July 2021). "Measuring fundamental jet properties with multiwavelength fast timing of the black hole X-ray binary MAXI J1820+070". In: *Monthly Notices of the Royal Astronomical Society* 504. ADS Bibcode: 2021MNRAS.504.3862T, pp. 3862–3883. ISSN: 0035-8711. DOI: 10.1093/mnras/stab820 (cit. on p. 177).

Teşileanu, O. et al. (Feb. 2014). "Young stellar object jet models: From theory to synthetic observations". en. In: *Astronomy & Astrophysics, Volume 562, id.A117, <NUMPAGES>9</NUMPAGES> pp.* 562, A117. ISSN: 0004-6361. DOI: 10.1051/0004-6361/201322627 (cit. on pp. 21, 154).

Tudor, V. et al. (Sept. 2017). "Disc-jet coupling in low-luminosity accreting neutron stars". In: *Monthly Notices of the Royal Astronomical Society* 470. ADS Bibcode: 2017MNRAS.470..324T, pp. 324–339. ISSN: 0035-8711. DOI: 10.1093/mnras/stx1168 (cit. on p. 6).

Uchida, Y. and K. Shibata (Jan. 1985). "Magnetodynamical acceleration of CO and optical bipolar flows from the region of star formation." In: *Publications of the Astronomical Society of Japan* 37, pp. 515–535 (cit. on p. 19).

Ustyugova, G. V. et al. (Feb. 1995). "Magnetohydrodynamic Simulations of Outflows from Accretion Disks". In: *The Astrophysical Journal* 439. ADS Bibcode: 1995ApJ...439L..39U, p. L39. ISSN: 0004-637X. DOI: 10.1086/187739 (cit. on p. 21).

— (May 1999). "Magnetocentrifugally Driven Winds: Comparison of MHD Simulations with Theory". In: *The Astrophysical Journal* 516. ADS Bibcode: 1999ApJ...516..221U, pp. 221–235. ISSN: 0004-637X. DOI: 10.1086/307093 (cit. on pp. 21, 174–176).

van den Eijnden, J. et al. (Jan. 2017). "Inclination dependence of QPO phase lags in black hole X-ray binaries". In: *Monthly Notices of the Royal Astronomical Society* 464.3, pp. 2643–2659. DOI: 10.1093/mnras/stw2634. arXiv: 1610.03469 [astro-ph.HE] (cit. on pp. 163–164).

van der Klis, M. (Jan. 1989). "Fourier techniques in X-ray timing". In: *Timing Neutron Stars*. Ed. by H. Ögelman and E. P. J. van den Heuvel. Vol. 262. NATO Advanced Study Institute (ASI) Series C, p. 27. DOI: 10.1007/978-94-009-2273-0_3 (cit. on p. 161).

van Leer, Bram (Mar. 1974). "Towards the Ultimate Conservation Difference Scheme. II. Monotonicity and Conservation Combined in a Second-Order Scheme". In: *Journal of Computational Physics* 14.4, pp. 361–370. DOI: 10.1016/0021-9991(74)90019-9 (cit. on p. 63).

— (Mar. 1977). "Towards the Ultimate Conservative Difference Scheme. IV. A New Approach to Numerical Convection". In: *Journal of Computational Physics* 23, p. 276. DOI: 10.1016/0021-9991(77)90095-X (cit. on p. 63).

Vignarca, F. et al. (Jan. 2003). "Tracing the power-law component in the energy spectrum of black hole candidates as a function of the QPO frequency". In: *Astronomy and Astrophysics* 397, pp. 729–738. DOI: 10.1051/0004-6361:20021542. arXiv: astro-ph/0210517 [astro-ph] (cit. on p. 164).

Virtanen, Pauli et al. (2020). "SciPy 1.0: Fundamental Algorithms for Scientific Computing in Python". In: *Nature Methods* 17, pp. 261–272. DOI: 10.1038/s41592-019-0686-2 (cit. on p. 86).

Vlahakis, N. and K. Tsinganos (Dec. 1997). "On the topological stability of astrophysical jets". In: *Monthly Notices of the Royal Astronomical Society* 292, p. 591. ISSN: 0035-8711. DOI: 10.1093/mnras/292.3.591 (cit. on pp. 90, 97–98).

Vlahakis, N. et al. (Oct. 2000). "A disc-wind model with correct crossing of all magnetohydrodynamic critical surfaces". In: *Monthly Notices of the Royal Astronomical Society* 318. ADS Bibcode: 2000MNRAS.318..417V, pp. 417–428. ISSN: 0035-8711. DOI: 10.1046/j.1365-8711.2000.03703.x (cit. on pp. 22, 80, 152, 175).

Vlahakis, Nektarios and Arieh Königl (Oct. 2003). "Relativistic Magnetohydrodynamics with Application to Gamma-Ray Burst Outflows. I. Theory and Semianalytic Trans-Alfvénic Solutions". In: *The Astrophysical Journal* 596. ADS Bibcode: 2003ApJ...596.1080V, pp. 1080–1103. ISSN: 0004-637X. DOI: 10.1086/378226 (cit. on p. 22).

Weber, Edmund J. and Leverett Davis Jr. (Apr. 1967). "The Angular Momentum of the Solar Wind". In: *The Astrophysical Journal* 148. ADS Bibcode: 1967ApJ...148..217W, pp. 217–227. ISSN: 0004-637X. DOI: 10.1086/149138 (cit. on p. 46).

Werner, Michael W. et al. (Nov. 2012). "Spitzer Observations of Hotspots in Radio Lobes". In: *The Astrophysical Journal* 759. ADS Bibcode: 2012ApJ...759...86W, p. 86. ISSN: 0004-637X. DOI: 10.1088/0004-637X/759/2/86 (cit. on p. 33).

Zanni, C. and J. Ferreira (Dec. 2009). "MHD simulations of accretion onto a dipolar magnetosphere. I. Accretion curtains and the disk-locking paradigm". In: *Astronomy and Astrophysics* 508.3, pp. 1117–1133. DOI: 10.1051/0004-6361/200912879 (cit. on pp. 126, 142).

Zanni, C. et al. (July 2007). "MHD simulations of jet acceleration from Keplerian accretion disks. The effects of disk resistivity". en. In: *Astronomy and Astrophysics, Volume 469, Issue 3, July III 2007, pp.811-828* 469.3, p. 811. ISSN: 0004-6361. DOI: 10.1051/0004-6361:20066400 (cit. on p. 175).

Zhang, Binzheng et al. (Jan. 2019). "Conservative averaging-reconstruction techniques (Ring Average) for 3-D finite-volume MHD solvers with axis singularity". In: *Journal of Computational Physics* 376, pp. 276–294. DOI: 10.1016/j.jcp.2018.08.020 (cit. on pp. 187, 190, 206–208).

Zhang, Liang et al. (May 2020). "A systematic analysis of the phase lags associated with the type-C quasi-periodic oscillation in GRS 1915+105". In: *Monthly Notices of the Royal Astronomical Society* 494.1, pp. 1375–1386. DOI: 10.1093/mnras/staa797. arXiv: 2003.08928 [astro-ph.HE] (cit. on p. 163).

Zhang, Shuang-Nan (Dec. 2013). "Black hole binaries and microquasars". In: *Frontiers of Physics* 8.6, pp. 630–660. DOI: 10.1007/s11467-013-0306-z. arXiv: 1302.5485 [astro-ph.HE] (cit. on p. 9).